



Atomic-scale study of pesticide interaction with soil mineral matter.

Bastien Belzunces

► To cite this version:

Bastien Belzunces. Atomic-scale study of pesticide interaction with soil mineral matter.. Theoretical and/or physical chemistry. Laboratoire de Chimie et Physique Quantiques, 2017. English. NNT : . tel-01850388

HAL Id: tel-01850388

<https://hal.science/tel-01850388>

Submitted on 27 Jul 2018

HAL is a multi-disciplinary open access archive for the deposit and dissemination of scientific research documents, whether they are published or not. The documents may come from teaching and research institutions in France or abroad, or from public or private research centers.

L'archive ouverte pluridisciplinaire **HAL**, est destinée au dépôt et à la diffusion de documents scientifiques de niveau recherche, publiés ou non, émanant des établissements d'enseignement et de recherche français ou étrangers, des laboratoires publics ou privés.

Université Fédérale



Toulouse Midi-Pyrénées

THÈSE

En vue de l'obtention du

DOCTORAT DE L'UNIVERSITÉ DE TOULOUSE

Délivré par : *l'Université Toulouse 3 Paul Sabatier (UT3 Paul Sabatier)*

Présentée et soutenue le 12/12/2017 par :

Bastien BELZUNCES

**Atomic-scale study of pesticide interaction with soil mineral
matter**

JURY

CORINNE
LACAZE-DUFAURE

Professeur

Présidente du jury

KARINE COSTUAS

Directeur de Recherche CNRS

Rapporteur

TZONKA MINEVA

Directeur de Recherche CNRS

Rapporteur

PIERRE MIGNON

Maître de Conférences

Examineur

JEAN-NOËL AUBERTOT

Directeur de Recherche INRA

Membre invité

FABIENNE BESSAC

Enseignant-Chercheur

Directeur

SOPHIE HOYAU

Maître de Conférences

Co-directeur

École doctorale et spécialité :

SDM : Physicochimie théorique - COP 01

Unité de Recherche :

Laboratoire de Chimie et Physique Quantiques (UMR 5626)

Directeur(s) de Thèse :

Fabienne BESSAC et Sophie HOYAU

Rapporteurs :

Karine COSTUAS et Tzonka MINEVA

Université Fédérale



Toulouse Midi-Pyrénées

THÈSE

En vue de l'obtention du

DOCTORAT DE L'UNIVERSITÉ DE TOULOUSE

Délivré par : *l'Université Toulouse 3 Paul Sabatier (UT3 Paul Sabatier)*

Présentée et soutenue le 12/12/2017 par :

Bastien BELZUNCES

**Atomic-scale study of pesticide interaction with soil mineral
matter**

JURY

CORINNE
LACAZE-DUFAURE

Professeur

Présidente du jury

KARINE COSTUAS

Directeur de Recherche CNRS

Rapporteur

TZONKA MINEVA

Directeur de Recherche CNRS

Rapporteur

PIERRE MIGNON

Maître de Conférences

Examineur

JEAN-NOËL AUBERTOT

Directeur de Recherche INRA

Membre invité

FABIENNE BESSAC

Enseignant-Chercheur

Directeur

SOPHIE HOYAU

Maître de Conférences

Co-directeur

École doctorale et spécialité :

SDM : Physicochimie théorique - COP 01

Unité de Recherche :

Laboratoire de Chimie et Physique Quantiques (UMR 5626)

Directeur(s) de Thèse :

Fabienne BESSAC et Sophie HOYAU


Rapporteurs :

Karine COSTUAS et Tzonka MINEVA

“All work and no play makes Jack a dull boy”

The Shining ; Stephen King, Diane Johnson & Stanley Kubrick

Remerciements

près trois années (et trois mois de préparation à la soutenance), emplies de péripéties, rebondissements, instants de paniques (aussi !...) mais heureusement d'innombrables bons moments, aussi bien apportés par la satisfaction du travail accompli, que par les rencontres et interactions avec les collègues ; je clôture finalement cette thèse par les remerciements qui s'imposent. Malgré leur côté conventionnel, il m'aurait été impossible de quitter cette aventure et ce laboratoire sans les exprimer.

Je commencerai donc tout naturellement par remercier les membres de mon jury d'avoir accepté d'en faire partie, d'avoir porté autant d'attention à la lecture de mon manuscrit, ainsi que pour les commentaires et discussions produits lors de la soutenance. Merci donc à mes rapporteurs, **Karine Costuas** et **Tzonka Mineva**, à mes examinateurs **Pierre Mignon** et **Corinne Lacaze-Dufaure**, qui a accepté de présider ce jury ; et enfin à **Jean-Noël Aubertot** pour sa participation en tant que membre invité. J'ai vraiment apprécié leur bienveillance vis-à-vis de mon travail, et leurs efforts dans le but de donner un aspect de discussion à la phase des questions lors de la soutenance, et non un classique rapport prof/étudiant ou examinateur/examiné tel qu'on le vit souvent lors des études supérieures.

A présent, je souhaite adresser tous mes remerciements aux deux personnes sans qui rien de tout ceci n'aurait été possible, mes directrices de thèse **Fabienne Bessac** et **Sophie Hoyau**. A l'inverse de la majorité des thèses que j'ai pu consulter, je me permettrai ici de ne pas en rester à de simples remerciements brefs et formels, au point d'en être impersonnels. En effet trois ans à travailler ensemble ce n'est pas rien, de plus nous avons la chance de très bien nous entendre, ce qui nous a permis de ne pas limiter nos conversations strictement à des sujets d'ordre professionnel, mais à des discussions nous permettant de refaire le monde, de pousser des coups de gueule, comme d'avoir de franches rigolades. Ce qui n'a rien ôté au sérieux et à la rigueur que l'exercice d'une thèse, et que la recherche

en général, exigeant.

Sophie, si je devais citer mon premier bon souvenir de thèse, je raconterais le jour de l'entretien avec toi et Fabienne, (avant même le début de la thèse de fait). En effet, alors que je me rendais à votre bureau, je t'ai croisée dans l'escalier et tu m'as fait la bise d'entrée. Ce qui est plutôt rare de la part d'un recruteur lorsque l'on se rend à un entretien ! Geste provoqué par le fait que nous nous connaissons depuis ma deuxième année de licence où je t'avais en TD. Et je suis toujours étonné que tu te sois souvenue de moi, je m'en sens d'ailleurs flatté, moi qui n'ai jamais été un élève brillant. Même s'il est vrai que nous nous étions recroisés lors de mon master. Je me souviens aussi qu'en sachant que tu faisais partie de la direction de ce sujet de thèse, je me réjouissais à l'idée de travailler avec toi car je conservais un très bon souvenir de toi en tant qu'enseignante (et je crois bien que c'est le cas de tous tes étudiants !). Je pense que cette anecdote s'explique aisément par ta bonne humeur constante (qui va de paire avec ton rire légendaire !), ton optimisme et ton énergie inépuisable. Je retiens aussi de toi ton dévouement sans faille lorsque l'on te demande de l'aide, alors même que tu croules sous les devoirs, contraintes et autres coups durs que te réservent chaque année l'enseignement et l'administration de la fac. Je te remercie pour tout cela.

Fabienne, au cours de ces trois ans, empiriquement, nous nous sommes accordés à dire que si Sophie est la représentante officielle de l'optimisme dans notre trio ; tu es celle qui nous aide à rester réalistes, humbles, et à garder les pieds sur Terre. Et s'il est vrai qu'en cela un équilibre adéquat est atteint entre vos caractères et vos approches complémentaires sur le plan scientifiques, tu n'en es pas pour autant une vraie pessimiste. Je te remercie de tout ton soutien au cours de ces trois années. En effet malgré ta double identité, à savoir chercheuse au LCPQ mais aussi enseignante à Purpan, tu t'es toujours inquiétée de mon avancement et de mes difficultés et tu es toujours prête à interrompre tes activités pour répondre à mes questions ou me conseiller. Ce qui t'as rendue toute aussi présente que Sophie dans mon encadrement. Et finalement, alors que tes absences pour travailler à Purpan pouvaient apparaître comme une difficulté au départ, ton affiliation à l'école, et par la même la mienne, ont été un point positif de la thèse selon moi. En effet j'ai apprécié mes rares interventions à Purpan, elles m'ont permis d'ouvrir l'horizon, de rencontrer des doctorants et des chercheurs d'une branche radicalement différente de la physique et de la chimie. Ce qui m'a exercé dans l'effort de vulgarisation de mes travaux et a aussi attisé ma curiosité à l'égard de l'agronomie et de ce milieu singulier que l'on nomme "Ecole d'ingénieurs"... Finalement je regrette de ne pas avoir eu plus souvent l'occasion d'y venir.

Pour conclure, j'ai beaucoup appris à vos côtés, travailler avec deux superviseuses enrichit les choix pris et les points de vue lors des recherches, je trouve donc cela préférable.

Pour tout ce que je viens d'évoquer, j'estime que j'ai de la chance de vous avoir eu en tant que directrices de thèse. Merci pour toute votre pédagogie, pour vos précieux conseils et votre dévouement (surtout lors des moments où je me disais que je vous faisais perdre votre temps !). Merci d'avoir cru en moi et de m'avoir donné l'opportunité de faire partie du monde de la recherche pendant trois années.

Je souhaite à présent remercier les deux groupes de recherche dont j'ai fait partie au sein du laboratoire.

Le groupe Modélisation, Agrégats, Dynamique (MAD) : **Mathias Rapacioli**, **Fernand Spiegelman** et **Florent Xavier Gadéa** pour leur aide et leur soutien lors de mes questionnements divers, **Aude Simon**, pour avoir partagé son bureau avec moi (et donc m'avoir supporté !) pendant trois ans, et pour s'être toujours rendue disponible pour me fournir de l'aide lorsque j'en avais besoin. Enfin, j'adresse mes remerciements tout particulièrement à **Jérôme Cuny** pour toute la formation qu'il m'a apporté durant cette thèse : en dynamique moléculaire et en méthodologie, en enseignement en m'ayant donné la chance d'enseigner en Travaux Dirigés, expérience dont je garde un très bon souvenir ; pour tout son investissement dans cette thèse, et pour la patience dont il a fait preuve vis-à-vis de mes difficultés. Merci également d'avoir participé activement à la correction du manuscrit et de m'avoir donné quelques petits cours particuliers afin de combler certaines de mes lacunes.

Le Groupe Méthodes et Outils de la chimie quantique (GMO), pour l'ouverture qu'il apporte par la grande diversité des thématiques de recherche qu'il rassemble. Les réunions de groupe m'ayant permis d'obtenir différents points de vue et commentaires sur mes travaux, et m'ayant de même permis de découvrir de nombreux autres aspects de la chimie théorique. J'en garde aussi le souvenir amusant des "Lotos de vin", concept fort sympathique et convivial qui m'a vu repartir avec quelques bouteilles (non **Arjan** je n'ai pas gagné tant que ça en trois ans !)...

Si ces trois ans ont été très agréables car j'ai pu y ressentir quotidiennement que j'aimais mon travail (sauf peut-être sur la fin...), de manière encore moins formelle, je souhaite maintenant remercier toutes les personnes qui ont contribué à rendre le quotidien agréable, composante très importante de tout travail.

Tout d'abord le "groupe du midi" pour leur bonne humeur, pour toutes ces fois où nous avons refait le monde ensemble : **Sophie** et son rire, **Fabienne** et ses anecdotes croustillantes, **Nadia** et sa jovialité (merci également d'avoir parfaitement géré la visio-conférence avec **Karine Costuas** le jour de la soutenance, nous aurions été bien embêtés sans toi), **Arjan** et son humour simple mais efficace, **Nicolas Elefantis** également pour son humour mais aussi sa mauvaise foi légendaire.

Je poursuivrai en remerciant l'ensemble des thésards et postdocs avec qui j'ai partagé

tant de pauses café et déjeuner et ce depuis le tout début. Au LCPQ : **Thomas** qui m'a initié au code Python, ce qui m'a été extrêmement utile durant cette thèse ; **Nathaniel** pour m'avoir permis de retrouver l'usage de mon PC portable (dont j'ai eu besoin jour et nuit dans les dernières semaines de rédaction) ; **Malika** avec qui j'ai partagé la sympathique expérience du Young Researchers Meeting 2016 de Londres ; **Kseniia** et nos trop rares parties d'échecs ; **Florian** avec qui je me suis régulièrement serré les coudes depuis le master ; **Sarah** et sa bonne compagnie, notamment lorsque nous étions à l'école d'été de Paris (PISACMS2015) ; et pour finir **Carles** et **Rubén** qui m'ont apporté tant de soutien lors des moments de doutes qui ont jalonné mes derniers mois de rédactions et de préparations à la soutenance, mais avec qui j'ai aussi tant partagé sur tous les sujets. Au LCAR : **Isabelle** et **Citlali** pour leur bonne humeur constante et leur humour ; **Julien**, **Eric** et **Mickaël** et nos nombreuses parties de babyfoot, **Vincent** et **Olivier**. Je tiens tout particulièrement à remercier **Etienne Mangaud** pour tout le soutien et les conseils qu'il m'a apporté aussi bien durant la rédaction qu'avant la soutenance, et plus généralement pour sa bonne compagnie. Merci à **Giuseppe** du LPT pour l'entraide échangée sur cette fin de thèse. Je terminerai ce paragraphe en remerciant **Lucy Cusinato** du LPCNO (mais pas seulement, car nous nous connaissons depuis la Licence !), pour l'aide occasionnelle qu'elle m'a fourni en thèse mais aussi en master, et pour tous nos échanges dans les moments de doute.

Merci également aux personnes bienveillantes du LCPQ et de l'IRSAMC qui ne rentreraient pas dans les catégories que je viens de mentionner. Je pense notamment à mes anciens enseignants de fac avec qui j'ai pu être collègue pendant cette thèse: **Thierry Leininger**, **Nathalie Guihéry**, **Nicolas Suaud**, **Romuald Poteau** et **Franck Jolibois**. Je pense également à **Patricia Bordais** dont la bonne humeur constante égaye tant le quotidien et à **Malika Bentour** dont les conversations ont été des bulles d'oxygène lors de certains week-ends et autres vacances d'été passés à travailler au LCPQ, alors dépourvu des âmes qui l'animent habituellement. Merci à toutes les personnes qui m'ont donné l'opportunité d'enseigner pendant deux ans à la fac, je pense entre autres à **Olivier Coutelier** de l'IMRCP dont les TP Polymères de M1 ont été très formateurs et ont été un défi à relever ; j'en garde un excellent souvenir.

J'adresse un grand merci à tous mes amis pour m'avoir toujours entouré, soutenu et m'avoir permis de souffler un peu dans les moments les plus éprouvants.

Et pour clôturer ces longs, et non moins sincères, remerciements, je ne remercierai jamais assez mes parents et mon frère pour avoir toujours cru en moi, m'avoir soutenu dans toutes mes entreprises (quel qu'en soit le prix) et m'avoir fait confiance dans mes choix d'études et de carrière.

Contents

Remerciements	9
List of Figures	21
List of Tables	29
List of acronyms.....	33
Abstract	35
Résumé	39
Introduction	43
I Pesticides	47
I.A Introduction.....	47
I.B TyPol database	51
I.C Atrazine.....	52
I.D Metamitron	54
I.E Fenhexamid	57

II	Soil	61
II.A	Horizons	62
II.B	General Soil composition	63
II. B.1	The inorganic phase or mineral matter	65
II. B. 1. α	Elementary composition	65
II. B. 1. β	Mineralogical composition	66
II. B. 1. γ	Mineralogical structure and general properties	67
II.C	Clay minerals	68
II. C.1	Montmorillonite and other clay minerals	69
II. C. 1. α	Phyllosilicates	69
II. C. 1. β	Smectites	72
II. C. 1. γ	Montmorillonite	74
III	Theoretical methods	79
III.A	Electronic structure	80
III. A.1	Wavefunction and Schrödinger equation	80
III. A.2	The Born-Oppenheimer approximation (BO)	81
III. A.3	Atoms and molecules: interacting electrons and nuclei	81
III. A.4	The Hartree method or mono-electronic approximation	82
III. A.5	The Hartree-Fock theory (HF)	83
III. A. 5. α	The Hartree-Fock equations	83
III. A. 5. β	The Self-Consistent Field method (SCF)	86
III. A. 5. γ	Linear Combination of Atomic Orbitals (LCAO)	86
III. A. 5. δ	Basis set	86
III. A. 5. ϵ	Roothaan equations	88
III.B	Density Functional Theory	89
III. B.1	Thomas-Fermi-Dirac approximation	89
III. B.2	Hohenberg-Kohn theorems	90
III. B.3	Kohn-Sham equations	91
III. B.4	Exchange-Correlation Functionals	92

III. B.5	DFT performances and PBE-D2 functional.....	95
III.C	Periodic systems for solid state models	97
III. C.1	Bloch theorem, real and reciprocal spaces	98
III. C.2	Planewave basis.....	99
III. C.3	Core-valence separation and pseudopotential approximation ...	100
III.D	Molecular Dynamics	102
III. D.1	Classical mechanics for nuclear motion	102
III. D.2	<i>Ab initio</i> molecular dynamics approaches.....	104
IV	Atrazine interaction with soil	109
IV.A	Atrazine in the gas phase	110
IV. A.1	Energetic values of interest.....	110
IV. A. 1. α	Interaction and complexation energies	110
IV. A. 1. β	RVS SCF energy decomposition scheme	110
IV. A.2	Complexation of atrazine with one Na ⁺ , one Ca ²⁺ and two Ca ²⁺ cation(s)	112
IV.B	Atrazine adsorbed on a surface	113
IV. B.1	Montmorillonite model.....	113
IV. B.2	Gaussian versus planewave basis sets on atrazine and complexes geometries and energies	114
IV. B.3	Atrazine adsorption on montmorillonite	118
V	Complexation of metamitron and fenhexamid with one and two Na⁺ or Ca²⁺ cations.....	139
V.A	Gaussian basis sets versus planewaves: calibration of gas phase pw calculation parameters.....	140
V.B	Dynamic exploration of the PES of Meta, Fen, Meta- (cation) _{<i>i,i=1,2</i>} and Fen-(cation) _{<i>i,i=1,2</i>}	146

VI	Adsorption on a Ca-Montmorillonite surface	173
VI.A	Starting structures and CPMD parameters	174
VI.B	Metamitron - Ca-montmorillonite	178
VI. B.1	PES exploration	178
VI. B.2	Optimized structures	178
VI.C	Fenhexamid - Ca-montmorillonite	185
VI. C.1	PES exploration	185
VI. C.2	Optimized structures	186
VI.D	Conclusion	196
VII	Pesticide hydration: solvation effects and fenhexamid desorption.	199
VII.A	Pesticide interaction with a watered - Ca -montmorillonite surface	200
VII. A.1	Starting structures and CPMD parameters	201
VII. A.2	Complexation sites hydration	204
VII. A.3	Surface hydration	205
VII.B	Pesticide desorption process from a hydrated - Ca -montmorillonite surface	209
VII. B.1	Umbrella Sampling	210
VII. B.2	Desorption of fenhexamid	213
VII. B.3	Free energy surface exploration	214
VII. B.4	Discussion	219
VII.C	Conclusion	221
	Conclusion	225

Résumé	231
1 Introduction	231
2 Pesticides	233
3 Le sol et la montmorillonite	236
4 Interaction de l'atrazine avec le sol	239
5 Complexation de la métamitronne et du fenhexamide avec un ou deux ions Na^+ et Ca^{2+}	244
6 Adsorption de la métamitronne et du fenhexamide sur une surface de Ca-montmorillonite	253
7 Effets de solvation et desorption du fenhexamide	258
8 Conclusion	267

List of Figures

I.1	Proportional agricultural surfaces of European countries in the year 2015 [1]	48
I.2	Amount of sold phytosanitary products (tons) in metropolitan France from 1996 to 2013 (reference: Union des Industries pour la Protection des Plantes (UIPP) Traitements: SOeS, 2016) [2,3] ; and from 2014 to 2015 [1]	49
I.3	Quantities of sold pesticides compared to UAA (kg/ha) of main European countries with agricultural activity in 2014 [1].	50
I.4	Atrazine semi-developed chemical formula.	53
I.5	Metamitron semi-developed chemical formula.	54
I.6	Fenhexamid semi-developed chemical formula.	58
II.1	Soil horizons (picture source: http://www.aucoeurdelarbre.ca/fr/hors-sentier/ section-profs/module4-html.php).	63
II.2	Example of the elementary composition of an American soil [4] expressed as concentra- tions in milligrams of element per kilogram of soil.	66
II.3	Representation of cations (<i>a</i>) in coordinations 4 (tetrahedron T, in dark blue) and (<i>b</i>) in coordination 6 (octahedron O, in light blue) with anions (red).	67
II.4	Isolated O^{2-} tetrahedron occupied with a Si^{4+} cation (<i>a</i>), single tetrahedral sheet (T) represented in the <i>xy</i> plane (<i>b</i>) and viewed from the <i>z</i> axis (<i>c</i>). Silicon cations and their associated tetrahedra (SiO_4) are in dark blue. Each basal oxygen O_b (red) is shared between two tetrahedra, apical oxygens $O_{a,down}$ (orange) point towards the same direction and will be shared with the octahedral sheet above.	70

II.5	Isolated O^{2-} octahedron occupied with an Al^{3+} cation (<i>a</i>), single octahedral sheet (O) viewed from the <i>y</i> axis (<i>b</i>) and from the <i>z</i> axis (<i>c</i>). Aluminium cations and their associated octahedra (AlO_6) are in light blue. Oxygens O_h (red) bearing hydrogen atoms (white) are not shared and belong to the O sheet only. In this example, O_h atoms are arranged on the diagonal corresponding to the <i>trans</i> -vacancy topology. Apical oxygens $\text{O}_{a,\text{down}}$ (orange) are shared with the T sheet below, and apical oxygens $\text{O}_{a,\text{up}}$ (yellow) are shared with the T sheet above.	71
II.6	Isomorphic substitutions (dark yellow) of 4 Al^{3+} in octahedral sites of the O sheet. . .	73
II.7	Montmorillonite surface viewed from the <i>y</i> axis (<i>a</i>), from the side (<i>b</i>), and from the <i>z</i> axis (<i>c</i>). This montmorillonite contains 4 substitutions of Al^{3+} by Mg^{2+} in the O sheet (dark yellow octahedra). Two Ca^{2+} cations (magenta) compensate the charge defect and are situated above substitutions, and above centers of ditrigonal ring of basal oxygens.	75
III.1	Bi-dimensional schematic representation of a cubic reciprocal space defined by the reciprocal vectors \mathbf{a}^* and \mathbf{b}^* . Every node of the reciprocal lattice is a unit cell of the direct lattice. The four nodes with their coordinates within the reciprocal lattice: $\Gamma(0,0)$, $X(\frac{1}{2},0)$, $Y(0,\frac{1}{2})$ and $M(\frac{1}{2},\frac{1}{2})$, represent the first Brillouin zone of the system. The circle colored in blue includes all the k-points used to build the planewave basis set for the k-point Γ . The diameter of this circle is defined by the energy cutoff E_{cutoff}	100
III.2	Schematic diagram of the true potential $V(\mathbf{r}) = -Z/\mathbf{r}$ associated to the true electronic wavefunction of an atom $\Psi(\mathbf{r})$, and of the pseudopotential $V(\mathbf{r})_{\text{pseudo}}$ with its corresponding wavefunction $\Psi(\mathbf{r})_{\text{pseudo}}$. \mathbf{r} is the distance vector from the nucleus, and Z is the nuclear charge. \mathbf{r}_c , the dotted line, is the cutoff radius beyond which the pseudopotential reproduce as exactly as possible the true potential. Below this cutoff, $V(\mathbf{r})$ and $\Psi(\mathbf{r})$ are replaced by smoother potential and wavefunction.	101
IV.1	(<i>a</i>) The triclinic unit cell of pyrophyllite ($a \neq b \neq c$ and $\alpha \neq \beta \neq \gamma \neq 90^\circ$), (<i>b</i>) the computational cell consists in 6 unit cells : $3a \times 2b \times c$ (in light turquoise) to minimize interaction energies between two atrazine images along <i>a</i> , <i>b</i> and <i>c</i> (30 Å) directions. Values are given in kcal/mol (identical for PBE/basis1 and PBE/basis2).	114
IV.2	Geometrical parameters near substitutions (O_{sub}) in (<i>c</i>) montmorillonite ($c = 9.354$ Å), (<i>d</i>) montmorillonite ($c = 30$ Å, distances in red are the most impacted going from the bulk to the surface), (<i>e</i>) atrazine-montmorillonite (PARA1, $c = 30$ Å, the distance in blue is the most modified by the adsorption) versus (<i>a</i>) pyrophyllite at the PBE-D2/pw level. Distances are in Å and angles in degrees. (<i>b</i>) The various labels of Mg-O_h distances: $\text{Mg-O}_h\mathbf{Ca}$ if Ca^{2+} is located just above the O_h oxygens, $\text{Mg-O}_h\mathbf{u}$ for other upper O_h oxygens and $\text{Mg-O}_h\mathbf{l}$ for other lower O_h oxygens.	120

V.1	Lowest-energy isomers of Meta-Ca ²⁺ and Fen-Ca ²⁺ complexes. Distances in Å, dihedrals (bold) in degrees and relative energies in kcal/mol obtained in PBE/basis2 (italics) and PBE-D2/pw 80 Ry (underlined) are reported.	144
VI.1	Three schematic orientations of the pesticides (green parallelepipeds) above the surface (layered blue).	174
VI.2	Starting structures of (a) Meta-Mont(CO-Phe) and (b) Meta-Mont(N-N). Distances are displayed in Å and dihedrals (bold) in degrees.	175
VI.3	Starting structures of (a) Fen-Mont(CO-Phe) _{para,eq} , (b) Fen-Mont(Cl-OH) _{para,ax} and (c) Fen-Mont(Cl-OH) _{ortho-short,ax} . Distances are displayed in Å and dihedrals (bold) in degrees.	177
VI.4	Meta-Mont isomers displayed with complexation families and relative energies (kcal/mol). Distances (black), cation distances to the molecule oxygens (red) and nitrogens (blue) are in Å. C1-C2-C3-N4] dihedrals (bold) are in degrees.	179
VI.5	Fen-mont isomers displayed with complexation families and relative energies (kcal/mol). Distances (black), cation distances to the molecule oxygens (red) and chlorines (green) are in Å. H7-N3-C4-C5] dihedrals (bold) are in degrees.	191
VI.6	Fen-mont isomers displayed with complexation families and relative energies (kcal/mol). Distances (black), cation distances to the molecule oxygens (red) and chlorines (green) are in Å. H7-N3-C4-C5] dihedrals (bold) are in degrees.	192
VII.1	Input and output structures of the 30 ps SCC-DFTB dynamics of the 18.6207 Å periodic cubic box of water molecules.	200
VII.2	Starting structures of the CPMD trajectories in $\phi_{solid}^{H_2O}$. Distances are displayed in Å.	202
VII.3	Distribution functions $f(d)$ of the distances in Å from the pesticides binding sites to Ca1, and their associated average values: (a) in Meta-Mont _{para} ^{H₂O} (CO(-Phe)) (red) and in Meta-Mont _{ortho-long} ^{H₂O} (N-N) (green and black) ; (b) in Fen-Mont _{para,ax} ^{H₂O} (CO(-Phe)) (red) and in Fen-Mont _{ortho-short,ax} ^{H₂O} (Cl-OH) (blue and purple).	204
VII.4	Distribution functions $f(d)$ of the calcium cation distances to the surface d_{Ca1-O_b} and d_{Ca2-O_b} (Å): (a) in Meta-Mont _{ortho} ^{H₂O} (N-N) (blue and black) and Meta-Mont _{para,ax} ^{H₂O} (CO(-Phe)) (red and green) ; (b) in Fen-Mont _{para,ax} ^{H₂O} (CO(-Phe)) (orange and light blue) and in Fen-Mont _{ortho,ax} ^{H₂O} (Cl-OH) (purple and grey) respectively.	206
VII.5	Snapshot of the Fen-Mont _{ortho,ax} ^{H₂O} (Cl-OH) trajectory. Fenhexamid and all H ₂ O molecules are represented in lines except the Ca2 inner hydration sphere (square-based pyramid) which is in ball and stick representation, as well as the surface and both cations.	207

VII.6	Representation of the WHAM method, applied to 6 windows of PMF on the reaction coordinate ξ . The F_i constant that must be determined in equation (VII.10) corresponds to the energy shift between a window of PMF (dotted line) and the complete free energy curve $A(\xi)$ (solid line). F_1 constant, associated to window 1, is represented as an example.	212
VII.7	Relative free energy surface $A(\xi)_{rel}$ (kcal/mol) (a), where ΔA_w values are the free energy differences between consecutive wells and where ΔA_b and ΔA_{b-} are the relative energies necessary to cross barriers, for the desorption and adsorption process respectively. The probability density functions $P(\xi)$ of the 11 windows are displayed in (b), each color corresponding to a different window i . ξ is the z coordinate of the pesticide center of mass.	215
VII.8	Last snapshots of windows 1 (a), 4 (b) and 10 (c) where distances are displayed in Å.	218
1	Quantité de produits phytosanitaires vendus (en tonnes) en France métropolitaine entre 1996 et 2013 (référence: Union des Industries pour la Protection des Plantes (UIPP) Traitements: SOeS, 2016) [2,3]; et de 2014 à 2015 [1]	233
2	Formule semi-développée de l'atrazine.	234
3	Formule semi-développée de la métamitronne.	235
4	Formule semi-développée du fenhexamide.	235
5	Les horizons du sol (source de l'image : http://www.aucoeurdelarbre.ca/fr/hors-sentier/section-profs/module4-html.php).	237
6	a) La structure en couches de la pyrophyllite et des smectites : T désigne les tétraèdres et O les octaèdres, δ représente la distance interfeuille ; b) L'environnement constitué par les oxygènes : des tétraèdres autour des siliciums et des octaèdres autour des aluminiums dans la pyrophyllite ; c) des substitutions isomorphiques se produisent dans la montmorillonite : par exemple un Al^{3+} a été remplacé par un Mg^{2+} dans la couche O, des Ca^{2+} sont ajoutés dans l'espace interfeuille pour compenser le défaut de charge. Les différents types d'oxygènes sont représentés : O_h correspond aux oxygènes connectés à des hydrogènes, O_b (pour basal en Anglais) sont impliqués dans des liaisons seulement avec des Si, O_a (axial) sont liés à des Si et des Al (ou Mg).	238
7	Pyrophyllite-atrazine : énergies d'interaction (ΔE_{int}) et d'adsorption (ΔE_{ads}) (en kcal/mol et en gras), charges de Hirshfeld [5] portées par l'atrazine (q_{atra}) et distances de l'atrazine (centre géométrique du cycle) à la surface (en Å et en rouge) aux niveaux PBE/pw et PBE-D2/pw. (a) Vue le long de la direction a ; (b) vue le long de la direction b pour le complexe pyrophyllite-atrazine optimisé au niveau PBE-D2/pw.	241

- 8 Montmorillonite-atrazine : énergies totales relatives (PARA1 est la référence), énergies d'interaction (ΔE_{int}) et d'adsorption (ΔE_{ads}) (en kcal/mol et en gras), charges de Hirshfeld [5] portées par l'atrazine (q_{atra}) et distances de l'atrazine (centre du cycle) à la surface (en Å et en rouge) au niveau PBE-D2/pw. Les vues sont le long de la direction a. 242
- 9 Isomère ORTHO des montmorillonite-molécule : l'énergie relative (PARA1 est la référence), les distances, énergies d'interaction (ΔE_{int}) et d'adsorption (ΔE_{ads}) de l'atrazine (en noir) ou d'atramod (en rouge) avec la surface au niveau PBE-D2. (a) Vue le long de la direction a ; (b) vue le long de la direction b. Les distances sont données en Å et les énergies en kcal/mol. La charge de Hirshfeld [5] portée par l'atrazine (q_{atra}). La structure ORTHO optimisée de la montmorillonite-atrazine a été utilisée pour montmorillonite-Atramod. 242
- 10 Pyrophyllite-atrazine : énergies d'interaction (ΔE_{int}) et d'adsorption (ΔE_{ads}) (en kcal/mol et en gras), charges de Hirshfeld portées par l'atrazine (q_{atra}) et distances de l'atrazine (centre géométrique du cycle) à la surface (en Å et en rouge) aux niveaux PBE/pw et PBE-D2/pw. (a) Vue le long de la direction a ; (b) vue le long de la direction b pour le complexe pyrophyllite-atrazine optimisé au niveau PBE-D2/pw. 243
- 11 (a) Conformère de la métamitrone, (b) conformères de basses énergies du fenhexamide : les distances sont en Å, les dièdres en degrés (en gras) aux niveaux PBE/basis1 et PBE/basis2 (en italique). $\vec{\mu}$ est le vecteur de moment dipolaire. 247
- 12 Les isomères de plus basses énergies de chaque famille pour Meta- Na^+ (première ligne) et Meta- Ca^{2+} (deuxième ligne). Les énergies relatives (à gauche) et de préparation (à droite) sont présentées en kcal/mol aux niveaux PBE/basis1 et PBE/basis2 (en italique). Les distances sont en Å, les dièdres en degrés (en gras) aux niveaux PBE/basis1 et PBE/basis2 (en italique). 248
- 13 Sept isomères de basses énergies de la métamitrone avec deux Na^+ (première ligne) et deux Ca^{2+} (deuxième ligne). Les énergies relatives (à gauche) et de préparation (à droite) sont présentées en kcal/mol aux niveaux PBE/basis1 et PBE/basis2 (en italique). Les distances sont en Å, les dièdres en degrés (en gras) aux niveaux PBE/basis1 et PBE/basis2 (en italique). 248
- 14 Les principaux isomères de basses énergies du fenhexamide avec un cation Na^+ . Les énergies relatives (à gauche) et de préparation (à droite) sont présentées en kcal/mol aux niveaux PBE/basis1 et PBE/basis2 (en italique). Les distances sont en Å et les dièdres en degrés (en gras) au niveau PBE/basis1. Pour les isomères les plus bas de chaque famille, des paramètres géométriques sont aussi donnés au niveau PBE/basis2 (en italique). Pour des délocalisations totalement brisées dans la famille CO-Phe, les cadres ont été colorés en violet. Au-delà de la limite matérialisée par la ligne pointillée, le groupe cyclohexyle a perdu sa conformation en chaise. 249

- 15 Les principaux isomères de basses énergies du fenhexamide avec un cation Ca^{2+} . Les énergies relatives (à gauche) et de préparation (à droite) sont présentées en kcal/mol aux niveaux PBE/basis1 et PBE/basis2 (en italique). Les distances sont en Å et les dièdres en degrés (en gras) au niveau PBE/basis1. Pour les isomères les plus bas de chaque famille, des paramètres géométriques sont aussi donnés au niveau PBE/basis2 (en italique). Pour des délocalisations totalement brisées dans la famille CO-Phe, les cadres ont été colorés en violet. Au-delà de la limite matérialisée par la ligne pointillée, le groupe cyclohexyle a perdu sa conformation en chaise excepté pour Fen- $\text{Ca}^{2+}(30)_{ax}$. 250
- 16 Les principaux isomères de basses énergies du fenhexamide avec deux cations Na^+ . Les énergies relatives (à gauche) et de préparation (à droite) sont présentées en kcal/mol aux niveaux PBE/basis1 et PBE/basis2 (en italique). Les distances sont en Å et les dièdres en degrés (en gras) au niveau PBE/basis1. Pour les isomères les plus bas de chaque famille, des paramètres géométriques sont aussi donnés au niveau PBE/basis2 (en italique). 251
- 17 Les principaux isomères de basses énergies du fenhexamide avec deux cations Ca^{2+} . Les énergies relatives (à gauche) et de préparation (à droite) sont présentées en kcal/mol aux niveaux PBE/basis1 et PBE/basis2 (en italique). Les distances sont en Å et les dièdres en degrés (en gras) au niveau PBE/basis1. Pour les isomères les plus bas de chaque famille, des paramètres géométriques sont aussi donnés au niveau PBE/basis2 (en italique). 252
- 18 Isomères Meta-Mont présentés avec leurs familles de complexation et leurs énergies relatives (kcal/mol). Les distances (en noir), les distances du cation à l'oxygène (en rouge) et aux azotes (en bleu) de la molécule sont en Å. Le dièdre C1-C2-C3-N4] (en gras) est en degrés. 255
- 19 Isomères Fen-mont présentés avec leurs familles de complexation et leurs énergies relatives (kcal/mol). Les distances (en noir), les distances du cation aux oxygènes (en rouge) et chlores (en vert) de la molécule sont en Å. Le dièdre H7-N3-C4-C5] (en gras) est en degrés. 256
- 20 Isomères Fen-mont présentés avec leurs familles de complexation et leurs énergies relatives (kcal/mol). Les distances (en noir), les distances du cation aux oxygènes (en rouge) et chlores (en vert) de la molécule sont en Å. Le dièdre H7-N3-C4-C5] (en gras) est en degrés. 257
- 21 Structures de départ des trajectoires CPMD en $\phi_{solid}^{H_2O}$, les distances sont présentées en Å. 260
- 22 Capture de la trajectoire de Fen-Mont $_{ortho,ax}^{H_2O}$ (CI-OH). Le fenhexamide et toutes les molécules H_2O sont représentés par des lignes exceptée la sphère d'hydratation interne de Ca2 (pyramide à base carrée) qui est en représentation boules et bâtons, comme le sont la surface et les cations. 262

23	Surface d'énergie libre relative $A(\xi)_{rel}$ (kcal/mol) (<i>a</i>), où les valeurs ΔA_w sont les différences d'énergies libres entre les puits consécutifs et où ΔA_b et ΔA_{b-} sont les énergies relatives nécessaires pour franchir les barrières, pour les processus de désorption et d'adsorption respectivement. Les fonctions de densité de probabilité $P(\xi)$ des 11 fenêtres d'exploration sont présentées en (<i>b</i>), chaque couleur correspond à une fenêtre différente <i>i</i> . ξ est la coordonnée <i>z</i> du centre de masse du pesticide.	265
24	Dernières captures des fenêtres 1 (<i>a</i>), 4 (<i>b</i>) et 10 (<i>c</i>) correspondant au trois puits d'énergie libre du profil énergétique obtenue (Figure 23). Les distances sont présentées en Å.	266

List of Tables

I.1	Average numbers of treatments applied on some types of French cultivations between 2013 and 2015 (reference: SSP - Agreste) [6].	50
I.2	Important experimental data for atrazine [7].	53
I.3	Important experimental data for metamilon [7].	55
I.4	Important experimental data for fenhexamid [7].	58
IV.1	MO basis sets and related energy contributions calculated with the RVS SCF method. Each MO basis set allows to determine the energy component in bold. MO sets in brackets are frozen during the SCF procedure. *BSSE scheme differs from counterpoise (only vacant MO accessible).	111
IV.2	Comparison of the structures and energies of two different atrazine conformers using a gaussian basis set in the gas phase and a periodic planewave calculation. Both computations were made using the PBE functional. Adding a dispersion correction to the PBE (PBE-D2) was also tested. Distances are given in Å, angles and dihedrals in degrees. Following the atom numbering of Figure 4 in the upcoming paper, α is the N6C1N2 <i>s</i> -triazine angle and <i>D</i> is the C1N2C3N4 dihedral. Computational cell parameters: a = 15.500 Å, b = 17.931 Å and c = 30 Å.	116
IV.3	Comparison of the structures and energies of two different Atra-Ca ²⁺ complexes using a gaussian basis set in the gas phase and a periodic planewave calculation. Both computations were made using the PBE functional. Distances are given in Å, angles and dihedrals in degrees. Following the atom numbering of Figure 4 in the upcoming paper, α is the angle made by the cation with the two atoms of the bidentate binding sites (left: N6CaCl14 ; right: N7CaN4) and <i>D</i> is a dihedral (left: C5N6CaCl14 ; right: N7CaN4C3). Computational cell parameters: a = 15.500 Å, b = 17.931 Å and c = 30 Å.	117


IV.4	Clay calculated average distances (in Å) in montmorillonite and atrazine-montmorillonite isomers at PBE-D2/pw level. Kinetic energy cutoff equal to 80 Ry. Distances in bold are the most impacted by complexation with atrazine.	121
IV.5	Clay calculated average angles (in degrees) in montmorillonite and atrazine-montmorillonite isomers at PBE-D2/pw level. Kinetic energy cutoff equal to 80 Ry. . .	121
V.1	E_{comp} in kcal/mol and E_{tot} in a.u. at PBE/pw level of the lowest-energy Meta- Na^+ isomer. 80 : kinetic energy cutoff sets to 80 Ry. 140 : kinetic energy cutoff sets to 140 Ry. T : a Tuckerman poisson solver scheme was used. c : cubic box length in Å.	140
V.2	E_{comp} complexation energies and dispersion contributions to the complexation (E_{disp}^{comp}) in kcal/mol of the lowest-energy Meta- Ca^{2+} isomer. d_{Phe-Ca} and d_{Ca-O} , the distances between Ca and the complexation site are given in Å. The D_{Meta} dihedral is given in degrees. The comparisons are made at the PBE/basis2, PBE/pw and PBE-D2/pw levels with pw cutoffs of 80 and 140 Ry and with a box of 13 or 20 Å.	142
V.3	E_{comp} complexation energies and dispersion contributions to the complexation (E_{disp}^{comp}) in kcal/mol of the lowest-energy Fen- Ca^{2+} isomer. d_{Phe-Ca} and d_{Ca-O} , the distances between Ca and the complexation site are given in Å. The D_{Fen} dihedral is given in degrees. The comparisons are made at the PBE/basis2, PBE/pw and PBE-D2/pw levels with pw cutoffs of 80 and 140 Ry and with a box of 15 or 20 Å.	142
V.4	Intramolecular bond lengths (Å) in PBE/basis2 and PBE-D2/pw 80 Ry of the lowest-energy Meta- Ca^{2+} and Fen- Ca^{2+} isomers of each binding site families.	143
V.5	Relative (ΔE), complexation (E_{comp}), interaction (E_{int}) energies and dispersion contributions in the complexation (E_{disp}^{comp}) and in the interaction (E_{disp}^{int}) in kcal/mol of the lowest-energy Meta- Ca^{2+} and Fen- Ca^{2+} isomers of each family. The comparisons are made at the PBE/basis2, PBE/pw and PBE-D2/pw levels with pw cutoffs of 80 and 140 Ry. In bold red, relative energies in agreement with the PBE/basis2 level. In bold, relative energies not in agreement with the PBE/basis2 level.	145
VI.1	Metamitron intramolecular distances (Å) in ϕ_{gas} (PBE/basis2) and ϕ_{solid}^{dry} (PBE-D2/pw) complexes.	181
VI.2	Meta-Mont distances or average distances (Å) in the Ca-montmorillonite surface. . . .	182
VI.3	Relative (ΔE), adsorption (E_{ads}), interaction (E_{int}) and preparation (E_{prep}) energies of the Meta-Mont isomers. $E_{prep}(\text{Pest})$, $E_{prep}(\text{Mont})$ and $E_{prep}(\text{total})$ are the metamitron, the Ca-montmorillonite and the total preparation energies respectively. Percentages in the preparation energies are the contributions in $E_{prep}(\text{total})$. E_{disp}^{ads} and E_{disp}^{int} are dispersion contributions to the adsorption and interaction energies. All energies are displayed in kcal/mol.	182

VI.4	Cation-binding site distances in Å and dihedrals in degrees of the lowest Fen-Ca ²⁺ and Fen-(Ca ²⁺) ₂ isomers with comparable complexations at the PBE/basis2 level, reported from Chapter V.	188
VI.5	Fenhexamid intramolecular distances (Å) in ϕ_{gas} (PBE/basis2) and ϕ_{solid}^{dry} (PBE-D2/pw) complexes.	193
VI.6	Fen-Mont distances or average distances (Å) in the Ca-montmorillonite surface.	194
VI.7	Relative (ΔE), adsorption (E_{ads}), interaction (E_{int}) and preparation (E_{prep}) energies of the Fen-Mont isomers. E_{prep} (Pest), E_{prep} (Mont) and E_{prep} (total) are the fenhexamid, the Ca-montmorillonite and the total preparation energies respectively. Percentages in the preparation energies are the contributions in E_{prep} (total). E_{disp}^{ads} and E_{disp}^{int} are dispersion contributions to the adsorption and interaction energies. All energies are displayed in kcal/mol.	194
VII.1	Distances between the binding sites and the complexed calcium cation Ca1 of Meta-Mont and Fen-Mont isomers, reported from the ϕ_{solid}^{dry} study, and corresponding average distances from the $\phi_{solid}^{H_2O}$, all displayed in Å.	205
VII.2	Distances between the calcium cations and the basal oxygens O_b of the surface, from the last $\phi_{solid}^{H_2O}$ snapshots and the ϕ_{solid}^{dry} isomers, displayed in Å.	208
VII.3	Parameters of the 11 biased CPMD trajectories. i is the window index, $\xi_{z(com)}^i$ is the arbitrary value of the reaction coordinate around which the harmonic potential must oscillates (cartesian z coordinate of the molecular center of mass), k_i is the associated harmonic constant and t_i the time of the simulation (ps).	214
VII.4	Average intercation distances and average distances from the calcium cations Ca1 and Ca2 to the basal, water and carbonyl oxygens in windows 1, 4 and 10. The same distances from Fen-Mont $_{para,ax}^{H_2O}$ are reported for comparison. All distances are in Å.	217
1	Nombres moyens de traitements appliqués sur certaines cultures françaises entre 2013 et 2015 (référence: SSP - Agreste) [6].	234

List of acronyms

Atra	Atrazine
BO	Born-Oppenheimer
BSSE	Basis Set Superposition Error
CPMD	Car-Parrinello Molecular Dynamics
DFT	Density Functional Theory
DFTB	Density Functional based Tight-Binding
Fen	Fenhexamid
GGA	Generalized Gradient Approximation
GTO	Gaussian Type Orbital
HF	Hartree-Fock
KS	Kohn-Sham
LCAO	Linear Combination of Molecular Orbitals
LDA	Local Density Approximation
MD	Molecular Dynamics
Meta	Metamitron
Mont	Ca-montmorillonite
PBE	Perdew-Burke-Ernzerhof
PES	Potential Energy Surface
PMF	Potential of Mean Force
pw	Plane Waves
RDF	Radial Distribution Function
RVS SCF	Reduced Variational Space Self-Consistent Field
SCF	Self-Consistent Field
STO	Slater Type Orbital
WHAM	Weighted Histogram Analysis Method

Abstract

esticides are widely employed molecules for crop protection in France and all over the world against insects, fungi or undesirable plants. When these substances are spread, they mainly diffuse on plants, in the atmosphere, but an important quantity reaches soils. In the present thesis, pesticide fate is under study. For this purpose, three pesticides have been selected: two herbicides, atrazine and metamitron, mainly used respectively on corn and sugar beets ; and a fungicide, fenhexamid, notably employed on grapes. Atrazine has been one of the most widespread pesticides for agriculture within the European Union until its prohibition in 2004.

In this study, only the soil mineral part is considered. Clay is one of the three major mineral families constituting soils. The most abundant smectite clay type, montmorillonite, has been chosen. The computational simulations conducted in this thesis use the Density Functional Theory (DFT) formalism.


The first part of this thesis treats a static study of atrazine interaction with pyrophyllite and montmorillonite. This work has shown the affinity of atrazine for montmorillonite, evidenced the importance of dispersion effects within such systems and thus the need in employing a DFT method with a dispersion correction. In the following chapters, Car-Parrinello Molecular Dynamics through DFT is used as a method of potential energy surface exploration of more and more complex systems. Indeed, this study begins with isolated pesticides, metamitron and fenhexamid, then their complexes with one or two Na^+ and Ca^{2+} , which are abundant cations in soil. Finally, the adsorption of these entities, in the presence of water or not, onto a montmorillonite surface, is considered using periodic calculations.

Within the second chapter of the present work, results from geometry optimisations in gas phase are presented. The stability of low energy conformers of metatitron and fenhexamid and isomers of their complexes with one or two cations of the same nature is analyzed. The most favorable complexation sites for these cations around the pesticides have been determined, as well as the complexation energies associated to these sites. As expected, whatever the pesticide, the complexation energy is larger with Ca^{2+} .

The third part develops the obtained results on the adsorption of metatitron and fenhexamid over the chosen clay model: a montmorillonite surface in which four isomorphic substitutions of Al^{3+} by Mg^{2+} have been done, inducing the presence of two Ca^{2+} cations in the interlayer to compensate the charge loss. Corresponding adsorption energies have been studied.

The last chapter of this thesis is organised in two sections. First, some of the most stable structures of each adsorbed pesticide onto the surface have been solvated. The aim being to understand solvation effects on these systems. In a second time, a study of fenhexamid desorption from the montmorillonite surface using a biased molecular dynamics method (Umbrella Sampling) along a specific reaction coordinate. This work allowed to quantify theoretically the free energy barrier to overcome to desorb fenhexamid from the hydrated montmorillonite.

Résumé

es pesticides sont des molécules utilisées en grandes quantités en France et dans le monde entier pour la protection des cultures contre insectes, champignons ou plantes indésirables. Lorsque ces substances sont répandues, elles se dispersent principalement sur les plantes, dans l'atmosphère mais une grande quantité rejoint aussi les sols. Dans cette thèse, le devenir de pesticides dans le sol est étudié. Pour cela, trois pesticides ont été sélectionnés : deux herbicides, l'atrazine et la métamitronne, principalement utilisés respectivement sur le maïs et les betteraves sucrières ; et un fongicide, le fenhexamide, notamment employé sur les vignes. L'atrazine était un des pesticides les plus répandus en agriculture au sein de l'Union Européenne jusqu'à son interdiction en 2004.

Dans ce travail, la partie minérale du sol est seule prise en compte. L'argile est une des trois grandes familles de minéraux constituant les sols. Une argile de type montmorillonite, la plus abondante des smectites, a été choisie. Les simulations menées lors de cette thèse emploient le formalisme de la Théorie de la Fonctionnelle de la Densité (DFT).

La première partie de cette thèse porte sur l'étude statique de l'interaction de l'atrazine avec la pyrophyllite et la montmorillonite. Ces travaux ont montré l'affinité de l'atrazine pour la montmorillonite, mis en évidence l'importance des effets de dispersion dans de tels systèmes et donc la nécessité d'utiliser une méthode de DFT avec une correction de dispersion. Dans les chapitres suivants, la Dynamique Moléculaire Car-Parrinello en DFT est utilisée comme méthode d'exploration des surfaces d'énergie potentielle de systèmes de plus en plus complexes. En effet, l'étude débute par les pesticides seuls, métamitronne et fenhexamide, puis leurs complexes avec un ou deux cations Na^+ et Ca^{2+} qui sont abondants dans les sols. Ensuite, l'adsorption de ces entités, en présence ou non d'eau, sur

une surface de montmorillonite, est envisagée à l'aide de calculs périodiques.

Dans le second chapitre de ce travail, des résultats issus d'optimisations de géométries en phase gazeuse sont présentés. La stabilité des conformères et isomères de basses énergies de la métamitronne et du fenhexamide seuls et complexés avec un ou deux cations de même nature est analysée. Les sites de complexation les plus favorables pour ces cations autour des pesticides ont pu être déterminés, ainsi que les énergies de complexation associées à ces sites. Comme attendu, quel que soit le pesticide, l'énergie de complexation est plus importante avec Ca^{2+} .


La troisième partie développe les résultats obtenus pour l'adsorption de la métamitronne et du fenhexamide sur le modèle d'argile choisi : une surface de montmorillonite dans laquelle quatre substitutions isomorphiques de Al^{3+} par Mg^{2+} ont été réalisées, nécessitant la présence de deux cations Ca^{2+} dans l'interfeuillet pour compenser la perte de charges. Les sites d'adsorption préférentiels des pesticides, ainsi que les énergies d'adsorption correspondantes ont été étudiés.

Le dernier chapitre de cette thèse s'organise en deux parties. Premièrement, certaines des structures les plus stables de chaque pesticide adsorbé sur la surface ont été solvatées. Le but étant de comprendre les effets de la solvatation sur ces systèmes. Dans un second temps, une étude de la désorption du fenhexamide de la surface de montmorillonite a été réalisée à l'aide d'une méthode de dynamique moléculaire biaisée (Umbrella Sampling) selon une coordonnée réactionnelle spécifique. Ce travail a permis de quantifier théoriquement la barrière d'énergie libre à franchir pour désorber le fenhexamide de la montmorillonite hydratée.

Introduction

*“If you wish to understand the fragrance of the rose, or the tenacity of the oak ;
if you are not satisfied until you know the secret paths by which the sunshine
and the air achieve these wonders ; [...] then take up chemistry.”*

Charles A. Coulson

esticides are a category of molecules that gathers all kind of chemical products synthesized for crop defense against insects, diseases or undesirable plants. In order to maximize field production, these substances are very employed in agriculture mainly, but also for maintenance of public and private areas such as parks and gardens. These molecules are widely used in Europe, for instance, the amount of sold products in France every year is counted in tens of thousands of tons [1–3]. France is thus one of the biggest pesticide consumers in the world. Consequently, the large employment of pesticides for agriculture raises health and environmental issues. Indeed, the presence of pesticides and degradation products can be measured in air, ground and drinkable water [8,9], micro- and macro- organisms, targetted crops and food [10].

The aim of this thesis is to study the interactions between pesticides and soil. The preliminary chapters to present the context of this work begin with a description of pesticide role in our society and a literature review on the three molecules of interest: atrazine, metamitron and fenhexamid (Chapter I). Then, a brief overview of soil organisation and composition will be given, followed by the presentation of montmorillonite, the clay mineral that has been chosen for this work (Chapter II). Further, as a last introduction of the present study, the consecutive chapter presents all the theoretical methods that have been employed to treat the considered systems.

This thesis is a step by step study of the nature and components of the interactions between pesticides and soil. For this purpose, four types of systems have been considered and correspond to the four next chapters:

- First, atrazine interaction with clay minerals has been studied by geometry optimisation of some isomers over the surface of modelized clays. This chapter is based on previous published work of the group on atrazine complexation with abundant environmental cations [11, 12].
- In a second time, two other pesticides, metamitron and fenhexamid, have been selected for this study and have been considered in interaction with the same set of cations than for atrazine. However, that study has included molecular dynamics for a larger exploration of pesticide isomers. This step of the present approach aims to study the pesticide-cation(s) interaction. Then, by comparison with pesticide behavior in solid phase, it will be possible to observe the influence of the surface on pesticide-cation(s) complexation.
- The third chapter considers metamitron and fenhexamid adsorbed on a dry montmorillonite model. Molecular dynamics simulations have then been run on both molecules. This step brings an improvement with respect to the static approach used in the work on atrazine.
- The final part of this work goes further by considering the previous systems with explicit water solvation. Indeed, real clay minerals, especially montmorillonite, are able to absorb an important amount of water in the interlayer. The next and last step of this thesis is thus a study of hydration effects on the pesticide-cation(s)-montmorillonite system. Furthermore, a series of biased dynamics have been run in parallel on a fenhexamid molecule adsorbed on the surface to drive desorption process and try to quantify free energy barriers along a specific reaction coordinate.


The approach of this thesis is a treatment of more and more complex models from isolated molecular systems to hydrated pesticides on clay surface.

Chapter I

Pesticides

“Error is a hardy plant... It flourisheth in every soil.”

Martin Farquhar Tupper

esticides, etymologically “pest killer”, from English *pest* and Latin *caedere* “kill, slaughter, hit” [13], designates all substances whose toxic properties allow to fight against pests, which may be insects (insecticide), plants (herbicide) or fungi (fungicide), ...

Pesticides employed for vegetal protection are officially named phytopharmaceutical, or commonly phytosanitary, products [14]. Such substances are widely produced and used all over the world, mainly for agriculture, but also in urban activity (parks, public green areas, gardens...) and in private properties. Pesticide issue gets more and more attention as it became a matter of environment preservation, food quality and thus public health.

I.A Introduction

Since the year 2004, France has presented the most important agricultural surface in Europe with 29,115.25 thousands hectares in 2015 corresponding approximately to 16 % of the whole European agricultural surface, above Spain (23,897.14 kha, 13 %), United Kingdom (17,147.00 kha, 9 %), Germany (16,730.70 kha, 9 %), Romania (13,835.47 kha, 7 %), and Italy (12,660.89 kha, 7 %) as shown on Figure I.1 ; knowing that data for Norway, Liechtenstein, Switzerland and Serbia are not available [1].

France has the leadership in agriculture among European countries, and is one of the main pesticide consumer in the world. Figure I.2 represents the evolution of total and

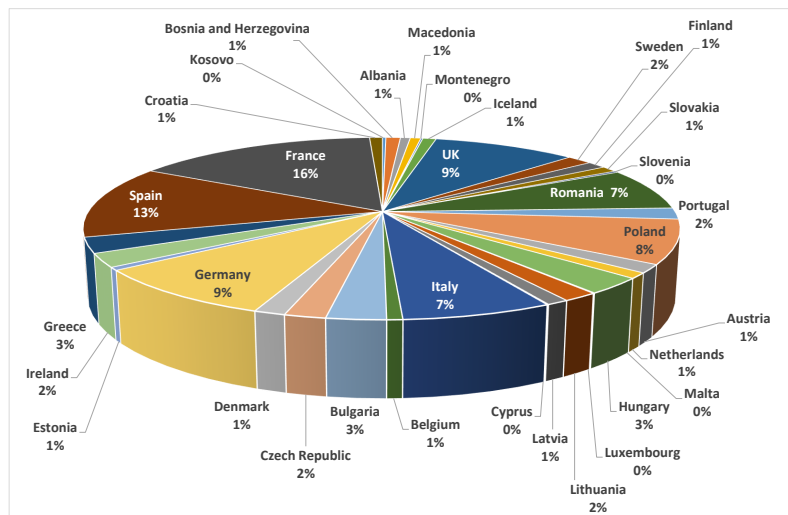


Figure I.1: Proportional agricultural surfaces of European countries in the year 2015 [1]

detailed pesticide sale in France every year from 1996 to 2015 [1–3]. A peak around 121 thousand tons of products has been reached in 1999, however the global tendency from that year is a decrease. In spite of the rise to 75 thousand tons in 2014, since the year 2009, the average sale of phytosanitary products is between 60 and 70 ktons per year. Globally, fungicide substances present the highest share of sold pesticides, followed by herbicides (44 % and 33 % in 2014 respectively). In 2011, pesticides French market represented a turnover of 69 billion euros. In terms of sold products, the last available data for Europe rank France as the second biggest consumer of pesticide substances after Spain. In EU-28, approximately 400 thousand tons of pesticides were sold in 2014: Spain represented 19.9 % of this amount, France 19.0 %, Italy 16.2 %, Germany 11.6 % and Poland 5.9 %.

In 2005, INRA (Institut National de la Recherche Agronomique) and CEMAGREF (Centre national du Machinisme Agricole du Génie Rural des Eaux et des Forêts) published a report on pesticides (Expertise Scientifique Collective (ESCo)) requested by Ecology and Agriculture French ministries. It highlighted the necessity to decrease pesticide use in order to reduce environment contamination and evidenced the possibility of maintaining a satisfying production, thanks to new cultivation systems, with an important reduction of chemical treatments. This report notably states that the average quantity of active pesticide substances spread on crops every year (until 2005) was from 5.1 to 5.4 kg/ha [15]. For further development of these new systems and to assess their performances, these ministries ordered a study to INRA: Ecophyto R&D, gathering a wide panel of expertises in the field.

In 2007, the “Grenelle de l’environnement”, an important political meeting for discussions and negotiations around environmental issues emphasized the pesticide problem. Later, the Ecophyto 2018 plan, established by the French agriculture ministry, stated to

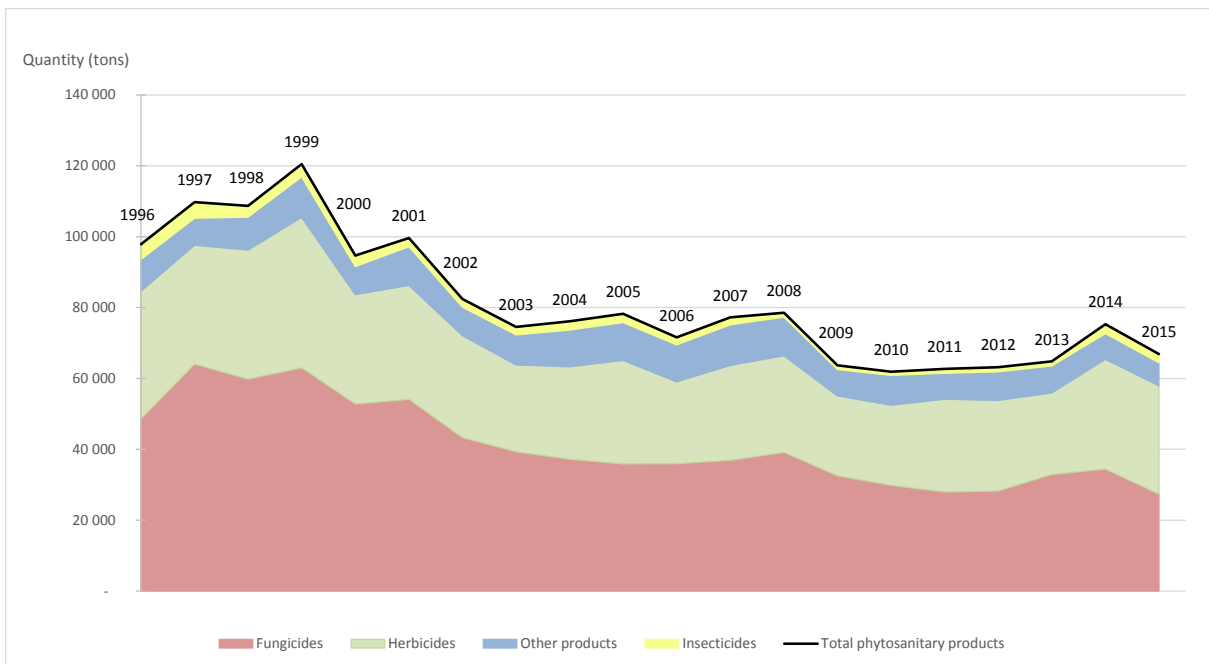
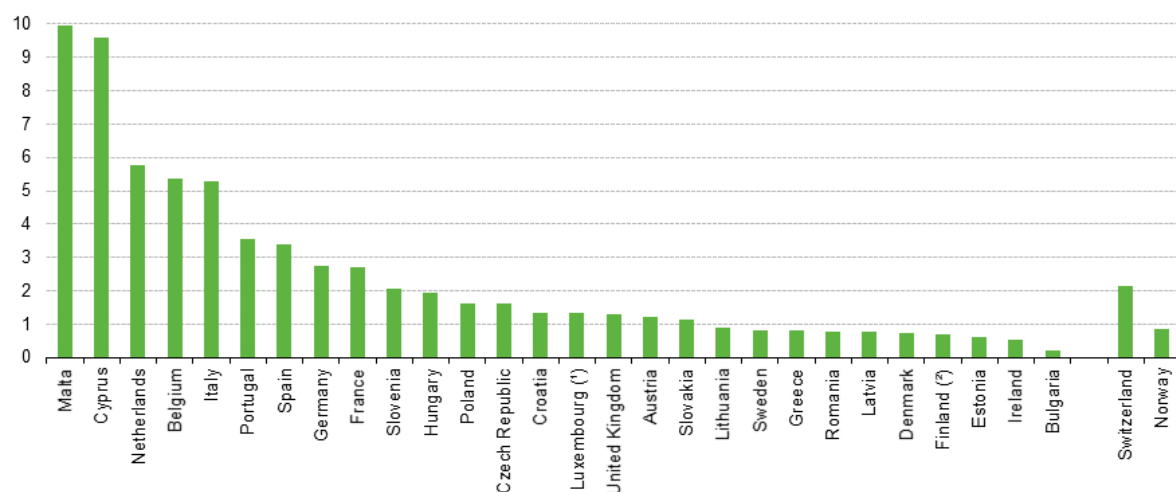


Figure I.2: Amount of sold phytosanitary products (tons) in metropolitan France from 1996 to 2013 (reference: Union des Industries pour la Protection des Plantes (UIPP) Traitements: SOeS, 2016) [2,3] ; and from 2014 to 2015 [1]

lower pesticide utilization of 50 % by the end of 2018. The evolution of pesticide sales in France (Figure I.2) suggests it will be a failure, even if from 2007, the average quantity of sold products globally decreased. However, last data show a reduction in the average quantity of pesticides used in kilograms per hectare: indeed the mean value until 2005 was 5.1 – 5.4 kg/ha ; in 2014, it was between 2.5 and 3.0 kg/ha ; estimated with the quantity of sold pesticides compared to hectares of Utilised Agricultural Area (UAA) within the country.

Pesticide consumption of European countries during the year 2014 are presented in Figure I.3 [1]. Calculating amounts of sold pesticides in kg/ha of UAA is more relevant to estimate how much countries use them for agriculture, than considering the total amount of sold pesticides like in Figure I.2 for France. Indeed, one can see that for some countries which do not have wide agricultural surfaces as Malta, Cyprus (which represent less of 1 % of the European agricultural surface each), their amount of sold pesticides in kg/ha are actually the two highest: approximately 10 and 9.5 kg/ha respectively. Then Netherlands and Belgium sell from 5 to 6 kg/ha, and Portugal, which represents 2 % of the European agricultural surface, sells more than 3 kg/ha. For countries with the biggest surfaces, amounts are between 2 and 6 kg/ha while other European countries are lower or equal to 2 kg/ha, except for Switzerland. Therefore, even if France manage to lower the quantities of sold pesticides within the country, it remains a big consumer. To give an insight on the



Note: Confidential data have been removed from the sums of pesticides sales. Data on total UAA from 2013.

(*) Fungicides and bactericides: 2012 data, other data: 2013.

(*) Urea is used only in forestry and is excluded from the total pesticide sales.

Figure I.3: Quantities of sold pesticides compared to UAA (kg/ha) of main European countries with agricultural activity in 2014 [1].

significant presence of pesticides in French agriculture, Table I.1 lists the last available data for the average number of treatments, for all kind of pesticides, over some fruits and vegetables between 2013 and 2015 [6]. We can notably see that the average number of treatments over one year can reach a very high level, especially for apple (36 treatments) and potato or peach (19) which are reputed for their sensitivity.

Average number of treatments							
2013	Carot	Cauliflower	Strawberry	Muskmelon	Leek	Lettuce	Tomato
	11	3	8	8	9	4	12
2014	Colza	Sunflower	Sugar beet	Potato	Sugar cane		
	7	3	5	19	4		
2015	Apple	Peach	Plum	Apricot	Cherry	Banana	
	36	19	12	13	11	8	

Table I.1: Average numbers of treatments applied on some types of French cultivations between 2013 and 2015 (reference: SSP - Agreste) [6].

A more reliable indicator, L'Indicateur de Fréquence de Traitement (IFT), gives the number of approved doses of pesticides applied per hectare of crop. The approved dose of a substance being the effective amount to apply on a given crop for a given target. That indicator was originally developed in Danemark during the 1980s and has been adopted in France by INRA and MAP (Ministère de l'Agriculture et de la Pêche) in 2006 after the ESCo report from the year before [16]. However, the most recent data concerning crops

in Table I.1 present an average fungicide IFT estimated around 12.0 and 15.5 for potato respectively for the years 2011 and 2014 [17]. In 2011, the average total IFT of potato was estimated around 15.6, while total IFT for sunflower was around 1.7 the same year [18].

To summarize, pesticides represent an ongoing problematic as their presence is very significant within our society and raise questions about the consequences on health and environment. This thesis focuses on three particular pesticides: atrazine, metamidon and fenhexamid which will be presented in the following sections. These substances have been chosen for their common use in agriculture, but also for their different physico-chemical characteristics and properties.

I.B TyPol database

The TyPol (Typology of Pollutants) database [19] is an algorithmic approach to classify pollutants regarding their molecular structure, but also their behavior in the environment. In total, TyPol gathers 215 organic pollutants: 191 parent compounds among which 116 pesticides, 30 polychlorinated biphenyls (PCB), 13 polycyclic aromatic hydrocarbons (PAH), 10 polychlorinated dibenzofurans (PCDF), 9 phthalates, 7 polychlorinated dibenzodioxins (PCDD) and 6 miscellaneous compounds (drugs, hormone, etc...) ; and 24 degradation products deriving from chloride pesticides. The approach proposed by TyPol is based on Partial Least Squares (PLS) regression [20,21] and hierarchical clustering: compounds of interest, and their degradation products can be classified in groups of molecules ("clusters" in the original paper), regarding specific environmental parameters (referenced on literature and databases), and molecular properties through molecular descriptors calculated via Dragon 5.5 for connectivity indices, regarding bi-dimensional chemical structures, and through the AM1 semi-empirical method in MOPAC for three-dimensional chemical structures, taken for a neutral and isolated molecule (gas phase).

This database uses five processes to describe environmental behavior: dissolution, volatilization, adsorption, degradation and bioaccumulation. These processes can all be described by different environmental parameters such as water solubility (S_w) and octanol-water partition coefficient (K_{ow}) for dissolution, vapor pressure (P_{vap}) and Henry's law constant (K_H) for volatilization, soil carbon organic content coefficient (K_{oc}) for adsorption, half-life ($DT50$) for degradation, or bioconcentration factor (BCF) for bioaccumulation and ecotoxicity estimation. These parameters have been used in the original paper of Servien *et al.* [19] to represent the five cited processes. This paper showed that the best classification of the 215 compounds is a set of 6 clusters taking all the data into account. Atrazine, metamidon and fenhexamid have been selected as they belong to three different clusters, defined by the following properties:

- Atrazine: belongs to cluster 1 which gathers compounds with relatively high polarizability, low K_{oc} and low $DT50$, the lowest BCF and K_{ow} , and the highest S_w . In addition, these substances have the lowest K_H and high P_{vap} .
- Metamitron: corresponds to cluster 5 with substances presenting high dipole moments and structures with high numbers of rotatable bonds. Their K_H , P_{vap} , K_{oc} and $DT50$ are medium, BCF and K_{ow} are low, and S_w is relatively high.
- Fenhexamid: found in cluster 4 where molecules have high polarizability, high numbers of hydrogens and carbons. They present low $DT50$ and P_{vap} , medium K_H and the highest K_{oc} .

These three commonly used pesticides have been chosen regarding their belonging to these different groups. Moreover, we will see in the next sections that a lot of experimental studies are available in literature.

I.C Atrazine

Atrazine (CAS* 1912-24-9) is a triazine herbicide ($C_8H_{14}ClN_5$) of semi-structural formula displayed on Figure I.4, also called 6-chloro-N2-ethyl-N4-isopropyl-1,3,5-triazine-2,4-diamine. This pesticide is widely employed in agriculture, notably on corn, sugar cane and wheat for its ability to prevent *pre*- and *post*- emergence of broad-leaved weeds and grasses by inhibiting photosynthesis, as metamitron that will be presented hereafter [7]. This herbicide substance has been introduced for the first time in 1957 but is a forbidden product in EU since the year 2004 for its consequences on health and environment. Table I.2 displays some of atrazine experimental data and main metabolites. These values show that atrazine has a quite high half-life ($DT50$) in soils, a low water solubility (35 mg/L at 20°C) and a high K_{ow} . According to Mudhoo *et al.*, atrazine is way more soluble in organic solvents: from 360 to 183,000 mg/L. However it is spread on crops with water spray at a usual concentration of 2.2 to 4.5 kg/ha [23].

Literature hardly links human cancer occurrence with atrazine exposure [24–28]. Atrazine can be found in drinking-water and may be involved in rates of premature birth and Small-for-Gestational-Age (SGA) in human newborns. Nevertheless, a correlation between these phenomena and this herbicide is hard to prove because of the presence of several other chemical pollutants in water [29–33]. Anyway, atrazine has been evidenced as an endocrine disrupter, mostly in rats [34–42] and aquatic life [43–48]. For that reason,

*Chemical Abstracts Service (CAS) is a division of the American Chemical Society (ACS) and the CAS registry number of a chemical substance is its unique numerical identifier in the ACS databank [22]

this substance and its transformation products are the first molecules under measurements in drinkable water [8] and rivers, among other herbicides [9, 49].

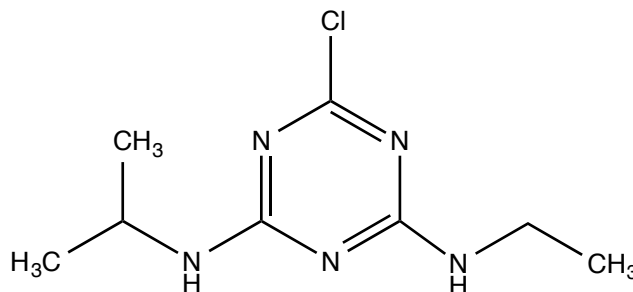


Figure I.4: Atrazine semi-developed chemical formula.

Molecular mass	215.68 g.mol ⁻¹
Solubility (water/20°C)	35 mg.L ⁻¹ (low)
Melting point	175.8°C
K _{ow} (pH 7/20°C)	5.01 × 10 ²
Soil degradation (DT50/aerobic)	75 days (typical)
	66 days (laboratory 20°C)
	29 days (field)
Main metabolites	6-deisopropyl atrazine (C ₅ H ₈ ClN ₅)
	Deethylatrazine (C ₆ H ₁₀ ClN ₅)
	2-hydroxyatrazine (C ₈ H ₁₅ N ₅ O)

Table I.2: Important experimental data for atrazine [7].

Studies on the molecule toxicity are still limited [48, 50–53] but a lot are available in literature concerning atrazine behavior in environment through several processes. For instance, experiments, physical and mathematical models are produced to try to understand and quantify transport and sorption of organic compounds, such as atrazine, in natural soils [54–58]. Sorption and desorption of this molecule towards particles of a mineral sand mining by-product in solution, the Neutralised Used Acid (NUA), have been investigated. It has shown high sorption levels of atrazine and other pesticides, for negligible desorption amounts and no degradation of the pesticides during the processes. NUA could thus be an efficient and low-cost way to remove atrazine and other pesticides from water [27]. In this area, the employment of polymers has been proven to be successful for atrazine removal from water [59–61] as well as zeolites [62–65] or carbon nanotubes [66–70].

Smectites affinity with organic molecules is widely studied, specially with montmorillonite, the most abundant smectite on Earth, as we will present it in Chapter II.

Literature developing montmorillonite as a solution for atrazine extraction from water is very rich. Potassium homoionic montmorillonite has shown a good efficiency in adsorbing and concentrating atrazine and its metabolites [71] that can be enhanced with intercalated polymers [72]. A relationship between atrazine orientation and the hydration level of smectites interlayer has been established, stating that atrazine takes a parallel orientation to the basal surface when only one layer of water molecule is found in the smectite. For a higher hydration level (three water layers), the molecule is tilted at an acute angle with the surface [73]. A comparison of atrazine sorption on saturated Al- and Ca-smectites showed stronger sorption on Al-smectites, likely due to the trivalency of Al cation, compared to divalent Ca cation, and an associated higher polarization of water molecules [74]. Among the three kinds of smectite: K-, Na- and Ca-montmorillonite all present efficient sorption of atrazine and other herbicides [75] and are research tracks for pesticides (and more generally pollutants) removal from water, through the study of adsorption-desorption processes [76–79].

I.D Metamitron

Metamitron (CAS 41394-05-2), is the common name of 4-amino-4,5-dihydro-3-methyl-6-phenyl-1,2,4-triazin-5-one ($C_{10}H_{10}N_4O$), an organic molecule belonging to triazinone family [7], of semi-structural formula presented on Figure I.5. Some of its main experimental properties and known metabolites are displayed in Table I.3.

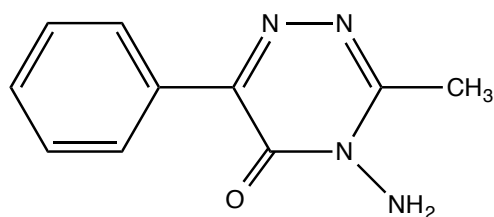


Figure I.5: Metamitron semi-developed chemical formula.

According to these data and literature, metamitron persists in sugar beet plants up to 15 days and has a half-life (DT_{50}) of 30 days in soil [10]. It has a high aqueous solubility at 20°C ($1,770 \text{ mg}\cdot\text{L}^{-1}$), a low K_{ow} of 7.08, and its main known metabolite is the desamino-metamitron. This substance has been first reported in 1975 and has probably been introduced on the same year [7]. It is very widely employed in agriculture for its selective herbicide effect, mainly on fodder and sugar beet crops. It allows to

Molecular mass	202.21 g.mol ⁻¹
Solubility (water/20°C)	1,770 mg.L ⁻¹ (high)
Melting point	166.6 °C
Degradation point	250 °C
K _{ow} (pH 7/20°C)	7.08
Soil degradation (DT50/aerobic)	30 days (typical)
	19 days (laboratory 20°C)
	11.1 days (field)
Main metabolite	Desamino-metamitron (C ₁₀ H ₉ N ₃ O)

Table I.3: Important experimental data for metamitron [7].

prevent *pre*- and *post*- emergence of annual broad-leaved weeds and turf grass among cultures, by inhibiting their photosynthesis process [80].

Its use is widespread in Western Europe as sugar beet is a crop that knew an important expansion in cultivation and production from 1989 (17 million tons) to 2000 (19 million tons), in order to follow the increasing demand in sugar during that period [81]. Metamitron was by far the most employed herbicide on sugar beets in Germany, France, Netherlands, UK, Spain and Belgium in 2000. For instance, the same year, 544 tons of metamitron substances have been used on French sugar beet cultivations, above chloridazon with 169 tons, knowing that France presented 427,000 ha of cultivated sugar beets. Among the cited countries, metamitron represented 46 % of market share making it the largest herbicide used at that time. Then in decreasing order follow: chloridazon, ethofumesate, phenmedipham, glyphosate, lenacil, quinmerac, desmedipham and clopyralid. Other substances represented less than 2 % of the market: riflusulfuron-methyl, dimethenamid, s-metolachlor, cycloxydim, fluazifop-P-butyl, propaquizafop, quizalofop-P, haloxyfop [81].

All the agricultural, environmental and public health issues raised by the employment of such substances has lead to a large amount of surveys and experimental studies on metamitron. Assessment of its presence, transport and fate in environment is done in air, plants, crops, among microorganisms and animals by bioaccumulation, surface and ground waters, and finally soils. Concerning fate of metamitron in soils, several approaches can be adopted as a lot of parameters are involved in its persistence, exchange and degradation, involving bio-process or not. Generally, influence of microorganisms, herbicide availability in the soil liquid phase (soil solution) and size of the mineral particles (sand, silt or clay) are important factors in metamitron degradation rate [82], as well as temperature [83]. On a mineral point of view, sorption of metamitron and exchange between mineral matter and soil solution can be investigated. Surveys have been conducted in differ-

ent countries around the world: sorption on a wide range of different soil horizons and types have been studied in Southern Spain [84]. In Finnish soils, fate of metamitron, glyphosate, glufosinate-ammonium, phenmedipham and ethofumesate was evaluated [85], and metamitron presents a relatively good mobility compared to the other ones [86]. An experimental and mathematical study allowed to establish generalized equations derived for sorption/desorption description, in order to be implemented in pesticide fate models, knowing that adsorption rate in soils have a time-dependence due to the chemical degradation of the herbicide [87]. This study also showed the histeretic characteristic of metamitron and other herbicides desorptions. Metamitron notably presents decreasing mobility and leaching risk with aging in soils.

Some studies focus more on the solvation properties of metamitron in surface and ground waters [8,9]. Photodegradation of this molecule solvated in surface waters is also an important research topic: metamitron can be rapidly photodegraded to its main metabolite, desamino-metamitron, in aqueous solution and the influence of soil particles presence or not on the photolysis rate have been evidenced [88]. Its photodegradation has also been studied depending on the solvents [89,90] and in presence of quantum sized titanium particles, giving different degradation products with a new reaction scheme in a photoreactor [91]. A study of its degradation in a sandy-clay soil, both in a laboratory and in a field using lysimeters, was conducted and leads to different half-life and thus different kinetic orders for each case [92].

Then, a “biologic” point of view can also be adopted in the sense that the molecule persistence, accumulation in plants, crops or animals [93,94] and its biodegradation by microorganisms commonly found in soils is a wide field of interest: metamitron was notably proven to follow a first order reaction kinetics [10].

For biodegradation in soils, it is interesting to note that some microorganisms use metamitron as a carbon source: it has been observed in pure cultures of *Arthrobacter* sp. DSM 20389, a common bacteria in soils ; where the amide bond in the triazinone ring undergo a hydrolytic cleavage [95]. Pure cultures of *Rhodococcus* sp. 0246b can also degrade the phenyl ring of metamitron to incorporate carbon in their cells [96]. Carbon dioxide is the ultimate product, with biogenic residues, of the C₆-metamitron in soil which can be interpreted as a complete detoxification [97,98].

This research field includes a very large panel of analysis tools and methods of detection: from high resolution Gas Chromatography coupled to Mass Spectrometry (GC-MS) [99,100], Gas Chromatography coupled to an Electron Capture Detector (GC-ECD) [80] and Liquid Chromatography-Mass Spectrometry (LC-MS) [8,100], to ¹³C-[97,98] and ¹⁴C-labeling to track the fate of metamitron and its metabolites after a possible degradation [96,101]. We can also cite High Pressure Liquid Chromatography

(HPLC) [10,102,103] and voltammetric [104,105], vibrational spectrometry [106] methods for metamitron detection in different media.

Metamitron is a molecule that has been used for several decades and is still very largely employed in Europe for its selective herbicide effect mainly on sugar beet crops. Even if its persistence is not so long, the frequent use of this substance raises questions on its consequences on environment. We just saw that a lot of experimental studies on metamitron's fate are available in literature, but to the best of our knowledge, investigations with a theoretical approach involving computational chemistry have not been done yet. Considering its spread utilization, the rich literature and the innovative aspect of an atomic scale study on this molecule, metamitron is a good candidate for this thesis.

The third pesticide molecule that has been chosen for the present work is fenhexamid, a very common fungicide.

I.E Fenhexamid

N-(2,3-dichloro-4-hydroxyphenyl)-1-methylcyclohexanecarboxamide ($C_{14}H_{17}Cl_2NO_2$), or fenhexamid (CAS 126833-17-8), is a molecule of the hydroxyanilide family used for its fungicide effect on a large variety of cultivated fruits or flowers like grapes and strawberries mainly, but also kiwi fruit, tomato, different kinds of berries, eggplant, sunflower or ornamentals. It is a foliar treatment, discovered in 1989 and first reported and marketed in 1998 [7], intended to protect plant leaves notably against *Botrytis cinerea* [107] and *Monilinia*, two fungi. However, for wine production, botrytized grapes may be desirable [108], depending on the wine that is aimed by the cultivation, that is why it is sometimes called “noble-rot”. But for grapes quality or other kinds of wine, it must be avoided as it modifies aromas and color before making the fruits go rotten. In case of wine production, it alters fermentation processes. *Botrytis cinerea* and *Monilinia* can also appear in postharvest storage period and cause important fruit losses. Thereupon, very recent studies on biological methods with antifungal effect gave very promising results against such diseases, thanks to volatile organic compounds derived from plants and microorganisms [109–112].

Fenhexamid is an efficient fungicide as it disrupts fungus membrane function and inhibits spore germination [7]. Figure I.6 presents the semi-structural formula of this substance and Table I.4 gives some important experimental data.

Fenhexamid molecule has a low aqueous solubility at 20°C (24.0 mg.L⁻¹ and high K_{ow}), is not persistent in soil according to the soil degradation values that are lower than one day, and it has two main known metabolites which are deschlorofenhexamid and

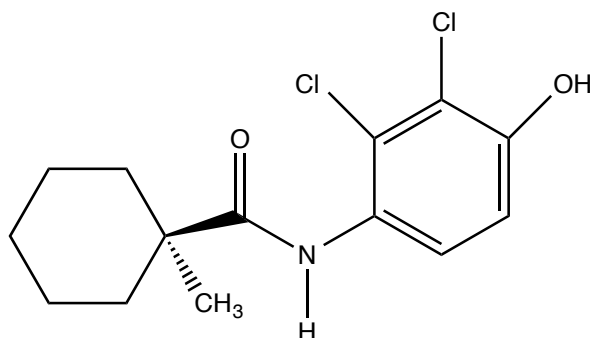


Figure I.6: Fenhexamid semi-developed chemical formula.

Molecular mass	302.20 g.mol ⁻¹
Solubility (water/20°C)	24.0 mg.L ⁻¹ (low)
Melting point	153.8 °C
Degradation point	230 °C
K _{ow} (pH 7/20°C)	3.24 × 10 ³
Soil degradation (DT50/aerobic)	0.43 days (typical)
	0.43 days (laboratory 20°C)
Main metabolites	Deschlorofenhexamid (C ₁₄ H ₁₉ NO ₂)
	Biphenyl-fenhexamid (C ₂₈ H ₃₂ Cl ₄ N ₂ O ₄)

Table I.4: Important experimental data for fenhexamid [7].

biphenyl-fenhexamid.

To the best of our knowledge, in spite of its wide usage in agriculture, the literature around the fenhexamid molecule is quite poor, especially about its fate in the environment. Studies, listed hereafter, focus more on detection of its presence in drinkable or ground water, wine and food.

Determination of fenhexamid presence have been investigated and evidenced in tomatoes [113], grapes [114] and especially in grape seed oil because of its good oil-solubility ($\log(K_{ow}) > 2.5$) [115], and in several fruits as well [116]. In 2012, analysis of fenhexamid [117] and its reactivity in water samples was investigated depending on their chlorine containing levels [118]. Fenhexamid is significantly reactive in water samples with low chlorine levels ($< 2 \mu\text{g.ml}^{-1}$) but follow a pseudo-first-order kinetics of degradation in excess of chlorine. This kind of issue is interesting for quality control of drinking water production for example. Concerning food quality, a recent paper presents addition of charcoal in grapes juice during the fermentation process as a solution to minimize fungicide residues in wine without penalising aroma and color [119]. Other solutions to remove fenhexamid residues are developed like purification of water by degrading the molecule

thanks to microorganisms [120]. The degradation products of this fungicide are also a field of interest, they have been studied for instance on silicon support under environmental conditions with or without UV radiation exposure (from the laboratory or from outdoor exposure), and some of its metabolites were evidenced [121].

Concerning soil investigations: recently an evaluation of the impact of fenhexamid on environment was done by controlling the presence of microorganisms of interest in soils [122]. On another side, amending vineyard soil with wine lees has proven to have an influence on fenhexamid adsorption on soil [123]. About fenhexamid interaction with clay, the behavior of fenhexamid in soil and water has been studied in an Italian paper of 2007 and showed that the fungicide has a good affinity towards smectite (31 %) and very good one with humic acid (73 %) [124]. It also describes fenhexamid as a molecule with a low persistence in soil if the microflora activity is present ($DT_{50} \approx 1$ day), without microorganisms it remains stable. Finally, this paper evidences the ability of the bacterium *Bacillus megaterium* to metabolize fenhexamid with a hydroxylation reaction of its cyclohexane ring, and the influence of pH over solvated fenhexamid stability. It shows better stability at acid pH than in neutral or alkaline media. Moreover, a study of 2009 shows the higher affinity of fenhexamid for adsorption on organo-modified clays (Cloisite 30B and 20A: clays containing interlayer organic cations with different functional groups), compared to adsorption on an unmodified clay, being a sodium montmorillonite (Na-montmorillonite) [125]. This paper shows how clays can be a solution to remove fenhexamid from water and trap this pesticide at high amounts.

Fenhexamid is a widely used fungicide employed in agriculture, particularly for vineyards. Despite its very short half-life time ($DT_{50} < 1$ day), its interaction with clay minerals is an interesting topic as it can have a significant reactivity in ground water, and thus in future drinkable water, depending on its surroundings (soil composition). In addition it showed a good affinity towards montmorillonite and has been studied as an alternative to purify water.


The forthcoming chapter presents soil which is a very complex system on all points of view. Giving first a global insight about its composition, properties and characteristics, its final aim will be to describe the montmorillonite clay mineral which is the type of crystalline solid chosen to model pesticide interaction with soil.

Chapter II

Soil

“If there is one way better than another, it is the way of nature.”

Aristotle

oil is a very complex system that undergoes permanent modifications in its composition. Thus, properties of a soil are dynamical data: physical, chemical and biological. Quoting R.Calvet, and according to Jenny’s approach in 1980: “soil is an ecosystem and must be considered as a natural body with its own organisation and its own history” [126, 127]. Let us try to clarify how soil can be described by considering its five main characteristics:

1. Soil is a porous material and can contain potentially mobile liquid and/or gas phase. Several *micro*- or *macro*- organisms can grow and live inside these media.
2. Soil composition and limits vary in the three directions of space: vertically, variations appear through the existence of layers with different characteristics and composition, and in addition with different thickness depending on the location. These layers are called “horizons” and are detailed in the upcoming section.
3. Soil characteristics depend on time as well: a lot of non-instantaneous phenomena, for instance water content or ionic composition of soil, evolve at various speeds and influence soil properties. These phenomena are very important in geology as well as in pedology.
4. Soil is an open thermodynamical system. Whatever the scale, a soil exchanges matter and energy with the surroundings. Therefore, defining a volume, a space and a time scale is mandatory to study soil.

5. Most of the time, phenomena occurring in soils are irreversible thermodynamically. It may be a source of error as models often consider them as reversible. Thus, experimental data are needed.

In the following sections, we will give a general description of soil organisation and main components at different scales, starting from a macroscopic scale (soil horizons, phases and granulometry), to the microscopic scale (atomic and mineral compositions).

For the macroscopic part, let us begin with the vertical organisation of soil: horizons, then the four soil phases and eventually the granulometric aspect.

II.A Horizons

Soil is made of layers with different compositions and properties called “horizons”, the thickness of these horizons can be quite different depending on the location on Earth. Figure [II.1](#) presents the six layers organisation of soil, here listed in deepness order, from the soil surface to the deepest layer:

- O horizon: this layer is found on the surface and is mainly composed by organic matter coming from dead plants and animals. For this reason, it is more commonly present under forests than in grassland areas.
- A horizon: this horizon can be referred as the “topsoil” and is the first layer containing minerals but also an important organic part. This is where most of the biological activity occurs, by the presence of worms, insects, fungi and bacteria. A high amount of plant roots is also found in this layer.
- E horizon: generally occurs between A and B horizons but is not always found in soils. Called “E” for “eluviated”, this zone undergoes an important leaching of clay, iron and aluminium oxides, leaving resistant minerals concentrated in E.
- B horizon: leached minerals from E horizon ends up in B horizon underneath. Therefore, leached minerals accumulates there, especially in humid regions. This horizon is commonly called “subsoil” and is thus mainly mineral but also contains organic materials coming from the leaching of the above horizons. This process is called illuviation or illuvium: the displacement of material from one layer to another one through rainwater flowing. The B layer is less accessible to plant roots.

- C horizon: it is the last layer before the bedrock and is thus mostly composed of parent material coming from it (D horizon) but slightly altered. This layer is not affected by water, mineral or soil particles movement.
- D horizon: the bedrock, its composition is only mineral, the parent material that can be found in C horizon comes from here.

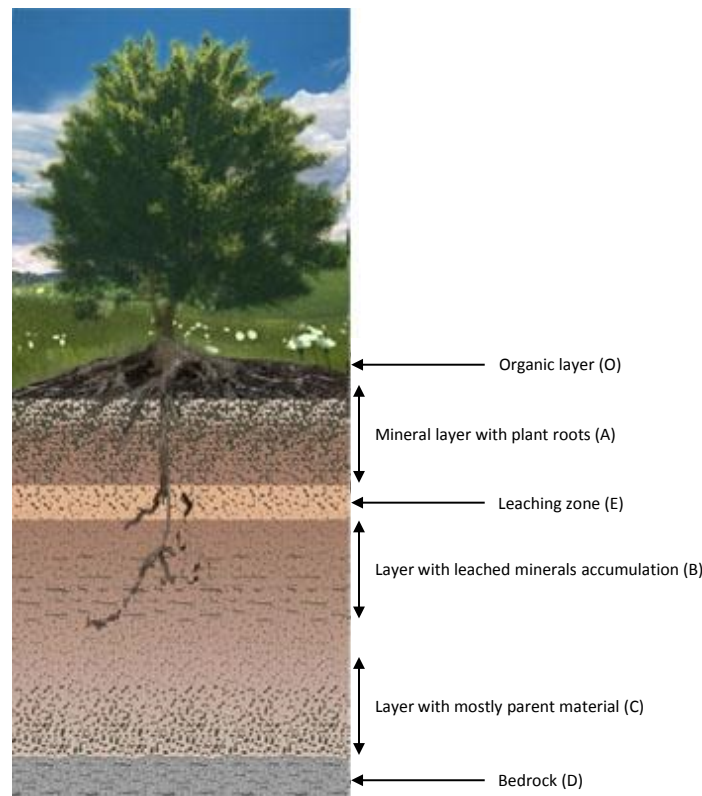


Figure II.1: Soil horizons (picture source: <http://www.aucoeurdelarbre.ca/fr/hors-sentier/section-profs/module4-html.php>).

In spite of the “organised” structure of soil, the compositions and properties of the layers are not completely different. In particular, A horizon is a great meeting zone for different kind of phases, chemical substances, living organisms, ...

The next section will give an overview on the soil composition.

II.B General Soil composition

Soil has a layered organisation, however it may be described as a system composed of four phases:

1. The gas phase with a composition very similar to air.
2. The liquid phase, mainly water, with a wide variety of solvated chemical species, also called “soil solution”.
3. The organic phase includes all bioorganisms in soil: microscopic and macroscopic, living or dead animals and vegetals.
4. The solid phase, or inorganic phase, made of all kinds of minerals.

In a soil, the four phases are not separated but highly interact and exchange, making a whole complex system with a wide range of physical and chemical phenomena. The relative proportions of each phase vary, depending on mechanical constraints and hydric state.

The gas phase

Also called the “soil atmosphere”, the gas phase contained in soil has a comparable composition to air but may change depending for example on deepness and on surrounding biological activity.

The soil solution

The liquid phase has a very irregular composition as it is mainly water. A great diversity of substances are found in that “solution”, organic or inorganic molecules, ionic or neutral species... The concentrations of these species depend on several phenomena: called “source phenomena” if they increase the concentrations of given substances (dissolution, desorption,...), and “well phenomena” if they lower their concentrations (precipitation, adsorption,...). In the soil solution, two families of species are found: micro-elements with a concentration below 1 mmol.m^{-3} , and macro-elements, more concentrated and thus in important quantity in soil. The main chemical species being HCO_3^- , NO_3^- , Na^+ , Mg^{2+} , Si^{4+} , SO_4^{2-} , Cl^- , K^+ , Ca^{2+} and O_2 . Obviously H^+ and OH^- are also found depending on the pH of water.

The organic phase

The organic phase can constitute from 1 % to 10 % of soil mass. Its physics and chemistry contributes to soil structure stability.

There are two categories of organic species in soil:

- Living organisms which can be vegetal (plant roots) or animal: microorganisms (bacteria, fungi or algae) ; microfauna (protozoa) ; mesofauna (dust mites or nematodes) ; and macrofauna (worms or insects).
- Dead organic matter including a very large variety of molecule and substances: from very simple isolated molecules like carboxylic acids or amino acids, to bigger molecules like proteins, lipids or molecular aggregates.

II. B.1 The inorganic phase or mineral matter

The inorganic phase is composed by minerals of different natures depending directly on the kind of bedrock beneath. In this subsection, we will globally describe the mineral matter of soils beginning with the general composition in terms of chemical elements, following with the definitions of the two families of minerals (primary and secondary) and some general properties about the stability of minerals.

II. B. 1.α Elementary composition

The two main chemical elements present in soil are by far oxygen and silicon, followed by aluminium in a relatively important quantity, then different cations. Data gathered from American soil [4] represent the elementary soil composition quite well, they are reported on Figure II.2. Considering their average concentration in mg.kg^{-1} , oxygen is the main element in soil with 490,000 mg.kg^{-1} , silicon is second with 310,000 mg.kg^{-1} , then come aluminium (47,000 mg.kg^{-1}), iron (18,000 mg.kg^{-1}) and a series of alkaline or alkaline earth metals: potassium (15,000 mg.kg^{-1}), calcium (9,200 mg.kg^{-1}), sodium (5,900 mg.kg^{-1}), magnesium (4,400 mg.kg^{-1}) and finally the least present element among those with a rate above 1,000 mg.kg^{-1} is titanium (2,400 mg.kg^{-1}). Other elements can be found with very low concentrations (between 0.5 and 60 mg.kg^{-1}) like lithium, beryllium, vanadium, chromium, cobalt or nickel.

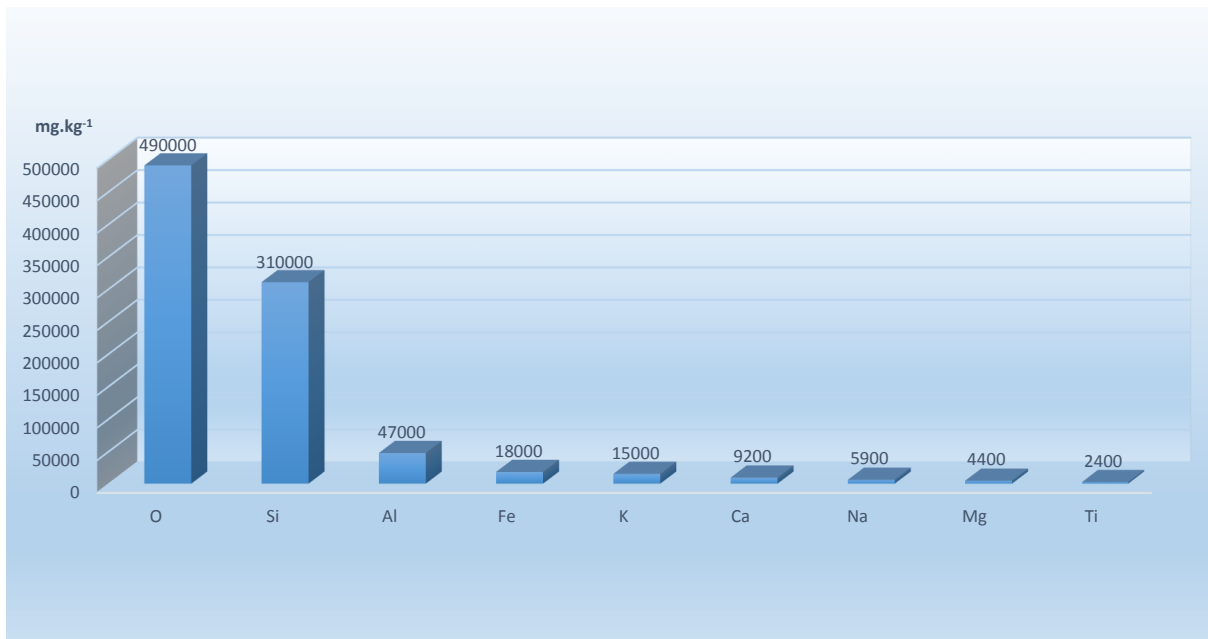


Figure II.2: Example of the elementary composition of an American soil [4] expressed as concentrations in milligrams of element per kilogram of soil.

II. B. 1.β Mineralogical composition

Minerals can be classified in two families:

- **Primary minerals**

This first family gathers minerals found in soil but originating from the bedrock (D horizon). These primary minerals are more or less fragmented but very slightly or even not altered. Their crystalline structure and elementary composition make them more or less sensitive to chemical reactions or phenomena which could transform them in other kind of minerals (secondary ones). Among them we can cite epidote, tourmaline, zircon or rutile which are some of the most resistant to alterations and are usually intact in soil. More vulnerable minerals such as quartz, feldspar, mica, amphibole, pyroxene and olivine give secondary minerals by chemical mechanisms.

- **Secondary minerals**

Secondary minerals are produced by alteration of the primary minerals and also by their spontaneous precipitation. Therefore, their abundance depends a lot on the composition of the bedrock and of pedogenesis process. This second family of minerals is very wide, let us cite kaolinite, smectite (pyrophyllite and montmorillonite are smectites), vermiculite, chlorite, allophane, imogolite, gibbsite, goethite, hematite, ferrihydrite, birnessite, calcite or gypsum.

II. B. 1.γ Mineralogical structure and general properties

Soil minerals are ionic solids, as the main chemical elements in soil are ionic oxygen (O^{2-}), silicon (Si^{4+}) and aluminium (Al^{3+}), the structure of soil mineral matter is mainly composed of Si–O and Al–O ionic bonds. The structure and stability of minerals are characterized by three important parameters: the ionic electric charge, the distances between ions regarding ionic radii, and the coordination number being the number of anions surrounding each cation in a crystalline structure. At a given coordination number (coord), ionic radius r_{ionic} depends on the valence of the ions: the bigger is the valence, the shorter is the ionic radius, for instance $r_{ionic}(Li^{+}_{coord6}) > r_{ionic}(Mg^{2+}_{coord6}) > r_{ionic}(Al^{3+}_{coord6})$. However, for a given valence, the bigger is the coordination number, the bigger is the ionic radius: $r_{ionic}(Al^{3+}_{coord6}) > r_{ionic}(Al^{3+}_{coord4})$. A coordination number of 4 corresponds to a tetrahedron (T) of anions around a cation, and a coordination of 6 is an octahedron (O) (Figure II.3). This structure organisation in solids follows the Pauling's rules.

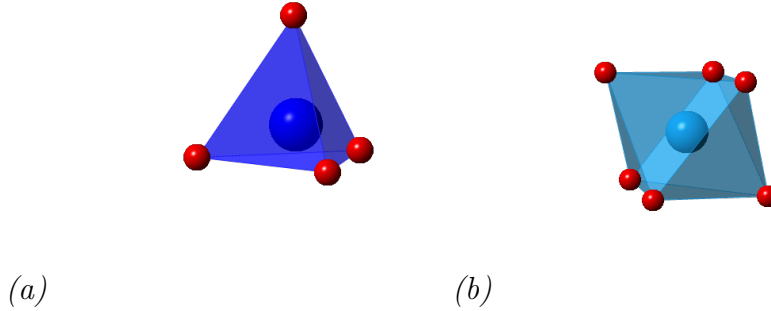


Figure II.3: Representation of cations (a) in coordinations 4 (tetrahedron T, in dark blue) and (b) in coordination 6 (octahedron O, in light blue) with anions (red).

General characteristics of soil have been presented regarding its layered organisation, elementary and mineral compositions. The present thesis focuses on the interaction between pesticides and montmorillonite mineral. It has been chosen as it is the most abundant smectite and is thus widespread on Earth. Moreover, it presents agricultural and industrial interesting applications, due to the clay swelling property which makes possible the absorption and adsorption of hydrated substances.

The next section will start with a general introduction about clay minerals, followed by a description of the structure and properties of montmorillonite.

II.C Clay minerals

The term “clay” usually has two different meanings that could be confusing: in granulometry^{*}, “clay” refers to a family of grain size (below 2 μm) ; while in mineralogy, it refers to a part of the phyllosilicates, a subclass of silicate minerals. However, some clay minerals are not phyllosilicates like quartz or feldspar, or not even silicates.

On an agricultural aspect, clay soils have always been known as good and fertile but hard to work due to their mechanical properties. Notably, clay soils are appreciated for high water retention capacity due to swelling ability which allows to minimize irrigation. First studies on clay minerals are the work of Henri Le Châtelier in 1887 named “About the action of heat on clays” [128] and from Lowenstein in 1909 [129]. Later, the first X-ray analysis of clay minerals were conducted by Hedding, a Swedish researcher in 1923 ; and Rinne, a German researcher in 1924. They found the crystalline organisation of clays and discover that they do not have a wide range of characteristics. Around the same period, at the United States Geological Survey (USGS), Byers, Ross and collaborators determine mineralogical compositions of different clay materials. Structures of smectites have been proposed by Hofman, Endell and Wilm in 1931. The British researcher MacEwan studied reactions of organic compounds over clay minerals.

In general, the very wide applications of clay materials in industry, agriculture or even art lead clays to be a subject of great interest within the scientific community over the decades: in agronomy, geology, mineralogy, physics, chemistry... An international association has even been created in 1948: the Comité International Pour l’Etude des Argiles (CIPEA), which became the Association Internationale Pour l’Etude des Argiles (AIPEA) in 1963 [130]. Some kind of clays, like montmorillonite, also have swelling properties, especially regarding water, which made them very interesting for industrial products: diapers or cat litters ; but also in the pharmaceutical field where clays are used against dehydrating diseases like gastroenteritis. A wide topic of interest around clay minerals nowadays also concerns waste storage, particularly for nuclear waste [131–133].

^{*}Granulometry is a type of soil analysis regarding grain size. It is A. M. Atterberg (1846-1916) who first proposed to separate mineral particles considering their apparent diameter and established the limits of each granulometric domain, these limits have been adopted by the International Soil Science Society [126] and are the following: for particles with an apparent diameter below 2 mm, three granulometric classes have been identified: clay (< 2 μm), silt (2 μm - 50 μm) and sand (50 μm - 2000 μm).

II. C.1 Montmorillonite and other clay minerals

Montmorillonite belongs to the smectite family, which is a part of the phyllosilicates group. Let us first present phyllosilicates, then smectites before describing montmorillonite and see why it has been chosen for the present study. The following sections are largely inspired from the book of Raoul Calvet [126].

II. C. 1.α Phyllosilicates

Phyllosilicates is a group of minerals that are, ideally, a stacking of a continuous sheet of oxygen tetrahedra (T) on top of a continuous sheet of oxygen octahedra (O). Both kind of polyhedra are constituted with O^{2-} anions and are occupied by a cation in the center which can be Si^{4+} , Al^{3+} or Fe^{3+} for T and Al^{3+} , Fe^{3+} , Fe^{2+} or Mg^{2+} for O typically. Ca^{2+} , Na^{+} and K^{+} , in spite of their abundance in soils, are too large to occupy T or O centers. Figure II.4.(a) displays the shape of a single tetrahedron of oxygen anions with a Si^{4+} cation occupying its center, and (b) and (c) the organisation of a T sheet. Each tetrahedron shares one of its three corners (or oxygen ions) with one of the neighboring tetrahedra, these oxygens are called basal oxygen atoms O_b . The fourth oxygen of each tetrahedron is free and called apical oxygen atoms O_a . This web of tetrahedra forms an “infinite” two-dimensional hexagonal mesh pattern in the a , b crystallographic directions. From the c axis, the tetrahedra are organised in hexagons (Figure II.4.(c)).

Beneath the T sheet is found the O sheet. Each octahedron shares edges with adjacent ones. The O sheet can present two different topologies: indeed, OH functions present in octahedra can have positions along one edge (*cis*-oriented octahedron) or along the diagonal (*trans*-oriented octahedron) as on Figure II.5.(c). OH groups are in opposite positions on both sides of the vacant octahedra, this example is a *trans-vacancy*.

The free corners O_a of all tetrahedra point to the same side of the sheet and connect T and O sheets to form a common plane with the octahedral anionic position labelled O_h when bearing a hydrogen atom. O_h anions lie near the center of each T sixfold ring, but are not shared with tetrahedra.

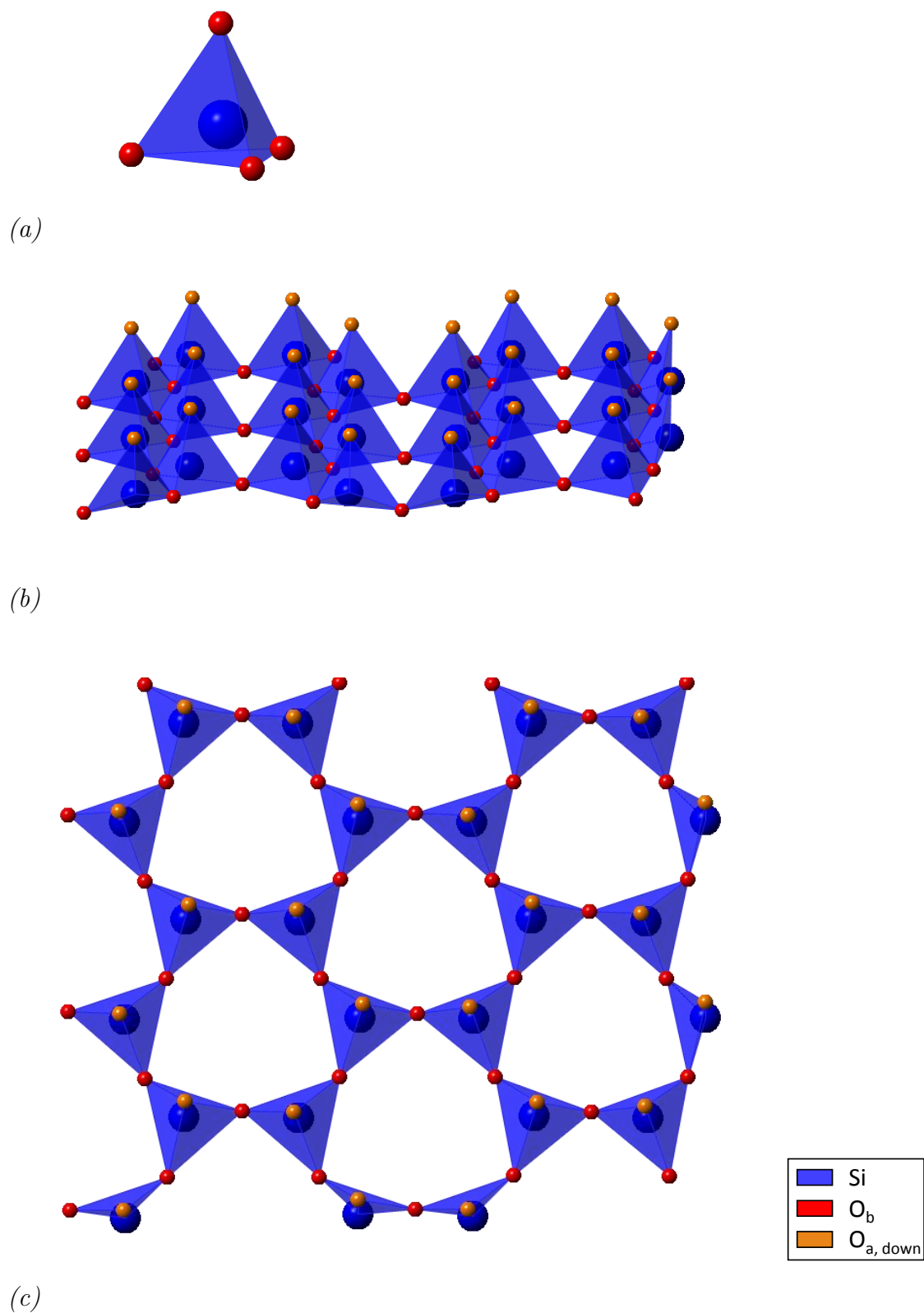


Figure II.4: Isolated O^{2-} tetrahedron occupied with a Si^{4+} cation (a), single tetrahedral sheet (T) represented in the xy plane (b) and viewed from the z axis (c). Silicon cations and their associated tetrahedra (SiO_4) are in dark blue. Each basal oxygen O_b (red) is shared between two tetrahedra, apical oxygens $\text{O}_{a,down}$ (orange) point towards the same direction and will be shared with the octahedral sheet above.

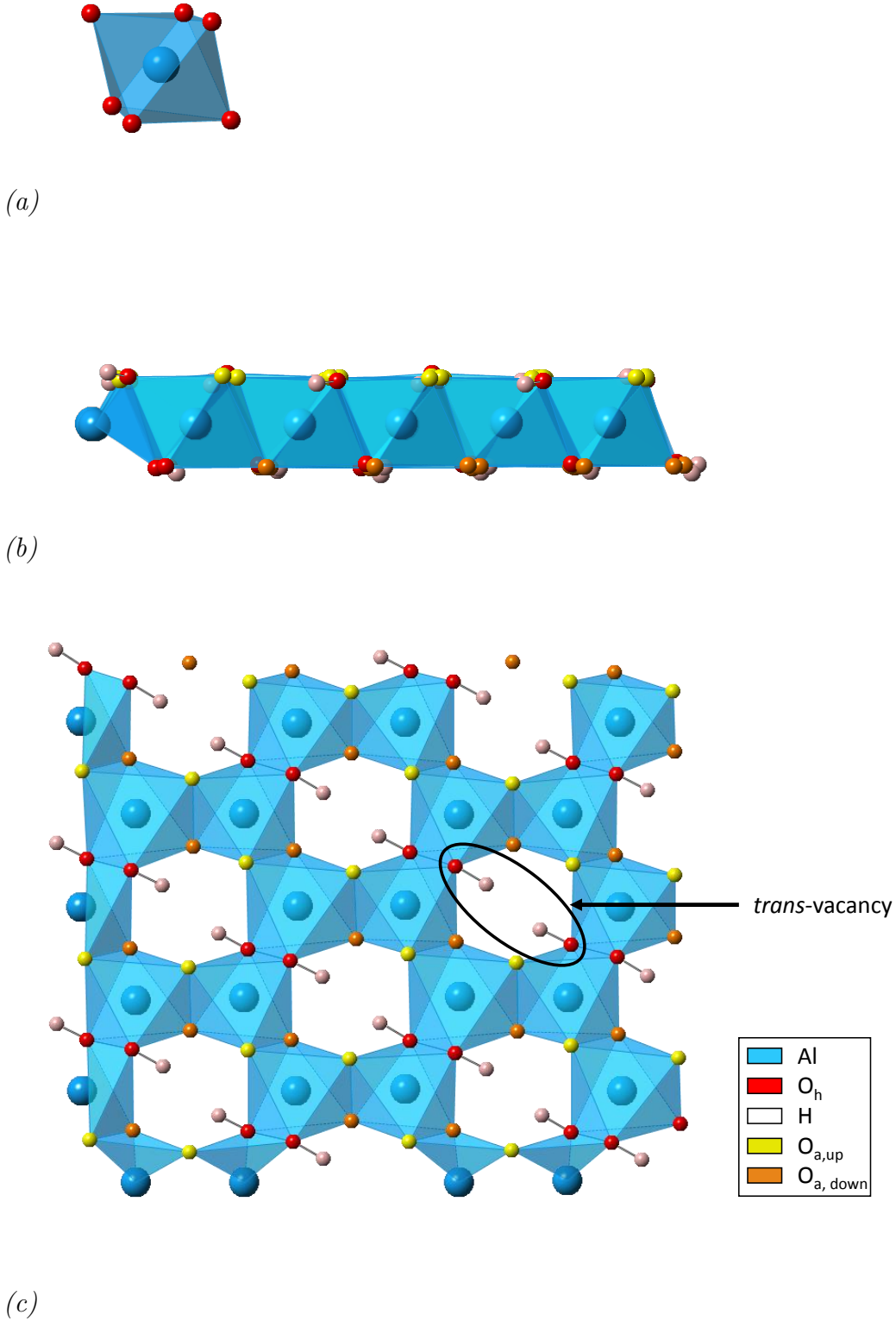


Figure II.5: Isolated O^{2-} octahedron occupied with an Al^{3+} cation (a), single octahedral sheet (O) viewed from the y axis (b) and from the z axis (c). Aluminium cations and their associated octahedra (AlO_6) are in light blue. Oxygens O_h (red) bearing hydrogen atoms (white) are not shared and belong to the O sheet only. In this example, O_h atoms are arranged on the diagonal corresponding to the *trans*-vacancy topology. Apical oxygens $O_{a,down}$ (orange) are shared with the T sheet below, and apical oxygens $O_{a,up}$ (yellow) are shared with the T sheet above.

Mineral groups: different stacking

The general structure of phyllosilicates have been described, however, three different stackings of these sheets are possible, leading to three groups of minerals (the examples in parenthesis are only clay minerals):

- 1:1 minerals (or T/O): as described above, a sheet of tetrahedra is associated with an octahedral one. The thickness of the 1:1 layer is approximately 0.7 nm. This group gathers the kaolin group (kaolinite, dickite, nacrite, halloysite, endellite, odinite, ...) and the serpentine group (lizardite, antigorite, chrysotile, amesite, carlosturanite and greenalite, ...).
- 2:1 minerals (or T/O/T): an octahedral sheet is sandwiched between two opposing tetrahedral sheets, this makes a layer around 1.0 nm thickness. Smectite (montmorillonite for instance), pyrophyllite, vermiculite, illite, talc, mica or chlorite belong to this group.
- 2:1:1 minerals (or T/O/T/O): two octahedral sheets associated with two tetrahedral sheets, with a thickness around 1.4 nm.

Diocahedral and trioctahedral minerals

In phyllosilicates, a diocahedral mineral is when $\frac{2}{3}$ of the octahedral sites are occupied by cations within the O layer. A mineral is trioctahedral when all of them are occupied.

II. C. 1. β Smectites

Montmorillonite, a 2:1 phyllosilicate, is a diocahedral smectite of general formula: $(M_{x+y}^{+}.nH_2O)(R_{2-y}^{3+}R_y^{2+})(Si_{4-x}Al_x)O_{10}(OH)_2$ such as beidellite, nontronite and volkonskoite as well, where x and y are respectively the layer charge resulting from tetrahedral and octahedral sites, R^{2+} and R^{3+} are respectively the divalent and trivalent octahedral cations, and M^{+} is a monovalent interlayer cation.

Exchangeable cations in the interlayer

One of the main properties of smectites is to contain water in the interlayer space, in which exchangeable cations are solvated. In the previous general formula, the interlayer cation was considered as monovalent (Na^{+} , K^{+} , ...), but it can also be divalent (Ca^{2+} , Mg^{2+} , ...). The interlayer space is found between series of T/O/T sheets. Cations are

situated in the interlayer as compensating positive charges towards the negatively charged clay layer, as isomorphic substitutions occur in the T or O sheets.

Isomorphic substitutions

Isomorphic substitutions occur in both T or O sheets: in T centers, Si^{4+} can be replaced by Al^{3+} up to 15 % of the T sites ; in the O sites, substitutions by Mg^{2+} , Fe^{2+} , Zn^{2+} , Ni^{2+} or even Li^{+} (rarely) may be found, as in Figure II.6. These substitutions are called “isomorphic” in the sense that in spite of the changes in charge and nature of the cation, the type of O^{2-} polyhedron (T or O here) is kept, and thus the coordination of the cation as well. Most of the time, tetravalent cations are substituted by trivalent ones ($\text{Si}^{4+} \rightarrow \text{R}^{3+}$) and trivalent cations by divalent ones ($\text{Al}^{3+} \rightarrow \text{R}^{2+}$). A complete replacement of aluminium cations by another kind would correspond to a specific smectite mineral: for instance, a smectite where all Al^{3+} are substituted by Mg^{2+} cations is a saponite ; with only Fe^{2+} in the Oh sheet, it is a nontronite...

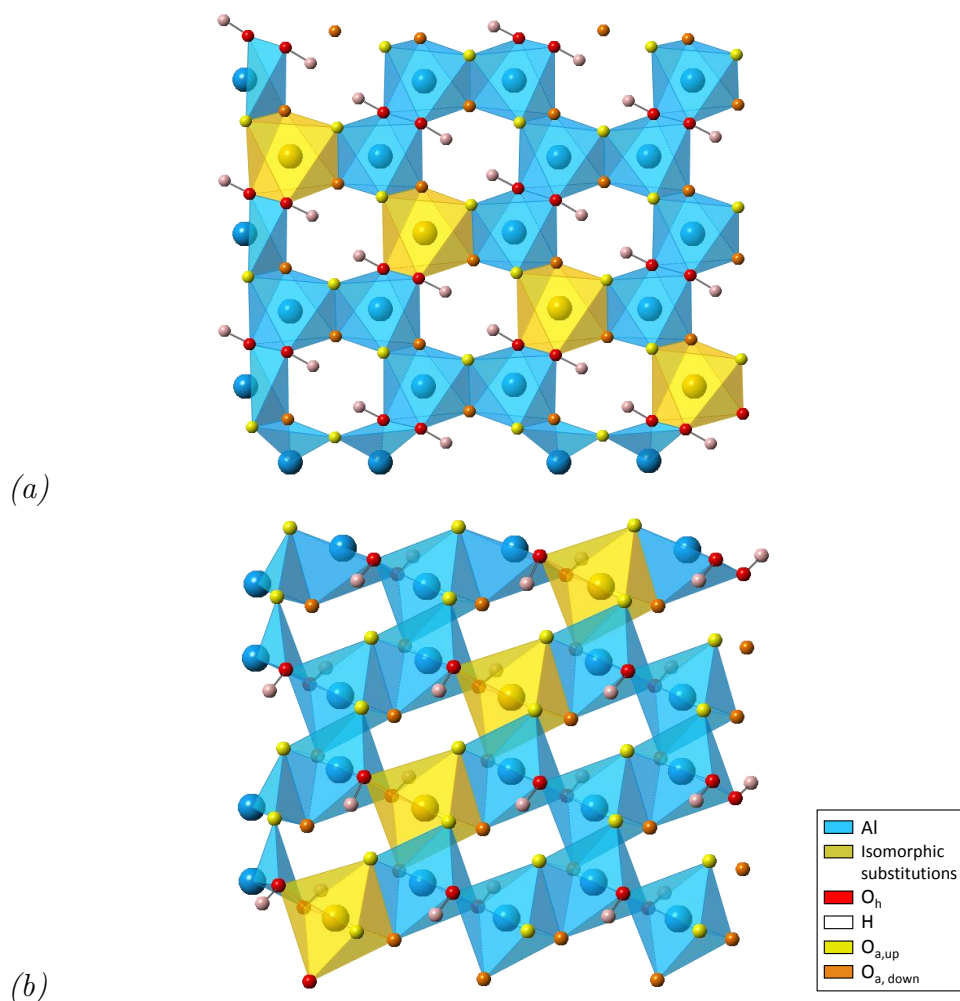


Figure II.6: Isomorphic substitutions (dark yellow) of 4 Al^{3+} in octahedral sites of the O sheet.

The effect of isomorphic substitution on singly-charged interlayer cation hydration (Li^+ , Na^+ and K^+) in montmorillonite has been investigated considering three different kinds of substitution: tetrahedral, octahedral and both [134]. Hydration (water-cation affinity) and adsorption of the cation on the surface (cation-surface affinity) are competitive phenomena directly influenced by the cation nature and the type of substitution. Indeed the negative charge repartition over the surface oxygens is different regarding the substitutions, and modifies the affinity of the cation towards the surface and thus hydration. Li^+ has the best binding energy with water, then comes Na^+ and finally K^+ ; this order is reversed when the cations interact with a montmorillonite surface. Montmorillonite with K^+ as compensating cation (K-montmorillonite), has a lower swelling ability than Na- or Ca-montmorillonite.

II. C. 1. γ Montmorillonite

For the present study, a montmorillonite clay mineral has been chosen and modeled as it is the most abundant smectite on Earth. A very rich literature can be found about montmorillonite, and this mineral presents interesting properties regarding swelling ability, usable for waste storage (notably nuclear waste) and organic catalysis for pharmaceutical applications, water purification and ecology. The general chemical formula of montmorillonite is $(\text{M}_y^+.n\text{H}_2\text{O})(\text{Al}_{2-y}^{3+}\text{Mg}_y^{2+})\text{Si}_4^{4+}\text{O}_{10}(\text{OH})_2$.

In this thesis, montmorillonite will be modeled theoretically. However, experimentally, the X-ray structure of the Ca-montmorillonite model we will consider, is not available in literature. Consequently, the model that has been built for simulations in the following chapters is inspired from the pyrophyllite X-ray structure given in the work of Wardle *et al.* [135], with the following unit cell parameters: $a = 5.161 \text{ \AA}$, $b = 8.957 \text{ \AA}$ and $c = 9.351 \text{ \AA}$; $\alpha = 91.03^\circ$, $\beta = 100.37^\circ$ and $\gamma = 89.75^\circ$. Indeed, pyrophyllite and montmorillonite have similar structures, except that isomorphic substitutions do not occur in pyrophyllite. Then, Al^{3+} cations have been substituted with Mg^{2+} in order to obtain a Ca-montmorillonite mineral in which more than 15 % of substitutions are present in the O sheet, and where the charge defect is compensated in the interlayer with calcium cations, the total system being neutral. Further details on the modeled montmorillonite and the computational cell that has been used for simulations are given in Chapter IV [136]. Figure II.7 displays a layer of the model of Ca-montmorillonite that has been employed for this thesis.

Isomorphic substitutions accompanied with compensating cations in the interlayer space are typical characteristics of montmorillonite. As $\frac{2}{3}$ of O centers are occupied, *cis*- and *trans*- vacancies occur as on Figure II.6. In 2001, Emmerich *et al.* proposed an experimental method to switch from a Na^+ -saturated *cis*-vacant montmorillonite to a

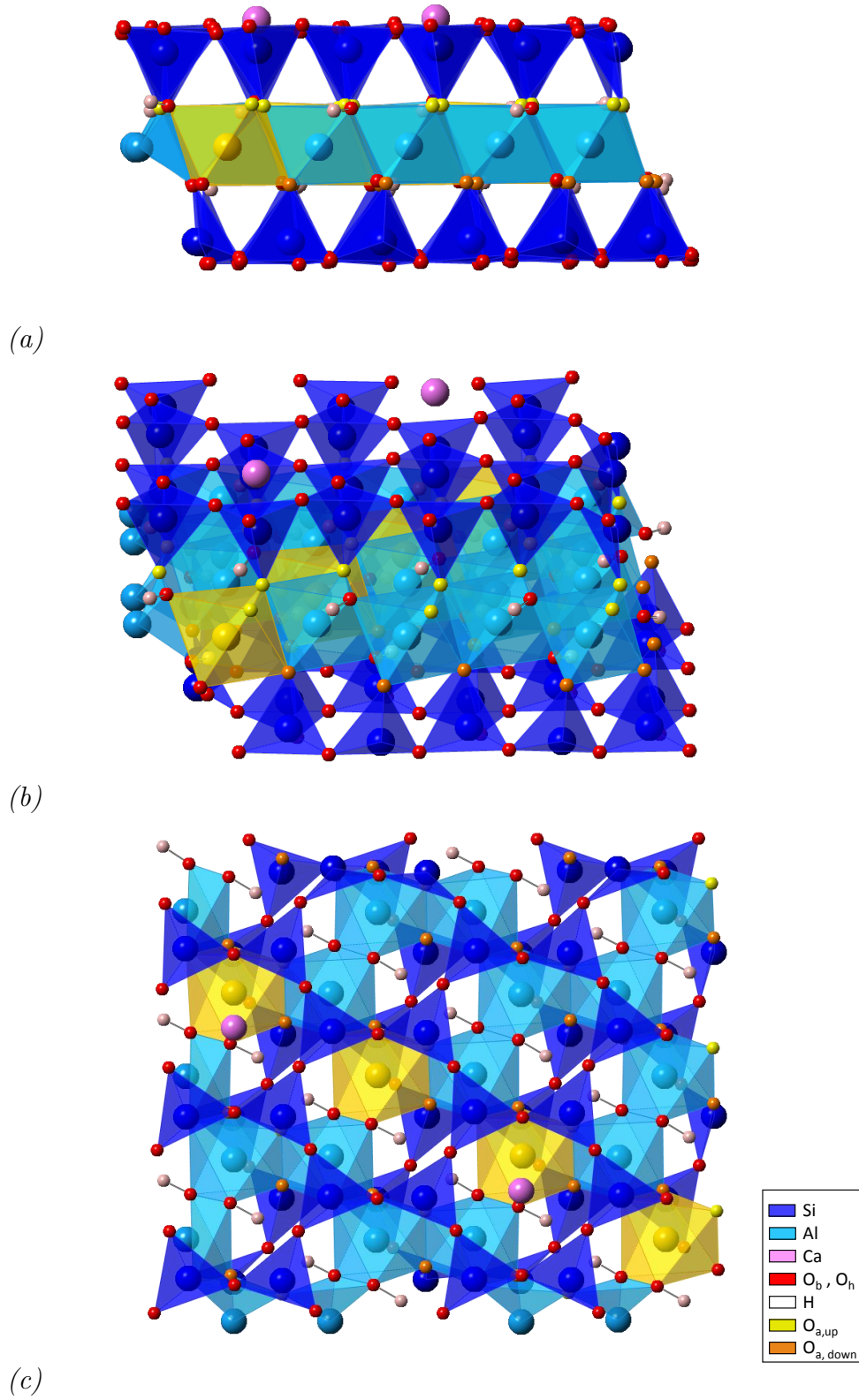


Figure II.7: Montmorillonite surface viewed from the y axis (a), from the side (b), and from the z axis (c). This montmorillonite contains 4 substitutions of Al^{3+} by Mg^{2+} in the O sheet (dark yellow octahedra). Two Ca^{2+} cations (magenta) compensate the charge defect and are situated above substitutions, and above centers of ditrigonal ring of basal oxygens.

trans-vacant one and studied both physico-chemical properties [137]. A paper in 2005 showed that *cis*-vacant octahedral sequences corresponds to a $C2/m$ symmetry, when a *trans*-vacant sequence has a $C2$ symmetry, and these two symmetries can be found in a same sample [138]. Another issue with montmorillonite and smectites structure is the unknown position of the hydroxyl groups (OH) within the structure. Tunega et al. in 2007 showed by a theoretical approach the slight influence of *cis*-OH and *trans*-OH vacancies, depending in the chemical nature of substitutions, on the total energy of the structure in smectites [139]. It also evidenced that structures with substitutions in the O sheet are generally more stable in *trans*-coordination.

A lot of studies have been conducted for the comprehension of montmorillonite swelling and interlayer substance transport and retention processes for environmental issues. Indeed, an interesting property of montmorillonite is its ability to swell and absorb an important quantity of water in interlayer space: the more montmorillonite is hydrated, the more the interlayer opens and the more it hosts water molecules, and reciprocally until a critical distance. In 2008, Salles and coworkers studied experimentally the impact of the interlayer cation nature, of the hydration state of montmorillonite (and thus the interlayer opening), and of the isomorphic substitution positions on the cation displacement in the interlayer by conductivity measurements [140]. More recently, Salles also published on the influence of these parameters on the diffusion coefficients of cations in a montmorillonite saturated in alkali cations, with the combination of complex impedance spectroscopy measurements and water adsorption isotherms [141]. Montmorillonite swelling and interlayer cation behavior has also been studied by means of theoretical methods and in comparison with experiments. Rotenberg published on cation exchange in clay by mean of theoretical simulations and microcalorimetry experiments [142, 143]. The swelling properties of Ca^{2+} and Na^{+} -montmorillonite has been investigated with Monte-Carlo theoretical simulations compared with X-ray experiments [144]. It gives rise to a discussion on the importance of swelling depending on the method and conditions, and on the cations, involving ion-ion correlation in Na^{+} -, Ca^{2+} -, or mixed-montmorillonite. A comparison between the swelling properties and behavior of Na^{+} -, Mg^{2+} - and mixed $\text{Na}^{+}/\text{Mg}^{2+}$ - montmorillonites has also been studied and showed the predominant influence of the interlayer cation on the swelling by means of Monte-Carlo calculations [145]. As well, the importance of considering the dispersion interactions in Density Functional Theory (DFT) calculations has been shown in the water-surface interaction of pyrophyllite and montmorillonite, and thus its influence on the interlayer distance [146]. A lot more studies have been conducted on the behavior of interlayer cations related to swelling in montmorillonite through numerical simulations and electronic structure studies [147]: importance of H-bonding in the hysteresis swelling process [148] ; mechanics of the structure depending on interactions between the cations,

the surface and water at different hydration levels through Molecular Dynamics (MD) study [149, 150] ; influence of three types of isomorphic substitutions (T, O and O-T types) on the hydration of interlayer alkali cations with MD simulations [134] ; hydration of particular cation in the interlayer (Na^+ , Mg^{2+} , Ca^{2+}) and even of more exotic ones (Sr^{2+} and Ba^{2+}) through DFT [151] ; and a study of layer structure through $^{23}\text{Na}^+$ theoretical NMR by means of DFT revealing sensitivity to isomorphic substitutions within the layer of a dehydrated montmorillonite [152].

Another wide field of investigation about montmorillonite is the study of its possibility towards catalysis and adsorption processes: adsorption of RNA/DNA bases on a Na-Montmorillonite have been investigated to understand RNA polymerization with DFT, and shows the importance of dispersive interactions and H-bonds between the bases and the surface [153, 154]. Influence of CO_2 introduction (CO_2 storage) [155] and fate of cytosine [156] in a watered interlayer of a Na-montmorillonite through MD simulations have been studied. As well, the adsorption of light organic molecules (water, ethanol, toluene, ...) on a model of dry-smectite clay, based on the Kunipia-F clay model [157] ; and the adsorption of dinitrophenol herbicides in aqueous systems have been considered to understand their interactions with montmorillonite [158]. As we saw in Chapter I, atrazine interaction with clay minerals has been largely investigated, as well as other pesticides such as simazine, metribuzin [159] and 2,4-dichlorophenoxyacetic acid [160]. Getting closer to the methodology of this thesis, Car-Parrinello MD was employed to predict solvation of hydronium in a hydrated Na-montmorillonite with one, two or three layers of water molecules in the interlayer space [161].

This chapter presented a brief description of soil general composition, then the structure of soil mineral matter has been emphasized. Montmorillonite has been described as it is the chosen mineral for the present thesis, and an overview of the wide available literature about it has been given. The following chapter is a brief development of the theoretical methods employed for the computational simulations and study of the three selected pesticides and the Ca-montmorillonite model.

Chapter III


Theoretical methods

*“Erwin with his psi can do calculations quite a few.
But one thing has not been seen: just what does psi really mean ?”*

Erich Hückel

“Anyone who is not shocked by quantum theory has not understood it.”

Niels Bohr

 heoretical chemistry is a branch of science that proposes methods to describe matter at an atomic or molecular level. Two types of theories can be employed: wavefunction based methods (Hartree-Fock and post-Hartree-Fock), and density based methods (Density Functional Theory). Depending on the nature and size of the system, these methods are more or less accurate and their main issue is their computational cost.

The aim of the present thesis is to study pesticide interaction with soil mineral matter. Atrazine, metamitron and fenhexamid are organic molecules while pyrophyllite and montmorillonite are solids. These systems contain from twenty to a few hundred atoms and because of their different properties and size, molecules and solids will not be treated with the same methods. This chapter presents the theoretical basis and approximations that have been employed in the present work.

III.A Electronic structure

III. A.1 Wavefunction and Schrödinger equation

In the early 20th century, De Broglie emitted the hypothesis that any kind of matter behaves like a wave. This concept is the wave-particle duality: any elementary particle, photon or electron for instance, may be described both as a particle and as a wave. Then, the wavefunction postulate was introduced in quantum mechanics. It establishes that for any system of particles, there is an associated wavefunction $\Psi(\mathbf{r}, t)$ dependent of time t and vector \mathbf{r} , the position of the particle of coordinates x, y, z . In this work, wavefunction will be employed for electrons only and without time dependency. Therefore, it will only be a function of space: $\Psi(\mathbf{r})$. Quantum mechanics postulates that if the wavefunction of a system is known, all its properties can be determined. To represent a physical system, the wavefunction has to respect a few features:

- $\Psi(\mathbf{r})$ has to be a solution of the Schrödinger equation, described hereafter (III.2).
- $\Psi(\mathbf{r})$ must be continuous and differentiable, $\frac{\partial \Psi(\mathbf{r})}{\partial \mathbf{r}}$ as well.
- The product of $\Psi(\mathbf{r})$ with its conjugate $\Psi^*(\mathbf{r})$ gives electrons probability density of presence. Over the whole space, it is equal to 1 as the wavefunction is normalized:

$$\int \Psi^*(\mathbf{r})\Psi(\mathbf{r})d\mathbf{r} = \int |\Psi(\mathbf{r})|^2 d\mathbf{r} = 1 \quad (\text{III.1})$$

In a paper of 1926 [162,163], Erwin Schrödinger gave a new form to quantum chemistry by introducing the fundamental time-independent equation:

$$\hat{H}\Psi(\mathbf{r}) = E\Psi(\mathbf{r}) \quad (\text{III.2})$$

establishing that a Hamiltonian operator \hat{H} applied to the wavefunction $\Psi(\mathbf{r})$ of a system, gives eigenvalues E (the total energy of the system), and eigenvectors $\Psi(\mathbf{r})$. Therefore, solving the Schrödinger equation allows to know the wavefunction of the system and thus all its properties. This is why the main purpose of theoretical chemistry is to solve this equation.

In the following, we will see several approximations and methods to solve this very complicated problem.

III. A.2 The Born-Oppenheimer approximation (BO)

Atoms have two components: a nucleus and one or several electron(s) around it. An atomic nucleus is composed by protons and neutrons weighting respectively $m_p = 1.673 \times 10^{-27}$ kg and $m_n = 1.675 \times 10^{-27}$ kg. Electrons are way lighter than protons and neutrons: $m_e = 9.109 \times 10^{-31}$ kg making the nucleus more than 1800 times heavier than each electron separately. This important difference allows to say that the motion of electrons is immensely faster than the movement of nuclei. The Born-Oppenheimer approximation (BO) [164] thus establishes that nuclei may be considered as fixed in space, while electrons movement is instantaneous. It is also called the adiabatic approximation in the sense that there is no energy exchange between nuclei and electrons. It simplifies a lot the theoretical treatment of chemical systems, especially for solving the Schrödinger equation statically, but also for dynamical simulations.

This approximation works very well and makes calculations computationally less expensive. Nevertheless, it may present a limitation for the treatment of hydrogen atoms, in which the difference between the masses of the unique electron and the nucleus is not as important as in heavier atoms.

III. A.3 Atoms and molecules: interacting electrons and nuclei

Atoms and molecules can be seen as systems of electrons, noted i , in interaction with atomic nuclei, noted I . Using this notation, the hamiltonian operator, is written as the sum of the kinetic \hat{T} and potential \hat{V} energy operators of the system:

$$\begin{aligned}\hat{H} &= \hat{T} + \hat{V} \\ &= -\underbrace{\frac{\hbar^2}{2m_e} \sum_i \nabla_i^2}_{\hat{T}_e} - \underbrace{\sum_I \frac{\hbar^2}{2M_I} \nabla_I^2}_{\hat{T}_n} + \underbrace{\frac{1}{2} \sum_{i \neq j} \frac{e^2}{|\mathbf{r}_i - \mathbf{r}_j|}}_{\hat{V}_{e-e}} + \underbrace{\frac{1}{2} \sum_{I \neq J} \frac{Z_I Z_J e^2}{|\mathbf{R}_I - \mathbf{R}_J|}}_{\hat{V}_{n-n}} - \underbrace{\sum_{i,I} \frac{Z_I e^2}{|\mathbf{r}_i - \mathbf{R}_I|}}_{\hat{V}_{e-n}}\end{aligned}\quad (\text{III.3})$$

where \hat{T}_e is the kinetic energy of electrons, \hat{T}_n the kinetic energy of nuclei, \hat{V}_{e-e} the electron-electron repulsive potential, \hat{V}_{n-n} the nucleus-nucleus repulsive potential, and \hat{V}_{e-n} the electron-nucleus attractive potential. \mathbf{r} and \mathbf{R} are respectively the electron and nucleus position vectors dependent of coordinates x, y, z . \hbar is the Planck constant, m_e is the mass of an electron, e the fundamental charge, M_I and Z_I are the mass and charge of nuclei respectively. Working in the BO approximation allows to set the nuclei kinetic energy \hat{T}_n to zero. As nuclei are fixed, the internuclei potential \hat{V}_{n-n} becomes a constant contribution that will be omitted from now on. Furthermore, all along this thesis, it will

be convenient to work in atomic units, where $\hbar = m_e = e = 4\pi\epsilon_0 = 1$, which simplifies equation (III.3). Finally it can be rewritten as the Born-Oppenheimer Hamiltonian:

$$\hat{H}_{BO} = -\underbrace{\frac{1}{2} \sum_i \nabla_i^2}_{\hat{T}_e} + \underbrace{\frac{1}{2} \sum_{i \neq j} \frac{1}{|\mathbf{r}_i - \mathbf{r}_j|}}_{\hat{V}_{e-e}} - \underbrace{\sum_{i,I} \frac{Z_I}{|\mathbf{r}_i - \mathbf{R}_I|}}_{\hat{V}_{e-n}} \quad (\text{III.4})$$

The system can be considered as interacting electrons within an external potential $V_{ext}(\mathbf{r})$ originating from nuclei. Thus, the electronic hamiltonian operator \hat{H}_e can be written as the sum of the kinetic energy of the electrons, the Coulomb electron-electron interaction, and an external potential:

$$\hat{H}_e = \hat{T}_e + \hat{V}_{e-e} + V_{ext}(\mathbf{r}) \quad (\text{III.5})$$

Equation (III.5) still presents an important issue: the position of each electron depends on the positions of all the other electrons and reciprocally. This is electronic correlation. The \mathbf{r}_i and \mathbf{r}_j variables are inseparable. Thus, the repulsive Coulomb potential \hat{V}_{e-e} is indeterminate. It is necessary to use approximations to be able to solve the Schrodinger equation. Two types of methods are possible: wavefunction based methods and density based methods.

The first method presented hereafter is based on wavefunction: the Hartree method, also called mono-electronic or orbital approximation. It is the most basic wavefunction method and represents the foundations of theoretical chemistry.

III. A.4 The Hartree method or mono-electronic approximation

The mono-electronic approximation, developed by Hartree in 1928 [165], proposes to solve the Coulomb interaction problem by considering all the N electrons of a given system as independent from each other. Therefore, the total electronic Hartree Hamiltonian is the sum of N mono-electronic Hamiltonian operators \hat{h}_i as:

$$\hat{H}_H = \sum_{i=1}^N \hat{h}_i \quad (\text{III.6})$$

i being the index of electrons.

Then, each electron, independently of its spin, can be described by its own wavefunction $\psi_i(\mathbf{r}_i)$ and the exact wavefunction of this system, dependent of the N electronic positions \mathbf{r}_i , can be written as the product:

$$\Psi(\mathbf{r}_1, \mathbf{r}_2, \dots, \mathbf{r}_N) = \psi_1(\mathbf{r}_1)\psi_2(\mathbf{r}_2) \dots \psi_N(\mathbf{r}_N) \quad (\text{III.7})$$

$$= \prod_{i=1}^N \psi_i(\mathbf{r}_i) \quad (\text{III.8})$$

Here, eigenvectors and eigenvalues can be defined for each electron independently. The Coulombian interaction is taken into account as it is expressed as the interaction of each electron with the mean field created by all the other ones.

However, the Hartree method does not include the Pauli exclusion principle and has been improved in that sense. It is the Hartree-Fock theory.

III. A.5 The Hartree-Fock theory (HF)

III. A. 5.α The Hartree-Fock equations

The Hartree-Fock (HF) method does not treat orbitals only but spin-orbitals by introducing electronic spin σ_i as a new variable of the wavefunction:

$$\Psi(\mathbf{r}_1\sigma_1, \mathbf{r}_2\sigma_2, \dots, \mathbf{r}_N\sigma_N) = \prod_{i=1}^N \psi_i(\mathbf{r}_i, \sigma_i) \quad (\text{III.9})$$

\mathbf{r}_i and σ_i being decorrelated, a mono-electronic wavefunction can be associated to two electrons of opposite spin. That is why, in the following, σ_i will not be considered in the notations and spin-orbitals will be noted $\psi_i(\mathbf{r}_i)$. The wavefunction must be antisymmetric to follow the Pauli exclusion principle [166]. Thus, any permutation of two electrons within the wavefunction induces a change of sign:

$$\Psi(\mathbf{r}_1, \mathbf{r}_2, \dots, \mathbf{r}_N) = -\Psi(\mathbf{r}_2, \mathbf{r}_1, \dots, \mathbf{r}_N) \quad (\text{III.10})$$

The wavefunction can be expressed in terms of the sum of all possible permutations as:

$$\begin{aligned} \Psi &= \Psi(\mathbf{r}_1, \mathbf{r}_2, \dots, \mathbf{r}_N) - \Psi(\mathbf{r}_2, \mathbf{r}_1, \dots, \mathbf{r}_N) + \dots \\ &= \psi_1(\mathbf{r}_1)\psi_2(\mathbf{r}_2) \dots \psi_N(\mathbf{r}_N) - \psi_2(\mathbf{r}_1)\psi_1(\mathbf{r}_2) \dots \psi_N(\mathbf{r}_N) + \dots \end{aligned} \quad (\text{III.11})$$

where only the permutation of electrons 1 and 2 is explicitly written.

$N!$ permutations are possible and the complete expression can take the form of a Slater determinant [167, 168]:

$$\Psi = \frac{1}{\sqrt{N!}} \begin{vmatrix} \psi_1(\mathbf{r}_1) & \psi_2(\mathbf{r}_1) & \dots & \psi_N(\mathbf{r}_1) \\ \psi_1(\mathbf{r}_2) & \psi_2(\mathbf{r}_2) & \dots & \psi_N(\mathbf{r}_2) \\ \vdots & \vdots & \ddots & \vdots \\ \psi_1(\mathbf{r}_N) & \psi_2(\mathbf{r}_N) & \dots & \psi_N(\mathbf{r}_N) \end{vmatrix} \quad (\text{III.12})$$

with the wavefunction normalization factor $1/\sqrt{N!}$, associated to normalized orbitals.

Fock has included the antisymmetrization and the Pauli principle in the wavefunction by expressing it as a Slater determinant. In this thesis, we will only work with electronic ground states. The **variational principle** states that for a given Ψ , the lowest energy that can be expected is the ground state energy E_0 :

$$\hat{H} |\Psi\rangle = E |\Psi\rangle \iff \frac{\langle \Psi | \hat{H} | \Psi \rangle}{\langle \Psi | \Psi \rangle} = E \geq E_0 \quad (\text{III.13})$$

Thus, in order to get as close as possible to the ground state energy of the system, the energy obtained with Ψ as a Slater determinant will be minimized, regarding the variations of the mono-electronic functions $\psi(\mathbf{r}_i)$ and their normalization constraint. That optimisation of the wavefunction leads to the Hartree-Fock equations:

$$\hat{F} \psi_i(\mathbf{r}_i) = \sum_{j=1}^N \epsilon_{ij} \psi_j(\mathbf{r}_i) \quad (\text{III.14})$$

The Fock operator \hat{F} being expressed as:

$$\hat{F} = \underbrace{-\frac{1}{2} \nabla_{\mathbf{r}_i}^2 - V_{ext}(\mathbf{r}_{iI})}_{\hat{h}_i} + \sum_{j=1}^N (\hat{J}_j - \hat{K}_j) \quad (\text{III.15})$$

with \hat{h}_i the mono-electronic hamiltonian equals to the sum of the kinetic energy and the electrostatic potential experienced by electron i within the external potential originating from the P nuclei: $V_{ext}(\mathbf{r}_{iI}) = \sum_{I=1}^P \frac{Z_I}{r_{iI}}$ (Z_I is the charge of the I -th nucleus).

\hat{J} is the Coulomb operator, or Hartree term, which is the mean potential undergone by i in the field of the other $N - 1$ electrons. Finally, the exchange operator \hat{K} can be interpreted as the contribution of the wavefunction antisymmetry to the energy (linked to the Pauli exclusion principle).

Therefore, the energy of a mono-electronic wavefunction can be calculated as:

$$\begin{aligned}
 \epsilon_i &= \langle \psi_i | \hat{F} | \psi_i \rangle \\
 &= \langle \psi_i | -\frac{1}{2} \nabla_{\mathbf{r}_i}^2 - V_{ext}(\mathbf{r}_{iI}) + \sum_{j=1}^N (\hat{J}_j - \hat{K}_j) | \psi_i \rangle \\
 &= \langle \psi_i | -\frac{1}{2} \nabla_{\mathbf{r}_i}^2 - V_{ext}(\mathbf{r}_{iI}) | \psi_i \rangle + \sum_{i,j=1}^N (\hat{J}_{ij} - \hat{K}_{ij}) \quad (\text{III.16})
 \end{aligned}$$

$$\text{knowing} \quad \left\{ \begin{aligned} \langle \psi_i | \hat{J}_j | \psi_i \rangle &= \int \int \psi_i^*(i) \psi_j^*(j) \left(\frac{1}{\mathbf{r}_{ij}} \right) \psi_i(i) \psi_j(j) d\mathbf{r}_i d\mathbf{r}_j = \hat{J}_{ij} \quad (\text{III.17}) \\ \langle \psi_i | \hat{K}_j | \psi_i \rangle &= \int \int \psi_i^*(i) \psi_j^*(j) \left(\frac{1}{\mathbf{r}_{ij}} \right) \psi_j(i) \psi_i(j) d\mathbf{r}_i d\mathbf{r}_j = \hat{K}_{ij} \quad (\text{III.18}) \end{aligned} \right.$$

Finally, the total Hartree-Fock energy is the sum of all orbital energies ϵ_i as:

$$E_{HF} = \sum_{i=1}^N \langle \psi_i | -\frac{1}{2} \nabla_{\mathbf{r}_i}^2 - V_{ext}(\mathbf{r}_{iI}) | \psi_i \rangle + \frac{1}{2} \sum_{i,j=1}^N (\hat{J}_{ij} - \hat{K}_{ij}) \quad (\text{III.19})$$

This notation avoids to count every bi-electronic interaction twice. Let us note that in the last equation (III.19), j can be equal to i , which corresponds to the Coulomb interaction and exchange of an electron with itself: \hat{J}_{ii} and \hat{K}_{ii} . However, those terms are equals and cancel each other, which means that the self-interaction issue does not occur (unlike in Density Functional Theory as we will see in the following).

The only approximation in the HF method is the description of each electron by a mono-electronic wavefunction. As electrons are independent in this theory, the electronic correlation, which corresponds to the mutual influence between the motion of an electron with the motions of all the $N-1$ electrons, is not considered. Thus, the difference between the exact energy of a system and its HF energy E_{HF} is the correlation energy E_c . E_{HF} is superior to the exact energy as the absence of correlation between electrons increases their repulsion. We will see later that several methods can be used to take E_c in consideration and calculate the exact energy.

In practice, Hartree-Fock equations can be solved iteratively to find an optimized Ψ by minimizing E_{HF} . This process, that uses the variational principle, is the Self-Consistent Field method.

III. A. 5. β The Self-Consistent Field method (SCF)

The Self-Consistent Field method (SCF) is the mathematical and computational method to optimize the wavefunction of a system iteratively.

Every iteration is done in three steps:

1. Set up nuclear coordinates, number of electrons and give an ensemble of guess mono-electronic functions $\tilde{\psi}_i$ corresponding to the guess wavefunction $\tilde{\Psi}_0$. Usually, the guess $\tilde{\psi}_i$ are wavefunctions obtained from the extended Hückel method.
2. Calculate the bi-electronic operators \hat{J}_{ij} , \hat{K}_{ij} and determine the mono-electronic \hat{h}_i .
3. Solve HF equations with the calculated \hat{F} .
4. Compare the obtained \tilde{E}_0 with the one from the previous iteration. A convergence criterion (arbitrary) has to be specified on the energy, depending on the desired accuracy of the result. The process goes back to step 2 if the convergence criterion is not reached, with the calculated orbitals as guess orbitals. Following the variational principle, \tilde{E}_0 has to be as low as possible knowing that $\tilde{E}_0 \geq E_0$.

III. A. 5. γ Linear Combination of Atomic Orbitals (LCAO)

On a practical aspect, the direct mathematical and computational description of N mono-electronic functions ψ_i in a system is very resource consuming. In order to lighten these calculations, several known basis functions, analytically easy to solve, are employed. The set of these functions is called the basis set. The linear combination of several basis functions χ_k to build a mono-electronic wavefunction ψ_i is defined as:

$$\psi_i = \sum_{k=1}^N C_{ik} \chi_k \quad (\text{III.20})$$

where the weight of each function χ_k in every wavefunction ψ_i , is defined by a specific coefficient C_{ik} . An SCF procedure allows to determine these coefficients while Ψ is optimized. At a molecular level, the Linear Combination of Atomic Orbitals (LCAO) method [169–172] is employed on Atomic Orbitals (AO), and a set of associated coefficients is determined to describe Molecular Orbitals (MO).

III. A. 5. δ Basis set

In this thesis, most of the systems of interest are periodic, that is why, planewave basis sets will be used (see III.C). However, for heterogeneous electronic systems like atoms or molecules, two types of basis functions are commonly employed:

- **Slater Type Orbitals (STO)**

Slater-Type Orbitals (STO) [173] are expressed as:

$$\chi_S(r, \theta, \phi, \zeta) = N r^{n^*-1} \exp(-\zeta r) Y_{lm}(\theta, \phi) \quad (\text{III.21})$$

where N is a normalization constant, r , θ and ϕ spherical electronic coordinates and n^* the effective quantum number. Empirical values are assigned to n^* , depending on n , the real principal quantum number of the considered electron. l and m are respectively the azimuthal and magnetic quantum numbers. ζ is the orbital factor given by the expression $\zeta = \frac{Z-s}{n^*}$ with Z the nuclear charge and s a screening constant ($Z - s$ is often noted Z_{eff} , as the effective charge experienced by the electron). Finally $Y_{lm}(\theta, \phi)$ are spherical harmonics. This form is equivalent to a hydrogen-like electronic wavefunction, in which nodes are neglected.

- **Gaussian Type Orbitals (GTO)**

The general form of a Gaussian function [174] is:

$$\chi_G(r, \alpha) = N x^n y^m z^l \exp(-\alpha r^2) \quad (\text{III.22})$$

where n , l and m are still the quantum numbers, r the spherical electronic coordinate, x , y and z the cartesian electronic coordinates, and α a space extension constant. A convenient property of GTOs is that the product of two Gaussian functions is a Gaussian. Numerically, it allows to simplify calculations involving products of basis functions.

The LCAO method is exact for an infinite number of basis functions, however it is impossible to compute. Therefore, regarding the type of system and the desired accuracy of the results, the basis set size has to be defined and optimized. The larger is a basis, the more accurate it gets, but bigger is the computational cost. In a minimal basis, each AO is represented by a single basis function, composed of several functions. For instance, STO- n G basis describe each AO of a system with a single function composed of n Gaussian functions, designed to correspond to an STO [175]. Basis where each AO is build with two basis functions are called double- ζ basis, with three functions triple- ζ basis, ... When two atoms bind, their AOs undergo deformations and produce MOs. In that case, the accuracy of the basis can be improved with polarization functions, which enhance the basis flexibility and allow electronic charge delocalization. To describe regions of space farther from the nucleus, which is useful for the study of anions or excited states, diffuse functions can be employed.

Another type, split-valence basis sets, have been proposed, such as the very popular Pople basis sets [176], which have specific names depending on the number and type of basis functions employed to represent AOs. For instance, the standard **6-31G*** double- ζ basis set, where one function composed of 6 Gaussians describes the core orbitals and two functions of 3 and 1 Gaussians represent the valence orbitals. In this notation, “G” stands for “Gaussian” and “-” represents the core-valence splitting. A star (*) means that a polarization function of d type is used on heavy atoms (heavier than He), if two stars appear in the name (**), a polarization function d is employed for heavy atoms and another of p type for hydrogen and helium. If the basis contains more polarization functions, their number and type is specified in parenthesis as in the **6-311+G(2d,2p)** triple- ζ basis set for instance. In this case, the core AOs are described with a single function of 6 Gaussians, the valence with three functions composed of 3, 1 and 1 Gaussians, and (2d,2p) means that 2 polarization functions of d type are used for heavy atoms, and 2 of p type for hydrogen. Finally, the + sign indicates that a diffuse function of p type on heavy atoms is used. When a basis name contains the (++) notation, it means that two diffuse functions are employed: one on heavy atoms, one on hydrogen and helium. Polarization and diffuse functions are always composed of only one Gaussian.

The two examples that have been described (**6-31G*** and **6-311+G(2d,2p)**) are the basis sets that will be employed for the gas phase study of metamitron and fenhexamid in interaction with cations, in Chapter V.

III. A. 5.ε Roothaan equations

The development of Equation (III.14) within the LCAO method leads to a system of equations called the Roothaan equations [177]. For a given mono-electronic function ψ_i , described by basis functions indexed k and l , the i^{th} equation is expressed as:

$$\sum_{k=1}^R (F_{kl} - S_{kl}\epsilon_i) C_{ik} = 0 \quad ; \quad i = 1, 2, \dots, N \quad (\text{III.23})$$

with R the number of basis functions indexed k or l , and N the number of mono-electronic functions.

F_{kl} is the Fock number such as $F_{kl} = \langle \chi_k | \hat{F}_{kl} | \chi_l \rangle$, S_{kl} is the basis function overlap as $S_{kl} = \langle \chi_k | \chi_l \rangle$, ϵ_i is the energy associated to ψ_i and C_{ik} is the basis function coefficient. The system of Roothaan equations for the i^{th} mono-electronic wavefunction ψ_i can be expressed by the matrix equation:

$$\mathbf{FC} = \mathbf{SC}\epsilon_i \quad (\text{III.24})$$

where \mathbf{F} , \mathbf{C} , \mathbf{S} are respectively the matrices of Fock numbers, basis function coefficients and overlap matrix. Thus, a set of N energies ϵ_i is calculated. As we mentioned it before, a guess set of basis function coefficients is given at the first step of an SCF procedure to determine them. Usually, the extended Hückel method is employed.

The Hartree-Fock method is the basic wavefunction-based theory to describe electronic structure. It allows to solve the Schrödinger equation by doing only one approximation: each electron of the system is described by a mono-electronic wavefunction in the mean-field of all the other ones. The only issue of this method is the electronic correlation that cannot be considered within this approximation. More sophisticated wavefunction-based methods, called *post-Hartree-Fock* have been proposed to include the electronic correlation term in the calculations: the Coupled-Cluster method (CC) [178–181], variational methods such as Configuration Interaction (CI) [182] and Multi-Configurational Self-Consistent Field (MRSCF) [183] or perturbative methods as Møller-Plesset (MP) [184]. These theories can produce very accurate results but consume a lot of computational resources. For instance, the second order Møller-Plesset method (MP2) applied to a system containing N electrons has a computational cost in N^5 , while for the CI method it is in $N!$.

Thus, a very low number of atoms can be treated with these methods. In the present thesis, the systems of interest go from pesticide molecules (25-36 atoms), to hydrated pesticide on a montmorillonite surface (> 600 atoms). It is necessary to use a method that allows to take electronic correlation into account and to treat a relatively high number of atoms accurately for a reasonable computational cost. Density Functional Theory, a density-based method, is a good compromise between all these considerations, with a resource cost in N^4 .

III.B Density Functional Theory

The Density Functional Theory (DFT) establishes that the energy and state of a system can be fully described by its electronic density $n(\mathbf{r})$. Instead of dealing with the total wavefunction of the system, which depends on $3N$ variables for a N -electron system, it treats $n(\mathbf{r})$ that depends only on the three space variables x, y, z in vector \mathbf{r} . This theory is very popular in theoretical chemistry and physics and can be employed in a lot of different fields.

III. B.1 Thomas-Fermi-Dirac approximation

DFT originates from the work published by Llewellyn Hilleth Thomas [185] and Enrico Fermi [186] in 1927, stating a new approximation in quantum physics: the total electronic

energy in atoms may be considered as an explicit functional of the density:

$$E_{TF}[n(\mathbf{r})] = \underbrace{C_k \int n(\mathbf{r})^{5/3} d\mathbf{r}}_{T_{TF}[n(\mathbf{r})]} + \underbrace{\frac{1}{2} \iint \frac{n(\mathbf{r}) n(\mathbf{r}')}{|\mathbf{r} - \mathbf{r}'|} d\mathbf{r} d\mathbf{r}'}_{V_{e-e}[n(\mathbf{r})]} - \underbrace{Z \int \frac{n(\mathbf{r})}{r} d\mathbf{r}}_{V_N[n(\mathbf{r})]} \quad (\text{III.25})$$

where electron-nucleus attractive potential $V_N[n(\mathbf{r})]$ is expressed in a classical form, Z being the nuclear charge. In the Thomas-Fermi model, the electronic kinetic energy $T_{TF}[n(\mathbf{r})]$ is based on the homogeneous electronic gas such as:

$$C_k = \frac{3}{10} (3\pi^2)^{2/3}$$

A first issue with their theory was the missing treatment of electronic exchange. In 1930, Dirac formulated a local approximation for exchange [187] and improved the form of the functional with the Thomas-Fermi-Dirac total energy such as:

$$E_{TFD}[n(\mathbf{r})] = T_{TF}[n(\mathbf{r})] + V_{e-e}[n(\mathbf{r})] - V_N[n(\mathbf{r})] + C_x \int n(\mathbf{r})^{4/3} d\mathbf{r} \quad (\text{III.26})$$

$$\text{with } C_x = -\frac{3}{4} \left(\frac{3}{\pi} \right)^{1/3}$$

where C_k and C_x the kinetic and exchange constants are expressed in atomic units.

However, this method is too crude to give an accurate description of electronic total energy in atoms: the electronic kinetic and exchange energies are strongly approximated, the electron repulsive potential is expressed as a Hartree potential and correlation effects are neglected [188–190]. The main issue of the Thomas-Fermi-Dirac theory is the expression of the electronic kinetic energy which is unknown. Anyway, the achievement of this model is its ability to express the total energy in terms of electronic density.

III. B.2 Hohenberg-Kohn theorems

In 1964, Pierre Hohenberg and Walter Kohn [191] (HK), established two theorems to formulate DFT as an exact theory of many-body systems. Within this method, it is assumed that all the ground-state properties of a system can be known, if its electronic density $n_0(\mathbf{r})$ is known.

For any system of interacting electrons in any external potential $V_{ext}(\mathbf{r})$:

- Theorem I: the external potential is uniquely determined, up to a constant, by the ground state electronic density $n_0(\mathbf{r})$. In other words, there is a one-to-one mapping between $n_0(\mathbf{r})$ and $V_{ext}(\mathbf{r})$. Therefore, a universal functional $F_{HK}[n(\mathbf{r})]$

can be defined to calculate the ground-state energy E_0 associated to $n_0(\mathbf{r})$.

- Theorem II: For any particular $V_{ext}(\mathbf{r})$, the exact ground state energy of the system E_0 is the global minimum value of $F_{HK}[n(\mathbf{r})]$, and the density $n(\mathbf{r})$ that minimizes this functional is the exact ground state density $n_0(\mathbf{r})$. This is the variational principle applied to the electronic density.

Thanks to the HK theorems, a different expression has been proposed for the total energy of any electronic system as a density functional:

$$E_{HK}[n(\mathbf{r})] = \underbrace{T[n(\mathbf{r})] + V_{e-e}[n(\mathbf{r})]}_{F_{HK}[n(\mathbf{r})]} + \int V_{ext}(\mathbf{r}) n(\mathbf{r}) d\mathbf{r} \quad (\text{III.27})$$

where the sum of the electronic kinetic $T[n(\mathbf{r})]$ and potential $V_{e-e}[n(\mathbf{r})]$ energy functionals is the universal HK functional, and the external potential corresponds to the electron-nucleus interaction.

However, the problem of knowing the mathematical form of the electron kinetic energy and repulsive electron potential remains.

III. B.3 Kohn-Sham equations

Walter Kohn and Lu Jeu Sham (KS) proposed a new approach in 1965 [192]: for any system of interacting electrons with a given density in an external potential $V_{ext}(\mathbf{r})$, the total energy functional can be expressed as the one of the equivalent non-interacting system (with equivalent $n(\mathbf{r})$) experiencing the same $V_{ext}(\mathbf{r})$, added to an electronic exchange and correlation functional $E_{xc}[n(\mathbf{r})]$:

$$E_{KS}[n(\mathbf{r})] = T_s[n(\mathbf{r})] + V_{Hartree}[n(\mathbf{r})] + \int V_{ext}(\mathbf{r}) n(\mathbf{r}) d\mathbf{r} + E_{xc}[n(\mathbf{r})] \quad (\text{III.28})$$

The density $n(\mathbf{r})$ is expressed in terms of mono-electronic wavefunctions $\psi_i(\mathbf{r})$, called Kohn-Sham orbitals, as:

$$n(\mathbf{r}) = \sum_{i=1}^N |\psi_i(\mathbf{r})|^2 \quad (\text{III.29})$$

and the expressions of the kinetic energy and repulsive potential of non-interacting electrons is known:

$$T_s[n(\mathbf{r})] = -\frac{1}{2} \sum_{i=1}^N \langle \psi_i | \nabla_i^2 | \psi_i \rangle \quad (\text{III.30})$$

$$V_{Hartree}[n(\mathbf{r})] = \frac{1}{2} \iint \frac{n(\mathbf{r}) n(\mathbf{r}')}{|\mathbf{r} - \mathbf{r}'|} d\mathbf{r} d\mathbf{r}' \quad (\text{III.31})$$

The only unknown term is $E_{xc}[n(\mathbf{r})]$ which is equal to the energy difference between the interacting and non-interacting systems:

$$E_{xc}[n(\mathbf{r})] = T[n(\mathbf{r})] - T_s[n(\mathbf{r})] + V_{e-e}[n(\mathbf{r})] - V_{Hartree}[n(\mathbf{r})] \quad (\text{III.32})$$

Then, the ground-state energy of the system is calculated by resolution of the system of Kohn-Sham equations: $\hat{H}^{KS} \psi_i(\mathbf{r}) = \epsilon_i \psi_i(\mathbf{r})$ and minimization of $E_{KS}[n(\mathbf{r})]$ during an SCF procedure on the KS orbitals. A minimum can be identified by derivation of the energy with respect to density, thus the Kohn-Sham Hamiltonian is expressed as:

$$\hat{H}^{KS} = \frac{\partial E[n(\mathbf{r})]}{\partial n(\mathbf{r})} = -\frac{1}{2} \nabla_i^2 + \int \frac{n(\mathbf{r}')}{|\mathbf{r} - \mathbf{r}'|} d\mathbf{r}' + V_{ext}(\mathbf{r}) + \frac{\partial E_{xc}[n(\mathbf{r})]}{\partial n(\mathbf{r})} \quad (\text{III.33})$$

The first term is the electronic kinetic energy potential, the second one is the new Hartree potential and the last term is the exchange-correlation potential $V_{xc}(\mathbf{r})$.

The validity of this approach is assumed, as it has never been proven for a real system. Unlike HF method, the use of mono-electronic wavefunction ψ_i is not an approximation in DFT as, in a non-interacting system, they are the real wavefunctions. In conclusion, the only unknown term in the whole KS approach is the exchange-correlation functional, thus, if it can be calculated, the ground-state density and total energy of the real interacting system can be obtained.

III. B.4 Exchange-Correlation Functionals

Nowadays, there is still no exact solution to calculate $E_{xc}[n(\mathbf{r})]$, however a lot of exchange-correlation functionals have been developed over the years to approximate this term and allow to use DFT in practice. Each functional is more or less adapted to given chemical systems and produces results with different accuracies. This section presents the three most famous families of functionals.

Local Density Approximation (LDA)

In their original paper, Kohn and Sham already proposed the Local Density Approximation (LDA) [192], where, at each point of space, $n(\mathbf{r})$ is considered as the density of a homogeneous electron gas:

$$E_{xc}^{LDA}[n(\mathbf{r})] = \int \left(\epsilon_x^{hom}(n(\mathbf{r})) + \epsilon_c^{hom}(n(\mathbf{r})) \right) n(\mathbf{r}) d\mathbf{r} \quad (\text{III.34})$$

where $\epsilon_x^{hom}(n(\mathbf{r}))$ can be determined analytically [193], and $\epsilon_c^{hom}(n(\mathbf{r}))$ can be calculated by simulations, it has notably been done accurately by Monte Carlo methods [194, 195]. This approximation has been developed for polarized systems as the Local Spin Density Approximation (LSDA), by introducing spin densities $n^\uparrow(\mathbf{r})$ and $n^\downarrow(\mathbf{r})$:

$$E_{xc}^{LSDA}[n^\uparrow(\mathbf{r}), n^\downarrow(\mathbf{r})] = \int \left(\epsilon_x^{hom}(n^\uparrow(\mathbf{r}), n^\downarrow(\mathbf{r})) + \epsilon_c^{hom}(n^\uparrow(\mathbf{r}), n^\downarrow(\mathbf{r})) \right) n(\mathbf{r}) d\mathbf{r} \quad (\text{III.35})$$

It treats the system locally as a homogeneous electron gas at each point of space, thus such a functional is expected to give its best performance for solids (especially metals). In very inhomogeneous systems like atoms or molecules, for farther and farther positions from the systems, the density must go continuously to zero and this approximation should poorly describe density. However, L(S)DA functionals can give pretty good results in the description of inhomogeneous systems. This property is due to an underestimation of the exchange energy and an overestimation of the correlation energy, which tend to balance each other. These errors limit the use of this approximation.

The introduction of density gradients in the exchange-correlation functional, leading to GGA functionals, brings enough accuracy to make DFT sufficiently good to describe properties in a wide range of chemical systems.

Generalized Gradient Approximation (GGA)

LDA treats density as homogeneous, which becomes inappropriate for systems that have strong density fluctuations in space, like atoms or molecules. A more elaborated type of functional introduces the density gradient as supplementary variable in the exchange-correlation functional, this is the Generalized Gradient Approximation (GGA) [196, 197]:

$$E_{xc}^{GGA}[n(\mathbf{r})] = \int \left(\epsilon_x(n(\mathbf{r}), |\nabla n(\mathbf{r})|) + \epsilon_c(n(\mathbf{r}), |\nabla n(\mathbf{r})|) \right) n(\mathbf{r}) d\mathbf{r} \quad (\text{III.36})$$

for unpolarized systems. Several GGA functionals have been developed over the years [198], notably two categories can be identified [199]. The first one is more designed for the description of inhomogeneous systems than for solid-state physics. These functionals give good results for molecular properties such as atomization energy and reaction barriers.

The Becke, Lee, Yang, Parr (BLYP) [200,201] and Perdew-Wang (PW91) [202,203] being some of the most popular. Anyway, they usually give better results for solids than LDA, and present good agreements with experiments. The second group of GGA functionals focuses more on the ability to describe solid-state physics better than LDA. On the other hand, they do not produce very accurate results for atoms and molecules. The Perdew-Burke-Ernzerhof (PBE) [204] notably gives pretty good results for solids and specifically for montmorillonite [134,136,146,152–156,161] and other minerals [157,205–207]. As this functional has been employed all along this work, we will discuss some of its quality and drawbacks in a further section (see III. B.5).

In spite of the large improvement introduced by GGA, density functionals fail to describe long-range exchange and correlation implied in van der Waals forces. Indeed, they decrease exponentially for an increasing distance r , instead of decreasing in $-1/r$. As we will see in section III. B.5, for systems in which dispersion interactions play an important role, this kind of interaction can be treated with adapted corrections to the functional (DFT-D). In addition, in both LDA and GGA, errors due to self-interaction in the Hartree term are not adequately corrected.

The third and last most famous family of functionals for the exchange-correlation term in the Kohn-Sham energy are hybrid functionals, designed to correct these errors.

Hybrid functionals

These functionals are called hybrid as they contain a combination of Hartree-Fock exchange, as suggested by Becke in 1993 [208], and exchange-correlation obtained with one or several Density Functional Approximation (LSDA or GGA). The general expression for a hybrid exchange-correlation energy functional can be written as:

$$E_{xc}^{hybrid} = \alpha E_x^{HF} + \beta E_x^{DFT} + E_c^{DFT} \quad (\text{III.37})$$

where E_x^{HF} is the exchange energy calculated at the HF level. However this exchange is not exact as in HF theory, because the mono-electronic wavefunctions employed for the calculations are KS orbitals, and not HF orbitals. That is why a part of the exchange energy is calculated at HF level, and another part at DFT level (E_x^{DFT}), with associated coefficients α and β respectively. Then correlation E_c^{DFT} is calculated at DFT level as well. Depending on the system of interest, several energy functionals of different types (LDA or GGA) can be combined for exchange or correlation separately:

$$E_{xc}^{hybrid} = \alpha E_x^{HF} + \beta E_x^{LDA} + \gamma E_x^{GGA} + \delta E_c^{LDA} + \epsilon E_c^{GGA} \quad (\text{III.38})$$

$\alpha, \beta, \gamma, \delta, \epsilon$ are tunable coefficients, fitted empirically. For instance, B3LYP, which is

the most popular hybrid functional, combines E_x^{HF} with a Becke (B) exchange correction [200], and a combination of LDA and LYP (GGA) functionals for correlation [201]. Depending on the method, several B3LYP functionals exist, containing different LDA functionals and different coefficients. B3LYP can be employed for molecular systems as well as for periodic structures. Indeed, it performs very well in calculating properties of minerals [209–212].

In spite of their success in theoretical chemistry, the “tunable” aspect of hybrid functionals make them a bit controversial as it does not match with the *ab initio* purpose of DFT. The main problem in using hybrid functionals for periodic systems is their higher computational cost. Indeed, choosing a suitable functional for a DFT study requires to find a good balance between quality and accuracy of the results on one hand, time and computational cost on the other hand.

III. B.5 DFT performances and PBE-D2 functional

The objective of this thesis is to understand pesticide interaction with a montmorillonite surface, thus an exchange-correlation functional able to give good results on mineral solids and on organic molecules is necessary.

LDA are excluded regarding accuracy issues for molecules and inhomogeneous systems, as mentioned earlier, montmorillonite being an inhomogeneous solid as shown in the previous chapter.

Hybrid functionals can be very accurate but are computationally too expensive considering the size of the system (> 600 atoms).

Finally, GGA functionals propose a good balance between accuracy and resources consumption. A very large panel of functionals is available and it is necessary to choose carefully. Studies show that benchmarks cannot conclude on what is the best functional to use. It strongly depends on the information that is under study, notably when dispersion interactions are involved [213]. Literature presents the PBE functional [204] as suitable for montmorillonite [134, 152, 157, 161], and for molecular systems in interaction with montmorillonite when combined with dispersion correction (PBE-D) [146, 153–156], as well as for other clay minerals in which effects of non-bonding interactions are important [205, 206]. Indeed, corrections are usually needed as DFT methods often fail in describing non-bonding interactions accurately [214, 215], even if some hybrid functionals perform better for van der Waals (vdW) interactions [216]. Then, it is important to consider the performance of PBE and PBE-D functionals in water description, as its role on pesticide adsorption will be studied (see Chapter VII). A correct description of H-bonding is necessary as it will occur in the pesticide-water-montmorillonite systems, especially be-

tween surface oxygens and molecules. It has been shown over several databases that PBE, compared to many DFT functionals (notably hybrid ones), is one of the best GGAs for hydrogen bonding description [217, 218]. The paper of Goumans *et al.* also suggests H-bonding to be slightly better described by the PBE functional in a planewave basis, than by B3LYP in the case of a fully hydroxylated (001) α -quartz surface [219]. Moreover, PBE describes H-bonding in good agreement with MP2 and CC methods [220] and performs well in silica derived material treatment [221]. However, the PBE functional presents limitations in describing water structure. PBE tends to over-structure water compared to experiment [222–228] regarding the Radial Distribution Function (RDF) and diffusion coefficient. This crystalline-like aspect of water in PBE is well-known and comes from a strong directional description of H-bonds between H_2O molecules [229].

To summarize, it is necessary to add long-range dispersion corrections to the PBE functional to treat pesticide-montmorillonite interactions with a reasonable accuracy considering the importance of dispersive effects in such systems. In that sense, a Grimme D2 correction will be added to PBE. The general expression for the total energy in DFT with Grimme long-range dispersion correction as described in Stefan Grimme’s original paper from 2004 [230] is written:

$$E_{DFT-D} = E_{KS-DFT} + E_{disp} \quad (\text{III.39})$$

with E_{KS-DFT} the Kohn-Sham energy calculated with the chosen functional, in our case, with the PBE functional the total energy is:

$$E_{PBE-D} = E_{KS-PBE} + E_{disp} \quad (\text{III.40})$$

E_{disp} is an empirical dispersion correction such as:

$$E_{disp} = -s_6 \sum_{i=1}^{N-1} \sum_{j=i+1}^N \frac{C_6^{ij}}{R_{ij}^6} f_{damping}(R_{ij}) \quad (\text{III.41})$$

N being the number of atoms in the chemical system, C_6^{ij} the dispersion coefficient specific for each pair of atoms i and j , R_{ij} the interatomic distance in a pair, and s_6 a scaling factor that has to be adapted to the chosen functional. The damping function $f_{damping}$ is necessary to avoid singularities for small R_{ij} , its expression is:

$$f_{damping}(R_{ij}) = \frac{1}{1 + e^{-d(R_{ij}/R_0-1)}} \quad (\text{III.42})$$

with R_0 the sum of atomic vdW radii and d a tunable constant defining the steepness of the damping function depending on the system and the exchange-correlation functional.

The Grimme's dispersion correction can be used at different order. The original paper proposed the first order version of the correction (DFT-D1) [230], which includes the expression of E_{disp} as in equation (III.41) with the C_6^{ij} parameters of each pair of atoms ij calculated as an average value of each atom coefficient C_6^i and C_6^j :

$$C_6^{ij} = 2 \frac{C_6^i C_6^j}{C_6^i + C_6^j} \quad (\text{III.43})$$

A further improvement of this method, the second order dispersion correction DFT-D2, was then proposed in 2006 by Grimme *et al.* [231] with C_6^{ij} expressed under the form of a geometric mean such as:

$$C_6^{ij} = \sqrt{C_6^i C_6^j} \quad (\text{III.44})$$

This method has proven to give better results than DFT-D1. As the expression of C_6^{ij} is not the same in both methods, the value of s_6 , specific to each density functional, is different within the D1 and D2 approaches. Furthermore, a third-order DFT-D3 version of Grimme's dispersion correction has been developed later, which adds a three-body term in the expression of E_{disp} and is more efficient, accurate and less empiric compared to the previous versions [232].

In the present thesis, the PBE-D2 functional will be used for pesticide-montmorillonite systems to treat dispersion interactions which play a major role in this kind of systems. This corrected functional will be used as it is implemented in the CPMD software package [233], knowing that the D3 version is not available in this software.

III.C Periodic systems for solid state models

Solid-state physics is a different branch of physical chemistry and cannot be treated with the same methods than molecules, complexes or clusters. Crystalline solids present organised structures in the three dimensions of space. Building finite models of such systems (clusters) may be a solution to analyze their local properties, but cannot reproduce their general behavior accurately. Solids are extended systems considered as infinite structures in three dimensions. DFT assumes to apply for any system, thus it can be employed for infinite systems. Such systems thus contain an infinite number of electrons and requires an infinite number of Kohn-Sham equations to solve. For perfect crystals, this issue can be avoided.

III. C.1 Bloch theorem, real and reciprocal spaces

First, to reproduce an infinite perfect solid, a primitive unit cell can be defined in this structure, and describes the complete crystal by periodic translations in three dimensions. A primitive cell is described by six parameters: three vectors \mathbf{a} , \mathbf{b} , \mathbf{c} and α , β , γ the angles between them. Several combinations of these parameters lead to different kinds of unit cells called Bravais lattices. The atoms within the unit cell are reproduced periodically in three-dimensional space through translation vectors \mathbf{t} such as:

$$\mathbf{t} = n_a \mathbf{a} + n_b \mathbf{b} + n_c \mathbf{c} \quad (\text{III.45})$$

n_a , n_b and n_c being integer numbers, positive, negative or zero. The primitive unit cell formed by \mathbf{a} , \mathbf{b} and \mathbf{c} has a volume Ω :

$$\Omega = \mathbf{a} \cdot (\mathbf{b} \wedge \mathbf{c}) \quad (\text{III.46})$$

In such systems, the Bloch theorem allows to describe electronic structure with mono-electronic functions, called Bloch functions, defined as:

$$\psi_{i,\mathbf{q}}(\mathbf{r}) = e^{i\mathbf{q} \cdot \mathbf{r}} u_{i,\mathbf{q}}(\mathbf{r}) \quad (\text{III.47})$$

where $u_{i,\mathbf{q}}(\mathbf{r})$ is a wavefunction having the Bravais lattice periodicity and $e^{i\mathbf{q} \cdot \mathbf{r}}$ is a planewave defined by the wave-vector \mathbf{q} . The development of the Bloch theorem shows that \mathbf{q} is a vector in the reciprocal space, which corresponds to the Fourier transform of the real space. Similarly to the real space, the reciprocal space is described by a unit cell called Brillouin zone and defined by three vectors such as:

$$\mathbf{a}^* = \frac{2\pi}{\Omega} \mathbf{b} \wedge \mathbf{c} , \quad \mathbf{b}^* = \frac{2\pi}{\Omega} \mathbf{c} \wedge \mathbf{a} , \quad \mathbf{c}^* = \frac{2\pi}{\Omega} \mathbf{a} \wedge \mathbf{b} \quad (\text{III.48})$$

and by translation vectors:

$$\mathbf{t}^* = m_{a^*} \mathbf{a}^* + m_{b^*} \mathbf{b}^* + m_{c^*} \mathbf{c}^* \quad (\text{III.49})$$

where m_{a^*} , m_{b^*} and m_{c^*} are integer numbers, negative, positive or zero. The smallest Brillouin zone that can be defined for a given reciprocal space is called First Brillouin Zone.

$u_{i,\mathbf{q}}(\mathbf{r})$ having the lattice periodicity, $\psi_{i,\mathbf{q}}(\mathbf{r})$ can be estimated by considering only the \mathbf{q} in the First Brillouin Zone, noted \mathbf{k} in the following, as any \mathbf{q} vector can be expressed

as a $\mathbf{k} + \mathbf{t}^*$ sum. A new expression of Kohn-Sham equations can be given as:

$$\left\{ -\frac{1}{2}(\nabla_i + i\mathbf{k})^2 + V_{Hartree}(\mathbf{r}) + V_{ext}(\mathbf{r}) + E_{xc}(\mathbf{r}) \right\} u_{i,\mathbf{k}}(\mathbf{r}) = \epsilon_{i,\mathbf{k}} u_{i,\mathbf{k}}(\mathbf{r}) \quad (\text{III.50})$$

This theorem allows to avoid an infinite number of Kohn-Sham equations to solve, instead, a finite number of equations is solved for an infinite number of \mathbf{k} -points within the First Brillouin Zone. At every \mathbf{k} -points, equation (III.50) leads to a set of eigenvalues $\epsilon_{i,\mathbf{k}}$. The total electronic structure of the system is represented by i functions $\epsilon_{i,\mathbf{k}} = f(\mathbf{k})$ composing the band structure of the system. $u_{i,\mathbf{k}}(\mathbf{r})$ varies slightly between close \mathbf{k} -points which allows to limit the number of employed \mathbf{k} -points and thus the number of Kohn-Sham equations to solve. Symmetries in the First Brillouin Zone allows to reduce this number.

III. C.2 Planewave basis

In the LCAO method, mono-electronic wavefunctions of a periodic system can be developed in planewave basis, which are the most commonly used for such systems. In the present work, all periodic systems will be treated with planewave basis. Therefore, mono-electronic wavefunctions are expressed as:

$$\psi_{i,\mathbf{k}}(\mathbf{r}) = \sum_{\mathbf{q}} C_{i,\mathbf{k},\mathbf{q}} e^{i\mathbf{q} \cdot \mathbf{r}} = \sum_{\mathbf{q}} C_{i,\mathbf{q}} e^{i(\mathbf{k}+\mathbf{t}) \cdot \mathbf{r}} \quad (\text{III.51})$$

where the $u_{i,\mathbf{k}}(\mathbf{r})$ periodicity implies that only C_i coefficients associated to planewaves with a $(\mathbf{k} + \mathbf{t})$ wave-vector have non-zero values.

To better visualize what is the reciprocal space and the propagation wave-vector \mathbf{k} , Figure III.1 represents a bi-dimensional reciprocal space where dots are unit cells, all in contact with their neighbours. Each one of these dots is described by a wave-vector $(\mathbf{k} + \mathbf{t})$ and thus called a \mathbf{k} -point. This example specifies four \mathbf{k} -points to build the first Brillouin zone: Γ the origin, X , Y and M . The basis is defined by a cutoff energy E_{cutoff} that gives the threshold of the basis:

$$\frac{1}{2}|\mathbf{k} + \mathbf{t}|^2 < E_{cutoff} \quad (\text{III.52})$$

All planewave of wave-vector $(\mathbf{k} + \mathbf{t})$ and lower energy than E_{cutoff} is included within the basis. Planewave basis are not adapted to molecular systems, as electronic structures of such systems vary roughly in space and thus would need a high E_{cutoff} to be correctly described.

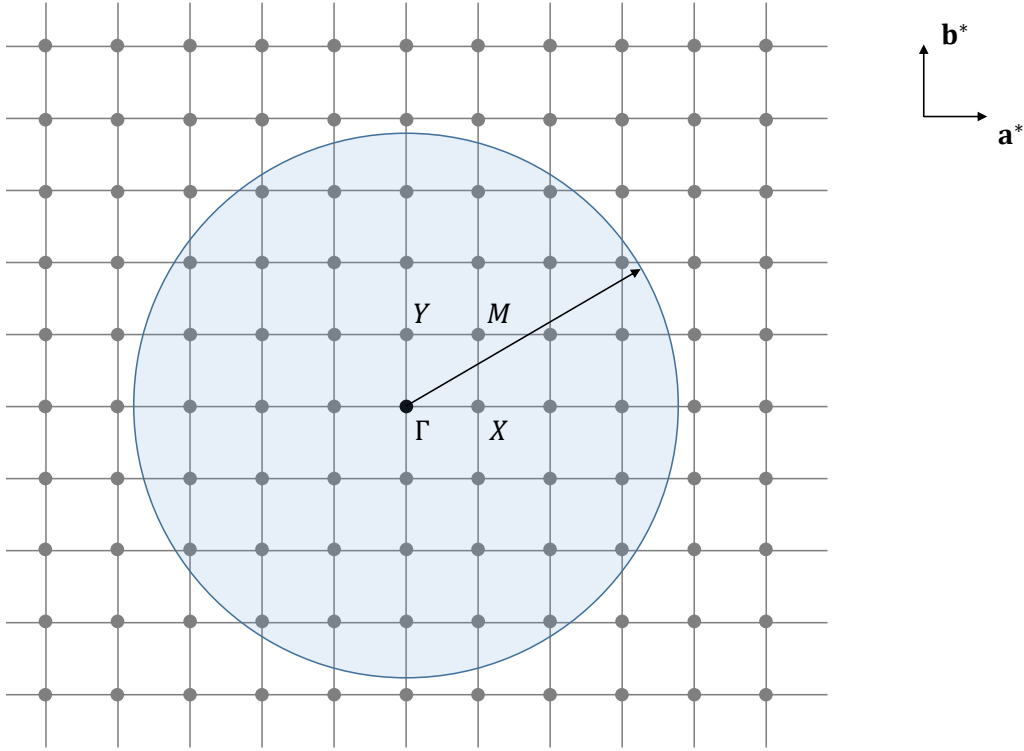


Figure III.1: Bi-dimensional schematic representation of a cubic reciprocal space defined by the reciprocal vectors \mathbf{a}^* and \mathbf{b}^* . Every node of the reciprocal lattice is a unit cell of the direct lattice. The four nodes with their coordinates within the reciprocal lattice: $\Gamma(0,0)$, $X(\frac{1}{2},0)$, $Y(0,\frac{1}{2})$ and $M(\frac{1}{2},\frac{1}{2})$, represent the first Brillouin zone of the system. The circle colored in blue includes all the \mathbf{k} -points used to build the planewave basis set for the \mathbf{k} -point Γ . The diameter of this circle is defined by the energy cutoff E_{cutoff} .

III. C.3 Core-valence separation and pseudopotential approximation

Chemistry is ruled by valence electrons, which are in the highest-energy occupied AOs. These electrons intervene when bonds are created between atoms to build molecules. However, core electrons are only slightly influenced by molecular surroundings. Moreover, core electrons are hardly accessible for bonding as their energy is much lower than valence electrons, and their probability of presence is much closer to atomic cores. In the pseudopotential approximation, valence electrons are treated explicitly with a basis set while core electrons are included in an effective potential $V(\mathbf{r})_{eff}$. This potential is produced by an effective charge Z_{eff} acting on valence electrons and such as $Z_{eff} = Z + Z_{core}$, where Z and Z_{core} are the nuclear and the core electrons charges respectively. It makes calculations cheaper as the number of electrons that are explicitly described is reduced to the valence ones. The pseudopotential approximation in a planewave basis set uses a cutoff radius \mathbf{r}_c to define two regions of space where the pseudopotential acts differently.

From the nucleus to the cutoff value the real wavefunction $\Psi(\mathbf{r})$ and its associated potential $V(\mathbf{r}) = -Z/\mathbf{r}$ are replaced by a smoother nodeless pseudo-wavefunction $\Psi(\mathbf{r})_{pseudo}$ and a pseudopotential $V(\mathbf{r})_{pseudo}$. Beyond \mathbf{r}_c , the pseudopotential and its corresponding wavefunction are meant to follow the true $V(\mathbf{r})$ and $\Psi(\mathbf{r})$ as closely as possible [234]. This behavior is illustrated on Figure III.2. Indeed, the valence electron wavefunctions present several and narrow oscillations in the core region. A high number of planewaves would be needed to explicitly describe them and the computational cost would highly increase, especially for an important accuracy.

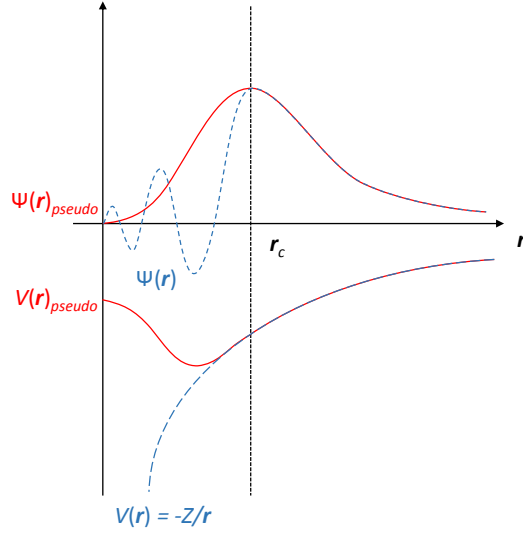


Figure III.2: Schematic diagram of the true potential $V(\mathbf{r}) = -Z/\mathbf{r}$ associated to the true electronic wavefunction of an atom $\Psi(\mathbf{r})$, and of the pseudopotential $V(\mathbf{r})_{pseudo}$ with its corresponding wavefunction $\Psi(\mathbf{r})_{pseudo}$. \mathbf{r} is the distance vector from the nucleus, and Z is the nuclear charge. \mathbf{r}_c , the dotted line, is the cutoff radius beyond which the pseudopotential reproduce as exactly as possible the true potential. Below this cutoff, $V(\mathbf{r})$ and $\Psi(\mathbf{r})$ are replaced by smoother potential and wavefunction.

The only purpose of this approximation is to lower the computational cost, knowing that it is proportional to the size of the basis. A main goal in pseudopotential development being to produce a pseudo-wavefunction as smooth as possible to lower the resource cost. According to Hamann, Schlüter and Chiang, four properties are desirable to have an accurate and transferable pseudopotential [235]:

1. For a given atomic configuration, the real and pseudo wavefunction eigenvalues for valence electrons are equivalent.
2. The real and pseudo atomic wavefunctions are identical beyond the cutoff radius r_c .
3. Integrations of the real and pseudo charge densities from 0 to r agree when $r > r_c$ for each valence state. This insures the norm conservation.

4. The real and pseudo wavefunctions have equivalent logarithmic derivatives and first energy derivatives for $r > r_c$

On a practical aspect, the higher is r_c , the less the basis set needs to be large.

In the present thesis, Troullier-Martins (TM) pseudopotentials will be employed as they show a good efficiency for systems including first-row elements [236].

III.D Molecular Dynamics

To summarize the previous sections of this chapter: DFT will be used to describe electronic structures in pesticide-montmorillonite periodic systems, and PBE-D2 is the chosen functional. Planewave functions are convenient to treat periodicity and will thus be employed while the TM pseudopotentials are used in wavefunctions. Molecular Dynamics (MD) methods will allow us to include temperature effects to simulations and explore the Potential Energy Surfaces (PES) of the systems of interest. This section presents the basics of MD methods.

III. D.1 Classical mechanics for nuclear motion

Within the BO approximation, nuclei may be considered as fixed compared to the very fast motion of electrons. For the same reason, in MD studies, nuclei and electrons are treated differently: electrons are quantum objects and are consequently described by quantum mechanics. In contrast, nuclei are treated as classical objects because of their “slow” motion ; their trajectories are thus described by the classical Newton’s equation of motion.

Newton’s equation of motion and propagation

Let us consider a set of N nuclei treated as classical masses M_I , with I a given nucleus of this set, interacting with a potential $V(\mathbf{R}_1, \dots, \mathbf{R}_N)$ as a function of all nucleus positions \mathbf{R}_I . During a MD trajectory, the position of each nucleus evolves from a given time step t to the next one $t + \delta t$ under the forces due to all the other nuclei at t . The Newtonian equations of motion of every nucleus are under the form:

$$M_I \ddot{\mathbf{R}}_I = - \frac{\partial V(\mathbf{R}_1, \dots, \mathbf{R}_N)}{\partial \mathbf{R}_I} = \mathbf{F}_I(\mathbf{R}_1, \dots, \mathbf{R}_N) \quad (\text{III.53})$$

where $\ddot{\mathbf{R}}_I$ is the acceleration vector of the I nucleus and \mathbf{F}_I the total force vector acting on it. As positions evolve with time, an algorithm is necessary for the trajectory propagation, knowing the initial positions $\mathbf{R}_I(t = 0)$, velocities $\mathbf{v}_I(t = 0)$ and forces on nuclei $\mathbf{F}_I(t = 0)$.

At time t , such algorithm must be able to calculate the positions, velocities and forces at $t + \delta t$ efficiently.

Several features define the quality of a propagator, among them we can cite the conservation of the total energy along the trajectory and the time reversibility of the propagation (as classical mechanics is deterministic: the positions, velocities and accelerations have to be accessible in both directions of time). On a practical aspect, a good algorithm should provide $\mathbf{R}_I(t + \delta t)$ and $\mathbf{v}_I(t + \delta t)$ simultaneously, and handle a large time step. A lot of different algorithms have been developed through the years to perform MD [237], let us mention:

- the Gear Predictor-corrector [238, 239], pretty efficient for small time steps δt but not reversible and very consuming in computer resources.
- the Verlet algorithm [240], time reversible but only good for short simulations as it does not conserve the total energy of the system on long trajectories. This is due to the accumulation of slight errors on the kinetic energy which is calculated from the momentum \mathbf{p} at every step.
- the Leap-frog Verlet algorithm [241] which improves the Verlet algorithm by proposing an explicit propagation of velocities. Thus positions and velocities are propagated in parallel and independently. However, the respective propagation equations of \mathbf{R} and \mathbf{v} do not allow to know positions and velocities simultaneously, which is one of the main drawbacks of this algorithm.
- the Velocity-Verlet algorithm [242] solves the problem of knowing positions and velocities simultaneously by explicitly computing positions and velocities at $t + \delta t$ and also halfway velocities at $t + \frac{1}{2}\delta t$, which gives the three propagation equations:

$$\mathbf{v}_i\left(t + \frac{1}{2}\delta t\right) = \mathbf{v}_i(t) + \frac{1}{2}\mathbf{a}_i(t)\delta t \quad (\text{III.54a})$$

$$\mathbf{R}_i(t + \delta t) = \mathbf{R}_i(t) + \mathbf{v}_i\left(t + \frac{1}{2}\delta t\right)\delta t \quad (\text{III.54b})$$

$$\mathbf{v}_i(t + \delta t) = \mathbf{v}_i\left(t + \frac{1}{2}\delta t\right) + \frac{1}{2}\mathbf{a}_i(t + \delta t)\delta t \quad (\text{III.54c})$$

where \mathbf{a}_i is the acceleration of the system. It is time reversible, propagates velocities and performs a good total energy conservation, which allows to work on long simulation times. The main limitation being that the time step cannot be large, this algorithm is considered as one of the most efficient nowadays.

So far, nuclei and electron motions have been totally separated and the previous section focused on classical motion of nuclei. In the following section, different methods are presented to propagate electron trajectories.

III. D.2 *Ab initio* molecular dynamics approaches

Ab Initio Molecular Dynamics (AIMD) approaches are MD methods that use electronic structure description to obtain the set of forces $\mathbf{F}_1(t) \dots \mathbf{F}_N(t)$ acting on all nuclei positions $\mathbf{R}_1(t) \dots \mathbf{R}_N(t)$ of the system during a trajectory. Within the BO approximation, nuclei are treated classically while electrons propagate through quantum dynamics. Therefore, at each time step t , nuclei are fixed and the time-independent Schrödinger equation is solved for electrons to get the current energy of the system and calculate new forces $\mathbf{F}_I(t)$. This method is the **Born-Oppenheimer Molecular Dynamics (BOMD)** [243, 244]. An advantage of this type of MD is that, as the Schrödinger equation is solved at each step, the wavefunction is always optimized, which means that the system follows the PES during its exploration. However, matrix diagonalizations at every time step can be very expensive to compute, depending on the size of the system and on the method to solve the Schrödinger equation.

In the present thesis, DFT has been chosen, which is a lot cheaper than sophisticated wavefunction methods, however, for systems going up to 600 atoms, BOMD is very expensive.

Car-Parrinello Molecular Dynamics (CPMD) [245] is a way cheaper approach to do AIMD and will be the employed method in this work. Indeed, CPMD allows to propagate electrons, not as quantum entities anymore, but as classical objects: a fictitious mass μ is associated to mono-electronic orbitals, and allows an electronic classical propagation. Then, electrons and nuclei propagations are coupled thanks to a Lagrangian operator, developed hereafter. Thanks to this approach, the total energy is not minimized at every step as in BOMD, which makes simulations a lot less expensive. The Schrödinger equation is solved to obtain the non-optimized electronic total energy and calculate the forces acting on nuclei. However, the non-optimized electronic wavefunction of the system Ψ'_0 leads to a PES sampling energetically higher than the fundamental PES corresponding to the optimized wavefunction Ψ_0 .

The Newton equations III.53 of each method can be written and compared such as:

$$\text{BOMD: } M_I \ddot{\mathbf{R}}_I(t) = -\nabla_I \min_{\Psi_0} \langle \Psi_0 | \hat{H}_e | \Psi_0 \rangle \quad (\text{III.55})$$

$$\text{CPMD: } M_I \ddot{\mathbf{R}}_I(t) = -\nabla_I \langle \Psi'_0 | \hat{H}_e | \Psi'_0 \rangle \quad (\text{III.56})$$

Therefore, in the CPMD method, nuclei and electrons are both classical objects that propagates separately along a trajectory. However, to keep the system as close as possible to the real ground state PES and conserve a physical meaning, it is necessary to maintain

a maximum correlation between nuclei and mono-electronic orbitals. In the following, the CPMD Lagrangian and the nuclear and electronic equations of motion are developed.

Car-Parrinello Lagrangian and equations of motion

The Lagrangian of a dynamical system is defined as the difference between its kinetic and potential energies:

$$\hat{L}(r_i, p_i, t) = \hat{T}(r_i, p_i, t) - \hat{V}(r_i, t) \quad (\text{III.57})$$

Therefore, the Car-Parrinello Lagrangian is defined as:

$$\hat{L}_{CP} = \underbrace{\frac{1}{2} \sum_I M_I \dot{\mathbf{R}}_I^2}_{T_I} + \underbrace{\frac{1}{2} \mu \sum_i \langle \dot{\psi}_i | \dot{\psi}_i \rangle}_{T_e} - \underbrace{\sum_i \langle \psi_i | \hat{H}_e | \psi_i \rangle}_E + \underbrace{\sum_{i,j} \Lambda_{ij} (\langle \psi_i | \psi_j \rangle - \delta_{ij})}_{C_{ortho}} \quad (\text{III.58})$$

where T_I is the nuclear kinetic energy with M_I the nuclear mass, T_e the fictitious kinetic energy of the mono-electronic orbital ψ_i with the fictitious mass μ , E the electronic total energy calculated with the hamiltonian H_e , and C_{ortho} a constraint in order to maintain the orthonormalization of orbitals i and j , with Λ_{ij} a matrix of Lagrange multipliers and δ_{ij} the Kronecker delta such as:

$$\delta_{ij} = \langle \psi_i | \psi_j \rangle = \begin{cases} 0 & ; \quad i \neq j \\ 1 & ; \quad i = j \end{cases} \quad (\text{III.59a})$$

The main question in CPMD is to choose a reasonable value for the fictitious mass μ in order to keep the propagations of nuclei and orbitals consistent. If μ is too low, orbitals move too fast compared to nuclei ; if μ is too large, electrons does not move fast enough to follow nuclei motion. In both cases, the physico-chemical consistency of the system is totally lost. Therefore, it is necessary to tune the value of the fictitious mass, regarding the chosen time step of the simulation and the system nature.

Euler-Lagrange equations

Two classical propagations happen during CPMD simulations: nuclear motions on one hand and mono-electronic orbital motions on the other hand.

These propagations have associated equations of motion, which are obtained through the Euler-Lagrange equations:

$$\left\{ \begin{array}{l} \frac{d}{dt} \frac{\partial \hat{L}}{\partial \dot{\mathbf{R}}_I} = \frac{\partial \hat{L}}{\partial \mathbf{R}_I} \\ \frac{d}{dt} \frac{\partial \hat{L}}{\partial \dot{\psi}_i^*} = \frac{\partial \hat{L}}{\partial \psi_i^*} \end{array} \right. \quad \begin{array}{l} \text{(III.60a)} \\ \text{(III.60b)} \end{array}$$

The development of each side of equations (III.60) gives the following:

$$\Leftrightarrow \left\{ \begin{array}{l} M_I \ddot{\mathbf{R}}_I = -\frac{\partial}{\partial \mathbf{R}_I} \langle \Psi | \hat{H}_e | \Psi \rangle + \frac{\partial}{\partial \mathbf{R}_I} \sum_{i,j} \Lambda_{ij} (\langle \psi_i | \psi_j \rangle - \delta_{ij}) \\ \mu_i \ddot{\psi}_i = -\frac{\delta}{\delta \psi_i^*} \langle \Psi | \hat{H}_e | \Psi \rangle + \frac{\delta}{\delta \psi_i^*} \sum_j \Lambda_{ij} \psi_j \end{array} \right. \quad \begin{array}{l} \text{(III.61a)} \\ \text{(III.61b)} \end{array}$$

Equations (III.61a) and (III.61b) are respectively the equations of motion of nuclei and mono-electronic orbitals.

A last important consideration to take in the implementation of all methods of AIMD is the calculation of the forces acting on nuclei at each step, as the gradient of the potential energy must be calculated every step to get the forces \mathbf{F}_I (III.53), and is computationally expensive. The Hellmann-Feynman theorem can be used to lighten these calculations.

Forces propagation: Hellmann-Feynman theorem

The numerical resolution of the right part of equation (III.61a) is computationally heavy and can be simplified with the following Hellmann-Feynman theorem [246, 247]:

$$\nabla_I \langle \Psi | \hat{H}_e | \Psi \rangle = \langle \Psi | \nabla_I \hat{H}_e | \Psi \rangle \quad \text{(III.62)}$$

only true if the employed basis set is complete or independent of \mathbf{R}_I (planewaves typically), or if the wavefunction is exact. This theorem allows to avoid wavefunction derivation which is expensive to calculate. A limitation of this theorem is that it is only convenient for ground state wavefunctions Ψ_0 . That is why it can be used all along BOMD simulations, however, for CPMD, it can be used only for forces applied on an optimized starting wavefunction.

Concerning the present work, all CPMD trajectory will be executed in planewave basis, thus the Hellmann-Feynman applies.

To summarize, this chapter and the previous ones presented the pesticides, model of soil mineral matter and theories chosen for this thesis, thanks to literature review. Three molecules have been selected: atrazine, metamitron and fenhexamid, to study pesticide interaction with a clay mineral, montmorillonite. For this purpose, the main theoretical method to explore the PES of such periodic interacting systems is CPMD in DFT, using the PBE-D2 exchange-correlation functional, and a planewave basis with the TM pseudopotentials to treat wavefunctions. The forthcoming chapters develop the different systems that have been considered within this work ; the associated methodologies, based on the theories we just described ; and the results and discussions drawn from these studies.

Chapter IV

Atrazine interaction with soil

*“It is also a good rule not to put too much confidence in experimental results
until they have been confirmed by theory.”*

Arthur Eddington

All the studies about pesticides in this work imply a multi-scale approach from the gas phase to the condensed phase to analyze step by step the effects of each improvement of the model. Previous publications of the group concern atrazine and atrazine complexes with sodium and calcium cations in the gas phase. Detailed investigations of the contributions to the interaction were made through a Reduced Variational Space Self-Consistent Field (RVS SCF) decomposition scheme. In a second time, atrazine was deposited on clay surfaces: pyrophyllite and montmorillonite. The choice of the clay surface (substitutions and compensating cations) and the size of the computational cell is detailed thereafter. In this work, a static approach allowed to optimize several atrazine/surface isomers involving various locations and orientations of the pesticide molecule. Both optimized structures and adsorption energies are presented in the paper attached thereafter.

IV.A Atrazine in the gas phase

IV. A.1 Energetic values of interest

IV. A. 1.α Interaction and complexation energies

In the gas phase, the complexation energy E_{comp} is a negative value which characterizes the stabilization of the complexes with respect to both isolated entities. In our case, for pesticide-cation complexes, the complexation energy E_{comp} corresponds to the energy difference between the complex and the cation and the pesticide. For complexation, optimized geometry of each entity is used:

$$E_{comp} = E_{pest-cat(opt)} - E_{pest(opt)} - E_{cat} \quad (E_{comp} \leq 0) \quad (IV.1)$$

The interaction energy E_{int} corresponds to the energy difference between the complex and both cation and pesticide in the geometry of the complex:

$$E_{int} = E_{pest-cat(opt)} - E_{pest} - E_{cat} \quad (E_{int} \leq 0) \quad (IV.2)$$

The preparation energy E_{prep} is the required energy to promote the molecule from its isolated structure to its geometry in the complex:

$$E_{prep} = E_{pest} - E_{pest(opt)} \quad (E_{prep} > 0) \quad (IV.3)$$

The addition of E_{int} and E_{prep} leads to E_{comp} :

$$E_{comp} = E_{int} + E_{prep} \quad (IV.4)$$

IV. A. 1.β RVS SCF energy decomposition scheme

More information can be extracted from E_{int} previously defined by performing a Reduced Variational Space Self Consistent Field (RVS SCF) [248] energy decomposition. By this way, the different contributions to the interaction energy are determined. In the case of two entities in interaction, the process involves SCF optimized monomer Molecular Orbitals (MO) in dimer calculations. The wavefunction of one monomer is frozen while the wavefunction of the other is optimized self-consistently [248]. A truncation of the variational space is possible by removing the virtual orbitals of either fragment (Table IV.1). This method, as it is implemented in the Gamess package [249, 250], has allowed to calculate the different contributions to the interaction energy. If only occupied MOs of each entity are used the sum of the electrostatic contribution E_{elec} , and the Pauli repul-

sion E_{exch} is obtained. E_{elec} is determined thanks to a Morokuma decomposition scheme without antisymmetrization of the wavefunction built from both monomer MOs [251]. To determine the other contributions, some occupied MOs are frozen and some virtuals are taken into account (see Table IV.1):

- the polarization of each entity by the other: E_{pol} (for example, $E_{pol(pest)}$ is the polarization energy of the pesticide by the cation),
- the Charge Transfer (CT) from one entity to the other: E_{CT} (for instance, $E_{CT(pest-cat)}$ is the charge transfer from the pesticide to the cation),
- the Basis Set Superposition Error (BSSE) contribution of each entity: $E_{BSSE(pest)}$ and $E_{BSSE(cat)}$.

MO basis set	Energy contributions
$pest_{occ}$	E_{pest}
cat_{occ}	E_{cat}
$pest_{occ} + cat_{occ}$	$E_{pest} + E_{cat} + \mathbf{E_{exch}} + \mathbf{E_{elec}}$
$[pest_{occ}] + cat_{occ} + cat_{vac}$	$E_{pest} + E_{cat} + E_{exch} + E_{elec} + \mathbf{E_{pol(cat)}}$
$[pest_{occ}] + cat_{occ} + cat_{vac} + pest_{vac}$	$E_{pest} + E_{cat} + E_{exch} + E_{elec} + E_{pol(cat)} + \mathbf{E_{CT(cat-pest)}} + \mathbf{E_{BSSE(cat)}}^*$
$[cat_{occ}] + pest_{vac}$	$E_{cat} + \mathbf{E_{BSSE(cat)}}^*$
$[cat_{occ}] + pest_{occ} + pest_{vac}$	$E_{pest} + E_{cat} + E_{exch} + E_{elec} + \mathbf{E_{pol(pest)}}$
$[cat_{occ}] + pest_{occ} + pest_{vac} + cat_{vac}$	$E_{pest} + E_{cat} + E_{exch} + E_{elec} + E_{pol(pest)} + \mathbf{E_{CT(pest-cat)}} + \mathbf{E_{BSSE(pest)}}^*$
$[pest_{occ}] + cat_{vac}$	$E_{pest} + \mathbf{E_{BSSE(pest)}}^*$

Table IV.1: MO basis sets and related energy contributions calculated with the RVS SCF method. Each MO basis set allows to determine the energy component in bold. MO sets in brackets are frozen during the SCF procedure.

*BSSE scheme differs from counterpoise (only vacant MO accessible).

This last contribution, the BSSE, must be calculated to correct the overestimation of the complex energy due the incompleteness of the basis set. The Basis Set Superposition Error is the name given by Liu and McLean to the overestimation of the intermolecular attraction produced with *ab initio* calculations in weakly bound chemical systems [252, 253]. The cause of this error comes from the fact that, the occupied orbitals of each monomer are better described within the complex than separately [254]. This is due to the availability of the neighboring monomer basis set in the complex which extends the basis set of each monomer. It exists different ways to correct E_{int} from BSSE in considering either only the virtual orbitals (RVS scheme) or both occupied and virtual orbitals (counterpoise correction [255]) of the neighboring monomer.

IV. A.2 Complexation of atrazine with one Na^+ , one Ca^{2+} and two Ca^{2+} cation(s)

In preliminary works, atrazine (Atra) complexes with Na^+ and Ca^{2+} , two important environmental cations were studied [11]. The methodology consists in a static study and is developed on several points of investigation: first the study of one of atrazine metabolite, 2-chloro-1,3,5-triazine-4,6-diamine (denoted AtraMod in the paper) allowed to identify the complexation sites of each cation around the molecule, starting from five structures with a cation in interaction with electron rich binding sites: nitrogen and chlorine atoms. Secondly geometry optimisations at various computational levels were performed with a wide panel of methods: ranging from Hartree-Fock to Coupled Cluster and including DFT/B3LYP and Møller-Plesset with two different basis sets: 6-31G* (basis1) and 6-311+G(2d,2p) (basis2).

The main conclusions are:

- Starting with five different structures for each cation, three families of isomers have been identified for AtraMod-cation and Atra-cation complexes. With Na^+ , AtraMod was a good model to identify the families of isomers for atrazine. Relative energies of the complex families are even correctly reproduced. However the results for AtraMod with Ca^{2+} allow to find only correct binding sites.
- The energetic order of the three lowest-energy AtraMod complexes is the same for a given cation whatever the computational level. However, in the case of Atra- Ca^{2+} , both lowest-energy isomers (different binding sites) are iso-energetic and thus, the energy order depends on the computational level. Moreover, AtraMod and Atra complexes with a calcium cation present more favorable complexation energy than the similar complexes with sodium. As expected regarding the charge, calcium cation interaction is much stronger than sodium one.
- Electrostatic contributions calculated via different schemes (RVS decomposition, replacing the cation by a point charge or through multipole expansion) showed as expected, that the main contribution to the interaction between AtraMod and a cation comes from electrostatics. In the case of Ca^{2+} , the polarization contribution is also decisive to describe the interaction.

Finally, the complexation energy of atrazine with calcium is stronger than with sodium (at the B3LYP/basis2 level: $E_{comp}(\text{Atra-Ca}^{2+}) = -125.1$ kcal/mol and $E_{comp}(\text{Atra-Na}^+) = -39.5$ kcal/mol).

Then, a wide variety of isomers of atrazine in interaction with two calcium cations were optimized at both B3LYP/basis1 and B3LYP/basis2 levels [12]. The three most stable isomers belong to different families but present complexation sites involving nitrogen and chlorine atoms, in a monodentate or bidentate interaction. Those optimized structures constitute good starting points when atrazine is adsorbed on a clay surface. For the lowest-energy isomer, the interaction energy E_{int} (-186.10 kcal/mol) compensates approximately the repulsion energy between both Ca^{2+} cations (7.3 Å) ($+182.67$ kcal/mol) at B3LYP/basis1. After adding preparation energy, a repulsive complexation energy of $+21.76$ or $+9.80$ kcal/mol is obtained using basis1 or basis2 respectively. In the same way, complexation enthalpies and free energies are also repulsive. From gas to condensed phase, other contributions should lead to attractive adsorption energies.

In the following, atrazine interacts with a clay surface. The first paper confirmed that interaction of atrazine with Ca^{2+} is significantly stronger than with Na^+ [11], thus calcium is chosen as clay compensating cation. Calcium cation positions over the surface would probably play an important role on the pesticide adsorption energy as inter-cation repulsion is significantly large (see results of the second paper [12]). Moreover, dispersion effects between the surface and the pesticide would emphasize the attractive contributions of the interaction.

IV.B Atrazine adsorbed on a surface

IV. B.1 Montmorillonite model

Montmorillonite, the most abundant type of smectite clay, has been chosen. Montmorillonite is a mineral with a layered structure. Isomorphic substitutions naturally happen in each layer (octahedral AlO_6 , or tetrahedral SiO_4). Al^{3+} and Si^{4+} are generally substituted by Mg^{2+} and Al^{3+} respectively. The resulting negative charge default is compensated by the presence in the interlayer space of metal cations such as Na^+ or Ca^{2+} . To maximize interaction with the pesticide, Ca^{2+} compensating cation has been chosen. To end up with satisfying model for montmorillonite, the following requirements have to be fulfilled:

- substitutions in the octahedral sheet (O) $> \approx 15$ % ;
- one atrazine molecule adsorbed at the surface should not interact with its images.

The montmorillonite model has been built from pyrophyllite, a similar layered mineral for which X-ray data are available ($a = 5.161$ Å, $b = 8.957$ Å and $c = 9.351$ Å ; $\alpha =$

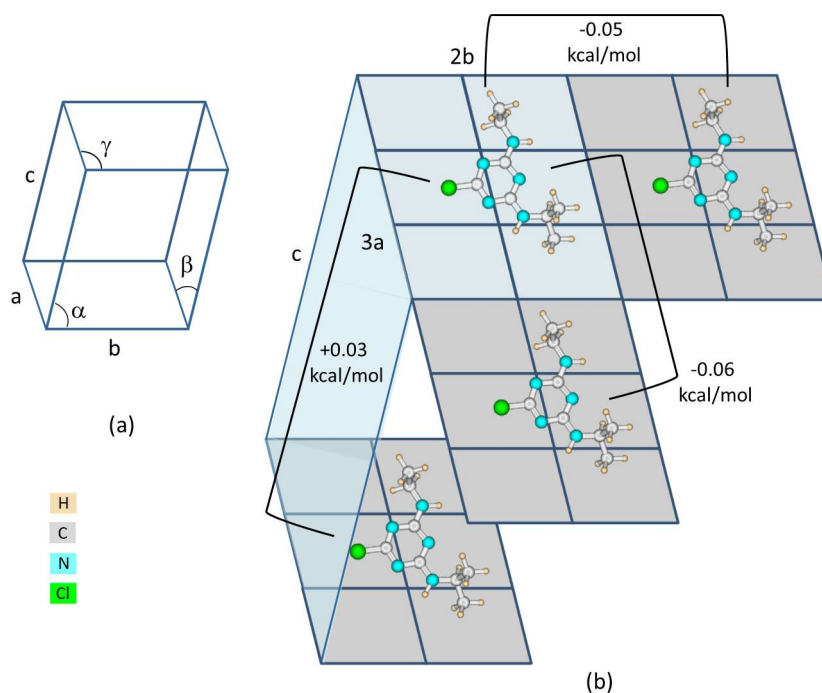


Figure IV.1: (a) The triclinic unit cell of pyrophyllite ($a \neq b \neq c$ and $\alpha \neq \beta \neq \gamma \neq 90^\circ$), (b) the computational cell consists in 6 unit cells : $3a \times 2b \times c$ (in light turquoise) to minimize interaction energies between two atrazine images along a , b and c (30 Å) directions. Values are given in kcal/mol (identical for PBE/basis1 and PBE/basis2).

91.03° , $\beta = 100.37^\circ$ and $\gamma = 89.75^\circ$) [135]. The computational cell was extended and consists of 6 unit cell ($\times 3$ in the a direction and $\times 2$ in the b direction, see Figure IV.1). This computational cell contains four consecutive isomorphous substitutions in the O sheet where Al^{3+} have been replaced by Mg^{2+} cations. This quantity represents $\sim 16.7\%$ of substituted aluminium cations and produces a -4 negative charge that can be compensated by two Ca^{2+} ($d_{\text{Ca}-\text{Ca}} \approx 10$ Å).

Then, atrazine is deposited on a clay surface, using Atr- Ca^{2+} or Atr- $(\text{Ca}^{2+})_2$ isomers as starting structures. Thus a comparison between gaussian basis sets and planewaves (pw) is presented thereafter.

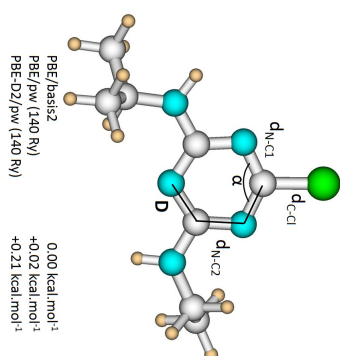
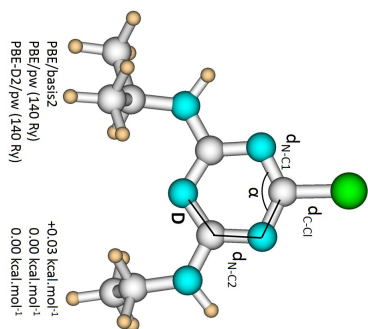
IV. B.2 Gaussian versus planewave basis sets on atrazine and complexes geometries and energies

On Table IV.2, two atrazine conformers, which were the lowest in energy in our previous work, are depicted. On Table IV.3, two Atr- Ca^{2+} isomers significantly separated in relative energy, including the most stable, are drawn. Their relative energies and their structural parameters have been computed at both PBE/basis2 using Gaussian software

and PBE/pw using CPMD software (with a 80 (only for the lowest-energy conformer and isomer) or 140 Rydberg kinetic energy cutoff, at the Γ point and in the previously described computational cell). In the case of atrazine, a PBE-D2/pw optimisation was also performed as isolated atrazine is used to compute adsorption energies with the montmorillonite surface. As we worked with charge species, the influence of a Tuckerman poisson solver (employed to isolate the system from its periodic images by reducing the electrostatic potential smoothly to zero at the unit cell boundaries) has also been tested on both geometries and energies.

The main discrepancy on distances between the two methods is of 0.01 Å for Atra, and 0.04 Å for Atra-Ca²⁺. Distances driven by electrostatic interactions are obviously the most affected by the method. Angles and dihedrals are very similar whatever the method even when the cation is involved. Finally, the differences in relative energy are lower than the accuracy of the methods: 0.03 kcal/mol for Atra conformers and 0.17 kcal/mol for Atra-Ca²⁺ isomers. No significant change is thus observable within the periodic PBE/pw relaxation as compared to the gas phase PBE/basis2 whatever the cutoff or the use of Tuckerman Poisson solver. In the case of Atra, a PBE-D2/pw optimisation was also performed as isolated atrazine is used to compute adsorption energies. The dispersion correction effect is negligible on the structures (0.001 Å on distances, 0.1° on angles and 0.4° on dihedrals) and weak on relative energies (0.2 kcal/mol).

Finally, results of calculations concerning atrazine adsorbed on montmorillonite at PBE-D2/pw (80 Ry, without Tuckerman Poisson solver and within a $15.500 \times 17.931 \times 30$ Å cell) can be compared to the gas phase atrazine and atrazine-Ca²⁺ complexes computed at PBE/basis2 or at PBE/pw (80 Ry, with/without Tuckerman Poisson solver and within a $15.500 \times 17.931 \times 30$ Å cell) in order to point out the influence of the adsorption of the molecule onto the surface.



	d_{N-C1}	d_{C-Cl}	d_{N-C2}	α	D	d_{N-C1}	d_{C-Cl}	d_{N-C2}	α	D
PBE/basis2	1.323	1.760	1.356	129.2	+0.15	1.319	1.761	1.356	129.3	+0.42
PBE/pw (80 Ry/a×b×c box)	1.324	1.750	1.355	128.9	-0.10					
PBE/pw (140 Ry/a×b×c box)	1.323	1.750	1.355	128.9	-0.06	1.319	1.750	1.357	129.0	+0.32
PBE/pw (780 Ry/a×b×c box)	1.324	1.750	1.355	128.9	-0.01					
PBE-D2/pw (140 Ry/a×b×c box)	1.324	1.750	1.354	129.0	+0.11	1.320	1.750	1.355	129.1	+0.73

Table IV.2: Comparison of the structures and energies of two different atrazine conformers using a gaussian basis set in the gas phase and a periodic plane-wave calculation. Both computations were made using the PBE functional. Adding a dispersion correction to the PBE (PBE-D2) was also tested. Distances are given in Å, angles and dihedrals in degrees. Following the atom numbering of Figure 4 in the upcoming paper, α is the N6C1N2 *s*-triazine angle and D is the C1N2C3N4 dihedral. Computational cell parameters: a = 15.500 Å, b = 17.931 Å and c = 30 Å.

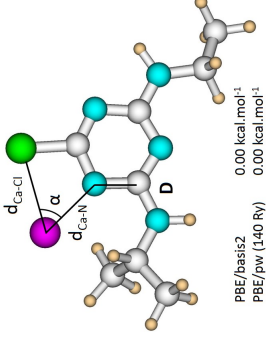
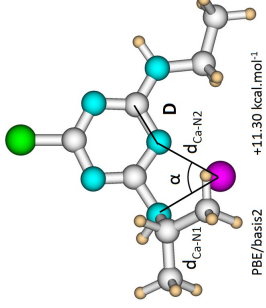
						
	E_{comp}	d_{Ca-Cl}	d_{Ca-N}	α	D	
PBE/basis2	-132.3	2.796	2.222	61.1	-176.2	
PBE/pw (80 Ry/a×b×c box)	-137.98	2.791	2.215	61.3	-175.9	
PBE/pw (140 Ry/a×b×c box)	-137.81	2.793	2.213	61.2	-176.0	
PBE/pw (T80 Ry/a×b×c box)	-137.97	2.790	2.215	61.3	-176.1	
		d_{Ca-N1}	d_{Ca-N2}	α	D	
		2.400	2.267	59.9	-174.0	
		2.364	2.259	60.5	-172.5	

Table IV.3: Comparison of the structures and energies of two different Atraz-Ca²⁺ complexes using a gaussian basis set in the gas phase and a periodic planewave calculation. Both computations were made using the PBE functional. Distances are given in Å, angles and dihedrals in degrees. Following the atom numbering of Figure 4 in the upcoming paper, α is the angle made by the cation with the two atoms of the bidentate binding sites (left: N6CaCl14 ; right: N7CaN4) and D is a dihedral (left: C5N6CaCl14 ; right: N7CaN4C3). Computational cell parameters: $a = 15.500$ Å, $b = 17.931$ Å and $c = 30$ Å.

IV. B.3 Atrazine adsorption on montmorillonite

In the following paper, a static approach of the adsorption of atrazine on the montmorillonite model was published. Four different isomers of atrazine-Ca-montmorillonite complexes (Atra-Mont) were chosen: three presenting the *s*-triazine cycle face-to-face with the clay surface (PARA1, PARA2 and PARA3), and one where this cycle is orthogonal to the montmorillonite surface (ORTHO). Moreover, one atrazine-pyrophyllite isomer was studied. Finally, atrazine is physisorbed on the pyrophyllite surface thus dispersion corrections are mandatory to describe the atrazine/pyrophyllite interaction. Without dispersion, atrazine-pyrophyllite distance is 0.2 Å longer and the adsorption energy is about 0 kcal/mol. Therefore, the paper evidences the necessity to introduce dispersion corrections along the optimisation process for pesticide interaction with a clay surface. The D2 empirical dispersion correction of S. Grimme is available in CPMD and has so been used [230, 231]. At PBE-D2/pw level, adsorption energies of atrazine on montmorillonite ($-15 < \Delta E_{ads} < -30$ kcal/mol) are two to three times larger than on pyrophyllite (≈ -10 kcal/mol). For the lowest-energy isomers (PARA1 and PARA3), the adsorption involves one Ca^{2+} cation in a monodentate way as well as the chlorine atrazine atom. The resulting Ca-Cl distance is only a little longer than in the gas phase ($\approx +0.03$ Å) pointing out a strong interaction between the pesticide and the surface and then, a large adsorption energy. At the same time, deformation (or preparation) energies are small < 4 kcal/mol and come mainly from atrazine. The structural modifications of the montmorillonite clay surface concern essentially the calcium position of the interacting cation ($+0.13$ Å on both Ca1-O_b and Ca1-O_h , see Table IV.4 and Figure IV.2 (d) and (e)). In the published version of the article, the montmorillonite results given at $c = 30$ Å have been mistakenly replaced by values at $c = 9.534$ Å. Thus, Tables IV.4 and IV.5, as well as Figure IV.2 replaces Tables 3 and 4, and Figure 2 of the paper. The clay internal geometrical modifications attributed in the paper to the adsorption of atrazine comes for real from the transition between the bulk and the surface. Indeed, the deformations concern distances around substitutions underneath calcium cations (see distances in red on Figure IV.2 (d)). During the transition, both calcium cations move closer to the surface (≈ -0.20 Å on Ca-O_h and Ca-O_b distances). The other distances and all the angles are only very slightly modified. When atrazine is adsorbed, the only relevant modification concerns the involved Ca^{2+} cation that moves away from the surface ($\approx +0.15$ Å see distance in blue on Figure IV.2 (e)). The small deformation (preparation) energies of MONT (< 2 kcal/mol) are consistent with the moderate changes in the surface. The chosen substitutions imply an inter-cation distance of ≈ 10 Å, not much compatible with an involvement of both cations in the adsorption for atrazine. Changing atrazine by metamitron or fenhexamid, adsorption sites and inter-cation distances will evolve and both cations might be involved in the

adsorption (see Chapter VI). Thus, the substitution positions have a decisive influence on both the geometry of the complex and its adsorption energy. In future development of this study, it would be interesting to investigate other Ca-montmorillonite models.

This static approach of atrazine adsorption on both pyrophyllite and montmorillonite allows to validate the use of PBE-D2/pw (80 Ry within a $15.500 \times 17.931 \times 30$ Å cell at the Γ point). As expected after the gas phase study, the large and negative adsorption energies testify of the increase of attractive effects in particular of the dispersion contribution when the surface is involved. In the following, a dynamic approach will be applied on one hand to explore in more details the PES of pesticide complexes in the gas phase, and on the other hand, to describe more exhaustively the adsorption of the pesticide with the surface.

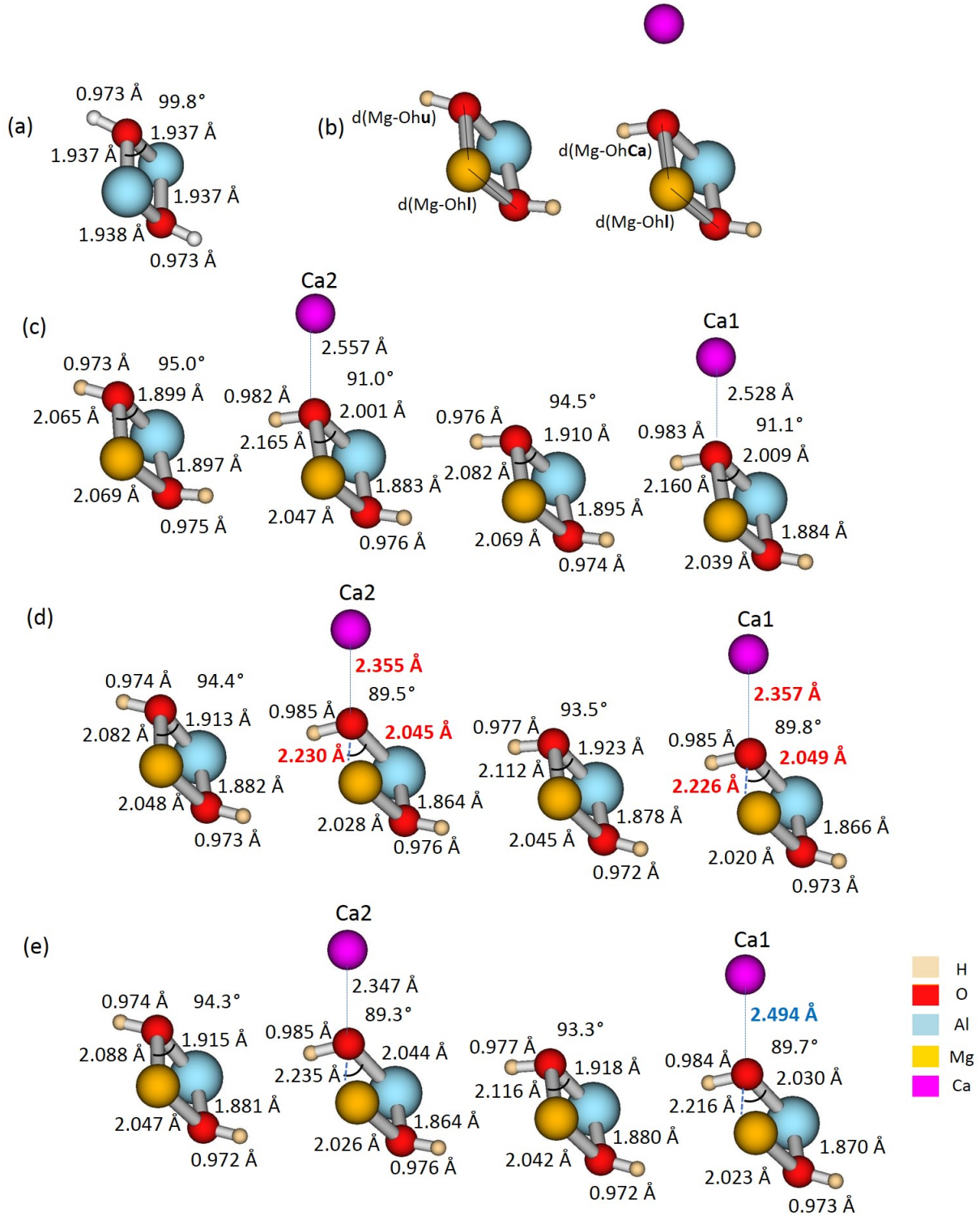


Figure IV.2: Geometrical parameters near substitutions (O_{sub}) in (c) montmorillonite ($c = 9.354$ Å), (d) montmorillonite ($c = 30$ Å, distances in red are the most impacted going from the bulk to the surface), (e) atrazine-montmorillonite (PARA1, $c = 30$ Å, the distance in blue is the most modified by the adsorption) versus (a) pyrophyllite at the PBE-D2/pw level. Distances are in Å and angles in degrees. (b) The various labels of Mg-O_h distances: Mg-O_hCa if Ca²⁺ is located just above the O_h oxygens, Mg-O_hu for other upper O_h oxygens and Mg-O_hl for other lower O_h oxygens.

Mont			Para1	Para2	Para3	Ortho
<i>c</i>	9.354	30	30	30	30	30
d_{Si-O_b}	1.629	1.629	1.629	1.629	1.629	1.629
d_{Si-O_a}	1.635	1.638	1.638	1.638	1.638	1.638
d_{Al-O_a}	1.969	1.974	1.974	1.974	1.974	1.974
d_{Al-O_h}	1.938	1.940	1.940	1.940	1.940	1.940
d_{Mg-O_a}	2.084	2.085	2.085	2.085	2.085	2.084
$d_{Mg-O_h \mathbf{Ca}}$	2.162	2.228	2.225	2.233	2.226	2.233
d_{Mg-O_h}	2.087	2.056	2.057	2.056	2.056	2.056
$d_{Mg-O_h \mathbf{u}}$	2.074	2.097	2.102	2.099	2.099	2.101
$d_{Mg-O_h \mathbf{l}}$	2.056	2.035	2.034	2.034	2.034	2.033
d_{O_h-H}	0.978	0.978	0.978	0.978	0.978	0.978
d_{Ca1-O_h}	2.557	2.355	2.347	2.359	2.498	2.408
d_{Ca2-O_h}	2.528	2.357	2.494	2.402	2.344	2.365
d_{Ca1-O_b}	0.466	0.246	0.392	0.303	0.225	0.245
d_{Ca2-O_b}	0.497	0.249	0.233	0.252	0.407	0.324
$d_{Atrazine-O_b}$	-	-	3.091	3.267	3.196	5.187

Table IV.4: Clay calculated average distances (in Å) in montmorillonite and atrazine-montmorillonite isomers at PBE-D2/pw level. Kinetic energy cutoff equal to 80 Ry. Distances in bold are the most impacted by complexation with atrazine.

Mont			Para1	Para2	Para3	Ortho
<i>c</i>	9.354	30	30	30	30	30
$\widehat{AlO_aAl}$	99.1	98.8	98.8	98.8	98.8	98.8
$\widehat{AlO_aMg}$	96.9	96.1	96.1	96.1	96.1	96.1
$\widehat{AlO_hAl}$	98.1	98.2	98.2	98.2	98.3	98.2
$\widehat{AlO_hMg}$	94.8	97.4	97.2	97.5	97.2	97.4
$\widehat{HO_hAl}$	113.0	113.6	113.7	113.7	113.7	113.7
$\widehat{HO_hMg}$	107.1	111.5	111.5	111.8	111.5	111.6
$\widehat{O_aAlO_a}$	88.2	88.3	88.3	88.3	88.3	88.3
$\widehat{O_aAlO_h}$	92.8	92.7	92.6	92.6	92.6	92.6
$\widehat{O_aMgO_a}$	87.7	88.3	88.3	88.3	88.3	88.3
$\widehat{O_aMgO_h}$	93.7	93.9	93.8	93.9	93.9	93.9
$\widehat{O_hAlO_h}$	83.5	83.3	83.3	83.3	83.3	83.3
$\widehat{O_hMgO_h}$	80.8	80.1	80.1	79.9	80.1	80.0
$\widehat{O_aSiO_b}$	110.7	111.0	111.1	111.0	111.1	111.1
$\widehat{O_bSiO_b}$	108.0	107.6	107.6	107.6	107.6	107.6
$\widehat{SiO_aAl}$	125.6	126.0	126.0	126.1	126.0	126.0
$\widehat{SiO_aMg}$	121.4	121.9	121.9	121.8	121.8	121.8
$\widehat{SiO_bSi}$	133.3	133.2	133.2	133.2	133.2	133.2

Table IV.5: Clay calculated average angles (in degrees) in montmorillonite and atrazine-montmorillonite isomers at PBE-D2/pw level. Kinetic energy cutoff equal to 80 Ry.

Theoretical Study of the Atrazine Pesticide Interaction with Pyrophyllite and Ca^{2+} -Montmorillonite Clay Surfaces

Bastien Belzunces,^[a,b,d] Sophie Hoyau,^[a,b] Magali Benoit,^[c] Nathalie Tarrat,^[c] and Fabienne Bessac^{*[a,b,d]}

Atrazine, a pesticide belonging to the s-triazine family, is one of the most employed pesticides. Due to its negative impact on the environment, it has been forbidden within the European Union since 2004 but remains abundant in soils. For these reasons, its behavior in soils and water at the atomic scale is of great interest. In this article, we have investigated, using DFT, the adsorption of atrazine onto two different clay surfaces: a pyrophyllite clay and an Mg-substituted clay named montmorillonite, with Ca^{2+} compensating cations on its surface. The calculations show that the atrazine molecule is physisorbed on the pyrophyllite surface, evidencing the necessity to use dispersion-corrected computational methods. The adsorption energies of atrazine on montmorillonite are two to three times larger than on pyrophyllite, depending on the adsorption pattern. The computed adsorption energy is of about -30 kcal

mol^{-1} for the two most stable montmorillonite-atrazine studied isomers. For these complexes, the large adsorption energy is related to the strong interaction between the chlorine atom of the atrazine molecule and one of the Ca^{2+} compensating cations of the clay surface. The structural modifications induced by the adsorption are localized: for the surface, close to substitutions and particularly below the Ca^{2+} cations; in the molecule, around the chlorine atom when Ca^{2+} interacts strongly with this basic site in a monodentate mode. This study shows the important role of the alkaline earth cations on the adsorption of atrazine on clays, suggesting that the atrazine pesticide retention will be significant in Ca^{2+} -montmorillonite clays. © 2016 Wiley Periodicals, Inc.

DOI: 10.1002/jcc.24530

Introduction

In the EU, REACH legislation (Registration, Evaluation, Authorization and restriction of Chemicals) imposes on manufacturers to provide eco-toxicological data for substances with produced volumes higher than one metric ton per year. About 30,000 existing substances have to be registered by 2018 by the Member states.^[1,2] Beyond specific regulatory obligations, questions concern chemical substances that are potentially present in the environment. From 30,000 to 100,000 chemical substances are concerned by environmental risks assessment.^[3] However, their behavior in the environment and their transfer to environmental components such as water, soil or air have been studied for only a very small proportion of the chemicals because these studies are time-consuming and/or cost prohibitive. To address this gap, *in silico* approaches are an attractive alternative allowing the evaluation of the behavior of organic compounds within reasonable timeframe and costs. Among the priority substances, atrazine (2-chloro-*N*⁴-ethyl-*N*⁶-isopropyl-1,3,5-triazine-4,6-diamine), belonging to the s-triazine family, is one of the most employed pesticides.^[4,5] It has been forbidden within the European Union since 2004 and is still being used in about 80 countries all over the world. The use of atrazine is highly controversial because of its negative impact on the environment. Therefore, even if it has been widely studied, the behavior of this compound in soils and water at the atomic scale remains misunderstood and is of great interest.^[6–12] Some atrazine properties are presented in Table 1. This pesticide has a moderate hydrophobicity as shown by the octanol/water partition coefficient ($\log K_{ow} = 2.75 < 3$). Thus, bioaccumulation of atrazine is low. With a pK_a of 1.6, atrazine is a

very weak base. At the same time, atrazine is almost insoluble in water at ambient temperature as its solubility is below 0.1 mol L^{-1} . Consequently, in a preliminary approach, depositing atrazine on a dry clay seems reasonable.

In this work, we have studied the adsorption of atrazine on two clay surfaces: pyrophyllite and montmorillonite, the most abundant type of smectite clays. Smectites and pyrophyllites are both minerals with a layered structure (Fig. 1a). Each layer is made of three successive sheets: one octahedral (O) sheet in between two tetrahedral (T) sheets. Oxygen atoms (O^{2-}) are the vertices of octahedrons and tetrahedrons. Tetrahedrons point in direction of the octahedrons and share an O^{2-} anion with them. Tetrahedral sites are all occupied by silicon Si^{4+} cations. Octahedral positions are either vacant, for one third,

[a] B. Belzunces, S. Hoyau, F. Bessac

Laboratoire de Chimie et Physique Quantiques, 118, route de Narbonne, Université de Toulouse, UPS, IRSAMC, Toulouse, F-31062, France
E-mail: fabienne.bessac@purpan.fr

[b] B. Belzunces, S. Hoyau, F. Bessac

CNRS (UMR 5626), F-31062, Toulouse, France

[c] M. Benoit, N. Tarrat

CEMES - Centre d'Elaboration de Matériaux et d'Etudes Structurales - CNRS (UPR 8011), 29 rue Jeanne Marvig, Toulouse, F-31055, France

[d] B. Belzunces, F. Bessac

Ecole d'Ingénieurs de Purpan, 75, Université de Toulouse, INPT, voie du TOEC, BP 57611, Toulouse Cedex 03, F-31076, France

Contract grant sponsor: HPC resources of CALMIP supercomputing center; Contract grant number: 2015-[P1222]; Contract grant sponsor: HPC resources from CINES; Contract grant number: 2015-[cpq7002]; Contract grant sponsor: CIM3 (Labex NEXT); Contract grant sponsor: French government for Bastien Belzunces' PhD funding.

© 2016 Wiley Periodicals, Inc.

Table 1. Properties of atrazine pesticide.

Solubility (mol L ⁻¹), 26°C ^[13]	log Kow ^[14]	pKa ^[15]
1.61×10^{-4}	2.75	1.6

or occupied by aluminum Al³⁺ cations. Such clay minerals are defined as dioctahedral. In dioctahedral minerals, the vacancies are *cis* or *trans* with respect to the hydroxyl groups. Minisini et al.^[16] and Tunega et al.^[17] have shown that the energy difference between the *cis*- and *trans*-vacant isomers is insignificant. In our studies, we focus on the *trans*-vacant isomer, which is predominant in nature.

The main differences between pyrophyllite and montmorillonite are the isomorphous substitutions that can naturally happen in montmorillonite clays in each layer and that are absent in pyrophyllite (Fig. 1b). In montmorillonite clays, tetrahedral sheet substitutions (Tsub) of Si⁴⁺ are limited to around 15% of the sites, and octahedral sheet substitutions (Osub) of Al³⁺ are generally more frequent. Mg²⁺ is the dominant cation to replace Al³⁺ in Osub (Fig. 1c) and Al³⁺ is the dominant cation to replace Si⁴⁺ in Tsub. As a consequence of isomorphous substitutions, negative charges are created, which are counterbalanced by the presence of metal cations such as Na⁺ or Ca²⁺ in the interlayer space. These exchangeable cations play an important role, in particular, in water retention by the mineral and thus in the swelling properties of montmorillonite clays. In the case of pyrophyllite, as isomorphous substitutions do not occur, the electric charge of the layered structure is zero and the interlayer distance is fixed. Consequently, pyrophyllite does not have swelling properties.

Because of environmental issues but also for their interesting chemistry, several authors got interested into organic chemicals interacting with clay minerals,^[18] in particular montmorillonite by using computational chemistry methods.^[19–29] For instance, DNA bases on acidic external surface of montmorillonite has been studied by P. Mignon and M. Sodupe.^[30–34] V. Aggarwal et al.^[35,36] have investigated adsorption of polar organic compounds onto montmorillonite. P. Clausen et al. have computed the adsorption of volatile molecules.^[37,38] To the best of our knowledge, no theoretical studies focusing on the interaction between atrazine and clays have been performed. However, in earlier studies, the complexes between atrazine and two abundant soil cations, Na⁺ and Ca²⁺, have been studied by means of Hartree–Fock, density functional theory (B3LYP), Møller–Plesset perturbation theory (MP2), and Coupled Cluster theory (CCSD(T)).^[39,40] These studies evidenced, among other effects, that the complexation of atrazine-(Ca²⁺)₂ isomers onto a clay surface will lead to an attractive complexation energy thanks to dispersive effects between the pesticide and the surface. That will be the subject of the present paper. After the computational details (Computational details), pyrophyllite and montmorillonite models used in this work will be described as well as the definition and the method to compute interaction, deformation and adsorption energies (Models). In the next part (Results and Discussion), results will be exposed and discussed. First, we will present and discuss the energetics and geometries of one atrazine-pyrophyllite complex. Then, atrazine-montmorillonite complexes, in which atrazine lies face-to-face or orthogonally to the surface, will be under investigation.

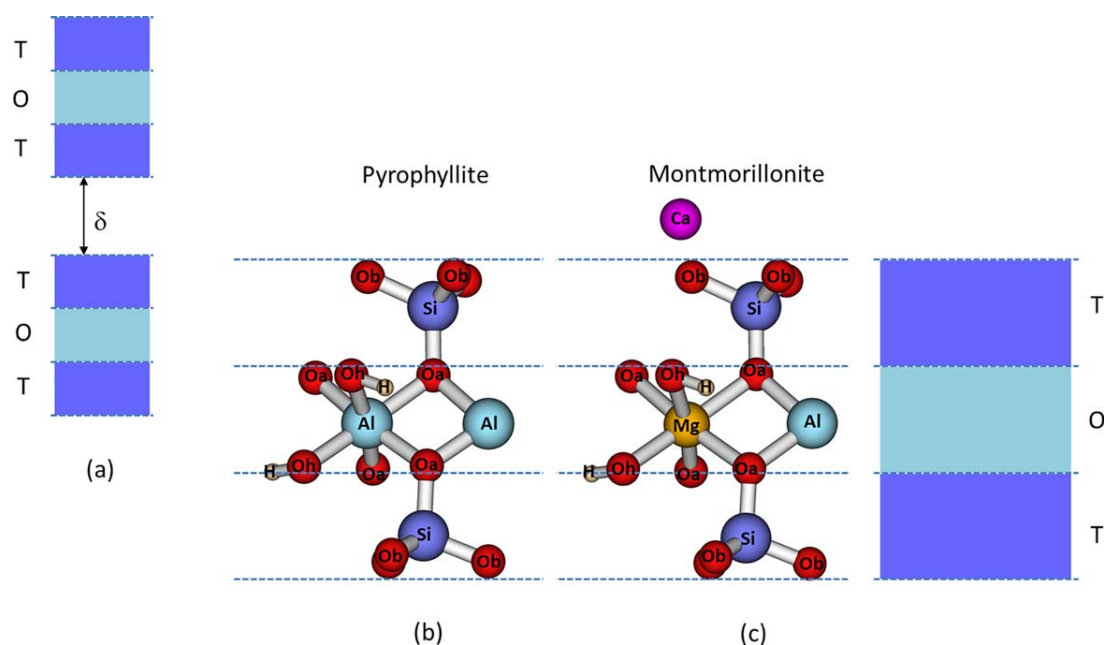


Figure 1. a) The layered structure of pyrophyllite and smectite clay minerals: T stands for Tetrahedron and O for Octahedron, δ is the interlayer distance; b) The Oxygen environment: tetrahedral around silicon and octahedral around aluminum in pyrophyllite; c) Isomorphous substitutions occur in montmorillonite: example of Al³⁺ replaced by Mg²⁺ in the O sheet, Ca²⁺ are added in the interlayer space to compensate the charge default. The various types of oxygen atoms are represented: Oh correspond to oxygen connected to hydrogens, Ob (basal) are involved in bonds with Si atoms only, Oa (axial) are bonded to both Si and Al (or Mg). [Color figure can be viewed at wileyonlinelibrary.com]

Table 2. Experimental X-ray parameters of the unit cell of pyrophyllite from R. Wardle et al.^[52] used as a starting point for periodic DFT optimizations. Optimized unit cell parameters calculated using the PBE functional without (PBE/pw) or with dispersion in the D2 Grimme scheme (PBE-D2/pw), 140 Ry as plane-wave energy cutoff and the Monkhorst–Pack sample of the Brillouin zone $3 \times 2 \times 2$ which corresponds to 12 *k*-points per unit cell. In brackets, the differences between the calculations results and the X-ray values are given.

	Unit cell XR parameters R. Wardle et al. ^[52]	Optimized unit cell PBE/pw 140 Ry $3 \times 2 \times 2$	Optimized unit cell PBE-D2/pw 140 Ry $3 \times 2 \times 2$
<i>a</i> (Å)	5.161	5.167 (+6 × 10 ^{−3})	5.167 (+6 × 10 ^{−3})
<i>b</i> (Å)	8.957	8.968 (+1 × 10 ^{−2})	8.965 (+8 × 10 ^{−3})
<i>c</i> (Å)	9.351	9.357 (+6 × 10 ^{−3})	9.354 (+3 × 10 ^{−3})
α (°)	91.03	91.03	91.03
β (°)	100.37	100.38 (+1 × 10 ^{−2})	100.37
γ (°)	89.75	89.76 (+1 × 10 ^{−2})	89.76 (+1 × 10 ^{−2})
Volume (Å ³)	425.2	426.5	426.1

Computational Details

The structures were investigated using density-functional theory (DFT) with generalized gradient approximation (GGA) under periodic boundary conditions in the plane-wave (pw) pseudopotential scheme using the Car–Parrinello Molecular Dynamics (CPMD) software.^[41–43] We used the Perdew–Burke–Ernzerhof^[44] (PBE) exchange–correlation functional. Atomic norm-conserving pseudopotentials were derived with the Martins–Troullier^[45] (MT) procedure and applied using the Kleinman–Bylander^[46] scheme to treat nonlocal terms. For Mg atoms, a nonlinear core correction (NLCC) pseudopotential was used.^[47] The kinetic energy cutoff was fixed to 140 Rydberg in association with the $3 \times 2 \times 2$ *k*-point mesh for the full cell optimization (lattice parameters + internal atomic coordinates) of pyrophyllite (unit cell in Supporting Information Fig. S1a). For both pyrophyllite and montmorillonite clay systems, a 80 Rydberg kinetic energy cutoff with the $1 \times 1 \times 1$ *k*-point mesh was used for geometry optimizations (internal atomic coordinates) or single point energy calculations (computational cell in Supporting Information Fig. S1b). The *k*-point grid for the integration in the Brillouin zone (BZ) was determined by the Monkhorst–Pack procedure.^[48] All atoms were allowed to fully relax along the calculated forces until residual force components were less than 5×10^{-4} a.u. The lattice parameters were optimized within 1×10^{-3} a.u., the wavefunctions within 1×10^{-6} a.u. Optimizations were carried out including the forces coming from the empirical Grimme's correction for dispersion. This correction, implemented in the CPMD package under its D2 version,^[49] is based on pairwise interatomic potentials of the form $C_6 R^{-6}$, where C_6 values are derived from ionization potentials and static polarizabilities of the considered atom. Hereafter calculations carried out with the CPMD software will be denoted as PBE/pw and PBE-D2/pw without and with the dispersion correction, respectively. Charges have been computed using the Hirshfeld population analysis.^[50]

Details concerning atrazine and atrazine- Ca^{2+} complexes using gaussian basis sets, DFT with the PBE functional and the Gaussian03 package^[51] are available for comparison in Supporting Information.

Models

Pyrophyllite model

Pyrophyllite unit cells constitute our building blocks for clay surfaces. We started from experimental X-ray data from R.

Wardle et al.^[52] (Table 2). Cell parameters and volume are given in Table 2 for the X-ray data and the periodic calculations with and without dispersion effects. The discrepancies between experimental and computational cell parameters are less than 1×10^{-2} Å for *a*, *b*, and *c* and less than 1×10^{-2} degree for α , β , and γ (see unit cell on Supporting Information Fig. S1a). Experimental and computed internal structural parameters of pyrophyllite are given in Tables 3 and 4. Our values are comparable or overall slightly closer to the experimental data^[52] than those of Clausen et al.^[38] computed with cell parameters fixed to the experimental values. Geometrical parameters very slightly depend on *c* distance, that is, the geometry optimization of pyrophyllite we have performed with *c* = 30 Å to simulate a surface leads to geometrical parameters nearly equal to those computed with *c* = 9.35 Å (discrepancy of at the most 0.003 Å for the average Oh–H distance and 0.6° for the OaSiOb angle). Finally, X-ray distances and angles are overall correctly reproduced at both PBE/pw and PBE-D2/pw levels with a difference of at the most 0.03 Å and 2 degrees (Si–Oa and OaAlOh, respectively).

Montmorillonite model

To build a montmorillonite model, only the most abundant isomorphic substitutions were considered, that is, in the octahedral sheet (Fig. 1c). In this framework, substitutions in the octahedral sheet have to be more abundant than 15%. Therefore, to build a model allowing the interaction of atrazine with two Ca^{2+} located on the clay surface, the computational cell was extended and consists of six unit cells ($3a \times 2b$, Supporting Information Fig. S1b) and four substitutions of Al^{3+} by Mg^{2+} were introduced. This cell has four isomorphic substitutions in the octahedral sheet (~16.7% of substitutions) and the negative layer charge produced (−4 e) is compensated by two Ca^{2+} cations in the interlayer, which were placed above substitutions, as far as possible from each other to minimize the electrostatic repulsion. Substitutions never concern neighboring positions. This initial structure was optimized at the PBE-D2/pw level (with a 80 Rydberg kinetic energy cutoff and a $1 \times 1 \times 1$ *k*-point mesh) using the pyrophyllite lattice parameters except for *c* (30 Å) to simulate a surface.

The average clay deformation due to isomorphic substitutions (Al^{3+} by Mg^{2+}) and compensating Ca^{2+} cation addition was analyzed in comparing montmorillonite to pyrophyllite

Table 3. Clay calculated average distances (in Å) in pyrophyllite, pyrophyllite-atrazine, montmorillonite, and montmorillonite-atrazine isomers at the PBE-D2/pw level. As a comparison, the experimental distances,^[52] the PBE/pw distances computed in the present work and by Clausen et al.^[38] are given for pyrophyllite. Kinetic energy cutoff equal to 80 Ry, except [a] kinetic energy cutoff equal to 140 Ry. Distances in bold are the most impacted by complexation with atrazine.

	Pyrophyllite						Montmorillonite				
	Exp ^[52] Pyro	PBE ^[38] Pyro	PBE/pw Pyro ^[a]	PBE-D2/pw			PBE-D2/pw				
				Pyro ^[a]	Pyro	Pyro-Atra	Mont	Mont-Atra			
								Para1	Para2	Para3	Ortho
c	9.351	25	9.357	9.354	30	30	30	30	30	30	30
d(Si-Ob)	1.615	1.625	1.624	1.624	1.624	1.625	1.629	1.629	1.629	1.629	1.629
d(Si-Oa)	1.623	1.644	1.651	1.654	1.655	1.655	1.635	1.638	1.638	1.638	1.638
d(Al-Oa)	1.953	1.932	1.965	1.968	1.969	1.969	1.969	1.974	1.974	1.974	1.974
d(Al-Oh)	1.938	1.896	1.934	1.937	1.935	1.935	1.938	1.940	1.940	1.940	1.940
d(Mg-Oa)							2.084	2.085	2.085	2.085	2.084
d(Mg-OhCa)							2.162	2.225	2.233	2.226	2.233
d(Mg-Oh)							2.087	2.057	2.056	2.056	2.056
d(Mg-Ohu)							2.074	2.102	2.099	2.099	2.101
d(Mg-Ohl)							2.056	2.034	2.034	2.034	2.033
d(Oh-H)		0.964	0.972	0.973	0.976	0.976	0.978	0.978	0.978	0.978	0.978
d(Ca1-Oh)							2.557	2.347	2.359	2.498	2.408
d(Ca2-Oh)							2.528	2.494	2.402	2.344	2.365
d(Ca1-Ob)							0.466	0.392	0.303	0.225	0.245
d(Ca2-Ob)							0.497	0.233	0.252	0.407	0.324
d(AtraCycle-Ob)						3.559		3.091	3.267	3.196	5.187

Table 4. Clay computed average angles (in degrees) in pyrophyllite, pyrophyllite-atrazine, montmorillonite, and montmorillonite-atrazine isomers at the PBE-D2/pw level. As a comparison, the experimental angles,^[52] the Clausen et al. angles^[38] and the PBE/pw angles computed in the present work are given for pyrophyllite. Kinetic energy cutoff equal to 80 Ry, except [a] kinetic energy cutoff equal to 140 Ry. When several angles involving the same atom connectivity have been clearly identified, the average value of each kind is also presented (in italics). Angles in bold are the most impacted by complexation with atrazine.

	Pyrophyllite						Montmorillonite				
	Exp ^[52] Pyro	PBE ^[38] Pyro	PBE/pw Pyro ^[a]	PBE-D2/pw			PBE-D2/pw				
				Pyro ^[a]	Pyro	Pyro-Atra	Mont	Mont-Atra			
								Para1	Para2	Para3	Ortho
c	9.351	25	9.357	9.354	30	30	30	30	30	30	30
AlOaAl	100.2	102	99.4	99.1	99.1	99.1	99.1	98.8	98.8	98.8	98.8
AlOaMg							96.9	96.1	96.1	96.1	96.1
AlOhAl	100.2	103	100.0	99.8	99.8	99.8	98.1	98.2	98.2	98.3	98.2
AlOhMg							94.8	97.2	97.5	97.2	97.4
HOHAl		121	117.1	116.6	117.1	117.0	113.0	113.7	113.7	113.7	113.7
HOHMg							107.1	111.5	111.8	111.5	111.6
OaAlOa			88.3	88.4	88.3	88.3	88.2	88.3	88.3	88.3	88.3
			80.6	81.0	80.9	80.9					
	94.0	92	94.1	94.0	93.5	93.4					
OaAlOh			93.6	93.5	93.2	93.5	92.8	92.6	92.6	92.6	92.6
	94.2	94	94.3	94.2	94.2	94.3					
	94.1	92	92.2	92.1	92.0	92.0					
OaMgOa							87.7	88.3	88.3	88.3	88.3
OaMgOh							93.7	93.8	93.9	93.9	93.9
OhAlOh			80.0	80.2	80.2	80.2	83.5	83.3	83.3	83.3	83.3
OhMgOh							80.8	80.1	79.9	80.1	80.0
OaSiOb	109.4	109	109.3	109.2	109.8	109.7	110.7	111.1	111.0	111.1	111.1
ObSiOb	109.5	109	109.1	109.2	109.2	109.2	108.0	107.6	107.6	107.6	107.6
SiOaAl			125.7	125.8	125.7	125.7	125.6	126.0	126.1	126.0	126.0
SiOaMg							121.4	121.9	121.8	121.8	121.8
SiObSi			134.1	134.1	133.8	133.7	133.3	133.2	133.2	133.2	133.2
	132.3	130	130.9	131.0	130.4	130.4					
	140.7	142	140.7	140.3	140.9	140.8					

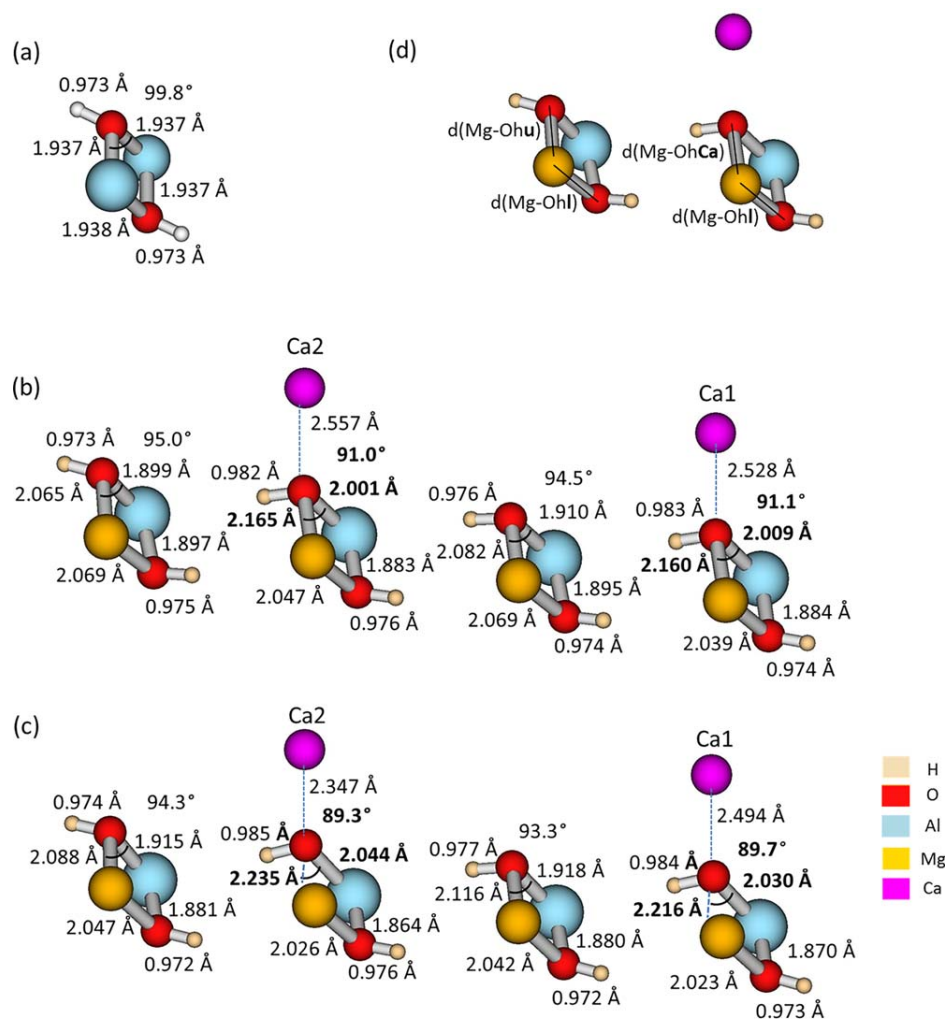


Figure 2. Geometrical parameters near substitutions (Osub) in (b) montmorillonite and (c) montmorillonite-atrazine (PARA1) versus (a) pyrophyllite at the PBE-D2/pw level. Distances are in Å and angles in degrees. (d) The various labels of Mg-Oh distances: Mg-OhCa if Ca^{2+} is located just above the Oh oxygens, Mg-Ohu for other upper Oh oxygens and Mg-Ohl for all lower Oh Oxygens. [Color figure can be viewed at wileyonlinelibrary.com]

($c = 30$ Å). The clay average distances are only slightly modified (the largest difference is 0.02 Å for Si-Oa, the others are negligible, see Table 3). Overall, average angles change only slightly (Table 4). However, angles involving Si atoms (T sheets) are modified by 0.1 to 1.2 degrees. The largest variations concern the angles including Al and Oh atoms (O sheet). Indeed, the third of Oh atoms are close to substitutions and induces differences of 3.9 and 3.3 degrees for average values of HOHAl and OHAlOh, respectively.

The local geometry around the substitution is clearly modified; particularly near the Ca^{2+} cations (Figs. 2a for pyrophyllite and 2b for montmorillonite). Indeed, Al-Oh distances near substitutions are reduced by 0.03–0.04 Å if Ca^{2+} is not located above the substitution. However, if the compensating cation Ca^{2+} lies just above the substitution, the Al-Oh distance increases significantly for the upper Oh oxygen (noted Ohu) (+0.06–0.07 Å compared to pyrophyllite) whereas it decreases for the lower Oh oxygens, noted Ohl. The discrepancy between the shorter and the larger Al-Oh distances around the substitutions is of

0.12–0.13 Å. The same difference is observed for Mg-Oh distances in the vicinity of Ca^{2+} . The interaction between the Ca^{2+} cations and the upper Oh is responsible for these geometrical modifications. In the same way, Mg-Oh distances are larger by 0.12 Å for Ohu located under Ca^{2+} cations than for the Ohl. For the Oh far from Ca^{2+} , distances are slightly larger than the latest (from +0.02 to +0.04 Å). The Ca^{2+} -Oh optimized distances are 2.557 and 2.528 Å in montmorillonite.

Atrazine on clay surfaces

Surface model. For the calculations of the isolated atrazine and surfaces as well as of the atrazine-surface complexes, a triclinic cell ($15.500 \times 17.931 \times 30.000$ Å³) was used that corresponds to $3a \times 2b \times 30$ Å³, with a and b being the optimized pyrophyllite unit cell parameters at PBE-D2/pw (kinetic energy cutoff: 140 Ry; and $3 \times 2 \times 2$ k-point mesh) and c large enough to avoid the interaction with the periodic images in the direction normal to the surface. In order to ensure that there is no interaction with

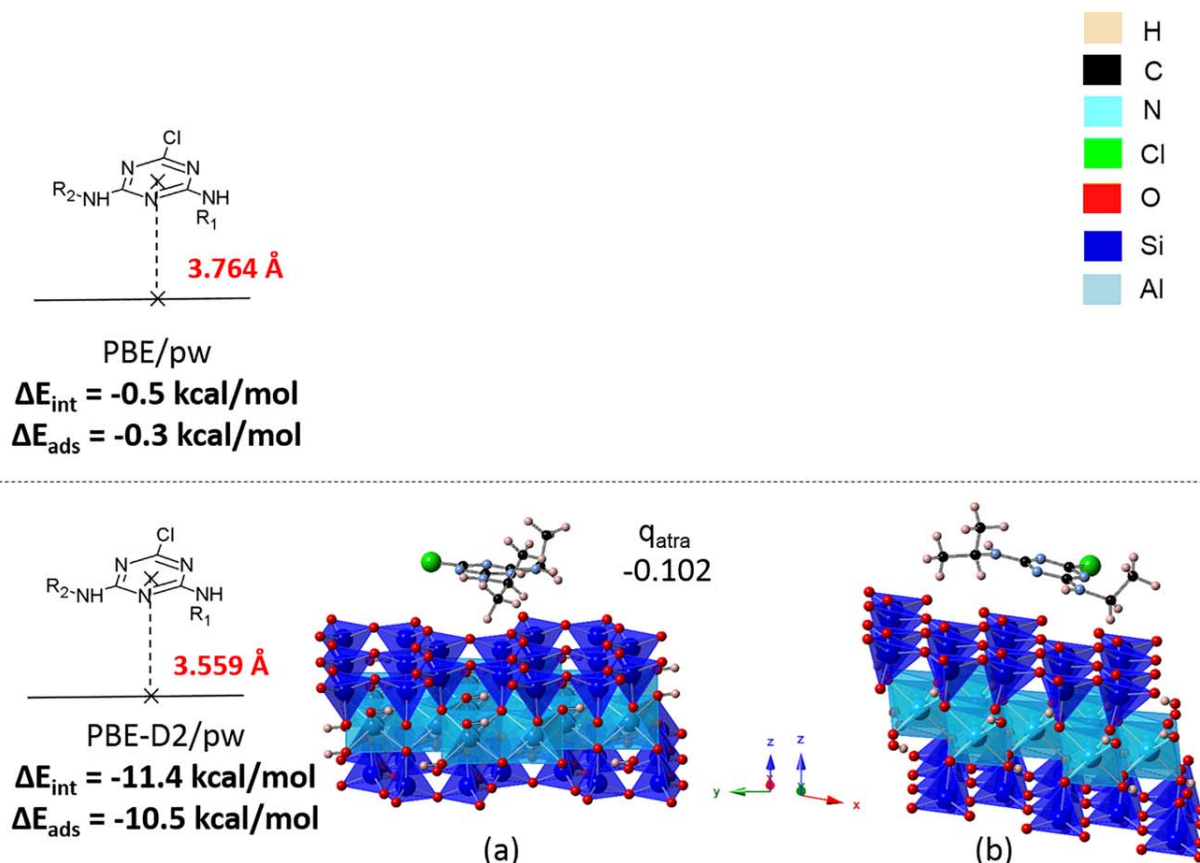


Figure 3. Pyrophyllite-atrazine: interaction (ΔE_{int}) and adsorption (ΔE_{ads}) energies (in kcal mol⁻¹, in bold), Hirshfeld charge^[50] bore by atrazine (q_{atra}) and surface to atrazine (cycle geometrical center) distances (in Å, in red) at the PBE/pw and PBE-D2/pw levels. a) View along the *a* direction; b) view along the *b* direction for the optimized pyrophyllite-atrazine complex at the PBE-D2/pw level. [Color figure can be viewed at wileyonlinelibrary.com]

the periodic images, calculations with different *c* parameters were performed. The results are given in Supporting Information (Table S1). A schematic representation of the atrazine molecule over the computational cell is given on Figure S1b. We ensured that the interaction energy of the closest two atrazine molecules on the six unit cells surface is negligible (Fig. S1b in Supporting Information for details).

Interaction and adsorption energies. The interaction energies between the atrazine molecule and the surface were calculated as

$$\Delta E_{\text{int}} = E_{\text{AtrazineSurf}} - E_{(\text{Atrazine})\text{cplx}} - E_{(\text{Surf})\text{cplx}} \quad (1)$$

where $E_{\text{AtrazineSurf}}$ is the energy of the atrazine-surface complex at its optimized geometry, and $E_{(\text{Atrazine})\text{cplx}}$ and $E_{(\text{Surf})\text{cplx}}$ are the energies of the isolated atrazine and surface, respectively, each one in the geometry they have in the complex.

The adsorption energies between the atrazine molecule and the surface were calculated as

$$\Delta E_{\text{ads}} = E_{\text{AtrazineSurf}} - E_{\text{Atrazine}} - E_{\text{Surf}} \quad (2)$$

where $E_{\text{AtrazineSurf}}$ is the energy of the atrazine-surface complex at its optimized geometry, and E_{Atrazine} and E_{Surf} are the energies of the isolated atrazine and surface, respectively, optimized in a ($3a \times 2b \times 30 \text{ Å}^3$) cell.

The difference between interaction and adsorption energies gives access to the deformation energy (noted ΔE_{def}) of the molecule and of the surface due to the adsorption.

Results and Discussion

As in previous works, we studied atrazine molecule and atrazine- Ca^{2+} complexes, we made some tests to ensure that the results on structures and energetics obtained with both a PBE gaussian basis set and a PBE plane wave basis set approaches are comparable (see Supporting Information, Figs. S2 and S3 for details).

Atrazine-pyrophyllite complex

The atrazine was deposited face-to-face onto a pyrophyllite surface ($c = 30 \text{ Å}$, Fig. 3). This orientation was chosen to maximize the influence of dispersive effects to evaluate their importance for this type of complexes. The geometry of the atrazine-pyrophyllite complex (Pyro-Atra) was optimized at the PBE/pw and PBE-D2/pw levels. Under complexation, the geometry of the atrazine molecule is slightly modified (see Fig. 4). At the PBE-D2/pw level, the variations are of 0.003 Å for the distances, 0.1 degree for the *s*-triazine cycle angles and up to 1.7 degree for the amino group angles which depend on alkyl chain orientation. The pyrophyllite deformation is also

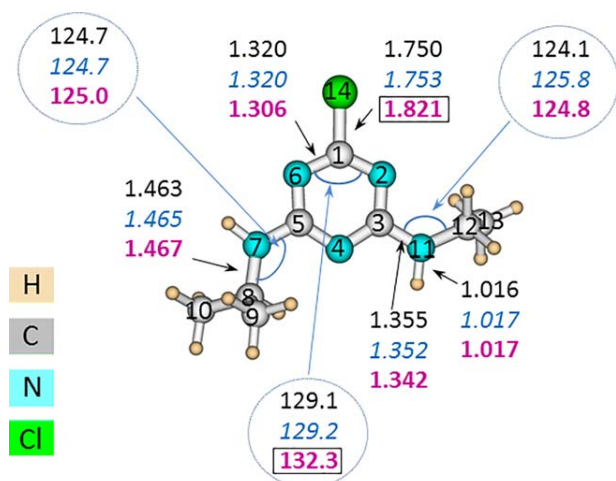


Figure 4. Numbering of atoms and selected geometrical parameters for atrazine (in black), in interaction with pyrophyllite (in blue italics) and with montmorillonite in PARA1 (in bold pink) at the PBE-D2/pw level. Values corresponding to largest deviations are framed. Distances are given in Å and angles (encircled) in degrees. [Color figure can be viewed at wileyonlinelibrary.com]

minimal when interacting with the atrazine molecule (0.001 Å for SiOb and 0.3 degree for OaAlOh at the most at the PBE-D2/pw level, see Tables 3 and 4).

Without dispersion, both adsorption and interaction energies are close to zero (−0.31 and −0.47 kcal mol^{−1}, see Fig. 3 and Table 5). The distance between the plane containing the more external clay oxygen atoms and the center of the *s*-triazine cycle is 3.764 Å. The orientation of the molecule with respect to the surface remains similar when introducing dispersion, whereas the atrazine-surface distance shortens to 3.559 Å. At the same time, both adsorption and interaction energies strengthen to −10.53 and −11.41 kcal mol^{−1}, respectively. In this case, the deformation energy is weak (0.88 kcal mol^{−1}: 0.25 kcal mol^{−1} for pyrophyllite and 0.63 kcal mol^{−1} for atrazine, see Table 6). Taken into account the adsorption planar mode, the distance between the molecule and the surface, the small deformation, the magnitude of the interaction energy and the small charge transfer to atrazine

($q_{\text{atra}} = -0.102$, Fig. 3), one could assume that the molecule is physisorbed on the pyrophyllite surface. Dispersion effects being tremendous for physisorbed aromatic molecules (−12.46 kcal mol^{−1} for Pyro-Atra, Table 5), only the PBE-D2/pw method has been used to optimize geometries in the following.^[53]

Atrazine-montmorillonite complex

To study the atrazine-montmorillonite complex, four structures were optimized: three face-to-face, labeled PARA, (Fig. 5) and one where the *s*-triazine cycle is orthogonal to the clay surface, denoted ORTHO (Fig. 6). PARA isomers were designed so that the molecule interacts with both Ca²⁺ cations similarly as they do in the two lowest atrazine-(Ca²⁺)₂ isomers previously obtained in the gas phase.^[39] From PARA1 to PARA2, atrazine was rotated around the *z*-axis of about +90°. In PARA3, the optimized atrazine conformation of PARA2 was modified: the ethyl chain was rotated to reproduce its position in the lowest isomer optimized in the gas phase. Finally, PARA1 and PARA3 have the strongest adsorption energies (−27.42 and −26.73 kcal mol^{−1}, respectively). PARA2 is higher by 12.22 kcal mol^{−1} than PARA1. For all PARA isomers, adsorption and interaction energies are close (Table 6). The largest deformation energies correspond to PARA3 (3.80 kcal mol^{−1}) and PARA1 (3.59 kcal mol^{−1}). In all cases, atrazine is more distorted than the montmorillonite surface ($\Delta E_{\text{def}}(\text{Atra}) > 56\% \Delta E_{\text{def}}$, see Table 6). The atrazine-surface distance has been computed between the geometrical center of the *s*-triazine cycle of atrazine and the plane containing the Ob oxygen atoms (Fig. 1). This distance will be noted Atracycle-Ob in the following. It is related to the order in relative, adsorption and interaction energies: $d_{\text{PARA1}} = 3.091 \text{ Å} < d_{\text{PARA3}} = 3.196 \text{ Å} < d_{\text{PARA2}} = 3.267 \text{ Å}$ (Fig. 5).

When montmorillonite is complexed with atrazine, local geometry modifications around substitutions are important, particularly near Ca²⁺. For each isomer, the Mg-Oh distances of the upper Oh oxygens (Mg-Oh_u and Mg-Oh_{Ca}, see Fig. 2d for labels and Table 3 for average values) near substitutions increase in average by 0.03 Å for Mg-Oh_u and by 0.07 Å if Ca²⁺ is above (Mg-Oh_{Ca}) in comparison with bare

Table 5. Interaction and adsorption energies between the atrazine molecule and the surface. Energies in kcal mol^{−1} calculated using the PBE functional without (PBE/pw) or with dispersion in the D2 Grimme scheme (PBE-D2/pw), 80 Ry as plane-wave energy cutoff and the Monkhorst-Pack sample of the Brillouin zone which corresponds to the Γ -point. In italics are reported the energies for the same geometries in which the alkyl chains of the atrazine are replaced by hydrogen atoms (2-chloro-4,6-diamino-1,3,5-triazine).

	PBE/pw		PBE-D2/pw					
	ΔE_{int}	ΔE_{ads}	ΔE_{int} without dispersion	Dispersion term	ΔE_{int}	ΔE_{ads} without dispersion	Dispersion term	ΔE_{ads}
PYROPHYLLITE								
Pyro-Atra	−0.47	−0.31	+1.05	−12.46	−11.41	+1.45	−11.98	−10.53
MONTMORILLONITE								
PARA1			−12.99	−18.02	−31.01	−9.65	−17.77	−27.42
			−13.23	−11.53	−24.76			
PARA2			−0.61	−15.88	−16.49	+0.15	−15.35	−15.20
PARA3			−12.41	−18.12	−30.53	−8.85	−17.88	−26.73
ORTHO			−2.59	−13.73	−16.32	−1.04	−12.95	−13.99
			−0.29	−3.27	−3.56			

Table 6. Interaction, deformation and adsorption energies between the atrazine molecule and the surface. Energies in kcal mol^{−1} calculated using the PBE functional with dispersion in the D2 Grimme scheme, 80 Ry as plane-wave energy cutoff and the Monkhorst–Pack sample of the Brillouin zone which corresponds to the Γ -point.

	ΔE_{int}	$\Delta E_{\text{def}}(\text{Atra})$	$\Delta E_{\text{def}}(\text{Surf})$	ΔE_{ads}
PYROPHYLLITE				
Pyro-Atra	−11.41	+0.63	+0.25	−10.53
MONTMORILLONITE				
PARA1	−31.01	+2.22	+1.37	−27.42
PARA2	−16.49	+1.00	+0.29	−15.20
PARA3	−30.53	+2.14	+1.66	−26.73
ORTHO	−16.32	+1.96	+0.37	−13.99

montmorillonite. The discrepancy between the Mg–Oh distances of the upper (Mg–OhCa) and the lower oxygens (Mg–OhI) near Ca²⁺ increases similarly in the PARA series. For instance, it goes from 0.12 for montmorillonite to 0.20 Å when complexing atrazine in PARA1 (Figs. 2b and 2c). The Al–Oh distance also increases for the upper Oh by about 0.02–0.04 Å near Ca²⁺ when atrazine is adsorbed (Figs. 2b and 2c). The modification of this distance induced by the presence of the Ca²⁺ cation (0.07 Å, Figs. 2a and 2b) is twice larger than that induced by the adsorption of atrazine (0.03 Å, Figs. 2b and 2c).

The Ca²⁺ cations move closer to the surface when atrazine is adsorbed. Indeed, the average Ca–Ob distance shortens from 0.482 Å in montmorillonite to [0.278–0.316] Å in PARA isomers. Furthermore, the distance of Ca²⁺ to the surface is even shorter as atrazine is further from the cations. It is the case of PARA2, the adsorption energy of which is the smallest (in absolute value as $\Delta E_{\text{ads}} < 0$) (−15.20 kcal mol^{−1}) and the Atracycle–Ob (3.267 Å) and average Atracycle–Ca (2.989 Å) distances are the longest. Atracycle–Ca is the average distance between Atracycle–Ca1 and

Atracycle–Ca2: the distances between the plane containing the *s*-triazine cycle of atrazine and the corresponding Ca²⁺ cation. For PARA1 and PARA3, adsorption energies are similar (−27.42 and −26.73 kcal mol^{−1}, respectively) and the largest. The dispersion term is equal in both cases (−17.77 and −17.88 kcal mol^{−1}, respectively, Table 5). These isomers correspond to Atracycle–Ob (3.091 and 3.196 Å) and Atracycle–Ca (2.778 and 2.880 Å) distances shorter than in PARA2. The charge transfer from atrazine to the surface is, indeed, larger for PARA1 and PARA3 ($q_{\text{atra}} = 0.383$ and 0.327, respectively) than for PARA2 ($q_{\text{atra}} = 0.272$).

For PARA2, the Ca²⁺–Oh distances are reduced by 0.13 to 0.20 Å (Table 3) as compared to montmorillonite. In PARA1 (Fig. 2c) the Ca2–Oh distance decreases even more significantly from 2.557 to 2.347, the second Ca–Oh distance is less reduced from 2.528 and 2.494 Å. In this isomer, the distance between Ca²⁺ and Cl, the closest atom in atrazine is 2.833 Å (Fig. 7), a little longer than in the corresponding isomer of atrazine–(Ca)₂²⁺ in the gas phase (2.681 Å). The same behavior is observed in PARA3. In this case, the chlorine atom of atrazine interacts with Ca1 cation with a Ca–Cl distance of 2.839 Å (Fig. 7).

In PARA1, the local deformation of atrazine is significant: the distance C1–Cl increases by 0.07 Å (Fig. 4) and the *s*-triazine angle N6C1N2 by 3.2 degrees (Fig. 4). The latter geometrical parameters are identical for atrazine adsorbed in PARA3. The strong interaction between the Cl–atrazine atom and its closest Ca²⁺ cation could explain that PARA1 and PARA3 are the lowest montmorillonite–atrazine isomers. In the case of PARA1 (PARA3), the distance between Ca2 (Ca1) and the upper Oh atom near the substitution decreases even more as the atrazine–Ca2 (atrazine–Ca1) distance is larger. Locally, the clay deformation induced by the atrazine molecule around Ca2

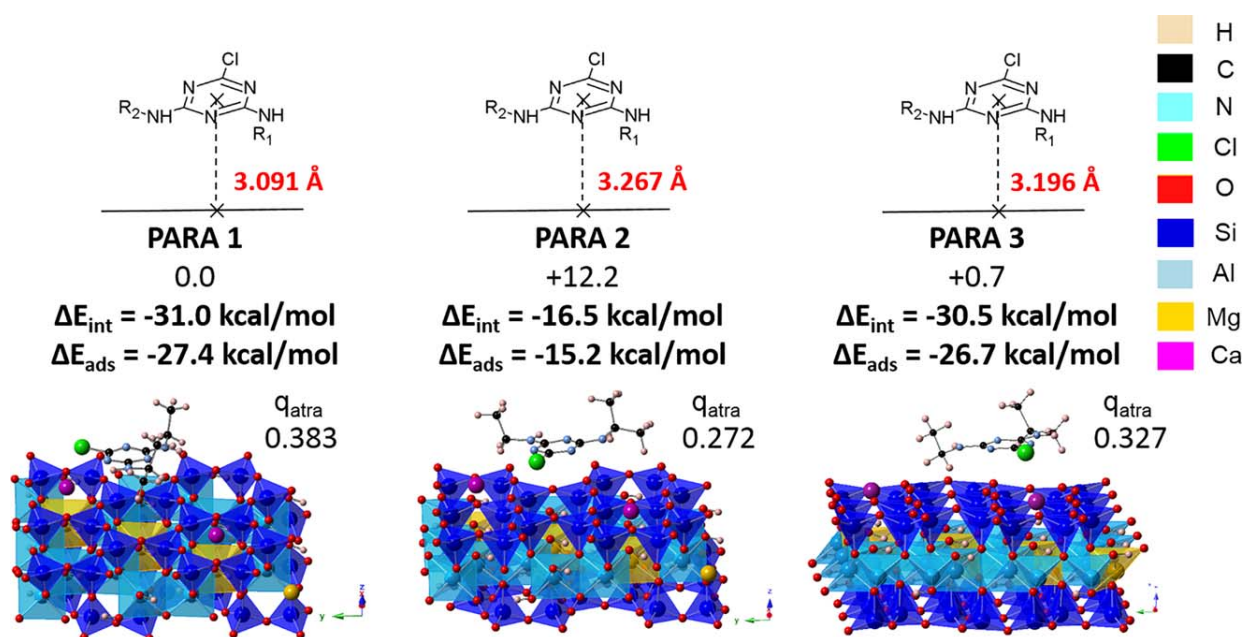


Figure 5. Montmorillonite-atrazine: relative total energies (PARA 1 is the reference), interaction (ΔE_{int}) and adsorption (ΔE_{ads}) energies (in kcal mol^{−1}, in bold), Hirshfeld charge^[50] bore by atrazine (q_{atra}) and surface to atrazine (cycle center) distances (in Å, in red) at the PBE-D2/pw level. Views along the *a* direction. [Color figure can be viewed at wileyonlinelibrary.com]

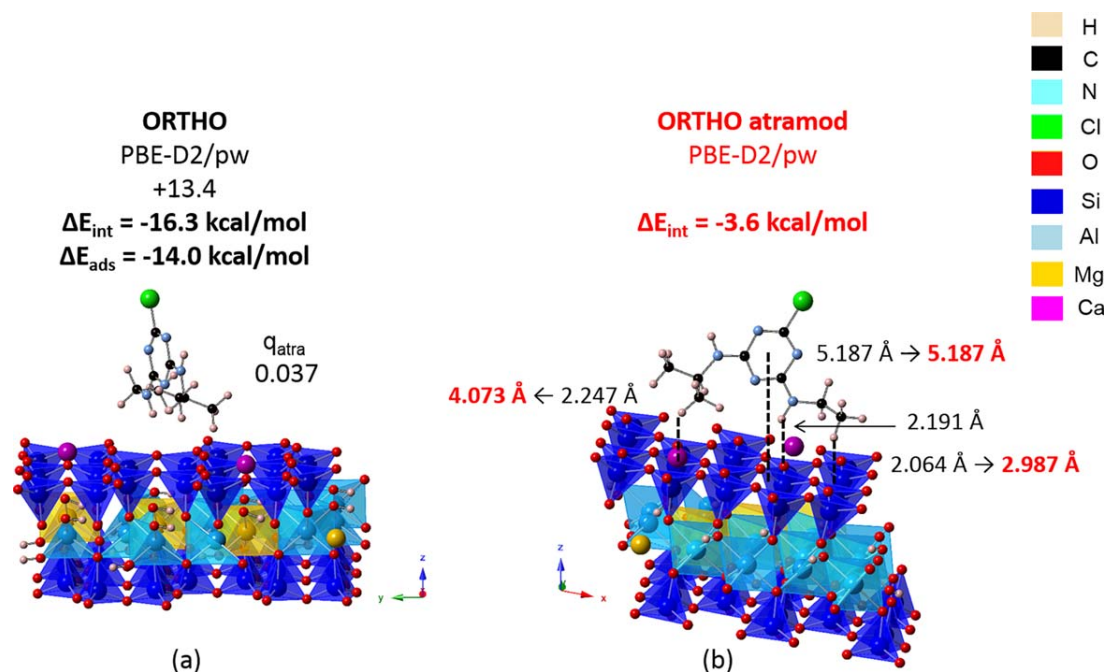


Figure 6. Montmorillonite-molecule ORTHO isomer: relative energy (PARA 1 is the reference), distances, interaction (ΔE_{int}) and adsorption (ΔE_{ads}) energies of atrazine (in black) or atramod (in red) with the surface at the PBE-D2 level. a) View along the *a* direction; b) view along the *b* direction. Distances are given in Å and energies in kcal mol⁻¹. Hirshfeld charge^[50] bore by atrazine (q_{atra}). The ORTHO montmorillonite-atrazine optimized structure has been used for montmorillonite-atramod. [Color figure can be viewed at wileyonlinelibrary.com]

(Ca1) is larger than in PARA2. Moreover, deformation energies are the largest for PARA1 and PARA3, notably the $\Delta E_{\text{def}}(\text{Surf})$ part (Table 6). In both isomers, as the atrazine and the surface are becoming closer, the deformation terms are increasing for both entities, the atrazine and the surface. Nevertheless, the benefit realized on adsorption energies are more important than the loss. In PARA2, both Ca²⁺ cations interact with atrazine via nitrogen atoms (either the two amino, or one amino and one of the *s*-triazine cycle) with long distances (4.978 and 4.148 Å, see Fig. 7) and not via the Cl atom. This different interaction mode explains the smallest adsorption energy of PARA2.

The ORTHO isomer was obtained starting from PARA1, by rotating the molecule of about +90° around the *x*-axis. In the optimized ORTHO isomer (Fig. 6), the distance between the center of the *s*-triazine cycle and the surface is 5.187 Å and the closest atoms to the surface are hydrogen atoms from the ethyl and closest amino groups, which are distant from the surface by 2.094 Å and 2.191 Å (distance between the hydrogen atom and the plane containing the Ob oxygen atoms), respectively. For this isomer, the basic atoms are far from the surface, the atrazine-surface charge transfer is then the smallest in the series ($q_{\text{atra}} = 0.037$). As for the PARA isomers, the Ca²⁺ cations stand close to the surface (0.245 and 0.324 Å, see Table 3). The same deformation of the clay surface can be observed for ORTHO than for PARA2, especially concerning Mg-Oh and Al-Oh distances near substitutions (Table 3). Computed deformation energies are, by the way, similar for the surface (0.29 for PARA2 and 0.37 kcal mol⁻¹ for ORTHO). The atrazine geometrical parameters are also modified under

complexation leading to $\Delta E_{\text{def}}(\text{Atra})$ of 1.00 and 1.96 kcal mol⁻¹, respectively. Moreover, Ca-Oh distances are similar in ORTHO (2.408 and 2.365 Å) and PARA2 (2.359 and 2.402 Å). The Ca2-N7 and Ca1-N11 distances (5.604 and 4.968 Å, respectively) are longer when the ORTHO conformer is adsorbed than in the PARA series (Fig. 7). However, ORTHO so obtained leads to an adsorption energy of -13.99 kcal mol⁻¹ and lies 13.42 kcal mol⁻¹ above PARA1. Its adsorption energy comparable to PARA2 can probably be explained by the larger polarization by Ca²⁺ cations of alkyl chains which are closer in this case (Fig. 7). This is related to the larger atrazine deformation energy in ORTHO than in PARA2. Indeed, in a previous study, we have already shown the importance of such alkyl chains polarization in atrazine-(Ca²⁺)₂ complexes in the gas phase.^[39]

As can be seen in Table 5, the dispersion part of the adsorption energy is slightly smaller for ORTHO than for PARA1, -12.95 versus -17.77 kcal mol⁻¹. The latter dispersion contribution is significantly larger than the one of Pyro-Atra (-11.98 kcal mol⁻¹), which was expected as they correspond both to face-to-face atrazine-clay surface interaction with a shorter atrazine-surface distance in PARA1 (3.091 Å) compared to Pyro-Atra (3.559 Å).

To roughly analyze the origin of the dispersion, the alkyl groups of atrazine were replaced by hydrogens in both ORTHO and PARA1 isomers (the structures were not optimized). By replacing alkyl chains by hydrogens, the 2-chloro-4,6-diamino-1,3,5-triazine, an atrazine by-product, noted atramod, is obtained (Fig. 6). In both cases, the *s*-triazine cycle-surface distance remains unchanged. However, in ORTHO, the closest atoms to the surface are the two hydrogens of the amino group (2.191 and 2.987 Å) which bear the ethyl chain. The interaction energy without

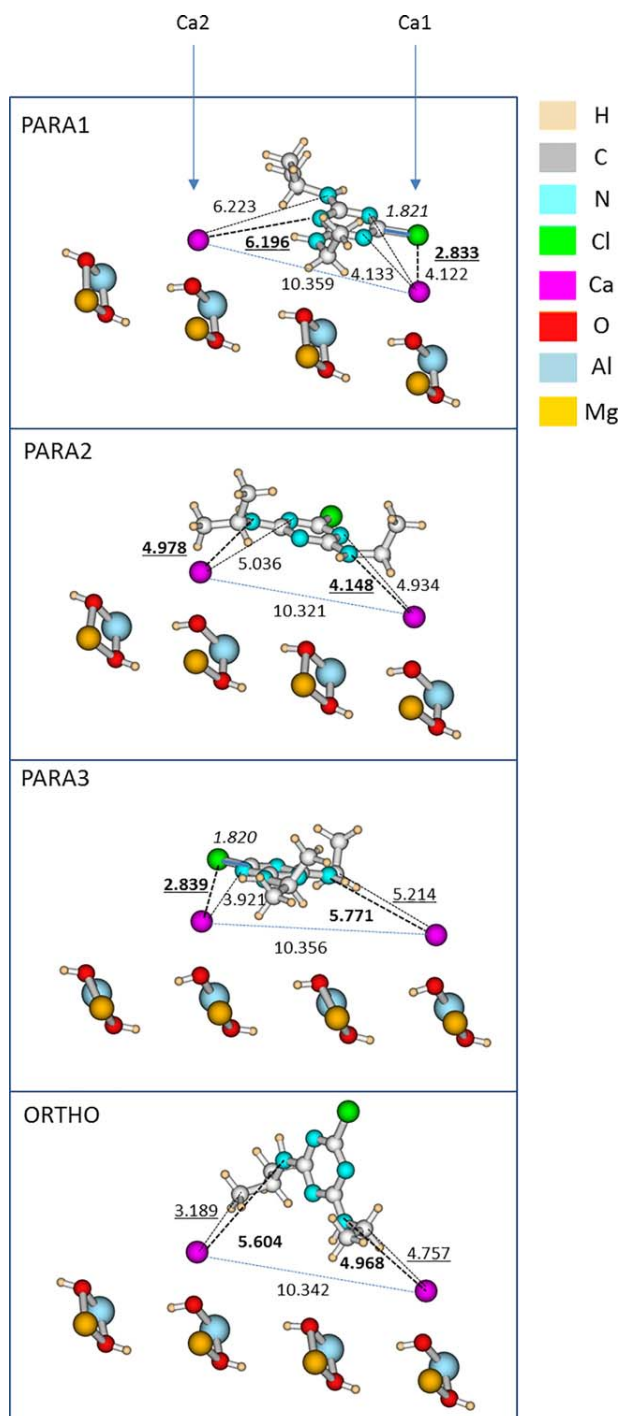


Figure 7. Geometrical parameters of the interaction between the atrazine molecule and the Ca^{2+} cations of montmorillonite in PARA1, PARA2, PARA3, and ORTHO structures at the PBE-D2/pw level. For a sake of clarity, only atoms near substitutions have been represented for the clay surface. The shortest atrazine- Ca^{2+} distances (in Å) corresponding to interaction with basic sites and/or carbon atoms are presented. The smallest distance between each Ca^{2+} and atrazine is underlined and the shortest distance from each cation to a basic atom is given in bold. [Color figure can be viewed at wileyonlinelibrary.com]

dispersion is small with or without alkyl chains for ORTHO (-2.59 versus -0.29 kcal mol $^{-1}$, see Table 5) and similar for PARA1 (~ -13 kcal mol $^{-1}$). The dispersion term is larger than the

interaction energy without dispersion for PARA1 (-18.02 vs. -11.53 kcal mol $^{-1}$). It decreases, when replacing alkyl chains by hydrogen atoms, for each isomer but more dramatically in ORTHO (-13.73 to -3.27 kcal mol $^{-1}$). The dispersion contribution due to the alkyl chains is noticeably larger for ORTHO. It can be estimated to about -6 kcal mol $^{-1}$ for PARA1 and -11 kcal mol $^{-1}$ for ORTHO. We can also evaluate the part due to the delocalized electronic system at about -12 kcal mol $^{-1}$ for PARA1 and -3 kcal mol $^{-1}$ for ORTHO.

To conclude, PARA1 and Pyro-Atra dispersion is mainly due to the interaction between the clay surface and the π electronic system of the *s*-triazine cycle as expected. The same cannot be said for ORTHO in which dispersion essentially comes from the interaction of the surface with the alkyl groups.

Conclusions

In this work, we have investigated the adsorption of atrazine onto two different clay surfaces: a pyrophyllite clay and an Mg-substituted clay named montmorillonite, in which Ca^{2+} cations have been added on the surface to counter-balance the charges induced by the substitutions of Al^{3+} by Mg^{2+} . After having built the models for these two clay surfaces, different adsorption sites of atrazine on these surfaces have been studied.

The calculations show that the atrazine molecule is physisorbed on the pyrophyllite surface, evidencing the necessity to use dispersion-corrected computational methods. The adsorption energies of atrazine on montmorillonite are two to three times larger than on pyrophyllite, depending on the adsorption pattern. Interaction and adsorption energies are close for all isomers. Thus, the deformation energy is small ($\sim 10\%$ ΔE_{int}). In all cases, when atrazine is complexed to montmorillonite, the Ca^{2+} cations move closer to the surface. Atrazine adsorption induces significant structural modifications of the montmorillonite clay surface, particularly close to substitutions (i.e., in the octahedral sheet). The changes are even greater below the Ca^{2+} compensating cations. For the two most stable studied complexes, the large adsorption energy is related to the strong interaction between the chlorine atom of the atrazine molecule and one of the Ca^{2+} compensating cations with a Ca-Cl distance only a little longer than in the gas phase. The atrazine molecule is, in both cases, deformed around the chlorine atom due to the large interaction with Ca^{2+} and the clay deformation is all the more important near the Ca^{2+} cation the least complexed to atrazine. Therefore, the substitution positions will probably have a decisive role on both the geometry of the complex and the adsorption energy between the atrazine and the montmorillonite surface. This particular point is under study and will be the subject of a following paper.

This study shows the important role of the alkaline earth cations on the adsorption of atrazine on clays, confirming the conclusion of our previous studies on the atrazine- Ca^{2+} complexes. The results obtained suggest that the atrazine pesticide will be retained in clays containing Ca^{2+} cations. However, to get a complete picture of the pesticide retention in clay minerals, more realistic models need to be investigated (different types of pesticides and cations, the effect of temperature, the presence,


or not, of water molecules in the interlayer space, etc.). Particularly, an exhaustive montmorillonite-atrazine conformational study has to be performed using molecular dynamics and is one of our current preoccupations. The next step will consist in adding a large number of water molecules to mimic the soil solution also in a dynamical approach. Only long simulation time will allow us to observe desorption phenomenon and solvation in water. Other pesticides of the TyPol databank^[54] in interaction with the montmorillonite surface are also under study. These various studies are in progress in our group and the results will be presented in forthcoming papers, which will strive after giving some clues on the presence of pesticides in groundwater tables.

Acknowledgment

The authors would like to thank Jérôme Cuny for fruitful discussions.

Keywords: clay minerals · atrazine pesticide · theoretical calculations · adsorption energy · interaction energy

How to cite this article: B. Belzunces, S. Hoyau, M. Benoit, N. Tarrat, F. Bessac. *J. Comput. Chem.* **2017**, *38*, 133–143. DOI: 10.1002/jcc.24530

 Additional Supporting Information may be found in the online version of this article.

- [1] J. Ahlers, F. Stock, B. Werschkun, *Environ. Sci. Pollut. Res.* **2008**, *15*, 656.
- [2] European Council Regulation 793/93/EEC on the evaluation and control of risks of existing substances, L161, **1993**.
- [3] D. C. G. Muir, P. H. Howard, *Environ. Sci. Technol.* **2006**, *40*, 7157.
- [4] D. J. Kyle, *Photochem. Photobiol.* **1985**, *41*, 107.
- [5] J. Hirschberg, L. E. E. McIntosh, *Science* **1983**, *222*, 1346.
- [6] M. S. Mills, E. M. Thurman, *Environ. Sci. Technol.* **1994**, *28*, 600.
- [7] E. M. Thurman, D. A. Goolsby, M. T. Meyer, M. S. Mills, M. L. Pomes, D. W. Kolpin, *Environ. Sci. Technol.* **1992**, *26*, 2440.
- [8] L. Cornejo, R. Celis, C. Dominguez, M. C. Hermosin, J. Cornejo, *Appl. Clay Sci.* **2008**, *42*, 284.
- [9] M. C. Hermosin, J. Cornejo, *J. Environ. Quality* **1993**, *22*, 325.
- [10] P. Benoit, E. Barriuso, S. Houot, R. Calvet, *Eur. J. Soil Sci.* **1996**, *47*, 567.
- [11] P. Benoit, I. Madrigal, C. M. Preston, C. Chenu, E. Barriuso, *Eur. J. Soil Sci.* **2008**, *59*, 178.
- [12] L. Mamy, E. Barriuso, B. Gabrielle, *Pest Manag. Sci.* **2005**, *61*, 905.
- [13] T. M. Ward, J. B. Weber, *J. Agric. Food Chem.* **1968**, *16*, 959.
- [14] D. S. Brown, E. W. Flagg, *J. Environ. Quality* **1981**, *10*, 382.
- [15] C. MacBean, *e-Pesticide Manual*, 15th ed., ver. 5.1; British Crop Protection Council: Alton, UK.
- [16] B. Minisini, F. Tsobnang, *Appl. Surf. Sci.* **2005**, *242*, 21.
- [17] D. Tunega, B. A. Goodman, G. Haberhauer, T. G. Reichenauer, M. H. Gerzabek, H. Lischka, *Clays Clay Miner.* **2007**, *55*, 220.
- [18] J. P. Prates Ramalho, A. V. Dordio, A. J. Palace Carvalho, *Adsorption* **2013**, *19*, 937.
- [19] D. Tunega, M. H. Gerzabek, G. Haberhauer, H. Lischka, *Eur. J. Soil Sci.* **2007**, *58*, 680.
- [20] V. K. Voora, W. A. Al-Saidi, K. D. Jordan, *J. Phys. Chem. A* **2011**, *115*, 9695.
- [21] L. Gorb, R. Lutchny, Y. Zub, D. Leszczynska, J. Leszczynski, *J. Mol. Struct. THEOCHEM* **2006**, *766*, 151.
- [22] D. R. Katti, P. Ghosh, S. Schmidt, K. S. Katti, *Biomacromolecules* **2005**, *6*, 3276.
- [23] A. Rennig, A. Slutter, L. Tribe, *Int. J. Quantum Chem.* **2008**, *108*, 538.
- [24] T. L. Robinson, A. Michalkov, L. Gorb, J. Leszczynski, Studies in hydrogen-bonded systems—A collection of Invited Papers in honour of Professor Lucjan Sobczyk, on the occasion of his 80th Birthday **2007**, 844–845, 48.
- [25] S. P. Newman, T. Di Cristina, P. V. Coveney, W. Jones, *Langmuir* **2002**, *18*, 2933.
- [26] L. Aristilde, B. Lanson, L. Charlet, *Langmuir* **2013**, *29*, 4492.
- [27] S. Pirillo, C. R. Luna, I. López-Corral, A. Juan, M. J. Avena, *J. Phys. Chem. C* **2015**, *119*, 16082.
- [28] A. Michalkova, T. L. Robinson, J. Leszczynski, *Phys. Chem. Chem. Phys.* **2011**, *13*, 7862.
- [29] K. El Adraa, V. Timon, J. F. Lambert, A. R. Al-Rabaa, F. Jaber, M. Jaber, F. Tielens, *J. Phys. Chem. C* **2012**, *116*, 26414.
- [30] P. Mignon, P. Geerlings, R. Schoonheydt, *J. Phys. Chem. C* **2007**, *111*, 12376.
- [31] P. Mignon, M. Sodupe, *Phys. Chem. Chem. Phys.* **2012**, *14*, 945.
- [32] P. Mignon, M. Sodupe, *J. Phys. Chem. C* **2013**, *117*, 26179.
- [33] P. Mignon, P. Ugliengo, M. Sodupe, *J. Phys. Chem. C* **2009**, *113*, 13741.
- [34] P. Mignon, P. Ugliengo, M. Sodupe, E. R. Hernandez, *Phys. Chem. Chem. Phys.* **2010**, *12*, 688.
- [35] V. Aggarwal, Y. Y. Chien, B. J. Teppen, *Eur. J. Soil Sci.* **2007**, *58*, 945.
- [36] V. Aggarwal, H. Li, B. Teppen, *J. Environ. Toxicol. Chem.* **2006**, *25*, 392.
- [37] P. Clausen, W. Andreoni, A. Curioni, E. Hughes, C. J. G. Plummer, *J. Phys. Chem. C* **2009**, *113*, 15218.
- [38] P. Clausen, W. Andreoni, A. Curioni, E. Hughes, C. J. G. Plummer, *J. Phys. Chem. C* **2009**, *113*, 12293.
- [39] F. Bessac, S. Hoyau, *Comput. Theor. Chem.* **2013**, *1022*, 6.
- [40] F. Bessac, S. Hoyau, *Comput. Theor. Chem.* **2011**, *966*, 284.
- [41] D. Marx, J. Hutter, In *Modern Methods and Algorithms of Quantum Chemistry*; J. Grotendorst, Eds.; Forschungszentrum Jülich, **2000**; pp. 301–449.
- [42] D. Marx, J. Hutter, *Ab Initio Molecular Dynamics*; Cambridge University Press, **2009**.
- [43] W. Andreoni, A. Curioni, *Parallel Comput.* **2000**, *26*, 819.
- [44] J. P. Perdew, K. Burke, M. Ernzerhof, *Phys. Rev. Lett.* **1996**, *77*, 3865.
- [45] N. Troullier, J. L. Martins, *Phys. Rev. B* **1991**, *43*, 1993.
- [46] L. Kleinman, D. M. Bylander, *Phys. Rev. Lett.* **1982**, *48*, 1425.
- [47] S. G. Louie, S. Froyen, M. L. Cohen, *Phys. Rev. B* **1982**, *26*, 1738.
- [48] H. J. Monkhorst, J. D. Pack, *Phys. Rev. B* **1976**, *13*, 5188.
- [49] S. Grimme, *J. Comput. Chem.* **2006**, *27*, 1787.
- [50] F. L. Hirshfeld, *Theor. Chim. Acta* **1977**, *44*, 129.
- [51] Gaussian 03, Revision C.02, M. J. Frisch, G. W. Trucks, H. B. Schlegel, G. E. Scuseria, M. A. Robb, J. R. Cheeseman, J. A. Montgomery, Jr., T. Vreven, K. N. Kudin, J. C. Burant, J. M. Millam, S. S. Iyengar, J. Tomasi, V. Barone, B. Mennucci, M. Cossi, G. Scalmani, N. Rega, G. A. Petersson, H. Nakatsuji, M. Hada, M. Ehara, K. Toyota, R. Fukuda, J. Hasegawa, M. Ishida, T. Nakajima, Y. Honda, O. Kitao, H. Nakai, M. Klene, X. Li, J. E. Knox, H. P. Hratchian, J. B. Cross, V. Bakken, C. Adamo, J. Jaramillo, R. Gomperts, R. E. Stratmann, O. Yazyev, A. J. Austin, R. Cammi, C. Pomelli, J. W. Ochterski, P. Y. Ayala, K. Morokuma, G. A. Voth, P. Salvador, J. J. Dannenberg, V. G. Zakrzewski, S. Dapprich, A. D. Daniels, M. C. Strain, O. Farkas, D. K. Malick, A. D. Rabuck, K. Raghavachari, J. B. Foresman, J. V. Ortiz, Q. Cui, A. G. Baboul, S. Clifford, J. Cioslowski, B. B. Stefanov, G. Liu, A. Liashenko, P. Piskorz, I. Komaromi, R. L. Martin, D. J. Fox, T. Keith, M. A. Al-Laham, C. Y. Peng, A. Nanayakkara, M. Challacombe, P. M. W. Gill, B. Johnson, W. Chen, M. W. Wong, C. Gonzalez, J. A. Pople, Gaussian Inc.: Wallingford, CT, **2004**.
- [52] R. Wardle, G. W. Brindley, *Am. Mineral.* **1972**, *57*, 732.
- [53] D. Tunega, T. Bucko, A. Zaoui, *J. Chem. Phys.* **2012**, *137*, 114105.
- [54] R. Servien, L. Mamy, Z. Li, V. Rossard, E. Latrille, F. Bessac, D. Patureau, P. Benoit, *Chemosphere* **2014**, *111*, 613.

Received: 11 October 2016

Accepted: 16 October 2016

Published online on 12 November 2016

Supplementary material for

Theoretical study of the atrazine pesticide interaction with
pyrophyllite and Ca^{2+} -montmorillonite clay surfaces.

Bastien Belzunces^{§‡}, Sophie Hoyau^{§‡}, Magali Benoit[†], Nathalie Tarrat[†], Fabienne Bessac^{§‡‡}*

[§]Université de Toulouse; UPS; IRSAMC; Laboratoire de Chimie et Physique Quantiques;
118, route de Narbonne ; F-31062 Toulouse, France.

[‡]CNRS (UMR 5626); F-31062 Toulouse, France.

[†]CEMES - Centre d'Elaboration de Matériaux et d'Etudes Structurales - CNRS (UPR 8011)
Groupe MC2, 29 rue Jeanne Marvig; F-31055 Toulouse, France.

^{*}Université de Toulouse; INPT; Ecole d'Ingénieurs de Purpan; 75, voie du TOEC, BP 57611,
F-31076 Toulouse Cedex 03, France.

FIGURES

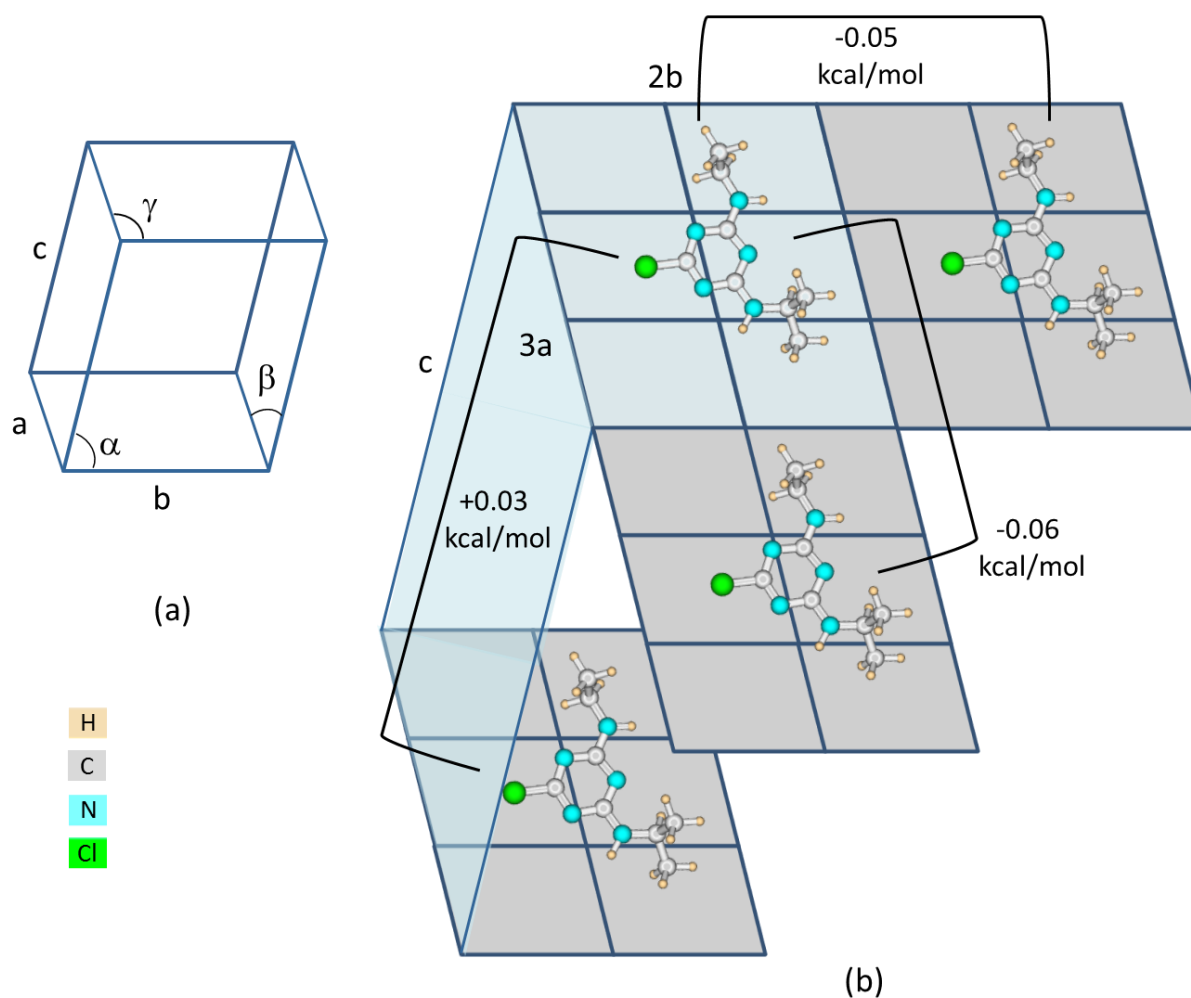


Figure S1. (a) The triclinic unit cell of pyrophyllite ($a \neq b \neq c$ and $\alpha \neq \beta \neq \gamma \neq 90^\circ$); (b) The computational cell consists in 6 unit cells: $3a \times 2b \times c$ (in light turquoise) to minimize interaction energies between two atrazine images along a , b and c (30 Å) directions. Values are given in kcal mol⁻¹ (identical for PBE/6-31G* and PBE/6-311+G(2d,2p))³⁷.

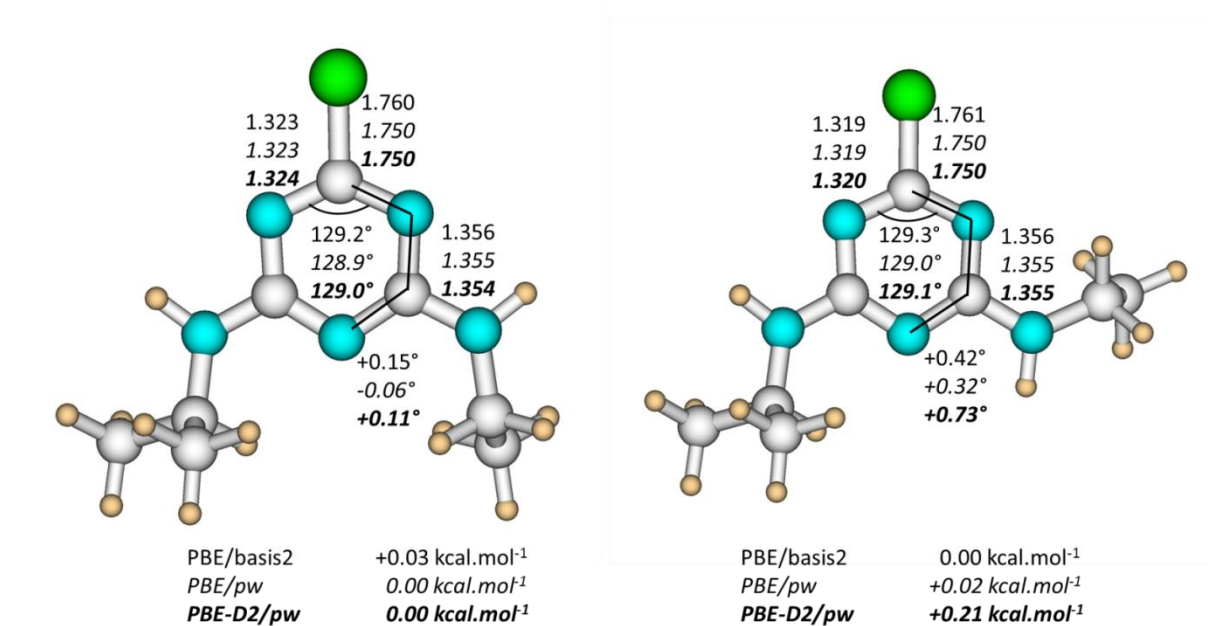


Figure S2. Representative geometrical parameters and relative energies of the two lowest atrazine conformers in the gas phase: gaussian basis set (6-311+G(2d,2p)) or plane-wave basis set with the PBE functional are presented (in italics), as a comparison PBE-D2 (in italics and bold) computations are also given in the plane-wave case. Distances are given in Å, angles and dihedrals in degrees.³⁷

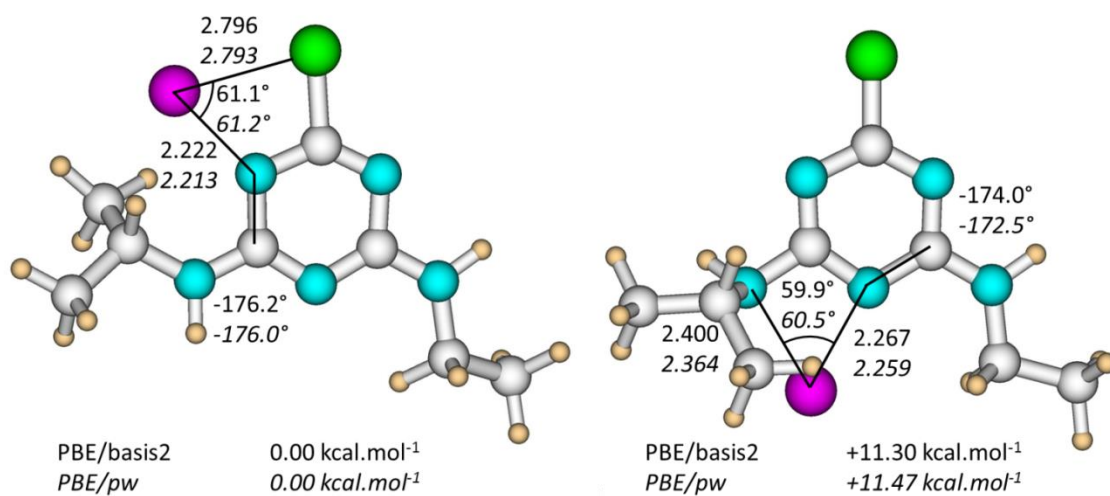


Figure S3. Representative geometrical parameters and relative energies of two different atrazine- Ca^{2+} complexes using either a gaussian basis set (6-311+G(2d,2p)) or a plane-wave basis set (in italics) in the gas phase using the PBE functional. Distances are given in Å, angles and dihedrals in degrees.³⁷

TABLES

Table S1. Adsorption and interaction energies of atrazine onto pyrophyllite and montmorillonite (PARA1, PARA2, PARA3 and ORTHO) computed at the PBE-D2/pw level as a function of the value of the c parameter. ^a SP22/30: single point calculations for c= 22 Å with a geometry optimized for c= 30 Å.


	c (Å)	ΔE_{int} (kcal/mol)	ΔE_{ads} (kcal/mol)
PYROPHYLLITE			
Pyro-Atra	22	-14.10	-13.15
	SP22/30 ^a	-11.49	-10.79
	30	-11.41	-10.53
MONTMORILLONITE			
PARA1	22	-31.47	-27.64
	SP22/30 ^a	-31.33	-27.85
	30	-31.01	-27.42
PARA2	22	-19.03	-17.60
	SP22/30 ^a	-16.85	-15.52
	30	-16.49	-15.20
PARA3	22	-31.45	-27.38
	SP22/30 ^a	-30.74	-27.11
	30	-30.53	-26.73
ORTHO	22	-17.52	-14.48
	SP22/30 ^a	-15.75	-13.38
	30	-16.32	-13.99

Chapter V

Complexation of metमितron and fenhexamid with one and two Na^+ or Ca^{2+} cations

“The molecule also has a body. When this body is hit, the molecule feels hurt all over.”

Alexander I. Kitaigorodski

 In the previous chapter, the adsorption of the atrazine pesticide on pyrophyllite and on a model of Ca-montmorillonite clay is studied. Results of atrazine and atrazine complexes with one and two cations (Na^+ or Ca^{2+}) were the base to choose the investigated isomers of Atra-Mont. Such a static approach allows to calibrate our method of investigation of pesticides adsorption on a clay surface.

In the present chapter, to explore in more details the PES of metमितron (Meta), fenhexamid (Fen) and their complexes, a dynamic approach is used. Sampling the PES implies to work within a planewave framework, however, each selected structure is then optimized with a gaussian basis set (basis1: 6-31G* or basis2: 6-311+G(2d,2p)). Working with gaussian basis sets allows to determine thermodynamic values in the gas phase and to analyze in details the contributions to the interaction energies. Thus, this chapter starts with a comparison between optimized geometries in the gaussian or the planewave framework to verify the agreement between both approaches and to validate the choices of the planewave calculation parameters. In a second part, the main results of the published work on complexation of metमितron and fenhexamid with one and two Na^+ or Ca^{2+}

cations in the gas phase are presented and the article is attached.

V.A Gaussian basis sets versus planewaves: calibration of gas phase pw calculation parameters

Table V.1 gives complexation and total energies for the lowest-energy Meta- Na^+ isomer at PBE/pw level for 80 and 140 Ry kinetic energy cutoffs and using a Tuckerman poisson solver scheme or not [256]. Simultaneously, the cubic box length, c , increases from 11 to 30 Å. Without the poisson solver, the complexation energy hardly converges between $c = 25$ and 30 Å. Thus, the Tuckerman correction has been employed for the future dynamic simulations and geometry optimisations at PBE/pw as a cubic box has been chosen in this case. With the Tuckerman scheme, the convergence on E_{comp} is obtained as c is going from 13 to 15 Å. Therefore, the chosen box length is $c = 13$ Å for Meta. In the case of Fen, the box length is enlarged to 15 Å. As previously pointed out for atrazine, the kinetic energy cutoff has a small influence on E_{comp} (with and without poisson solver).

c (Å)	E_{tot} 80	E_{comp} 80	E_{comp} 140	E_{tot} T80	E_{comp} T80	E_{comp} T140
11	-165.535351	-65.41	-65.02	-165.439267	-47.40	-47.06
13	-165.509718	-55.62	-55.23	-165.430422	-41.94	-41.54
15	-165.493779	-51.13	-50.74	-165.430645	-43.05	-42.65
17	-165.486761	-48.60	-48.21	-165.433692	-43.13	-42.77
19	-165.478969	-47.04	-46.65	-165.433064	-43.15	-42.78
21	-165.473251	-46.03	-45.64	-165.432771	-43.18	-42.77
23	-165.469363	-45.36	-44.96	-165.433200	-43.20	-42.79
25	-165.465396	-44.86	-44.47	-165.432602	-43.18	-42.78
30	-165.458832	-44.14	-43.76	-165.432220	-43.18	-42.78

Table V.1: E_{comp} in kcal/mol and E_{tot} in a.u. at PBE/pw level of the lowest-energy Meta- Na^+ isomer. 80 : kinetic energy cutoff sets to 80 Ry. 140 : kinetic energy cutoff sets to 140 Ry. T : a Tuckerman poisson solver scheme was used. c : cubic box length in Å.

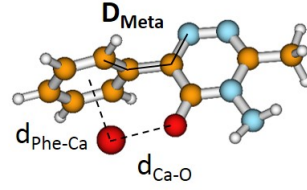
In the following, the influence of the box length, of the cutoff and of the D2 correction will be analyzed on both geometry and complexation energy of the lowest-energy isomers of Meta- Ca^{2+} (see Table V.2) and Fen- Ca^{2+} (see Table V.3). On geometries, the kinetic energy cutoff and the box length (at PBE/pw) have only a very few influence with respect to the PBE/basis2 ($< 1.5 \times 10^{-2}$ Å). Even the local geometry around the complexation site is not impacted by these parameters. When the D2 dispersion correction is added, the discrepancies do not exceed 5×10^{-2} Å (on $d_{\text{Phe-Ca}}$ for Meta- $\text{Ca}^{2+}(1)$).

On the complexation energy, whatever the computational level, the kinetic energy cutoff has only a very little influence (< 0.03 kcal/mol). For Fen- Ca^{2+} , changing the box length from 15 to 20 Å affects E_{comp} by ≈ 1 kcal/mol, which is within the accuracy of the

methods. Thus, $c = 15 \text{ \AA}$ is an appropriate choice for Fen complexes. On the contrary for Meta, E_{comp} is going from -139 to -143 kcal/mol changing the box length from 13 to 20 \AA . At $c = 20 \text{ \AA}$, E_{comp} is converged (-143 kcal/mol also at $c = 50 \text{ \AA}$). A difference of about 3 kcal/mol between a gaussian basis set and a planewave approach is observed in both cases, *i.e.*, 2% on E_{comp} , which is acceptable. For both Meta- $\text{Ca}^{2+}(1)$ and Fen- $\text{Ca}^{2+}(1)$, D2 empirical dispersion corrections induce a systematic overestimation (in absolute value) of about $5 - 6 \text{ kcal/mol}$ on E_{comp} whatever the box length and the cutoff. This difference corresponds to the dispersion energy value (E_{comp}^{disp}). The empirical dispersion correction has been refined by S. Grimme in the D3 scheme including in particular three body terms [232]. D3 corrections have been tested within the Gaussian software [257]. The PBE-D3/basis2 results on Fen- $\text{Ca}^{2+}(1)$ reduce the D2 dispersion overestimation by about 5 kcal/mol and lead to more accurate E_{comp} . However as D3 is not implemented in CPMD, D2 corrections have to be used to compute adsorption energies of pesticide on clay surfaces.

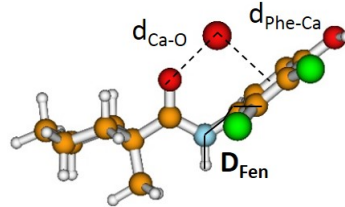
The same parameters are tested on geometries and relative energies of lowest-energy isomers of complexation families for Meta- Ca^{2+} and Fen- Ca^{2+} complexes. As previously mentioned, geometries are in great agreement in the gas phase when using either a gaussian basis set (PBE/basis2) or planewaves (PBE-D2/pw 80 Ry) whatever the complexation site. Intramolecular distances are given in Table V.4. On Figure V.1, geometrical parameters around the complexation sites are gathered.

For Meta- Ca^{2+} isomers, relative energy order of the families is correctly reproduced at PBE-D2/pw. However, for Fen- Ca^{2+} complexes, the three presented isomers are iso-energetic at PBE-D2/pw whereas Fen- $\text{Ca}^{2+}(17)$ is 2.4 kcal/mol higher than Fen- $\text{Ca}^{2+}(1)$ at PBE/basis2 (see Figure V.1). To recover correct relative energies for Fen- $\text{Ca}^{2+}(1)$ and (17), a box length of 20 \AA has to be used (see values in red in Table V.5).



	E_{comp}	E_{comp}^{disp}	d_{Phe-Ca}	d_{Ca-O}	D_{Meta}
PBE/basis2	-139.95		2.434	2.166	-96.5
PBE/pw (80 Ry/13 Å box)	-138.70		2.431	2.149	-96.6
PBE/pw (140 Ry/13 Å box)	-138.73		2.432	2.147	-96.5
PBE/pw (80 Ry/20 Å box)	-143.12		2.426	2.156	-96.5
PBE/pw (140 Ry/20 Å box)	-143.14		2.424	2.154	-96.2
PBE/pw (80 Ry/50 Å box)	-143.15		2.425	2.157	-96.5
PBE-D2/pw (80 Ry/13 Å box)	-144.07	-5.50	2.477	2.137	-96.4
PBE-D2/pw (140 Ry/13 Å box)	-144.09	-5.46	2.479	2.135	-96.2
PBE-D2/pw (80 Ry/20 Å box)	-148.42	-5.40	2.466	2.143	-96.6
PBE-D2/pw (140 Ry/20 Å box)	-148.44	-5.40	2.464	2.143	-95.5

Table V.2: E_{comp} complexation energies and dispersion contributions to the complexation (E_{disp}^{comp}) in kcal/mol of the lowest-energy Meta- Ca^{2+} isomer. d_{Phe-Ca} and d_{Ca-O} , the distances between Ca and the complexation site are given in Å. The D_{Meta} dihedral is given in degrees. The comparisons are made at the PBE/basis2, PBE/pw and PBE-D2/pw levels with pw cutoffs of 80 and 140 Ry and with a box of 13 or 20 Å.



	E_{comp}	E_{comp}^{disp}	d_{Phe-Ca}	d_{Ca-O}	D_{Fen}
PBE/basis2	-141.52		2.634	2.121	-88.6
PBE/pw (80 Ry/15 Å box)	-143.43		2.478	2.113	-88.1
PBE/pw (140 Ry/15 Å box)	-143.46		2.481	2.115	-88.2
PBE/pw (80 Ry/20 Å box)	-144.69		2.478	2.108	-88.3
PBE/pw (140 Ry/20 Å box)	-144.70		2.479	2.110	-88.5
PBE-D2/basis2	-147.36	-5.85	2.500	2.112	-89.6
PBE-D3/basis2	-142.71	-1.18	2.478	2.118	-88.0
PBE-D2/pw (80 Ry/15 Å box)	-149.23	-5.88	2.498	2.106	-89.3
PBE-D2/pw (140 Ry/15 Å box)	-149.25	-5.89	2.497	2.107	-89.3
PBE-D2/pw (80 Ry/20 Å box)	-150.44	-5.87	2.500	2.102	-89.3
PBE-D2/pw (140 Ry/20 Å box)	-150.45	-5.84	2.497	2.101	-89.5

Table V.3: E_{comp} complexation energies and dispersion contributions to the complexation (E_{disp}^{comp}) in kcal/mol of the lowest-energy Fen- Ca^{2+} isomer. d_{Phe-Ca} and d_{Ca-O} , the distances between Ca and the complexation site are given in Å. The D_{Fen} dihedral is given in degrees. The comparisons are made at the PBE/basis2, PBE/pw and PBE-D2/pw levels with pw cutoffs of 80 and 140 Ry and with a box of 15 or 20 Å.

Sites	Isomers	d_{C3-N4}	d_{N4-N5}	d_{N5-C6}	d_{N-NH_2}	d_{CO}	d_{C-C16}	d_{C-C18}	d_{C-OH}	d_{O-H}
PBE/basis2										
	Meta	1.329	1.352	1.322	1.410	1.238	-	-	-	-
CO-Phe	Meta-Ca ²⁺ (1)	1.326	1.340	1.329	1.381	1.298	-	-	-	-
N-N	Meta-Ca ²⁺ (2)	1.333	1.376	1.332	1.381	1.214	-	-	-	-
Phe-N	Meta-Ca ²⁺ (4)	1.341	1.341	1.337	1.369	1.220	-	-	-	-
CO-NH2	Meta-Ca ²⁺ (6)	1.350	1.328	1.321	1.452	1.293	-	-	-	-
	Fen(1) _{ax}	-	-	-	-	1.230	1.749	1.747	1.362	0.977
CO-Phe	Fen-Ca ²⁺ (1) _{eq}	-	-	-	-	1.287	1.718	1.722	1.329	0.982
CO-Cl-Cl	Fen-Ca ²⁺ (4) _{eq}	-	-	-	-	1.282	1.763	1.747	1.338	0.976
cyclo-CO-Cl	Fen-Ca ²⁺ (17) _{ax}	-	-	-	-	1.287	1.785	1.731	1.336	0.978
PBE-D2/pw 80 Ry										
	Meta	1.329	1.351	1.322	1.409	1.238	-	-	-	-
CO-Phe	Meta-Ca ²⁺ (1)	1.327	1.339	1.327	1.379	1.299	-	-	-	-
N-N	Meta-Ca ²⁺ (2)	1.331	1.376	1.330	1.380	1.214	-	-	-	-
Phe-N	Meta-Ca ²⁺ (4)	1.340	1.339	1.336	1.371	1.220	-	-	-	-
CO-NH2	Meta-Ca ²⁺ (6)	1.348	1.330	1.321	1.451	1.292	-	-	-	-
	Fen(1) _{ax}	-	-	-	-	1.231	1.739	1.737	1.366	0.983
CO-Phe	Fen-Ca ²⁺ (1) _{eq}	-	-	-	-	1.288	1.707	1.714	1.334	0.987
CO-Cl-Cl	Fen-Ca ²⁺ (4) _{eq}	-	-	-	-	1.284	1.752	1.735	1.343	0.980
cyclo-CO-Cl	Fen-Ca ²⁺ (17) _{ax}	-	-	-	-	1.288	1.772	1.723	1.341	0.983

Table V.4: Intramolecular bond lengths (Å) in PBE/basis2 and PBE-D2/pw 80 Ry of the lowest-energy Meta-Ca²⁺ and Fen-Ca²⁺ isomers of each binding site families.

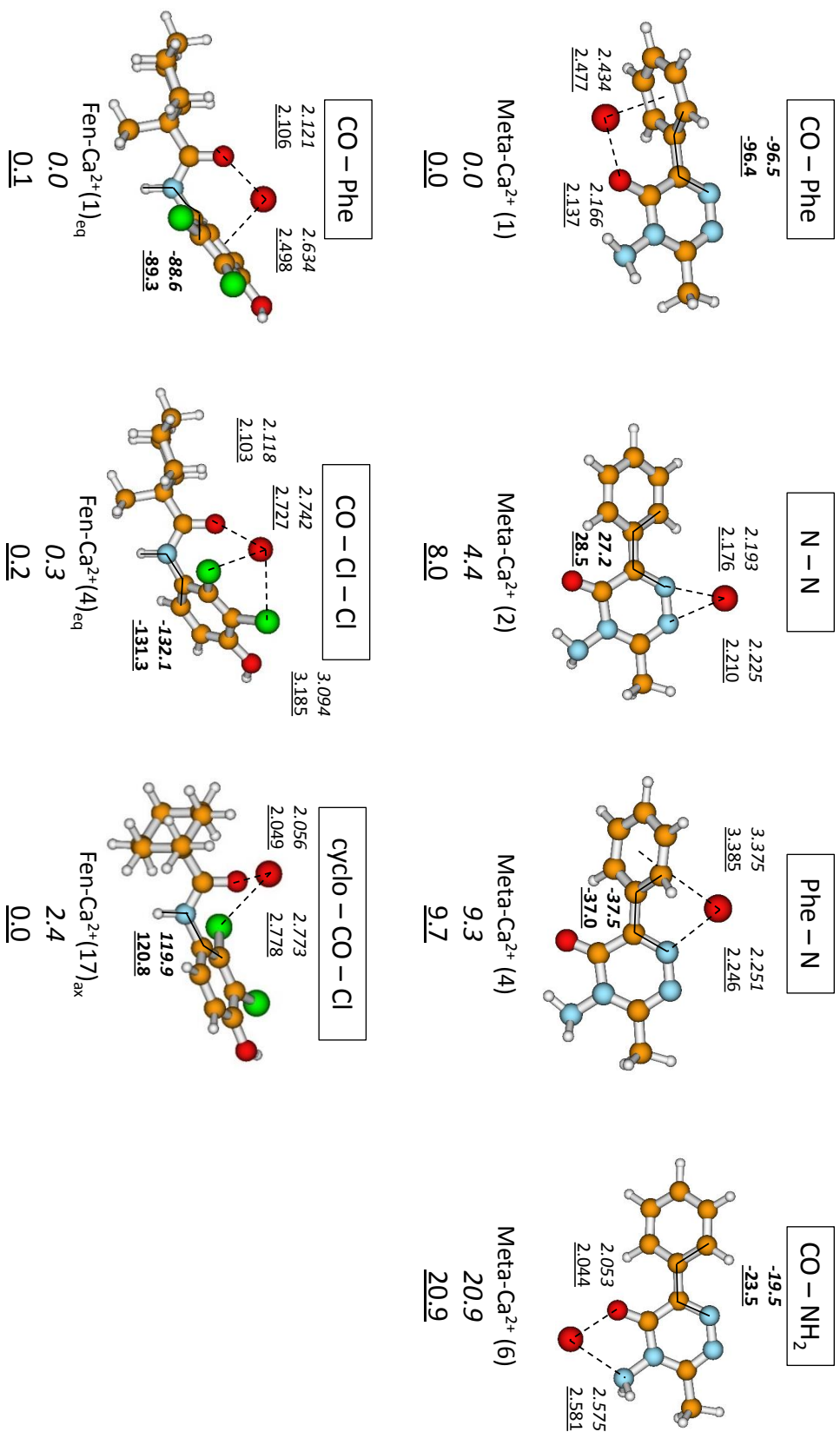


Figure V.1: Lowest-energy isomers of Meta- Ca^{2+} and Fen- Ca^{2+} complexes. Distances in Å, dihedrals (bold) in degrees and relative energies in kcal/mol obtained in PBE/basis2 (italics) and PBE-D2/pw 80 Ry (underlined) are reported.

Sites	Isomers	ΔE	E_{comp}	E_{disp}^{comp}	E_{int}	E_{disp}^{int}
PBE/basis2						
CO-Phe	Meta-Ca ²⁺ (1)	0.0	-139.95	-	-153.25	-
N-N	Meta-Ca ²⁺ (2)	4.4	-135.60	-	-139.87	-
Phe-N	Meta-Ca ²⁺ (4)	9.3	-130.66	-	-136.87	-
CO-NH2	Meta-Ca ²⁺ (6)	20.9	-119.10	-	-136.45	-
CO-Phe	Fen-Ca ²⁺ (1) _{eq}	0.0	-141.52	-	-153.66	-
CO-Cl-Cl	Fen-Ca ²⁺ (4) _{eq}	0.3	-141.22	-	-158.38	-
cyclo-CO-Cl	Fen-Ca ²⁺ (17) _{ax}	2.4	-139.11	-	-151.14	-
PBE/pw (80 Ry/15 Å box)						
CO-Phe	Fen-Ca ²⁺ (1) _{eq}	0.8	-143.43	-	-156.07	-
cyclo-CO-Cl	Fen-Ca ²⁺ (17) _{ax}	0.0	-144.24	-	-154.36	-
PBE/pw (80 Ry/20 Å box)						
CO-Phe	Fen-Ca ²⁺ (1) _{eq}	0.0	-144.69	-	-157.44	-
cyclo-CO-Cl	Fen-Ca ²⁺ (17) _{ax}	1.9	-142.82	-	-154.80	-
PBE/pw (140 Ry/15 Å box)						
CO-Phe	Fen-Ca ²⁺ (1) _{eq}	0.7	-143.46	-	-155.99	-
cyclo-CO-Cl	Fen-Ca ²⁺ (17) _{ax}	0.0	-144.17	-	-154.24	-
PBE-D2/pw (80 Ry/13 Å box)						
CO-Phe	Meta-Ca ²⁺ (1)	0.0	-144.07	-	-157.57	-
N-N	Meta-Ca ²⁺ (2)	8.0	-136.11	-	-140.28	-
Phe-N	Meta-Ca ²⁺ (4)	9.7	-134.38	-	-140.08	-
CO-NH2	Meta-Ca ²⁺ (6)	20.9	-123.19	-	-139.99	-
PBE-D2/pw (80 Ry/15 Å box)						
CO-Phe	Fen-Ca ²⁺ (1) _{eq}	0.1	-149.23	-5.89	-161.85	-5.74
CO-Cl-Cl	Fen-Ca ²⁺ (4) _{eq}	0.2	-149.09	-4.68	-165.63	-4.37
cyclo-CO-Cl	Fen-Ca ²⁺ (17) _{ax}	0.0	-149.35	-5.44	-159.61	-4.86
PBE-D2/pw (140 Ry/15 Å box)						
CO-Phe	Fen-Ca ²⁺ (1) _{eq}	0.0	-149.25	-5.89	-161.81	-5.74
cyclo-CO-Cl	Fen-Ca ²⁺ (17) _{ax}	0.2	-149.01	-5.01	-158.78	-4.46
PBE-D2/pw (80 Ry/20 Å box)						
CO-Phe	Fen-Ca ²⁺ (1) _{eq}	0.0	-150.4	-5.87	-163.2	-5.74
cyclo-CO-Cl	Fen-Ca ²⁺ (17) _{ax}	2.0	-148.4	-5.89	-160.6	-5.76
PBE-D2/pw (140 Ry/20 Å box)						
CO-Phe	Fen-Ca ²⁺ (1) _{eq}	0.0	-150.45	-5.84	-163.21	-5.74
cyclo-CO-Cl	Fen-Ca ²⁺ (17) _{ax}	2.2	-148.29	-5.91	-160.70	-5.12

Table V.5: Relative (ΔE), complexation (E_{comp}), interaction (E_{int}) energies and dispersion contributions in the complexation (E_{disp}^{comp}) and in the interaction (E_{disp}^{int}) in kcal/mol of the lowest-energy Meta-Ca²⁺ and Fen-Ca²⁺ isomers of each family. The comparisons are made at the PBE/basis2, PBE/pw and PBE-D2/pw levels with pw cutoffs of 80 and 140 Ry. In bold red, relative energies in agreement with the PBE/basis2 level. In bold, relative energies not in agreement with the PBE/basis2 level.

To conclude, the box length of 13 Å and 15 Å for Meta- Ca^{2+} and Fen- Ca^{2+} respectively are sufficient to correctly describe geometrical parameters. Thus, dynamic simulations are performed using such cubic boxes. However, to compute accurate relative and complexation energies, a box length of 20 Å without dispersion correction must be used. For gas phase systems, D2 dispersion correction is not recommended to evaluate complexation energies.

Nevertheless, as the snapshots are optimized using PBE/basis2, geometries, relative and complexation energies should be accurate. In the following, the computational cell used to deposit the pesticides on the montmorillonite surface is large enough ($15.500 \times 17.931 \times 30 \text{ Å}^3$) to avoid such energetic problems (relative energy inversions for Fen and complexation energy overestimation for Meta).

V.B Dynamic exploration of the PES of Meta, Fen, Meta-(cation)_{*i,i=1,2*} and Fen-(cation)_{*i,i=1,2*}

Metamitron and fenhexamid (the active substances of herbicide and fungicide products respectively) as well as complexes with one or two Ca^{2+} and Na^+ cations have been studied by means of molecular dynamic simulations to widely explore the PES. A large panel of structures, conformers for both pesticides and complexes corresponding to various families (different complexation sites) have then been optimized using PBE/basis1 and PBE/basis2 levels (gaussian basis set approach).

For Meta, only one conformer has been obtained. For Fen, 11 minima have been characterized with relative energies under 10 kcal/mol.

For Meta- Na^+ and Meta- Ca^{2+} complexes, the four families obtained do not overlap in relative energies. Moreover, the basis set has a small influence on energies and PBE/basis1 gives the right energetic order for the various families.

For Meta- Na^+ , a complexation on both nitrogen atoms of triazine cycle (N-N) is preferred due to a favorable interaction of Na^+ approximately along the dipole moment direction of the molecule. For Ca^{2+} , a complexation on the carbonyl oxygen and the π system of the triazine cycle (CO-Phe) is clearly favored whereas the energetic order of other families is the same as with Na^+ .

Finally, to compute accurate complexation energies, PBE/basis2 has to be used particularly to reduce BSSE. For Meta- Ca^{2+} , more accurate geometries are also optimized at this level (in particular, Phe-Ca distances, which need a better description of polarization).

For Meta-(cation)₂ complexes, the three characterized families are combination of

Meta-cation complexation sites. Finally, for Na⁺ and Ca²⁺, the family energetic order is the same whatever the basis set. The lowest-energy isomer implies a combination of the previous N-N and CO-Phe complexation sites. The influence of the basis set on cation distances to the complexation site is larger than in Meta-cation complexes and PBE/basis2 will be preferred in this case.

Due to the higher complexity of the Fen landscape, the Fen-cation and Fen-(cation)₂ PES are more complicated to explore. More families exist (5) and only three are common for Na⁺ and Ca²⁺. Moreover, the family order depends on the basis set: PBE/basis2 has to be used to recover the right energetic order.

For Na⁺, the preferred complexation site implies the carbonyl oxygen and the closest chlorine. In the case of Ca²⁺, a complexation on the carbonyl oxygen and the π system of the substituted phenyl is more favorable (as for Meta). Finally, basis set has a none negligible influence even on geometries particularly for calcium complexes. To reduce BSSE and to treat correctly the CT contribution, basis2 must be used.

For Fen-(cation)₂, a large number of isomers has been optimized for which the complexation sites are not a combination of the previous ones. The energetic order of the families is the same for Na⁺ and Ca²⁺ (as for Meta). The lowest-energy isomer implies in both cases a bidentate interaction on the hydroxyl oxygen and the closest chlorine and a monodentate complexation of the second cation on the carbonyl oxygen, this cation polarizing the cyclohexyl group.

Considering, Fen and Meta, complexation values are of the same order of magnitude:

- E_{comp} are around -40 kcal/mol with one Na⁺, -140 kcal/mol with one Ca²⁺, -22 kcal/mol with two Na⁺ and -30 (Meta) and -60 (Fen) kcal/mol for two Ca²⁺.
- ΔG_{comp} are around -32 kcal/mol with one Na⁺, -130 kcal/mol with one Ca²⁺, -7 kcal/mol with two Na⁺ and -10 (Meta) and -40 (Fen) kcal/mol for two Ca²⁺.

A detailed analysis of the contributions to the interaction energy is presented in this paper. In sodium complexes (one or two Na⁺), E_{elec} represents about $\frac{2}{3}$ and E_{pol} $\frac{1}{3}$ of the sum of the attractive terms. While for calcium complexes, only 50 % corresponds to E_{elec} , 40 % to E_{pol} and 10 % to E_{CT} . The difference in contribution proportions between Na⁺ and Ca²⁺ pesticide complexes will probably lead to different adsorption on Na-montmorillonite and Ca-montmorillonite. Adsorption on Ca-montmorillonite is the subject of the following chapters. The isomers characterized in the attached paper will be starting structures for dynamic simulation on pesticide-clay systems. In Chapter VI,

a dry Ca-montmorillonite is the substrate. To compare our results with macroscopic values, hydration of pesticide-clay systems is envisaged in the last chapter, in particular adsorption and desorption processes.



Contents lists available at ScienceDirect

Computational and Theoretical Chemistry

journal homepage: www.elsevier.com/locate/comptc

Pesticide interaction with environmentally important cations: A molecular dynamics and DFT study of metamitron and fenhexamid

Bastien Belzunces^{a,b}, Sophie Hoyau^{a,b}, Jérôme Cuny^{a,b}, Fabienne Bessac^{a,b,c,*}^a Université de Toulouse, UPS, IRSAMC, Laboratoire de Chimie et Physique Quantiques, 118, route de Narbonne, F-31062 Toulouse, France^b CNRS (UMR 5626), F-31062 Toulouse, France^c Université de Toulouse, INPT, Ecole d'Ingénieurs de Purpan, 75, voie du TOEC, BP 57611, F-31076 Toulouse Cedex 03, France

ARTICLE INFO

Article history:

Received 30 June 2017

Received in revised form 28 July 2017

Accepted 2 August 2017

Available online 4 August 2017

Keywords:

Pesticide

Metamitron

Fenhexamid

Pesticide-(cation)_{i,j=1,2} complexes

Theoretical calculations

Energy decomposition

ABSTRACT

Metamitron (Meta), 4-amino-3-methyl-6-phenyl-1,2,4-triazin-5-one, and fenhexamid (Fen), N-(2,3-dichloro-4-hydroxyphenyl)-1-methylcyclohexanecarboxamide, are active substances of herbicide and fungicide products, respectively, employed in agriculture. When these molecules are spread on crops, an important amount reaches the soil and diffuse through water to deep layers of the soil structure and thus to groundwater tables. To get some insight into the interaction of pesticides with soil, in particular clay surfaces, we have run theoretical calculations. This paper presents preliminary results of this wide and challenging work. Metamitron, fenhexamid and their complexes with one or two Ca²⁺ and Na⁺, which are among the most abundant cations into soils, are under investigation. Conformational searches have been performed thanks to Car-Parrinello molecular dynamics (CPMD) simulations from which geometries as well as relative, complexation and interaction energies have been extracted. Thermodynamical complexation values have been calculated for complexes of Meta or Fen with one or two cation(s) in order to understand the complex stability. We found that complexation free energies are comparable for Meta and Fen: around −32 kcal/mol with one sodium cation, ≈−130 kcal/mol with one Ca²⁺, and −7 kcal/mol with two Na⁺. With two Ca²⁺, complexation free energy is four times larger in absolute value for Fen (−40 kcal/mol) than for Meta due to longer inter-cation distances in Fen-(Ca²⁺)₂ complexes. The larger values obtained with Ca²⁺ in the gas phase suggest a strong adsorption of Meta and Fen with Ca²⁺-montmorillonite clay surfaces.

© 2017 Elsevier B.V. All rights reserved.

1. Introduction

For health and environmental reasons, detection, fate and transport of pesticides in water, soil and even food is of great interest in both experimental and theoretical chemistry [1–6]. A lot of studies have been conducted on adsorption of organic compounds over clay minerals in order to understand soil contamination by pesticides [7–11], physical and chemical processes in soils [12–14], and physico-chemistry of environmentally important cations [15–18]. Studies of interaction between biomolecules such as DNA bases and montmorillonite have also been an active topic to improve knowledge in catalysis, drug delivery, or for biomedical developments [19–21].

Among the large amount of pesticides, metamitron (Meta), 4-amino-3-methyl-6-phenyl-1,2,4-triazin-5-one (C₁₀H₁₀N₄O), and

* Corresponding author at: Université de Toulouse, UPS, IRSAMC, Laboratoire de Chimie et Physique Quantiques, 118, route de Narbonne, F-31062 Toulouse, France.
E-mail address: fabienne.bessac@purpan.fr (F. Bessac).

fenhexamid (Fen), N-(2,3-dichloro-4-hydroxyphenyl)-1-methylcyclohexanecarboxamide (C₁₄H₁₇Cl₂NO₂), an herbicide and a fungicide, respectively, have been chosen in the present study. Metamitron belongs to the triazinone family and is mainly employed on fodder and sugar beets to prevent *pre* and *post* emergence of broad-leaved weeds and turf grass by inhibiting their photosynthesis process [1]. Fenhexamid is a fungicide product of the hydroxylanilide family and is used on a wide range of fruits or flowers: grapes, berries, tomato, eggplant or sunflower especially against *Botrytis cinerea* and *Monilinia* [22,2]. An important amount of these two substances or their metabolites can be found in soils as they are commonly employed in agriculture. From physical and chemical point of views, metamitron and fenhexamid display different behavior with regards to adsorption processes into soils. Indeed, their mobilities have been experimentally characterized: medium to very high for Meta and medium to low for Fen [23,24]. Furthermore, half-life of metamitron can go up to 480 days [6,23] and to more than 110 days for fenhexamid [2,25]. It worth pointing out that those values strongly depends on environmental

parameters such as temperature, pressure, pH, aerobic or anaerobic conditions or soil composition.

According to Calvet [26,27], soil may be seen as a system made of three phases in interaction: solid, made of three kind of minerals: clay, sand and silt; liquid, the soil solution containing organic and inorganic substances dissolved in water; and gas, also called “soil atmosphere” due to its composition often similar to air. An assessment of the chemical elements in soil shows that atomic ions are present in large amount with the following abundance order: $O^{2-} > Si^{4+} > Al^{3+} > Fe^{2+/3+} > Ca^{2+} > K^+ > Na^+ > Mg^{2+}$. O, Si and Al are the main components of the solid phase. Furthermore, those cations can also be found in the soil where they can interact with pesticides and lead to complexes.

In the present work, we intend to understand these latter interactions by studying Meta and Fen complexed with one or two exchangeable cations. For that purpose, among the most abundant cations in soil, Na^+ and Ca^{2+} have been chosen because they are respectively monovalent and divalent. Furthermore, despite their different charges, their ionic radii are very similar: $r_{Na^+} = 0.95 \text{ \AA}$ and $r_{Ca^{2+}} = 0.99 \text{ \AA}$ which allow us to evaluate the influence of the cationic charge only over the interaction. Such a study has been recently conducted on complexes of atrazine with one or two Ca^{2+} and one Na^+ cations using computational chemistry methods [28,29]. To the best of our knowledge, the interaction of Meta and Fen with atomic cations present in soils has never been studied theoretically. This work has been conducted as a first step to understand fate and behavior of Meta and Fen in soils. It starts with a molecular dynamics (MD) exploration of metamitron and fenhexamid conformations, followed by a density functional theory (DFT) [30] study of their low-energy complexes with one and then two environmentally important cations: Na^+ and Ca^{2+} .

The outline of the article is as follows: in the first part, computational details for both plane-wave and gaussian basis set calculations are presented. Then, structures and relative energies of pesticides and their complexes with one or two Na^+ and Ca^{2+} cations are commented. Finally, thermodynamical complexation values are discussed and contributions to the interaction energies from RVS SCF decomposition are analyzed. The main outcomes and perspectives are summarized in the conclusion.

2. Computational details

2.1. Plane-wave calculations

Calculations were performed using DFT [30] with the Perdew-Burke-Ernzerhof (PBE) [31] functional as implemented in the

CPMD package [32]. Valence-core interactions have been described using Troullier-Martins norm-conserving pseudopotentials [33] in combination with a plane-wave basis set. To ensure a proper convergence of our results with respect to the kinetic energy cut-off, tests over metamitron, fenhexamid and their complexes were conducted with cut-off values ranging from 80 to 140 Ry. All calculations were performed with a kinetic energy cut-off of 80 Ry and at the Γ point only. A cubic box of 30 \AA length has been used for neutral species in order to minimize interactions between the molecule and its periodic images. For charged species, we employed the Tuckerman Poisson solver [34] to isolate the system from its periodic images. In that case, cell sizes ranging from 11 to 30 \AA have been tested for metamitron in order to check the convergence of the complexation energies and geometries (see Table S1 in supplementary material). The weak variations allowed us to select a 13 \AA cubic unit-cell for Meta complexes. Considering the larger size of Fen, a 15 \AA cubic unit-cell has been used for the corresponding complexes.

Car-Parrinello molecular dynamics simulations [35] were performed within the microcanonical ensemble (NVE). Hydrogen atoms were substituted by deuterium, the electron fictitious mass was set to 600 a.u. and a time step of 5.0 a.u. was applied. For Fen, two starting geometries have been used: either with the R group ($R = 2,3\text{-dichloro-4-hydroxyphenylcarboxamid}$) in axial position on the cyclohexyl, Fen_{ax} , (Fig. 1(a)) or in equatorial position, Fen_{eq} , (Fig. 1(b)). On the figures, ax and eq indices are provided when relevant, i.e. when the cyclohexyl adopts a chair shape conformation. In the text, those indices are not always reminded to lighten the report. For Meta, only one starting structure has been chosen (Fig. 1(c)). The three CPMD simulations have been performed for 25 ps each, at an average temperature of 800 K that allows a wide exploration of the potential energy surface (PES).

PES of the complexes being more difficult to explore, we built the starting configurations as follows: for each pesticide, among the snapshots of the previous conformational exploration, we picked the structure with the highest potential energy. For each complex (Meta, Fen_{ax} , Fen_{eq} with one or two Na^+ or Ca^{2+} cations), 5 random positions of the cation(s) were generated leading to 60 initial configurations. To avoid generating highly correlated structures, we ensure that each random position generated for the cations were at least 2 \AA further from all the other position. They were used as starting geometries of 60 MD simulations of 12.5 ps each. To characterize the stationary points for pesticide and pesticide-cation(s) PES, we have optimized 20 configurations extracted from the aforementioned MD trajectories. From each trajectory, we selected the structures with the 10 highest and the 10

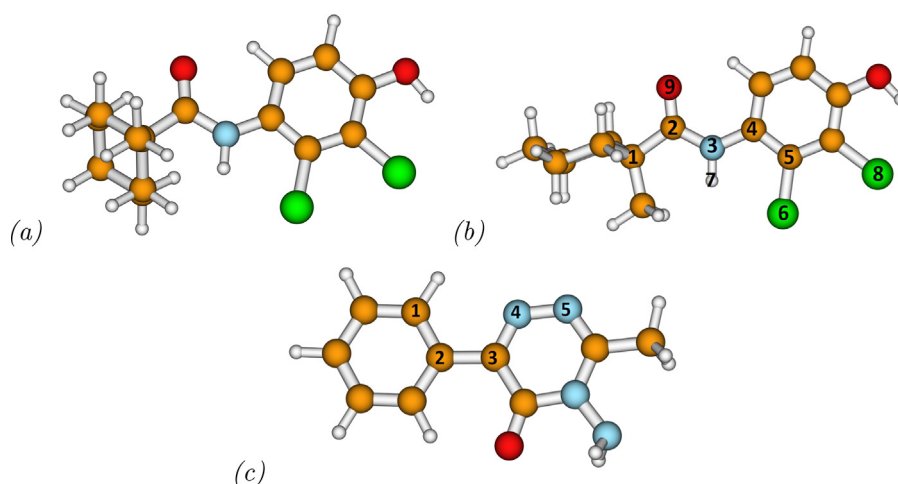


Fig. 1. Starting structures of Fen_{ax} (a), Fen_{eq} (b) and Meta (c). Main atoms are numbered.

Table 1

MO basis sets and related energy contributions calculated with the RVS SCF method. Each MO basis set allows to determine the energy component in bold. MO sets in brackets are frozen during the SCF procedure.

MO basis set	Energy contributions
pest_{occ}	E_{pest}
cat_{occ}	E_{cat}
pest_{occ} + cat_{occ}	E_{pest} + E_{cat} + E_{exch} + E_{elec}
[pest_{occ}] + cat_{occ} + cat_{vac}	E_{pest} + E_{cat} + E_{exch} + E_{elec} + E_{pol} (cat)
[pest_{occ}] + cat_{occ} + cat_{vac} + pest_{vac}	E_{pest} + E_{cat} + E_{exch} + E_{elec} + E_{pol} (cat) + E_{CT} (cat–pest) + E_{BSSE} (cat)^a
[cat_{occ}] + pest_{vac}	E_{cat} + E_{BSSE} (cat)^a
[cat_{occ}] + pest_{occ} + pest_{vac}	E_{pest} + E_{cat} + E_{exch} + E_{elec} + E_{pol} (pest)
[cat_{occ}] + pest_{occ} + pest_{vac} + cat_{vac}	E_{pest} + E_{cat} + E_{exch} + E_{elec} + E_{pol} (pest) + E_{CT} (pest–cat) + E_{BSSE} (pest)^a
[pest_{occ}] + cat_{vac}	E_{pest} + E_{BSSE} (pest)^a

^a BSSE scheme differs from counterpoise (only vacant MO accessible).

lowest energies taking care by a visual analysis that they are structurally uncorrelated. The optimizations were conducted with gaussian basis set calculations using the Gaussian09 software [36].

2.2. Gaussian basis set calculations

The geometry optimizations were performed through DFT with the PBE functional [30,31]. The standard 6-31G* basis set was used for the first row atoms (H, C, N and O). For the second row atoms (Na and Cl) and for Ca, we respectively employed the Francl et al. [37] and the Blaudeau et al. [38] basis sets. To investigate the influence of the basis set over energies and structures, the basis set was extended to the standard 6-311+G(2d,2p) for the first row atoms. For Na and Cl, the corresponding MacLean–Chandler basis set was used [39] and for Ca, the corresponding Blaudeau et al. [38] basis was chosen. To simplify notations and stay consistent with previous papers [28,29], in the following, we call the first basis set “basis1” and the extended basis set “basis2”. Analytical frequency calculations have been performed on all the optimized structures to confirm they are minima on the PES. In the following, only conformers and isomers with energies up to 10 kcal/mol above the lowest-energy structure are reported and discussed, except if an higher energy species of particular interest has been found. For cation and di-cations species, in addition to MD conformational searches, some structures were constructed by hand, exchanging Na⁺ by Ca²⁺ or vice versa, to confirm that it is a minimum on the corresponding PES.

For all the pesticide-cation(s) complexes, the complexation energy E_{comp} corresponds to the energy difference between the complex and both cation(s) and pesticide in its optimized geometry. The interaction energy E_{int} corresponds to the energy difference between the complex and both cation(s) and pesticide in the geometry of the complex:

$$E_{comp} = E_{pest-(cat)_i} - E_{pest(opt)} - iE_{(cat)} \quad (1)$$

$$E_{int} = E_{pest-(cat)_i} - E_{pest} - E_{(cat)_i} \quad (2)$$

In the complex with two cations ($i = 2$), $E_{(cat)_i}$ is the cation pair energy in the geometry of the complex (it includes the repulsion energy between both cations). Then, the counterpoise correction was employed to compute the Basis Set Superposition Error (BSSE) [40]. The preparation energy E_{prep} is the required energy to promote the molecule from its isolated structure to its geometry in the complex:

$$E_{prep} = E_{pest} - E_{pest(opt)} \quad (E_{prep} > 0) \quad (3)$$

E_{comp} can also be determined from Eqs. (1)–(3) as:

$$E_{comp} = E_{int} + E_{prep} + E_{int(cat-cat)} \quad (4)$$

where $E_{int(cat-cat)}$ is the interaction energy between the cations if $i = 2$. It is calculated as the difference between the energy of the cations in the complex and the energy of each cation separately:

$$E_{int(cat-cat)} = E_{(cat)_i} - iE_{(cat)} \quad (i = 2) \quad (5)$$

A reduced variational space self consistent field (RVS SCF) [41] energy decomposition has been performed in order to determine the different contributions to the interaction energy. In the case of two entities in interaction, it involves SCF optimized monomer Molecular Orbitals (MO) in dimer calculations. The wavefunction of one monomer is frozen while the wavefunction of the other is optimized self-consistently [41]. A truncation of the variational space is possible by removing the unoccupied orbitals of either fragment (Table 1). This method, as it is implemented in the Gamess package [42,43], has allowed us to calculate the electrostatic contribution E_{elec} , the Pauli repulsion E_{exch} , the polarization of each entity by the other E_{pol} (for example, $E_{pol(pest)}$ is the polarization energy of the pesticide by the cation), the Charge Transfer (CT) from one entity to the other E_{CT} (for instance, $E_{CT(pest-cat)}$ is the charge transfer from the pesticide to the cation), and the BSSE contribution of each entity $E_{BSSE(pest)}$ and $E_{BSSE(cat)}$. E_{elec} is determined thanks to a Morokuma decomposition scheme without antisymmetrization of the wavefunction built from both monomers MO [44]. All these terms contribute to the interaction energy between pesticide and cation(s) and have been calculated at HF//PBE levels with previously defined basis sets.

3. Results and discussion

Among the large number of starting geometries extracted from the molecular dynamics simulations, only one conformer has been obtained for metamidron, 11 for fenhexamid and 5, 5, 5, 3, 24, 35, 29, 14 for Meta-Na⁺, Meta-Ca²⁺, Meta-(Na⁺)₂, Meta-(Ca²⁺)₂, Fen-Na⁺, Fen-Ca²⁺, Fen-(Na⁺)₂ and Fen-(Ca²⁺)₂, respectively (see Figs. 2–9 for main isomers and Figs. S1–S5 in supplementary material for additional structures).

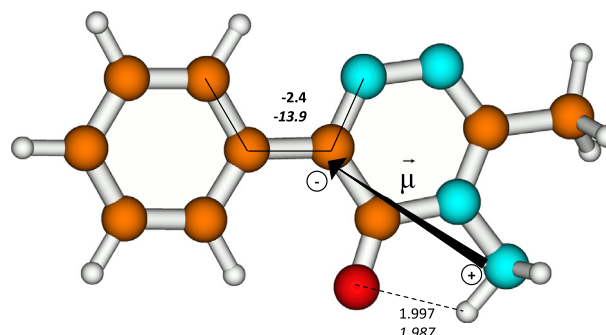


Fig. 2. Metamidron conformer: distances in Å, dihedrals (bold) in degrees at PBE/basis1 and PBE/basis2 in italics. $\bar{\mu}$ is the dipole moment vector.

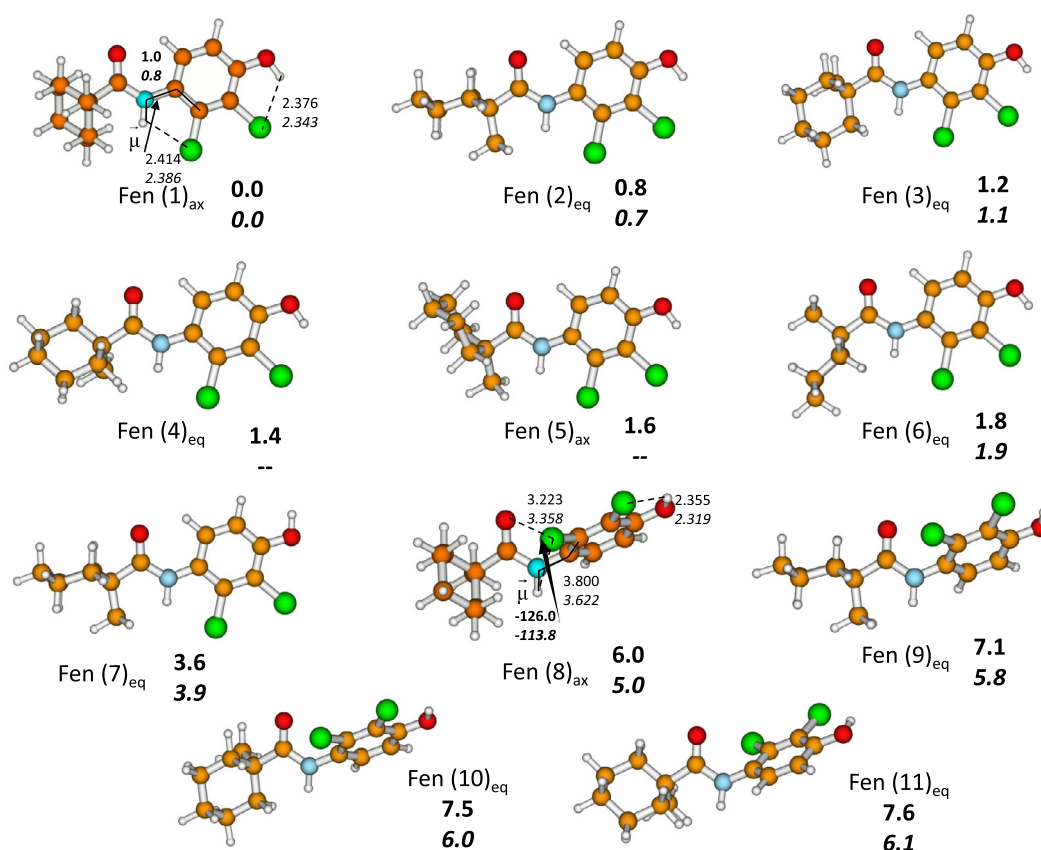


Fig. 3. Fenhexamid low-lying conformers with their relative energies in kcal/mol. Distances are given in Å, dihedrals (bold) in degrees at PBE/basis1 and PBE/basis2 in italics. μ is the dipole moment vector.

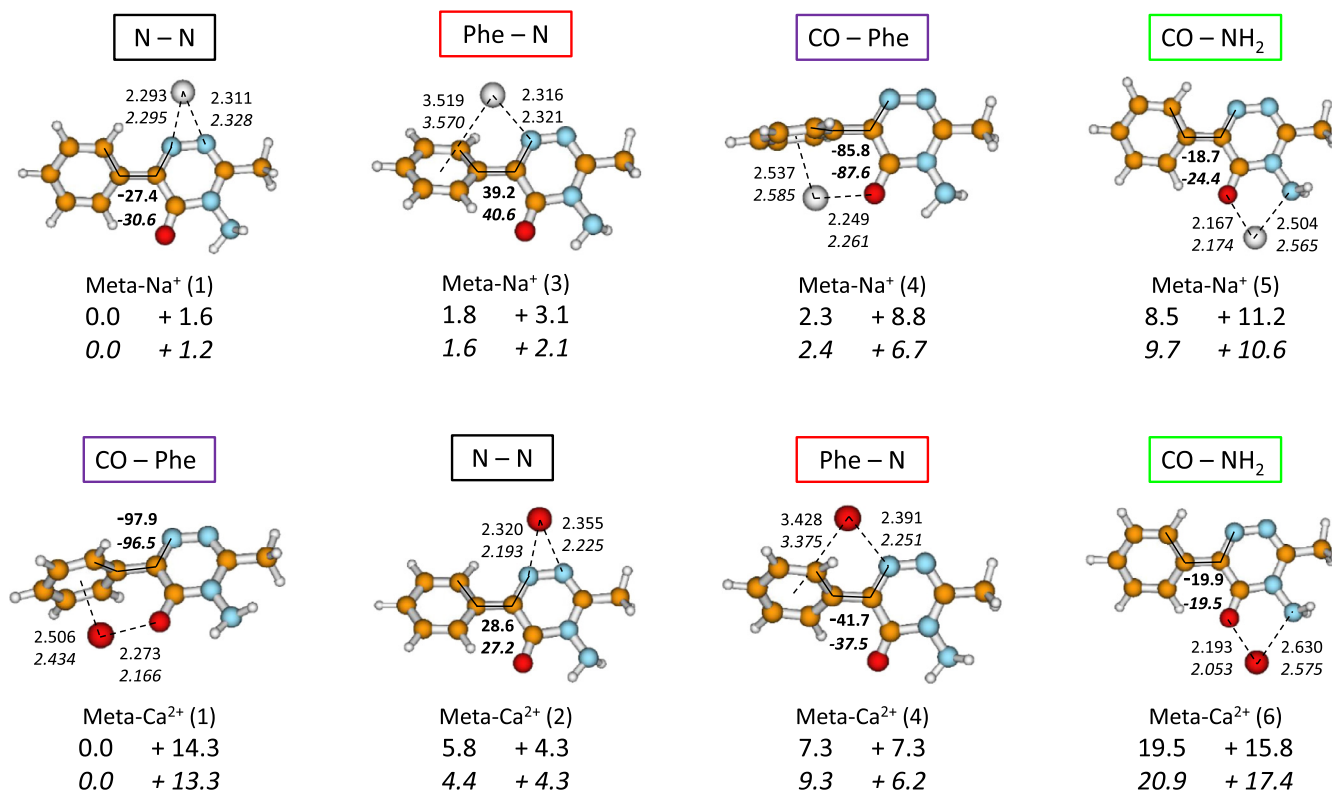


Fig. 4. The lowest-energy isomer of each family for Meta-Na⁺ (top) and Meta-Ca²⁺ (bottom). Relative (left) and preparation energies (right) are displayed in kcal/mol at PBE/basis1 and PBE/basis2 (in italics) levels. Distances are in Å and dihedrals (bold) in degrees at the PBE/basis1 and PBE/basis2 (in italics) levels.

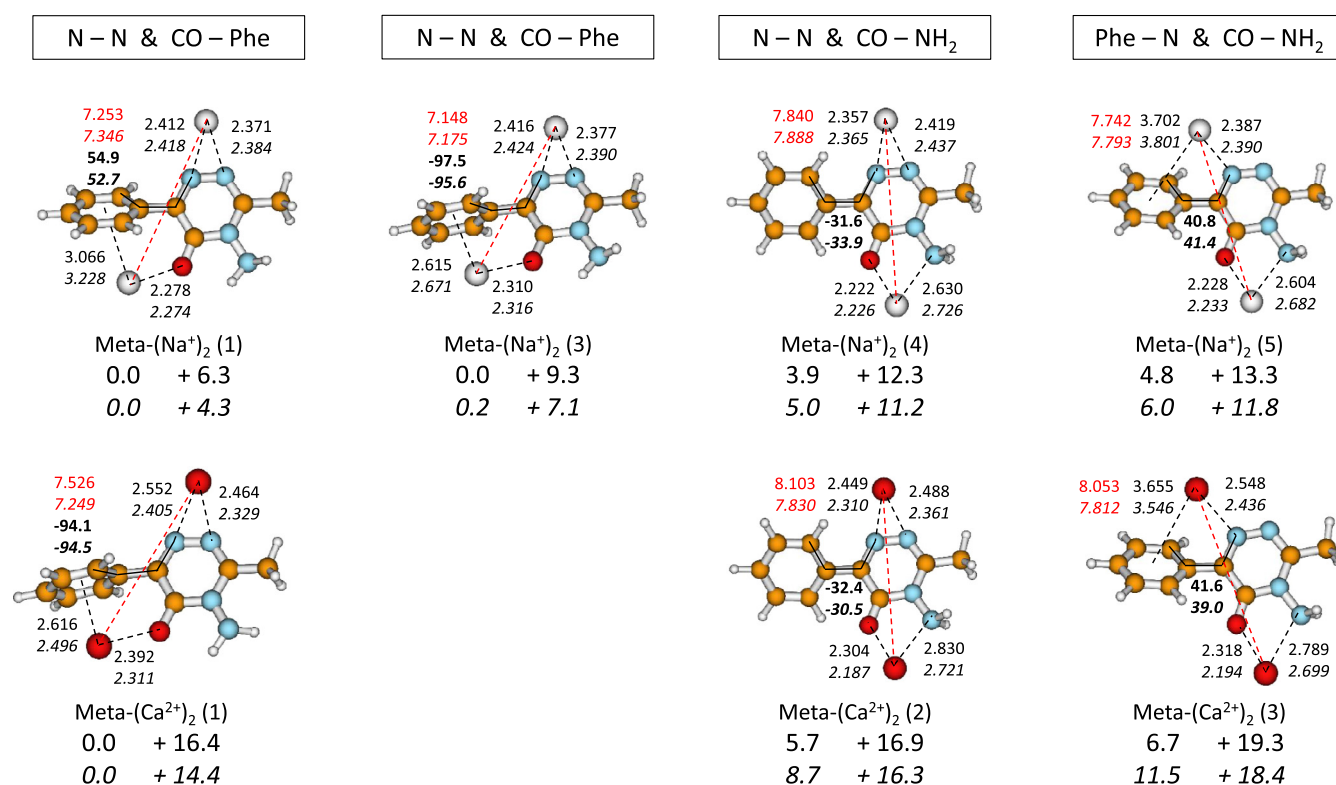


Fig. 5. Seven low-lying isomers of metamitron with two Na⁺ (top) and two Ca²⁺ (bottom). Relative (left) and preparation energies (right) are displayed in kcal/mol at PBE/basis1 and PBE/basis2 (in italics) levels. Distances are in Å and dihedrals (bold) in degrees at the PBE/basis1 and PBE/basis2 (in italics) levels.

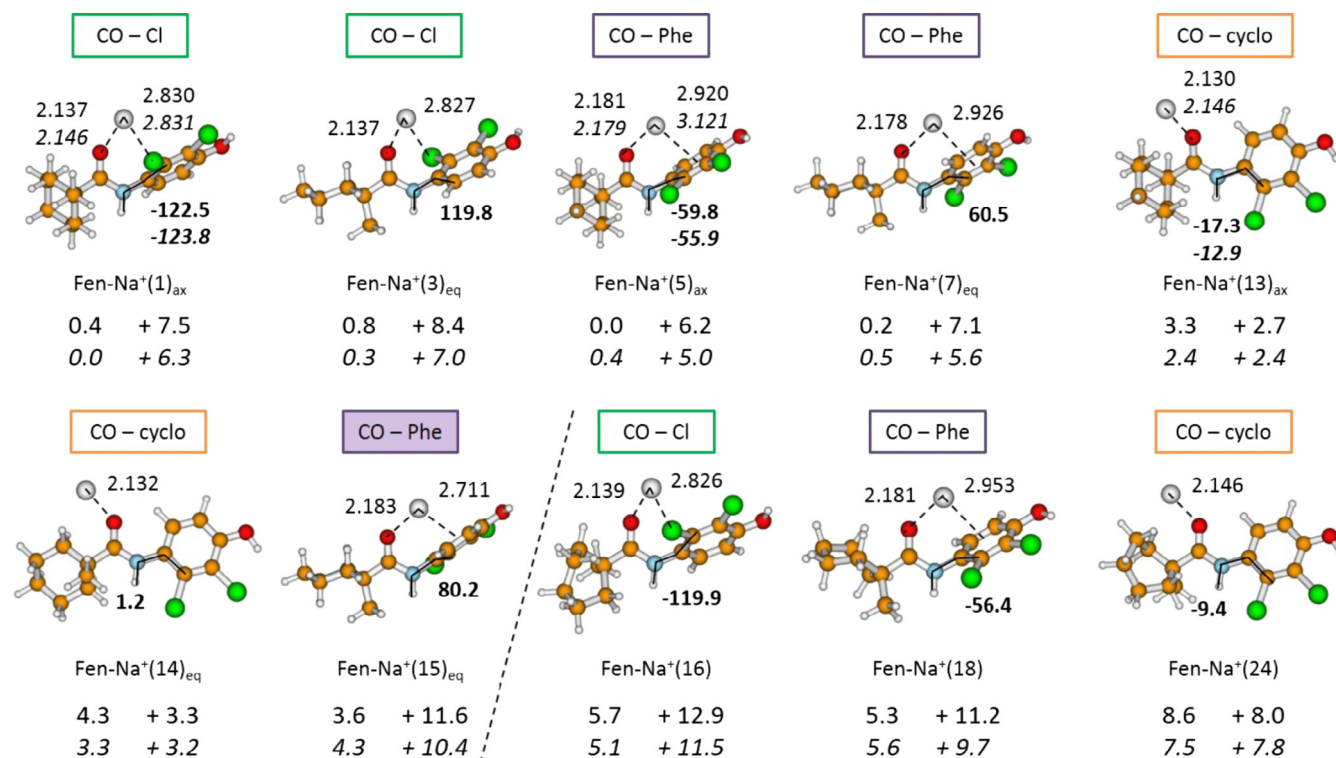


Fig. 6. The main low-lying isomers of fenhexamid with one cation Na⁺. Relative (on the left) and preparation energies (on the right) are displayed in kcal/mol at PBE/basis1 and PBE/basis2 (in italics) levels. Distances are in Å and dihedrals (bold) in degrees at the PBE/basis1. For the lowest isomers of each family, geometrical parameters are also given at PBE/basis2 (in italics). For totally broken delocalization in CO-Phe, the frames have been filled in purple. Beyond the limit materialized by the dot line, the cyclohexyl group is out of chair shape.

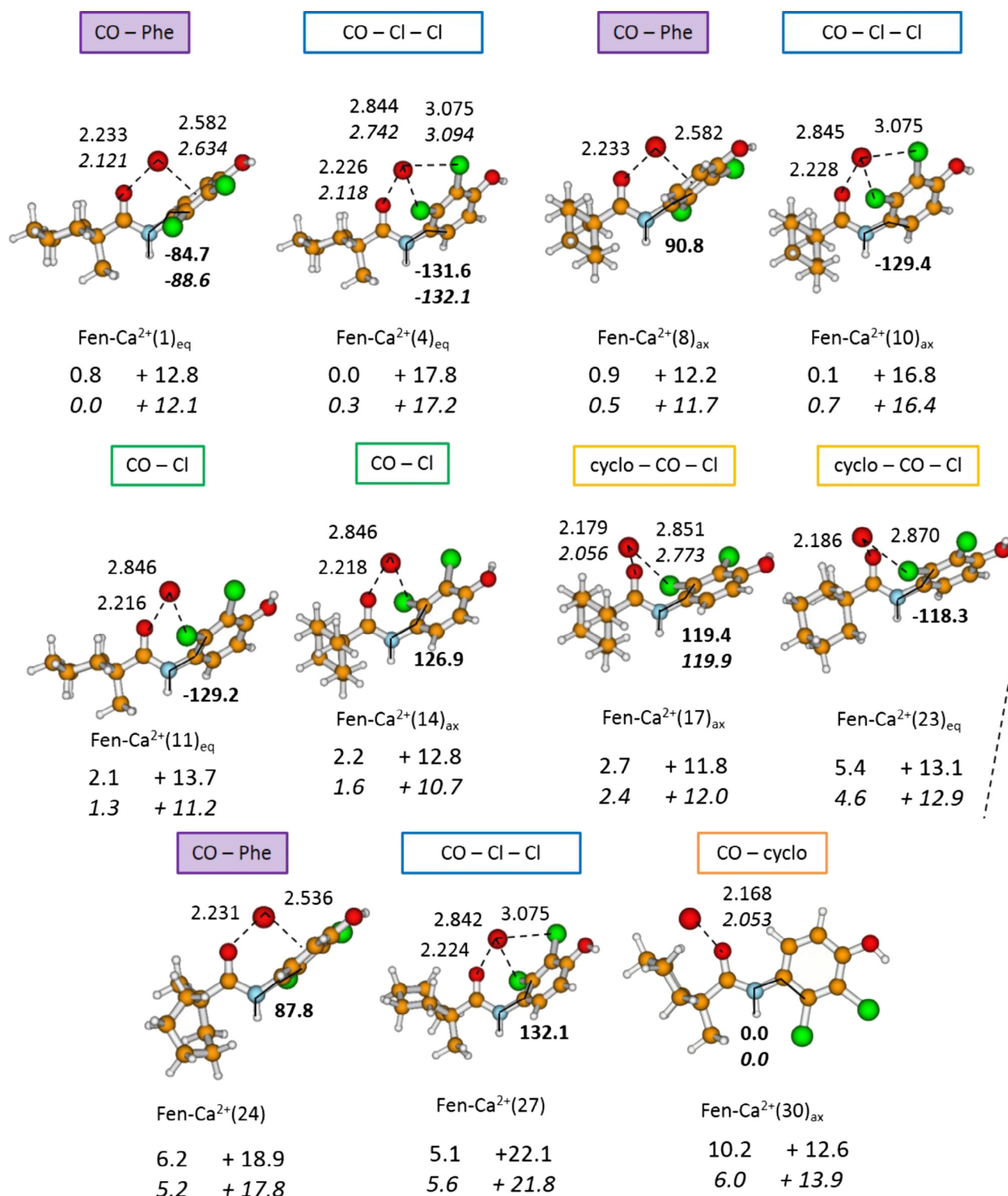


Fig. 7. The main low-lying isomers of fenhexamid with one cation Ca²⁺. Relative (on the left) and preparation energies (on the right) are displayed in kcal/mol at PBE/basis1 and PBE/basis2 (in italics) levels. Distances are in Å and dihedrals (bold) in degrees at the PBE/basis1. For the lowest isomers of each family, geometrical parameters are also given at PBE/basis2 (in italics). For totally broken delocalization in CO-Phe, the frames have been filled in purple. Beyond the limit materialized by the dot line, the cyclohexyl group is out of chair shape except for Fen-Ca²⁺(30)_{ax}.

3.1. Pesticides: structures and relative energies

3.1.1. Metamitron

Despite the 25 ps of MD simulation allowing flexibility within the structure, the 20 snapshots we selected and

optimized have led to the same minimum (see Fig. 2). This result was expected since the planar form of Meta enables the conjugation of the 14 π electrons from the phenyl and the triazinone cycle. Moreover, the structure of metamitron has only a few degrees of freedom. In this conformation, a weak

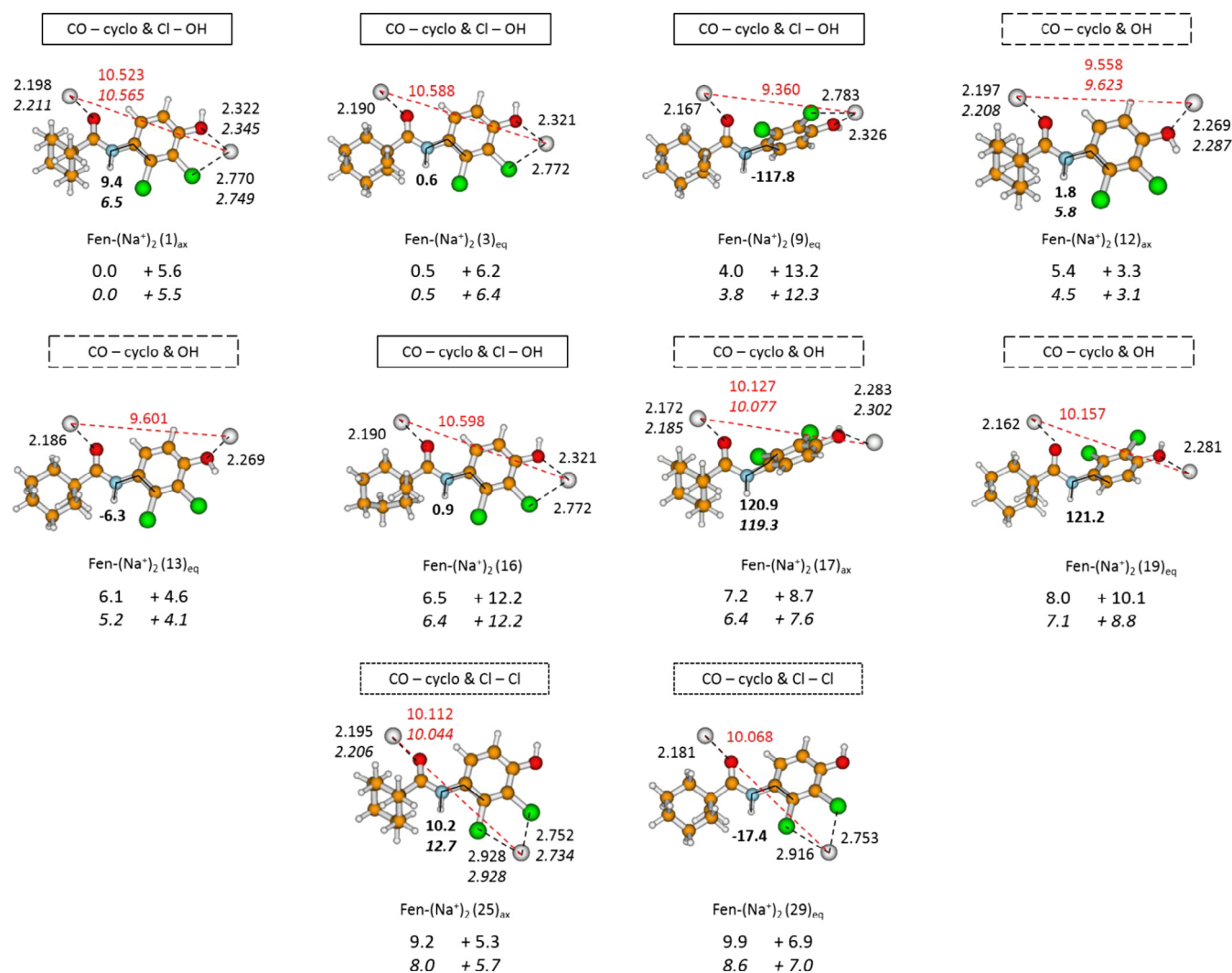


Fig. 8. The main low-lying isomers of fenhexamid with two Na⁺ cations. Relative (on the left) and preparation energies (on the right) are displayed in kcal/mol at PBE/basis1 and PBE/basis2 (in italics) levels. Distances are in Å and dihedrals (bold) in degrees at the PBE/basis1. For the lowest isomers of each family, geometrical parameters are also given at PBE/basis2 (in italics).

interaction between one of the NH₂ hydrogen and the carbonyl oxygen is observed.

3.1.2. Fenhexamid

40 structures have been optimized, leading to 11 low-energy conformers lying in a range of 10 kcal/mol (see Fig. 3). In all conformers, the cyclohexyl group takes a chair shape. According to literature, the cyclohexane adopts a chair conformation in more than 99.9% of cases at room temperature [45,46]. Promoting the cyclohexane from a chair to a twist-boat shape requires to cross an energy barrier of +10.8 kcal/mol and the potential energy difference between chair and twist-boat is +5.5 kcal/mol. A detailed analysis of the conformer structures reveals that Fen has three main structural degrees of freedom. The first one, that has the greatest impact in terms of relative energy, is the H7-N3-C4-C5 dihedral. Indeed, the seven lowest-energy minima of Fen display a delocalisation of the π system along the peptide bond (CO-NH) and the di-chloro, hydroxy-phenyl group that is allowed by a dihedral of $\approx 0^\circ$. From Fen(8), the π delocalization is partially broken (H7-N3-C4-C5 dihedral $\approx \pm 120^\circ$). More interestingly, considering basis1, the Fen(1)/Fen(8), Fen(2)/Fen(9), Fen(3)/Fen(10) and Fen(4)/Fen(11) pairs of conformers are structurally identical except for the H7-N3-C4-C5 dihedral, which always induces an energy

difference of 5–6 kcal/mol that can thus be attributed to the breaking of the π delocalisation. The second degree of freedom is related to the intra-molecular hydrogen bond involving the hydroxyl hydrogen and the closest Cl atom that exists in all isomers except Fen(7). The 3 kcal/mol energy difference between Fen(7) and Fen(2) that display the same structural features can be imputed to this hydrogen bond stabilisation. The last degree of freedom is the position of the R fragment: axial in Fen(1), Fen(5) and Fen(8) or equatorial in all the other conformers. The relative energies of both conformer types overlap. For instance, Fen(1)_{ax} and Fen(2)_{eq} only differ by the orientation of R and their energy difference of 0.8 kcal/mol can thus be related to the position of this fragment. In that case, the axial conformation of R (and thus the equatorial conformation of CH₃) is preferred as it minimizes the steric hindrance between the axial hydrogens on the cyclohexyl and the methyl hydrogens (see [supplementary material Table S2](#) for more details).

3.2. Pesticide – (cation)_i complexes, $i = 1, 2$: structures and relative energies

Metamitron and fenhexamid are neutral molecules. Therefore, the most favorable binding sites for the cation(s) should be the

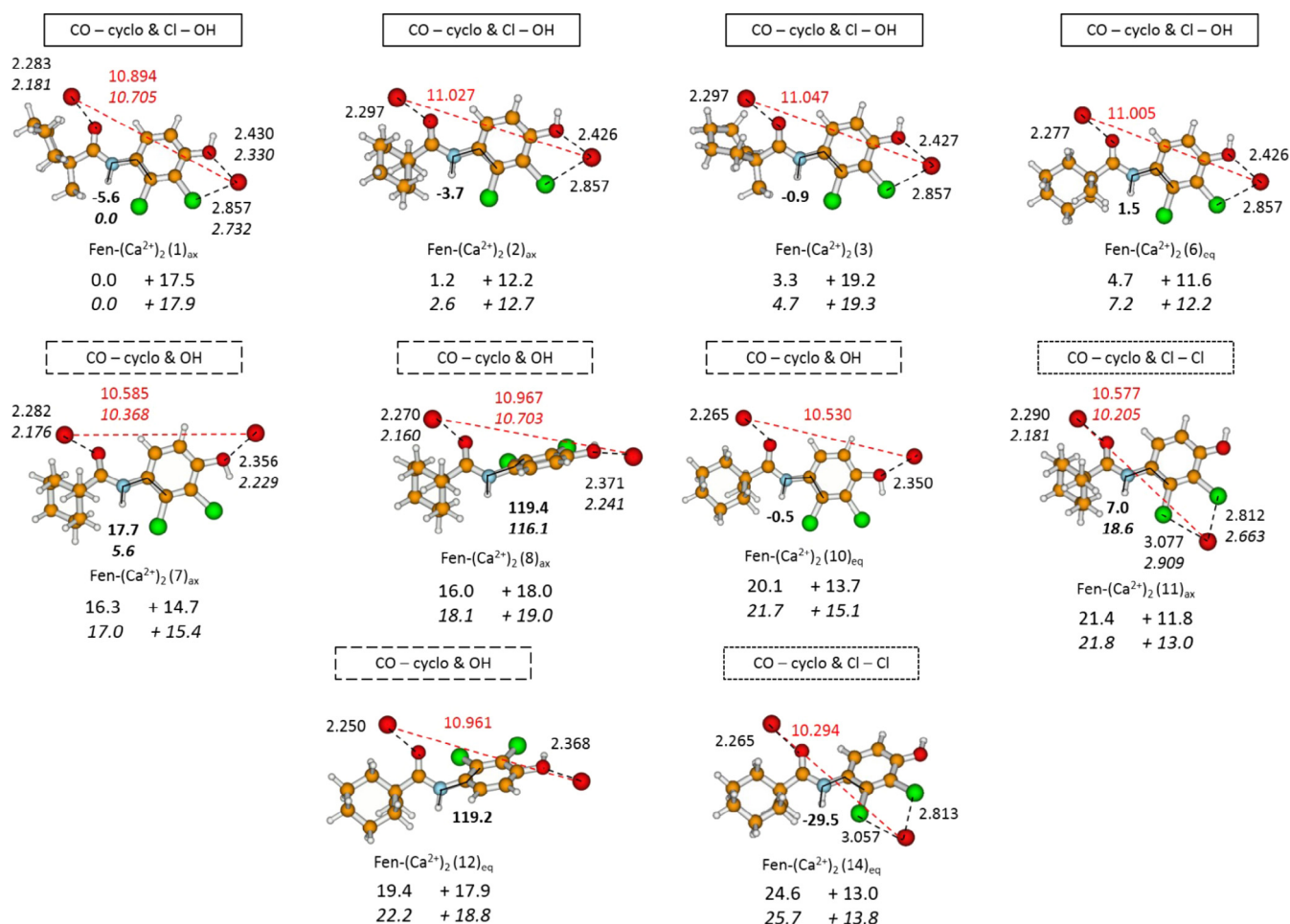


Fig. 9. The main low-lying isomers of fenhexamid with two Ca²⁺ cations. Relative (on the left) and preparation energies (on the right) are displayed in kcal/mol at PBE/basis1 and PBE/basis2 (in italics) levels. Distances are in Å and dihedrals (bold) in degrees at the PBE/basis1. For the lowest isomers of each family, geometrical parameters are also given at PBE/basis2 (in italics).

electron rich ones such as chlorines, oxygens, nitrogens and the π system of the triazinone, the phenyl or of the substituted phenyl.

3.2.1. Metamitron – cation

Whatever the nature of the cation, geometry optimisations lead to four families corresponding to different bidentate binding sites for the cation (see Fig. 4). In the family denoted N-N, the cation interacts with both consecutive nitrogen atoms of the triazinone cycle. In this case, the cation lies in the plane of the aromatic cycle. The Phe-N family regroups isomers with a binding site involving both phenyl π system and the closest triazinone nitrogen. When the cation binds both carbonyl oxygen and phenyl π system, the family is labelled CO-Phe. For Phe-N and CO-Phe families, π delocalisation between phenyl and triazinone is partially or totally broken, respectively. The last family is named CO-NH₂ and involves a binding of the cation with both carbonyl oxygen and NH₂ group.

For each cation, the four families do not overlap in relative energy. Furthermore, the energetical order between those families is the same whatever the basis set. Consequently, results with basis1 will be commented thereafter. For Na⁺, the two N-N isomers are the lowest in energy followed by the only representatives of the Phe-N, CO-Phe and CO-NH₂ families at 1.8, 2.3 and 8.5 kcal/mol, respectively. The N-N family is favored due to a complexation site close to the dipole moment direction (see Fig. 2). For Ca²⁺, the main difference with Na⁺ is that the CO-Phe isomer is strongly stabilized and becomes the lowest-energy structure. The order remains the same for families N-N (5.8 kcal/mol for the lowest in

energy: Meta-Ca²⁺(2)), Phe-N (7.3 kcal/mol for Meta-Ca²⁺(4)) and CO-NH₂ (19.5 kcal/mol for Meta-Ca²⁺(6)). The latter isomer has been obtained from the optimization of the corresponding Meta-Na⁺(5) isomer for comparison. For Meta-Ca²⁺ complexes, the stabilization of the CO-Phe family is enhanced by the interaction with higher order electric moments than the dipole moment. A more detailed analysis of contributions in particular E_{CT} , E_{pol} and E_{elec} , will be presented in the RVS SCF analysis paragraph.

For sodium complexes, both geometries and relative energies depend only slightly on the basis set (see Fig. 4). The complexation site distances are always a bit larger using basis2. This results from BSSE effects as shown in the RVS SCF analysis paragraph. The main discrepancies concern the phenyl or NH₂ interactions ($+5$ – 6×10^{-2} Å). For the three first families, the relative energies are identical whatever the basis set (at the most 0.2 kcal/mol) whereas for the CO-NH₂ family, it is slightly larger (1.2 kcal/mol).

Basis set effects are more important for Meta-Ca²⁺ isomers. Indeed, distances between the cation and the binding sites are shortened (from 0.05 to 0.14 Å) with basis2 essentially due to a better description of the polarization contribution (see computed polarizabilities PBE/basis1 versus PBE/basis2 in Table 2). A larger difference (from 1.4 to 2 kcal/mol) on relative energies is also obtained due to the same effect.

3.2.2. Metamitron – (cation)₂

Fig. 5 shows the low-lying isomers of Meta in interaction with two cations of the same type. Five isomers have been located with

Table 2
Polarizability α (in Bohr³) and dipole moment μ (in Debye) of metatriton and fenhexamid at the PBE/basis1, HF/basis1//PBE/basis1, PBE/basis2 and HF/basis2//PBE/basis2 levels. Percentages of deviation from PBE/basis2 results are given for all the other levels of calculations.

	Meta				Fen			
	μ		α		μ		α	
PBE/basis1	3.2425	–3.0%	150.24	–14.0%	2.0417	–15.5%	190.07	–14.6%
HF/basis1//PBE/basis1	3.2945	–1.4%	132.64	–24.1%	2.6645	+10.3%	169.17	–24.0%
PBE/basis2	3.3420		174.77		2.4165		222.58	
HF/basis2//PBE/basis2	3.4292	+2.6%	153.90	–11.9%	2.8760	+19.0%	194.79	–12.5%

Na⁺ and three with Ca²⁺. For each cation, the isomers can be classified in three families corresponding to combination of two interaction sites already described for Meta – cation complexes. In Fig. 5, Meta-(Na⁺)₂(3) has been added for comparison with Meta-(Ca²⁺)₂(1) as they display the same structural features. Both cations settle in order to maximize the interaction with the molecule and to minimize inter-cation charge repulsion. Thus, the cations cannot be on the same “side” of the molecule: N-N and Phe-N, CO-Phe and CO-NH₂, CO-Phe and Phe-N sites cannot combine. Finally, for both cations and whatever the basis set, the energetic order is the same: N-N & CO-Phe, N-N & CO-NH₂ (Na⁺: 3.9 kcal/mol, Ca²⁺: 5.7 kcal/mol with basis1) and Phe-N & CO-NH₂ (Na⁺: 4.8 kcal/mol, Ca²⁺: 6.7 kcal/mol with basis1).

The effect of the basis set on both distances and relative energies is intensified as compared to Meta – cation complexes. For Na⁺, the distances are increased with basis2 by 0.16 Å at the most, which results from BSSE effects. The largest difference in relative energy is +1.2 kcal/mol from basis1 to basis2. In the case of Ca²⁺, both polarization and repulsion effects lead to larger variations increasing the basis set. The most significant decrease concerns the Ca–Ca distance (from –0.2 to –0.3 Å). The aforementioned effects imply an increase of up to 4.8 kcal/mol on the relative energies.

3.2.3. Fenhexamid – cation

Due to the complexity of the Fen energy landscape, the PES of Fen complexes is also more complicated to explore. Indeed, Fen-cation isomers have been sorted into 5 families, 3 of which being common for both cations: CO-Cl, CO-Phe and CO-cyclo. In the first family, so called CO-Cl, the cation interacts with the carbonyl oxygen and the closest chlorine atom. For the representatives of this family, the H7–N3–C4–C5 dihedral is around $\pm 120^\circ$. CO-Phe isomers are characterized by a cation coordination with the carbonyl oxygen and the π system of the phenyl group. In that case, the delocalization between the peptide bond and the phenyl is partially or totally broken (H7–N3–C4–C5 equals either $\pm 60^\circ$ or $\pm 80^\circ$). For Ca²⁺, all the CO-Phe isomers have a totally broken delocalization. In the CO-cyclo family, the cations interact mainly with the carbonyl oxygen and lies close to the cyclohexyl to increase polarization. In this case, delocalization remains almost total (H7–N3–C4–C5 from 0 to $\pm 20^\circ$).

For Ca²⁺, two other families have been identified. The CO-Cl-Cl isomers display a tridentate interaction with both chlorine atoms and the carbonyl oxygen (H7–N3–C4–C5 $\approx \pm 130^\circ$). In this case, no hydrogen bond between the hydroxyl hydrogen atom and the closest chlorine is formed. In the cyclo-CO-Cl family, the cation coordinates the carbonyl oxygen and the closest chlorine atom. Moreover, Ca²⁺ is oriented towards the cyclohexyl group to enhance the polarization contribution in contrast to the CO-Cl family (H7–N3–C4–C5 $\approx \pm 120^\circ$). In all these Fen-cation families, both axial and equatorial positions for the R fragment are observed. In the case of Na⁺, both kinds of isomers are quasi degenerated with a slight preference for the axial one, as for uncomplexed Fen. On the contrary, with Ca²⁺, the equatorial position is favored (except for the cyclo-CO-Cl family, see thereafter). This inversion is due

to the different steric hindrance induced by the cations as demonstrated in [supplementary material](#).

Unlike metatriton complexes, the basis set has a tremendous influence on the energetic order of the families. Situations where significant variations of the energetic contributions are observed will be discussed in details in the RVS SCF analysis paragraph. Although the relative energy difference between basis1 and basis2 does not exceed the accuracy of the method (≈ 1 kcal/mol), the isomers have been ordered and discussed considering the PBE/basis2 relative energies.

For Fen-Na⁺ isomers, we discuss in details only the 15 first isomers. Beyond this limit, materialized by a dot line in Fig. 6, the cyclohexyl group is out of chair shape. The energetic order of the families is the same before and after this frontier. The four lowest-energy isomers belong to the CO-Cl family (≤ 0.3 kcal/mol). The following family, CO-Phe, includes isomers 5–12 (0.4–2.3 kcal/mol). The stabilization of the CO-Cl family compared to the CO-Phe one results from a favorable position of the cation with respect to the orientation of the dipole moment $\vec{\mu}$ that is illustrated on the structure of Fen(8) in Fig. 3. This leads to a larger electrostatic contribution to the interaction energy (see E_{elec} of Fen-Na⁺(1)_{ax} and Fen-Na⁺(5)_{ax} in Table 5). Isomers 13 and 14, with relative energies between 2.4 and 3.3 kcal/mol, are part of the CO-cyclo group. Isomer 15 with a relative energy of 4.3 kcal/mol belongs to the CO-Phe family. It is however rather particular because of the totally broken delocalization between the peptide bond and the phenyl group (H7–N3–C4–C5 = 80.2°). As a consequence, the preparation energy is larger for Fen-Na⁺(15) (+10.4 kcal/mol) than for all the other isomers with a chair shape cyclohexyl.

Finally, the basis set has a negligible influence on the geometry of the Fen-Na⁺ isomers except for the CO-Phe family. Overall, for CO-Cl and CO-cyclo, the variations on the geometrical parameters of the interaction do not exceed 10^{-2} Å for the distances, and about 5° for the dihedrals. In the CO-Phe family, the distance between Na⁺ and the carbonyl oxygen remains roughly unchanged whereas the Na⁺–Phe distance increases (about 0.2 Å to the center of the phenyl) while enlarging the basis set. This is due to BSSE and CT contribution, both larger with basis1 for the CO-Phe family (see RVS SCF analysis with basis1 and basis2 of Fen-Na⁺(5)_{ax} in Table 6).

For Ca²⁺, 23 isomers are below the limit beyond which the cyclohexyl is deformed ($\Delta E \leq 4.6$ kcal/mol). Only those isomers will be discussed in details. Nevertheless, we located higher energy structures among which one CO-cyclo isomer, Fen-Ca²⁺(30) (6.0 kcal/mol), that lies higher in energy and displays a chair shape structure. The two first families, CO-Phe and CO-Cl-Cl, are imbricated but an organization scheme is observed: isomers where the R group is in equatorial position lie lower in energy (≤ 0.5 kcal/mol), then come the axial isomers ($0.5 \leq \Delta E \leq 0.7$ kcal/mol). For both positions, CO-Phe representatives are slightly more stable than CO-Cl-Cl ones. The contribution that distinguishes both families is the CT term, which is larger for CO-Phe isomers (see Table 5 for RVS SCF analysis of Fen-Ca²⁺(1)_{eq} versus Fen-Ca²⁺(4)_{eq}). Let's notice that using basis1, while the equatorial/axial order is maintained (quasi degenerated), the family order is reversed and

the families are not imbricated anymore. The third family is CO-Cl between 1.3 and 1.7 kcal/mol (Fen-Ca²⁺(11)–(15)) and a last representative at 3.4 kcal/mol (Fen-Ca²⁺(22)). It gathers three equatorial isomers followed by three axials. Then, one CO-Cl-Cl representative lies at 2.4 kcal/mol (Fen-Ca²⁺(16), see [supplementary material](#)) and is 1.7 kcal/mol (1.2 with basis1) higher than Fen-Ca²⁺(10). The latter energy difference corresponds to a change in fenhexamid conformation from Fen(1) to Fen(5) (1.6 kcal/mol using basis1). Between both isomers of the cyclo-CO-Cl family presented in [Fig. 7](#) (Fen-Ca²⁺(17): 2.4 and Fen-Ca²⁺(23): 4.6 kcal/mol) exist three equatorial and one axial CO-Phe isomers in which the bond between the hydroxyl hydrogen and the closest Cl atom is broken. Unlike all the families, in the cyclo-CO-Cl family, the axial conformation is favored with respect to the equatorial form due to a larger polarization contribution (see RVS SCF analysis in [Table 5](#) (17) versus (23)).

Concerning geometries, distances from Ca²⁺ to the phenyl or to the furthest chlorine, increase from basis1 to basis2 since the BSSE is reduced. In contrast, Ca-O9 and Ca-Cl6 distances decrease when the basis set enlarges (around –0.1 Å). This is due to the non negligible CT in Fen-Ca²⁺ isomers. Ca²⁺ natural charges computed at PBE/basis2 are smaller than at PBE/basis1 (see [Table 3](#)) indicating a larger CT.

3.2.4. Fenhexamid – (cation)₂

For fenhexamid complexes with two cations, 29 isomers have been found for Na⁺ (see [Fig. 8](#)) and 14 for Ca²⁺ (see [Fig. 9](#)). The complexation sites previously described with one cation are not combined in Fen-(cation)₂ isomers due to cation-cation repulsion. For both cations, the three same families have been obtained in which one cation complexes the carbonyl oxygen and polarizes the cyclohexyl group. Consequently, axial positions are always favored in order to maximize cyclohexyl polarization. Thus, those families differ by the complexation mode of the second cation:

- CO-cyclo & Cl-OH: the second cation is engaged in a bidentate interaction with the hydroxyl oxygen and the closest chlorine;
- CO-cyclo & OH: it interacts only with the hydroxyl oxygen;
- CO-cyclo & Cl-Cl: it complexes both chlorine atoms.

The energetic order of those families is the same for Na⁺ and Ca²⁺: CO-cyclo & Cl-OH, CO-cyclo & OH and CO-cyclo & Cl-Cl, and does not depend on the basis set.

For Fen-(Na⁺)₂, the three families are successive except for two structures (15, 16) with an out of chair shape cyclohexyl. Whatever the family, the delocalization of the peptide bond and the

substituted phenyl leads to the most stable isomers. The first family gathers isomers 1–11 with relative energies ranging from 0 to 4.3 kcal/mol. In the CO-cyclo & OH family, two groups are identifiable. A first one where the delocalization is conserved allowing a shorter Na-Na distance (≈ 9.6 Å): isomers 12 (4.5 kcal/mol) to 14 (6.0 kcal/mol). For isomers 17 (6.4 kcal/mol) to 24 (7.5 kcal/mol), the delocalization is partially broken but a larger Na-Na distance (≈ 10.1 Å) reduces the inter-cation repulsion. The last family with Cl-Cl bidentate interaction includes isomers 25 (8.0 kcal/mol) to 29 (8.6 kcal/mol).

For Fen-(Ca²⁺)₂, the CO-cyclo & Cl-OH family is more stable than the two others: isomers 1–6 with relative energies up to 7.2 kcal/mol. For these complexes, the delocalization is maintained and the Ca-Ca distance is rather long around 11 Å. First, axial isomers lie below 2.6 kcal/mol, then, axial out of chair shape isomers arise (4.7–6.1 kcal/mol). Finally, one equatorial isomer is found with a relative energy of 7.2 kcal/mol. Both other families overlap and are higher in energy from 17.0 to 25.7 kcal/mol due to two factors: either the shorter Ca-Ca distance (≈ 10.5 Å) leading to a larger inter-cation repulsion; or the partially broken delocalization. Overall axial position, delocalization and OH complexation are stabilizing factors.

3.3. Complexation with Na⁺ and Ca²⁺ cations

3.3.1. Thermodynamics

[Table 4](#) displays complexation energies, enthalpies and free energies for the lowest isomer of each pesticide with one or two cations at PBE/basis1, PBE/basis2//PBE/basis1 and PBE/basis2 levels. Considering Meta or Fen, complexation values are of the same order of magnitude. Complexation energies are around –40 kcal/mol with one sodium cation, –140 kcal/mol with one Ca²⁺, –22 kcal/mol with two Na⁺ and –30 (Meta) to –60 (Fen) kcal/mol with two Ca²⁺. Cation charge influences the contributions to the interaction energy, in particular, electrostatic and polarization terms. Hence, complexation energies with one Ca²⁺ are larger in absolute values. When two cations interact with the pesticides, repulsion between both cations also plays an important role and a balance between minimal repulsion and maximal attractive contributions occurs. Distances between the two cations are about 7.2 Å for Meta and around 10.7 Å for Fen. For Na⁺, despite this bond length difference, similar complexation energies are obtained. In the case of Ca²⁺, repulsion gets the upper hand over electrostatic contribution plus polarization in Meta-(Ca²⁺)₂ leading to a twice smaller complexation energy (in absolute value). Let's notice that

Table 3

Natural charges from NBO population analysis for Fen-Na⁺(1) and (5) as well as for Fen-Ca²⁺(1) and (4) at PBE and HF//PBE levels.

		HF/basis1 //PBE/basis1	HF/basis2 //PBE/basis2	PBE/basis1	PBE/basis2
Fen-Na ⁺ (1)	Na	+0.97	+0.95	+0.93	+0.94
	O9	–0.89	–0.89	–0.74	–0.75
	Cl6	+0.03	+0.03	+0.06	+0.08
	Cl8	+0.00	+0.02	+0.03	+0.05
Fen-Na ⁺ (5)	Na	+0.97	+0.96	+0.94	+0.95
	O9	–0.87	–0.88	–0.72	–0.74
	Cl6	+0.05	+0.05	+0.09	+0.10
	Cl8	+0.07	+0.07	+0.10	+0.11
Fen-Ca ²⁺ (1)	Ca	+1.90	+1.78	+1.85	+1.65
	O9	–0.97	–0.95	–0.82	–0.78
	Cl6	+0.13	+0.14	+0.17	+0.19
	Cl8	+0.11	+0.12	+0.16	+0.18
Fen-Ca ²⁺ (4)	Ca	+1.87	+1.75	+1.79	+1.60
	O9	–0.98	–0.95	–0.83	–0.79
	Cl6	+0.05	+0.09	+0.08	+0.15
	Cl8	+0.05	+0.09	+0.09	+0.14

Table 4 $E_{\text{comp}}^{\text{uncorr}}$, E_{comp} (BSSE corrected), ΔH_{comp} , ΔG_{comp} (kcal/mol) at the PBE/basis1, PBE/basis2//PBE/basis1 and PBE/basis2 levels of important isomers.

	Meta-Na ⁺ (1) N-N	Fen-Na ⁺ (5) _{ax} CO-Phe	Meta-Ca ²⁺ (1) CO-Phe	Fen-Ca ²⁺ (4) _{eq} CO-Cl-Cl	Meta-(Na ⁺) ₂ (1) N-N & CO-Phe	Fen-(Na ⁺) ₂ (1) _{ax} CO-cyclo & Cl-OH	Meta-(Ca ²⁺) ₂ (1) N-N & CO-Phe	Fen-(Ca ²⁺) ₂ (1) _{ax} CO-cyclo & Cl-OH
PBE/basis1								
$E_{\text{comp}}^{\text{uncorr}}$	-46.37	-44.89	-124.89	-125.64	-32.49	-29.48	-14.35	-35.51
E_{comp}	-43.52	-40.80	-120.37	-121.41	-25.46	-24.35	-7.24	-30.39
ΔH_{comp}	-42.94	-40.64	-120.21	-121.01	-24.60	-23.73	-6.85	-30.27
ΔG_{comp}	-35.26	-33.41	-110.90	-111.61	-9.89	-9.68	+10.19	-14.17
PBE/basis2//PBE/basis1								
$E_{\text{comp}}^{\text{uncorr}}$	-42.27	-40.62	-138.56	-139.57	-25.48	-23.46	-28.59	-55.07
E_{comp}	-41.63	-39.64	-138.07	-139.03	-23.97	-21.96	-27.92	-54.40
ΔH_{comp}	-41.05	-39.48	-137.90	-138.63	-23.10	-21.33	-27.53	-54.28
ΔG_{comp}	-33.38	-32.25	-128.59	-129.22	-8.40	-7.28	-10.48	-38.18
	Meta-Na ⁺ (1) N-N	Fen-Na ⁺ (1) _{ax} CO-Cl	Meta-Ca ²⁺ (1) CO-Phe	Fen-Ca ²⁺ (1) _{eq} CO-Phe	Meta-(Na ⁺) ₂ (1) N-N & CO-Phe	Fen-(Na ⁺) ₂ (1) _{ax} CO-cyclo & Cl-OH	Meta-(Ca ²⁺) ₂ (1) N-N & CO-Phe	Fen-(Ca ²⁺) ₂ (1) _{ax} CO-cyclo & Cl-OH
PBE/basis2								
$E_{\text{comp}}^{\text{uncorr}}$	-42.28	-40.64	-139.95	-141.52	-25.49	-23.46	-31.04	-57.87
E_{comp}	-41.64	-39.67	-139.43	-140.96	-24.01	-21.97	-30.29	-57.13
ΔH_{comp}	-40.98	-39.27	-139.07	-140.58	-23.00	-21.11	-29.84	-57.26
ΔG_{comp}	-33.23	-32.05	-129.50	-131.83	-8.45	-6.71	-12.38	-41.48

with Fen and Meta complexation energies with two cations are attractive contrary to atrazine previously studied [29].

In the following, basis set and geometry effects on the complexation values will be discussed. With Na⁺ cation, using basis1 even with BSSE correction, complexation energies are slightly overestimated (3–11% in comparison with basis2). In the case of Ca²⁺, basis1 underestimates BSSE corrected complexation energies (14% with one cation and up to 76% with two cations). This discrepancy is essentially due to the underestimation of polarization using basis1. Indeed, it can be seen that computed polarizabilities given in Table 2, are largely underestimated at PBE/basis1 (~15%).

As noticed in our previous DFT studies on atrazine complexes, geometry optimization level has only a little influence on the computed complexation energies in basis2. At PBE/basis2//PBE/basis1, complexation energies are in very good agreement with PBE/basis2 (relative error < 1.5%) except for complexes with two Ca²⁺ cations (relative error at most 8% for Meta-(Ca²⁺)₂).

To obtain thermodynamic values at a T temperature (298.15 K) and a P pressure (1 atm), vibrational, translational and rotational energies and entropies have to be computed. A vibrational frequency calculation performed with Gaussian09 enables to calculate these thermodynamic corrections evaluating the corresponding partition functions defined in statistical thermodynamics. It has been carried out for the lowest conformers or isomers at PBE/basis1 and PBE/basis2 levels.

In all cases, the correction from energy to enthalpy is rather small (<1 kcal/mol) whatever the vibrational frequency computational level. The entropic $-T\Delta S_{\text{comp}}$ correction is about 8 kcal/mol for complexes with one cation and around 15 kcal/mol for two cation complexes. Such as the previous correction, this term slightly depends on the computational level. The main entropic difference between one and two cation complexes comes from the translational entropy of the additional cation (about 10 kcal/mol whatever the cation). A smaller contribution is due to the entropy difference between pesticide-cation and pesticide-(cation)₂ complexes (3–4 kcal/mol). Finally, complexation free energies are around -30 kcal/mol with one sodium cation, -130 kcal/mol with one Ca²⁺, around -7 kcal/mol with two Na⁺ and -12.4 (Meta) to -41.5 (Fen) kcal/mol with two Ca²⁺.

3.3.2. RVS SCF analysis

In the previous paragraph, complexation values in particular E_{comp} have been discussed within the PBE framework. In the following, the different contributions to the interaction energy E_{int}

will be computed at HF levels and commented. Dipole moments and polarizabilities of pesticides are given in Table 2 at various computational levels. Our reference level is PBE/basis2. Whatever the pesticide, Meta or Fen, the computed polarizability is underestimated when basis1 is used (~15%) and with HF (~12%). Thus, the polarization contribution is always underestimated in the RVS SCF decomposition analysis. Concerning dipole moments (μ), it depends on the pesticide:

- Meta: μ is slightly underestimated using basis1 (3% at most) and a bit overestimated at HF/basis2//PBE/basis2 (~3%);
- Fen: μ is underestimated using PBE/basis1 (16%) but overestimated with HF (from 10 (basis1) to 20% (basis2)).

Thus, in our decomposition, E_{elec} will be correctly described for Meta whatever the basis set whereas for Fen, the error on the computed electrostatic contribution will be larger, particularly with basis2. Charge transfer is almost non-existent with Na⁺, and weak with Ca²⁺ as can be seen from cation natural charges in Table 3. Moreover, it is underestimated at HF levels. This was expected for alkaline and alkaline-earth metal cations. It is worth pointing out that for transition-metal cations, for instance Fe^{2+/3+} also present in soils, the interaction with a pesticide would involve a larger part of covalency and so a stronger charge transfer. Otherwise, computed values of electronic affinity (EA) of Ca²⁺ and ionization potential (IP) of Fen are reported in Table S6. $EA_{\text{Ca}^{2+}}$ is smaller and IP_{Fen08} is larger at HF levels leading to smaller CT contributions. For comparison, $EA_{\text{Na}^{+}}$ has been computed and found notably smaller than $EA_{\text{Ca}^{2+}}$ (123.4 versus 276.2 kcal/mol at PBE/basis2) in agreement with the negligible CT in sodium complexes. Table S7 presents E_{comp} , E_{prep} and E_{int} for the lowest isomers of both CO-Phe (1) (the most stable with basis2) and CO-Cl-Cl (4) (the most stable using basis1) Fen-Ca²⁺ families at PBE and HF levels. The relationship between E_{comp} and E_{int} is as follows: $E_{\text{comp}} = E_{\text{int}} + E_{\text{prep}} + E_{\text{int(cat-cat)}}$. In our previous studies, we have demonstrated that preparation energies computed at both DFT and HF levels are usually similar [28,29]. Here, it is also verified. In most cases, the difference does not exceed 1 kcal/mol except for Fen-Ca²⁺(4)_{eq} using basis2 ($\Delta E_{\text{prep}} = 4.1$ kcal/mol). Anyway, the relative E_{comp} and E_{int} orders are conserved for isomers 1 and 4 at HF level compared to PBE whatever the basis set. Indeed, isomer (4) is always the lowest for E_{int} whatever the basis set but for E_{comp} , (1) is the lowest using basis2 and (4) is the most stable with basis1 (HF or PBE).

Thus, RVS SCF analysis of the interaction energy has been performed at the HF/basis1//PBE/basis1 level of theory for the lowest isomer of each complex of Meta and Fen with one or two cation(s) (see Table 5). In some cases, other representative(s) have been considered in order to support our discussion. As can be seen in Table 5, the electrostatic contribution prevails over, the polarization term is significant and the charge transfer is weak in Na⁺ complexes and slightly larger with Ca²⁺. For one or two Na⁺, E_{elec} and E_{pol} represents two thirds of the sum of the attractive terms, E_{pol} counts for about one third and E_{CT} is almost negligible. For one or two Ca²⁺, E_{elec} represents 50% of the sum of the attractive terms, E_{pol} counts for about 40% and E_{CT} is $\approx 10\%$. With two Na⁺, the electrostatic contribution is more important with Meta than with Fen, the tendency is similar with two Ca²⁺ when at the same time, E_{pol} decreases. In all cases, BSSE corrections at HF/basis1 level represents less than 4% of E_{int} . Comparing Meta and Fen complexed by one Na⁺, E_{exch} and E_{pol} remain unchanged. On the contrary, E_{elec} is greater for Fen whereas the dipole moment is lower (see Table 2). The electrostatic contribution is not easily rationalizable as previously shown for atrazine complexes [28,29]. Mainly two reasons could be invoked: the position of the cation with respect to the dipole moment orientation and the participation to E_{elec} from quadrupole, octupole and higher order moments. Finally, E_{CT} is slightly higher for Fen.

Considering one Ca²⁺ complexation, the lowest complex for each pesticide, Meta and Fen, concerns the same type of site: CO-Phe (always true for Meta, with basis2 for Fen). In this case, E_{int} computed with basis1 is greater for Meta (−131.7 versus −125.1 kcal/mol) as well as E_{elec} and E_{CT} . E_{exch} and E_{pol} remain of similar magnitudes going from Meta to Fen. Overall, the percentage of each contribution is equivalent in Meta and Fen complexes with one Ca²⁺.

Fen-Ca²⁺(4)_{eq}, the most stable in basis1, belongs to CO-Cl-Cl family. Its interaction energy is about 6 kcal/mol higher than Fen-Ca²⁺(1)_{eq} (CO-Phe family). E_{elec} and E_{pol} terms are larger in isomer (4) (−85.57 versus −79.73 kcal/mol, −68.89 versus −66.06 kcal/mol respectively). On the contrary, E_{CT} is about 3 kcal/mol less important in isomer (4), which is corroborated by a natural charge on Ca²⁺ smaller in isomer (4) (1.87 versus 1.90 at HF/basis1//PBE/basis1 see Table 3). Nevertheless, E_{comp} is greater for Fen-Ca²⁺(4)_{eq}: the energy to bring Fen to the geometry it adopts in the complex is more important for isomer (4) than in the case of isomer (1) ($\Delta E_{prep} \approx 5$ kcal/mol at PBE levels).

Fen-Ca²⁺ isomers (17) and (23) belong to cyclo-CO-Cl family. The position of the R fragment (R = 2,3-dichloro-4-hydroxyphenyl carboxamid) on the cyclohexyl differs for these two isomers: axial position in isomer (17) and equatorial position in isomer (23). Isomer (17) lies about 2.5 kcal/mol lower in energy than isomer (23). The differences for all the RVS terms except E_{pol} are negligible and

for the preparation energies are small comparing Fen-Ca²⁺(17)_{ax} and Fen-Ca²⁺(23)_{eq}. Thus, the axial position is preferred due to the strengthening of E_{pol} by 3 kcal/mol in isomer (17). Dealing with the complexation of Meta and Fen by two cations, $E_{int (cat-cat)}$ has to be considered. Due to born charges, $E_{int (cat-cat)}$ is much larger for Ca²⁺ than for Na⁺: it ranges from 30 to 50 kcal/mol for Na⁺ and from 120 to 180 kcal/mol for Ca²⁺. Indeed distances between both cations are always smaller when Meta is complexed instead of Fen (≈ 7 Å versus ≈ 10 Å).

Considering complexation by two Na⁺, E_{int} is larger for Meta than for Fen (−75.6 and −61.5 kcal/mol respectively) mainly due to the electrostatic term (−65.0 versus −52.5 kcal/mol), which well matches with dipole moment values: 3.3 Debye for Meta and 2.7 for Fen (see Table 2).

When the pesticides are complexed by two Ca²⁺ cations, E_{int} remains larger for Meta than for Fen (−189.7 and −160.3 kcal/mol respectively), essentially due to E_{elec} strengthened going from Fen to Meta (−27 kcal/mol). On the other hand, accounting two Ca²⁺ complexation, Fen is favored compared to Meta (−30.4 kcal/mol versus −7.2 for Meta, see Table 4). Indeed, $E_{int (Ca^{2+}-Ca^{2+})}$ increases by ≈ 50 kcal/mol going from Fen to Meta.

For Fen-Na⁺(5)_{ax} and Fen-Ca²⁺(1)_{eq}, the complexation site is the same, CO-Phe, complexation distances remains quite similar, the difference between both pair members resides in the nature of the cation and thus in the born charge going from +1 to +2. If the preponderant electrostatic term comes from the interaction between the pesticide dipole moment (μ) and the cation point charge (q), E_{elec} varies proportionally to the charge ($\frac{q\mu}{r^2}$). Going from Na⁺ to Ca²⁺, a multiplication by approximately a factor two of the value of E_{elec} is verified (−36.7 compared to −79.7 kcal/mol for Fen-Na⁺(5)_{ax} and Fen-Ca²⁺(1)_{eq} respectively). As well, E_{pol} varying proportionally to square charges ($\frac{q^2\alpha}{2r^4}$), a multiplication by approximately a factor four of the value of E_{pol} going from Na⁺ to Ca²⁺ complexation is verified in Table 5 (−16.6 compared to −66.1 kcal/mol for Fen-Na⁺(5)_{ax} and Fen-Ca²⁺(1)_{eq} respectively). In the two following pairs of complexes: Meta-(Na⁺)₂(1) and Meta-(Ca²⁺)₂(1) and Fen-(Na⁺)₂(1)_{ax} and Fen-(Ca²⁺)₂(1)_{ax}, the same multiplication factors are observed (charge going from 2 to 4 for those complexes with two cations).

Moreover in Table 6, the influences of the choice of the bases on the RVS decomposition and/or the geometry optimization have been reported for Fen-Ca²⁺(1)_{eq} (CO-Phe family) and Fen-Ca²⁺(4)_{eq} (CO-Cl-Cl family) isomers. RVS SCF analyses computed at HF/basis1 lead to about 50% of E_{elec} , 41% of E_{pol} and 9% of E_{CT} with respect to the sum of the attractive terms for both isomers. Performing the decomposition at HF/basis2, E_{pol} participates in percentages as much as E_{elec} (48% versus 46%) for both complexes. As expected regarding polarizabilities, the polarization term is greater with

Table 5

RVS SCF decomposition analysis (energies in kcal/mol) at the HF/basis1//PBE/basis1 level for isomers of Meta and Fen with one and two cations.

Complexes	Sites	E_{int}^{uncorr}	E_{int}	$E_{int (cat-cat)}$	E_{elec}	E_{exch}	E_{pol}	E_{CT}	BSSE
Meta-Na ⁺ (1)	N-N	−41.44	−42.71		−33.76 (65%)	+10.75	−16.66 (32%)	−1.67 (3%)	+1.27
Meta-Ca ²⁺ (1)	CO-Phe	−133.36	−131.72		−84.71 (50%)	+37.94	−65.72 (39%)	−18.61 (11%)	+1.64
Meta-Ca ²⁺ (2)	N-N	−111.24	−110.04		−71.83 (50%)	+33.72	−63.63 (45%)	−7.34 (5%)	+1.20
Meta-(Na ⁺) ₂ (1)	N-N & CO-Phe	−78.56	−75.56	+46.45	−64.99 (72%)	+15.13	−21.48 (24%)	−4.11 (5%)	+3.00
Meta-(Ca ²⁺) ₂ (1)	N-N & CO-Phe	−192.36	−189.69	+176.34	−133.59 (59%)	+38.68	−75.07 (33%)	−18.83 (8%)	+2.68
Fen-Na ⁺ (1) _{ax}	CO-Cl	−49.47	−48.14		−40.72 (68%)	+11.70	−16.07 (27%)	−2.97 (5%)	+1.33
Fen-Na ⁺ (5) _{ax}	CO-Phe	−45.72	−44.18		−36.70 (64%)	+11.49	−16.58 (29%)	−3.93 (7%)	+1.54
Fen-Ca ²⁺ (1) _{eq}	CO-Phe	−126.50	−125.06		−79.73 (49%)	+37.90	−66.06 (41%)	−16.55 (10%)	+1.44
Fen-Ca ²⁺ (4) _{eq}	CO-Cl-Cl	−132.83	−131.54		−85.57 (51%)	+36.90	−68.89 (41%)	−13.38 (8%)	+1.29
Fen-Ca ²⁺ (17) _{ax}	cyclo-CO-Cl	−125.41	−124.27		−83.02 (51%)	+38.18	−67.39 (42%)	−11.22 (7%)	+1.14
Fen-Ca ²⁺ (23) _{eq}	cyclo-CO-Cl	−122.79	−121.59		−82.29 (52%)	+37.71	−64.41 (41%)	−11.08 (7%)	+1.18
Fen-(Na ⁺) ₂ (1) _{ax}	CO-cyclo & Cl-OH	−63.31	−61.49	+31.56	−52.47 (67%)	+16.53	−21.68 (28%)	−3.77 (5%)	+1.82
Fen-(Ca ²⁺) ₂ (1) _{ax}	CO-cyclo & Cl-OH	−161.91	−160.27	+121.89	−106.62 (51%)	+51.96	−88.06 (42%)	−16.53 (8%)	+1.64

Table 6RVS SCF decomposition analysis (kcal/mol) at the HF/basisRVS//PBE/basisGeom level of Fen-Na⁺(5)_{ax}, Fen-Ca²⁺(1)_{eq} and Fen-Ca²⁺(4)_{eq}.

Complexes	Sites	basisRVS	basisGeom	E_{int}^{uncorr}	E_{int}	E_{elec}	E_{exch}	E_{pol}	E_{CT}	BSSE
Fen-Na ⁺ (5) _{ax}	CO-Phe	1	1	−45.72	−44.18	−36.70 64%	+11.49	−16.58 29%	−3.93 7%	+1.54
		2	2	−44.18	−44.01	−37.27 65%	+13.74	−19.71 34%	−0.61 1%	+0.17
Fen-Ca ²⁺ (1) _{eq}	CO-Phe	1	1	−126.50	−125.06	−79.73 49%	+37.90	−66.06 41%	−16.55 10%	+1.44
		1	2	−123.09	−121.56	−90.31 50%	+59.63	−73.37 41%	−16.80 9%	+1.52
Fen-Ca ²⁺ (4) _{eq}	CO-Cl-Cl	1	1	−132.83	−131.54	−85.57 51%	+36.90	−68.89 41%	−13.38 8%	+1.29
		1	2	−129.70	−128.33	−94.57 51%	+56.97	−76.05 41%	−13.98 8%	+1.38
Fen-Ca ²⁺ (1) _{eq}	CO-Phe	2	1	−135.61	−135.28	−80.29 45%	+44.52	−85.37 48%	−12.78 7%	+0.32
		2	2	−135.47	−135.13	−90.51 45%	+66.53	−93.08 47%	−16.45 8%	+0.34
Fen-Ca ²⁺ (4) _{eq}	CO-Cl-Cl	2	1	−140.80	−140.39	−82.50 46%	+41.06	−86.21 48%	−11.52 6%	+0.41
		2	2	−140.60	−140.18	−91.31 46%	+61.41	−93.77 47%	−15.02 7%	+0.42

basisRVS = basis2. On the other hand, E_{elec} varies only slightly when changing the basisRVS basis set confirming that E_{elec} is not driven only by charge-dipole interaction.

Finally, for both isomers, the main changes optimizing geometries with basis2 instead of basis1 correspond to a shortening of Ca-Cl6 distance for Fen-Ca²⁺(4)_{eq} and of Ca-O9 distance for both 1 and 4 isomers. Therefore, E_{exch} (repulsion energy between Ca²⁺ and Fen) is larger using basis2 by about 20 kcal/mol (basisGeom = basis2, see Table 6) whatever the isomer and the basisRVS. At the same time, E_{pol} and E_{elec} increase in absolute value by ≈7 kcal/mol and 10 kcal/mol respectively. Concerning, E_{CT} as previously mentioned, a CO-Phe complexation implies a larger CT contribution than CO-Cl-Cl whatever the HF/basisRVS//PBE/basisGeom level (ΔE_{CT} from 1.2 to 3 kcal/mol).

4. Conclusion

In this work, we have used molecular dynamical simulations to perform a quasi-exhaustive conformational analysis of pesticides (metamitron and fenhexamid) and their complexes with one or 2 cations (Na⁺ and Ca²⁺). For isolated metamitron, only one conformer has been localized in which the π electrons from the phenyl and the triazinone cycles are delocalized. In the case of fenhexamid, 11 conformers have been found below 10 kcal/mol. The seven first (relative energy < 4 kcal/mol) present delocalization of the π system between the peptide bond (CO-NH) and the dichloro,hydroxy-phenyl group. In the lowest-energy conformer, the R group is in axial position on the cyclohexyl due to the larger methyl steric hindrance. For Meta complexes, geometries and relative energies slightly depend on basis set. Thus, the isomer energetic order is the same whatever the basis set. In the lowest-energy isomer, Na⁺ complexes Meta on both consecutive N atoms of the triazinone cycle favoring dipole moment interaction. For Ca²⁺, the cation interacts with the carbonyl oxygen and the phenyl π electron cloud (CO-Phe). In this case, the interaction implies higher order electric moments as well as a larger CT contribution. Complexation of Meta with 2 cations combines both previous complexation sites. Unlike Meta complexes, the basis set has a tremendous influence on Fen-cation isomers. Complexation families are different with Na⁺ and Ca²⁺. Two families are common: CO-Cl and CO-Phe. CO-Cl implies an interaction of the cation with the carbonyl oxygen and the closest chlorine atom, this interaction on the dipole

moment direction is the most favorable for Na⁺. CO-Phe interaction type is preferred with Ca²⁺ because of CT term such as in Meta-Ca²⁺. For Fen-Na⁺, axial position of the R group is slightly favored (as for isolated Fen). In the contrary, R in equatorial becomes the most stable situation, Ca²⁺-Methylamidocyclohexane group causes more steric hindrance than methyl. For Fen-(cation)₂, family energetic order is the same whatever the cation and the basis set. Families are not combination of the one cation complexation sites. For both cation, CO-cyclo & Cl-OH family, conserving delocalization, is preferred: one cation interacts with the carbonyl O and polarizes the cyclohexyl, the second complexes the hydroxyl O and the closest chlorine. This family is clearly lower for Ca²⁺ due to a minimal inter-cation repulsion (maximal inter-cation distance). RVS SCF decomposition is a great tool to analyze contributions and understand the reasons of complex stability. In those complexes, for one or two Na⁺, E_{elec} represents two thirds of the sum of the attractive terms, E_{pol} counts for about one third and E_{CT} is almost negligible. For one or two Ca²⁺, E_{elec} represents 50% of the sum of the attractive terms, E_{pol} counts for about 40% and E_{CT} is ≈10%. Finally, thermodynamical complexation values are of the same order of magnitude considering Meta or Fen. Complexation energies are around −40 kcal/mol with one sodium cation, −140 kcal/mol with one Ca²⁺, −22 kcal/mol with two Na⁺. With two Ca²⁺, complexation energy is twice larger in absolute value for Fen (−60 kcal/mol) than for Meta due to longer inter-cation distances in Fen-(Ca²⁺)₂ complexes. At the same time, PBE/basis2//PBE/basis1 gives comparable results to PBE/basis2, and thus could be an alternative to investigate larger systems. Computed complexation free energies are negative whatever the complex (Meta/Fen with one or two cation(s)) unlike atrazine-(Ca²⁺)₂ studied in previous work. Thus, the studied structures in this work are interesting starting points to be deposited on clay surfaces. Finally, we aim to relate the macroscopic differences in behavior of pesticides into a soil with atomic scale values we could obtain. Therefore, pesticide interaction with hydrated clay surfaces or bulks are studies in progress in our group in order to get some hints on adsorption and desorption processes. To ally computational efficiency as well as result accuracy on large systems, force field or semi-empirical methods could be a great compromise. For exchangeable alkaline and alkaline-earth cations, polarization contributions are essential to describe pesticide/cation interaction. Thus, the chosen force field should be polarizable, for example ReaxFF[47]. In the case of semi-empirical framework, DFTB (Density Functional based Tight

binding) with a self-consistent redistribution of charges (SCC-DFTB [48]) would be an interesting way to explore.

Funding sources

This work was granted access to the HPC resources of CALMIP supercomputing center under the allocation 2016-[P1222] and of CINES under the allocation 2016-[cpq7002] made by GENCI.

Appendix A. Supplementary material

Supplementary data associated with this article can be found, in the online version, at <http://dx.doi.org/10.1016/j.comptc.2017.08.003>.

References

- [1] S. Tandon, S. Kumar, N.K. Sand, Development and validation of GC-ECD method for the determination of metolamiton in soil, *Int. J. Anal. Chem.* 2015 (2015) 1–5, <http://dx.doi.org/10.1155/2015/592763>.
- [2] C. Abbate, D. Borzi, P. Caboni, A. Baglieri, M. Gennari, Behavior of fenhexamid in soil and water, *J. Environ. Sci. Health Part B* 42 (7) (2007) 843–849, <http://dx.doi.org/10.1080/03601230701555088>.
- [3] Y.-S. Wang, M.-R. He, C.-Y. Zhang, S.-H. Fan, J. Ma, H.-F. Li, Determination of multiresidual fungicides in environmental water samples by high performance liquid chromatography tandem mass spectrometry, *Chin. J. Anal. Chem.* (Chinese Version) 40 (11) (2013) 1764–1771, <http://dx.doi.org/10.3724/sp.j.1096.2012.20100>.
- [4] U. Schulte-Oehlmann, J. Oehlmann, F. Keil, Before the curtain falls: endocrine-active pesticides – a german contamination legacy, in: *Reviews of Environmental Contamination and Toxicology*, Springer Science + Business Media, 2011, pp. 137–159, http://dx.doi.org/10.1007/978-1-4419-9860-6_5.
- [5] F.A. Esteve-Turrillas, A. Abad-Fuentes, J.V. Mercader, Determination of fenhexamid residues in grape must, kiwifruit, and strawberry samples by enzyme-linked immunosorbent assay, *Food Chem.* 124 (4) (2011) 1727–1733, <http://dx.doi.org/10.1016/j.foodchem.2010.07.112>.
- [6] L. Mamy, E. Barriuso, Desorption and time-dependent sorption of herbicides in soils, *Eur. J. Soil Sci.* 58 (1) (2007) 174–187, <http://dx.doi.org/10.1111/j.1365-2389.2006.00822.x>.
- [7] G. Sheng, C.T. Johnston, B.J. Teppen, S.A. Boyd, Adsorption of dinitrophenol herbicide from water by montmorillonites, *Clays Clay Miner.* 50 (1) (2002) 25–34, <http://dx.doi.org/10.1346/000986002761002630>.
- [8] V. Aggarwal, H. Li, B.J. Teppen, Triazine adsorption by saponite and beidellite clay minerals, *Environ. Toxicol. Chem.* 25 (2) (2006) 392, <http://dx.doi.org/10.1897/05-264r.1>.
- [9] D. Tunega, M.H. Gerzabek, G. Haberhauer, H. Lischka, Formation of 2,4-d complexes on montmorillonites – an ab initio molecular dynamics study, *Eur. J. Soil Sci.* 58 (3) (2007) 680–691, <http://dx.doi.org/10.1111/j.1365-2389.2006.00853.x>.
- [10] D. Muñoz-Santiburcio, J. Ortega-Castro, C. Sainz-Díaz, F. Huertas, A. Hernández-Laguna, Theoretical study of the adsorption of 2-nitro-1-propanol on smectite surface models, *J. Mol. Struct.: THEOCHEM* 912 (1–3) (2009) 95–104, <http://dx.doi.org/10.1016/j.theochem.2009.01.001>.
- [11] B. Belzunces, S. Hoyau, M. Benoit, N. Tarrat, F. Bessac, Theoretical study of the atrazine pesticide interaction with pyrophyllite and Ca²⁺-montmorillonite clay surfaces, *J. Comput. Chem.* 38 (3) (2017) 133–143, <http://dx.doi.org/10.1002/jcc.24530>.
- [12] A.J. Aquino, D. Tunega, G. Haberhauer, M.H. Gerzabek, H. Lischka, Adsorption of organic substances on broken clay surfaces: a quantum chemical study, *J. Comput. Chem.* 24 (15) (2003) 1853–1863, <http://dx.doi.org/10.1002/jcc.10342>.
- [13] P. Clausen, W. Andreoni, A. Curioni, E. Hughes, C.J.G. Plummer, Adsorption of low-molecular-weight molecules on a dry clay surface: an ab initio study, *J. Phys. Chem. C* 113 (28) (2009) 12293–12300, <http://dx.doi.org/10.1021/jp811383y>.
- [14] S.V. Churakov, G. Kosakowski, An ab initio molecular dynamics study of hydronium complexation in na-montmorillonite, *Phil. Mag.* 90 (17–18) (2010) 2459–2474, <http://dx.doi.org/10.1080/14786430903559474>.
- [15] A. Berghout, D. Tunega, A. Zaoui, Density functional theory (DFT) study of the hydration steps of Na⁺/Mg²⁺/Ca²⁺/Sr²⁺/Ba²⁺-Exchanged montmorillonites, *Clays Clay Miner.* 58 (2) (2010) 174–187, <http://dx.doi.org/10.1346/ccmn.2010.0580204>.
- [16] P. Mignon, P. Ugliengo, M. Sodupe, E.R. Hernandez, Ab initio molecular dynamics study of the hydration of Li⁺, Na⁺ and K⁺ in a montmorillonite model. Influence of isomorphic substitution, *Phys. Chem. Chem. Phys.* 12 (3) (2010) 688–697, <http://dx.doi.org/10.1039/b915689e>.
- [17] L. Sun, J.T. Tanskanen, J.T. Hirvi, S. Kasa, T. Schatz, T.A. Pakkanen, Molecular dynamics study of montmorillonite crystalline swelling: roles of interlayer cation species and water content, *Chem. Phys.* 455 (2015) 23–31, <http://dx.doi.org/10.1016/j.chemphys.2015.04.005>.
- [18] F. Salles, J.-M. Douillard, O. Bildstein, S.E. Ghazi, B. Prélôt, J. Zajac, H.V. Damme, Diffusion of interlayer cations in swelling clays as a function of water content: case of montmorillonites saturated with alkali cations, *J. Phys. Chem. C* 119 (19) (2015) 10370–10378, <http://dx.doi.org/10.1021/jp512986d>.
- [19] P. Mignon, P. Ugliengo, M. Sodupe, Theoretical study of the adsorption of RNA/DNA bases on the external surfaces of Na⁺-montmorillonite, *J. Phys. Chem. C* 113 (31) (2009) 13741–13749, <http://dx.doi.org/10.1021/jp901699q>.
- [20] P. Mignon, M. Sodupe, Theoretical study of the adsorption of DNA bases on the acidic external surface of montmorillonite, *Phys. Chem. Chem. Phys.* 14 (2) (2012) 945–954, <http://dx.doi.org/10.1039/c1cp22454a>.
- [21] P. Mignon, M. Sodupe, Structural behaviors of cytosine into the hydrated interlayer of na + -montmorillonite clay. An ab initio molecular dynamics study, *J. Phys. Chem. C* 117 (49) (2013) 26179–26189, <http://dx.doi.org/10.1021/jp4103383>.
- [22] A. Panebianco, I. Castello, G. Cirvilleri, G. Perrone, F. Epifani, M. Ferrara, G. Polizzi, D.R. Walters, A. Vitale, Detection of botrytis cinerea field isolates with multiple fungicide resistance from table grape in sicily, *Crop Prot.* 77 (2015) 65–73, <http://dx.doi.org/10.1016/j.cropro.2015.07.010>.
- [23] E.E.F.S. Authority, Conclusion Regarding the Peer Review of the Pesticide Risk Assessment of the Active Substance Metamitron, <http://dx.doi.org/10.2903/j.efsa.2008.185r>.
- [24] B. CropScience, Bayer CropScience fiche de données de sécurité conformément au règlement (ce) no. 1907/2006 URL <<https://www.cropscience.bayer.fr/fr-FR/-/media/Bayer%20CropScience/Country-Belgium-Internet/products/msds/MSDS%20Teldor.pdf>>.
- [25] E.E.F.S. Authority, Conclusion on the Peer Review of the Pesticide Risk Assessment of the Active Substance Fenhexamid, <http://dx.doi.org/10.2903/j.efsa.2014.3744>. URL <<http://www.efsa.europa.eu/fr/efsajournal/pub/3744>>.
- [26] R. Calvet, Le sol: propriétés et fonctions, no. vol. 1 in Le sol: propriétés et fonctions, Editions France Agricole, 2003. URL <<https://books.google.fr/books?id=stjPwnBDH-EC>>.
- [27] R. Calvet, Le sol, Agriproduction: univers agricole, Ed. France Agricole, 2013. URL <<https://books.google.fr/books?id=a88xnwEACAAJ>>.
- [28] F. Bessac, S. Hoyau, Pesticide interaction with environmentally important cations: a theoretical study of atrazine, *Comput. Theor. Chem.* 966 (1–3) (2011) 284–298, <http://dx.doi.org/10.1016/j.comptc.2011.03.024>.
- [29] F. Bessac, S. Hoyau, Pesticide interaction with environmentally important cations: a theoretical study of atrazine in interaction with two Ca²⁺ cations, *Comput. Theor. Chem.* 1022 (2013) 6–13, <http://dx.doi.org/10.1016/j.comptc.2013.06.025>.
- [30] W. Kohn, L.J. Sham, Self-consistent equations including exchange and correlation effects, *Phys. Rev.* 140 (4A) (1965) A1133–A1138, <http://dx.doi.org/10.1103/physrev.140.a1133>.
- [31] J.P. Perdew, K. Burke, M. Ernzerhof, Generalized gradient approximation made simple, *Phys. Rev. Lett.* 77 (18) (1996) 3865–3868, <http://dx.doi.org/10.1103/physrevlett.77.3865>.
- [32] CPMD, <<http://www.cpmd.org/>>, Copyright IBM Corp 1990–2015, Copyright MPI für Festkörperforschung Stuttgart, 1997–2001.
- [33] N. Troullier, J.L. Martins, Efficient pseudopotentials for plane-wave calculations, *Phys. Rev. B* 43 (3) (1991) 1993–2006, <http://dx.doi.org/10.1103/physrevb.43.1993>.
- [34] G.J. Martyna, M.E. Tuckerman, A reciprocal space based method for treating long range interactions in ab initio and force-field-based calculations in clusters, *J. Chem. Phys.* 110 (6) (1999) 2810, <http://dx.doi.org/10.1063/1.477923>.
- [35] R. Car, M. Parrinello, Unified approach for molecular dynamics and density-functional theory, *Phys. Rev. Lett.* 55 (22) (1985) 2471–2474, <http://dx.doi.org/10.1103/physrevlett.55.2471>.
- [36] M.J. Frisch, G.W. Trucks, H.B. Schlegel, G.E. Scuseria, M.A. Robb, J.R. Cheeseman, G. Scalmani, V. Barone, B. Mennucci, G.A. Petersson, H. Nakatsuji, M. Caricato, X. Li, H.P. Hratchian, A.F. Izmaylov, J. Bloino, G. Zheng, J.L. Sonnenberg, M. Hada, M. Ehara, K. Toyota, R. Fukuda, J. Hasegawa, M. Ishida, T. Nakajima, Y. Honda, O. Kitao, H. Nakai, T. Vreven, J.A. Montgomery, Jr., J.E. Peralta, F. Ogliaro, M. Bearpark, J.J. Heyd, E. Brothers, K.N. Kudin, V.N. Staroverov, R. Kobayashi, J. Normand, K. Raghavachari, A. Rendell, J.C. Burant, S.S. Iyengar, J. Tomasi, M. Cossi, N. Rega, J.M. Millam, M. Klene, J.E. Knox, J.B. Cross, V. Bakken, C. Adamo, J. Jaramillo, R. Gomperts, R.E. Stratmann, O. Yazyev, A.J. Austin, R. Cammi, C. Pomelli, J.W. Ochterski, R.L. Martin, K. Morokuma, V.G. Zakrzewski, G.A. Voth, P. Salvador, J.J. Dannenberg, S. Dapprich, A.D. Daniels, F. Farkas, J.B. Foresman, J. V. Ortiz, J. Cioslowski, D.J. Fox, Gaussian09 Revision E.01, Gaussian Inc. Wallingford CT 2009.
- [37] M.M. Franc, Self-consistent molecular orbital methods. XXIII. A polarization-type basis set for second-row elements, *J. Chem. Phys.* 77 (7) (1982) 3654, <http://dx.doi.org/10.1063/1.444267>.
- [38] J.-P. Blaudeau, M.P. McGrath, L.A. Curtiss, L. Radom, Extension of gaussian-2 (g2) theory to molecules containing third-row atoms k and ca, *J. Chem. Phys.* 107 (13) (1997) 5016, <http://dx.doi.org/10.1063/1.474865>.
- [39] A.D. McLean, G.S. Chandler, Contracted gaussian basis sets for molecular calculations. I. Second row atoms, z=11–18, *J. Chem. Phys.* 72 (10) (1980) 5639, <http://dx.doi.org/10.1063/1.438980>.
- [40] S. Boys, F. Bernardi, The calculation of small molecular interactions by the differences of separate total energies. some procedures with reduced errors, *Mol. Phys.* 19 (4) (1970) 553–566, <http://dx.doi.org/10.1080/00268977000101561>.

- [41] W.J. Stevens, W.H. Fink, Frozen fragment reduced variational space analysis of hydrogen bonding interactions. Application to the water dimer, *Chem. Phys. Lett.* 139 (1) (1987) 15–22, [http://dx.doi.org/10.1016/0009-2614\(87\)80143-4](http://dx.doi.org/10.1016/0009-2614(87)80143-4).
- [42] M.W. Schmidt, K.K. Baldridge, J.A. Boatz, S.T. Elbert, M.S. Gordon, J.H. Jensen, S. Koseki, N. Matsunaga, K.A. Nguyen, S. Su, T.L. Windus, M. Dupuis, J.A. Montgomery, General atomic and molecular electronic structure system, *J. Comput. Chem.* 14 (11) (1993) 1347–1363, <http://dx.doi.org/10.1002/jcc.540141112>.
- [43] M.S. Gordon, M.W. Schmidt, *Advances in electronic structure theory*, in: *Theory and Applications of Computational Chemistry*, Elsevier BV, 2005, pp. 1167–1189, <http://dx.doi.org/10.1016/b978-044451719-7/50084-6>.
- [44] K. Morokuma, Molecular orbital studies of hydrogen bonds. III. c(double bond) o[middle dot][middle dot][middle dot]h[single bond]o hydrogen bond in h2co [middle dot][middle dot][middle dot]h2o and h2co[middle dot][middle dot] [middle dot]2h2o, *J. Chem. Phys.* 55 (3) (1971) 1236, <http://dx.doi.org/10.1063/1.1676210>.
- [45] M.A. Wilson, D. Chandler, Molecular dynamics study of cyclohexane interconversion, *Chem. Phys.* 149 (1–2) (1990) 11–20, [http://dx.doi.org/10.1016/0301-0104\(90\)80127-j](http://dx.doi.org/10.1016/0301-0104(90)80127-j).
- [46] M. Squillacote, R.S. Sheridan, O.L. Chapman, F.A.L. Anet, Spectroscopic detection of the twist-boat conformation of cyclohexane. Direct measurement of the free energy difference between the chair and the twist-boat, *J. Am. Chem. Soc.* 97 (11) (1975) 3244–3246, <http://dx.doi.org/10.1021/ja00844a068>.
- [47] A.C.T. van Duin, S. Dasgupta, F. Lorant, W.A. Goddard, Reaxff: a reactive force field for hydrocarbons, *J. Phys. Chem. A* 105 (41) (2001) 9396–9409, <http://dx.doi.org/10.1021/jp004368u>.
- [48] M. Elstner, D. Porezag, G. Jungnickel, J. Elsner, M. Haugk, T. Frauenheim, S. Suhai, G. Seifert, Self-consistent-charge density-functional tight-binding method for simulations of complex materials properties, *Phys. Rev. B* 58 (1998) 7260–7268, <http://dx.doi.org/10.1103/PhysRevB.58.7260>.

Supplementary material - Pesticide interaction with environmentally important cations: A molecular dynamics and DFT study of metamidon and fenhexamid

Bastien Belzunces, Sophie Hoyau, Jérôme Cuny and Fabienne Bessac

Table S1: E_{comp} in kcal/mol and E_{tot} in a.u. at PBE/pw level of Meta- Na^+ . 80 : kinetic energy cutoff sets to 80 Ry. 140 : kinetic energy cutoff sets to 140 Ry. T : a Tuckerman poisson solver scheme was used. c : cubic box length in Å.

c (Å)	E_{tot} 80	E_{comp} 80	E_{comp} 140	E_{tot} T80	E_{comp} T80	E_{comp} T140
11	-165.535351	-65.41	-65.02	-165.439267	-47.40	-47.06
13	-165.509718	-55.62	-55.23	-165.430422	-41.94	-41.54
15	-165.493779	-51.13	-50.74	-165.430645	-43.05	-42.65
17	-165.486761	-48.60	-48.21	-165.433692	-43.13	-42.77
19	-165.478969	-47.04	-46.65	-165.433064	-43.15	-42.78
21	-165.473251	-46.03	-45.64	-165.432771	-43.18	-42.77
23	-165.469363	-45.36	-44.96	-165.433200	-43.20	-42.79
25	-165.465396	-44.86	-44.47	-165.432602	-43.18	-42.78
30	-165.458832	-44.14	-43.76	-165.432220	-43.18	-42.78

In all Fen-cation families, both axial and equatorial positions for R fragment are observed. In the case of Na^+ , both kinds of isomers are quasi degenerated with a slight preference for the axial one, as for Fen. In the contrary, with Ca^{2+} , the equatorial position is favored (except for the cyclo-CO-Cl family, see thereafter). This inversion is due to the different steric hindrance induced by the cations as demonstrated in supplementary material. To confirm this hypothesis, single point calculations on model systems (R group reduced to cation-CO-NH₂) have been performed. These models have been built from both lowest-energy CO-Phe isomers corresponding to an axial/equatorial pair. For Na^+ -Methylamidocyclohexane, the axial form is slightly lower in energy (0.11 kcal/mol at PBE/basis2 level), with Ca^{2+} , the equatorial isomer is 0.72 kcal/mol more stable than the axial one (see Table S2 in supplementary material). To be sure that the inversion is due to the nature of the cation not to the local geometry, each cation has been replaced by the other. The results confirm the larger Ca^{2+} -CO-NH₂ steric hindrance than CH₃.

Table S2: Methylamidocyclohexane and amidocyclohexane: $\Delta E = E_{eq} - E_{ax}$ in kcal/mol at different level of calculation: PBE/basis1, PBE/basis2 and PBE/pw (Kinetic energy cutoff sets to 80 Ry. A Tuckerman poisson solver scheme was used in a cubic box length of 15 Å). D2: dispersion correction used.

ΔE	PBE/basis1	PBE/basis2	PBE/pw	
				- D2
Amidocyclohexane				
-0.60	-1.17	-1.30	-0.70	
Methylamidocyclohexane				
1.25	1.01	1.00	0.95	
Na^+ -Methylamidocyclohexane				
		0.11		
		$\text{Na}^+ \rightarrow \text{Ca}^{2+}$		
		-0.50		
Ca^{2+} -Methylamidocyclohexane				
		-0.72		
		$\text{Ca}^{2+} \rightarrow \text{Na}^+$		
		0.25		

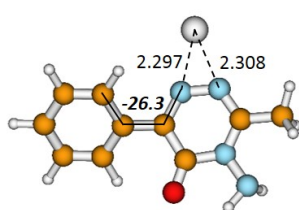
Table S3: Electronic affinity and ionization potential of Ca^{2+} cation and Fen08 conformer at HF/basis1//PBE/basis2, HF/basis2//PBE/basis2, PBE/basis1//PBE/basis2 and PBE/basis2//PBE/basis2 levels (in kcal/mol).

	$\text{EA}_{\text{Ca}^{2+}}$	$\text{IP}_{\text{Fen}(08)}$
HF/basis1//PBE/basis2	+260.8	+188.7
HF/basis2//PBE/basis2	+260.9	+191.1
PBE/basis1//PBE/basis2	+275.3	+173.6
PBE/basis2//PBE/basis2	+276.2	+180.2

Table S4: $E_{\text{comp}}^{\text{uncorr}}$, E_{prep} and $E_{\text{int}}^{\text{uncorr}}$ for $\text{Fen-Ca}^{2+}(1)_{\text{eq}}$ and $\text{Fen-Ca}^{2+}(4)_{\text{eq}}$ complexes at PBE/basis1, PBE/basis2, HF/basis1//PBE/basis1 and HF/basis2//PBE/basis2 levels of theory. Relative $E_{\text{comp}}^{\text{uncorr}}$ and $E_{\text{int}}^{\text{uncorr}}$ are given in italics. All energies are given in kcal/mol.

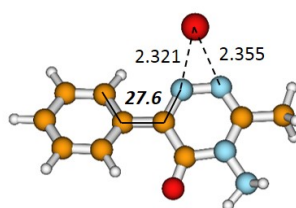
Fen- $\text{Ca}^{2+}(\text{a})_{\text{eq}}$	PBE/basis1		PBE/basis2		HF/basis1//PBE/basis1		HF/basis2//PBE/basis2	
a	1	4	1	4	1	4	1	4
$E_{\text{comp}}^{\text{uncorr}}$	-124.8	-125.6	-141.5	-141.2	-113.7	-114.2	-122.6	-119.5
	<i>0.8</i>	<i>0.0</i>	<i>0.0</i>	<i>0.3</i>	<i>0.5</i>	<i>0.0</i>	<i>0.0</i>	<i>3.1</i>
E_{prep}	12.8	17.8	12.1	17.2	12.8	18.6	13.0	21.3
$E_{\text{int}}^{\text{uncorr}}$	-137.6	-143.6	-153.6	-158.4	-126.5	-132.8	-135.6	-140.8
	<i>6.0</i>	<i>0.0</i>	<i>4.8</i>	<i>0.0</i>	<i>6.3</i>	<i>0.0</i>	<i>5.2</i>	<i>0.0</i>

Meta- Na^+ (2)



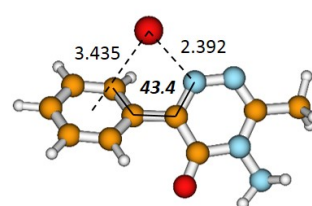
0.4 + 1.7
0.3 + 1.2

Meta- Ca^{2+} (3)



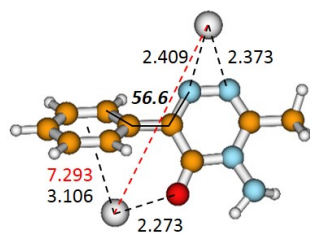
6.4 + 4.3
4.8 + 4.4

Meta- Ca^{2+} (5)



7.8 + 8.0
9.7 + 6.8

Meta- $(\text{Na}^+)_2$ (2)



0.1 + 6.4
0.0 + 4.4

Figure S1: Additional isomers of metamitron with one Na^+ , one Ca^{2+} and two Na^+ . Relative and preparation energies are displayed in kcal/mol at the PBE/basis1 and PBE/basis2 (in italics) levels.

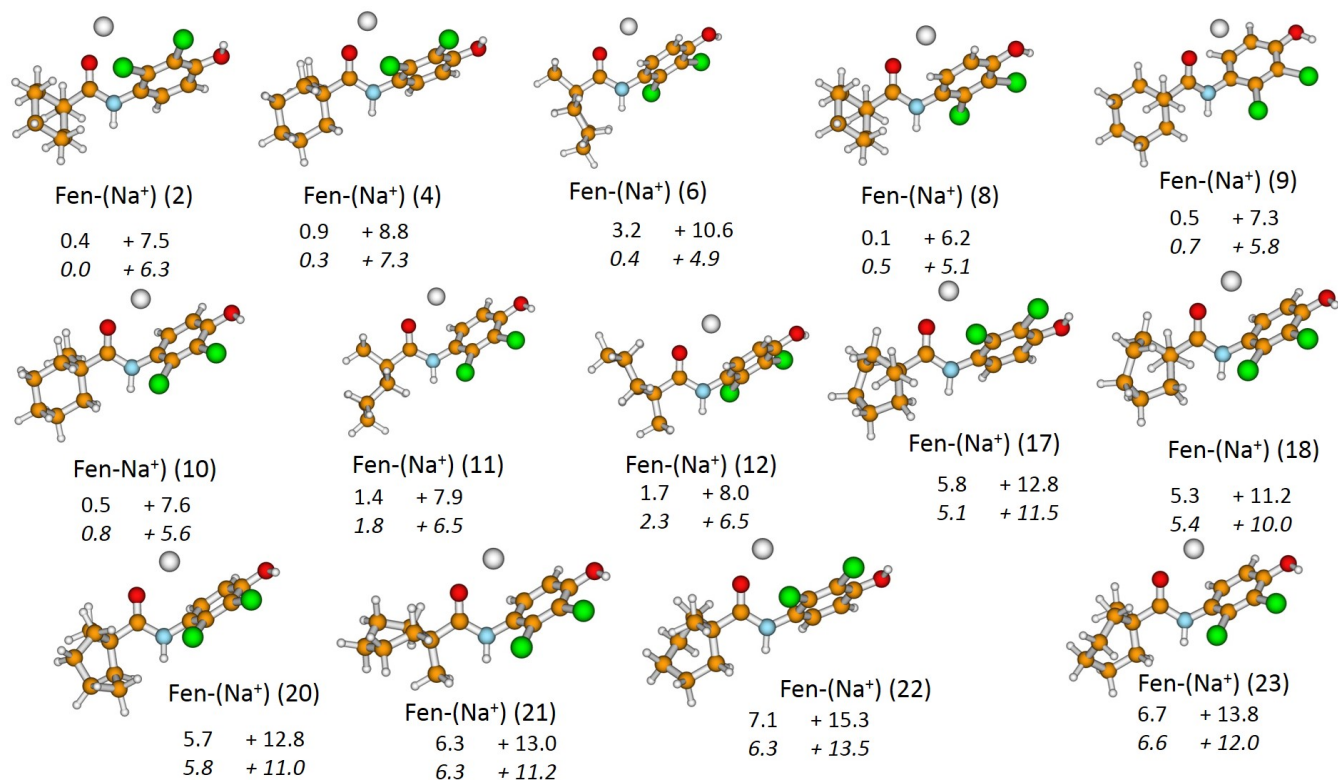


Figure S2: Additional isomers of fenhexamid with one Na^+ . Relative and preparation energies are displayed in kcal/mol at the PBE/basis1 and PBE/basis2 (in italics) levels.

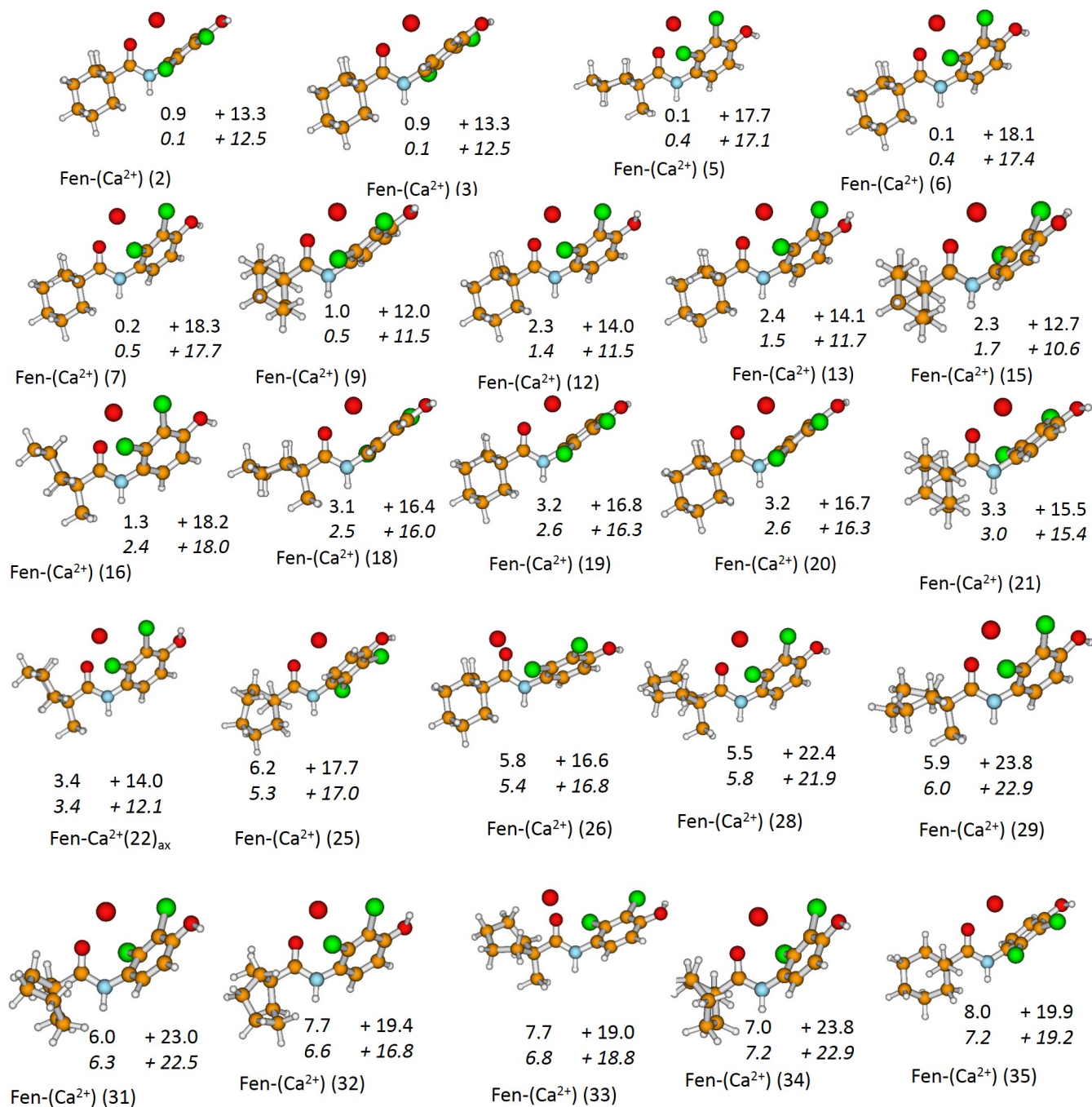


Figure S3: Additional isomers of fenhexamid with one Ca^{2+} . Relative and preparation energies are displayed in kcal/mol at the PBE/basis1 and PBE/basis2 (in italics) levels.

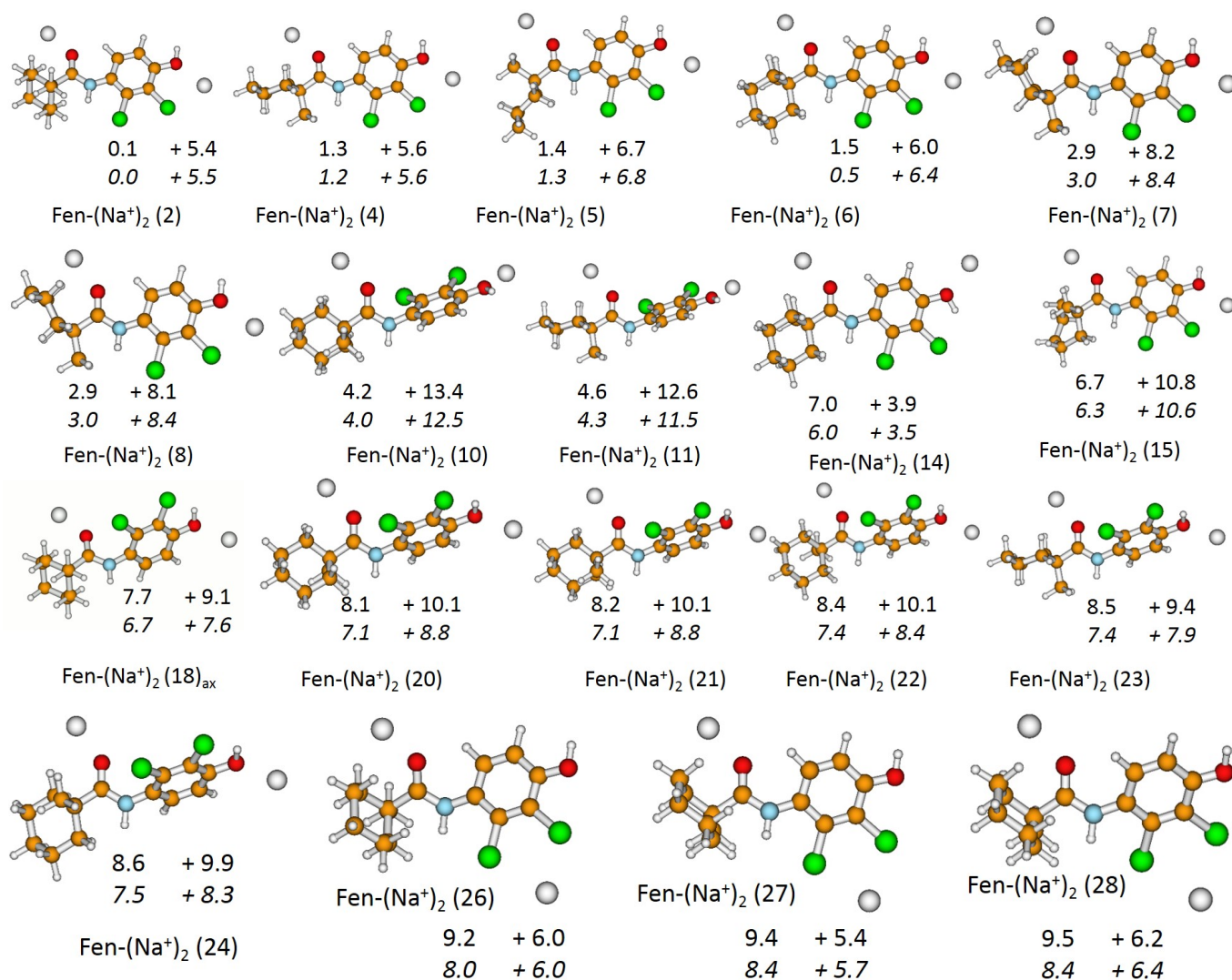


Figure S4: Additional isomers of fenhexamid with two Na⁺. Relative and preparation energies are displayed in kcal/mol at the PBE/basis1 and PBE/basis2 (in italics) levels.

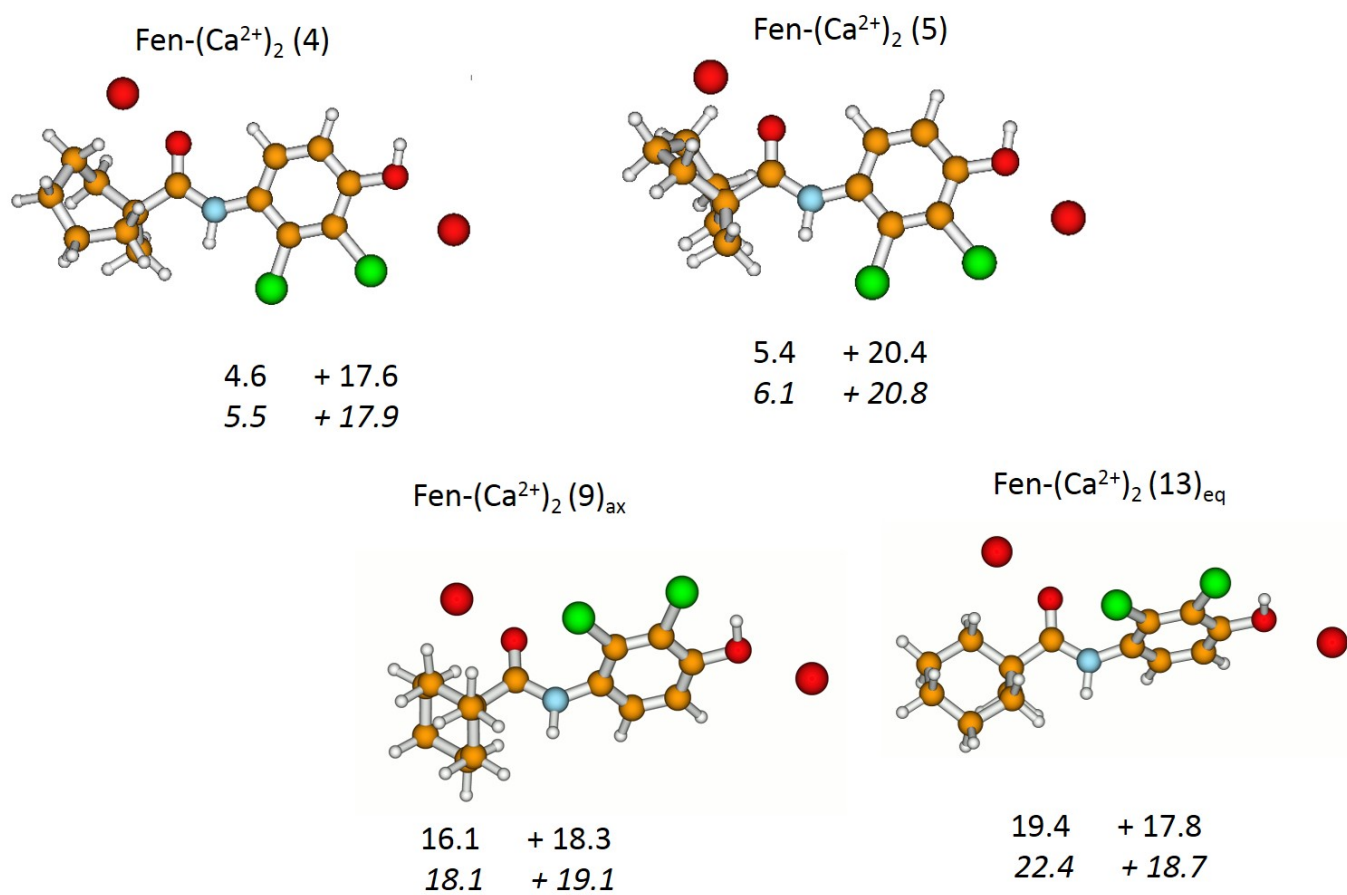



Figure S5: Additional isomers of fenhexamid with two Ca²⁺. Relative and preparation energies are displayed in kcal/mol at the PBE/basis1 and PBE/basis2 (in italics) levels.

Chapter VI

Adsorption on a Ca-Montmorillonite surface

“It is by logic that we prove, but by intuition that we discover.”

Jules Henri Poincaré

 In the foregoing chapter, CPMD simulations have been employed in NVE ensembles by means of DFT/PBE to explore as widely as possible the conformations of metamitron and fenhexamid on one hand, and their most probable isomers in presence of one or two Na^+ or Ca^{2+} cations on the other hand. These results showed, in agreement with the previous paper on atrazine complexes with the same cations, that Ca^{2+} in interaction with metamitron or fenhexamid presents a complexation energy around -140 kcal/mol, much stronger than complexation with Na^+ . For this reason, as for atrazine, a Ca-montmorillonite surface has been chosen as a model to study metamitron and fenhexamid interaction with the soil mineral matter. As isomers of the pesticides adsorbed on the modeled Ca-montmorillonite surface will be explored, periodic DFT is used with a D2 Grimme dispersion correction (PBE-D2) [231], in a planewave basis (pw) with an energy cutoff of 80 Ry as discussed in the previous chapter.

VI.A Starting structures and CPMD parameters

This section presents the starting structures that have been chosen for the exploration of metamitron and fenhexamid isomers put in adsorption on the Ca-montmorillonite model, noted Mont in the following.

In the following, we will use indexes to name three typical positions of the pesticides above the Ca-montmorillonite surface, represented on Figure VI.1, regarding the long or short side of the molecule, and the orientation of the aromatic cycles.

When both cycles (triazine and phenyl) of metamitron, or the phenyl of fenhexamid are in a parallel orientation with the surface, isomers are indexed “*para*”. When these cycles are orthogonal to Mont, they are in “*ortho – long*” position, as pesticides interact with the surface on the long side. The third index “*ortho – short*” designates isomers where the pesticide is nearly orthogonal to the surface and exposes the short side.

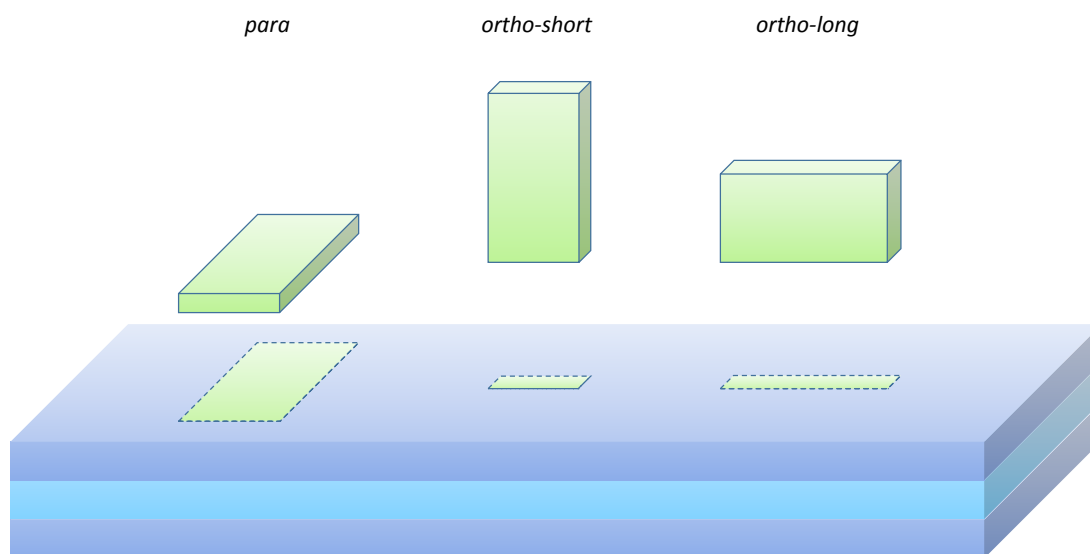


Figure VI.1: Three schematic orientations of the pesticides (green parallelepipeds) above the surface (layered blue).

Two and three CPMD trajectories have been run for metamitron and fenhexamid respectively:

- **Metamitron - Ca-montmorillonite**

According to the study conducted in the previous chapter on metamitron-cation(s) complexes, the most stable isomers that have been found with one or two Ca^{2+}

presented the same two lowest binding sites: between the phenyl π system and the carbonyl oxygen (CO-Phe), and on the two consecutive nitrogens of the triazine cycle (N-N). However, considering the small size of the molecule, and the distance between two consecutive calcium cations in the optimized Mont: $d_{Ca-Ca}(\text{Mont}(\text{opt})) = 10.341$ Å at the PBE-D2/pw level, it is impossible to adsorb metamitron on the surface and get the double N-N & CO-Phe complexation with both cations as in gas phase, where $d_{Ca-Ca} = 7.249$ Å for Meta-(Ca²⁺)₂(1) at PBE/basis2.

For this reason, two MD trajectories have been simulated for Meta over Mont:

- a complexation on CO-Phe ;
- a complexation on N-N.

As starting structures, the molecule has been adsorbed in the geometry of the lowest-energy complex with two cations Meta-(Ca²⁺)₂ (1), and has been put in interaction above one of the calcium cations on the surface. Figure VI.2 displays the two starting geometries : Meta-Mont(CO-Phe) and Meta-Mont(N-N). The binding sites distances are longer than in Meta-(Ca²⁺)₂ (1) in gas phase to minimize repulsion between the molecule and the surface.

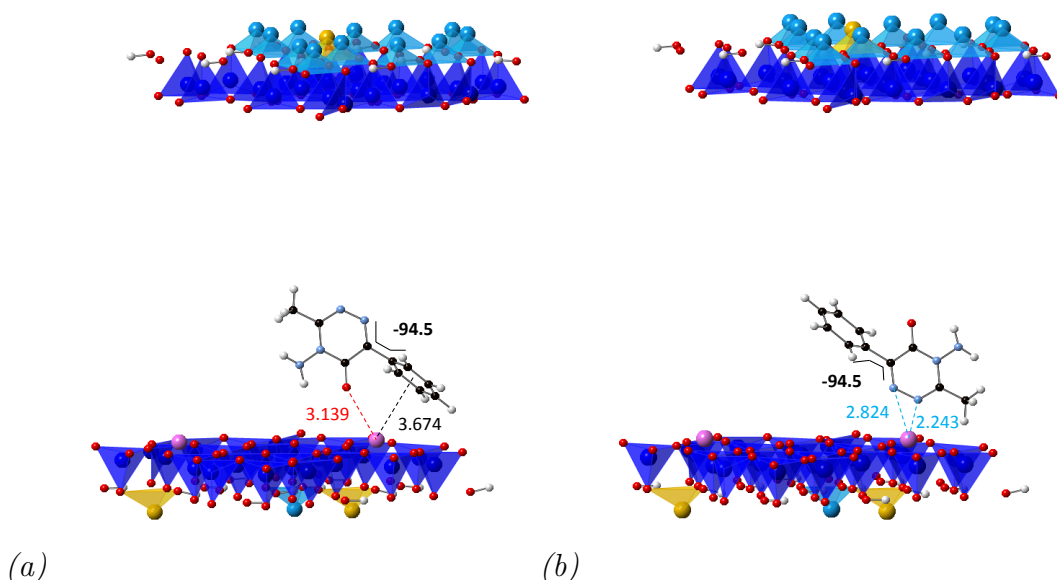


Figure VI.2: Starting structures of (a) Meta-Mont(CO-Phe) and (b) Meta-Mont(N-N). Distances are displayed in Å and dihedrals (bold) in degrees.

- **Fenhexamid - Ca-Montmorillonite**

The lowest families of isomers obtained for Fen with:

- one Ca^{2+} : **CO-Phe_{eq}** ;
- two Ca^{2+} : **cyclo-CO & Cl-OH_{ax}**.

In addition all Fen- $(\text{Ca}^{2+})_2$ isomers with relative energies ≤ 7 kcal/mol (PBE/basis2) belong to the **cyclo-CO & Cl-OH** family. Three starting structures have been considered for fenhexamid and are presented in Figure VI.3:

The first one, Fen-Mont(CO-Phe)_{para,eq}, is Fen in the geometry of the lowest isomer with one calcium cation, Fen- $\text{Ca}^{2+}(1)_{eq}$, presenting a CO-Phe adsorption over one of the cations, in a parallel orientation on Mont (Figure VI.3 (a)).

The second starting structure, Fen-Mont(Cl-OH)_{para,ax}, has the molecule in the geometry of Fen- $(\text{Ca}^{2+})_2(1)_{ax}$ (**cyclo-CO & Cl-OH family**), parallel to the surface with a starting interaction on the Cl-OH binding site. Moreover, the molecule is oriented towards the second cation to favour a double complexation during the MD trajectory (Figure VI.3 (b)). Unlike metamitron, here a double complexation is possible as the Ca-Ca distance obtained in Fen- $(\text{Ca}^{2+})_2$ in the gas phase is of 10.705 Å (PBE/basis2) comparable with 10.341 Å for the d_{Ca-Ca} in Mont at PBE-D2/pw.

Then, a third trajectory has been run: Fen-Mont(Cl-OH)_{ortho-short,ax}, where the same molecular structure and binding site than in Fen-Mont(Cl-OH)_{para,ax} have been chosen but with the pesticide in *ortho – short* orientation (Figure VI.3 (c)).

The second lowest family of complexation in Fen- (Ca^{2+}) , **CO-Cl-Cl**, has not been selected as a starting structure. Indeed it is expected to be obtained during the MD trajectory of Fen-Mont(CO-Phe)_{para,eq}, as both structures are quite similar.

These three starting structures cover three main features to explore: the orientation of the molecule (*para* or *ortho*), the positions of the chemical groups around the cyclohexyl (*ax* or *eq*), and the involvement of different complexation sites explored in the gas phase study (CO-Phe and cyclo-CO & Cl-OH), with the expectation of exploring a maximum of isomers and binding sites.

- **CPMD parameters**

A CPMD simulation of 12 ps (120,000 steps of 0.1 fs equivalent to 4.0 a.u) has been run on each of the starting structures: Meta-Mont(CO-Phe), Meta-Mont(N-N), Fen-Mont(CO-Phe)_{para,eq}, Fen-Mont(Cl-OH)_{para,ax} and Fen(Cl-OH)_{ortho-short,ax} in the NVE ensemble at respective average temperatures of 888 K, 932 K, 897 K, 873 K and 962 K to bring a lot of energy in the system and maximize the chances

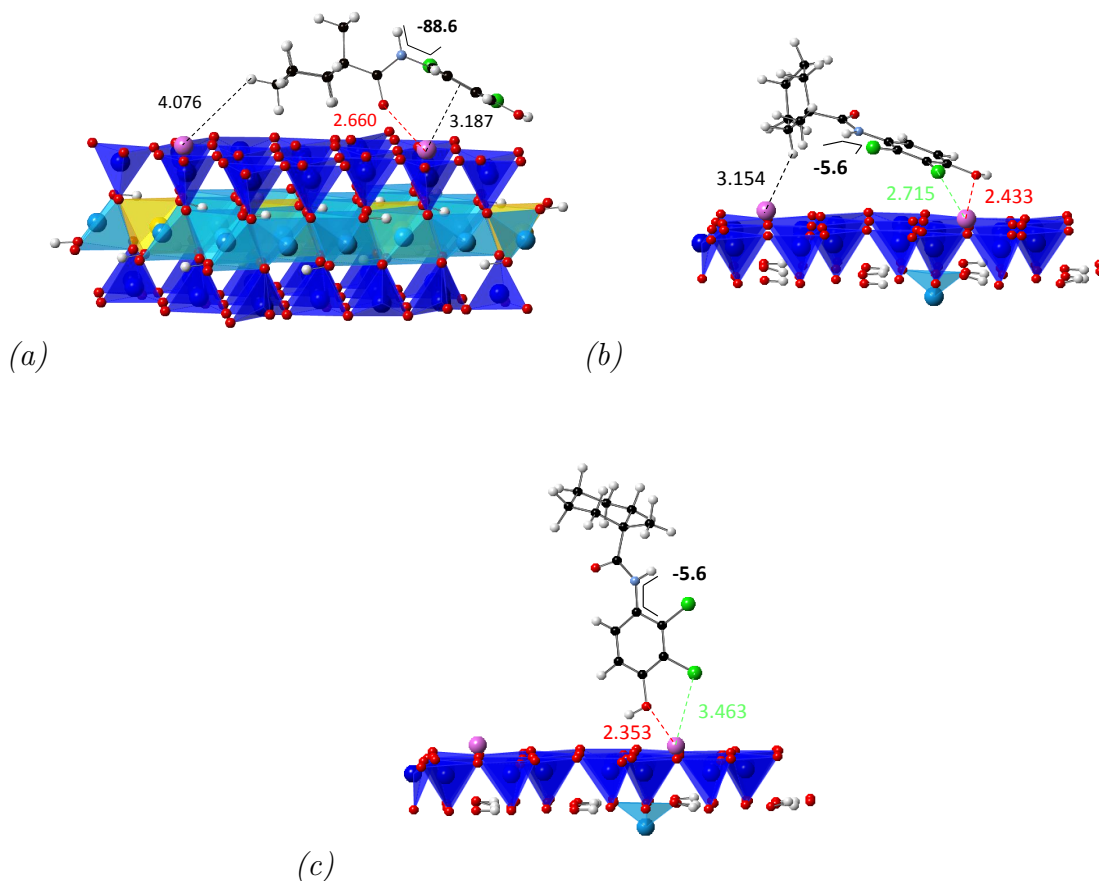


Figure VI.3: Starting structures of (a) Fen-Mont(CO-Phe)_{para,eq}, (b) Fen-Mont(Cl-OH)_{para,ax} and (c) Fen-Mont(Cl-OH)_{ortho-short,ax}. Distances are displayed in Å and dihedrals (bold) in degrees.

to widely explore the PES. A fictitious electronic mass $\mu = 350.0$ a.u. has been used here, and the D2 Grimme’s dispersion correction has been added to the PBE functional (PBE-D2) as in the atrazine-Mont (Atra-Mont) study (Chapter IV [136]). All other CPMD parameters are the same as in the gas phase study.

The next sections present the results of the PES exploration and the optimized structures at PBE-D2/pw level, as well as the related energies, first for metamitron and then for fenhexamid.

From now on, to simplify the discussions, ϕ_{gas} and ϕ_{solid}^{dry} will be used as notations to replace the terms “gas phase” and “dry solid phase”. The numbering of atoms in Meta and Fen will be the same as in the paper of the previous chapter.

VI.B Metamitron - Ca-montmorillonite

VI. B.1 PES exploration

- **Meta-Mont(CO-Phe)**

As the trajectory starts, the distance between the carbonyl oxygen and the calcium cation shortens during the very first steps. The molecule stays bound to Ca^{2+} through CO oxygen along the whole dynamics with an oxygen-calcium distance always $\leq 3.00 \text{ \AA}$. Nevertheless, Phe is not always involved in the interaction with the cation and can rotate to get back to a parallel orientation with the triazine cycle and restore total delocalization. Metamitron can adopt a *para* orientation towards the surface with a conservation of the CO oxygen interaction with the cation. Finally, the bidentate interaction CO-NH₂ that has been found in ϕ_{gas} (Meta-Ca²⁺(6)) is also explored.

- **Meta-Mont(N-N)**

The starting structure presented a totally broken delocalization ($\text{C1-C2-C3-N4} \mid = -94.5^\circ$), but along the trajectory, as in Meta-Mont(CO-Phe), it is regularly recovered when Phe rotates to be coplanar with the triazine cycle, leading to both *para* and *ortho* isomers. During the whole MD simulation, metamitron stays adsorbed on the N-N site, sometimes only on one of the nitrogens.

As metamitron can never be in a double complexation over the Mont surface ($d_{\text{Ca}-\text{Ca}} \approx 7 - 8 \text{ \AA}$ in Meta-(Ca²⁺)₂/ ϕ_{gas}), all the Meta-Mont optimized structures will be compared to the complexes with one cation: Meta-Ca²⁺ isomers.

VI. B.2 Optimized structures

According to the trajectories we have just described, starting with N-N and CO-Phe complexation sites, 9 snapshots have been extracted and optimized from these simulations. The corresponding isomers, noted Meta-Mont, are displayed on Figure VI.4 with respective binding sites, geometrical parameters and relative energies. The family name and molecule orientation (*para*, *ortho - short* and *ortho - long*) are also precised.

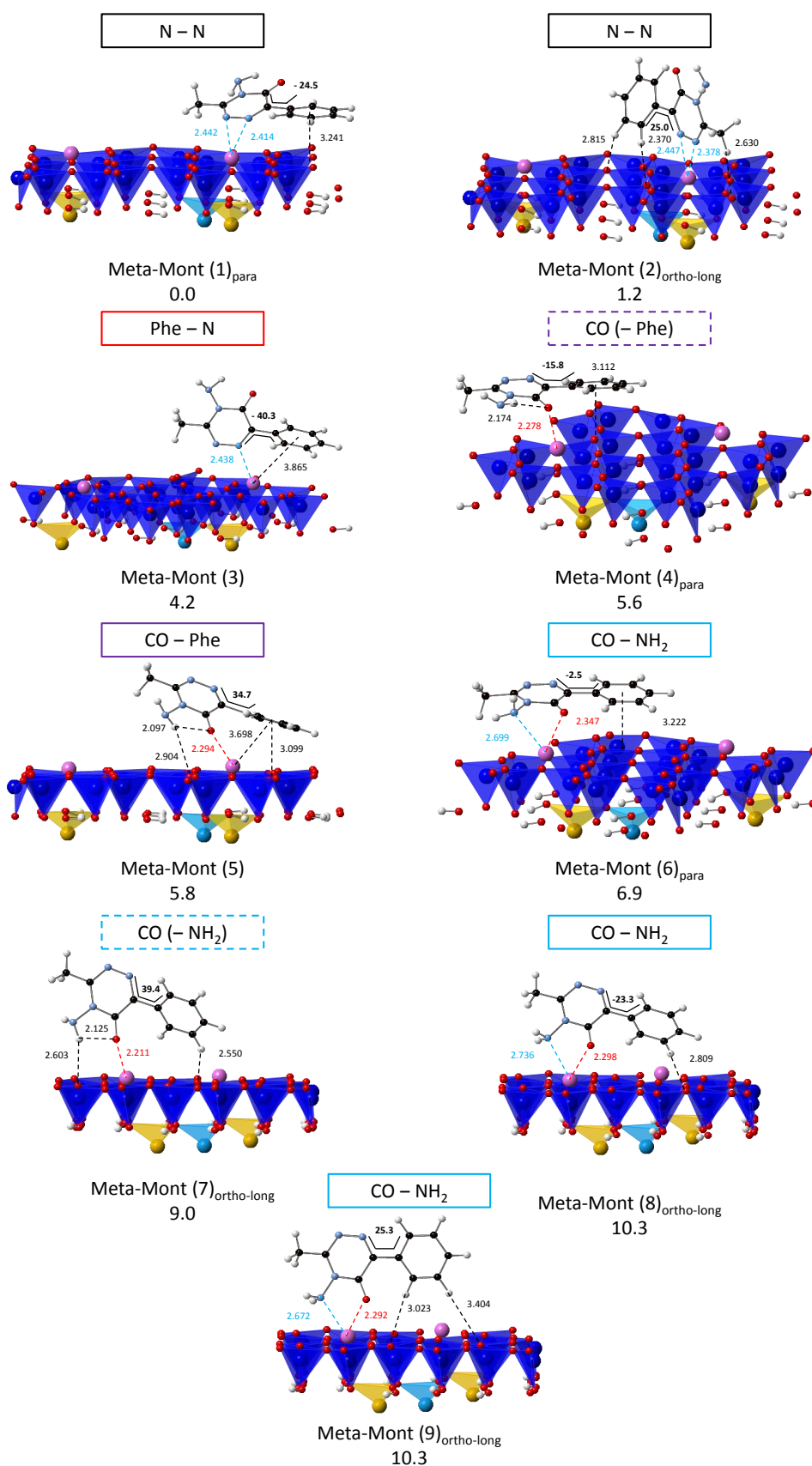


Figure VI.4: Meta-Mont isomers displayed with complexation families and relative energies (kcal/mol). Distances (black), cation distances to the molecule oxygens (red) and nitrogens (blue) are in Å. C1-C2-C3-N4] dihedrals (bold) are in degrees.

Family energetic order

Four families of bidentate complexations have been obtained. All involve only one cation. These families are similar to those obtained in ϕ_{gas} : they do not overlap, however the relative energetic order is not the same as Meta- Ca^{2+} isomers in ϕ_{gas} ($\text{CO-Phe} < \text{N-N} < \text{Phe-N} < \text{CO-NH}_2$). However, the order is consistent with Meta- Na^+ in ϕ_{gas} . Meta-Mont isomers have relative energies $0 \leq \Delta E < 11$ kcal/mol and present the following complexation sites:

- **N-N**: the lowest-energy family, with adsorption on the consecutive nitrogens of the triazine cycle ($\Delta E = 0.0$ and 1.2 kcal/mol), with Ca^{2+} coplanar with the triazine cycle (Meta-Mont(2)_{ortho-long}), as in ϕ_{gas} , or out of plan (Meta-Mont(1)_{para}).
- **Phe-N**: between the π system of the phenyl and the closest nitrogen atom (Meta-Mont(3) ; $\Delta E = 4.2$ kcal/mol) ;
- **CO-Phe**: between the carbonyl oxygen and the π electrons of the phenyl (Meta-Mont(5) ; $\Delta E = 5.8$ kcal/mol) ;
- **CO-NH₂**: between the carbonyl oxygen and the amine nitrogen (Meta-Mont(6)_{para}, (8)_{ortho} and (9)_{ortho} ; $\Delta E = 6.9$ and 10.3 kcal/mol).

Monodentate complexes have been found as well: Meta-Mont(4)_{para} ($\Delta E = 5.6$ kcal/mol) noted **CO(-Phe)** as the geometry has a similar form as Meta-Mont(5)(**CO-Phe**) but with Meta parallel to the surface and with a more important π delocalization. Similarly, the monodentate complex Meta-Mont(7)_{ortho}(**CO(-NH₂)**) with $\Delta E = 9.0$ kcal/mol, is derived from the **CO-NH₂** family.

In the **N-N** and **CO-NH₂** families, *para* and *ortho-long* orientations have been obtained. The *para* isomer is preferred in both families due to a larger dispersion interaction with the surface.

However, as families of complexation do not overlap, *ortho-long* isomers can be more stabilized than *para*: Meta-Mont(2)_{ortho-long}(**N-N**) is lower in energy than Meta-Mont(4)_{para}(**CO(-Phe)**). Thus the complexation site is predominant to explain the energetic order.

Isomer geometry compared to ϕ_{gas}

The distances between the binding sites and the calcium cation increase in all Meta-Mont structures by $0.1 - 0.3$ Å compared to Meta- $\text{Ca}^{2+}/\phi_{gas}$. The Ca^{2+} -Phe distance in the **CO-Phe** family is particularly elongated (≈ 1.3 Å) in Meta-Mont(5) compared to Meta- Ca^{2+} (1), due to the sharing of the π system interaction of Phe between the calcium

cation and the surface. The global increasing of the molecule-cation distances in all isomers is due to repulsion and steric hindrance induced by the surface, and consequently to a weaker interaction between the pesticide and Ca^{2+} . This point will be discussed below with the adsorption energies.

Table VI.1 displays intramolecular distances of ϕ_{gas} and Meta-Mont complexes. In ϕ_{gas} , among Meta- Ca^{2+} isomers, bond lengths can vary with amplitudes of 0.02 Å for d_{C3-N4} and d_{N5-C6} , 0.05 Å for d_{N4-N5} , up to 0.08 – 0.09 Å in d_{N-NH_2} and d_{C-O} . The comparison of these intramolecular distances in each complex with Meta shows a deviation of $\pm 0.02 - 0.04$ Å, with a higher elongation for d_{C-O} when it is involved in the binding site: longer of ≈ 0.06 and ≈ 0.05 Å in Meta- $\text{Ca}^{2+}(2)(\text{CO-Phe})$ and $(6)(\text{CO-NH}_2)$ respectively.

Isomers	Complexation	d_{C3-N4}	d_{N4-N5}	d_{N5-C6}	d_{N-NH_2}	d_{C-O}
PBE/basis2						
Meta	-	1.329	1.352	1.322	1.410	1.238
Meta- $\text{Ca}^{2+}(1)$	CO-Phe	1.326	1.340	1.329	1.381	1.298
Meta- $\text{Ca}^{2+}(2)$	N-N	1.333	1.376	1.332	1.381	1.214
Meta- $\text{Ca}^{2+}(4)$	Phe-N	1.341	1.341	1.337	1.369	1.220
Meta- $\text{Ca}^{2+}(6)$	CO-NH₂	1.350	1.328	1.321	1.452	1.293
PBE-D2/pw						
Meta-Mont(1) _{para}	N-N	1.326	1.358	1.323	1.399	1.229
Meta-Mont(2) _{ortho-long}	N-N	1.326	1.357	1.320	1.397	1.228
Meta-Mont(3)	Phe-N	1.328	1.350	1.321	1.399	1.231
Meta-Mont(4) _{para}	CO(-Phe)	1.337	1.338	1.322	1.393	1.274
Meta-Mont(5)	CO-Phe	1.330	1.348	1.321	1.400	1.263
Meta-Mont(6) _{para}	CO-NH₂	1.332	1.345	1.318	1.425	1.255
Meta-Mont(7) _{ortho-long}	CO(-NH₂)	1.331	1.347	1.321	1.402	1.262
Meta-Mont(8) _{ortho-long}	CO-NH₂	1.327	1.357	1.314	1.426	1.245
Meta-Mont(9) _{ortho-long}	CO-NH₂	1.327	1.358	1.313	1.422	1.246

Table VI.1: Metamitron intramolecular distances (Å) in ϕ_{gas} (PBE/basis2) and ϕ_{solid}^{dry} (PBE-D2/pw) complexes.

In ϕ_{solid}^{dry} , the same tendency as in ϕ_{gas} can be observed: when bonds are involved in the complexation, they undergo elongations. However this tendency is weaker: d_{N-NH_2} and d_{C-O} undergo the widest variations: ≈ 0.04 Å, while other bonds show variations ≤ 0.02 Å. The maximum elongation being 0.03 Å for d_{C-O} in Meta-Mont(4)_{para}(**CO(-Phe)**).

Compared to the structure of isolated Meta, bond length deviations in ϕ_{solid}^{dry} are lower than in ϕ_{gas} (see discussion on $E_{prep}(Pest)$ in the following). These lower modifications suggest that the interaction with the cation is not as strong as in ϕ_{gas} . This point will be discussed in the following, regarding the adsorption energies (E_{ads}).

Table VI.2: Meta-Mont distances or average distances (\AA) in the Ca-montmorillonite surface.

Isomers	Complexation	d_{Ca1-O_h}	d_{Ca2-O_h}	d_{Ca1-O_h}	d_{Ca2-O_h}	$d_{(Al-O_a)}$	$d_{(Al-O_h)}$	$d_{(Mg-O_a)}$	$d_{(Mg-O_h)}$	$d_{(H-O_h)}$	$d_{(Si-O_a)}$	$d_{(Si-O_h)}$
Mont(opt)	-	0.252	0.249	2.360	2.358	1.973	1.940	2.084	2.055	0.978	1.638	1.629
Meta-Mont(1) _{para}	N-N	0.525	0.236	2.626	2.349	1.971	1.939	2.083	2.056	0.978	1.639	1.629
Meta-Mont(2) _{ortho-long}	N-N	0.515	0.228	2.625	2.347	1.971	1.939	2.083	2.057	0.978	1.639	1.629
Meta-Mont(3)	Phe-N	0.524	0.223	2.624	2.347	1.971	1.939	2.084	2.057	0.978	1.639	1.629
Meta-Mont(4) _{para}	CO(-Phe)	0.471	0.229	2.575	2.370	1.971	1.939	2.084	2.054	0.978	1.639	1.629
Meta-Mont(5)	CO-Phe	0.561	0.232	2.663	2.342	1.971	1.939	2.083	2.056	0.978	1.639	1.629
Meta-Mont(6) _{para}	CO-NH ₂	0.544	0.227	2.656	2.352	1.971	1.939	2.084	2.056	0.978	1.639	1.629
Meta-Mont(7) _{ortho-long}	CO(-NH ₂)	0.442	0.238	2.549	2.353	1.971	1.939	2.084	2.057	0.978	1.639	1.629
Meta-Mont(8) _{ortho-long}	CO-NH ₂	0.527	0.231	2.633	2.355	1.972	1.939	2.084	2.057	0.978	1.639	1.629
Meta-Mont(9) _{ortho-long}	CO-NH ₂	0.526	0.235	2.634	2.353	1.971	1.939	2.084	2.057	0.978	1.639	1.629

Table VI.3: Relative (ΔE), adsorption (E_{ads}), interaction (E_{int}) and preparation (E_{prep} (Pest), E_{prep} (Mont) and E_{prep} (total)) are the metanition, the Ca-montmorillonite and the total preparation energies respectively. Percentages in the preparation energies are the contributions in E_{prep} (total). E_{disp}^{ads} and E_{disp}^{int} are dispersion contributions to the adsorption and interaction energies. All energies are displayed in kcal/mol.

Isomers	Complexation	ΔE	E_{ads}	E_{disp}^{ads}	E_{int}	E_{disp}^{int}	E_{prep} (Pest)	E_{prep} (Mont)	E_{prep} (total)
Meta-Mont(1) _{para}	N-N	0.0	-44.20	-18.30	-49.93	-17.92	+0.94 (16%)	+4.79 (84%)	+5.73
Meta-Mont(2) _{ortho-long}	N-N	1.2	-43.03	-11.80	-48.36	-11.48	+1.04 (20%)	+4.29 (80%)	+5.33
Meta-Mont(3)	Phe-N	4.2	-40.03	-16.16	-46.05	-15.97	+1.61 (27%)	+4.40 (73%)	+6.01
Meta-Mont(4) _{para}	CO(-Phe)	5.6	-38.64	-21.79	-46.37	-21.55	+3.69 (48%)	+4.05 (52%)	+7.74
Meta-Mont(5)	CO-Phe	5.8	-38.36	-17.20	-45.79	-16.76	+2.17 (29%)	+5.26 (71%)	+7.42
Meta-Mont(6) _{para}	CO-NH ₂	6.9	-37.32	-20.95	-52.04	-20.61	+9.48 (64%)	+5.25 (36%)	+14.73
Meta-Mont(7) _{ortho-long}	CO(-NH ₂)	9.0	-35.17	-11.28	-40.56	-10.96	+2.67 (50%)	+2.71 (50%)	+5.38
Meta-Mont(8) _{ortho-long}	CO-NH ₂	10.3	-33.91	-14.28	-49.28	-13.91	+10.77 (70%)	+4.60 (30%)	+15.37
Meta-Mont(9) _{ortho-long}	CO-NH ₂	10.3	-33.90	-10.78	-48.96	-10.27	+10.40 (69%)	+4.65 (31%)	+15.06

Cation distances to the basal (O_b) and hydroxyl (O_h) oxygens of the surface in all isomers, and montmorillonite inner distances for the lowest isomers of each family are displayed in Table VI.2. The comparison between Meta-Mont isomers and Mont(opt) show that all internal average distances stay relatively unchanged by the adsorption of the pesticide (a maximum deviation of $\approx 2 \times 10^{-3}$ Å is reached for $d_{\langle Al-O_a \rangle}$ and $d_{\langle Mg-O_h \rangle}$), regardless the site of complexation. On Ca2 (the non-complexed cation), $d_{\langle Ca2-O_b \rangle}$ and $d_{\langle Ca2-O_h \rangle}$ are shortened by only 0.01 – 0.03 Å in all isomers (the only exception being $d_{\langle Ca2-O_h \rangle}$ in Meta-Mont(4)_{para}, elongated by ≈ 0.01 Å). However, strong modifications can be seen for the complexed calcium cation (Ca1) distances to the surface: $d_{\langle Ca1-O_b \rangle}$ and $d_{\langle Ca1-O_h \rangle}$ simultaneously increase by ≈ 0.2 Å for monodentate and by ≈ 0.3 Å for bidentate sites of complexation.

Adsorption, interaction and preparation energies

Table VI.3 presents adsorption, interaction, preparation and dispersion energies of Meta-Mont isomers. The adsorption energy is calculated as: $E_{ads} = E_{int} + E_{prep}(\text{total})$. Thus, the adsorption is a compromise between the interaction and the preparation energies.

E_{ads} goes from –44.2 kcal/mol for the most favorable isomer (**N-N**) to –33.9 for the highest (**CO-NH₂**), which are very low in absolute value compared to the complexation energies of approximately –140 kcal/mol in Meta-Ca²⁺/ ϕ_{gas} isomers. With favorable dispersion interactions between the pesticide and the surface ($-21.8 \leq E_{disp}^{ads} \approx E_{disp}^{int} \leq -10.3$ kcal/mol), the adsorption energy would have been expected to be stronger in ϕ_{solid}^{dry} than in ϕ_{gas} . However, an opposite behavior is observed, it suggests that the interaction between the cation and the pesticide is lower than in ϕ_{gas} , and that the Ca²⁺ cation might have a charge lower than 2+. Furthermore, E_{ads} of Meta-Mont isomers has the same order of magnitude than the complexation energies of Meta-Na⁺ isomers in ϕ_{gas} (≈ -40 kcal/mol), which agrees with this hypothesis.

The interaction energy E_{int} is between –52.0 kcal/mol (Meta-Mont(6)_{para}(**CO-NH₂**)) and –40.6 kcal/mol. Meta-Mont(6)_{para}(**CO-NH₂**) has thus the most favorable interaction but also one of the strongest E_{prep} (+14.7 kcal/mol) which does not produce the most favorable adsorption energy (–37.3 kcal/mol).

Meta-Mont(1)_{para}(**N-N**), has the lowest E_{ads} as E_{int} is one of the strongest (–49.9 kcal/mol), and $E_{prep}(\text{total})$ is one of the weakest (+5.7 kcal/mol). The associated preparation of the pesticide is the lowest in the series: $E_{prep}(\text{pest}) \approx 0.9$ kcal/mol.

In all isomers, the total preparation energy is between +5.3 (**N-N**) and 15.4 kcal/mol (**CO-NH₂**). $E_{prep}(\text{Mont})$ is always $\approx 4-5$ kcal/mol except in Meta-Mont(7)_{ortho-long}(**CO-NH₂**): $E_{prep}(\text{Mont}) = +2.7$ kcal/mol, which is directly related to the lowest elongations

of the d_{Ca1-O_b} and d_{Ca1-O_h} distances due to the monodentate type of pesticide interaction with the cation (Table VI.2).

The preparation energy of the pesticide goes from +0.9 (**N-N**) to +10.8 kcal/mol (**CO-NH₂**) and is the contribution with the largest variation in $E_{prep}(\text{total})$ from an isomer to another. For a given family of complexation, $E_{prep}(\text{Pest})$ is always lower in Meta-Mont isomers than in ϕ_{gas} . For example, in **CO-Phe**, the C1-C2-C3-N4] dihedral is lower in Meta-Mont(5) (34.7°) than in Meta-Ca²⁺(1) (-96.5°), reducing the preparation energy to +2.2 kcal/mol instead of +13.3 kcal/mol. In isomers (1-5) $E_{prep}(\text{Pest})$ is always lower than $E_{prep}(\text{Mont})$, this tendency is reversed for isomers (6), (8) and (9).

In atrazine-Ca-montmorillonite isomers: PARA1, PARA2, PARA3 and ORTHO (Chapter IV [136]), the total preparation energies (the sum of the $\Delta E_{def}(\text{Atra})$ and $\Delta E_{def}(\text{Surf})$ terms) are lower in comparison: between +1.3 and +3.8 kcal/mol, with always $\Delta E_{def}(\text{Atra}) > \Delta E_{def}(\text{Surf})$. For these systems, the interaction energies are weaker ($-31.0 \leq \Delta E_{int} \leq -16.3$ kcal/mol) than in Meta-Mont. As we saw in the definition of E_{ads} , the more the E_{int} absolute value is high, the more the two entities in interaction may undergo strong deformations, and thus high E_{prep} , while preserving a favorable adsorption energy.

The dispersion contribution in the adsorption E_{disp}^{ads} and interaction E_{disp}^{int} energies are always of the same order for a given isomer, their values go from -21.8 (Meta-Mont(4)_{para}(**CO(-Phe)**) to -10.3 kcal/mol (Meta-Mont(9)_{ortho-long}(**CO-NH₂**)). As expected, the strongest dispersion contributions occur in *para* isomers ((1), (4) and (6)), mainly due to the interactions of the pesticide π system with the surface. For the same reason, but in the opposite way, the *ortho* isomers ((2) and (9)) present the weakest dispersive contributions.

Results on Meta-Mont and Atra-Mont isomers are comparable. The dispersion terms are of similar order (from -18.1 to -13.0 kcal/mol) and stronger for PARA isomers than in ORTHO. This similarity in dispersion is in good agreement with the relatively close polarizabilities of the two pesticides: $\alpha_{Atra} = 165 \text{ bohr}^3$ and $\alpha_{Meta} = 175 \text{ bohr}^3$ at the PBE/basis2 level.

VI.C Fenhexamid - Ca-montmorillonite

VI. C.1 PES exploration

- **Fen(CO-Phe)_{para,eq}**

The trajectory starts with Fen adsorbed on the CO-Phe site. Phe moves away from the interaction very early, around 0.4 ps, to leave only the carbonyl oxygen interacting with the cation. From this point, the distance of both cyclohexyl and Phe to the surface increases while the CO stays in close interaction with Ca^{2+} . Then, approximately at 0.8 ps, the molecule moves to create a CO-cyclo interaction with the cation, and goes back to CO only around 1.7 ps. This back and forth movement happens regularly all along the dynamics, oscillating between three types of complexation: CO-cyclo, CO and CO-Phe. However the cyclohexyl and the methyl undergo a lot of rotations around the asymmetric carbon C1: at first, the cyclohexyl is above the surface and the methyl points in the opposite direction (see Figure VI.3.(a)), then around 2.4 ps, they both rotate and interact with the surface. This rotation goes on to 2.8 ps where the methyl points towards the surface, the cyclohexyl being above. At 3.8 ps, the CH_3 and cyclo keep on rotating to interact with the surface again, but in the opposite direction than previously (they have both done a total rotation of 270° from the beginning). These groups keep this orientation until 7.0 ps of dynamics and finally accomplish a complete rotation around C1. From there, the rotation goes backward to allow the cyclohexyl and the methyl to interact with the surface again, around 11.5 ps. In the last half picosecond, the rotations of cyclo, CH_3 and R begin to conduct R to leave its equatorial position *eq* and gets much closer to an axial position *ax*, but with the cyclohexyl group out of chair shape.

- **Fen(Cl-OH)_{para,ax}**

As displayed in Figure VI.3.(b), Fen starts parallel to the surface, adsorbed on the bidentate Cl-OH site. The cyclohexyl is relatively close to the second calcium cation. During the first 4.5 ps, Fen flips over, always keeping the Cl-OH binding site on the cation: in 2 ps it rotates from *para* to *ortho* – *short* position, and follows this rotation until it comes back in *para* position on the opposite side of the cation. This way, the molecule is not oriented towards the second calcium cation of the unit cell as it used to be in the starting structure, but towards the nearest image of this cation. However, it is not close enough to form a double complexation. At some point around 5 ps, the Cl-OH interaction becomes monodentate on the hydroxyl only and stays monodentate until 8.5 ps. During this period, the cyclohexyl and the CH_3

undergo several rotations but stay in the *ax* orientation of the R group. Finally, the interaction with OH allows the molecule to get closer to the nearest cation from the next cell and a double complexation is set. The trajectory evolves in a way where the Cl-OH binding site is recovered while the cyclohexyl interacts with the closest cation, producing a cyclo & Cl-OH double interaction. Approximately from 8.5 to 10.5 ps, the molecule slides more and more towards the second cation so it finally allows the interaction of the cyclohexyl with the second Ca^{2+} to evolve in a shared interaction with the carbonyl. The result is a CO-cyclo & Cl-OH double complexation.

- **Fen(Cl-OH)_{ortho-short,ax}**

When the CPMD starts (see Figure VI.3.(c)), the Cl-OH binding site is lost in less than 1 ps and leaves a monodentate interaction between the hydroxyl oxygen and the cation. Then the molecule goes back and forth between these monodentate and bidentate interaction, staying orthogonal to the surface for a few picoseconds. After ~ 7 ps, fenhexamid is less and less orthogonal to the surface and starts to lean on it, pointing towards the second calcium cation. During this process, the OH- Ca^{2+} interaction is always conserved, involving or not the closest chlorine. Around 11 ps, fenhexamid is in a double interaction: Cl-OH on one Ca^{2+} (Ca1), the cyclohexyl on the other (Ca2). This double complexation is kept for approximately 1 ps until the molecule moves closer to Ca2 and allows the interaction of the carbonyl oxygen, losing the Cl-OH complexation on Ca1. Finally, the molecule stays adsorbed on the CO site and parallel to the surface, and the Phe rotates to take both orthogonal or parallel positions during the last picosecond of the trajectory.

VI. C.2 Optimized structures

The three CPMD trajectories described above allowed to find 9 Fen-Mont isomers. In addition, 2 supplementary geometries have been optimized to complete the exploration. Indeed, in the ϕ_{gas} study, the second lowest family of Fen- Ca^{2+} complexes implies a **CO-Cl-Cl** complexation site and has not been explored during any of the three CPMD trajectories. Then, Fen deposited on the surface in the geometry of Fen- $\text{Ca}^{2+}(4)_{eq}$ (ϕ_{gas}) (CO-Cl-Cl site) has been optimized. However, this optimisation led to the Fen-Mont(7)_{eq} isomer which belongs to the **CO-Cl** family. A second structure, Fen-Mont(11)_{eq}, has been obtained by geometry optimisation, in order to compare the effects of the *ax* and *eq* positions for *ortho* – *short* orientation.

Finally, 11 isomers, displayed in Figure VI.5 and VI.6, have been found and can be classified considering different characteristics: orientation towards the surface, single

or double complexations, nature of the binding site(s) and monodentate or bidentate complexations. In the following notation, parenthesis means that a binding site is monodentate but close to a bidentate form. For instance **CO(-Phe)** is a monodentate single complexation on the carbonyl oxygen, but with a geometry close to the bidentate form **CO-Phe**. When an isomer is in double complexation, the corresponding family is noted with a “&”, separating the names of the binding site on each Ca^{2+} .

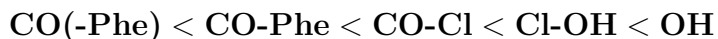
Family energetic order

During the MD trajectories, the molecule stayed nearly parallel to the surface most of the time to increase dispersion interaction, for that reason, most of the optimized snapshots have *para* geometries.

Two consecutive groups of isomers are distinguishable: *para* isomers (Fen-Mont(1-8)) which are the lowest as expected, and *ortho – short* isomers (Fen-Mont(9-11)). In Fen-Mont(1)_{ax}, Phe does not have a real parallel position but is considered as *para* as its intermediate orientation tends to favor dispersion interaction with the surface. Fen-Mont(10)_{ax} is not really orthogonal to the surface as well, but does not lean on the surface, that is why it is noted as an *ortho – short* isomer.

Then, single (only one Ca^{2+}) and double (two Ca^{2+}) complexations of the pesticide are possible and these categories of geometry overlap: the lowest isomer Fen-Mont(1)_{ax}(**CO(-Phe)**) ($\Delta E = 0$ kcal/mol) presents a single complexation on the carbonyl oxygen while the second lowest, Fen-Mont(2)_{ax}(**CO-cyclo & (Cl-OH)**), shows a double complexation between the carbonyl and the cyclohexyl for one cation, and between the hydroxyl oxygen and closest chlorine for the second.

The relative energetic orders for single and double complexation geometries are respectively:



and



Compared to ϕ_{gas} , three identical families have been found: 2 single complexations, **CO-Phe** and **CO-Cl**, and 1 double complexation, **CO-cyclo & Cl-OH**.

Hereafter, we will first consider the families of single complexation isomers, and then the double will be discussed.

For discussion, Table VI.4 reports the cation-binding site distances and the dihedrals of Fen-Ca²⁺ and Fen-(Ca²⁺)₂ lowest isomers in ϕ_{gas} similar families.

Isomers	Complexation	H7-N3-C4-C5]	d_{Ca-O}	d_{Ca-Phe}	d_{Ca-Cl6}	d_{Ca-Cl8}	d_{Ca-OH}
PBE/basis2							
Fen-Ca ²⁺ (1) _{eq}	CO-Phe	-88.6	2.121	2.634	-	-	-
Fen-Ca ²⁺ (11) _{eq}	CO-Cl	-121.3	2.081	-	2.749	-	-
Fen-(Ca ²⁺) ₂ (1) _{ax}	CO-cyclo & Cl-OH	0.0	2.181	-	-	2.732	2.330
Fen-(Ca ²⁺) ₂ (7) _{ax}	CO-cyclo & OH	5.6	2.176	-	-	-	2.229

Table VI.4: Cation-binding site distances in Å and dihedrals in degrees of the lowest Fen-Ca²⁺ and Fen-(Ca²⁺)₂ isomers with comparable complexations at the PBE/basis2 level, reported from Chapter V.

Among all ϕ_{solid}^{dry} isomers, 5 single complexations have been found:

- **CO(-Phe)**: a monodentate complexation on the carbonyl oxygen in Fen-Mont(1)_{ax} ($\Delta E = 0.0$ kcal/mol) and (8)_{eq} ($\Delta E = 16.1$ kcal/mol), where Fen geometry is close to the bidentate **CO-Phe** form. Phe in (1)_{ax} is not really orthogonal to the surface, a π electron interaction is maintained, that is why it will be considered as a *para* isomer ;
- **CO-Phe**: an interaction between the carbonyl oxygen and the π system of the phenyl: Fen-Mont(3)_{ax} ($\Delta E = 2.5$ kcal/mol) and Fen-Mont(6)_{eq} ($\Delta E = 14.1$ kcal/mol) ;
- **CO-Cl**: a bidentate interaction on the carbonyl and the nearest chlorine Cl6 (as in ϕ_{gas}) : Fen-Mont(7)_{eq} ($\Delta E = 14.4$ kcal/mol) ;
- **Cl-OH**: complexation on the hydroxyl oxygen and the closest chlorine Cl8 in Fen-Mont(9)_{ax} ($\Delta E = 18.8$ kcal/mol) and Fen-Mont(11)_{eq} ($\Delta E = 26.0$ kcal/mol). This type of interaction has been found in ϕ_{gas} but only for isomers with two calcium cations (Fen-(Ca²⁺)₂).
- **OH**: a monodentate complexation on the hydroxyl oxygen in Fen-Mont(10)_{ax} ($\Delta E = 21.0$ kcal/mol), which has been found only for Fen-(Ca²⁺)₂ as well.

Let us notice that the carbonyl oxygen is implied in the interaction with Ca²⁺ in the three lowest-energy ϕ_{solid}^{dry} single complexation isomers.

The lowest-energy isomer Fen-Mont(1)_{ax} surprisingly involves one Ca²⁺ cation essentially in a monodentate interaction with the carbonyl oxygen ($d_{Ca-Phe} = 5.29$ Å).

The bidentate **CO-Phe** isomers Fen-Mont(3)_{ax} and (6)_{eq} ($\Delta E = 2.5$ and 14.1 kcal/mol) are lower in energy than (7)_{eq}(**CO-Cl**) ($\Delta E = 14.4$ kcal/mol), the calcium cation preference for CO-Phe than CO-Cl is found again as in ϕ_{gas} .

The corresponding d_{Ca-O} distance in ϕ_{solid}^{dry} (Fen-Mont(1)_{ax}, (3)_{ax} and (7)_{eq}), is the less modified with respect to ϕ_{gas} (see Table VI.4) with a maximum elongation of 0.2 Å (as in Meta-Mont isomers). Other distances to the complexation site, d_{Ca-Cl6} and d_{Ca-Phe} , are elongated by 0.4 Å (Fen-Mont(7)_{eq}(**CO-Cl**)) and 1.7 Å (Fen-Mont(3)_{ax}(**CO-Phe**)) respectively. The larger elongations highly depend on the position and orientation of the phenyl above the surface, and on the strength of the Phe-surface interaction.

The lowest-energy *ortho-short* families, Fen-Mont(9)_{ax}**Cl-OH** and (10)_{ax}**OH**, present binding sites that have been found only for double complexations in ϕ_{gas} . Thus they can be compared to Fen-(Ca²⁺)₂(1)_{ax} and Fen-(Ca²⁺)₂(7)_{ax} respectively. d_{Ca-Cl8} and d_{Ca-OH} are only longer by ≈ 0.3 and 0.1 Å in ϕ_{solid}^{dry} , as adsorption in *ortho-short* orientation does not require a strong modification of the pesticide conformation (see the discussion on E_{prep} hereafter).

For double complexations, 3 families have been found with $2 \leq \Delta E \leq 12$ kcal/mol:

- **CO-cyclo (& Cl-OH)**: Fen-Mont(2)_{ax} isomer ($\Delta E = 2.1$ kcal/mol) shows an interaction of Ca1 with the carbonyl oxygen on one hand, polarizing the cyclohexyl on the other hand. The hydroxyl oxygen and the closest chlorine Cl8 are oriented towards the second cation. d_{Ca-O} is longer than in Fen-(Ca²⁺)₂(1)_{ax} by only ≈ 0.1 Å, while d_{Ca-Cl8} and d_{Ca-OH} are longer by ≈ 1 and 1.5 Å respectively, which shows that the interaction of Ca1 on CO oxygen is favored. That is why Cl-OH is in parenthesis in this notation ;
- **(CO-)cyclo & Cl-OH**: corresponds to Fen-Mont(4)_{ax} ($\Delta E = 8.5$ kcal/mol) which has very similar geometry and family as the previous isomer, but with a favored Cl-OH interaction. Indeed, d_{Ca-O} is elongated by ≈ 1.5 Å compared to Fen-(Ca²⁺)₂(1)_{ax} while d_{Ca-Cl8} and d_{Ca-OH} only longer by ≈ 0.7 and 0.2 Å respectively.
- **(CO-)cyclo & OH**: the last type of double complexation is in Fen-Mont(5)_{ax} isomer where the pesticide interacts with Ca2 through polarization of the cyclohexyl, with the CO oxygen oriented towards the cation. Moreover, Ca1 interacts with the hydroxyl oxygen in a monodentate binding with a d_{Ca-OH} distance longer by only ≈ 0.2 Å compared to Fen-(Ca²⁺)₂(7)_{ax}.

As for single complexation, an interaction of Ca1 on the carbonyl oxygen leads to the

lowest-energy isomer. The second criterion to explain the energetic order is the Phe-O_b distance: the longer this distance, the higher the relative energy.

Finally, all *para* isomers are lower than *ortho* – *short*, but considering other features: single/double complexations and monodentate/bidentate interactions, all the families overlap ; unlike Meta-Mont isomers, where families are consecutive. Concerning the orientation of *R* and CH₃ around the cyclohexyl, within the *para* and *ortho* – *short* optimized structures, the *ax* isomers are lower than the *eq*, regardless the family of complexation. However, the number of explored geometries is not large enough to draw any conclusion on this observation.

Unexpectedly, the lowest-energy structure presents a single complexation (Ca1), in a monodentate interaction. Although Ca-Ca distances are comparable (10.3 Å in ϕ_{solid}^{dry} and 10.5 Å in ϕ_{gas}), a “real” double complexation is not obtained in ϕ_{solid}^{dry} . Indeed, one of the binding sites is more favored than the other (CO oxygen in Fen-Mont(2)_{ax} versus Cl-OH in Fen-Mont(4)_{ax}).

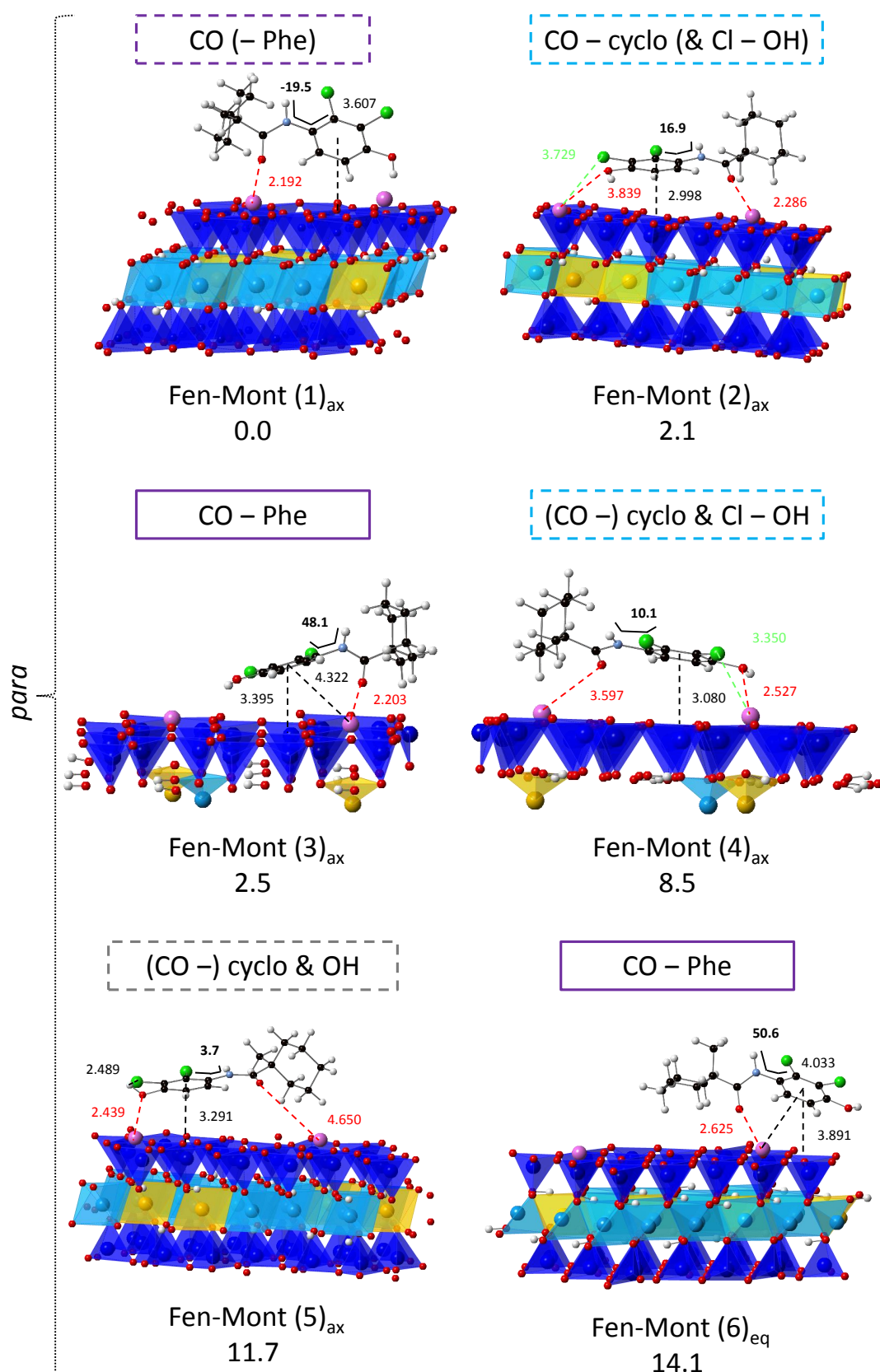


Figure VI.5: Fen-mont isomers displayed with complexation families and relative energies (kcal/mol). Distances (black), cation distances to the molecule oxygens (red) and chlorines (green) are in Å. H7-N3-C4-C5] dihedrals (bold) are in degrees.

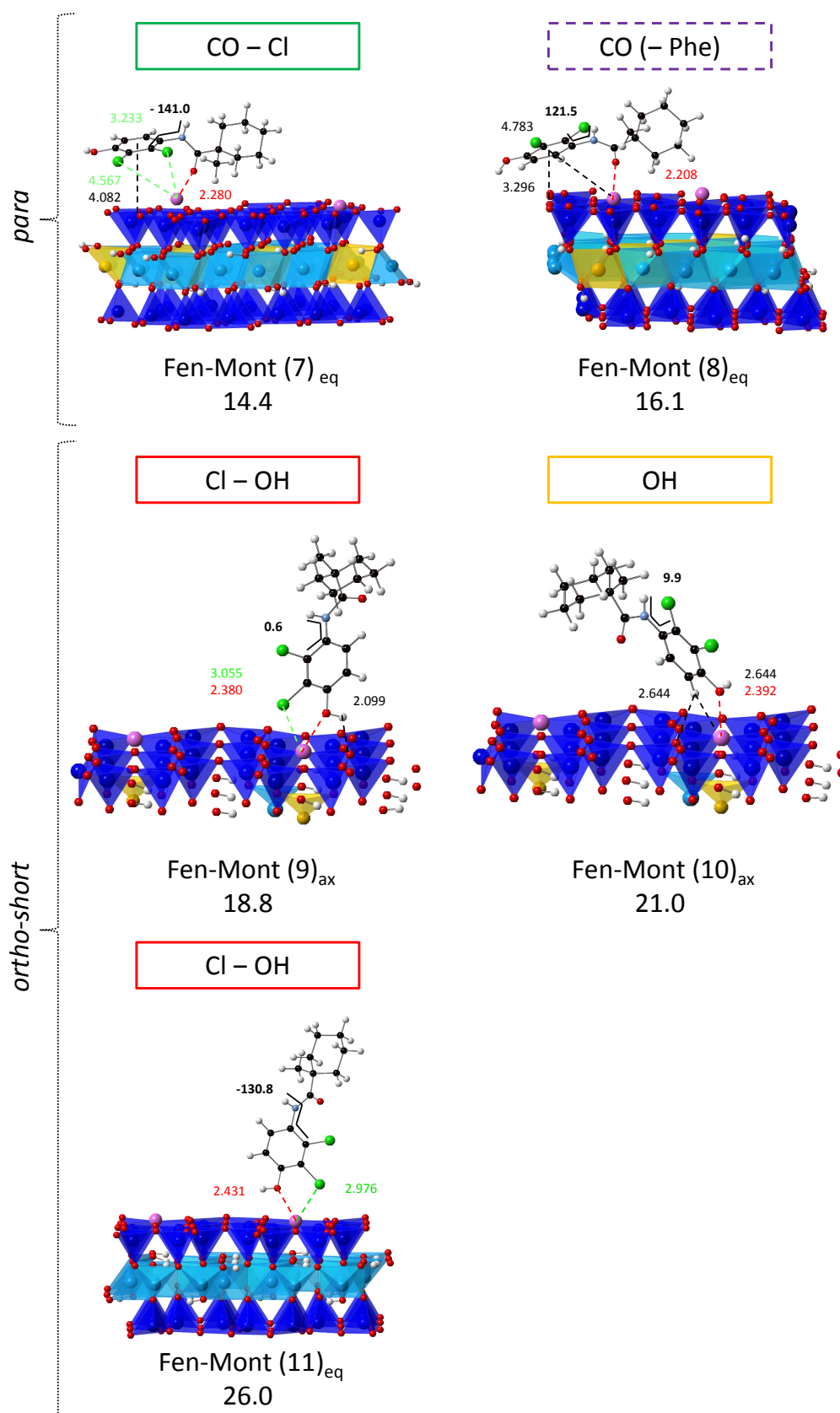


Figure VI.6: Fen-mont isomers displayed with complexation families and relative energies (kcal/mol). Distances (black), cation distances to the molecule oxygens (red) and chlorines (green) are in Å. H7-N3-C4-C5] dihedrals (bold) are in degrees.

Isomer geometry compared to ϕ_{gas}

Table VI.5 displays intramolecular distances in isolated Fen and ϕ_{gas} and ϕ_{solid}^{dry} complexes. The results are similar as for metamitron: the bond variations are lower in ϕ_{solid}^{dry} than ϕ_{gas} but never overtake 0.1 Å. When atoms or neighbour atoms are implicated in the complexation, bond lengths increase usually by 0.02 – 0.05 Å in ϕ_{gas} , and up to 0.08 Å for d_{C-OH} . For complexation in ϕ_{solid}^{dry} , d_{C-O} and d_{C-OH} increase by 0.03 – 0.05 Å while d_{C-Cl6} and d_{C-Cl8} are very slightly modified.

Isomers	Complexation	d_{C-O}	d_{O-H}	d_{C-OH}	d_{C-Cl6}	d_{C-Cl8}
PBE/basis2						
Fen(1) _{ax}	-	1.230	0.977	1.362	1.749	1.747
Fen-Ca ²⁺ (1) _{eq}	CO-Phe	1.287	0.982	1.329	1.718	1.722
Fen-Ca ²⁺ (11) _{eq}	CO-Cl	1.286	0.979	1.333	1.769	1.736
Fen-(Ca ²⁺) ₂ (1) _{ax}	CO-cyclo & Cl-OH	1.279	0.981	1.420	1.721	1.771
Fen-(Ca ²⁺) ₂ (7) _{ax}	CO-cyclo & OH	1.282	1.026	1.440	1.722	1.737
PBE-D2/pw						
Fen-Mont(1) _{ax}	CO(-Phe)	1.261	0.983	1.355	1.735	1.722
Fen-Mont(2) _{ax}	CO-cyclo & (Cl-OH)	1.255	0.980	1.367	1.731	1.733
Fen-Mont(3) _{ax}	CO-Phe	1.258	0.983	1.350	1.727	1.727
Fen-Mont(4) _{ax}	(CO-)cyclo & Cl-OH	1.233	0.981	1.397	1.728	1.734
Fen-Mont(5) _{ax}	(CO-)cyclo & OH	1.233	0.984	1.410	1.730	1.730
Fen-Mont(6) _{eq}	CO-Phe	1.252	0.991	1.351	1.742	1.731
Fen-Mont(7) _{eq}	CO-Cl	1.247	0.977	1.358	1.737	1.716
Fen-Mont(8) _{eq}	CO(-Phe)	1.258	0.981	1.356	1.729	1.723
Fen-Mont(9) _{ax}	Cl-OH	1.228	0.983	1.385	1.731	1.740
Fen-Mont(10) _{ax}	OH	1.229	0.988	1.396	1.730	1.734
Fen-Mont(11) _{eq}	Cl-OH	1.227	0.979	1.391	1.714	1.735

Table VI.5: Fenhexamid intramolecular distances (Å) in ϕ_{gas} (PBE/basis2) and ϕ_{solid}^{dry} (PBE-D2/pw) complexes.

Distances within the surface in Fen-Mont isomers are displayed in Table VI.6. As in Meta-Mont geometries, internal variations are very low, with a maximum deviation from Mont(opt) of $\approx 4 \times 10^{-3}$ Å. Nevertheless Ca²⁺ distances to the surface are strongly modified: d_{Ca1-O_b} is elongated by $\approx 0.12 - 0.48$ Å ; for single complexation isomers, d_{Ca2-O_b} is either equivalent or reduced by 0.06 Å at most ; for double complexations, d_{Ca2-O_b} increases from 0.06 to 0.18 Å. These variations are all the more large than the cation is implied in complexation with Fen (see discussion in the energetic analysis hereafter).

Table VI.6: Fen-Mont distances or average distances (\AA) in the Ca-montmorillonite surface.

Isomers	Complexation	d_{Ca1-O_b}	d_{Ca2-O_b}	d_{Ca1-O_h}	d_{Ca2-O_h}	$d_{(Al-O_a)}$	$d_{(Al-O_h)}$	$d_{(Mg-O_a)}$	$d_{(Mg-O_h)}$	$d_{(H-O_h)}$	$d_{(Si-O_a)}$	$d_{(Si-O_b)}$
Mont(opt)	-	0.252	0.249	2.360	2.358	1.973	1.940	2.084	2.055	0.978	1.638	1.629
Fen-Mont(1) _{ax}	CO(-Phe)	0.478	0.247	2.611	2.354	1.971	1.939	2.084	2.058	0.978	1.639	1.629
Fen-Mont(2) _{ax}	CO-cyclo & (Cl-OH)	0.552	0.354	2.662	2.424	1.971	1.939	2.084	2.056	0.978	1.639	1.629
Fen-Mont(3) _{ax}	CO-Phe	0.474	0.217	2.599	2.340	1.970	1.938	2.083	2.052	0.978	1.639	1.630
Fen-Mont(4) _{ax}	(CO-)cyclo & Cl-OH	0.480	0.433	2.555	2.553	1.971	1.939	2.084	2.055	0.978	1.638	1.629
Fen-Mont(5) _{ax}	(CO-)cyclo & OH	0.370	0.313	2.468	2.419	1.971	1.939	2.083	2.053	0.978	1.639	1.629
Fen-Mont(6) _{eq}	CO-Phe	0.543	0.235	2.659	2.348	1.974	1.940	2.086	2.059	0.978	1.637	1.629
Fen-Mont(7) _{eq}	CO-Cl	0.728	0.225	2.834	2.344	1.974	1.939	2.086	2.057	0.978	1.637	1.629
Fen-Mont(8) _{eq}	CO(-Phe)	0.488	0.194	2.667	2.319	1.973	1.937	2.083	2.051	0.978	1.635	1.631
Fen-Mont(9) _{ax}	Cl-OH	0.491	0.234	2.576	2.357	1.971	1.939	2.084	2.056	0.978	1.639	1.629
Fen-Mont(10) _{ax}	OH	0.367	0.250	2.474	2.364	1.971	1.939	2.083	2.057	0.978	1.639	1.629
Fen-Mont(11) _{eq}	Cl-OH	0.490	0.230	2.570	2.358	1.974	1.940	2.085	2.056	0.978	1.638	1.629

Table VI.7: Relative (ΔE), adsorption (E_{ads}), interaction (E_{int}) and preparation (E_{prep}) energies of the Fen-Mont isomers. $E_{prep}(\text{Pest})$, $E_{prep}(\text{Mont})$ and $E_{prep}(\text{total})$ are the fenhexamid, the Ca-montmorillonite and the total preparation energies respectively. Percentages in the preparation energies are the contributions in $E_{prep}(\text{total})$. E_{disp}^{ads} and E_{disp}^{int} are dispersion contributions to the adsorption and interaction energies. All energies are displayed in kcal/mol.

Isomers	Complexation	ΔE	E_{ads}	E_{disp}^{ads}	E_{int}	E_{disp}^{int}	$E_{prep}(\text{Pest})$	$E_{prep}(\text{Mont})$	$E_{prep}(\text{total})$
Fen-Mont(1) _{ax}	CO(-Phe)	0.0	-43.47	-17.48	-53.35	-17.03	+5.74	+4.14	+9.88
Fen-Mont(2) _{ax}	CO-cyclo & (Cl-OH)	2.1	-41.39	-25.37	-54.56	-24.82	+6.86	+6.31	+13.16
Fen-Mont(3) _{ax}	CO-Phe	2.5	-40.95	-18.73	-50.02	-18.73	+5.05	+4.02	+9.07
Fen-Mont(4) _{ax}	(CO-)cyclo & Cl-OH	8.5	-35.01	-27.06	-47.80	-26.82	+6.93	+5.86	+12.79
Fen-Mont(5) _{ax}	(CO-)cyclo & OH	11.7	-31.76	-20.77	-39.59	-21.25	+5.77	+2.05	+7.82
Fen-Mont(6) _{eq}	CO-Phe	14.1	-29.41	-13.64	-44.86	-13.46	+7.40	+8.05	+15.45
Fen-Mont(7) _{eq}	CO-Cl	14.4	-29.05	-19.91	-53.52	-19.38	+13.17	+11.31	+24.47
Fen-Mont(8) _{eq}	CO(-Phe)	16.1	-27.34	-18.94	-53.85	-18.62	+12.58	+13.93	+26.51
Fen-Mont(9) _{ax}	Cl-OH	18.8	-24.72	-8.05	-31.84	-7.95	+3.90	+3.22	+7.12
Fen-Mont(10) _{ax}	OH	21.0	-22.49	-7.75	-24.44	-7.66	+1.04	+0.92	+1.96
Fen-Mont(11) _{eq}	Cl-OH	26.0	-17.44	-8.32	-30.73	-8.18	+10.31	+2.98	+13.29

Adsorption, interaction and preparation energies

All energies that are discussed in the following are displayed in Table VI.7.

Fen-Mont adsorption energies go from -43.5 kcal/mol (Fen-Mont(1)_{ax}(**CO(-Phe)**)) to -17.44 kcal/mol (Fen-Mont(11)_{eq}(**Cl-OH**)), which is very similar to the adsorption energy scale of Meta-Mont isomers. Fen adsorption energies on Mont are a lot lower, in absolute value, than complexation energies with one Ca^{2+} in ϕ_{gas} . These values support the hypothesis of a lower cationic charge on Ca^{2+} , as the complexation energies of Meta and Fen in ϕ_{gas} with a single Ca^{2+} are ≈ -140 kcal/mol versus ≈ -40 kcal/mol with Na^+ .

Interaction energies in Fen-Mont isomers range from -54.6 kcal/mol (Fen-Mont(2)_{ax}(**CO-cyclo & (Cl-OH)**)) to -24.4 kcal/mol (Fen-Mont(10)_{ax}(**OH**)). The strongest interactions ($E_{int} \leq -50$ kcal/mol) are found when complexations involve the carbonyl oxygen: for Fen-Mont(1)_{ax}, (2)_{ax}, (3)_{ax}, (7)_{ax} and (8)_{ax}, all with $2.2 \leq d_{Ca-O} \leq 2.3$. The longer distance in Fen-Mont(6)_{ax} ($d_{Ca-O} = 2.625$ Å) partially explains its weaker interaction energy (-44.86 kcal/mol). As expected, *ortho* isomers present the weakest interactions with the surface ($E_{int} \geq -32$ kcal/mol), as for ORTHO isomer of Atra which presents the weakest adsorption and interaction energies in the series (Chapter IV [136]).

Total preparation energies show larger variations in Fen-Mont ($+1.96 \leq E_{prep}(\text{total}) \leq +26.51$ kcal/mol) than in Meta-Mont isomers ($+5.38 \leq E_{prep}(\text{total}) \leq +15.37$ kcal/mol). Overall, pesticide preparation energies tend to be lower ($+1 \leq E_{prep}(\text{Pest}) \leq +13$ kcal/mol in general) than in ϕ_{gas} ($E_{prep}(\text{Pest}) > +10$ kcal/mol). Indeed, the pesticide-cation interaction is not as favorable in ϕ_{solid}^{dry} , as the cationic charge of calcium ions is probably attenuated with respect to bare Ca^{2+} cations. Calcium is thus less available for interaction with the pesticide.

Unlike for Meta-Mont, preparation energy in Fen-Mont structures is fairly shared between the pesticide and the surface ($E_{prep}(\text{Pest}) \approx E_{prep}(\text{Mont})$), except in isomers (5)_{ax} and (11)_{eq} where $E_{prep}(\text{Pest})$ represents the main contribution in $E_{prep}(\text{total})$. In these two geometries, $E_{prep}(\text{Mont})$ is very low: $\approx +2$ and $\approx +3$ kcal/mol respectively. Indeed, for Fen-Mont(5)_{ax}, the cation distances to the surface increase by only $\approx 0.06 - 0.10$ Å, which are among the lowest d_{Ca-O_b} elongations, for a Ca^{2+} involved in the complexation (usually $\approx 0.2 - 0.3$ Å). This is due to the type of complexation (**(CO-)cyclo & OH**) which is “monodentate” on each cation, producing one of the weakest interaction energies (-39.59 kcal/mol).

In Fen-Mont(11)_{eq}(**Cl-OH**), d_{Ca1-O_b} increases a bit more (by ≈ 0.2 Å), as the binding site is bidentate, but E_{int} is even weaker (-30.73 kcal/mol) as the molecule is in *ortho* orientation. In addition its $E_{prep}(\text{Pest})$ is high ($+10.31$ kcal/mol), due in part to the large

dihedral ($\text{H7-N3-C4-C5}] = -130.8^\circ$), reducing π delocalization. Indeed, for isolated Fen, the first *eq* isomer with a broken delocalization is Fen(9)_{eq} and is about 5.8 kcal/mol higher than Fen(1)_{ax}, the lowest conformer. Therefore among the +10.31 kcal/mol of pesticide preparation energy in Fen-Mont(11)_{eq}, 5.8 kcal/mol originate from the broken delocalization and *eq* orientation. For comparison, Fen-Mont(9)_{ax}(**Cl-OH**), which present the same binding site but an *ax* orientation, and where the dihedral is -0.6° , has a pesticide preparation energy of +3.90 kcal/mol only. However, E_{int} and d_{Ca1-O_b} are of the same order of magnitude than in Fen-Mont(11)_{eq}.

The largest total preparation energies are found for Fen-Mont(7)_{eq} and (8)_{eq}, +24.47 and +26.51 kcal/mol respectively, although the strongest interaction energies (-53.52 and -53.85 kcal/mol) are observed. The largest surface deformations ($E_{prep}(\text{Mont}) \approx +11-14$ kcal/mol) is due to the significant elongation of d_{Ca1-O_b} in both geometries, compared to Mont(opt).

Among all isomers in ϕ_{solid}^{dry} that have been found for atrazine, metamitron and fenhexamid adsorbed on Ca-montmorillonite, Fen-Mont(7)_{eq} presents the longest cation-surface distance for the complexed Ca^{2+} ($d_{Ca1-O_b} = 0.728 \text{ \AA}$).

On the other hand, for single complexation isomers, the non-interacting cation (Ca2) generally gets slightly closer to the surface: d_{Ca2-O_b} is either unchanged (as in Fen-Mont(1)_{ax} and (10)_{ax}) or shortened, up to $\approx 0.06 \text{ \AA}$ as in Fen-Mont(8)_{eq}.

Dispersion contributions in the adsorption (E_{disp}^{ads}) and interaction (E_{disp}^{int}) energies, are always similar for a given isomer ($E_{disp}^{ads} \approx E_{disp}^{int}$). As expected, *para* isomers lead to stronger dispersive interaction ($-26.8 \leq E_{disp} \leq -13.5$ kcal/mol) than *ortho* – *short* ($-8.3 \leq E_{disp} \leq -7.7$ kcal/mol) as in Atra-Mont and Meta-Mont complexes.

The largest dispersion contributions have been found for Fen-Mont(2)_{ax}, (4)_{ax} and (5)_{ax} isomers with a double complexation mainly due to a nearly “perfect” orientation of Phe, parallel to the surface and with the shortest distances (2.998, 3.080 and 3.291 \AA respectively).

VI.D Conclusion

Five dynamic explorations of metamitron and fenhexamid in interaction with the Ca-montmorillonite model have been run, two for Meta-Mont and three for Fen-Mont complexes. They allowed to find a variety of optimized isomers and complexation families wider than for Atra-Mont, studied using a static exploration of the PES. Meta-Mont and Fen-Mont optimized adsorption energies are of the same order of magnitude (≈ -44

kcal/mol), but with higher absolute values than Atra-Mont (≈ -27 kcal/mol).

In ϕ_{gas} , double complexed Atra and Meta with calcium present inter-cation distances of $\approx 7 - 9$ Å [12], whereas d_{Ca-Ca} are longer in Fen isomers: $\approx 10 - 11$ Å. Considering that the inter-cation distance in Mont is 10.341 Å, a double complexation can only be envisaged for Fen. Indeed, Atra-Mont and Meta-Mont isomers only present complexations on one cation while three double complexation isomers have been found for Fen-Mont. Moreover, a complexation of Fen on cations is competitive with the lowest single complexation isomer (Fen-Mont(1)_{ax}(CO(-Phe)) regarding adsorption energies.

In an opposite way, in ϕ_{gas} , double complexations are systematically less favoured than single ones, due to the inter-cation repulsion. Indeed, this repulsion energy ranges from $\approx +140$ to $+180$ kcal/mol for Atra ($E_{Ca^{2+}-Ca^{2+}}$ in the paper of Bessac and Hoyau of 2013 [12]), and is approximately $+180$ kcal/mol for Meta, when it is $\approx +120$ kcal/mol for Fen ($E_{cat-cat}$ in Chapter V [258]), as in Fen- Ca^{2+} isomers, d_{Ca-Ca} is longer. Double complexation is even repulsive for Atra as it produces a positive complexation energy $E_{comp} = +9.80$ kcal/mol (B3LYP/basis2), whereas it is favored for Meta ($E_{comp} = -30.29$ kcal/mol (PBE/basis2)), and even more for Fen ($E_{comp} = -57.13$ kcal/mol (PBE/basis2)).

In ϕ_{solid}^{dry} , when the pesticide is put in interaction with the surface, the Ca-Ca repulsion is included in the surface energy. Consequently, adsorption energies of the pesticides are more favorable than complexation energies in ϕ_{gas} (see Chapters IV and V). In this case, cations stay close to the surface.


In the following chapter, the same type of systems will be simulated with explicit hydration, and the behavior of the adsorbed cations will be treated with high consideration, in order to analyse the solvation influence on such systems.

Chapter VII

Pesticide hydration: solvation effects and fenhexamid desorption.

*“Refrain from illusions, insist on work and not words,
patiently seek divine and scientific truth.”*

Last words of Maria Mendeleeva to her son Dmitri

 In the former chapter, structures of metamitron and fenhexamid adsorbed on a dry Ca-montmorillonite surface have been optimized. The description of soil in Chapter II showed that a quarter of its composition is mainly water. In addition, let us remind that montmorillonite is a mineral with a strong ability to swell and absorb water in its interlayer space. Metamitron and fenhexamid are both water-soluble species, up to 1,770 mg/L and 24.0 mg/L at 20°C respectively.

The present chapter is organised in two sections: first, a study of the hydration effects on pesticide interaction with the Ca-montmorillonite model, and the consequences on the surface. Both molecules will be simulated adsorbed on the surface in presence of water during CPMD trajectories controlled in temperature. In the second section, the desorption process of fenhexamid from the hydrated surface will be studied aiming to quantify desorption free-energy barriers.

VII.A Pesticide interaction with a watered - Ca - montmorillonite surface

This section treats hydration of pesticide-Mont systems based on some of the isomers (Meta-Mont and Fen-Mont) that have been optimized in the previous chapter. Let us describe first how the solvent is explicitly included in the simulations, then the starting structures of the CPMD simulations and the associated parameters. Finally, the results and observations will be displayed and discussed for each pesticide.

Water box

As an explicit solvation of the pesticides adsorbed on montmorillonite is envisaged, a box of water molecules has first been produced before its integration to the pesticide-Mont systems.

A grid of 216 water molecules arranged periodically at $d_{O-O} = 3 \text{ \AA}$ in the three directions of space, has been generated in a periodic cubic box of 18.6207 \AA side, corresponding to a density $\rho_{H_2O} = 1 \text{ g/cm}^3$. All intramolecular O-H distances are set to 0.96 \AA . This water molecule lattice is the starting structure of a BOMD simulation at 300 K during 30 ps, within the Self-Consistent Charge Density Functional based Tight-Binding method (SCC-DFTB) [259–261] as it is implemented in the deMonNano code [262]. This trajectory has been run within the NVT ensemble, with a Nose-Hoover thermostat [263–266].

The starting structure of water and the obtained structure after the 30 ps of simulation are represented on Figure VII.1.

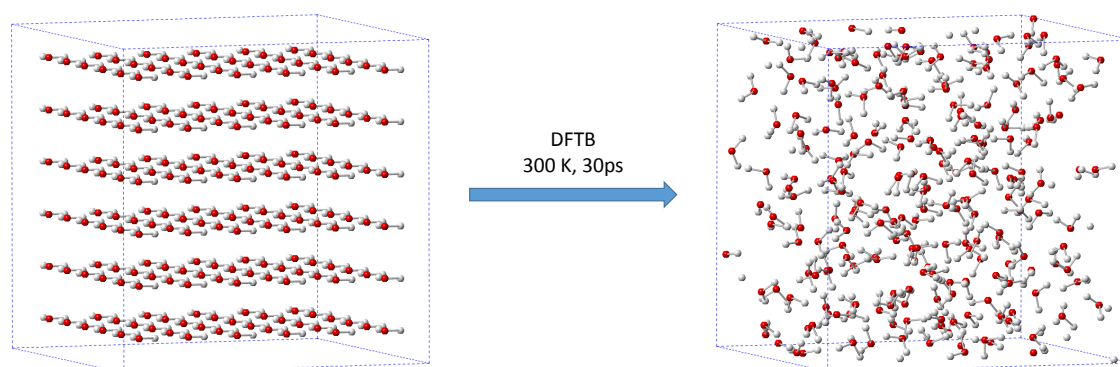


Figure VII.1: Input and output structures of the 30 ps SCC-DFTB dynamics of the 18.6207 \AA periodic cubic box of water molecules.

The average intermolecular distance $\langle d_{O-O} \rangle$ between all molecules has been computed at the end of the simulation and is equal to 2.75 \AA , which closely corresponds to the first

RDF peak of experimental water at 298 K [227, 267, 268].

VII. A.1 Starting structures and CPMD parameters

The output structure of the 216 water molecules contained in the cubic box, has been employed to introduce water in the four pesticide-Mont systems, that have been considered hereafter. The water structure of this box has been cut and arranged to fit the interlayer space and the shape of the pesticides in the starting structures. Finally, 135 H₂O molecules have been introduced for metamitron, and 132 molecules for fenhexamid, considering their slightly different volumes. Four structures have been considered for this solvation study (two for each pesticide) and are displayed in Figure VII.2. From now on, these hydrated solid phase systems will be noted as $\phi_{solid}^{H_2O}$ and Ca1 is the cation in interaction with the pesticide while Ca2 is the other one, as in the previous chapter. Before the description of these structures, it is necessary to indicate that these four simulations have been run before the complete exploration of the ϕ_{solid}^{dry} isomers in the previous chapter. That is why the following starting structures do not correspond to both lowest-energy Meta-Mont and Fen-Mont geometries. Consequently, a solvated Fen-Mont isomer in double complexation has not been considered. The four structures have initially been chosen in order to study Meta-Mont in *para* and *ortho-long* orientations, and Fen-Mont in *para* and *ortho-short* ones. Moreover, for both pesticides, a **CO(-Phe)** complexation site has been considered for comparison.

- **Metamitron -watered -Ca-montmorillonite**

For Metamitron, two isomers have been chosen, belonging to different families of complexation and with different orientations towards the surface in order to study adsorptions of different nature. Regarding the geometries and families obtained in ϕ_{solid}^{dry} , the first starting structure selected, Meta-Mont $_{ortho-long}^{H_2O}$, belongs to the **N-N** family with an *ortho* orientation, and corresponds to the solvation of a close form of Meta-Mont(2) $_{ortho-long}$ isomer ($\Delta E = 1.2$ kcal/mol (ϕ_{solid}^{dry})). The second structure, Meta-Mont $_{para}^{H_2O}$, is a **CO(-Phe)** isomer in *para* corresponding to Meta-Mont(4) $_{para}$ ($\Delta E = 5.6$ kcal/mol (ϕ_{solid}^{dry})).

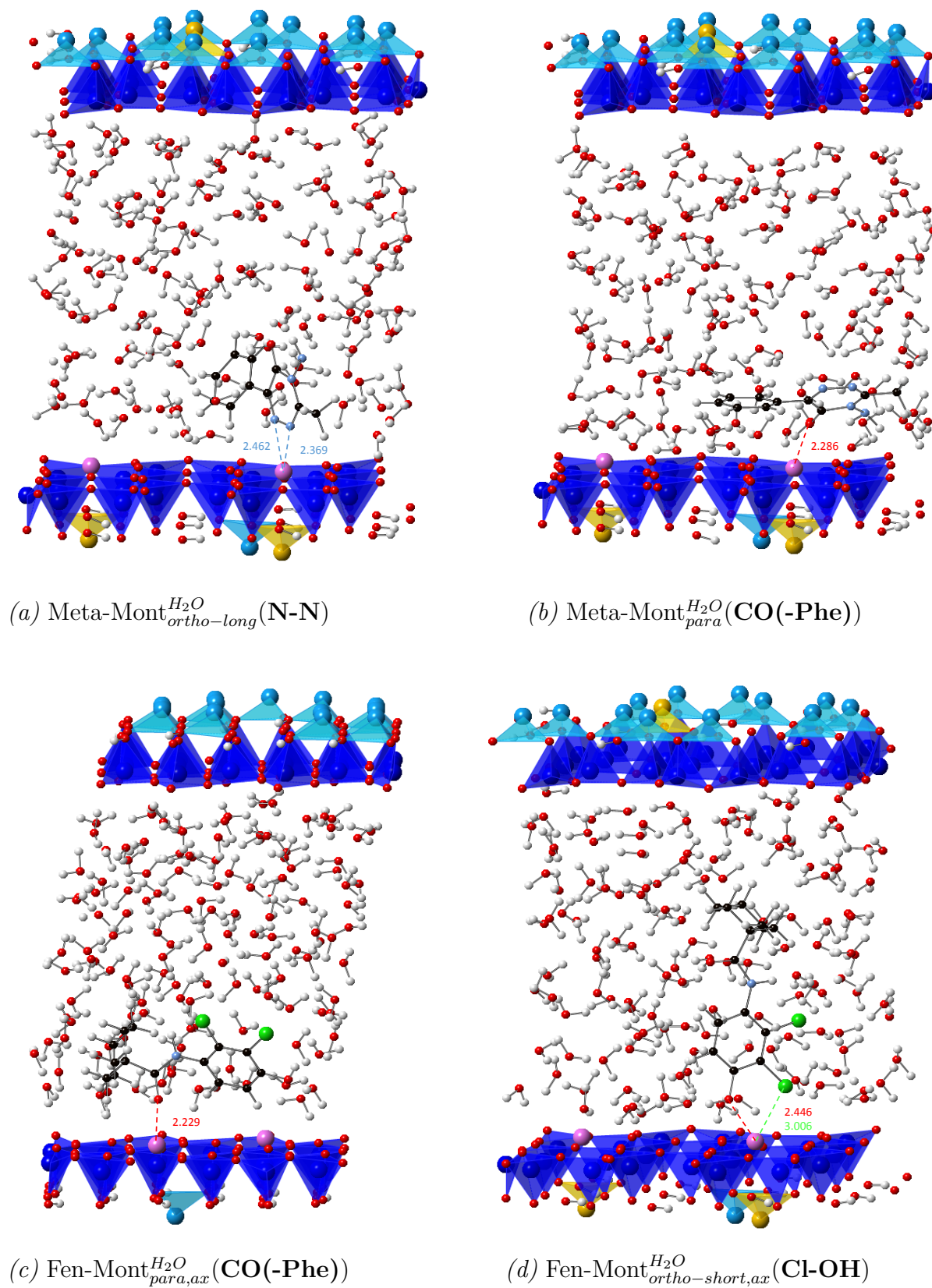


Figure VII.2: Starting structures of the CPMD trajectories in $\phi_{solid}^{H_2O}$. Distances are displayed in Å.

• Fenhexamid -watered -Ca-montmorillonite

For fenhexamid, axial structures in a single complexation have been chosen, but both *para* and *ortho* – *short* orientations are considered with two different binding sites:

- The first starting structure, named Fen-Mont $_{para}^{H_2O}$, is parallel to the surface and interacts with a cation through the carbonyl oxygen (**CO(-Phe)** family). It corresponds to the lowest isomer found in the previous study: Fen-Mont(1) $_{para,ax}$ ($\Delta E = 0.0$ kcal/mol (ϕ_{solid}^{dry})).
- The second structure corresponds to the Fen-Mont(9) $_{para,ax}$ isomer ($\Delta E = 18.8$ kcal/mol (ϕ_{solid}^{dry})), thus Fen interacts with Ca1 through a Cl-OH binding site (**Cl-OH** family), and is orthogonal to the surface. It is noted Fen-Mont $_{ortho-short}^{H_2O}$.

• CPMD parameters

The four trajectories have been run within the NVT ensemble during 12 ps with a Langevin thermostat [269–271] as it is implemented in the CPMD software package [233]. The timestep and the planewave cutoff are the same as in the previous isomer explorations (0.1 fs and 80 Ry) but with the fictitious electronic mass μ set to 400 a.u.

As presented in the theoretical chapter (III. B.5), the PBE functional (with or without dispersion correction) tends to over-structure water compared to experiments [222–228, 267]. Therefore, the thermostat of the simulations is set to 350 K instead of 298 K (ambient temperature), to try to overcome this over-structuration issue, and get intermolecular first neighbour distances as close as possible to 2.80 Å which is the most recent and accurate experimental value at ambient temperature. According to Naberukhin *et al.* [272], the X-ray diffraction results of Skinner *et al.* [268] are presented as the most recent and accurate experimental results for studies of water structure, and display the position and height of its RDF first peak at $r_1 = 2.80$ Å and $g_1 = 2.57$ respectively. Gillan *et al.* [228] compared RDF theoretical results gathered from several studies and evidenced that the PBE functional produces low first-neighbour distances, and show that the D2 dispersion correction does not improve the position of the first peak: $r_1 = 2.72$ Å for 64 water molecules simulated in CPMD/PBE-D2 at 324 K (NVE) (referenced on the paper of Lin *et al.* [273]). Concerning the molecular arrangements in water beyond the first peak, experimental data are still debated nowadays, due to the methods [272, 274, 275].

The global potential energy of each trajectory is stabilized after 4 ps, which is thus considered as the equilibration time and is not taken into account in the following analysis. After 4 ps, the average temperatures of the four simulations have been computed and is approximately of 330 K overall: 334 K for Meta-Mont^{H₂O}_{ortho-long}(N-N), 330 K for Meta-Mont^{H₂O}_{para}(CO(-Phe)), 331 K for Fen-Mont^{H₂O}_{para,ax}(CO(-Phe)), and 333 K for Fen-Mont^{H₂O}_{ortho-short,ax}(Cl-OH).

VII. A.2 Complexation sites hydration

Figure VII.3 displays the distribution functions of the distances between the pesticide binding sites and Ca1 in the four trajectories, with associated average distances, also reported in Table VII.1.

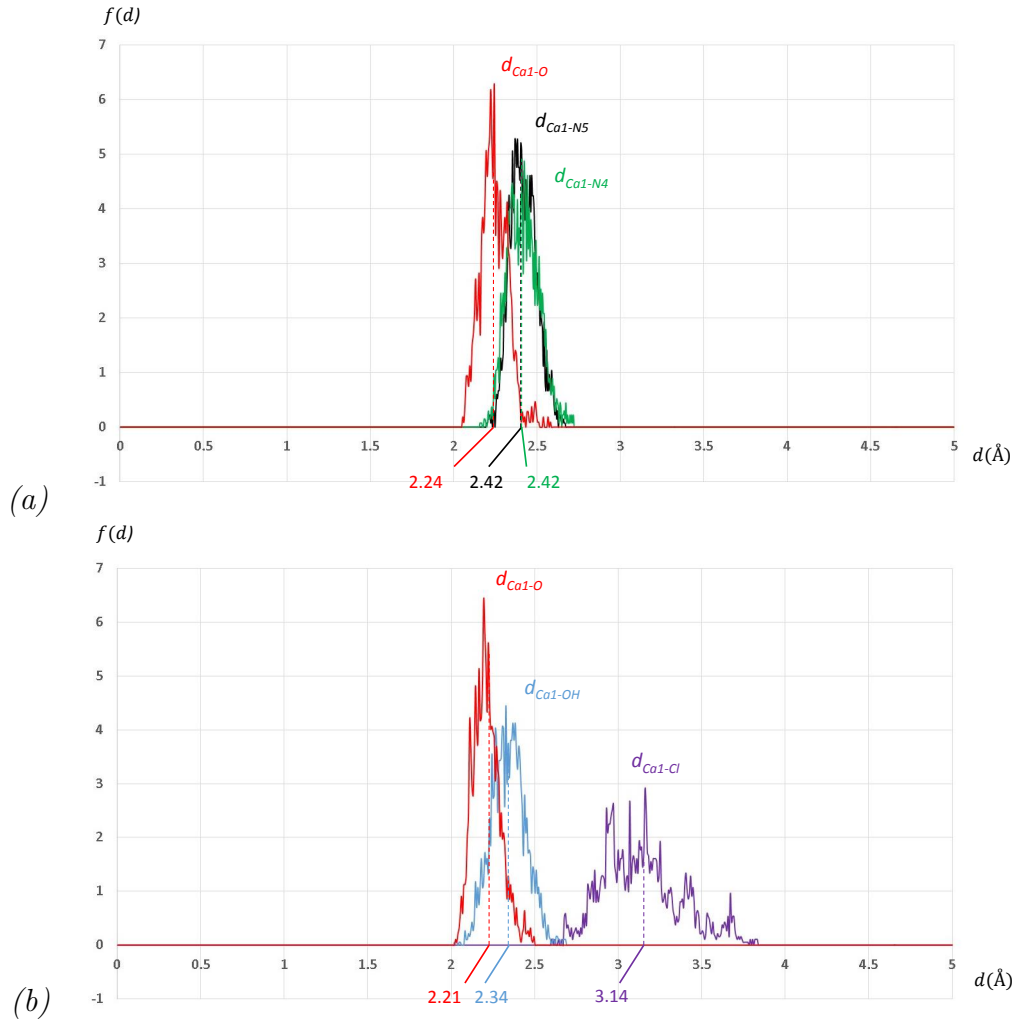


Figure VII.3: Distribution functions $f(d)$ of the distances in Å from the pesticides binding sites to Ca1, and their associated average values: (a) in Meta-Mont^{H₂O}_{para}(CO(-Phe)) (red) and in Meta-Mont^{H₂O}_{ortho-long}(N-N) (green and black) ; (b) in Fen-Mont^{H₂O}_{para,ax}(CO(-Phe)) (red) and in Fen-Mont^{H₂O}_{ortho-short,ax}(Cl-OH) (blue and purple).

Systems	Complexations	$\langle d_{Ca1-O} \rangle$	$\langle d_{Ca1-N4} \rangle$	$\langle d_{Ca1-N5} \rangle$	$\langle d_{Ca1-Cl} \rangle$	$\langle d_{Ca1-OH} \rangle$
ϕ_{solid}^{dry}						
Meta-Mont(2) _{ortho-long}	N-N	-	2.447	2.378	-	-
Meta-Mont(4) _{para}	CO(-Phe)	2.278	-	-	-	-
Fen-Mont(1) _{para,ax}	CO(-Phe)	2.192	-	-	-	-
Fen-Mont(9) _{ortho-short,ax}	Cl-OH	-	-	-	3.055	2.380
$\phi_{solid}^{H_2O}$						
Meta-Mont ^{H₂O} _{ortho-long}	N-N	-	2.42	2.42	-	-
Meta-Mont ^{H₂O} _{para}	CO(-Phe)	2.24	-	-	-	-
Fen-Mont ^{H₂O} _{para,ax}	CO(-Phe)	2.21	-	-	-	-
Fen-Mont ^{H₂O} _{ortho-short,ax}	Cl-OH	-	-	-	3.14	2.34

Table VII.1: Distances between the binding sites and the complexed calcium cation Ca1 of Meta-Mont and Fen-Mont isomers, reported from the ϕ_{solid}^{dry} study, and corresponding average distances from the $\phi_{solid}^{H_2O}$, all displayed in Å.

The hydration of the system does not have consequences on the interaction between the pesticides and the calcium cation. Indeed, the comparison between the ϕ_{solid}^{dry} lowest isomers and the $\phi_{solid}^{H_2O}$ results show the same trends:

- $2.2 \leq d_{Ca1-O} \leq 2.3$ Å for both pesticides ;
- $d_{Ca1-N4} \approx d_{Ca1-N5} \approx 2.4 - 2.5$ Å, for Meta, shows that the binding site stays bidentate all along the trajectory of Meta-Mont^{H₂O}_{ortho-long}((N-N)) ;
- $d_{Ca1-Cl} \approx 3.1$ Å while $d_{Ca1-OH} \approx 2.3 - 2.4$ Å for Fen which shows the stronger interaction with hydroxyl oxygen than with chlorine.

The carbonyl oxygen average distance to the cation is the same in Meta-Mont^{H₂O}_{para}(**CO(-Phe)**) and Fen-Mont(CO)^{H₂O}_{para,ax}(**CO(-Phe)**). However, the bidentate binding site in Fen-Mont^{H₂O}_{ortho-short,ax}(**Cl-OH**) can evolve to a monodentate interaction on the hydroxyl oxygen, so the d_{Ca1-Cl} distribution functions can go higher than 3.5 Å.

VII. A.3 Surface hydration

Concerning the solvation influence on Mont, the average distances between the calcium cations and the surface (the basal oxygens O_b) and the associated distribution functions are displayed in Figure VII.4.

Table VII.2 gives the d_{Ca-O_b} and average bond lengths within the surface for the last snapshot in each trajectory. The average distances in the ϕ_{solid}^{dry} isomers are also presented for comparison.

First, hydration of the surface has a slight influence on the Mont intrinsic structure as expected: internal distances slightly increase. The maximum elongation concerns

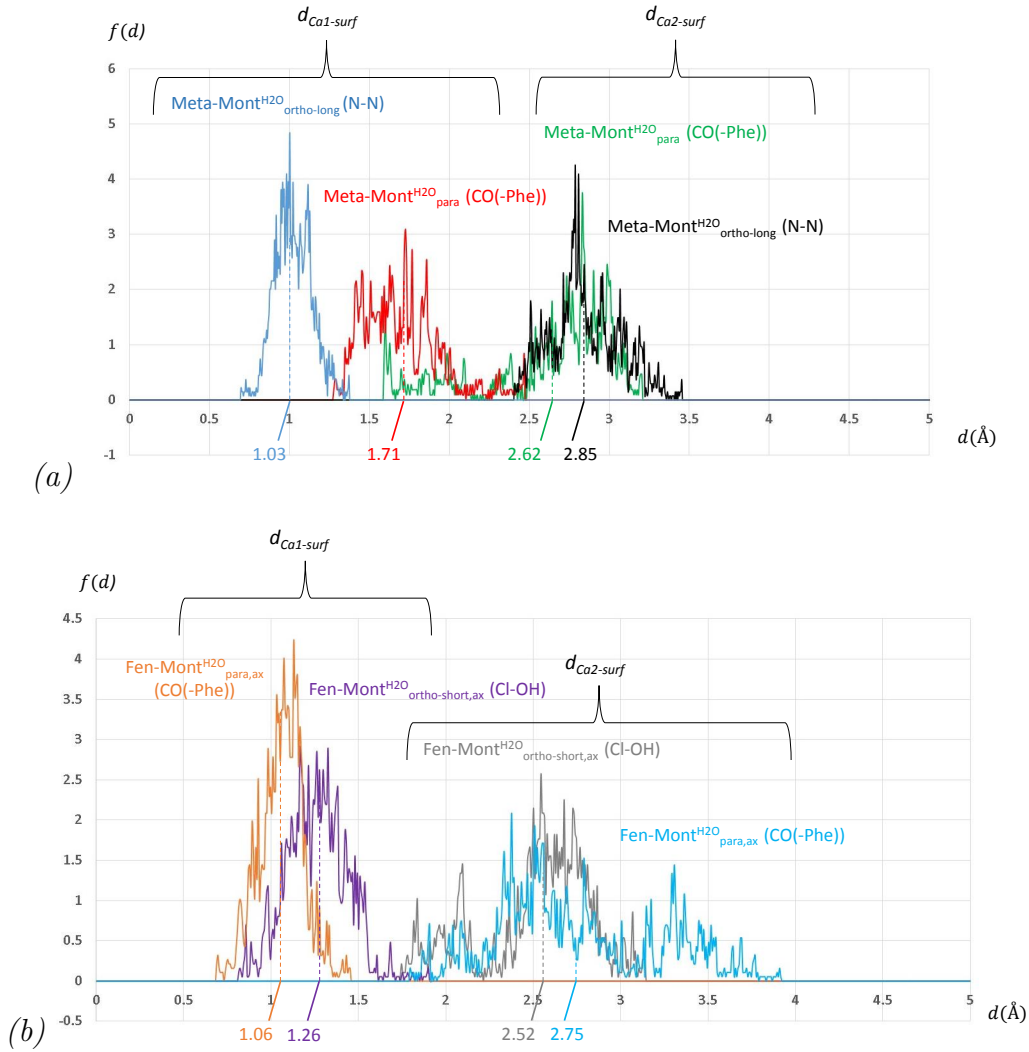


Figure VII.4: Distribution functions $f(d)$ of the calcium cation distances to the surface d_{Ca1-O_b} and d_{Ca2-O_b} (Å): (a) in Meta-Mont^{H₂O}_{ortho} (N-N) (blue and black) and Meta-Mont^{H₂O}_{para,ax} (CO(-Phe)) (red and green) ; (b) in Fen-Mont^{H₂O}_{para,ax} (CO(-Phe)) (orange and light blue) and in Fen-Mont^{H₂O}_{ortho,ax} (Cl-OH) (purple and grey) respectively.

geometric parameters around substitutions in particular d_{Mg-O_h} ($\approx +0.05$ Å) in Fen-Mont^{H₂O}_{ortho,ax} (Cl-OH).

The solvation presents a way stronger influence on the interlayer cations. Two types of cation solvations have been observed in clay minerals [276]: cations can be hydrated by several water molecules while they remain adsorbed on the clay surface (inner hydration sphere), or can be in a totally hydrated state, surrounded by water molecules and detached from the surface (outer hydration sphere).

In the simulations performed in this work, Ca2 is solvated in an inner hydration sphere composed of 5 H₂O molecules, arranged in a square-based pyramid as shown in Figure VII.5. At the same time, the $\langle d_{Ca2-O_b} \rangle$ distance strongly increases to an average value

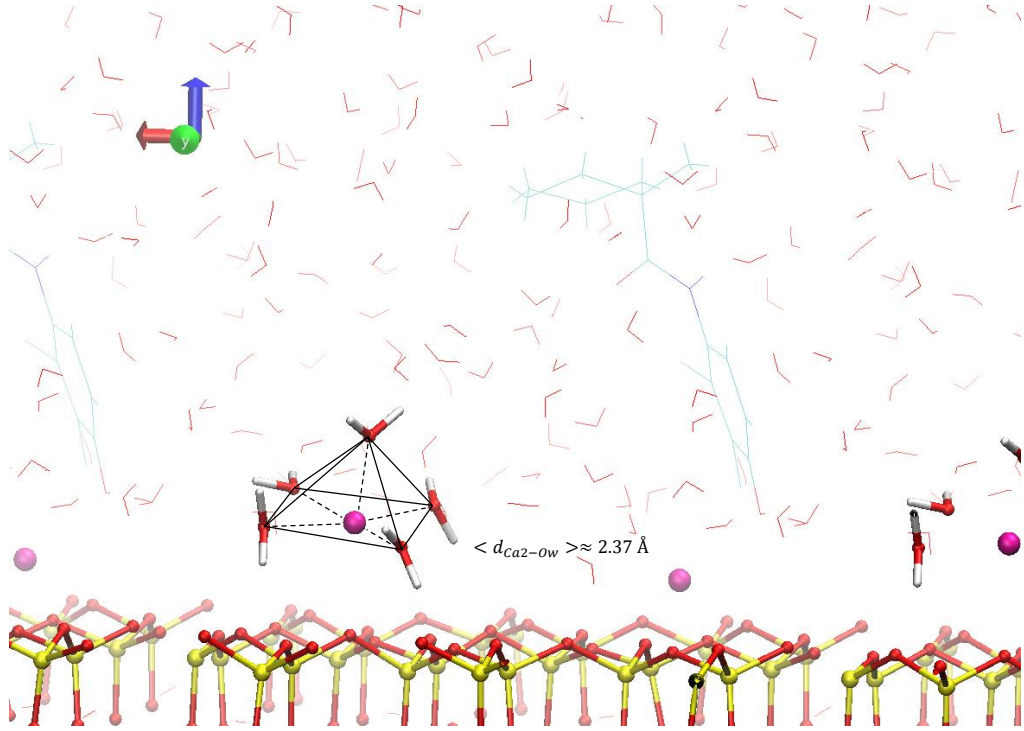


Figure VII.5: Snapshot of the Fen-Mont $^{H_2O}_{ortho,ax}$ (Cl-OH) trajectory. Fenhexamid and all H₂O molecules are represented in lines except the Ca2 inner hydration sphere (square-based pyramid) which is in ball and stick representation, as well as the surface and both cations.

between 2.52 and 2.85 Å depending on the simulation (see Figure VII.4), compared to $d_{Ca2-O_b} = 0.228 - 0.247$ Å in the ϕ_{solid}^{dry} isomers.

The average distances of the water molecule oxygens to Ca2 ($\langle d_{Ca2-O_w} \rangle$) in Meta-Mont $^{H_2O}_{ortho}$ (N-N), Meta-Mont $^{H_2O}_{para}$ (CO(-Phe)), Fen-Mont $^{H_2O}_{para,ax}$ (CO(-Phe)) and Fen-Mont $^{H_2O}_{ortho,ax}$ (Cl-OH) are 2.35, 2.39, 2.37 and 2.38 Å respectively, reported as $d_{Ca2-O_w} \approx 2.37$ Å on Figure VII.5. These values have been calculated on the period of time when Ca2 is solvated within the inner hydration sphere: during approximately 8, 7, 7 and 6 ps respectively.

$\langle d_{Ca1-O_b} \rangle$ increases in a lower proportion than $\langle d_{Ca2-O_b} \rangle$ as the interaction with the pesticide reduces Ca1 availability for interaction with water molecules. Indeed, $\langle d_{Ca1-O_b} \rangle$ goes from 1.03 to 1.71 Å, while it ranges from 0.471 to 0.515 Å in ϕ_{solid}^{dry} . The different values of $\langle d_{Ca1-O_b} \rangle$ might be due to the nature pesticides and the binding sites. However, Meta-Mont $^{H_2O}_{para}$ (CO(-Phe)) and Fen-Mont $^{H_2O}_{para,ax}$ (CO(-Phe)) are both complexed on the carbonyl oxygen and present very different $\langle d_{Ca1-O_b} \rangle$ distances: 1.71 and 1.06 Å respectively. This difference is mainly due to the local hydration state of Ca1. Indeed, the more Ca1 interacts with water, the longer $\langle d_{Ca1-O_b} \rangle$ is:

- In Fen-Mont $^{H_2O}_{para,ax}$ (CO(-Phe)), Ca1 interacts with only 1 H₂O molecule ($\langle d_{Ca1-O_b} \rangle = 1.06$ Å).

Systems	Complexations	d_{Ca1-O_b}	d_{Ca2-O_b}	d_{Ca1-O_h}	d_{Ca2-O_h}	d_{Al-O_a}	d_{Al-O_h}
ϕ^{dry}_{solid}							
Meta-Mont(2) <i>ortho-long</i>	N-N	0.515	0.228	2.625	2.347	1.971	1.939
Meta-Mont(4) <i>para</i>	CO(-Phe)	0.471	0.229	2.575	2.347	1.971	1.939
Fen-Mont(1) <i>para,ax</i>	CO(-Phe)	0.478	0.247	2.611	2.354	1.971	1.939
Fen-Mont(9) <i>ortho-short,ax</i>	Cl-OH	0.491	0.234	2.576	2.357	1.971	1.939
H_2O ϕ^{solid}							
Meta-Mont <i>ortho-long</i>	N-N	1.057	2.774	3.287	5.599	1.987	1.940
Meta-Mont <i>para</i>	CO(-Phe)	1.890	2.981	4.230	5.271	1.993	1.938
Fen-Mont <i>para,ax</i>	CO(-Phe)	1.124	2.803	3.407	5.071	1.989	1.930
Fen-Mont <i>ortho-short,ax</i>	Cl-OH	1.248	2.710	3.453	5.494	1.970	1.950
Systems	Complexations	d_{Mg-O_a}	d_{Mg-O_h}	d_{H-O_h}	d_{Si-O_a}	d_{Si-O_b}	
ϕ^{dry}_{solid}							
Meta-Mont(2) <i>ortho-long</i>	N-N	2.083	2.057	0.978	1.639	1.629	
Meta-Mont(4) <i>para</i>	CO(-Phe)	2.084	2.057	0.978	1.639	1.629	
Fen-Mont(1) <i>para,ax</i>	CO(-Phe)	2.084	2.058	0.978	1.639	1.629	
Fen-Mont(9) <i>ortho-short,ax</i>	Cl-OH	2.084	2.056	0.978	1.639	1.629	
H_2O ϕ^{solid}							
Meta-Mont <i>ortho-long</i>	N-N	2.054	2.092	1.000	1.643	1.636	
Meta-Mont <i>para</i>	CO(-Phe)	2.082	2.064	0.995	1.643	1.630	
Fen-Mont <i>para,ax</i>	CO(-Phe)	2.093	2.058	0.996	1.637	1.634	
Fen-Mont <i>ortho-short,ax</i>	Cl-OH	2.080	2.105	0.997	1.638	1.631	

Table VII.2: Distances between the calcium cations and the basal oxygens O_b of the surface, from the last $\phi^{H_2O}_{solid}$ snapshots and the ϕ^{dry}_{solid} isomers, displayed in Å.

- On the contrary, in Meta-Mont^{H₂O}_{para}(CO(-Phe)), 2 H₂O molecules solvate Ca1 ($\langle d_{Ca1-O_b} \rangle = 1.71 \text{ \AA}$).

In Meta-Mont^{H₂O}_{ortho}(N-N), Ca1 is complexed with one water molecule as in Fen-Mont^{H₂O}_{para,ax}(CO(-Phe)) with a similar $\langle d_{Ca1-O_b} \rangle$ (1.03 Å), whereas the complexation sites are different. Concerning Fen-Mont^{H₂O}_{ortho,ax}(Cl-OH), two water molecules hydrate Ca1 as in Meta-Mont^{H₂O}_{para}(CO(-Phe)) but with a shorter $\langle d_{Ca1-O_b} \rangle$ distance (1.26 Å). In this case, Ca1 availability to water is higher, this might be due to the *ortho* – *short* orientation of the pesticide.

It is worthwhile to note that in dry systems, the elongation of d_{Ca1-O_b} originating from the interaction of Ca1 with the pesticide, makes Ca2 get slightly closer to the surface while a totally opposite behavior occurs in the hydrated systems: Ca2 is highly solvated and gets twice further from the surface than Ca1.

We have seen the hydration influence on four pesticide isomers presenting different orientations and complexation sites with the cation. The next section will focus on the desorption process of the Fen hydrated pesticide.

VII.B Pesticide desorption process from a hydrated - Ca -montmorillonite surface

Along the foregoing chapters, atrazine, metamitron and fenhexamid have been studied considering the complexes they form in presence of one or two Na⁺ or Ca²⁺ in ϕ_{gas} . The second step has been to adsorb the pesticide on a dry Ca-montmorillonite surface. Then the solvation of these species over the surface has been considered. This methodology has been followed in order to understand the influence of each improvement of the model on the interaction.

The results from the previous chapters show that complexation energies of Meta and Fen with Ca²⁺ are very similar whether in ϕ_{gas} ($\approx -140 \text{ kcal/mol}$) or in ϕ_{solid}^{dry} ($\approx -40 \text{ kcal/mol}$). However, Fen seems more challenging to study as it can adopt a lot of different conformations and orientations towards the surface compared to Meta (see Chapter V). In this final section, fenhexamid has been chosen to study pesticide desorption from the hydrated clay surface. Indeed only one system has been simulated because of the time consumption represented by a single Umbrella Sampling in DFT, which is the method we will describe and use hereafter (the heavy cost of this work will be developed with the results in a further section).

The aim of this work is to quantify the free energy barrier that needs to be overcome to desorb fenhexamid from the watered Ca-montmorillonite.

To accomplish this desorption, an available method, Umbrella Sampling, consists in running a series of parallel biased molecular dynamics to move the system from a thermodynamical state to another corresponding to Fen adsorbed on Mont and desorbed respectively. This methodology is used to explore the free energy surface of a system along a chosen reaction coordinate, and allows to cross energy barriers. In the next section we will briefly present this method before a description of the MD trajectories and a discussion of the results.

VII. B.1 Umbrella Sampling

Umbrella Sampling is a biased exploration method of the free energy surface of a system, along a specific reaction coordinate $\xi(\mathbf{r}^N)$. This coordinate is arbitrary, can be mono- or multi-dimensional, and is a function of the N atomic positions \mathbf{r}^N of the system. The principle is to run several MD trajectories correctly distributed along ξ in order to explore the free energy surface between two thermodynamic states step by step. Each MD is biased with a harmonic potential $V_{bias}^i(\xi)$ and thus explores a “window” of free energy surface, centered on an arbitrary value of ξ . One of the main requirements of this method is a good overlap between all consecutive windows, to recover the surface shape.

This biased exploration of a window on the free energy surface is called Potential of Mean Force (PMF). It was first introduced by J. G. Kirkwood in 1935 [277] and improved later by G. M. Torrie and J. P. Valleau in 1977 [278,279] to enhance surface exploration by performing several MD trajectories, biased with harmonic potentials on the ξ coordinate, instead of a unique MD simulation on a very long time. PMF is the method of choice for the exploration of energy barriers.

The Helmholtz free energy (A), in PMF approach, is defined as:

$$A(\xi) = A(\xi_0) - k_B T \ln \left(\frac{P(\xi)}{P(\xi_0)} \right) \quad (\text{VII.1})$$

with k_B the Boltzmann constant, T the temperature, ξ_0 and thus $A(\xi_0)$ defined arbitrary as references for the calculation of the energy difference, $P(\xi)$ and $P(\xi_0)$ the respective probability functions of the system and of the reference, obtained as the average distribution:

$$P(\xi) = \frac{\int \delta[\xi'(\mathbf{r}^N) - \xi] e^{-\beta U(\mathbf{r}^N)} d\mathbf{r}^N}{\int e^{-\beta U(\mathbf{r}^N)} d\mathbf{r}^N} \quad (\text{VII.2})$$

with $\beta = 1/(k_B T)$ and $U(\mathbf{r}^N)$ the internal energy of the system.

$P(\xi)d\xi$ can be interpreted as the probability of finding the system in a small interval $d\xi$ around ξ .

The harmonic biased potential $V_{bias}^i(\xi)$ acting on the chosen coordinate ξ is expressed as:

$$V_{bias}^i(\xi) = \frac{1}{2} k (\xi - \xi_0^i)^2 \quad (\text{VII.3})$$

where k is the harmonic constant and ξ_0^i the value of ξ around which the i biased MD will explore the free energy surface.

Therefore the PMF of a window i is written as in Eq.(VII.1) in which $V_{bias}^i(\xi)$ is introduced:

$$A_i(\xi) = A(\xi_0) - k_B T \ln(P_{bias}^i(\xi)/P(\xi_0)) - V_{bias}^i(\xi) + F_i \quad (\text{VII.4})$$

where the biased probability distribution of a window $P_{bias}^i(\xi)$ is written as:

$$P_{bias}^i(\xi) = \frac{\int \delta[\xi'(\mathbf{r}^N) - \xi] e^{-\beta [U(\mathbf{r}^N) + V_{bias}^i(\xi')]} d\mathbf{r}^N}{\int e^{-\beta [U(\mathbf{r}^N) + V_{bias}^i(\xi')]} d\mathbf{r}^N} \quad (\text{VII.5})$$

and can be rewritten [280]:

$$\begin{aligned} P_{bias}^i(\xi) &= e^{-\beta V_{bias}^i(\xi)} P(\xi) \langle e^{-\beta V_{bias}^i(\xi)} \rangle^{-1} \\ &= e^{-\beta V_{bias}^i(\xi)} P(\xi) e^{+\beta F_i} \end{aligned} \quad (\text{VII.6})$$

where $P(\xi)$ is the non-biased probability distribution (from equation (VII.1)). F_i constants can be identified from equation (VII.6):

$$e^{-\beta F_i} = \langle e^{-\beta V_{bias}^i(\xi)} \rangle \quad (\text{VII.7})$$

The physical meaning of this constant is the free energy brought into the system by the introduction of the harmonic potential $V_{bias}^i(\xi)$.

Thus the F_i constant takes a specific value for each window i and needs to be determined in order to get a consistent and continuous free energy surface. As illustrated on Figure VII.6, each window gives a section of the PMF, centered on a given value ξ_0^i , and each piece of the surface is shifted in free energy compared to the others. F_i corresponds to the shift between a PMF window, and the complete $A(\xi)$. A good overlap between consecutive windows is essential. One of the most popular method to find the F_i and correct the shifts is the Weighted Histogram Approximation Method (WHAM) [281].

The WHAM is an iterative method to calculate the F_i constants of all the biased simulations and get the total corrected PMF simultaneously. First the total PMF is expressed from equation (VII.6):

$$P(\xi) = e^{+\beta V_{bias}^i(\xi)} P_{bias}^i(\xi) e^{-\beta F_i} \quad (\text{VII.8})$$

and doing an average of the sum of all the non-biased distribution of every windows:

$$P(\xi) = \frac{\sum_{i=1}^N P(\xi) n_i e^{-\beta[V_{bias}^i(\xi) - F_i]}}{\sum_{j=1}^N n_j e^{-\beta[V_{bias}^j(\xi) - F_j]}} = \frac{\sum_{i=1}^N n_i P_{bias}^i(\xi)}{\sum_{j=1}^N n_j e^{-\beta[V_{bias}^j(\xi) - F_j]}} \quad (\text{VII.9})$$

with N the number of windows (MD simulations), n_i and n_j the number of data statistically independant to build the biased distribution $P_{bias}^i(\xi)$. Then, the F_j constant may be determined using:

$$e^{-\beta F_j} = \sum_{\xi=\xi_{min}}^{\xi_{max}} e^{-\beta V_{bias}^j(\xi)} P(\xi) \quad (\text{VII.10})$$

ξ_{min} and ξ_{max} being the width of the j window.

Therefore, equations (VII.9) and (VII.10) are solved simultaneously by an iterative process, and allow to find the F_j , the mean canonical probability distribution $P(\xi)$ and the associated free energy surface $A(\xi)$ using equation (VII.1). In the following, the relative free energy surface in Section VII. B.3, Figure VII.7.(a) has been obtained with the WHAM method, as it is implemented in the code of Alan Grossfield [282].

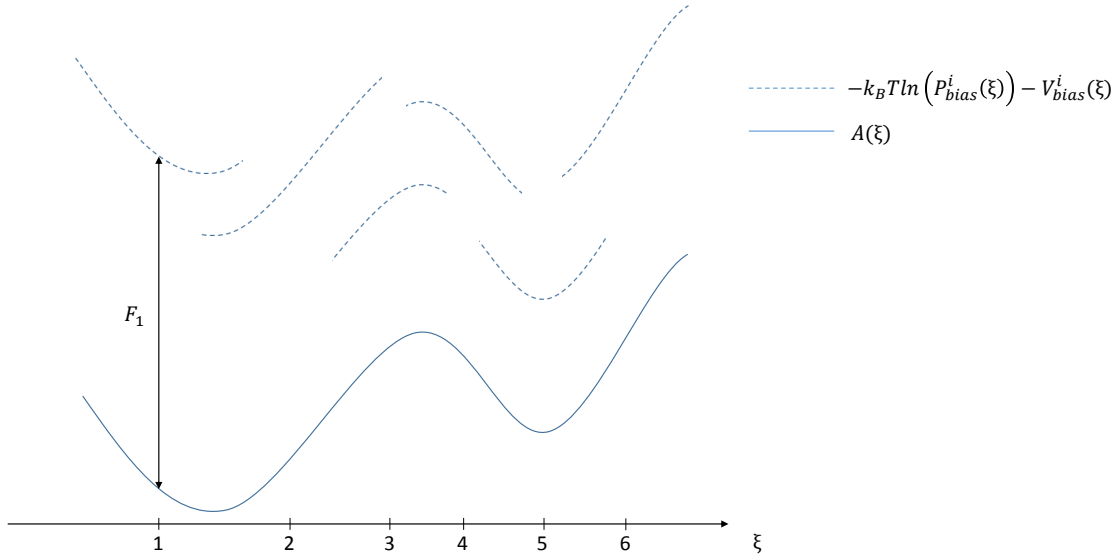


Figure VII.6: Representation of the WHAM method, applied to 6 windows of PMF on the reaction coordinate ξ . The F_i constant that must be determined in equation (VII.10) corresponds to the energy shift between a window of PMF (dotted line) and the complete free energy curve $A(\xi)$ (solid line). F_1 constant, associated to window 1, is represented as an example.

VII. B.2 Desorption of fenhexamid

Structures and parameters

The aim of this section is to quantify the free energy barrier to cross to desorb fenhexamid from a hydrated Ca-montmorillonite surface in the Fen-Mont $_{para,ax}^{H_2O}$ (**CO(-Phe)**) isomer which corresponds to the lowest-energy type of complexation that has been found in ϕ_{solid}^{dry} .

Umbrella sampling in DFT on a system containing more than 600 atoms is computationally extremely expensive. As displayed in Table VII.3 in the next section, 11 MD trajectories have been necessary to produce the free-energy surface exploration that is presented hereafter. Those trajectories represent 177 ps of dynamics. With a timestep of 0.1125 fs (4.5 u.a), 100 processors running in parallel and taking 30 s to produce each step, 1 ps of simulation is done in $\approx 8,900$ steps and costs $\approx 7,400$ hours of computational time. Therefore, 177 ps of parallel simulations cost approximately 1,300,000 hours. In real time, around 20,000 steps of a trajectory can be computed in one week, which represent 2.25 ps of simulation.

Careful considerations have then been taken to choose the reaction coordinate: the pesticide must start from a thermodynamical state where it is adsorbed on the Ca-montmorillonite, and follow a coordinate ξ increasing the distance to the surface to reach a second state in which it is desorbed.

In order to reproduce the physico-chemical behavior of the real system, the reaction coordinate ξ should not constrain too many degrees of freedom. The chosen coordinate in the present study is the z coordinate of the fenhexamid center of mass (com) (noted $\xi_{z(com)}$), which has to increase to desorb the pesticide. Let us emphasize that the position of Ca1, the calcium cation in interaction between the pesticide and the surface, is free to move. Ca1 is not constrained by the reaction coordinate. Indeed, the desorption process of fenhexamid is unknown and in particular, the implication of Ca1. In a first hypothesis, Ca1 is suspected to be desorbed in concert with the pesticide. As a matter of fact, 1 or 2 H₂O molecules interact with Ca1 in the previous Fen-Mont hydration trajectories (see Section VII.A). In a second hypothesis, Fen desorption process is considered separately from Ca1 behavior. This more general assumption has been chosen.

The last snapshot of Fen-Mont $_{para,ax}^{H_2O}$ (**CO(-Phe)**) trajectory in the hydration study (VII.A) has been chosen as the starting structure for window 1 (see Table VII.3) and has been modified by increasing the center of mass of the pesticide for other windows. Consequently Ca2 starts in an inner hydration sphere of 5 H₂O molecules in all simulations. The same simulation and thermostat parameters as in the previous section have been used, leading to trajectories at an approximate average temperature of 330 K as

well. However, μ is set to 500 u.a. which allows to increase the timestep to 0.1125 fs (4.5 u.a.).

From a window to another, the position of the pesticide in the interlayer has been shifted on the z axis regarding the value of $\xi_{z(com)}$. When it is necessary, water molecules overlapping with Fen have also been moved, but never between the pesticide and the surface to avoid any supplementary bias in the desorption process.

VII. B.3 Free energy surface exploration

Figure VII.7.(a) presents the relative free energy ($A(\xi)_{rel}$) profile that has been obtained with the 11 overlapping windows of exploration (indexed i) for $14 \leq \xi_{z(com)} \leq 20$ Bohr, and with the code of Alan Grossfield to apply the WHAM method [282]. Every single window i is represented by the distribution functions $P^i(\xi)$ on Figure VII.7.(b) and their associated parameters displayed in Table VII.3: the reaction coordinate $\xi_{z(com)}^i$, harmonic potential constant k_i and time of simulation t_i . As in the previous study on Pest-Mont hydration, a minimum of 4 ps has been removed from every simulations as thermalization time.

i	$\xi_{z(com)}^i$ (Bohr)	k_i (kcal.mol ⁻¹ .Bohr ⁻²)	t_i (ps)
1	14.71	4.0	20
2	15.37	8.0	20
3	15.60	32.0	13
4	16.03	4.0	20
5	16.80	16.0	12
6	16.85	32.0	13
7	17.10	32.0	16
8	17.36	16.0	25
9	18.30	16.0	14
10	18.68	4.0	11
11	20.00	4.0	13

Table VII.3: Parameters of the 11 biased CPMD trajectories. i is the window index, $\xi_{z(com)}^i$ is the arbitrary value of the reaction coordinate around which the harmonic potential must oscillates (cartesian z coordinate of the molecular center of mass), k_i is the associated harmonic constant and t_i the time of the simulation (ps).

The free energy profile shows three successive wells such as:

$$A(\xi)_{rel}(\textbf{Well 1}) < A(\xi)_{rel}(\textbf{Well 2}) < A(\xi)_{rel}(\textbf{Well 3}).$$

Well 1 ($A_{rel} = 0.0$ kcal/mol) and **2** ($A_{rel} \approx 1.5$ kcal/mol), are centered on $\xi_{z(com)} \approx 14.5$ Bohr and $\xi_{z(com)} \approx 16 - 16.5$ Bohr respectively, and separated by an energy barrier of $\Delta A_{b1} \approx +3$ kcal/mol. Then, a second energy barrier around $\Delta A_{b2} \approx +4.5$ kcal/mol

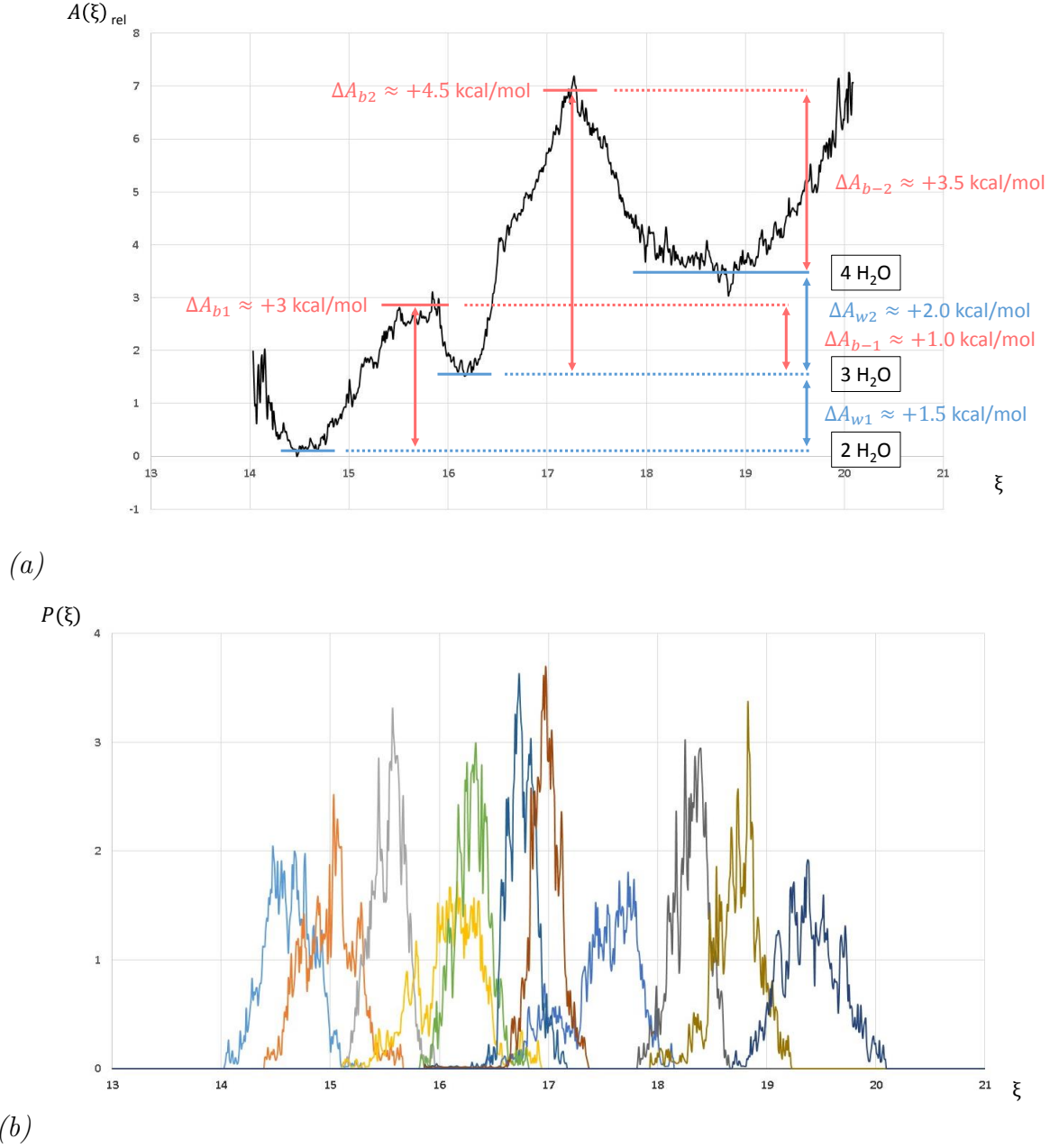


Figure VII.7: Relative free energy surface $A(\xi)_{rel}$ (kcal/mol) (a), where ΔA_w values are the free energy differences between consecutive wells and where ΔA_b and ΔA_{b-} are the relative energies necessary to cross barriers, for the desorption and adsorption process respectively. The probability density functions $P(\xi)$ of the 11 windows are displayed in (b), each color corresponding to a different window i . ξ is the z coordinate of the pesticide center of mass.

has been found between **Well 2** and **3**. **Well 3** ($A_{rel} \approx 3.5$ kcal/mol) is centered on $\xi \approx 18.5 - 19$ Bohr.

Concerning the energy barrier accuracy, two points can be risen:

- Umbrella sampling in DFT on a system containing more than 600 atoms is very expensive to compute. Then, the trajectories might not be long enough ($t_i \leq 20$ ps most of the time), and led to noisy distribution functions $P(\xi)$ and free-energy profile $A(\xi)$ (see Figure VII.7).
- Moreover, the free energy barriers are more difficult to explore than wells.

The last snapshots of these three simulations are represented on Figure VII.8 and all distances concerning the solvation of the cations and the complexation are reported in Table VII.4. Examining these structures, it is clear that each barrier corresponds to the insertion of a H₂O molecule between the pesticide and the surface to hydrate Ca1:

- **Well 1** is mainly explored within window 1. In this case, Fen is adsorbed on Ca1 at an average distance $\langle d_{Ca1-O} \rangle = 2.3$ Å and is located at an average $\langle d_{Ca1-O_b} \rangle = 1.6$ Å from the surface. Ca1 is hydrated with 2 water molecules at distances from 2.2 to 2.4 Å during the trajectory.
At the same time, $\langle d_{Ca2-O_b} \rangle$ increases a lot (around 3 Å) compared to the previous study on Fen-Mont^{H₂O}_{para,ax}. Ca2 goes from an inner (5 H₂O) to an outer hydration sphere composed of 8 water molecules at a mean distance of 2.6 Å from the cation. This solvation state occurs in the last 2 picoseconds of the trajectory (over 20 ps in total). Distances displayed on Figure VII.8.(a) have been computed within these 2 ps.
- **Well 2** has been explored in window 4. The hydration states of Ca1 and Ca2 represented in Figure VII.8.(b) are reached after 3 ps of simulation and kept all along the trajectory. Average distances on the Figure have been calculated within the 17 remaining picoseconds. Fen is still complexed on the cation as in **Well 1** ($\langle d_{Ca1-O} \rangle = 2.2$ Å), however $\langle d_{Ca1-O_b} \rangle$ is longer by 0.8 Å. It shows that, as the molecule distance to the surface gets longer, the Fen-Ca1 entity is desorbed. Consequently, a third H₂O molecule is able to interact with Ca1, underneath the pesticide. Ca2 is in an inner hydration sphere (5 H₂O) as in Fen-Mont^{H₂O}_{para,ax} (see Figure VII.5), and $\langle d_{Ca2-O_b} \rangle = 2.6$ Å.
- **Well 3** has been explored within window 10. As can be seen on Figure VII.8.(c), Ca1 has lost the interaction with Fen ($\langle d_{Ca1-O} \rangle = 3.7$ Å) and is solvated by 4 H₂O molecules, two of which are between the carbonyl oxygen and the cation. Unlike in

Well 2, Ca1 stays close to the surface ($\langle d_{Ca1-O_b} \rangle = 1.8 \text{ \AA}$) comparable with **Well 1**. This point will be discussed in the following. In this window, Ca2 reaches an outer hydration sphere (6 H₂O), and a shorter $\langle d_{Ca2-surf} \rangle$ than in **Well 1** (3.9 \AA). Ca2 is totally hydrated by the 6 water molecules after 9 ps, and average distances in Figure VII.8.(c) have been computed after this time (within 2 ps).

i	$\langle d_{Ca1-O_b} \rangle$	$\langle d_{Ca2-O_b} \rangle$	$\langle d_{Ca1-O} \rangle$	$\langle d_{Ca1-O_w} \rangle$	$\langle d_{Ca2-O_w} \rangle$	$\langle d_{Ca1-Ca2} \rangle$
1	1.6	5.7	2.3	-	2.6	12.3
4	2.4	2.6	2.2	-	2.4	10.6
10	1.8	3.9	3.7	-	2.4	9.9
Fen-Mont ^{H₂O} _{para,ax}	1.06	2.75	2.21	-	2.37	-

Table VII.4: Average intercation distances and average distances from the calcium cations Ca1 and Ca2 to the basal, water and carbonyl oxygens in windows 1, 4 and 10. The same distances from Fen-Mont^{H₂O}_{para,ax} are reported for comparison. All distances are in \AA .

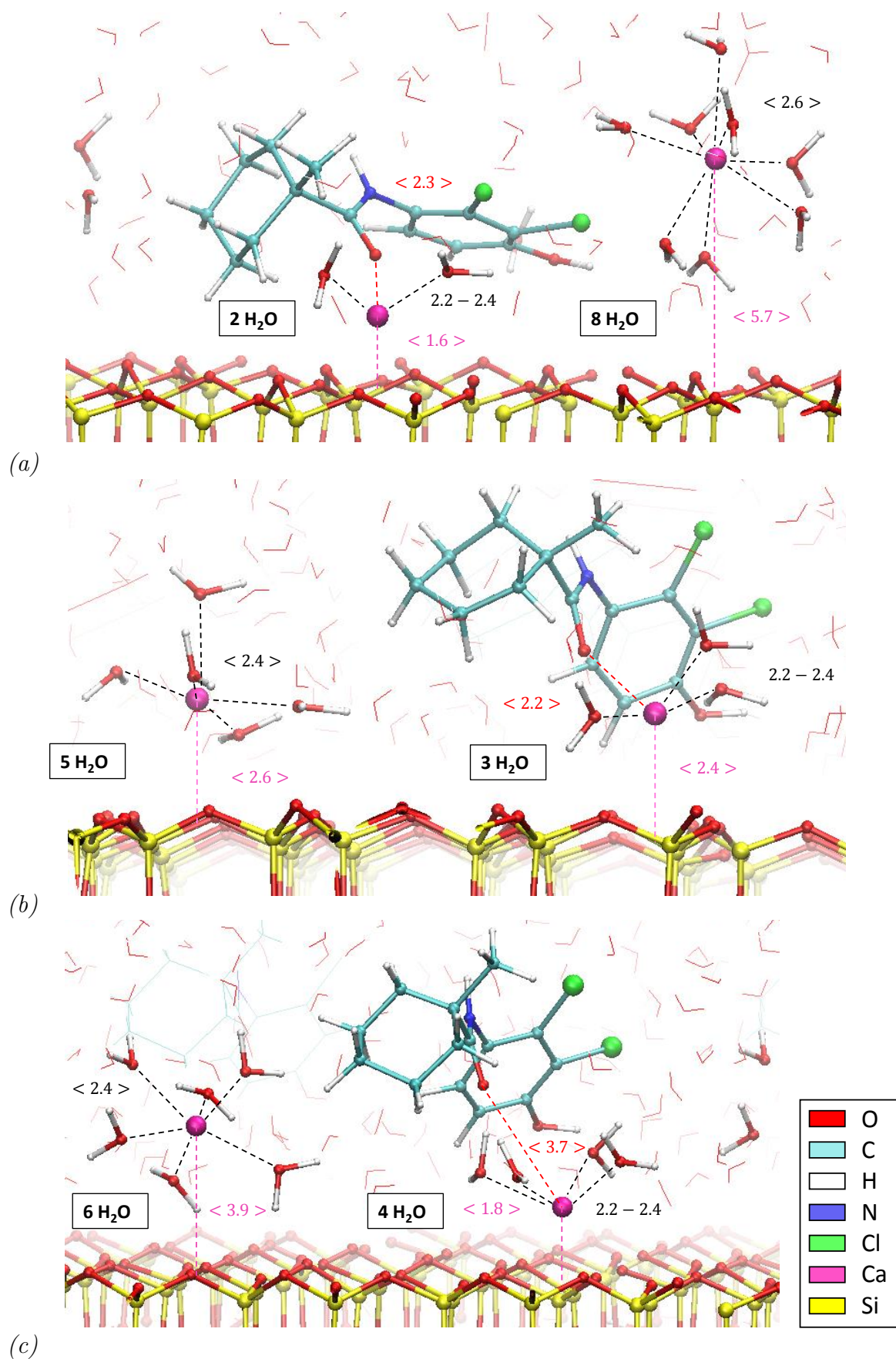


Figure VII.8: Last snapshots of windows 1 (a), 4 (b) and 10 (c) where distances are displayed in Å.

VII. B.4 Discussion

Thus the desorption energy profile in Figure VII.7.(a) presents three successive wells corresponding to higher and higher hydration state of Ca1 for an increasing ξ : $A(\xi)_{rel}(\text{Well 1})_{\text{Ca1}(\text{H}_2\text{O})_2} < A(\xi)_{rel}(\text{Well 2})_{\text{Ca1}(\text{H}_2\text{O})_3} < A(\xi)_{rel}(\text{Well 3})_{\text{Ca1}(\text{H}_2\text{O})_4}$. However the heights of the barriers between each well are low: $\Delta A \approx +3$ and $+4$ kcal/mol, knowing that DFT methods present an accuracy of approximately 1 kcal/mol. Each barrier corresponds to the insertion of a single water molecule under the pesticide. The hydration study of the previous section shows an increase of $\langle d_{\text{Ca1}-\text{O}_b} \rangle$ due to solvation. At the same time, the distance between the pesticide (complexed on Ca1) and the surface elongates, and thus favor water inclusion.

Indeed from **Well 1** to **Well 2**, Fen desorption seems consistent as the distance between the carbonyl oxygen and the surface increases, while Ca1 gets farther from the surface as well ($\langle d_{\text{Ca1}-\text{O}_b} \rangle = 1.6$ Å in **Well 1** and 2.4 Å in **Well 2**), and keeps a similar binding distance to the molecule as $\langle d_{\text{Ca1}-\text{O}} \rangle = 2.2 - 2.3$ Å in both trajectories (which is equivalent to the $\langle d_{\text{Ca1}-\text{O}} \rangle$ in Fen-Mont^{H₂O}_{para,ax} (2.21 Å) in the previous section). However, the trajectory in **Well 3** does not present the same behavior: the complexation between Ca1 and the carbonyl oxygen is weaker ($\langle d_{\text{Ca1}-\text{O}} \rangle = 3.5$ Å), and Ca1 stays adsorbed on the surface at an equivalent distance as in the first well: $\langle d_{\text{Ca1}-\text{O}_b} \rangle = 1.6$ and 1.8 Å in **Well 1** and **3** respectively. Nevertheless, the trajectory to explore window 10 (**Well 3**) has run for 11 ps only, which is approximately twice shorter than windows 1 and 4. Thus, if the simulation time is extended, Ca1 could either stay adsorbed (unlikely to occur) or desorb:

- to acquire first an inner hydration sphere before being fully solvated ;
- to be engaged in a hydrated complex with the pesticide.

As the desorption process is unknown, it is impossible to affirm that the cation should be desorbed in concert with the pesticide or not, both ways need to be considered.

One of the main question risen here is the possible occurrence of two different processes for the same reaction coordinate ξ . Indeed, all simulations have been run in parallel and thus have starting structures where the pesticide is more and more desorbed, but Ca1 is always connected to the surface. For small ξ values (**Well 1** and **2**), trajectories start with a structure where the pesticide is adsorbed with the cation on the surface. On the contrary, for larger ξ values, Fen tends to desorb without dragging Ca1 away. It brings us back to the first problematic presented in the Umbrella Sampling method: the choice of a

suitable ξ . Indeed, as only the position of fenhexamid center of mass has been constrained, the Ca1 calcium cation is free to desorb or to stay adsorbed on the surface.

One of the tracks to follow this work would be to perform a new set of trajectories for $\xi > 16$ Bohr from **Well 2** last snapshot (window 4), trying to desorb the Fen-Ca1 complex from the surface.

Concerning the solvation of Ca2, its hydration state is different in all wells: it presents coordinations of 5 H₂O (square-based pyramid) in **Well 2** as in $\phi_{solid}^{H_2O}$, of 6 H₂O (octahedron) in **Well 3**, and 8 H₂O molecules (distorted square antiprism [283,284]) in **Well 1**. Calcium cation hydration has been largely studied in literature both theoretically and experimentally [284–286]. Solvation of Ca²⁺ produces stable highly symmetric Ca(H₂O)_{*n*}²⁺ clusters, up to *n* = 8 molecules ; beyond, for *n* = 9, cluster dissociates to get back to a Ca(H₂O)₈²⁺ form [283]. Therefore, hydration of Ca2 by 8 H₂O molecules is the maximum stable solvation state (**Well 1**). However the most favored coordination is the octahedron (*n* = 6), but in general calcium cation hydration structure is highly variable [283,287,288]. The water molecule average distances obtained in **Well 2** and **3** ($\langle d_{Ca2-O_w} \rangle = 2.4$ Å) are in good agreement with the values obtained by Bako *et al.* at the CP/BLYP and DFT/BLYP levels: ≈ 2.40 and 2.41 Å respectively for Ca(H₂O)₅²⁺ and ≈ 2.42 Å for Ca(H₂O)₆²⁺. For Ca(H₂O)₈²⁺ they obtain a comparable distance: $d_{Ca2-O_w} = 2.510$ Å than the one obtained in **Well 1** (≈ 2.6 Å). Geometry optimisations of Ca(H₂O)_{*n*}²⁺ clusters at the DFT/B3LYP and MP2 levels in the paper of Megyes *et al.*, showed distances for these three forms: 2.360 Å (B3LYP) and 2.370 Å (MP2) (*n* = 5), 2.401 Å (*n* = 6) and 2.482 Å (*n* = 8) generally shorter than those obtained by X-ray diffraction ($2.43 - 2.46$ Å) [284].

More recently, a force-field (CLAYFF) combined with a water model (SPC/E) show a first hydration shell of 7 molecules for calcium on Ca-montmorillonite, with 13.7 Å of interlayer space. This interlayer being slightly larger than the experimental value [289]. This study also showed that Ca²⁺ prefers an outer hydration sphere, which is consistent with results obtained for Ca2 in **Well 1** and **Well 3**. More generally, calcium hydration spheres in montmorillonite highly depends on the size of the interlayer space (the clay swelling), temperature, pressure, pH and cations concentration in water [285,290].

Literature provides several studies on behavior of simple molecules in montmorillonite interlayer at different hydration levels [155,291,292]. However, to the best of our knowledge, a very few publications treat the adsorption/desorption process of organic molecules on montmorillonite surfaces. Recently, Mignon *et al.* published a comparable study of adsorbed cytosine on a hydrated Na-montmorillonite surface by means of short constraint MD simulations at 300 K (NVT ensemble) [156]. The distance between the carbonyl carbon of cytosine and a magnesium atom within the surface being controlled, noted d_{C2-Mg} in the original paper. The results of this paper show the influence of the molecule orien-

tation on the hydrated state of Na^+ and how sodium cation can desorb via its interaction with cytosine carbonyl oxygen and water. Similarly to fenhexamid in the present work, cytosine is complexed via its carbonyl oxygen to the montmorillonite surface, however, the surface cation is monovalent: Na^+ . Cytosine can be parallel or orthogonal to the surface regarding the aromatic ring orientation, similarly to atrazine (PARA, ORTHO), metamitron (*para*, *ortho* – *long*) and fenhexamid to a lesser extent (*para*, *ortho* – *short*). Initially, cytosine adopts a parallel orientation with molecule-surface distance below 4.9 Å and stays complexed with the cation. At larger distances, the molecule takes a nearly orthogonal orientation, Na^+ interacting on the carbonyl oxygen and the cycle nitrogen or being fully hydrated.

That study presents several similar aspects with the present section: desorption of an organic molecule in interaction with a surface montmorillonite cation through a carbonyl oxygen binding site. Then, both methods employ short constraint MD simulations allowing free motion of the molecule with respect to the reaction coordinate.

In the paper of Mignon *et al.* [156], cytosine and Na^+ desorption is observed with the increasing distance between the base and the surface, followed by a rotation from a parallel to an orthogonal orientation. These observations are in good agreement with the hypothesis of a desorption of the Fen- Ca^{2+} complex. In our case, a larger cation charge could favor either an outer hydration sphere, or a complexation with the pesticide.

The main innovation of this CP/DFT work on fenhexamid desorption from Ca-montmorillonite, is the quantitative determination of the free energy profile of the desorption process.

VII.C Conclusion

This last chapter presents a pesticide-montmorillonite solvation study in two sections. First, four CPMD simulations of hydrated metamitron and fenhexamid adsorbed on the surface have been run. These trajectories allowed to explore hydration of both Meta and Fen in parallel and orthogonal orientations towards the surface and with different binding sites: Meta-Mont ^{H_2O} _{*ortho-long*}(**N-N**), Meta-Mont ^{H_2O} _{*para*}(**CO(-Phe)**), Fen-Mont ^{H_2O} _{*para*}(**CO(-Phe)**) and Fen-Mont ^{H_2O} _{*ortho-short*}(**Cl-OH**). It showed that hydration of the complexes does not influence the binding site distances between pesticides and cations. However, as expected, surface cation behavior is largely influenced by solvation as the $d_{\text{Ca1-O}_b}$ and $d_{\text{Ca2-O}_b}$ strongly increase: by $\approx 0.5 - 1.4$ Å for Ca1 depending on its hydration with one or two H_2O molecules, and $\approx 2.5 - 2.7$ Å for Ca2 which interacts with an inner hydration sphere of 5 water molecules organised in a square-based pyramid. Concerning the internal structure of the surface, hydration tends to elongate distances between atoms up to a


maximum of 0.05 Å.

Then, the second section of this chapter treats the free energy surface exploration of the desorption process of the pesticide in the Fen-Mont_{para}^{H₂O}(CO(-Phe)). For that purpose, the Umbrella Sampling method has been chosen by means of DFT, 11 MD simulations have been run at 330 K in the NVT ensemble and a free energy profile has been obtained. The chosen reaction coordinate ξ for this exploration is the z component of fenhexamid center of mass which corresponds to an increasing distance between the molecule and the surface. The Ca²⁺ cation position has not been included in ξ as it was expected to desorb with the pesticide. The obtained profile presents three free energy wells separated by two barriers of 3.0 and 4.5 kcal/mol approximately, for an increasing distance between the binding site (the carbonyl oxygen) and the surface cation. Each barrier corresponds to the inclusion of a water molecule between the pesticide and the surface, hydrating Ca1 step by step, starting from a double coordination with water, to a triple, and then a quadruple hydration. Ca2 presents different first hydration spheres in the three wells: square-based pyramid (5 H₂O), octahedron (6 H₂O) and distorted square antiprism (8 H₂O), the latter being the maximum stable first hydration sphere according to literature. The results on Ca1 positions in the three wells seem to show that two different desorption paths overlap along the chosen reaction coordinate: desorption of the Fen-Ca²⁺ complex, as the evolution between **Well 1** and **2** suggests, or desorption of Fen only while Ca1 stays bound to the surface as in **Well 3**. A way to explore would be to run Umbrella Sampling simulations for $\xi > 20$ Bohr, starting from the structure of **Well 2** where Ca1 stays complexed on the carbonyl oxygen at a similar distance as in **Well 1**. Increasing the Ca1 distance from the surface will probably favor the complex desorption. Initially, these considerations have not been taken into account since simulations are very long to run and thus have been done in parallel. Considering results on Ca²⁺ hydration on montmorillonite and available results in literature on cytosine and cation desorption from montmorillonite, the Umbrella Sampling method applied to such systems is very promising to quantify free energy barrier despite huge resource cost.

Conclusion

“Science at its best provides us with better questions, not absolute answers”

Norman Cousins

 The aim of the present thesis is to improve understandings in the behavior of pesticides with soil mineral matter.

For this purpose, reports on pesticides in European agricultural practices and literature review allowed to choose three pesticides of interest for this study: atrazine, metamitron and fenhexamid. The interaction of these substances with montmorillonite, the most abundant smectite on Earth and thus a good representative of soil mineral phase, has been considered via a model of Ca-montmorillonite. This thesis is a multi-scale approach organised in four levels, starting from isolated molecular systems to condensed phase and gathering several DFT-based methods.

- First atrazine interaction with dry pyrophyllite and Ca-montmorillonite has been investigated by means of DFT/PBE-D2 geometry optimisations in a static approach. A preliminary adsorption of atrazine parallel to the pyrophyllite surface allowed to evidence the necessity of using dispersion corrections to treat molecule-surface interaction. The choice of a montmorillonite model in which compensating cations are calcium ions is based on previous studies published by the group, showing a way better complexation energy in gas phase between atrazine and Ca^{2+} (≈ -120 kcal/mol) than with Na^+ (≈ -40 kcal/mol), which are both abundant cations in soil. Several orientations, parallel (PARA) and orthogonal (ORTHO) to the surface, have been optimized for atrazine on Ca-montmorillonite (Mont) surface and reveal that the parallel adsorption energy of atrazine is two to three times stronger on Ca-montmorillonite than on pyrophyllite. The largest molecule adsorption is found for PARA with an adsorption energy around -30 kcal/mol. The strongest interactions

imply the atrazine chlorine and the surface Ca^{2+} , with a Ca-Cl distance comparable to the ones in Atra- Ca^{2+} gas phase complexes. Adsorption of atrazine whatever the orientation always makes the interacting Ca^{2+} cation get farther from the surface but only induces slight modifications in the internal structure of the solid.

- In a second time, Car-Parrinello Molecular Dynamics method is introduced. Potential energy surface explorations of metamitron and fenhexamid conformers and complexes with one or two Na^+ and Ca^{2+} cations have been performed in gas phase through simulations in the microcanonical ensemble. A unique conformer has been found for metamitron while fenhexamid presents 11 conformers below 10 kcal/mol in relative energy. Fenhexamid presents two types of structures regarding the positions of the R group around the cyclohexyl: axial and equatorial conformers. The lowest-energy conformer is axial.

Meta complexes with cation(s) display structures and associated relative energies slightly influenced by the basis set, while, on the opposite Fen complexes relative order changes with the basis. Complexation with one cation on Meta presents the same families of complexes but in different order depending on the nature of the cation. With two cations, families combine the binding sites of Meta with one cation.

In the case of Fen, complexation families are different but have three common types: CO-Cl, CO-Phe and CO-cyclo. Here, R axial position is slightly favored for Fen- Na^+ complexes while equatorial position is preferred in Fen- Ca^{2+} except when cyclohexyl is implied in the binding site. With two cations, Fen complex families have the same relative order whatever the cation and the basis set. Unlike Meta-cation, families with two cations are not combinations of families obtained with one cation.

The RVS SCF decomposition analysis allows to quantify the contributions to the interaction energy. It showed the predominance of electrostatic energy in the contribution to the attractive terms within the complexes. For Na^+ , two thirds of the attractive terms correspond to electrostatic energy, and one third to polarization energy. For Ca^{2+} , the electrostatic term represents 50 %, the polarization energy 40 %, and the charge-transfer ≈ 10 %.

Complexation energies of both pesticides with one Na^+ or Ca^{2+} are of similar order than with atrazine: -40 and -140 kcal/mol respectively, while the values are of -22 kcal/mol with two Na^+ . With two Ca^{2+} , Fen complexation energy is of -60 kcal/mol while the absolute value is twice lower for Meta.

Metamitron and fenhexamid complexes, whatever the number and nature of cations, give negative complexation free energies, which is not the case for Atra- $(\text{Ca}^{2+})_2$

where ΔG_{comp} is positive.

Finally, results at PBE/basis2//PBE/basis1 shows usually a good agreement with PBE/basis2 and could thus be an alternative to treat larger systems.

- The third step of this thesis has been to explore the PES of metamitron and fenhexamid adsorbed on a model of Ca-montmorillonite via CPMD/PBE-D2 simulations. The previous optimized complexes (Chapter V) have been used as starting structures. As expected, this dynamical approach allowed a larger exploration of isomers compared to the static approach used for Atra-Mont systems (Chapter IV).

In the case of Meta-Mont, families implying the same binding sites as in the gas phase have been obtained. Families are consecutive but the energetic order corresponds to Meta- Na^+ in the gas phase: a complexation on both nitrogens of the triazine cycle leads to the lowest-energy isomer. Both parallel and orthogonal orientations have been considered. In a given family, a *para* orientation is always preferred but the binding site criterion is determinant.

Although metamitron molecule cannot interact with two surface Ca^{2+} cations, Fen-Mont present double complexation geometries. For Fen-Mont, *para* isomers constitute the lowest-energy group. For single *para* isomers, a complexation on the carbonyl oxygen is observed. The lowest-energy isomer unexpectedly shows a single complexation in a nearly monodentate interaction with the carbonyl oxygen. Single and double complexations are competitive. As for single complexation, an interaction of Ca^{2+} on the carbonyl oxygen leads to the lowest-energy isomer. Whatever the pesticide, the adsorption energy is around -40 kcal/mol. As in the Atra-Mont study, the surface is nearly unmodified except the Ca^{2+} interacting position.

- The last chapter focuses on the hydration influence on pesticide-Mont complexes. Solvation slightly affects the binding site whatever the pesticide and the orientation. Mont internal geometry is also weakly modified. Concerning the Ca^{2+} hydration:
 - the non-interacting cation (Ca2) reaches an inner hydration sphere (5 H_2O) keeping an interaction with the surface ;
 - solvation of Ca1, implied in the binding site, depends on both the complexation site and the pesticide (up to 2 H_2O molecules).

The second aspect that has been investigated in the solvated systems is the desorption process of pesticides through series of biased MD trajectories along a reaction coordinate (Umbrella Sampling). The aim of this study was to explore the free energy surface and quantify the barrier to desorb fenhexamid, complexed through

the carbonyl oxygen, from the hydrated model of Ca-montmorillonite. Umbrella sampling has been done via 11 MD simulations (less than 20 ps most of the time) in DFT, and the chosen reaction coordinate ($\xi_{z(com)}$) is the z component of Fen center of mass. Two desorption processes can be hypothesized: a desorption of the molecule only, or a desorption of the pesticide-cation complex. The chosen reaction coordinate cannot allow to discriminate between both. The free energy profile along this coordinate, has been obtained for $14 \leq \xi_{z(com)} \leq 20$ Bohr, and corresponds to insertion of water molecules between the pesticide and the surface. In **Well 1**, the complexed cation (Ca1) is in interaction with 2 H₂O molecules. Then, two free energy barriers of ≈ 3.0 and 4.5 kcal/mol have been crossed and allowed to explore two wells:


- **Well 2**, approximately 1.5 kcal/mol higher than **Well 1**, where Ca1 is hydrated with 3 H₂O molecules ;
- **Well 3**, ≈ 2 kcal/mol higher than **Well 2** and with 4 H₂O molecules coordinated on Ca1.

In **Well 1** and **2**, the desorption of Fen-Ca²⁺ is observed by inclusion of water molecules. Although, in **Well 3**, the interaction between the pesticide and Ca²⁺ is weaker, the latter remaining adsorbed on the surface.

Further investigation starting from the structure of **Well 2** could lead to the Fen-Ca²⁺ desorption. Finally, these results emphasize the tricky problem of choosing the appropriate reaction coordinate particularly with the extremely high resources cost of Umbrella Sampling in CP/DFT.

Résumé

1 Introduction

es pesticides sont une catégorie de molécules regroupant tous types de produits destinés à la défense des plantes et plus particulièrement des cultures contre les insectes, maladies ou autres plantes indésirables. Dans le but d'optimiser la production en champs cultivables, ces substances sont très largement employées en agriculture, mais également pour la maintenance des espaces verts publics comme privés, tels que les parcs ou les jardins. De telles substances actives sont très répandues en Europe, par exemple la quantité de produits vendus en France chaque année se compte en dizaines de milliers de tonnes [1–3]. La France se trouve alors parmi les premiers consommateurs de pesticides au monde. Par conséquent, l'utilisation très large des pesticides pour l'agriculture soulève d'importantes questions concernant leur influence sur la santé publique et l'environnement. En effet, la présence des pesticides et de leurs produits de dégradation peut être mesurée dans l'air, le sol et l'eau potable [8, 9], comme dans les micro- et macro- organismes, les cultures traitées et la nourriture [10].

L'objectif de cette thèse est d'étudier les interactions entre les pesticides et le sol. Les chapitres préliminaires présentant le contexte de ce travail commencent avec la description du rôle des pesticides dans notre société et un état de l'art des trois pesticides d'intérêt : l'atrazine, la métamitronne et le fenhexamide (Chapitre I). Ensuite, de brèves généralités seront données concernant l'organisation du sol et sa composition, suivies d'une présentation de la montmorillonite, l'argile choisie pour ce travail (Chapitre II). Pour terminer l'introduction, le Chapitre III présente l'ensemble des méthodes théoriques qui ont été employées pour traiter les systèmes considérés.

Cette thèse est une étude de la nature et des composants des interactions entre les pesticides et le sol étape par étape. Dans ce but, quatre types de systèmes ont été pris

en compte et correspondent aux quatre chapitres suivants:

- Premièrement, l'interaction de l'atrazine avec les minéraux argileux a été étudiée par optimisation de géométrie de quelques uns de ses isomères lorsqu'elle est déposée sur la surface de modèles d'argile (Chapitre IV). Ce chapitre est basé sur de précédents travaux publiés et menés au sein de l'équipe de recherche sur la complexation de l'atrazine avec des cations naturellement abondants dans les sols [11, 12].
- Dans un second temps, deux autres pesticides, la métamitron et le fenhexamide, ont été sélectionnés pour cette étude et ont été considérés en interaction avec des cations de même nature et en même quantité que pour l'atrazine. Néanmoins, cette étude inclue la dynamique moléculaire dans sa méthodologie pour une exploration plus large des isomères de ces pesticides. Cette étape a pour but d'étudier l'interaction pesticide-cation(s). Puis, par comparaison avec le comportement des pesticides en phase solide, il sera possible d'observer l'influence de la surface d'argile sur les complexations pesticide-cation(s).
- Le chapitre suivant (Chapitre VI) traite de la métamitron et du fenhexamide adsorbés sur un modèle de montmorillonite sèche. Des simulations de dynamique moléculaire ont été lancées sur ces deux molécules. Une nouvelle fois, cette étape représente une évolution de la méthode par l'aspect dynamique, comparée au travail sur l'atrazine effectué grâce à une approche statique.
- La partie finale de ce travail va plus loin en considérant les systèmes précédents en présence d'un solvant explicite : l'eau. En effet, les minéraux argileux réels, et tout particulièrement la montmorillonite, sont capables d'absorber une importante quantité d'eau dans leurs interfeuillet. La prochaine et dernière étape de cette thèse est donc une étude des effets de l'hydratation sur les systèmes pesticide-cation(s)-montmorillonite. Pour tenter d'aller plus loin, des séries de dynamiques biaisées ont été effectuées en parallèle sur une molécule de fenhexamide adsorbée sur la surface, dans le but de conduire un processus de désorption et essayer de quantifier les barrières d'énergies libres rencontrées le long d'une coordonnée de réaction spécifique.

L'approche de cette thèse est un traitement de modèles de plus en plus complexes, de systèmes moléculaires isolés à des pesticides solvatés en interaction avec des surfaces d'argiles.

2 Pesticides

Stymologiquement, pesticide vient de l'Anglais *pest*, “insecte ou plante nuisible, parasite”, et du latin *caedere* qui signifie “tuer, frapper, abattre” [13]. Ce terme désigne donc tout type de substance destiné à combattre les êtres vivants indésirables, qu'ils soient des insectes (insecticides), des plantes (herbicides) ou des champignons (fongicides), ...

Les pesticides employés pour la protection de végétaux sont nommés “produits phytopharmaceutiques” ou plus communément “produits phytosanitaires” [14]. De telles substances sont très largement produites et utilisées dans le monde entier, principalement pour l'agriculture, mais aussi dans les espaces urbains (parcs, espaces verts, jardins, ...) et sur les propriétés privées. Cette large utilisation génère de plus en plus d'inquiétude vis-à-vis des questions environnementales et sanitaires soulevées par la présence des pesticides dans notre société.

Depuis 2004, la France présente la surface agricole la plus importante d'Europe avec 29 115,25 milliers d'hectares en 2015, correspondant approximativement à 16 % de la surface agricole totale en Europe [1].

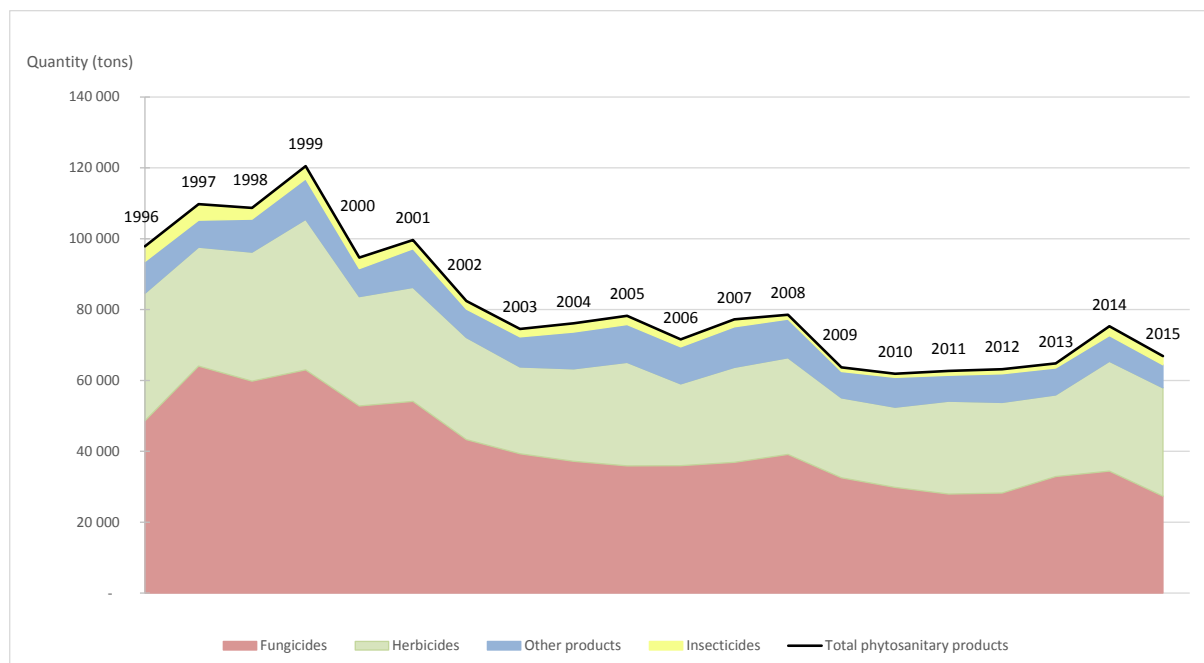


Figure 1: Quantité de produits phytosanitaires vendus (en tonnes) en France métropolitaine entre 1996 et 2013 (référence: Union des Industries pour la Protection des Plantes (UIPP) Traitements: SOeS, 2016) [2,3]; et de 2014 à 2015 [1]

La France est le leader agricole parmi les pays européens mais est aussi l'un des principaux consommateurs de pesticides au monde. La Figure 1 représente l'évolution de la vente totale et détaillée de pesticides en France chaque année entre 1996 et 2015 [1-3], indiquant un pic à 121 000 tonnes en 1999 suivi d'une tendance à la baisse. Depuis 2009, la moyenne de produits vendus est située entre 60 et 70 kilotonnes par an, illustrant bien l'importance de leur présence dans notre société. Un second aperçu de l'étendue de l'emploi des pesticides en agriculture est présenté par le Tableau 1, donnant le nombre moyen de traitements appliqués sur certaines cultures en France entre 2013 et 2015 [6].

Average number of treatment							
2013	Carot	Cauliflower	Strawberry	Muskmelon	Leek	Lettuce	Tomato
	11	3	8	8	9	4	12
2014	Colza	Sunflower	Sugar beet	Potato	Sugar cane		
	7	3	5	19	4		
2015	Apple	Peach	Plum	Apricot	Cherry	Banana	
	36	19	12	13	11	8	

Table 1: Nombres moyens de traitements appliqués sur certaines cultures françaises entre 2013 et 2015 (référence: SSP - Agreste) [6].

La grande présence des pesticides dans notre société soulève de nombreuses questions des points de vue de la santé publique et de l'environnement. Dans le but de développer les connaissances concernant l'interaction des pesticides avec l'environnement, et plus spécifiquement avec le sol, trois pesticides ont été sélectionnés pour la présente thèse: l'atrazine, la métamitron et le fenhexamide.

L'atrazine (CAS 1912-24-9) est un herbicide de la famille des triazines de formule brute $C_8H_{14}ClN_5$ et dont la forme semi-développée est présentée dans la Figure 2. Cette molécule a pour nom complet 6-chloro-N2-ethyl-N4-isopropyl-1,3,5-triazine-2,4-diamine et est très employée en agriculture, principalement sur le maïs, la canne à sucre et le blé, contre l'émergence de mauvaises herbes. Son pouvoir herbicide fonctionne par inhibition de leur processus de photosynthèse.

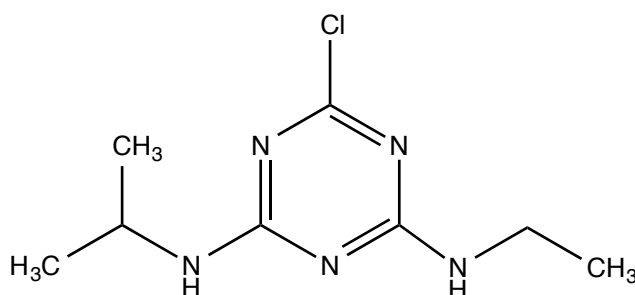


Figure 2: Formule semi-développée de l'atrazine.

La métamitronne (CAS 41394-05-2), également un herbicide permettant de lutter contre le même type de plante, est quant à elle principalement employée sur les cultures de betteraves fourragères et à sucre. Métamitronne est le nom commun de la 4-amino-4,5-dihydro-3-méthyl-6-phényl-1,2,4-triazin-5-one ($C_{10}H_{10}N_4O$), de formule semi-développée présentée en Figure 3 et appartient à la famille des triazinones [7].

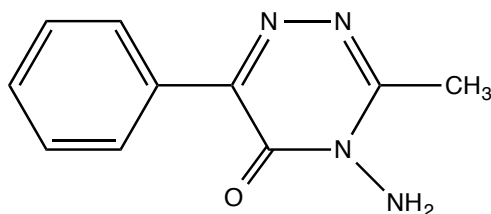


Figure 3: Formule semi-développée de la métamitronne.

Le dernier pesticide choisi pour cette étude est le fenhexamide (CAS 126833-17-8), un fongicide de nom complet N-(2,3-dichloro-4-hydroxyphényl)-1-méthylcyclohexanecarboxamide ($C_{14}H_{17}Cl_2NO_2$) et de formule semi-développée présentée dans la Figure 4. Cette molécule, de la famille des hydroxyanilides, est notamment utilisée pour ses effets protecteurs contre *Botrytis cinerea* [107] et *Monilinia* sur un large panel de cultures, parmi lesquelles nous pouvons citer la vigne et les fraises pour les plus concernées, mais aussi les kiwis, tomates, aubergines, différents types de baies, ainsi que des fleurs comme les tournesols ou les plantes ornementales.

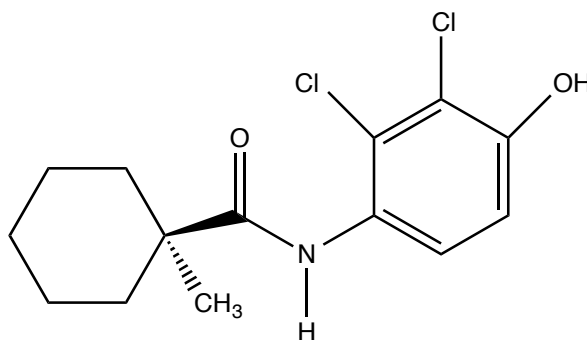



Figure 4: Formule semi-développée du fenhexamide.

Ces trois pesticides ont été choisis vis-à-vis de leur large utilisation en agriculture mais aussi à l'aide de la base de données TyPol (Typology of Pollutants) [19] contenant principalement des pesticides mais aussi d'autres formes de polluants. Cette base de données offre une approche statistique pour le classement des polluants en différents groupes (ou clusters) en fonction des paramètres environnementaux considérés qui peuvent être : la

solubilité dans l'eau (S_w), le coefficient de partage octanol-eau (K_{ow}), la pression de vapeur saturante (P_{vap}), la constante de Henry (K_H), le coefficient de partage carbone organique-eau (K_{oc}), le temps de demi-vie ($DT50$) ou le facteur de bioconcentration (BCF). Ces paramètres servent à décrire 5 processus environnementaux que sont la dissolution, la volatilisation, l'adsorption, la dégradation et la bioaccumulation. Tous ces paramètres ont été employés dans la publication originale [19] et ont révélé que la meilleure classification pour les 215 polluants de TyPol se fait via 6 clusters. Concernant les 3 pesticides choisis pour cette étude, ils appartiennent chacun à des clusters différents de cette classification ce qui a motivé leur sélection.

3 Le sol et la montmorillonite

 e sol est un système très complexe dont la composition est sujette à des modifications permanentes. D'un point de vue macroscopique, le sol est organisé en couches de compositions différentes appelées "horizons". L'ordre de ces horizons, accompagné d'une description générale de leurs composants, est schématisé sur la Figure 5.

De manière générale, la surface du sol est principalement composée de matière organique vivante et morte (horizon O), et plus l'on s'enfonce en profondeur dans le sol, plus la part majoritaire de matière organique cède la place à la matière minérale (horizons A, E et B). Finalement, les horizons les plus profonds (C et D) contiennent essentiellement de la matière minérale.

D'un point de vue global, le sol est composé de quatre phases en interaction : gazeuse (proche de l'air), liquide (principalement de l'eau contenant des minéraux et des composés organiques solvatés), une phase organique (minoritaire, incluant tous les organismes microscopiques ou macroscopiques) et une phase solide minérale.

Etant donné la complexité et la diversité d'un système tel que le sol, ce travail se focalisera essentiellement sur la description de la phase minérale. Le minéral de choix pour cette étude est la montmorillonite qui est un bon représentant du sol car il s'agit de la plus abondante des smectites. De plus, elle présente des applications agricoles et industrielles intéressantes et recherchées dues à ses propriétés absorbantes vis-à-vis de l'eau.

La montmorillonite est une smectite qui elle-même est un sous-groupe des phyllosilicates. C'est un minéral organisé en feuillets (Figure 6), eux-mêmes composés de trois sous-couches notées T/O/T (minéral 2:1) car il s'agit d'un empilement constitué d'une couche d'octaèdres (O) d'oxygènes O^{2-} occupés d'ions Al^{3+} . Cette couche O est alors entourée de part et d'autre par 2 couches de tétraèdres (T) d'anions O^{2-} occupés de cations

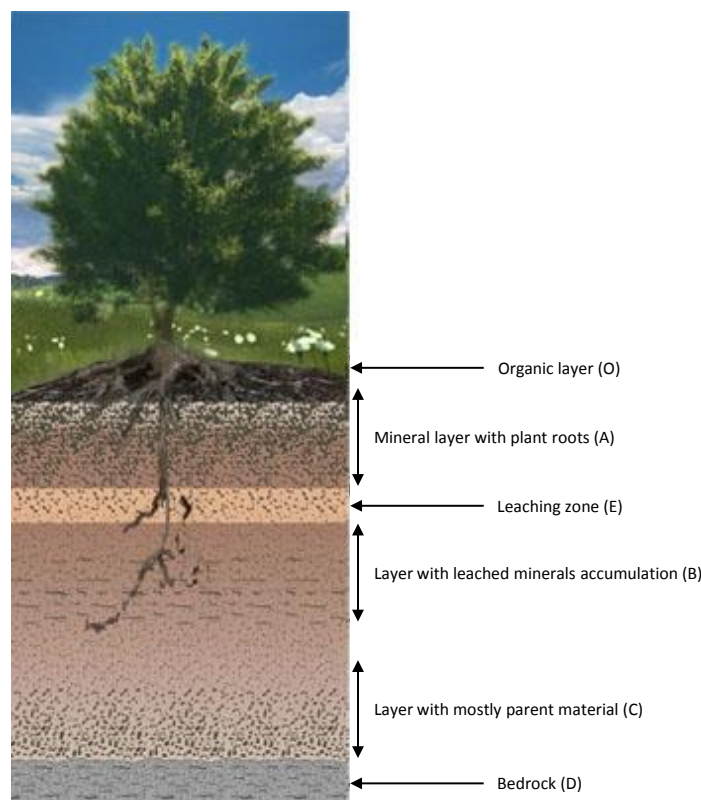


Figure 5: Les horizons du sol (source de l'image : <http://www.aucoeurdelarbre.ca/fr/hors-sentier/section-profs/module4-html.php>).

Si^{4+} . Tous les sites tétraédriques sont occupés alors qu'un tiers des sites octaédriques sont vacants, ce qui fait de cette structure un minéral dioctaédrique. Pour finir, la montmorillonite a la particularité de présenter des substitutions isomorphiques des cations dans les couches T et O. Généralement, les cations sont substitués par d'autres cations de charges inférieures : Si^{4+} peut être remplacé par Al^{3+} par exemple, et Al^{3+} peut être remplacé par Mg^{2+} ou Fe^{2+} entre autres ... Ces défauts de charges sont alors compensés par la présence de cations dans l'interfeuille, habituellement mono- ou di- valents tels que K^+ , Na^+ , Li^+ , Ca^{2+} , Mg^{2+} , ...

Dans le modèle de montmorillonite choisi pour ce travail, dont la maille élémentaire correspond à six fois la maille primitive de la montmorillonite ($3a \times 2b \times c$), quatre substitutions isomorphiques de Al^{3+} par Mg^{2+} ont été réalisées dans la couche octaédrique du feuillet d'argile. Le défaut de charge impliqué a alors été compensé par la présence de deux cations Ca^{2+} dans l'interfeuille. Les justifications de ce choix seront apportées dans la Section 4. Le modèle produit dans ce travail s'inspire de la structure de la pyrophyllite obtenue expérimentalement par rayon X dans les travaux de Wardle *et al.* [135] avec les paramètres de mailles suivants : $a = 5,161 \text{ \AA}$, $b = 8,957 \text{ \AA}$ and $c = 9,351 \text{ \AA}$; $\alpha = 91,03^\circ$, $\beta = 100,37^\circ$ and $\gamma = 89,75^\circ$. En effet, la pyrophyllite et la montmorillonite ont des

structures similaires mais se différencient principalement par la présence de substitutions isomorphiques dans les feuillets et donc de cations compensateurs dans l'interfeuille pour la montmorillonite (voir Figure 6). Les positions des sites octaédriques vacants et des groupements hydroxyles au sein de la montmorillonite peuvent être *cis* ou *trans* selon le cas. Ces cas ne sont pas identifiables par diffraction de rayons X et les positions des OH sont donc inconnus. Dans ce travail, le modèle de Ca-montmorillonite présente des vacances en positions *trans*. Cette structure a été choisie d'après les travaux de Tunega *et al.* en 2007, montrant que dans le cas général, les structures *trans* des phyllosilicates présentent une plus grande stabilité que les structures *cis* [139].

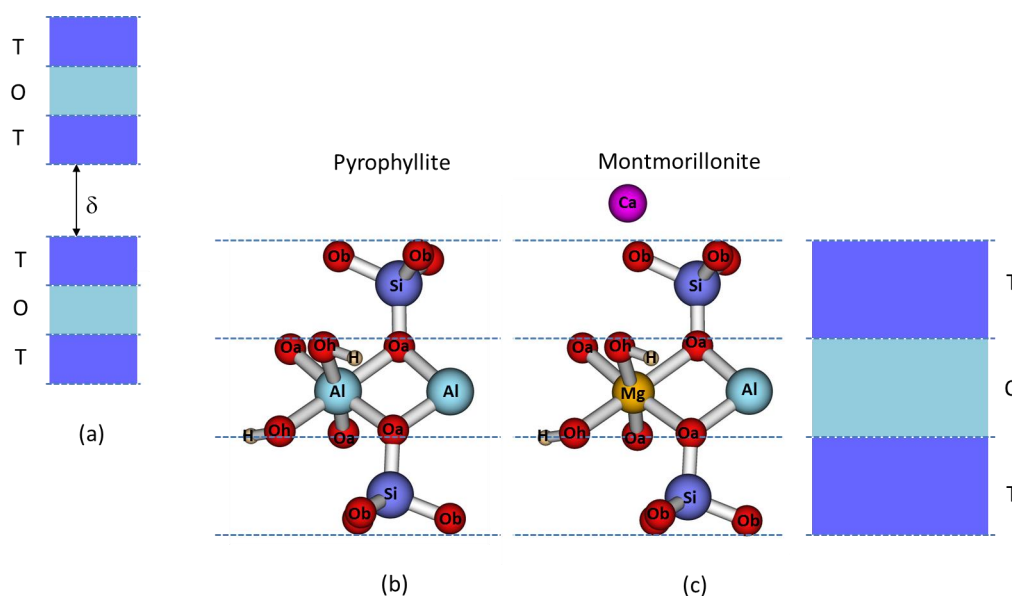



Figure 6: a) La structure en couches de la pyrophyllite et des smectites : T désigne les tétraèdres et O les octaèdres, δ représente la distance interfeuille ; b) L'environnement constitué par les oxygènes : des tétraèdres autour des siliciums et des octaèdres autour des aluminiums dans la pyrophyllite ; c) des substitutions isomorphiques se produisent dans la montmorillonite : par exemple un Al^{3+} a été remplacé par un Mg^{2+} dans la couche O, des Ca^{2+} sont ajoutés dans l'espace interfeuille pour compenser le défaut de charge. Les différents types d'oxygènes sont représentés : O_h correspond aux oxygènes connectés à des hydrogènes, O_b (pour basal en Anglais) sont impliqués dans des liaisons seulement avec des Si, O_a (axial) sont liés à des Si et des Al (ou Mg).

4 Interaction de l'atrazine avec le sol

es études menées sur les pesticides dans cette thèse impliquent une approche multi-échelle, depuis la phase gazeuse jusqu'à la phase condensée, pour analyser pas à pas les contributions de chaque constituant du modèle étudié.

L'atrazine en phase gaz

De précédentes publications au sein du groupe de recherche porte sur l'atrazine et les complexes qu'elle forme avec les ions sodium et calcium en phase gazeuse [11, 12]. Les différentes contributions aux énergies d'interaction ont été analysées à l'aide de la méthode de décomposition RVS SCF (Reduced Variational Space Self-Consistent Field) [248]. La publication de 2011 [11] est une étude statique de l'atrazine et de ses complexes avec Na^+ et Ca^{2+} . Cette étude se développe sur plusieurs points : tout d'abord l'étude d'un des métabolites de l'atrazine, la 2-chloro-1,3,5-triazine-4,6-diamine (notée AtraMod dans la publication), a permis d'identifier les sites de complexation de chaque cation autour de la molécule, en partant de cinq structures avec un cation en interaction sur un site riche en électrons : les atomes de chlore et d'azote. Deuxièmement, des optimisations de géométries à différents niveaux de calculs ont été menées en utilisant plusieurs méthodes : depuis la méthode Hartree-Fock jusqu'à celle du Coupled Cluster en passant par la DFT/B3LYP et Møller-Plesset d'ordre 2 (MP2) développées sur deux bases différentes : 6-31G* (basis1) et 6-311+G(2d,2p) (basis2). Les principales conclusions de ces travaux sont que l'ordre énergétique des trois complexes AtraMod-cation les plus stables est le même quelque soit le niveau de calcul, et ce pour un cation donné. Cependant, dans le cas de l'atrazine- Ca^{2+} , les deux isomères de plus basses énergies (avec différents sites de complexation) sont isoénergétiques, et donc leur ordre dépend du niveau de calcul. Par ailleurs, les complexes d'AtraMod et de l'atrazine avec le calcium présentent des énergies de complexation plus favorables que les mêmes complexes avec le sodium. Comme attendu vis-à-vis des charges des cations, l'interaction du calcium avec les molécules est nettement plus forte que celle du sodium. Pour aller plus loin, les contributions électrostatiques calculées à l'aide de la décomposition RVS SCF, ainsi que par un remplacement du cation par une charge ponctuelle, mais aussi par expansion du multipôle, ont montré que la principale contribution à l'interaction entre AtraMod et un cation provient de l'énergie électrostatique, comme attendu. Dans le cas de Ca^{2+} , la contribution de polarisation est également décisive dans la description de l'interaction.

Finalement, l'énergie de complexation de l'atrazine avec le calcium est plus forte qu'avec le sodium (au niveau B3LYP/basis2 : $E_{\text{comp}}(\text{atrazine-Ca}^{2+}) = -125,1 \text{ kcal/mol}$ et $E_{\text{comp}}(\text{atrazine-Na}^+) = -39,5 \text{ kcal/mol}$).

Par la suite, une seconde publication traite une large variété d'isomères de l'atrazine en présence d'un ou deux cation(s) Ca^{2+} optimisés aux niveaux de calculs B3LYP/basis1 et B3LYP/basis2 [12]. Les trois isomères les plus stables correspondent à différentes familles de complexes, mais présentent des sites de complexation impliquant les atomes d'azote et de chlore de la molécule, et ce en interaction de types monodentates ou bidentates. Ces structures optimisées constituent les points de départ pour notre étude de l'atrazine adsorbée sur une surface d'argile. Pour l'isomère de plus basse énergie, l'énergie d'interaction $E_{int} = -186,10$ kcal/mol compense approximativement l'énergie de répulsion entre les deux cations Ca^{2+} ($E_{rep} = +182,67$ kcal/mol) à une distance $d_{Ca-Ca} = 7,3$ Å au niveau B3LYP/basis1. Après avoir ajouté l'énergie de préparation, une énergie de complexation répulsive de +21,76 ou +9,80 kcal/mol est obtenue pour basis1 et basis2 respectivement. De la même manière, les enthalpies de complexation et les énergies libres sont aussi répulsives. De la phase gazeuse à la phase condensée, d'autres contributions sont attendues et devraient mener à des énergies d'adsorption attractives.

Dans la section ci-dessous, l'atrazine interagit avec une surface d'argile. Le premier article dont nous venons de donner les conclusions confirme que l'interaction entre l'atrazine et Ca^{2+} est nettement plus forte qu'avec Na^+ , pour cette raison, le calcium est le cation de choix en tant qu'ion compensateur dans l'interfeuillet du modèle de montmorillonite utilisé dans la suite. Les positions des cations sur la surface pourrait probablement jouer un rôle important dans l'énergie d'adsorption du pesticide du fait de l'importante répulsion entre deux ions calciums. De plus, les effets de dispersion entre la surface et le pesticide devraient renforcer les contributions attractives à l'énergie d'interaction.

Adsorption de l'atrazine sur un modèle de Ca-montmorillonite

Dans les travaux précédemment cités [11, 12], la molécule d'atrazine et ses complexes avec Ca^{2+} ont été étudiés, des tests ont alors été effectués dans le but de confirmer que les structures et les résultats énergétiques obtenus avec la fonctionnelle PBE en base de gaussiennes et en base d'ondes planes sont comparables.

Dans le Chapitre IV, l'atrazine est déposée sur une surface de pyrophyllite de paramètre $c = 30$ Å, le cycle aromatique étant parallèle à la surface (Figure 7). Cette orientation a été choisie pour maximiser l'influence des effets de dispersion et évaluer leur importance pour ce type de complexes. Les géométries des complexes atrazine-pyrophyllite (Pyro-Atra) ont été optimisées aux niveaux PBE/pw et PBE-D2/pw. De même, pour l'étude de complexes atrazine-montmorillonite, quatre structures ont été optimisées : trois en face à

face, nommées PARA (Figure 8) et une où le cycle *s*-triazine est orthogonal à la surface d'argile, notée ORTHO (Figure 9). Les isomères PARA ont été construits de manière à ce que la molécule interagisse avec les deux cations Ca^{2+} de la surface, tel qu'ils le font dans les deux complexes atrazine- $(\text{Ca}^{2+})_2$ de plus basses énergies obtenus en phase gazeuse [12].

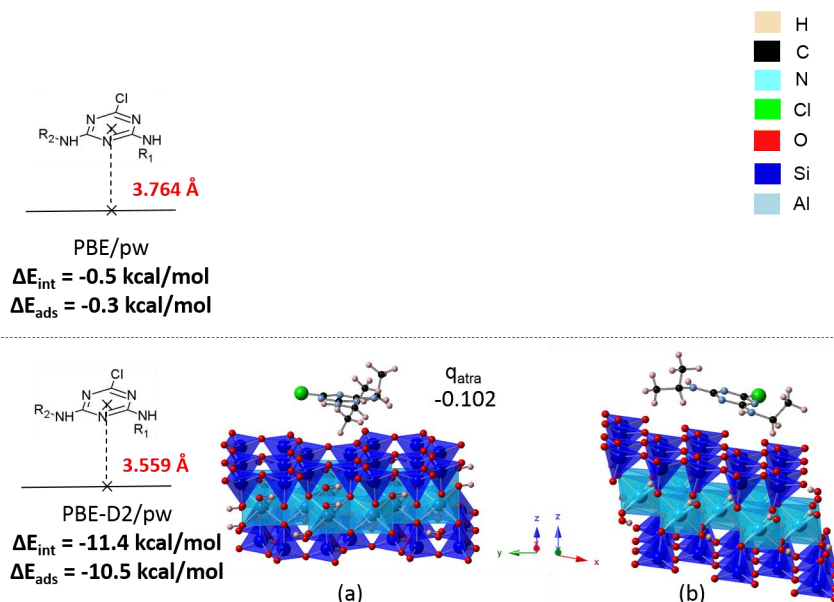


Figure 7: Pyrophyllite-atrazine : énergies d'interaction (ΔE_{int}) et d'adsorption (ΔE_{ads}) (en kcal/mol et en gras), charges de Hirshfeld [5] portées par l'atrazine (q_{atra}) et distances de l'atrazine (centre géométrique du cycle) à la surface (en Å et en rouge) aux niveaux PBE/pw et PBE-D2/pw. (a) Vue le long de la direction a ; (b) vue le long de la direction b pour le complexe pyrophyllite-atrazine optimisé au niveau PBE-D2/pw.

L'atrazine est physisorbée sur la surface de pyrophyllite, de ce fait des corrections de dispersion sont nécessaires pour décrire l'interaction entre ces deux entités. Sans dispersion, la distance atrazine-pyrophyllite est plus longue de 0,2 Å et l'énergie d'adsorption est d'environ 0 kcal/mol. De ce fait, ces résultats mettent en évidence le besoin d'introduire des corrections de dispersion au cours du processus d'optimisation des géométries pour l'interaction de pesticides avec une surface d'argile. La correction de dispersion empirique D2 de S. Grimme est disponible dans le logiciel CPMD et a donc été utilisée [230, 231]. Au niveau PBE-D2/pw, les énergies d'adsorption de l'atrazine sur la montmorillonite ($-15 < \Delta E_{\text{ads}} < -30 \text{ kcal/mol}$) sont deux à trois fois plus fortes que sur la pyrophyllite ($\approx -10 \text{ kcal/mol}$). Pour les isomères de plus basses énergies (PARA1 et PARA3), l'adsorption implique un cation Ca^{2+} de manière monodentate ainsi que l'atome de chlore de l'atrazine. La distance Ca-Cl qui en résulte est seulement un peu plus longue qu'en phase gazeuse ($\approx +0,03 \text{ Å}$) démontrant une interaction forte entre le pesticide et la surface, ainsi qu'une grande énergie d'adsorption. Dans le même temps, les énergies de déformation (ou préparation) sont petites $< 4 \text{ kcal/mol}$ et viennent principalement de

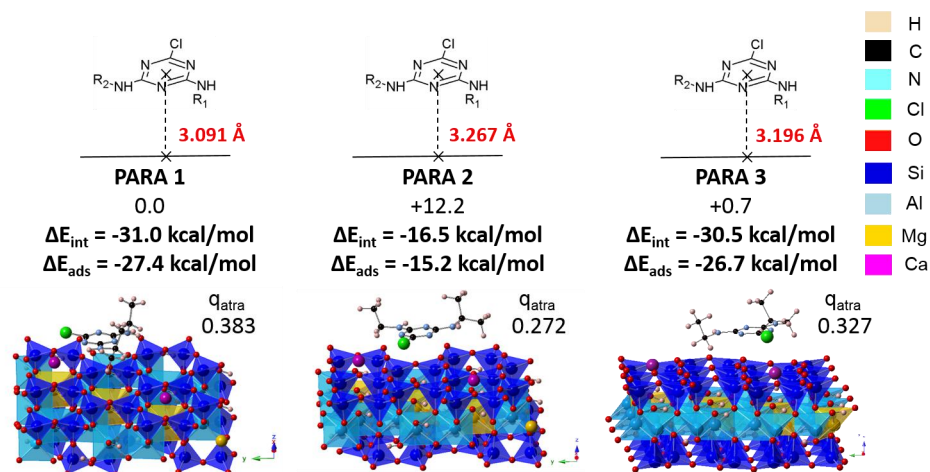


Figure 8: Montmorillonite-atrazine : énergies totales relatives (PARA1 est la référence), énergies d'interaction (ΔE_{int}) et d'adsorption (ΔE_{ads}) (en kcal/mol et en gras), charges de Hirshfeld [5] portées par l'atrazine (q_{atra}) et distances de l'atrazine (centre du cycle) à la surface (en Å et en rouge) au niveau PBE-D2/pw. Les vues sont le long de la direction a.

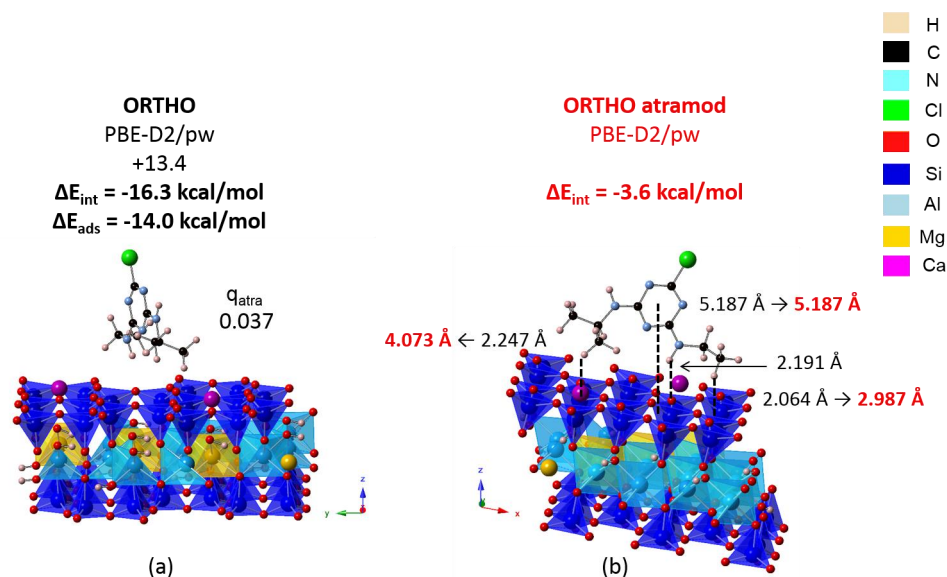


Figure 9: Isomère ORTHO des montmorillonite-molécule : l'énergie relative (PARA1 est la référence), les distances, énergies d'interaction (ΔE_{int}) et d'adsorption (ΔE_{ads}) de l'atrazine (en noir) ou d'atramod (en rouge) avec la surface au niveau PBE-D2. (a) Vue le long de la direction a ; (b) vue le long de la direction b. Les distances sont données en Å et les énergies en kcal/mol. La charge de Hirshfeld [5] portée par l'atrazine (q_{atra}). La structure ORTHO optimisée de la montmorillonite-atrazine a été utilisée pour montmorillonite-Atramod.

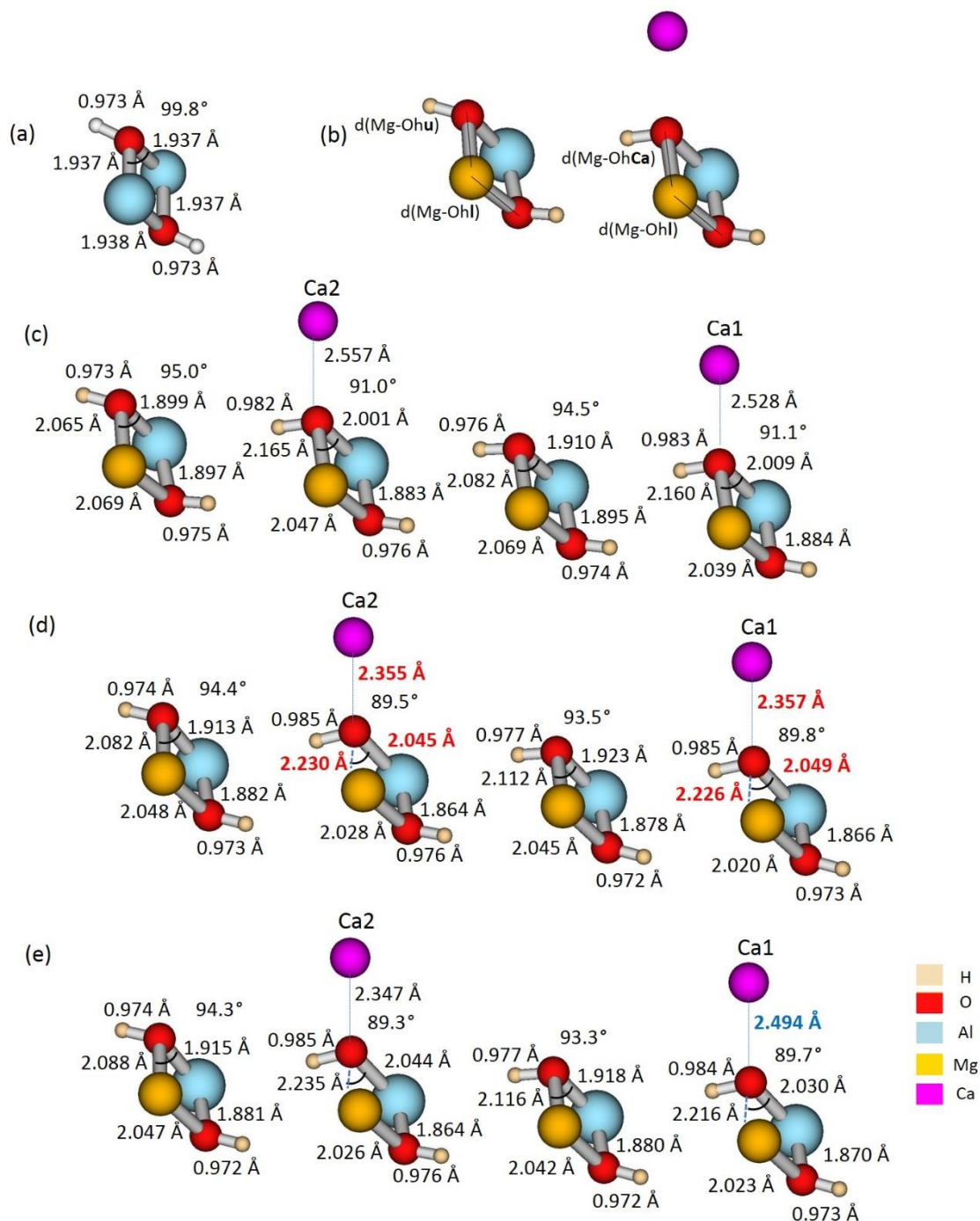


Figure 10: Pyrophyllite-atrazine : énergies d'interaction (ΔE_{int}) et d'adsorption (ΔE_{ads}) (en kcal/mol et en gras), charges de Hirshfeld portées par l'atrazine (q_{atra}) et distances de l'atrazine (centre géométrique du cycle) à la surface (en Å et en rouge) aux niveaux PBE/pw et PBE-D2/pw. (a) Vue le long de la direction a ; (b) vue le long de la direction b pour le complexe pyrophyllite-atrazine optimisé au niveau PBE-D2/pw.

l'atrazine. Les modifications structurales de la surface de montmorillonite concernent essentiellement la position du calcium interagissant ($+0,13 \text{ \AA}$ pour Ca1-O_b et Ca1-O_h comme visible dans la Figure 10 (d) et (e)). Les modifications internes de la surface d'argile proviennent de la transition entre les structures bulk ($c = 9,534 \text{ \AA}$) et la surface ($c = 30 \text{ \AA}$), durant cette transition les deux cations calcium se rapprochent de la surface ($\approx -0,20 \text{ \AA}$ pour les distances Ca-O_b et Ca-O_h). Toutes les autres distances ne sont que peu modifiées. Quand l'atrazine est adsorbée, la modification notable est l'éloignement de la surface du Ca^{2+} impliqué dans l'interaction ($\approx +0,15 \text{ \AA}$, voir la distance en bleu sur la Figure 10 (e)). Les petites énergies de déformation (ou préparation) de la montmorillonite ($< 2 \text{ kcal/mol}$) sont cohérentes avec les changements modérés dans la surface. Les substitutions choisies impliquent une distance inter-cations de $\approx 10 \text{ \AA}$, peu compatible avec une implication des deux cations dans l'adsorption de l'atrazine. Avec le remplacement de l'atrazine par la métamitronne ou le fenhexamide, les sites d'adsorption et les distances inter-cations devraient évoluer et les deux cations pourraient être impliqués dans l'adsorption (voir Chapitre VI). Les positions des substitutions ont donc une influence décisive sur la géométrie des complexes et leur énergie d'adsorption. Dans les futurs développements de ces travaux, il serait intéressant d'étudier d'autres modèles de Ca-montmorillonite.

Cette approche statique de l'adsorption de l'atrazine sur la pyrophyllite et une montmorillonite permet de valider l'utilisation du niveau de calcul PBE-D2/pw (80 Ry dans une maille primitive de $15,500 \times 17,931 \times 30 \text{ \AA}^3$ au point Γ). Comme attendu d'après l'étude en phase gazeuse, les importantes énergies d'adsorption négatives certifient l'augmentation des effets attractifs, et particulièrement ceux dus aux effets de dispersion, en présence de la surface. Dans la suite de cette thèse, une approche dynamique sera employée d'une part pour explorer plus amplement la Surface d'Energie Potentielle (SEP) des complexes de pesticides en phase gazeuse, et d'autre part, pour décrire de manière plus exhaustive l'adsorption de pesticides sur la surface.

5 Complexation de la métamitronne et du fenhexamide avec un ou deux ions Na^+ et Ca^{2+}

En introduction du Chapitre V, des tests de calibration ont été menés dans le but de valider l'utilisation de bases d'ondes planes par rapport aux bases de gaussiennes aux niveaux de calculs PBE/pw et PBE-D2/pw. Ces tests ont aussi permis de vérifier l'influence des paramètres tels que l'énergie de coupure des ondes planes, la taille de la cellule périodique employée et l'utilisation ou non du modèle de Tuckerman pour la résolution de l'équation de Poisson traitant les conditions aux limites [256], pour

des optimisations de géométries affranchies de leurs interactions avec leurs propres images périodiques.

Ces tests ont montré que l'emploi du modèle de Tuckerman est nécessaire car en son absence, les énergies de complexation convergent difficilement pour les systèmes avec un paramètre c compris entre 25 et 30 Å. La convergence est cependant atteinte en employant le modèle de Tuckerman pour un c allant de 13 à 15 Å. Il sera donc employé pour les optimisations de géométrie de ce chapitre. De plus dans le cas de la métamitron (Meta), une cellule cubique périodique de 13 Å est donc utilisée, étendue à 15 Å dans le cas du fenhexamide (Fen) dont les dimensions sont légèrement plus grandes. Comme cela a été montré pour l'atrazine (Atra), la valeur de l'énergie de coupure des ondes planes n'a qu'une faible influence sur l'énergie de complexation E_{comp} (avec ou sans Poisson solver). Concernant les géométries, l'énergie de coupure des ondes planes et la taille de la cellule périodique, n'ont qu'une légère influence au niveau PBE/pw ($< 1,5 \times 10^{-2}$ Å). Même la géométrie locale autour du site de complexation n'est pas impactée par ces paramètres. Quand la correction de dispersion D2 est ajoutée, les différences géométriques n'excèdent pas les 5×10^{-2} Å.

Sur l'énergie de complexation, quelque soit le niveau de calcul, l'énergie de coupure des ondes planes a une très légère influence ($< 0,03$ kcal/mol). Pour Fen- Ca^{2+} , modifier la taille de la boîte de 15 à 20 Å affecte E_{comp} de seulement ≈ 1 kcal/mol, ce qui est de l'ordre de la précision de la méthode. Donc, $c = 15$ Å est un choix approprié pour les complexes de Fen. Au contraire, pour Meta, E_{comp} va de -139 à -143 kcal/mol pour une taille de boîte allant de 13 à 20 Å. Pour $c = 20$ Å, E_{comp} est convergée (-143 kcal/mol également pour $c = 50$ Å). Une différence d'environ 3 kcal/mol entre la base de gaussiennes et l'approche ondes planes est observées dans les deux cas, c'est-à-dire 2 % sur E_{comp} , ce qui est acceptable. Pour Meta- $\text{Ca}^{2+}(1)$ et Fen- $\text{Ca}^{2+}(1)$, les corrections de dispersion empiriques D2 induisent une surestimation systématique (en valeur absolue) d'environ 5 – 6 kcal/mol sur E_{comp} quelque soit la taille de boîte et l'énergie de coupure. Cette différence correspond à la valeur de l'énergie de dispersion (E_{comp}^{disp}). La correction de dispersion empirique a été affinée par S. Grimme dans sa version D3 incluant en particulier les termes à trois corps [232]. Les corrections D3 ont été testées dans le logiciel Gaussian [257]. Les résultats au niveau PBE-D3/basis2 sur Fen- $\text{Ca}^{2+}(1)$ réduisent la surestimation de la dispersion D2 d'environ 5 kcal/mol et mènent à une E_{comp} plus précise. Cependant, D3 n'étant pas implémenté dans le logiciel CPMD, les corrections D2 ont donc été employées pour le calcul des énergies d'adsorption des pesticides sur les surfaces d'argile. Pour la phase gazeuse, utiliser la correction de dispersion D2 n'est pas recommandée pour l'évaluation des énergies de complexation. Néanmoins, les géométries optimisées au niveau PBE/basis2 dans Gaussian devraient présenter des énergies relatives

et de complexation suffisamment précises. Dans la suite, la cellule périodique utilisée pour déposer les pesticides sur les surfaces de montmorillonite est suffisamment grande ($15,500 \times 17,931 \times 30 \text{ \AA}^3$) pour éviter tout problème de précision énergétique.

Exploration dynamique des SEP de Meta, Fen, Meta-(cation)_{i,i=1,2} et Fen-(cation)_{i,i=1,2}

La métamitrone et le fenhexamide et leurs complexes avec un ou deux cations Ca^{2+} et Na^+ ont été étudiés aux moyens de simulations de dynamique moléculaire afin d'explorer aussi largement que possible les SEP. Un large panel de structures, les conformères des pesticides et leurs complexes correspondant à des familles variées (différents sites de complexation), a été optimisé aux niveaux PBE/basis1 et PBE/basis2 (bases de gaussiennes).

Pour Meta, un seul conformère a été obtenu. Pour Fen, 11 minima ont été caractérisés avec des énergies relatives sous le seuil des 10 kcal/mol (Figure 11).

Les complexes Meta-cation optimisés sont présentés dans la Figure 12. Pour les complexes Meta- Na^+ and Meta- Ca^{2+} , les quatre familles obtenues ne se recouvrent pas en énergies relatives. De plus, la base a une légère influence sur les énergies et PBE/basis1 donne le bon ordre énergétique pour les différentes familles.

Pour Meta- Na^+ , une complexation sur les deux atomes d'azote du cycle triazine (N-N) est préférée du fait de l'interaction favorable de Na^+ qui se fait approximativement le long de la direction du moment dipolaire de la molécule. Pour Ca^{2+} , une complexation sur l'oxygène du carbonyle et le système π du cycle triazine (CO-Phe) est clairement favorisée alors que l'ordre énergétique des autres familles est le même qu'avec Na^+ .

Finalement, afin de calculer des énergies de complexation précises, le niveau PBE/basis2 doit être employé en particulier pour réduire la BSSE (Basis Set Superposition Error en Anglais). Pour Meta- Ca^{2+} , des géométries optimisées plus précises ont aussi été obtenues à ce niveau de calcul (plus spécifiquement les distances Phe-Ca, qui ont besoin d'une meilleure description de la polarisation).

Dans le cas des complexes Meta-(cation)₂ (Figure 13), les trois familles qui ont été caractérisées sont des combinaisons des sites de complexation des systèmes Meta-(cation). Finalement, pour Na^+ et Ca^{2+} , l'ordre énergétique des familles est le même quelque soit la base utilisée. L'isomère de plus basse énergie implique la combinaison des sites de complexation N-N et CO-Phe précédents. L'influence de la base sur les distances du cation au site de complexation est plus grande que dans les complexes Meta-(cation) et le niveau PBE/basis2 sera préféré dans ce cas-ci.

Dû à la complexité supérieure de la géométrie de Fen, les SEP des systèmes Fen-cation et Fen-(cation)₂ sont plus difficiles à explorer. Plus de familles existent (5), et seulement

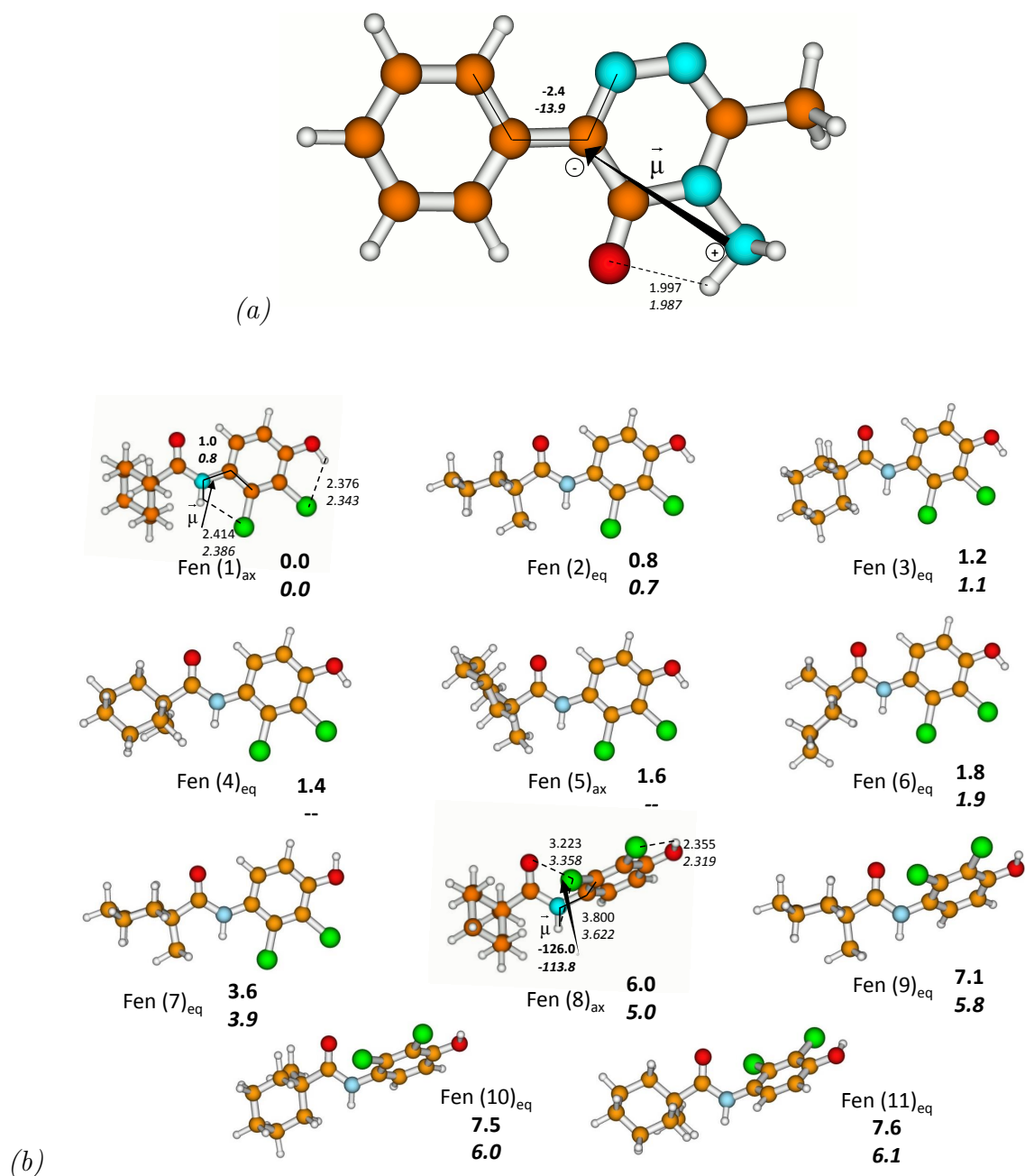


Figure 11: (a) Conformère de la métamitronne, (b) conformères de basses énergies du fenhexamide : les distances sont en Å, les dièdres en degrés (en gras) aux niveaux PBE/basis1 et PBE/basis2 (en italique). $\vec{\mu}$ est le vecteur de moment dipolaire.

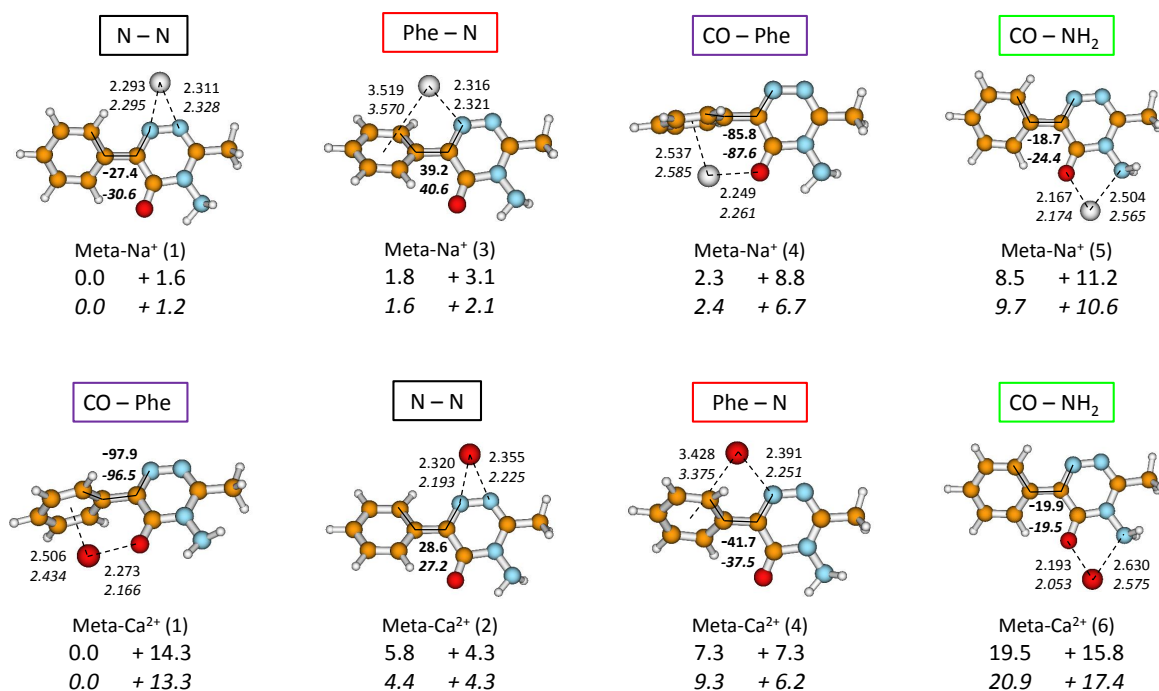


Figure 12: Les isomères de plus basses énergies de chaque famille pour Meta- Na^+ (première ligne) et Meta- Ca^{2+} (deuxième ligne). Les énergies relatives (à gauche) et de préparation (à droite) sont présentées en kcal/mol aux niveaux PBE/basis1 et PBE/basis2 (en italique). Les distances sont en Å, les dièdres en degrés (en gras) aux niveaux PBE/basis1 et PBE/basis2 (en italique).

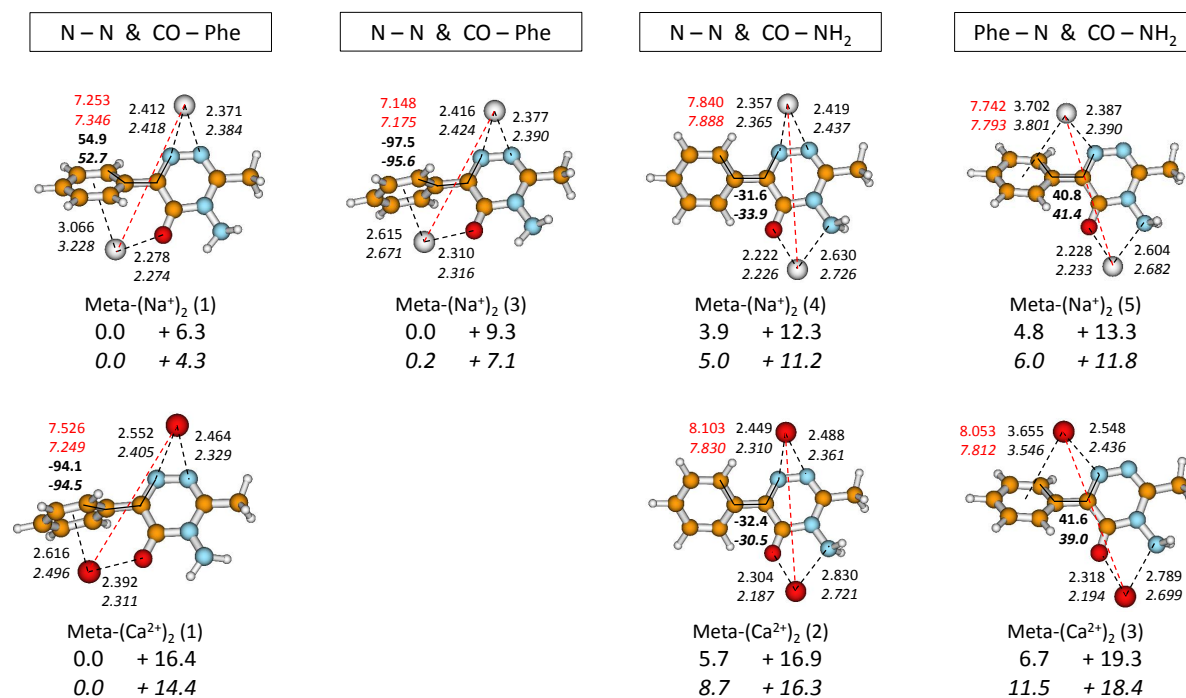


Figure 13: Sept isomères de basses énergies de la métamitrone avec deux Na^+ (première ligne) et deux Ca^{2+} (deuxième ligne). Les énergies relatives (à gauche) et de préparation (à droite) sont présentées en kcal/mol aux niveaux PBE/basis1 et PBE/basis2 (en italique). Les distances sont en Å, les dièdres en degrés (en gras) aux niveaux PBE/basis1 et PBE/basis2 (en italique).

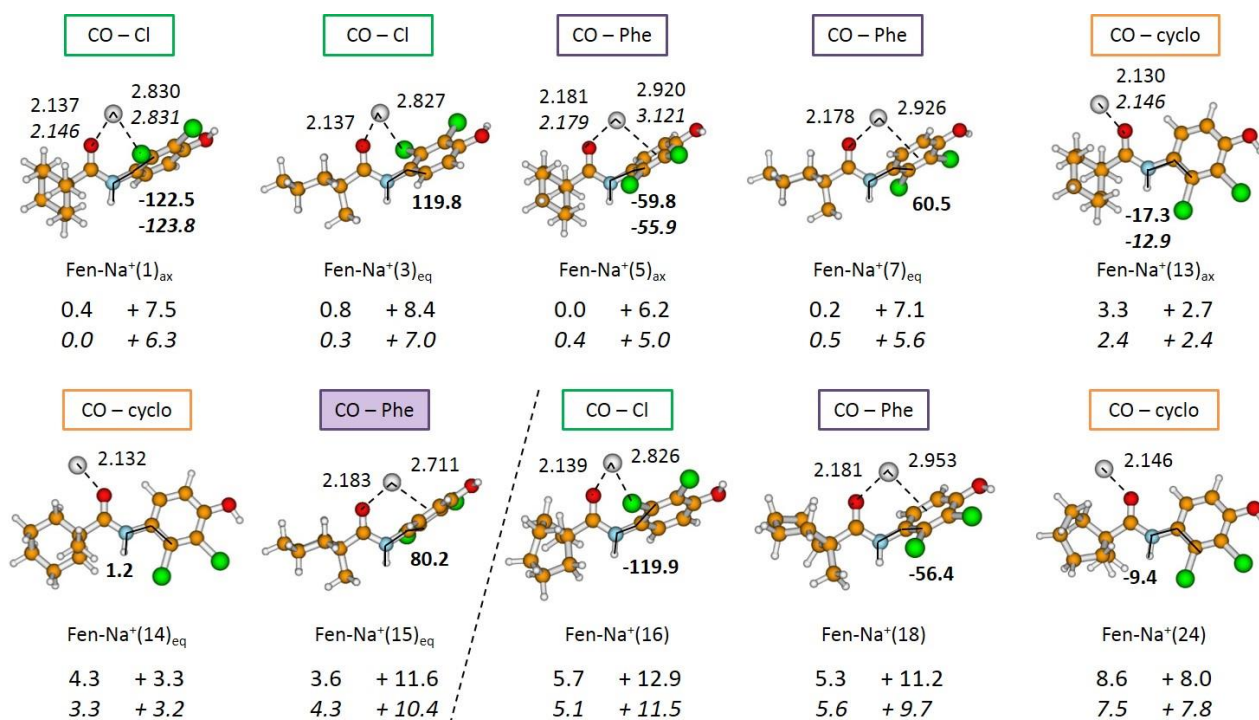


Figure 14: Les principaux isomères de basses énergies du fenhexamide avec un cation Na^+ . Les énergies relatives (à gauche) et de préparation (à droite) sont présentées en kcal/mol aux niveaux PBE/basis1 et PBE/basis2 (en italique). Les distances sont en Å et les dièdres en degrés (en gras) au niveau PBE/basis1. Pour les isomères les plus bas de chaque famille, des paramètres géométriques sont aussi donnés au niveau PBE/basis2 (en italique). Pour des délocalisations totalement brisées dans la famille CO-Phe, les cadres ont été colorés en violet. Au-delà de la limite matérialisée par la ligne pointillée, le groupe cyclohexyle a perdu sa conformation en chaise.

trois sont communes à Na^+ et Ca^{2+} . De plus, l'ordre des familles dépend de la base : PBE/basis2 doit être utilisée pour retrouver le bon ordre énergétique (Figure 14 et 15).

Dans le cas de Na^+ , le site de complexation privilégié implique l'oxygène du carbonyle et le chlore le plus proche. Pour Ca^{2+} , une complexation sur l'oxygène du carbonyle et le système π du phényle substitué est plus favorable (comme pour Meta). Enfin, la base a une influence non négligeable même sur les géométries, en particulier pour les complexes avec le calcium. Afin de réduire la BSSE et de traiter correctement la contribution du transfert de charge (Charge Transfer (CT) en Anglais), la basis2 doit être utilisée.

Pour Fen-(cation)₂, de nombreux isomères ont été optimisés pour lesquels les sites de complexation ne sont pas des combinaisons des précédents isomères (Figure 16 et 17). L'ordre énergétique des familles est le même pour Na^+ et Ca^{2+} (comme pour Meta). L'isomère le plus bas en énergie implique dans les deux cas une interaction bidentate sur l'oxygène de l'hydroxyle et le chlore le plus proche, et une interaction monodentate du second cation sur l'oxygène du carbonyle, ce cation polarisant le groupe cyclohexyle.

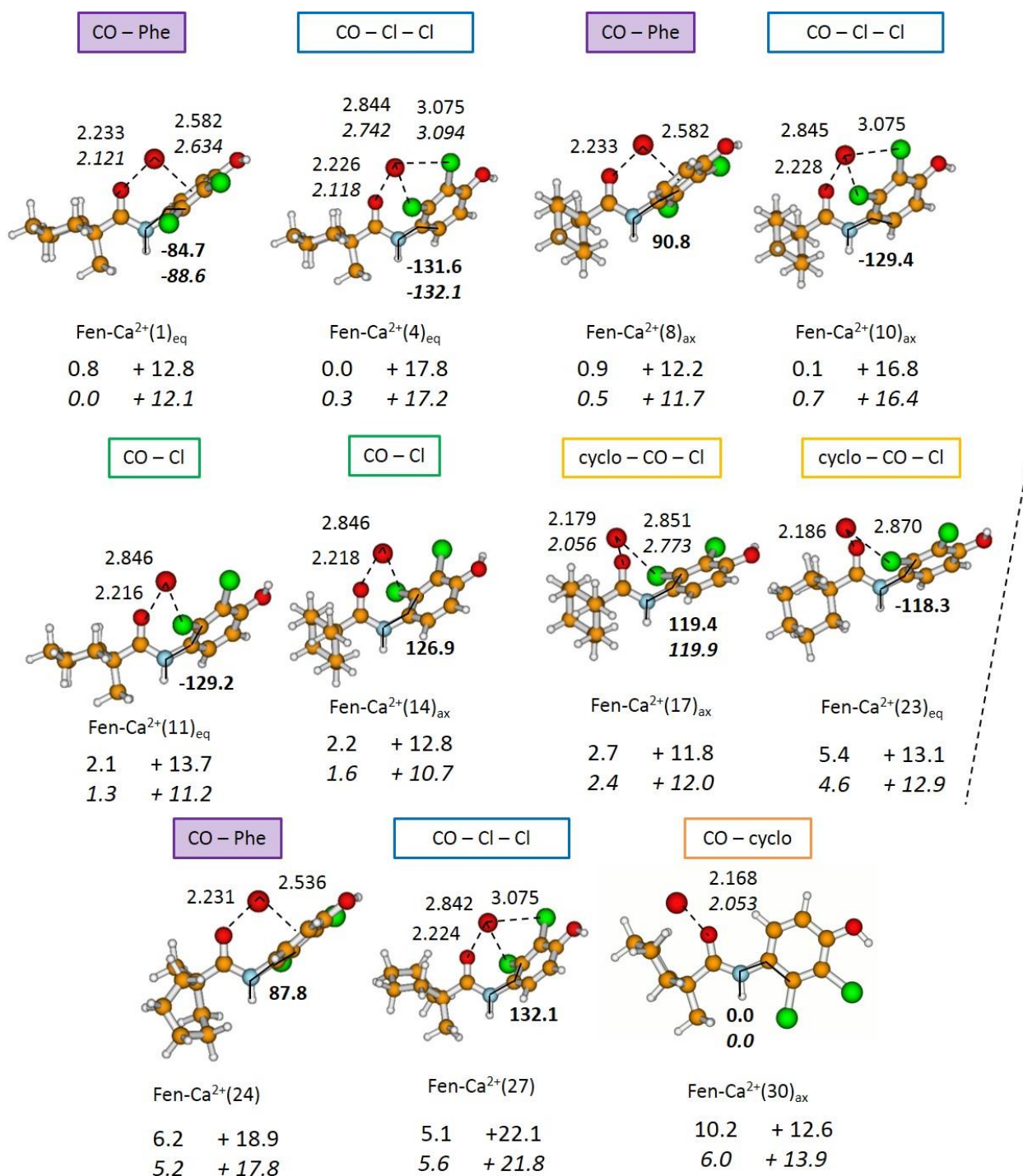


Figure 15: Les principaux isomères de basses énergies du fenhexamide avec un cation Ca^{2+} . Les énergies relatives (à gauche) et de préparation (à droite) sont présentées en kcal/mol aux niveaux PBE/basis1 et PBE/basis2 (en italique). Les distances sont en Å et les dièdres en degrés (en gras) au niveau PBE/basis1. Pour les isomères les plus bas de chaque famille, des paramètres géométriques sont aussi donnés au niveau PBE/basis2 (en italique). Pour des délocalisations totalement brisées dans la famille CO-Phe, les cadres ont été colorés en violet. Au-delà de la limite matérialisée par la ligne pointillée, le groupe cyclohexyle a perdu sa conformation en chaise excepté pour Fen- $\text{Ca}^{2+}(30)_{\text{ax}}$.

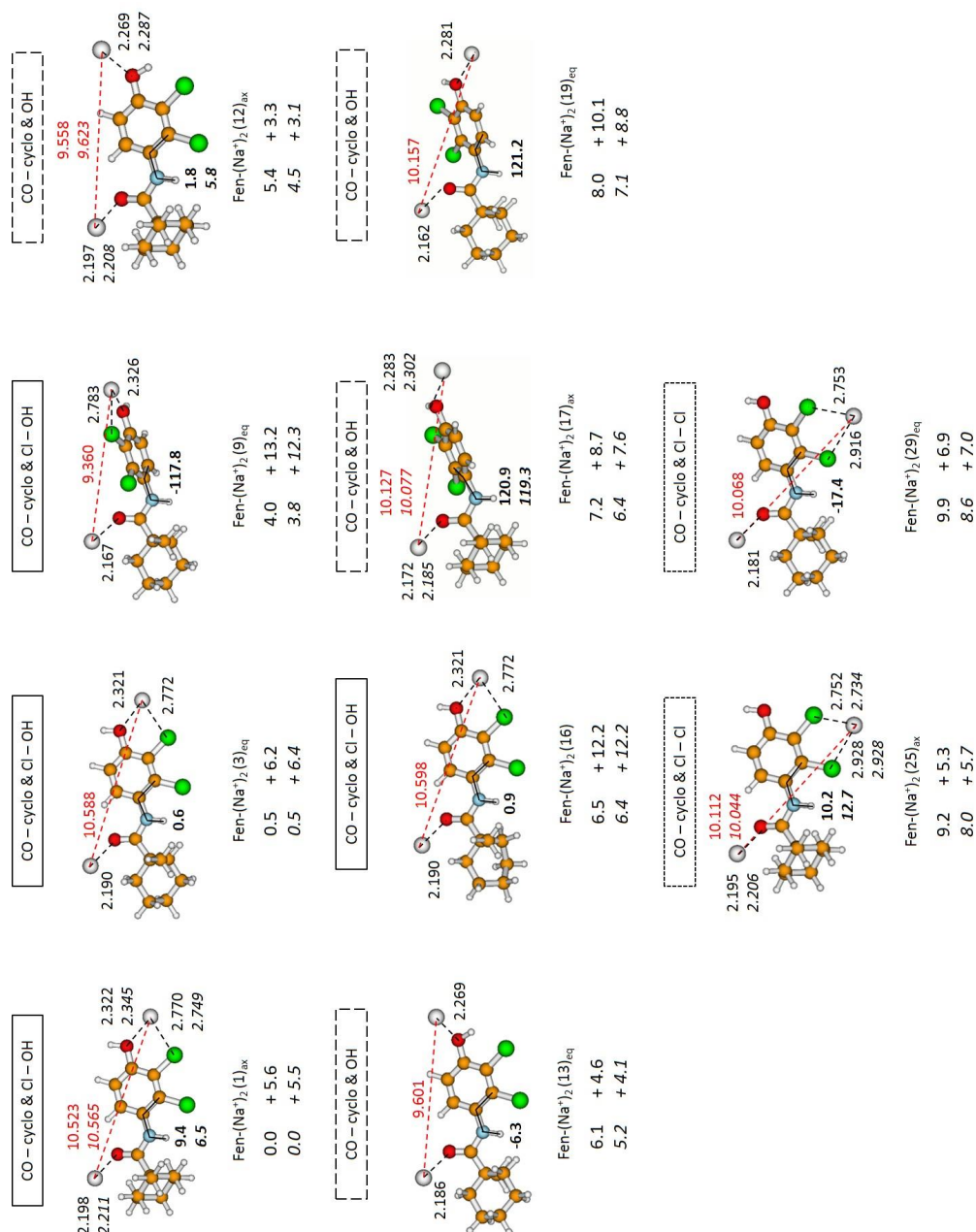


Figure 16: Les principaux isomères de basses énergies du fenhexamide avec deux cations Na^+ . Les énergies relatives (à gauche) et de préparation (à droite) sont présentées en kcal/mol aux niveaux PBE/basis1 et PBE/basis2 (en italique). Les distances sont en Å et les dièdres en degrés (en gras) au niveau PBE/basis1. Pour les isomères les plus bas de chaque famille, des paramètres géométriques sont aussi donnés au niveau PBE/basis2 (en italique).

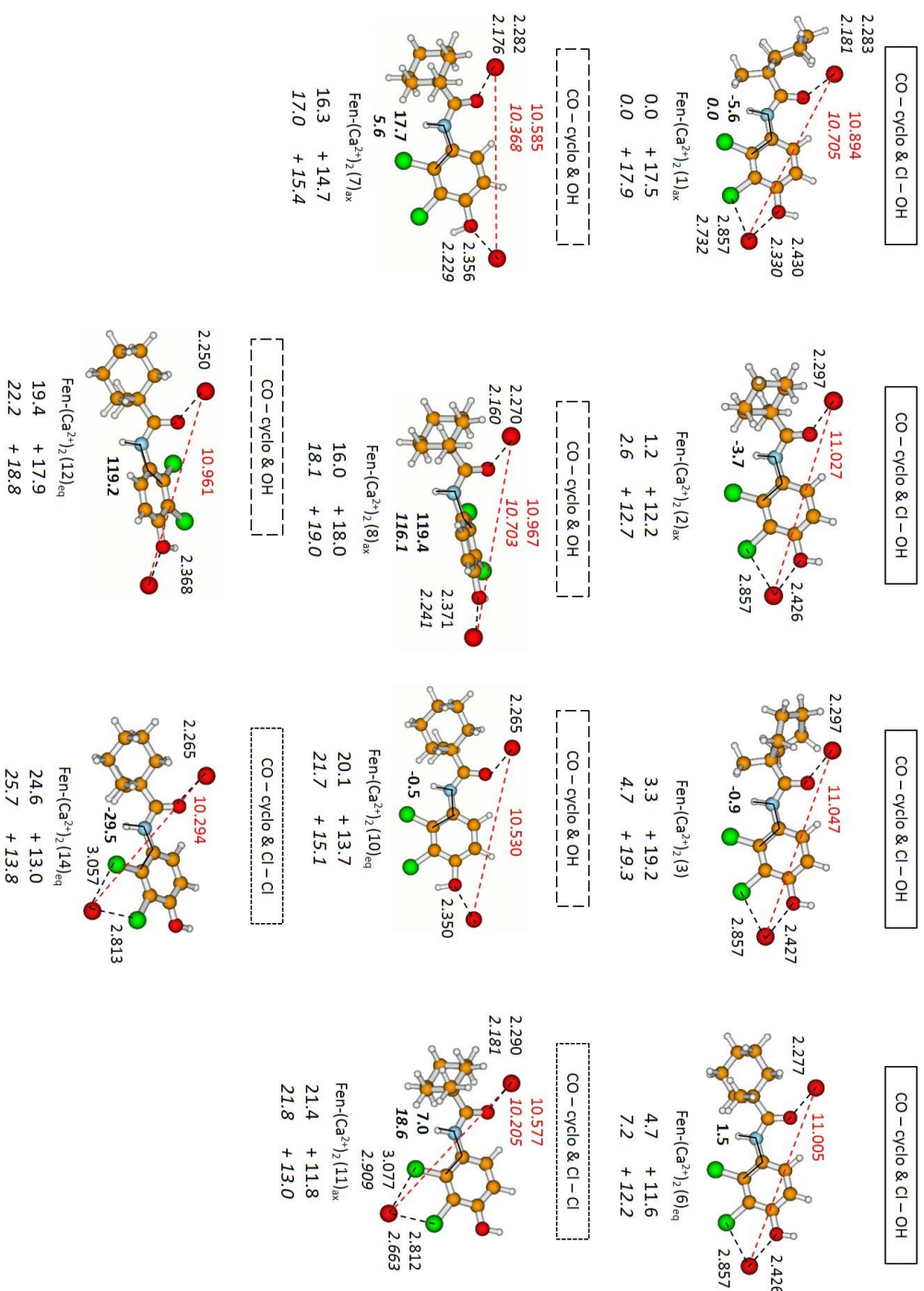


Figure 17: Les principaux isomères de basses énergies du fenhexamide avec deux cations Ca^{2+} . Les énergies relatives (à gauche) et de préparation (à droite) sont présentées en kcal/mol aux niveaux PBE/basis1 et PBE/basis2 (en italique). Les distances sont en Å et les dièdres en degrés (en gras) au niveau PBE/basis1. Pour les isomères les plus bas de chaque famille, des paramètres géométriques sont aussi donnés au niveau PBE/basis2 (en italique).

En prenant en compte Meta et Fen, les valeurs énergétiques correspondant aux complexations sont du même ordre de magnitude:

- E_{comp} est d'environ -40 kcal/mol avec un Na^+ , -140 kcal/mol avec un Ca^{2+} , -22 kcal/mol avec deux Na^+ et -30 (Meta) et -60 (Fen) kcal/mol pour deux Ca^{2+} .
- ΔG_{comp} est approximativement égale à -32 kcal/mol avec un Na^+ , -130 kcal/mol avec un Ca^{2+} , -7 kcal/mol avec deux Na^+ et -10 (Meta) et -40 (Fen) kcal/mol pour deux Ca^{2+} .

Une analyse détaillée des contributions à l'énergie d'interaction a été produite dans ce travail à l'aide de la méthode RVS SCF, précédemment utilisée pour l'atrazine. Dans les complexes avec le sodium (un ou deux Na^+), E_{elec} représente environ $\frac{2}{3}$ et E_{pol} $\frac{1}{3}$ de la somme des termes attractifs. Alors que pour les complexes incluant le calcium, seulement 50 % correspond à E_{elec} , 40 % à E_{pol} et 10 % E_{CT} . La différence dans les proportions des contributions entre les complexes de pesticides avec Na^+ et Ca^{2+} mènera probablement à différentes adsorptions sur des Na-montmorillonite et Ca-montmorillonite. L'adsorption sur une Ca-montmorillonite est le sujet du chapitre suivant (Chapitre VI).

6 Adsorption de la métamitrone et du fenhexamide sur une surface de Ca-montmorillonite

Dans la section précédente, des simulations CPMD ont été employées dans l'ensemble NVE au moyen de la DFT/PBE pour explorer autant que possible les conformations de la métamitrone et du fenhexamide d'une part, et leurs isomères les plus probables en présence d'un ou deux cations Na^+ ou Ca^{2+} d'autre part. Ces résultats ont montré, en accord avec la publication précédente sur les complexes de l'atrazine avec les mêmes cations, que Ca^{2+} en interaction avec la métamitrone ou le fenhexamide présente une énergie de complexation de -140 kcal/mol, bien plus forte que la complexation avec Na^+ . Pour cette raison, comme pour l'atrazine, une surface de Ca-montmorillonite a été choisie comme modèle pour étudier l'interaction de la métamitrone et du fenhexamide avec la matière minérale du sol. Comme les isomères des pesticides adsorbés sur le modèle de Ca-montmorillonite sont explorés, la DFT périodique est employée avec une correction de dispersion de Grimme de type D2 (PBE-D2) [231], dans une base d'ondes planes avec une énergie de coupure de 80 Ry.

Cinq explorations par dynamique moléculaire ont été effectuées, deux pour la métamitrone (Meta-Mont(CO-Phe) et Meta-Mont(N-N)), et trois pour le fenhexamide

(Fen-Mont(CO-Phe)_{para,eq}, Fen-Mont(Cl-OH)_{para,ax} et Fen-Mont(Cl-OH)_{ortho-short,ax}) adsorbés sur la Ca-montmorillonite. Ce type de système en phase solide sèche sera noté ϕ_{solid}^{dry} dans la suite. Ces simulations représentent chacune 12 ps de dynamique (120 000 pas de 0,1 fs) dans l'ensemble NVE à des températures moyennes de 888 K, 932 K, 897 K, 873 K et 962 K respectivement, avec des masses électroniques fictives $\mu = 350,0$ u.a. Tous les autres paramètres étant les mêmes que dans l'étude dynamique en phase gaz (ϕ_{gas}) de la métamitrone et du fenhexamide.

Cette méthode a permis de trouver une plus grande variété d'isomères optimisés et de familles de complexation pour chaque pesticide, que pour Atra-Mont où l'exploration de la SEP était statique. Les isomères trouvés pour la métamitrone et le fenhexamide adsorbés sur la surface de Ca-montmorillonite (notés Meta-Mont et Fen-Mont respectivement) sont présentés dans les Figures 18,19 et 20.

Les énergies d'adsorption des formes optimisées de Meta-Mont et Fen-Mont sont du même ordre de magnitude (≈ -44 kcal/mol), mais avec des valeurs absolues supérieures que pour Atra-Mont (≈ -27 kcal/mol).

En ϕ_{gas} , les formes doublement complexées d'Atra et de Meta présentent des distances inter-cation de $\approx 7 - 9$ Å [12], alors que la distance entre les deux calciums (d_{Ca-Ca}) est approximativement $10 - 11$ Å dans les isomères de Fen. Etant donné que la distance inter-cation dans Mont est de $10,341$ Å, une double complexation ne peut être envisagée que pour Fen. En effet, les isomères d'Atra-Mont et de Meta-Mont présentent seulement des complexations sur un cation alors que trois isomères doublement complexés ont été trouvés pour Fen-Mont. De plus, une complexation de Fen avec deux cations est compétitive avec l'isomère simplement complexé le plus bas en énergie (Fen-Mont(1)_{ax}(CO(-Phe)), au regard des énergies d'adsorption.

De manière opposée, en ϕ_{gas} , les doubles complexations sont systématiquement moins favorisées que les simples, dû à la répulsion inter-cation. Effectivement, l'ordre de grandeur de cette énergie de répulsion va de $\approx +140$ à $+180$ kcal/mol pour Atra ($E_{Ca^{2+}-Ca^{2+}}$ dans l'article de Bessac et Hoyau de 2013 [12]), et est approximativement de $+180$ kcal/mol pour Meta, quand elle est de $\approx +120$ kcal/mol pour Fen ($E_{cat-cat}$ [258]), sachant que dans les isomères Fen-(Ca²⁺)₂, d_{Ca-Ca} est plus longue. La double complexation est même répulsive pour Atra étant donné l'énergie de complexation positive qu'elle présente $E_{comp} = +9,80$ kcal/mol (B3LYP/basis2), elle est favorable pour Meta ($E_{comp} = -30,29$ kcal/mol (PBE/basis2)), et encore plus pour Fen ($E_{comp} = -57,13$ kcal/mol (PBE/basis2)).

Dans ϕ_{solid}^{dry} , quand le pesticide est mis en interaction avec la surface, la répulsion Ca-Ca est incluse dans l'énergie de la surface. Par conséquent, les énergies d'adsorption des pesticides sont plus favorables que les énergies de complexation en ϕ_{gas} . Dans ce cas, les

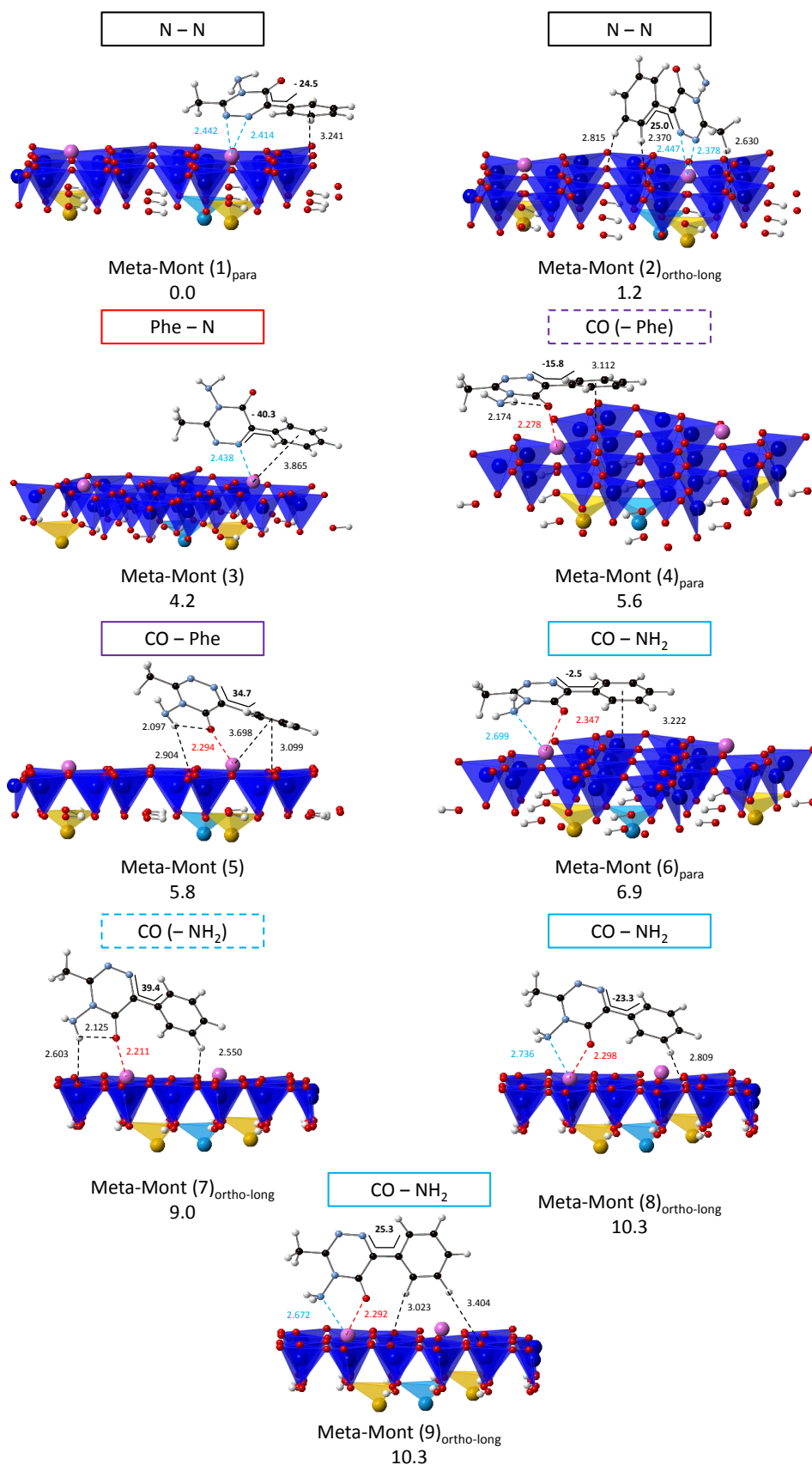


Figure 18: Isomères Meta-Mont présentés avec leurs familles de complexation et leurs énergies relatives (kcal/mol). Les distances (en noir), les distances du cation à l'oxygène (en rouge) et aux azotes (en bleu) de la molécule sont en Å. Le dièdre C1-C2-C3-N4] (en gras) est en degrés.

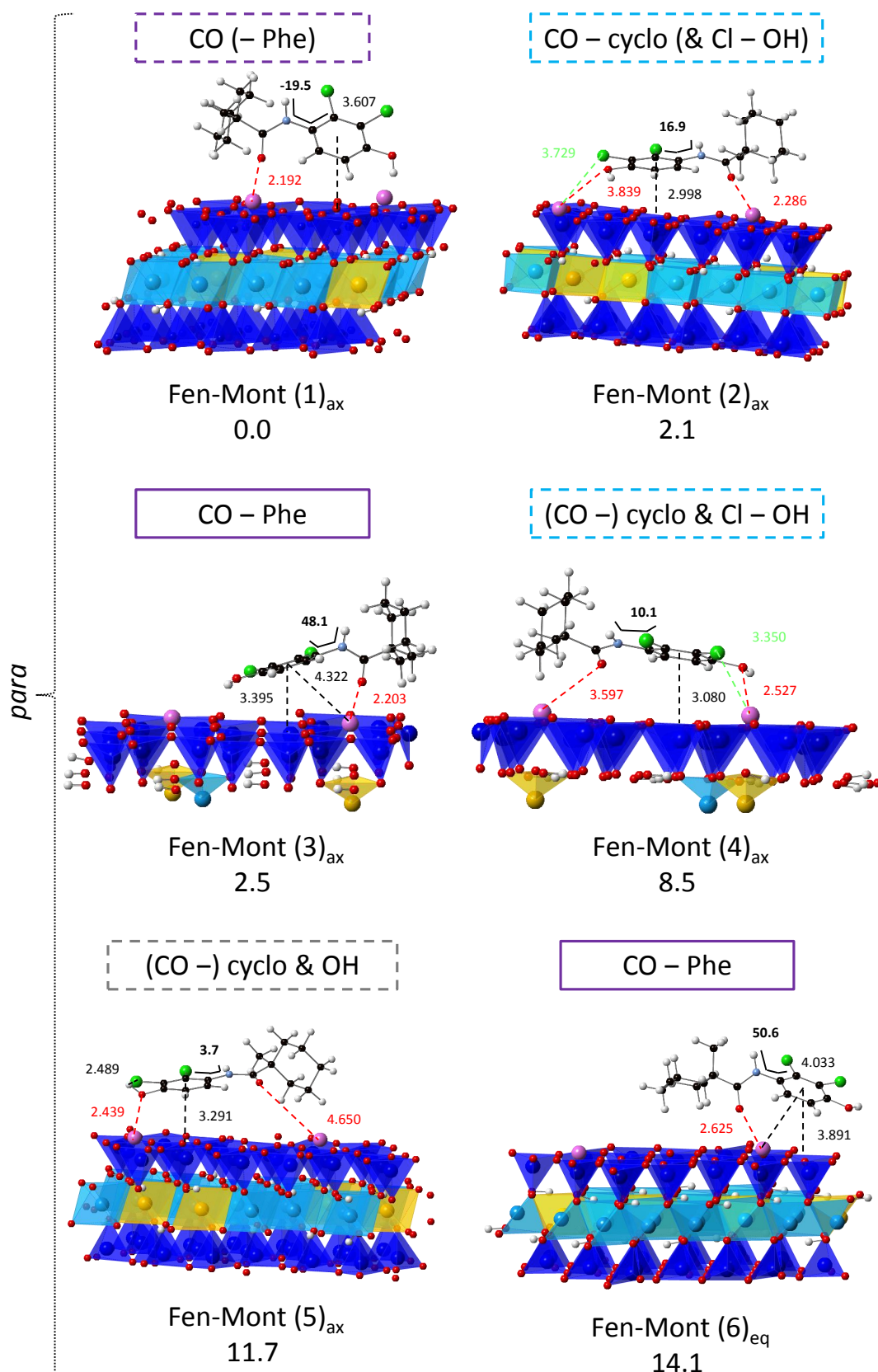


Figure 19: Isomères Fen-mont présentés avec leurs familles de complexation et leurs énergies relatives (kcal/mol). Les distances (en noir), les distances du cation aux oxygènes (en rouge) et chlores (en vert) de la molécule sont en Å. Le dièdre H7-N3-C4-C5] (en gras) est en degrés.

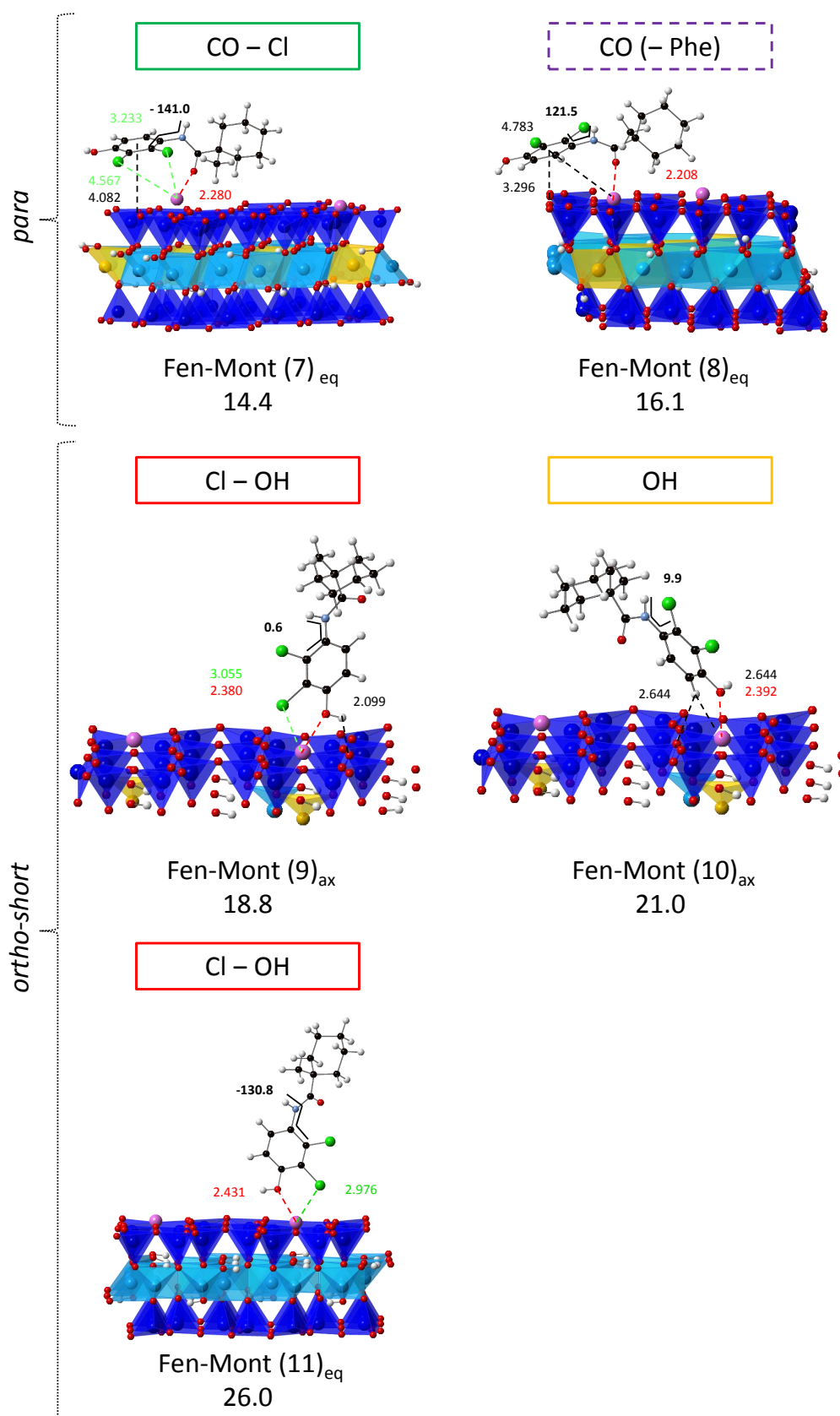



Figure 20: Isomères Fen-mont présentés avec leurs familles de complexation et leurs énergies relatives (kcal/mol). Les distances (en noir), les distances du cation aux oxygènes (en rouge) et chlores (en vert) de la molécule sont en Å. Le dièdre H7-N3-C4-C5] (en gras) est en degrés.

cations restent proches de la surface.

Les contributions de la dispersion dans les énergies d'adsorption (E_{disp}^{ads}) et d'interaction (E_{disp}^{int}) sont toujours similaires pour un isomère donné ($E_{disp}^{ads} \approx E_{disp}^{int}$) que cela soit pour Atra-Mont, Meta-Mont ou Fen-Mont. Comme attendu, les isomères *para* conduisent à de plus fortes interactions de dispersion que les isomères *ortho* – *long* pour Meta-Mont, et qu'*ortho* – *short* pour Fen-Mont. De même, les isomères PARA présentent de plus fortes interactions de dispersion que les isomères ORTHO pour Atra-Mont. Les ordres de magnitude de ces énergies sont similaires entre Atra-Mont (de $-18,1$ à $-13,0$ kcal/mol) et Meta-Mont ($-21,8 \leq E_{disp} \leq -10,3$ kcal/mol), et d'un ordre plus fort pour les isomères *para* de Fen-Mont ($-26,8 \leq E_{disp} \leq -13,5$ kcal/mol), mais moins forts pour les *ortho* – *short* ($-8,3 \leq E_{disp} \leq -7,7$ kcal/mol).

Dans la section suivante, le même type de systèmes a été pris en compte dans les simulations, mais avec l'hydratation explicite de ces systèmes. De plus, le comportement des cations adsorbés sera traité avec grande attention dans le but d'analyser l'influence de la solvation sur de tels systèmes.

7 Effets de solvation et desorption du fenhexamide

ans le chapitre précédent, les structures de la métamitrone et du fenhexamide adsorbés sur une surface sèche de Ca-montmorillonite ont été optimisées. La description du sol dans le Chapitre II indique qu'un quart de sa composition est principalement de l'eau. De plus, rappelons que la montmorillonite est un minéral avec une forte capacité de gonflement et d'absorption de l'eau dans son interfeuillet. La métamitrone et le fenhexamide sont tous deux des espèces solubles dans l'eau, jusqu'à 1 770 mg/L et 24,0 mg/L à 20°C respectivement.

Le Chapitre VII est organisé en deux parties : premièrement, une étude des effets de l'hydratation sur l'interaction des pesticides avec le modèle de Ca-montmorillonite, et les implications pour la surface est considérée. Les deux molécules seront simulées en adsorption sur la surface et en présence d'eau lors de trajectoires CPMD contrôlées en température. Dans la seconde partie, le processus de désorption du fenhexamide de la surface hydratée sera étudié dans le but de quantifier les barrières d'énergies libres de cette désorption.

Interaction des pesticides avec une surface hydratée de Ca-montmorillonite

Quatre structures ont été considérées pour cette étude de solvation (deux pour chaque pesticide) et sont présentées dans la Figure 21. Dans toute la suite, ces phases solides hydratées seront notées $\phi_{solid}^{H_2O}$ et Ca1 est le cation en interaction avec le pesticide alors que Ca2 est l'autre cation. Il est nécessaire de préciser que ces quatre simulations ont été effectuées avant l'exploration complète des isomères en ϕ_{solid}^{dry} du Chapitre VI. Pour cette raison, ces quatre structures de départ ne correspondent pas aux géométries des isomères Meta-Mont et Fen-Mont de plus basses énergies. Par conséquent, un isomère Fen-Mont doublement complexé n'a pas été considéré. Ces quatre structures ont été initialement choisies dans le but d'étudier Meta-Mont en orientations *para* et *ortho* – *long*, ainsi que Fen-Mont en *para* et *ortho* – *short*. Néanmoins, pour chaque pesticide, la complexation **CO(-Phe)** a été étudiée afin de permettre une comparaison.

Les quatre trajectoires ont été effectuées dans l'ensemble NVT pendant 12 ps avec un thermostat de Langevin [269–271] tel qu'il est implémenté dans le logiciel CPMD [233]. Le pas de temps et l'énergie de coupure des ondes planes sont les mêmes que dans l'exploration des isomères du chapitre précédent (0,1 fs et 80 Ry) mais avec une masse électronique fictive μ de 400 u.a.

Comme présenté dans le chapitre de théorie (Section III. B.5), la fonctionnelle PBE (avec ou sans correction de dispersion) tend à sur-structurer l'eau comparée à l'expérience [222–228, 267]. En conséquence, le thermostat des simulations est fixée à une valeur de 350 K au-lieu de 298 K (température ambiante), pour essayer de surmonter ce problème de sur-structuration, et obtenir des distances de premiers voisins (entre molécules d'eau) de 2,80 Å. Cette valeur expérimentale à température ambiante étant la plus récente et la plus précise actuellement [228, 268, 272–275].

Après un temps d'équilibration de 4 ps, l'énergie potentielle des quatre trajectoires est relativement stabilisée. Tous les résultats présentés dans la suite ont donc été produits après 4 ps de thermalisation. Sur les quatre simulations, la température moyenne est d'environ 330 K : 334 K pour Meta-Mont $_{ortho-long}^{H_2O}$ (N-N), 330 K pour Meta-Mont $_{para}^{H_2O}$ (**CO(-Phe)**), 331 K pour Fen-Mont $_{para,ax}^{H_2O}$ (**CO(-Phe)**), et 333 K pour Fen-Mont $_{ortho-short,ax}^{H_2O}$ (Cl-OH).

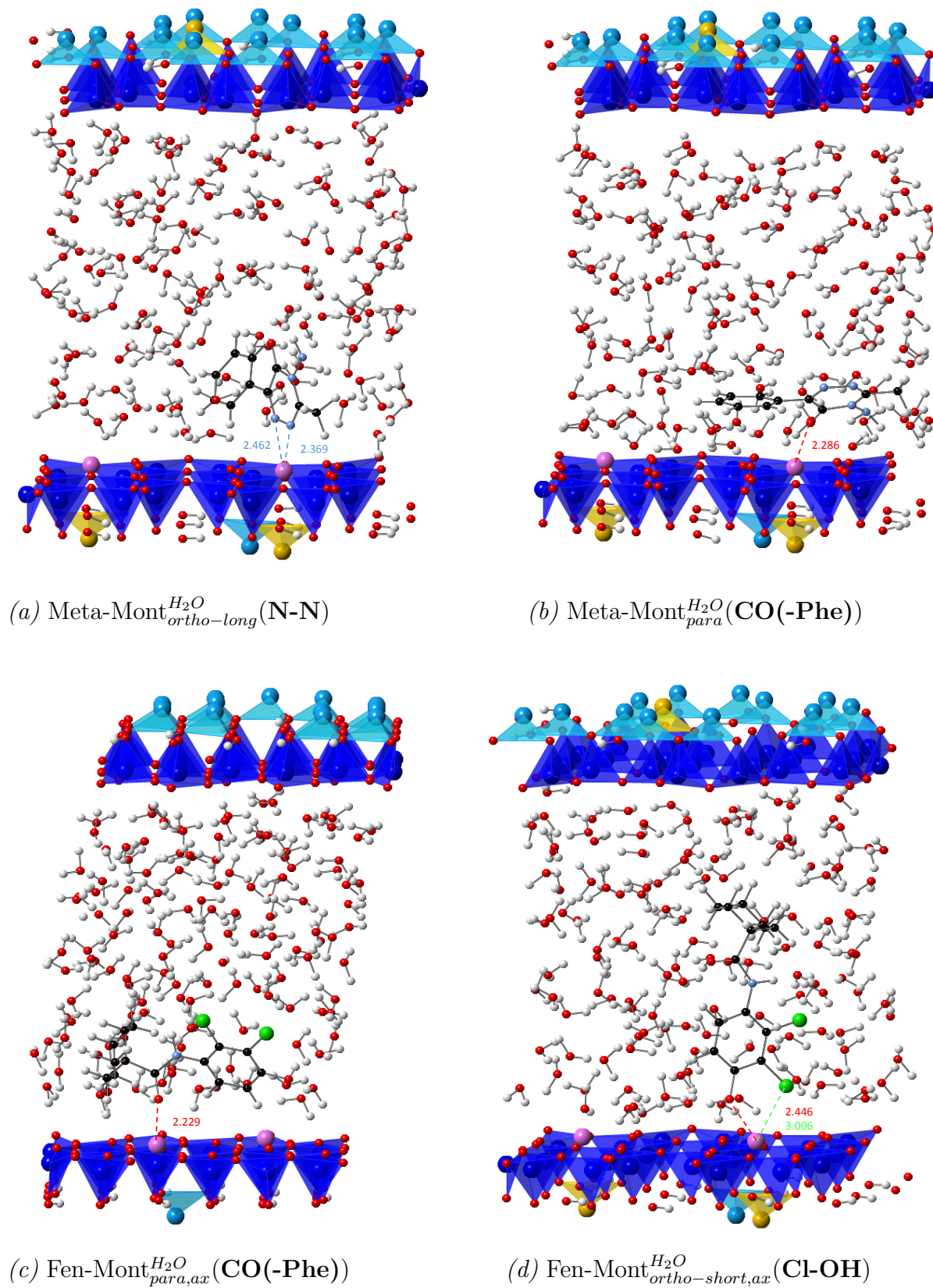


Figure 21: Structures de départ des trajectoires CPMD en $\phi^{H_2O}_{solid}$, les distances sont présentées en Å.

L'hydratation du système n'a pas de conséquences sur l'interaction entre les pesticides et les cations calciums. En effet, la comparaison entre les isomères les plus bas en ϕ_{solid}^{dry} et les résultats en $\phi_{solid}^{H_2O}$ présentent la même tendance :

- $2,2 \leq d_{Ca1-O} \leq 2,3$ Å pour les deux pesticides ;
- $d_{Ca1-N4} \approx d_{Ca1-N5} \approx 2,4 - 2,5$ Å, pour Meta, montre que le site de complexation reste bidentate tout au long de la trajectoire de Meta-Mont $_{ortho-long}^{H_2O}((N-N))$;
- $d_{Ca1-Cl} \approx 3,1$ Å alors que $d_{Ca1-OH} \approx 2,3 - 2,4$ Å pour Fen, ce qui montre la plus forte interaction de Ca1 avec l'oxygène de l'hydroxyle qu'avec le chlore.

A propos de l'hydratation de la surface, celle-ci a tout d'abord une légère influence sur la structure interne de la montmorillonite comme attendu : les distances internes augmentent. La solvation présente une influence nettement plus forte sur les cations de l'interfeuillet. Deux types d'hydratation des cations ont été observées dans les minéraux argileux [276] : les cations peuvent être hydratés par plusieurs molécules d'eau alors qu'ils restent adsorbés sur la surface d'argile (sphère de solvation interne), ou peuvent être totalement hydratés, entourés d'eau et détachés de la surface (sphère d'hydratation externe).

Dans les simulations effectuées dans ce travail, Ca2 est solvatoé dans une sphère d'hydratation interne composée de 5 H₂O, arrangées en pyramide à base carrée comme représenté en Figure 22.

En ce qui concerne la solvation de Ca1, il est observé que le niveau d'hydratation a une influence directe sur la distance moyenne $\langle d_{Ca1-O_b} \rangle$ entre Ca1 et les oxygènes de surfaces O_b, et ce quelque soit le site de complexation impliqué. En effet, Meta-Mont $_{para}^{H_2O}(\text{CO}(-\text{Phe}))$ et Fen-Mont $_{para,ax}^{H_2O}(\text{CO}(-\text{Phe}))$ sont tous les deux complexés sur l'oxygène du carbonyle mais présentent des distances $\langle d_{Ca1-O_b} \rangle$ très différentes : 1,71 et 1,06 Å respectivement. Cette différence est due au niveau de solvation de Ca1, plus celui-ci est élevé, plus la distance moyenne $\langle d_{Ca1-O_b} \rangle$ s'allonge:

- Dans Fen-Mont $_{para,ax}^{H_2O}(\text{CO}(-\text{Phe}))$, Ca1 interagit avec seulement 1 molécule H₂O ($\langle d_{Ca1-O_b} \rangle = 1,06$ Å).
- D'autre part, dans Meta-Mont $_{para}^{H_2O}(\text{CO}(-\text{Phe}))$, 2 molécules H₂O solvatent Ca1 ($\langle d_{Ca1-O_b} \rangle = 1,71$ Å).

Dans Meta-Mont $_{ortho}^{H_2O}(\text{N-N})$, Ca1 est complexé avec une molécule d'eau comme dans Fen-Mont $_{para,ax}^{H_2O}(\text{CO}(-\text{Phe}))$ avec une distance $\langle d_{Ca1-O_b} \rangle$ similaire (1,03 Å), alors que le site de complexation est différent. Concernant Fen-Mont $_{ortho,ax}^{H_2O}(\text{Cl-OH})$, deux molécules d'eau hydratent Ca1 comme dans Meta-Mont $_{para}^{H_2O}(\text{CO}(-\text{Phe}))$ mais avec une $\langle d_{Ca1-O_b} \rangle$

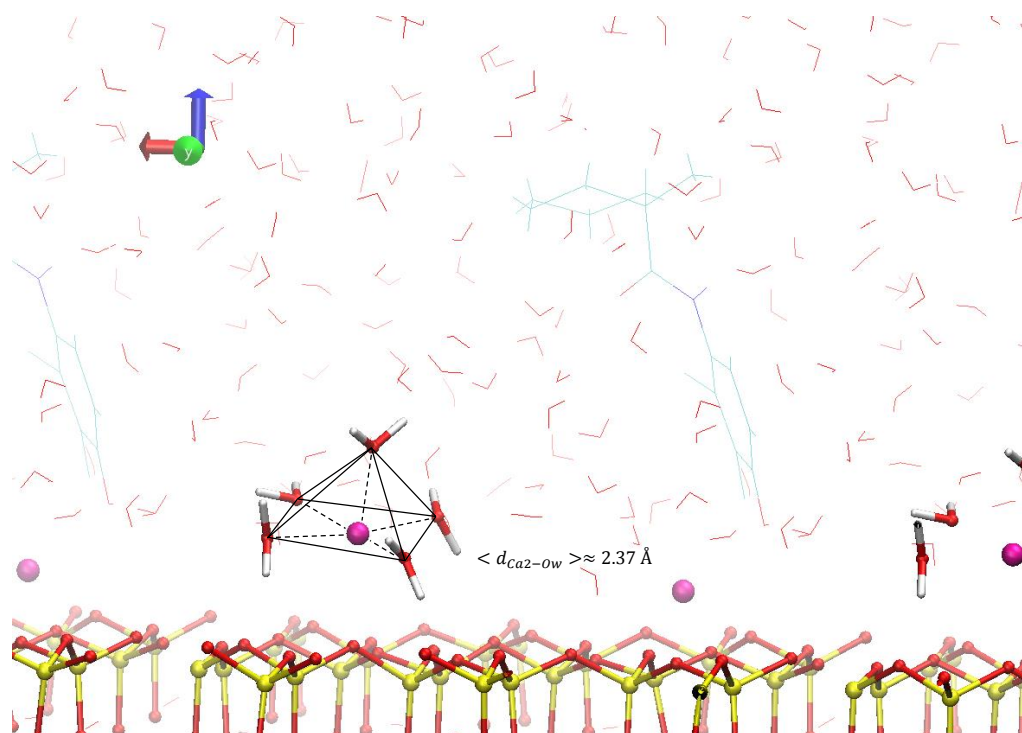


Figure 22: Capture de la trajectoire de Fen-Mont $^{H_2O}_{ortho,ax}$ (Cl-OH). Le fenhexamide et toutes les molécules H₂O sont représentés par des lignes exceptée la sphère d'hydratation interne de Ca2 (pyramide à base carrée) qui est en représentation boules et bâtons, comme le sont la surface et les cations.

plus courte (1,26 Å). Dans ce cas, la disponibilité de Ca1 vis-à-vis de l'eau est supérieure, cela pourrait être dû à l'orientation *ortho* – *short* du pesticide.

Il est intéressant de noter que dans les systèmes secs (ϕ_{solid}^{dry}), l'élongation de d_{Ca1-O_b} provenant de l'interaction de Ca1 avec le pesticide, provoque le léger rapprochement de Ca2 vers la surface alors qu'un comportement tout à fait opposé se produit dans les systèmes hydratés ($\phi_{solid}^{H_2O}$) : Ca2 solvate s'éloigne deux fois plus de la surface que Ca1.

Désorption du pesticide de la surface de Ca-montmorillonite hydratée

Au cours des chapitres précédents, l'atrazine, la métamitronne et le fenhexamide ont été étudiés vis-à-vis des complexes qu'ils forment en présence d'un ou deux cations Na⁺ ou Ca²⁺ en ϕ_{gas} . Ensuite, la seconde étape a été d'adsorber les pesticides sur une surface sèche de Ca-montmorillonite. Enfin la solvation de ces espèces sur la surface a été étudiée. Cette méthodologie a été menée dans le but de comprendre l'influence de chaque partie du modèle sur l'interaction.

Les résultats de ces chapitres montrent que les énergies de complexation de Meta et Fen avec Ca²⁺ sont très similaires que ce soit en ϕ_{gas} (≈ -140 kcal/mol) ou en ϕ_{solid}^{dry} (≈ -40 kcal/mol). Néanmoins, Fen semble être plus complexe et plus riche en possibilités

de résultats du fait de ces nombreuses conformations possibles et orientations par rapport à la surface, comparé à Meta (voir Chapitre V). Dans cette dernière partie, le fenhexamide a été choisi pour l'étude de la désorption d'un pesticide d'une surface d'argile hydratée.

Le but de ce travail est de quantifier la barrière d'énergie libre qui doit être franchie pour désorber le fenhexamide de la Ca-montmorillonite hydratée.

Pour accomplir cette désorption, une méthode disponible, l'Umbrella Sampling [277–280], consiste à lancer des séries de dynamiques moléculaires biaisées en parallèle afin de déplacer un système chimique d'un état thermodynamique à un autre, ici, Fen adsorbé sur Mont, vers un état où Fen est désorbé. Cette méthode est utilisée pour l'exploration de surfaces d'énergie libre d'un système le long d'une coordonnée de réaction choisie arbitrairement, et permet de franchir les barrières d'énergie. Par la suite, la méthode WHAM (Weighted Histogram Approximation Method en Anglais) [281] permet la reconstitution de manière itérative et auto-cohérente de la surface complète d'énergie libre, explorée à l'aide de multiples dynamiques moléculaires biaisées.

Le processus de désorption d'un seul et unique isomère, Fen-Mont $^{H_2O}_{para}$ (CO(-Phe)), a pu être étudié du fait du coût représenté par la méthode d'Umbrella Sampling en DFT sur un système de plus de 600 atomes. Au total, 11 simulations (ou fenêtres d'exploration) au niveau CPMD/PBE-D2 ont été effectuées en parallèle à 330 K en moyenne dans l'ensemble NVT et le profil énergétique présenté en Figure 23.(a) a été obtenu, associé au fenêtre d'exploration de la surface d'énergie libre en fonction de la coordonnée de réaction ξ choisie arbitrairement (Figure 23.(b)). La coordonnée ξ étant ici la composante z du centre de masse du fenhexamide, qui en augmentant correspond à une augmentation de la distance entre la molécule et la surface. La position du cation Ca^{2+} n'a pas été incluse dans ξ car sa désorption simultanée avec le pesticide était attendue. Le profil obtenu présente trois puits d'énergie libre séparés par deux barrières de 3,0 et 4,5 kcal/mol, pour une distance grandissante entre le site de complexation de la molécule (l'oxygène du carbonyle) et le cation de surface. Chaque barrière correspond à l'inclusion d'une molécule d'eau entre le pesticide et la surface, hydratant Ca1 pas à pas, en commençant par une double coordination avec l'eau, pour évoluer vers une triple, et finalement une quadruple hydratation, comme représenté sur la Figure 24. Ca2 présente différentes premières sphères d'hydratation dans les trois puits : une pyramide à base carrée (5 H_2O), un octaèdre (6 H_2O) et un antiprisme carré distordu (8 H_2O), ce dernier étant la plus grande première sphère d'hydratation stable que l'on puisse obtenir d'après la littérature [283]. Les résultats sur les positions de Ca1 dans les trois puits semblent montrer que deux chemins de désorption différents se recouvrent le long de la coordonnée de réaction ξ : la désorption du complexe Fen- Ca^{2+} , tel que l'évolution entre les puits 1 (**Well 1**, $\xi \approx 14,5$ Bohr) et 2 (**Well 2**, $\xi \approx 16 - 16,5$ Bohr) le suggère, ou bien la désorption de

Fen seul alors que Ca1 reste lié à la surface comme c'est le cas dans le puits 3 (**Well 3**, $\xi \approx 18,5 - 19$ Bohr). Une piste à explorer serait de lancer des simulations d'Umbrella Sampling pour $\xi > 20$ Bohr, en partant de la structure obtenue dans **Well 2** où Ca1 reste complexé sur l'oxygène du carbonyle à une distance similaire à celle dans **Well 1**. Augmenter la distance entre Ca1 et la surface encouragerait probablement la désorption du complexe. Initialement, ces considérations n'ont pas été prises en compte étant donné que les simulations sont très longues à effectuer et ont donc été faites en parallèle. Au regard des résultats obtenus pour l'hydratation de Ca^{2+} sur la montmorillonite et des résultats disponibles dans la littérature sur la désorption de la cytosine et du cation de la montmorillonite [156], la méthode de l'Umbrella Sampling appliquée à de tels systèmes est très prometteuse quant à la quantification de barrières d'énergie libre, en dépit de son coût de calcul colossal.

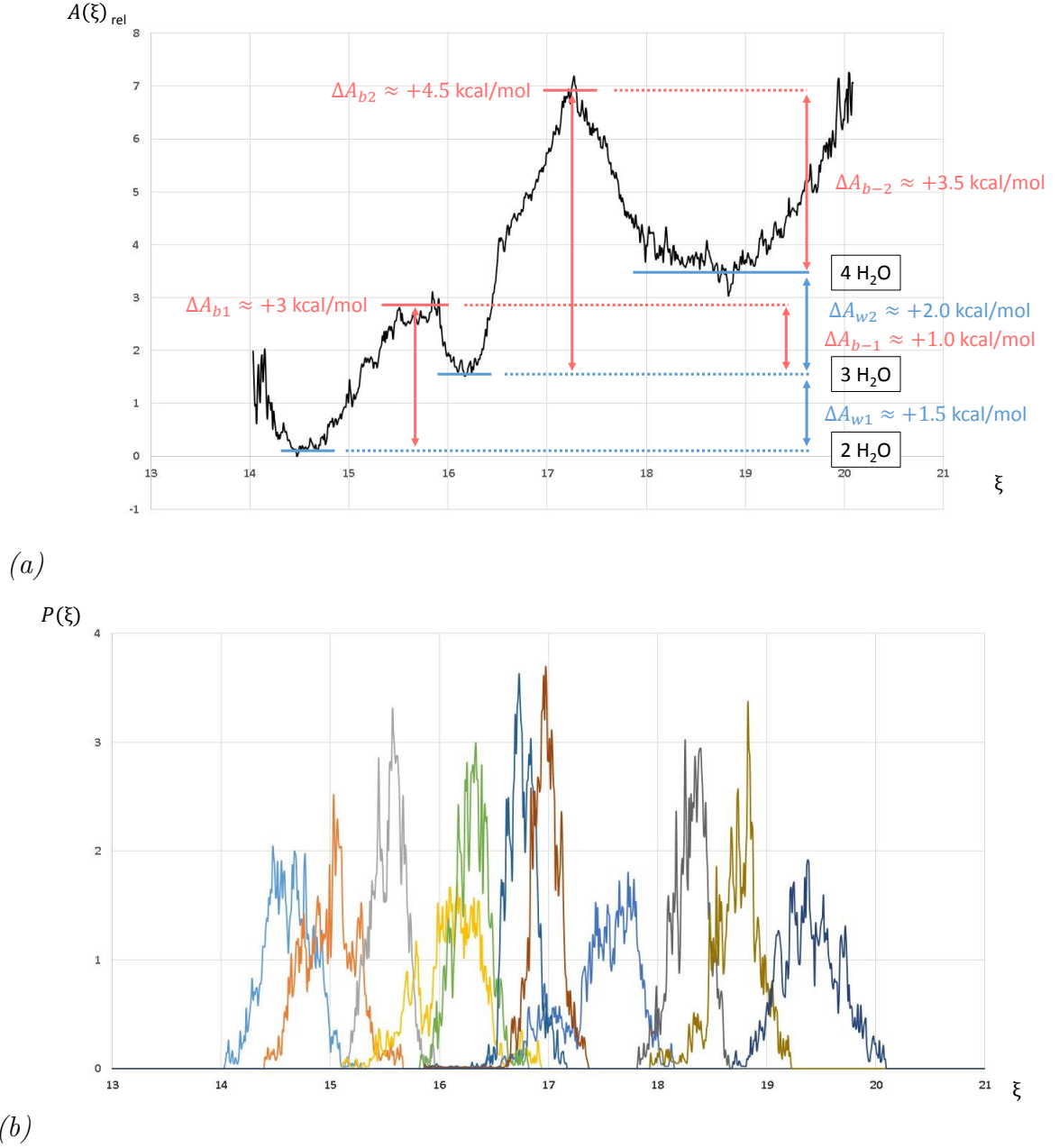


Figure 23: Surface d'énergie libre relative $A(\xi)_{rel}$ (kcal/mol) (a), où les valeurs ΔA_w sont les différences d'énergies libres entre les puits consécutifs et où ΔA_b et ΔA_{b-} sont les énergies relatives nécessaires pour franchir les barrières, pour les processus de désorption et d'adsorption respectivement. Les fonctions de densité de probabilité $P(\xi)$ des 11 fenêtres d'exploration sont présentées en (b), chaque couleur correspond à une fenêtre différente i . ξ est la coordonnée z du centre de masse du pesticide.

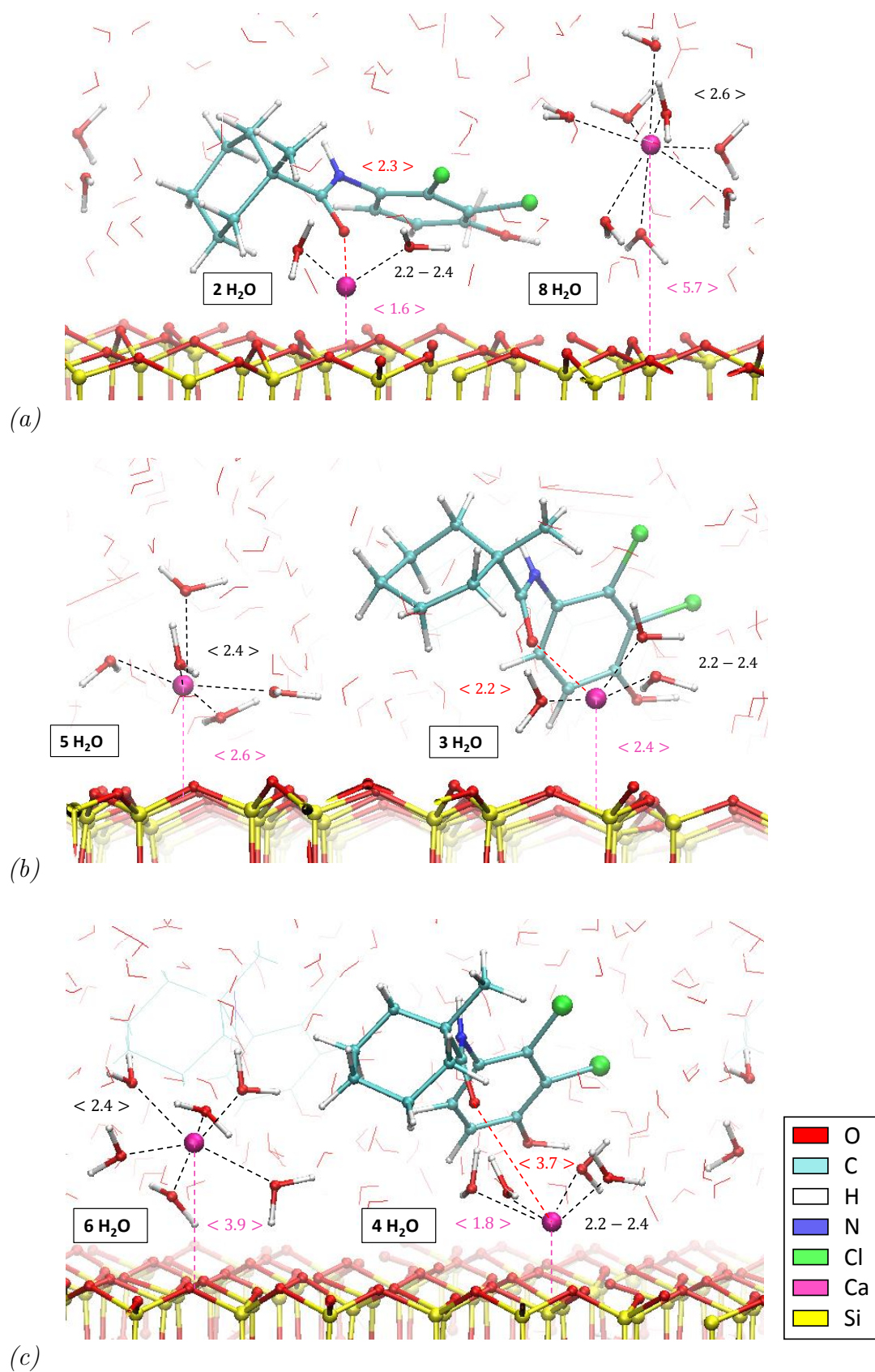


Figure 24: Dernières captures des fenêtres 1 (a), 4 (b) et 10 (c) correspondant au trois puits d'énergie libre du profil énergétique obtenue (Figure 23). Les distances sont présentées en Å.

8 Conclusion

L'objectif de cette étude est d'enrichir les connaissances du comportement des pesticides avec la matière minérale du sol.

En ce sens, des rapports et bases de données concernant les pesticides au sein des pratiques agricoles en Europe et l'état de l'art ont permis de choisir trois pesticides d'intérêt pour cette étude : l'atrazine, la métamitronne et le fenhexamide. L'interaction de ces substances avec la montmorillonite, la plus abondante smectite sur Terre et donc un cas représentatif de la phase minérale du sol, a été considérée à travers un modèle de Ca-montmorillonite. Cette thèse est une approche multi-échelle organisée en quatre étapes, allant de systèmes moléculaires isolés à la phase condensée et réunissant plusieurs méthodes de calculs basées sur la DFT.

- Tout d'abord, l'interaction de l'atrazine avec des surfaces sèches de pyrophyllite et de Ca-montmorillonite a été étudiée à l'aide d'optimisations de géométrie au niveau DFT/PBE-D2 de manière statique. Une adsorption préliminaire de l'atrazine parallèle à la surface de pyrophyllite a permis de démontrer la nécessité d'utiliser une correction de dispersion à la fonctionnelle PBE pour le traitement d'interactions molécule-surface. Le choix d'un modèle de montmorillonite dans lequel les cations compensateurs sont des ions calciums est basé sur des études préliminaires publiées par le groupe de recherche, montrant de bien meilleures énergies de complexation en phase gaz entre l'atrazine et Ca^{2+} (≈ -120 kcal/mol) qu'avec Na^+ (≈ -40 kcal/mol), tous deux des cations abondants dans les sols. Plusieurs orientations, parallèle (PARA) et orthogonale (ORTHO) à la surface, ont été optimisées pour l'atrazine sur la surface de Ca-montmorillonite (Mont) et ont révélé que l'énergie d'adsorption de l'atrazine parallèle est deux à trois fois plus forte sur la Ca-montmorillonite que sur la pyrophyllite. L'adsorption la plus importante étant trouvée pour PARA avec une énergie d'adsorption aux alentours de -30 kcal/mol. Les interactions les plus fortes impliquent l'atome de chlore de l'atrazine et un Ca^{2+} de la surface, avec une distance Ca-Cl comparable à celle dans les complexes Atr- Ca^{2+} en phase gaz. L'adsorption de l'atrazine, quelque soit son orientation, sur un cation Ca^{2+} provoque toujours un éloignement de ce cation vis-à-vis de la surface mais n'implique que de légères modifications de la structure interne de cette surface.
- Deuxièmement, la méthode de Dynamique Moléculaire Car-Parrinello est introduite. Les explorations de surfaces d'énergies potentielles des conformères et des complexes de la métamitronne et du fenhexamide avec un ou deux cations Na^+ ou Ca^{2+} en phase gaz ont été effectuées lors de simulations dans l'ensemble microcanonique. Un

conformère unique a été trouvé pour la métamitrone alors que le fenhexamide en a présenté 11 en-dessous de 10 kcal/mol d'énergie relative. Le fenhexamide possède deux types de structures par rapport à la position du groupement R autour du cyclohexyle : des conformères axiaux et équatoriaux. Le plus bas des conformères trouvés étant axial.

Les complexes de Meta avec un ou deux cations présentent des structures et des énergies relatives associées légèrement influencées par la base. La complexation d'un seul cation sur Meta produit les mêmes familles de complexes mais dans un ordre différent selon la nature du cation. Dans le cas de Fen, les familles de complexation sont différentes mais ont trois types en commun: CO-Cl, CO-Phe et CO-cyclo. Ici, la position de R en axial est légèrement favorisée pour les complexes Fen- Na^+ alors que la position équatoriale est préférée pour Fen- Ca^{2+} excepté quand le cyclohexyle est impliqué dans la complexation. Avec deux cations, les familles de complexes de Fen ont le même ordre en énergies relatives quelques soient le cation et la base utilisée. Contrairement aux complexes Meta-cation, les familles avec deux cations ne sont pas des combinaisons des familles obtenues avec un seul cation.

L'analyse par la décomposition RVS SCF permet de quantifier les différentes contributions à l'énergie d'interaction. Cela a permis de mettre en évidence la prédominance de la part d'énergie électrostatique dans les termes attractifs au sein des complexes. Pour Na^+ , deux tiers des termes attractifs correspondent à E_{elec} , et un tiers à E_{pol} . Pour Ca^{2+} , le terme électrostatique représente 50 %, l'énergie de polarisation 40 %, et le transfert de charge ≈ 10 %.

Les énergies de complexation des deux pesticides avec un Na^+ ou un Ca^{2+} sont d'ordres similaires à ceux avec l'atrazine : -40 et -140 kcal/mol respectivement, alors que les valeurs sont de -22 kcal/mol avec deux Na^+ . Avec deux Ca^{2+} , l'énergie de complexation de Fen est de -60 kcal/mol alors que sa valeur absolue dans le cas de Meta est deux fois plus basse.

Les complexes de la métamitrone et du fenhexamide, quelques soient le nombre et la nature des cations, donnent des énergies libres de complexation négatives, ce qui n'est pas le cas pour Atra- $(\text{Ca}^{2+})_2$ où ΔG_{comp} est positive.

Finalement, les résultats au niveau PBE/basis2//PBE/basis1 sont globalement en accord avec ceux obtenus en PBE/basis2 et ce niveau pourrait donc présenter une alternative pour le traitement de plus grands systèmes.

- La troisième étape de cette thèse a été une exploration de la SEP de la métamitrone et du fenhexamide adsorbés sur un modèle de Ca-montmorillonite à l'aide de simulations au niveau CPMD/PBE-D2. Les complexes optimisés précédemment (Chapitre

V) ont été utilisés comme structures de départ. Comme attendu, cette approche dynamique a permis une exploration plus large des isomères comparée à l’approche statique employée pour les systèmes Atra-Mont (Chapitre IV).

Dans le cas de Meta-Mont, les familles impliquant les mêmes sites de complexation qu’en phase gaz ont été obtenues. Les familles sont consécutives mais l’ordre énergétique correspond à Meta- Na^+ en phase gaz : une complexation sur les deux azotes du cycle triazine mène à l’isomère le plus bas. Les orientations parallèle et orthogonale ont toutes deux été considérées. Dans une famille donnée, une orientation *para* est toujours préférée mais le critère du site d’interaction est déterminant. Alors que la molécule de métamitrone ne peut interagir avec deux cations Ca^{2+} de surface, Fen-Mont présente des géométries à double complexation. Pour Fen-Mont, les isomères *para* constituent le groupe de plus basse énergie. Dans le cas d’isomères *para* avec une simple complexation, l’interaction se produit sur le carbonyle. Étonnamment, l’isomère de plus basse énergie présente une simple complexation dont l’interaction sur le carbonyle est proche d’un état monodentate. Les simples et doubles complexations sont compétitives. En effet, pour les simples complexations, une interaction de Ca^{2+} sur l’oxygène du carbonyle conduit à l’isomère de plus basse énergie. Quelque soit le pesticide, l’énergie d’adsorption est aux alentours de -40 kcal/mol. Comme pour l’étude d’Atra-Mont, la surface n’est pas modifiée significativement, excepté pour la position du Ca^{2+} interagissant.

- Le dernier chapitre se focalise sur l’influence de l’hydratation des complexes pesticide-Mont. La solvation affecte légèrement le site de complexation quelque soit le pesticide et son orientation. La géométrie interne de Mont est également légèrement modifiée. Concernant l’hydratation de Ca^{2+} :
 - le cation non-interagissant (Ca2) atteint une sphère de solvation “interne” (5 H_2O) en conservant l’interaction avec la surface ;
 - la solvation de Ca1, impliqué dans la complexation, dépend non seulement du site de complexation mais aussi du pesticide (jusqu’à 2 H_2O).

Le second aspect à avoir été pris en compte dans les systèmes solvatés est le processus de désorption du pesticide à travers des séries de trajectoires de dynamique moléculaire le long d’une coordonnée de réaction (Umbrella Sampling). Le but de cette étude était d’explorer la surface d’énergie libre et de quantifier la barrière de désorption du fenhexamide, complexé sur l’oxygène du carbonyle, du modèle hydraté de Ca-montmorillonite. L’Umbrella Sampling a été réalisé via 11 simulations (inférieures à 20 ps pour la plupart) en CPMD/DFT, et la coordonnée de réaction choisie ($\xi_{z(\text{com})}$) est la composante z du centre de masse du Fen. L’hypothèse de

deux processus de désorption peut être émise : une désorption de la molécule seule, ou bien une désorption du complexe pesticide-cation. La coordonnée de réaction choisie ne peut pas discriminer ces deux chemins possibles. Le profil d'énergie libre le long de cette coordonnée, a été obtenu pour $14 \leq \xi_{z(com)} \leq 20$ Bohr, et correspond à l'insertion de molécules d'eau entre le pesticide et la surface. Dans **Well 1**, le cation complexé (Ca1) est en interaction avec 2 H₂O. Ensuite, deux barrières énergétiques $\approx 3,0$ et $4,5$ kcal/mol ont été franchies et ont permis d'explorer deux puits:

- **Well 2**, approximativement supérieur à **Well 1** d'1,5 kcal/mol , où Ca1 est solvato par 3 H₂O ;
- **Well 3**, ≈ 2 kcal/mol au-dessus de **Well 2**, et avec Ca1 coordonné par 4 H₂O.

Dans **Well 1** et **2**, la désorption de Fen-Ca²⁺ est observée par inclusion d'eau. Cependant, dans **Well 3**, l'interaction entre le pesticide et Ca²⁺ est plus faible, ce dernier restant adsorbé sur la surface.

De plus amples recherches, partant de la structure correspondant à **Well 2**, pourraient mener à la désorption de Fen-Ca²⁺. Finalement, ces résultats mettent en évidence le problème délicat du choix d'une coordonnée de réaction appropriée, particulièrement avec le coût extrêmement élevé en ressources informatiques d'un Umbrella Sampling en CP/DFT.

Bibliography

- [1] <http://ec.europa.eu/eurostat>.
- [2] <http://www.statistiques.developpement-durable.gouv.fr/lessentiel/ar/2439/0/quantites-pesticides-vendues-france.html>.
- [3] <http://www.uipp.org/>.
- [4] Garrison Sposito. *The chemistry of soils*. Oxford University Press, Oxford New York, 2008.
- [5] F. L. Hirshfeld. Bonded-atom fragments for describing molecular charge densities. *Theoretica Chimica Acta*, 44(2):129–138, 1977.
- [6] <http://agreste.agriculture.gouv.fr/>.
- [7] <http://sitem.herts.ac.uk/aeru/ppdb/en/index.htm>.
- [8] Thorsten Reemtsma, Lutz Alder, and Ursula Banasiak. A multimethod for the determination of 150 pesticide metabolites in surface water and groundwater using direct injection liquid chromatography–mass spectrometry. *Journal of Chromatography A*, 1271(1):95–104, jan 2013.
- [9] Christoph Moschet, Etiënne L.M. Vermeirssen, Heinz Singer, Christian Stamm, and Juliane Hollender. Evaluation of in-situ calibration of chemcatcher passive samplers for 322 micropollutants in agricultural and urban affected rivers. *Water Research*, 71:306–317, mar 2015.
- [10] P. Janaki, S. Rathika, C. Chinnusamy, and N. K. Prabhakaran. Field dissipation of metamitron in soil and sugar beet crop. *Bulletin of Environmental Contamination and Toxicology*, 90(1):116–119, nov 2012.

- [11] Fabienne Bessac and Sophie Hoyau. Pesticide interaction with environmentally important cations: A theoretical study of atrazine. *Computational and Theoretical Chemistry*, 966(1-3):284–298, jun 2011.
- [12] Fabienne Bessac and Sophie Hoyau. Pesticide interaction with environmentally important cations: A theoretical study of atrazine in interaction with two Ca^{2+} cations. *Computational and Theoretical Chemistry*, 1022:6–13, oct 2013.
- [13] <http://www.cnrtl.fr/>.
- [14] <http://www.observatoire-pesticides.fr/>.
- [15] Rapport d’expertise collective : « Pesticides, agriculture et environnement », remis par l’INRA et le CEMAGREF - décembre 2005.
- [16] Brunet N., Guichard L., Omon B., Pingault N., Pleyber E., and Seiler A. L’indicateur de fréquence de traitements (ift) : un indicateur pour une utilisation durable des pesticides. *Courrier de l’environnement de l’INRA n°56*, pages 131–141, december 2008.
- [17] <http://www.lafranceagricole.fr/actualites/produits/-phytosanitaires-hausse-des-ift-entre-2011-et-2014-1,0,2688537963.html>.
- [18] http://agreste.agriculture.gouv.fr/IMG/pdf/dossier18_ift.pdf.
- [19] Rémi Servien, Laure Mamy, Ziang Li, Virginie Rossard, Eric Latrille, Fabienne Bessac, Dominique Patureau, and Pierre Benoit. TyPol – a new methodology for organic compounds clustering based on their molecular characteristics and environmental behavior. *Chemosphere*, 111:613–622, sep 2014.
- [20] Wold H. Estimation of principal component and related models by iterative least squares. *Krishnaiah, P.R. (Ed.), Multivariate Analysis. Academic Press, New York*, pages 391–420, 1966.
- [21] Lennart Eriksson, Patrik L. Andersson, Erik Johansson, and Mats Tysklind. Megavariate analysis of environmental QSAR data. part i – a basic framework founded on principal component analysis (PCA), partial least squares (PLS), and statistical molecular design (SMD). *Molecular Diversity*, 10(2):169–186, jun 2006.
- [22] <http://www.cas.org/>.

- [23] A. Mudhoo and V.K. Garg. Sorption, transport and transformation of atrazine in soils, minerals and composts: A review. *Pedosphere*, 21(1):11–25, feb 2011.
- [24] Nalini Sathiakumar, Elizabeth Delzell, and Philip Cole. Mortality among workers at two triazine herbicide manufacturing plants. *American Journal of Industrial Medicine*, 29(2):143–151, 1996.
- [25] Jennifer Sass and Paul W. Brandt-Rauf. Cancer incidence among triazine herbicide manufacturing workers. *Journal of Occupational and Environmental Medicine*, 45(4):343–344, apr 2003.
- [26] C. Hopenhayn-Rich, M. L. Stump, and S. R.” Browning. Regional assessment of atrazine exposure and incidence of breast and ovarian cancers in kentucky. *Archives of Environmental Contamination and Toxicology*, 42(1):127–136, Jan 2002.
- [27] Danielle P. Oliver, Yi Fong Pan, Jenny S. Anderson, Tsair Fuh Lin, Rai S. Kookana, Grant B. Douglas, and Laura A. Wendling. Sorption of pesticides by a mineral sand mining by-product, neutralised used acid (NUA). *Science of The Total Environment*, 442:255–262, jan 2013.
- [28] James W. Simpkins, James A. Swenberg, Noel Weiss, David Brusick, J. Charles Eldridge, James T. Stevens, Robert J. Handa, Russell C. Hovey, Tony M. Plant, Timothy P. Pastoor, and Charles B. Breckenridge. Atrazine and breast cancer: A framework assessment of the toxicological and epidemiological evidence. *Toxicological Sciences*, 123(2):441–459, jul 2011.
- [29] Jessica L. Rinsky, Claudia Hopenhayn, Vijay Golla, Steve Browning, and Heather M. Bush. Atrazine exposure in public drinking water and preterm birth. *Public Health Reports*, 127(1):72–80, jan 2012.
- [30] C M Villanueva. Atrazine in municipal drinking water and risk of low birth weight, preterm delivery, and small-for-gestational-age status. *Occupational and Environmental Medicine*, 62(6):400–405, jun 2005.
- [31] R Munger, P Isacson, S Hu, T Burns, J Hanson, C F Lynch, K Cherryholmes, P Van Dorpe, and W J Hausler. Intrauterine growth retardation in iowa communities with herbicide-contaminated drinking water supplies. *Environmental Health Perspectives*, 105(3):308–314, mar 1997.
- [32] Hugo Ochoa-Acuña, Jane Frankenberger, Leighanne Hahn, and Cristina Carbajo. Drinking-water herbicide exposure in indiana and prevalence of small-

- p>for-gestational-age and preterm delivery.
- Environmental Health Perspectives*
- , 117(10):1619–1624, jul 2009.
- [33] Paul D Winchester, Jordan Huskins, and Jun Ying. Agrichemicals in surface water and birth defects in the united states. *Acta Paediatrica*, 98(4):664–669, apr 2009.
- [34] Lawrence T. Wetzel, Louis G. Luempert, Charles B. Breckenridge, Merrill O. Tisdell, James T. Stevens, Ajit K. Thakur, Pamela J. Extrom, and J. Charles Eldridge. Chronic effects of atrazine on estrus and mammary tumor formation in female sprague-dawley and fischer 344 rats. *Journal of Toxicology and Environmental Health*, 43(2):169–182, oct 1994.
- [35] J.Charles Eldridge, Lawrence T. Wetzel, James T. Stevens, and James W. Simpkins. The mammary tumor response in triazine-treated female rats: A threshold-mediated interaction with strain and species-specific reproductive senescence. *Steroids*, 64(9):672–678, sep 1999.
- [36] R. L. Cooper. Atrazine disrupts the hypothalamic control of pituitary-ovarian function. *Toxicological Sciences*, 53(2):297–307, feb 2000.
- [37] T. E. Stoker. The effect of atrazine on puberty in male wistar rats: An evaluation in the protocol for the assessment of pubertal development and thyroid function. *Toxicological Sciences*, 58(1):50–59, nov 2000.
- [38] S. C. Laws. The effects of atrazine on female wistar rats: An evaluation of the protocol for assessing pubertal development and thyroid function. *Toxicological Sciences*, 58(2):366–376, dec 2000.
- [39] Chad D. Foradori, Laura R. Hinds, William H. Hanneman, Marie E. Legare, Colin M. Clay, and Robert J. Handa. Atrazine inhibits pulsatile luteinizing hormone release without altering pituitary sensitivity to a gonadotropin-releasing hormone receptor agonist in female wistar rats1. *Biology of Reproduction*, 81(1):40–45, jul 2009.
- [40] Chad D. Foradori, Arthur D. Zimmerman, Laura R. Hinds, Kristen L. Zuloaga, Charles B. Breckenridge, and Robert J. Handa. Atrazine inhibits pulsatile gonadotropin-releasing hormone (GnRH) release without altering GnRH messenger RNA or protein levels in the female rat1. *Biology of Reproduction*, 88(1), jan 2013.
- [41] Kristina Pogrmic-Majkic, Svetlana Fa, Vanja Dakic, Sonja Kaisarevic, and Radmila Kovacevic. Upregulation of peripubertal rat leydig cell steroidogenesis following 24

- h in vitro and in vivo exposure to atrazine. *Toxicological Sciences*, 118(1):52–60, jul 2010.
- [42] Kristina Pogrmic-Majkic, Dragana Samardzija, Svetlana Fa, Jelena Hrubik, Branka Glisic, Sonja Kaisarevic, and Nebojsa Andric. Atrazine enhances progesterone production through activation of multiple signaling pathways in FSH-stimulated rat granulosa cells: Evidence for premature luteinization1. *Biology of Reproduction*, 91(5), nov 2014.
- [43] Keith R. Solomon, David B. Baker, R. Peter Richards, Kenneth R. Dixon, Stephen J. Klaine, Thomas W. La Point, Ronald J. Kendall, Carol P. Weisskopf, Jeffrey M. Giddings, John P. Giesy, Lenwood W. Hall, and W. Marty Williams. Ecological risk assessment of atrazine in north american surface waters. *Environmental Toxicology and Chemistry*, 15(1):31–76, jan 1996.
- [44] T. B. Hayes, A. Collins, M. Lee, M. Mendoza, N. Noriega, A. A. Stuart, and A. Vonk. Hermaphroditic, demasculinized frogs after exposure to the herbicide atrazine at low ecologically relevant doses. *Proceedings of the National Academy of Sciences*, 99(8):5476–5480, apr 2002.
- [45] John A. McLachlan, Erica Simpson, and Melvenia Martin. Endocrine disrupters and female reproductive health. *Best Practice & Research Clinical Endocrinology & Metabolism*, 20(1):63–75, mar 2006.
- [46] Keith R. Solomon, James A. Carr, Louis H. Du Preez, John P. Giesy, Ronald J. Kendall, Ernest E. Smith, and Glen J. Van Der Kraak. Effects of atrazine on fish, amphibians, and aquatic reptiles: A critical review. *Critical Reviews in Toxicology*, 38(9):721–772, jan 2008.
- [47] Jason R. Rohr and Krista A. McCoy. A qualitative meta-analysis reveals consistent effects of atrazine on freshwater fish and amphibians. *Environmental Health Perspectives*, 118(1):20–32, sep 2009.
- [48] Sara E. Wirbisky, Gregory J. Weber, Kelly E. Schlotman, Maria S. Sepúlveda, and Jennifer L. Freeman. Embryonic atrazine exposure alters zebrafish and human miRNAs associated with angiogenesis, cancer, and neurodevelopment. *Food and Chemical Toxicology*, 98:25–33, dec 2016.
- [49] William A. Battaglin, Earl M. Thurman, Stephen J. Kalkhoff, and Stephen D. Porter. Herbicides and transformation products in surface waters of the midwestern united states. *Journal of the American Water Resources Association*, 39(4):743–756, aug 2003.

- [50] Dana B. Barr, Parinya Panuwet, Johnny V. Nguyen, Simeon Udunka, and Larry L. Needham. Assessing exposure to atrazine and its metabolites using biomonitoring. *Environmental Health Perspectives*, 2007.
- [51] Jonathan R Roy, Sanjoy Chakraborty, and Tandra R Chakraborty. Estrogen-like endocrine disrupting chemical affecting puberty in humans—review. 15:RA137–45, 07 2009.
- [52] Nahla Elsayed Omran and Wesam Mohamed Salama. The endocrine disruptor effect of the herbicides atrazine and glyphosate on biomphalaria alexandrina snails. *Toxicology and Industrial Health*, 32(4):656–665, nov 2013.
- [53] Yuanxiang Jin, Linggang Wang, Guanliang Chen, Xiaojian Lin, Wenyu Miao, and Zhengwei Fu. Exposure of mice to atrazine and its metabolite diaminochlorotriazine elicits oxidative stress and endocrine disruption. *Environmental Toxicology and Pharmacology*, 37(2):782–790, mar 2014.
- [54] Meng Mao and Li Ren. Simulating nonequilibrium transport of atrazine through saturated soil. *Ground Water*, 42(4):500–508, jul 2004.
- [55] Ihuaku Anagu, Joachim Ingwersen, Yaron Drori, Benny Chefetz, and Thilo Streck. Modeling concentration-dependent sorption–desorption hysteresis of atrazine in a sandy loam soil. *Journal of Environment Quality*, 40(2):538, 2011.
- [56] Shira Rubin, Ishai Dror, and Brian Berkowitz. Experimental and modeling analysis of coupled non-fickian transport and sorption in natural soils. *Journal of Contaminant Hydrology*, 132:28–36, may 2012.
- [57] Jaromir Dusek, Michal Dohnal, Michal Snehota, Martina Sobotkova, Chittaranjan Ray, and Tomas Vogel. Transport of bromide and pesticides through an undisturbed soil column: A modeling study with global optimization analysis. *Journal of Contaminant Hydrology*, 175-176:1–16, apr 2015.
- [58] Dorothea D. Giannouli and Vassilis Z. Antonopoulos. Evaluation of two pesticide leaching models in an irrigated field cropped with corn. *Journal of Environmental Management*, 150:508–515, mar 2015.
- [59] Djavanshir Djozan and Bahram Ebrahimi. Preparation of new solid phase micro extraction fiber on the basis of atrazine-molecular imprinted polymer: Application for GC and GC/MS screening of triazine herbicides in water, rice and onion. *Analytica Chimica Acta*, 616(2):152–159, jun 2008.

- [60] Małgorzata Kica and Sylwia Ronka. The removal of atrazine from water using specific polymeric adsorbent. *Separation Science and Technology*, 49(11):1634–1642, jul 2014.
- [61] Sylwia Ronka, Małgorzata Kujawska, and Honorata Juśkiewicz. Triazines removal by selective polymeric adsorbent. *Pure and Applied Chemistry*, 86(11), jan 2014.
- [62] Stefano Salvestrini, Pietropaolo Sagliano, Pasquale Iovino, Sante Capasso, and Carmine Colella. Atrazine adsorption by acid-activated zeolite-rich tuffs. *Applied Clay Science*, 49(3):330–335, jul 2010.
- [63] Tarek S. Jamil, Tarek A. Gad-Allah, Hanan S. Ibrahim, and Tamer S. Saleh. Adsorption and isothermal models of atrazine by zeolite prepared from egyptian kaolin. *Solid State Sciences*, 13(1):198–203, jan 2011.
- [64] Use of natural zeolites for organic compounds removal from water. pages 363–381, nov 2012.
- [65] Helen Paola Toledo-Jaldin, Alien Blanco-Flores, Víctor Sánchez-Mendieta, and Os-nieski Martín-Hernández. Influence of the chain length of surfactant in the modifi-cation of zeolites and clays. removal of atrazine from water solutions. *Environmental Technology*, pages 1–12, aug 2017.
- [66] X.M. Yan, B.Y. Shi, J.J. Lu, C.H. Feng, D.S. Wang, and H.X. Tang. Adsorption and desorption of atrazine on carbon nanotubes. *Journal of Colloid and Interface Science*, 321(1):30–38, may 2008.
- [67] Guang Min, Shuo Wang, Huaping Zhu, Guozhen Fang, and Yan Zhang. Multi-walled carbon nanotubes as solid-phase extraction adsorbents for determination of atrazine and its principal metabolites in water and soil samples by gas chromatography-mass spectrometry. *Science of The Total Environment*, 396(1):79–85, jun 2008.
- [68] Baoyou Shi, Xiaoyan Zhuang, Xiaomin Yan, Jiajuan Lu, and Hongxiao Tang. Ad-sorption of atrazine by natural organic matter and surfactant dispersed carbon nanotubes. *Journal of Environmental Sciences*, 22(8):1195–1202, aug 2010.
- [69] N. Rambabu, C. A. Guzman, J. Soltan, and V. Himabindu. Adsorption character-istics of atrazine on granulated activated carbon and carbon nanotubes. *Chemical Engineering & Technology*, 35(2):272–280, jan 2012.

- [70] Wang-Wang Tang, Guang-Ming Zeng, Ji-Lai Gong, Yang Liu, Xi-Yang Wang, Yuan-Yuan Liu, Zhi-Feng Liu, Long Chen, Xiu-Rong Zhang, and De-Zhu Tu. Simultaneous adsorption of atrazine and cu (II) from wastewater by magnetic multi-walled carbon nanotube. *Chemical Engineering Journal*, 211-212:470–478, nov 2012.
- [71] Lílían Zarpon, Gilberto Abate, Luciana B.O. dos Santos, and Jorge C. Masini. Montmorillonite as an adsorbent for extraction and concentration of atrazine, propazine, deethylatrazine, deisopropylatrazine and hydroxyatrazine. *Analytica Chimica Acta*, 579(1):81–87, oct 2006.
- [72] Gilberto Abate and Jorge Cesar Masini. Adsorption of atrazine, hydroxyatrazine, deethylatrazine, and deisopropylatrazine onto fe(III) polyhydroxy cations intercalated vermiculite and montmorillonite. *Journal of Agricultural and Food Chemistry*, 53(5):1612–1619, mar 2005.
- [73] Mark A. Chappell, David A. Laird, Michael L. Thompson, Hui Li, Brian J. Teppen, Vaneet Aggarwal, Cliff T. Johnston, and Stephen A. Boyd. Influence of smectite hydration and swelling on atrazine sorption behavior. *Environmental Science & Technology*, 39(9):3150–3156, may 2005.
- [74] B. L. Sawhney. Sorption of atrazine by al- and ca-saturated smectite. *Clays and Clay Minerals*, 45(3):333–338, 1997.
- [75] Edivaltrys Inayve Pissinati de Rezende, Patricio Guillermo Peralta-Zamora, Wilson de Figueiredo Jardim, Cristiane Vidal, and Gilberto Abate. Sorption and preconcentration of the herbicides atrazine, simazine, and ametryne on montmorillonite. *Analytical Letters*, 46(3):439–451, feb 2013.
- [76] D. A. Laird, E. Barriuso, R. H. Dowdy, and W. C. Koskinen. Adsorption of atrazine on smectites. *Soil Science Society of America Journal*, 56(1):62, 1992.
- [77] E. Barriuso, D. A. Laird, W. C. Koskinen, and R. H. Dowdy. Atrazine desorption from smectites. *Soil Science Society of America Journal*, 58(6):1632, 1994.
- [78] T. P. Ahammed Shabeer, Ajoy Saha, V. T. Gajbhiye, Suman Gupta, K. M. Manjaiah, and Eldho Varghese. Exploitation of nano-bentonite, nano-halloysite and organically modified nano-montmorillonite as an adsorbent and coagulation aid for the removal of multi-pesticides from water: A sorption modelling approach. *Water, Air, & Soil Pollution*, 226(3), feb 2015.

- [79] Gonzalo Bia, Patricia I. Ortiz, Valeria Pfaffen, and Laura Borgnino. Humic acid- $\text{Fe}(\text{hydr})\text{oxide}$ composites supported on montmorillonite: Synthesis, characterization, and atrazine adsorption. *Journal of Chemical & Engineering Data*, 62(11):3793–3801, sep 2017.
- [80] Shishir Tandon, Satyendra Kumar, and N. K. Sand. Development and validation of GC-ECD method for the determination of metatoltrien in soil. *International Journal of Analytical Chemistry*, 2015:1–5, 2015.
- [81] Brigitte Coyette, Francesca Tencalla, Ivo Brants, Yann Fichet, and Denis Rouchouze. Effect of introducing glyphosate-tolerant sugar beet on pesticide usage in Europe. *Pesticide Outlook*, 13(5):219–224, 2002.
- [82] Richard Allen and Allan Walker. The influence of soil properties on the rates of degradation of metatoltrien, metazachlor and metribuzin. *Pesticide Science*, 18(2):95–111, 1987.
- [83] F. Führ and W. Mittelstaedt. Effect of varying soil temperatures on the degradation of methabenzthiazuron, isocarbamid and metatoltrien. *Zeitschrift für Pflanzenernährung und Bodenkunde*, 142(5):657–668, 1979.
- [84] L. Cox, M.C. Hermosin, and J. Cornejo. Sorption of metatoltrien on soils with low organic matter content. *Chemosphere*, 32(7):1391–1400, apr 1996.
- [85] Pirkko Laitinen, Katri Siimes, Liisa Eronen, Sari Rämö, Leena Welling, Seija Oinonen, Leona Mattsoff, and Marja Ruohonen-Lehto. Fate of the herbicides glyphosate, glufosinate-ammonium, phenmedipham, ethofumesate and metatoltrien in two finnish arable soils. *Pest Management Science*, 62(6):473–491, 2006.
- [86] Sari Autio, Katri Siimes, Pirkko Laitinen, Sari Rämö, Seija Oinonen, and Liisa Eronen. Adsorption of sugar beet herbicides to finnish soils. *Chemosphere*, 55(2):215–226, apr 2004.
- [87] L. Mamy and E. Barriuso. Desorption and time-dependent sorption of herbicides in soils. *European Journal of Soil Science*, 58(1):174–187, feb 2007.
- [88] L Cox. Photolysis of metatoltrien in water in the presence of soils and soil components. *Chemosphere*, 33(10):2057–2064, nov 1996.
- [89] W.-U. Palm, M. Millet, and C. Zetzsch. Photochemical reactions of metatoltrien. *Chemosphere*, 35(5):1117–1130, sep 1997.

- [90] Dušan Mijin, Marina Savić, Perović Snežana, Ana Smiljanić, Olivera Glavaški, Mića Jovanović, and Slobodan Petrović. A study of the photocatalytic degradation of metamitron in ZnO water suspensions. *Desalination*, 249(1):286–292, nov 2009.
- [91] K Macounová, J Urban, H Krýsová, J Krýsa, J Jirkovský, and J Ludvík. Photodegradation of metamitron (4-amino-6-phenyl-3-methyl-1, 2, 4-triazin-5(4h)-one) on TiO₂. *Journal of Photochemistry and Photobiology A: Chemistry*, 140(1):93–98, apr 2001.
- [92] Costantino Vischetti, Cesare Marucchini, Cristiano Casucci, Liviana Leita, and Gianni Porzi. Transformation of metamitron in a sandy clay loam soil. *Agronomie*, 19(6):477–481, 1999.
- [93] Shibin C. Debnath, Arindam Kundu, Shyamal K. Das, Tapan K. Mandal, Anjan Bhattacharyya, Ashim Choudhury, and Animesh K. Chakraborty. Toxicokinetics, recovery, and metabolism of metamitron in goat. *Journal of Agricultural and Food Chemistry*, 51(20):5977–5984, sep 2003.
- [94] Debabrata Chanda, Shibin C. Debnath, Shyamal K. Das, Tapan K. Mandal, Anjan Bhattacharyya, Ashim Choudhury, and Animesh K. Chakraborty. Metabolism of metamitron in goat following a single oral administration of a nontoxic dose level: A continued study. *Journal of Agricultural and Food Chemistry*, 52(24):7377–7381, dec 2004.
- [95] Gabriele Engelhardt, Walter Ziegler, Peter R. Wollnofer, Heinrich J. Jarczyk, and Linthard Oehlmann. Degradation of the triazinone herbicide metamitron by arthrobacter spec. DSM 20369. *Journal of Agricultural and Food Chemistry*, 30(2):278–282, mar 1982.
- [96] N.R. Parekh, A. Walker, S.J. Roberts, and S.J. Welch. Rapid degradation of the triazinone herbicide metamitron by a rhodococcus sp. isolated from treated soil. *Journal of Applied Bacteriology*, 77(5):467–475, nov 1994.
- [97] Shizong Wang, Anja Miltner, and Karolina M. Nowak. Identification of degradation routes of metamitron in soil microcosms using ¹³C-isotope labeling. *Environmental Pollution*, 220:927–935, jan 2017.
- [98] Shizong Wang, Anja Miltner, Matthias Kästner, Andreas Schäffer, and Karolina M. Nowak. Transformation of metamitron in water-sediment systems: Detailed insight into the biodegradation processes. *Science of The Total Environment*, 578:100–108, feb 2017.

-
- [99] C. Planas, J. Caixach, F.J. Santos, and J. Rivera. Occurrence of pesticides in spanish surface waters. analysis by high resolution gas chromatography coupled to mass spectrometry. *Chemosphere*, 34(11):2393–2406, jun 1997.
- [100] Validation data of 127 pesticides using a multiresidue method by LC-MS/MS and GC-MS/MS in olive oil. Technical report, European Union Reference Laboratory, 2011. <http://www.crl-pesticides.eu/library/docs/fv/Validation-OliveOil.pdf>.
- [101] Laure Mamy, Enrique Barriuso, and Benoît Gabrielle. Environmental fate of herbicides trifluralin, metazachlor, metamitron and sulcotrione compared with that of glyphosate, a substitute broad spectrum herbicide for different glyphosate-resistant crops. *Pest Management Science*, 61(9):905–916, 2005.
- [102] Tomasz Tuzimski. Application of RP-HPLC-diode array detector after SPE to the determination of pesticides in pepper samples. *Journal of AOAC International*, 95(5):1357–1361, sep 2012.
- [103] Satyendra Kumar, Shishir Tandon, and N. K. Sand. Determination and method validation of metamitron in soil by RP-HPLC. *Bulletin of Environmental Contamination and Toxicology*, 92(2):165–168, nov 2013.
- [104] Alberto Sánchez Arribas, Esperanza Bermejo, Manuel Chicharro, and Antonio Zapardiel. Voltammetric detection of the herbicide metamitron at a bismuth film electrode in nondeaerated solution. *Electroanalysis*, 18(23):2331–2336, dec 2006.
- [105] Renáta Šelešovská, Lenka Janíková, and Jaromíra Chýlková. Green electrochemical sensors based on boron-doped diamond and silver amalgam for sensitive voltammetric determination of herbicide metamitron. *Monatshefte für Chemie - Chemical Monthly*, 146(5):795–805, dec 2014.
- [106] Javier Moros, Sergio Armenta, Salvador Garrigues, and Miguel de la Guardia. Quality control of metamitron in agrochemicals using fourier transform infrared spectroscopy in the middle and near range. *Analytica Chimica Acta*, 565(2):255–260, apr 2006.
- [107] Anna Panebianco, Ivana Castello, Gabriella Cirvilleri, Giancarlo Perrone, Filomena Epifani, Massimo Ferrara, Giancarlo Polizzi, Dale R. Walters, and Alessandro Vitale. Detection of botrytis cinerea field isolates with multiple fungicide resistance from table grape in sicily. *Crop Protection*, 77:65–73, nov 2015.

- [108] Xing jie Wang, Yong sheng Tao, Yun Wu, Rong yan An, and Zhuo ya Yue. Aroma compounds and characteristics of noble-rot wines of chardonnay grapes artificially botrytized in the vineyard. *Food Chemistry*, 226:41–50, jul 2017.
- [109] Marta Mari, Silvia Bautista-Baños, and Dharini Sivakumar. Decay control in the postharvest system: Role of microbial and plant volatile organic compounds. *Postharvest Biology and Technology*, 122:70–81, dec 2016.
- [110] A. Gotor-Vila, N. Teixidó, A. Di Francesco, J. Usall, L. Ugolini, R. Torres, and M. Mari. Antifungal effect of volatile organic compounds produced by *Bacillus amyloliquefaciens* CPA-8 against fruit pathogen decays of cherry. *Food Microbiology*, 64:219–225, jun 2017.
- [111] Alessandro Passera, Giovanni Venturini, Giovanna Battelli, Paola Casati, Francesca Penaca, Fabio Quaglino, and Piero Attilio Bianco. Competition assays revealed *Paenibacillus pasadenensis* strain r16 as a novel antifungal agent. *Microbiological Research*, 198:16–26, may 2017.
- [112] H. Calvo, P. Marco, D. Blanco, R. Oria, and M.E. Venturini. Potential of a new strain of *Bacillus amyloliquefaciens* BUZ-14 as a biocontrol agent of postharvest fruit diseases. *Food Microbiology*, 63:101–110, may 2017.
- [113] Elpiniki G. Amvrazi, Asimina T. Papadi-Psyllou, and Nikolaos G. Tsiropoulos. Pesticide enrichment factors and matrix effects on the determination of multiclass pesticides in tomato samples by single-drop microextraction (SDME) coupled with gas chromatography and comparison study between SDME and acetone-partition extraction procedure. *International Journal of Environmental Analytical Chemistry*, 90(3-6):245–259, mar 2010.
- [114] Paolo Cabras, Alberto Angioni, Vincenzo L. Garau, Filippo M. Pirisi, Franco Cabitza, Mario Pala, and Giovanni A. Farris. Fenhexamid residues in grapes and wine. *Food Additives and Contaminants*, 18(7):625–629, jul 2001.
- [115] Gavin Rose, Simon Lane, and Robert Jordan. The fate of fungicide and insecticide residues in Australian wine grape by-products following field application. *Food Chemistry*, 117(4):634–640, dec 2009.
- [116] Francesc A. Esteve-Turrillas, Antonio Abad-Fuentes, and Josep V. Mercader. Determination of fenhexamid residues in grape must, kiwifruit, and strawberry samples by enzyme-linked immunosorbent assay. *Food Chemistry*, 124(4):1727–1733, feb 2011.

-
- [117] Marija Vukcevic, Ana Kalijadis, Marina Radisic, Biljana Pejic, Mirjana Kostic, Zoran Lausevic, and Mila Lausevic. Application of carbonized hemp fibers as a new solid-phase extraction sorbent for analysis of pesticides in water samples. *Chemical Engineering Journal*, 211-212:224–232, nov 2012.
- [118] T. Rodríguez-Cabo, M. Paganini, I. Carpinteiro, L. Fontenla, I. Rodríguez, M. C. Pietrogrande, and R. Cela. Liquid chromatography time-of-flight mass spectrometry evaluation of fungicides reactivity in free chlorine containing water samples. *Journal of Mass Spectrometry*, 48(2):216–226, feb 2013.
- [119] G. Nicolini, T. Román Villegas, L. Tonidandel, S. Moser, and R. Larcher. Small amounts of charcoal during fermentation reduce fungicide residues without penalising white wine aroma compounds and colour. *Australian Journal of Grape and Wine Research*, 22(3):376–383, jun 2016.
- [120] Andrea Baglieri, Sarah Sidella, Valeria Barone, Ferdinando Fragalà, Alla Silkina, Michèle Nègre, and Mara Gennari. Cultivating chlorella vulgaris and scenedesmus quadricauda microalgae to degrade inorganic compounds and pesticides in water. *Environmental Science and Pollution Research*, 23(18):18165–18174, jun 2016.
- [121] T. Rodríguez-Cabo, I. Rodríguez, M. Ramil, and R. Cela. Assessment of silicone as support to investigate the transformation routes of organic chemicals under environmental conditions and UV exposure. application to selected fungicides. *Analytical and Bioanalytical Chemistry*, 405(12):4187–4198, feb 2013.
- [122] Facundo Rivera-Becerril, Diederik van Tuinen, Odile Chatagnier, Nadine Rouard, Jérémie Béguet, Catherine Kuszala, Guy Soulas, Vivienne Gianinazzi-Pearson, and Fabrice Martin-Laurent. Impact of a pesticide cocktail (fenhexamid, folpel, deltamethrin) on the abundance of glomeromycota in two agricultural soils. *Science of The Total Environment*, 577:84–93, jan 2017.
- [123] Maria Vittoria Pinna, Marilena Budroni, Giovanni Antonio Farris, and Alba Pusino. Fenhexamid adsorption behavior on soil amended with wine lees. *Journal of Agricultural and Food Chemistry*, 56(22):10824–10828, nov 2008.
- [124] Cristina Abbate, Daniela Borzì, Pierluigi Caboni, Andrea Baglieri, and Mara Gennari. Behavior of fenhexamid in soil and water. *Journal of Environmental Science and Health, Part B*, 42(7):843–849, sep 2007.
- [125] Andrea Baglieri, Daniela Borzì, Cristina Abbate, Michèle Nègre, and Mara Gennari. Removal of fenhexamid and pyrimethanil from aqueous solutions by clays and

- organoclays. *Journal of Environmental Science and Health, Part B*, 44(3):220–225, mar 2009.
- [126] Raoul Calvet. *Le sol*. Ed. France Agricole, Paris, 2013.
- [127] Hans Jenny. *The Soil Resource : Origin and Behavior*. Springer New York, New York, NY, 1980.
- [128] Faiza Bergaya. *Handbook of clay science*. Elsevier, Amsterdam London, 2006.
- [129] E. Lowenstein. *Zeitschr. anorg. Chemie*, 63:69, 1909.
- [130] <https://www.aipea.org/>.
- [131] Sergio Pérez-Conesa, José M. Martínez, and Enrique Sánchez Marcos. Hydration and diffusion mechanism of uranyl in montmorillonite clay: Molecular dynamics using an ab initio potential. *The Journal of Physical Chemistry C*, 121(49):27437–27444, nov 2017.
- [132] Bruno Campos, Javier Aguilar-Carrillo, Manuel Algarra, Mário A. Gonçalves, Enrique Rodríguez-Castellón, Joaquim C.G. Esteves da Silva, and Iuliu Bobos. Adsorption of uranyl ions on kaolinite, montmorillonite, humic acid and composite clay material. *Applied Clay Science*, 85:53–63, nov 2013.
- [133] W.P. Li, X.Y. Han, X.Y. Wang, Y.Q. Wang, W.X. Wang, H. Xu, T.S. Tan, W.S. Wu, and H.X. Zhang. Recovery of uranyl from aqueous solutions using amidoximated polyacrylonitrile/exfoliated na-montmorillonite composite. *Chemical Engineering Journal*, 279:735–746, nov 2015.
- [134] Pierre Mignon, Piero Ugliengo, Mariona Sodupe, and Eduardo R. Hernandez. Ab initio molecular dynamics study of the hydration of Li^+ , Na^+ and K^+ in a montmorillonite model. Influence of isomorphic substitution. *Phys. Chem. Chem. Phys.*, 12(3):688–697, 2010.
- [135] R. Wardle and G. W. Brindley. *American Mineralogist*, 57:732–750, 1972.
- [136] Bastien Belzunces, Sophie Hoyau, Magali Benoit, Nathalie Tarrat, and Fabienne Bessac. Theoretical study of the atrazine pesticide interaction with pyrophyllite and Ca^{2+} -montmorillonite clay surfaces. *Journal of Computational Chemistry*, 38(3):133–143, nov 2016.
- [137] Katja Emmerich and Günter Kahr. The cis- and trans-vacant variety of a montmorillonite: an attempt to create a model smectite. *Applied Clay Science*, 20(3):119–127, nov 2001.

- [138] T. Beermann and O. Brockamp. Structure analysis of montmorillonite crystallites by convergent-beam electron diffraction. *Clay Minerals*, 40(1):1–14, mar 2005.
- [139] Daniel Tunega, Bernard A. Goodman, Georg Haberhauer, Thomas G. Reichenauer, Martin H. Gerzabek, and Hans Lischka. Ab initio calculations of relative stabilities of different structural arrangements in dioctahedral phyllosilicates. *Clays and Clay Minerals*, 55(2):220–232, apr 2007.
- [140] Fabrice Salles, Sabine Devautour-Vinot, Olivier Bildstein, Michel Jullien, Guillaume Maurin, Jean-Charles Giuntini, Jean-Marc Douillard, and Henri Van Damme. Ionic mobility and hydration energies in montmorillonite clay. *The Journal of Physical Chemistry C*, 112(36):14001–14009, sep 2008.
- [141] Fabrice Salles, Jean-Marc Douillard, Olivier Bildstein, Samira El Ghazi, Bénédicte Prélot, Jerzy Zajac, and Henri Van Damme. Diffusion of interlayer cations in swelling clays as a function of water content: Case of montmorillonites saturated with alkali cations. *The Journal of Physical Chemistry C*, 119(19):10370–10378, may 2015.
- [142] Benjamin Rotenberg. *Modélisation multi-échelles du comportement de l’eau et des ions dans les argiles*. PhD thesis, 01 2007.
- [143] Benjamin Rotenberg, Jean-Pierre Morel, Virginie Marry, Pierre Turq, and Nicole Morel-Desrosiers. On the driving force of cation exchange in clays: Insights from combined microcalorimetry experiments and molecular simulation. *Geochimica et Cosmochimica Acta*, 73(14):4034–4044, jul 2009.
- [144] M. Segad, Bo Jönsson, T. Åkesson, and B. Cabane. Ca/Na montmorillonite: Structure, forces and swelling properties. *Langmuir*, 26(8):5782–5790, apr 2010.
- [145] Artur Meleshyn and Claus Bunnenberg. Swelling of Na/Mg-montmorillonites and hydration of interlayer cations: A monte carlo study. *The Journal of Chemical Physics*, 123(7):074706, aug 2005.
- [146] Vamsee K. Voora, W. A. Al-Saidi, and Kenneth D. Jordan. Density functional theory study of pyrophyllite and m-montmorillonites ($m = \text{li, na, k, mg, and ca}$): Role of dispersion interactions. *The Journal of Physical Chemistry A*, 115(34):9695–9703, sep 2011.
- [147] P. Boulet, H.C. Greenwell, S. Stackhouse, and P.V. Coveney. Recent advances in understanding the structure and reactivity of clays using electronic structure

- calculations. *Journal of Molecular Structure: THEOCHEM*, 762(1-3):33–48, apr 2006.
- [148] Tim J. Tambach, Peter G. Bolhuis, Emiel J. M. Hensen, and Berend Smit. Hysteresis in clay swelling induced by hydrogen bonding: accurate prediction of swelling states. *Langmuir*, 22(3):1223–1234, jan 2006.
- [149] Steven R. Schmidt, Dinesh R. Katti, Pijush Ghosh, and Kalpana S. Katti. Evolution of mechanical response of sodium montmorillonite interlayer with increasing hydration by molecular dynamics. *Langmuir*, 21(17):8069–8076, aug 2005.
- [150] Linlin Sun, Jukka T. Tanskanen, Janne T. Hirvi, Seppo Kasa, Timothy Schatz, and Tapani A. Pakkanen. Molecular dynamics study of montmorillonite crystalline swelling: Roles of interlayer cation species and water content. *Chemical Physics*, 455:23–31, jul 2015.
- [151] Abid Berghout, Daniel Tunega, and Ali Zaoui. Density functional theory (DFT) study of the hydration steps of $\text{Na}^+/\text{Mg}^{2+}/\text{Ca}^{2+}/\text{Sr}^{2+}/\text{Ba}^{2+}$ -Exchanged montmorillonites. *Clays and Clay Minerals*, 58(2):174–187, apr 2010.
- [152] Carla G. Fonseca, Gustavo S.G. de Carvalho, Fernando Wypych, Renata Diniz, and Alexandre A. Leitão. Na^+ as a probe to structural investigation of dehydrated smectites using NMR spectra calculated by DFT. *Applied Clay Science*, 126:132–140, jun 2016.
- [153] Pierre Mignon, Piero Ugliengo, and Mariona Sodupe. Theoretical study of the adsorption of RNA/DNA bases on the external surfaces of Na^+ -montmorillonite. *J. Phys. Chem. C*, 113(31):13741–13749, aug 2009.
- [154] Pierre Mignon and Mariona Sodupe. Theoretical study of the adsorption of DNA bases on the acidic external surface of montmorillonite. *Phys. Chem. Chem. Phys.*, 14(2):945–954, 2012.
- [155] Evgeniy M. Myshakin, Wissam A. Saidi, Vyacheslav N. Romanov, Randall T. Cygan, and Kenneth D. Jordan. Molecular dynamics simulations of carbon dioxide intercalation in hydrated na-montmorillonite. *The Journal of Physical Chemistry C*, 117(21):11028–11039, may 2013.
- [156] Pierre Mignon and Mariona Sodupe. Structural behaviors of cytosine into the hydrated interlayer of na + -montmorillonite clay. an ab initio molecular dynamics study. *J. Phys. Chem. C*, 117(49):26179–26189, dec 2013.

-
- [157] Pascal Clausen, Wanda Andreoni, Alessandro Curioni, Eric Hughes, and Christopher J. G. Plummer. Adsorption of low-molecular-weight molecules on a dry clay surface: An ab initio study. *J. Phys. Chem. C*, 113(28):12293–12300, jul 2009.
- [158] Guangyao Sheng, Cliff T. Johnston, Brian J. Teppen, and Stephen A. Boyd. Adsorption of dinitrophenol herbicides from water by montmorillonites. *Clays and Clay Minerals*, 50(1):25–34, feb 2002.
- [159] Vaneet Aggarwal, Hui Li, and Brian J. Teppen. TRIAZINE ADSORPTION BY SAPONITE AND BEIDELLITE CLAY MINERALS. *Environmental Toxicology and Chemistry*, 25(2):392, 2006.
- [160] D. Tunega, M. H. Gerzabek, G. Haberhauer, and H. Lischka. Formation of 2,4-d complexes on montmorillonites – an ab initio molecular dynamics study. *Eur J Soil Science*, 58(3):680–691, jun 2007.
- [161] Sergey V. Churakov and Georg Kosakowski. An ab initio molecular dynamics study of hydronium complexation in na-montmorillonite. *Philosophical Magazine*, 90(17-18):2459–2474, apr 2010.
- [162] E. Schrödinger. Quantisierung als eigenwertproblem. *Annalen der Physik*, 384(4):361–376, 1926.
- [163] E. Schrödinger. An undulatory theory of the mechanics of atoms and molecules. *Physical Review*, 28(6):1049–1070, dec 1926.
- [164] M. Born and R. Oppenheimer. Zur quantentheorie der molekeln. *Annalen der Physik*, 389(20):457–484, 1927.
- [165] D. R. Hartree. The wave mechanics of an atom with a non-coulomb central field. part i. theory and methods. *Mathematical Proceedings of the Cambridge Philosophical Society*, 24(01):89, jan 1928.
- [166] W. Pauli. *Z.Physik*, 31:719, 1925.
- [167] J. C. Slater. Note on hartree's method. *Physical Review*, 35(2):210–211, jan 1930.
- [168] V. Fock. Näherungsmethode zur lösung des quantenmechanischen mehrkörperproblems. *Zeitschrift für Physik*, 61(1-2):126–148, jan 1930.
- [169] Erich Huckel. Zur quantentheorie der doppelbindung. *Zeitschrift für Physik*, 60(7-8):423–456, jul 1930.

- [170] Erich Huckel. Quantentheoretische beiträge zum benzolproblem. *Zeitschrift für Physik*, 70(3-4):204–286, mar 1931.
- [171] Erich Huckel. Quantentheoretische beiträge zum benzolproblem. *Zeitschrift für Physik*, 72(5-6):310–337, may 1931.
- [172] Erich Huckel. Quantentheoretische beiträge zum problem der aromatischen und ungesättigten verbindungen. III. *Zeitschrift für Physik*, 76(9-10):628–648, sep 1932.
- [173] J. C. Slater. Atomic shielding constants. *Physical Review*, 36(1):57–64, jul 1930.
- [174] S. F. Boys. Electronic wave functions. i. a general method of calculation for the stationary states of any molecular system. *Proceedings of the Royal Society A: Mathematical, Physical and Engineering Sciences*, 200(1063):542–554, feb 1950.
- [175] W. J. Hehre, R. F. Stewart, and J. A. Pople. Self-consistent molecular-orbital methods. i. use of gaussian expansions of slater-type atomic orbitals. *The Journal of Chemical Physics*, 51(6):2657–2664, sep 1969.
- [176] R. Krishnan, J. S. Binkley, R. Seeger, and J. A. Pople. Self-consistent molecular orbital methods. XX. a basis set for correlated wave functions. *The Journal of Chemical Physics*, 72(1):650–654, jan 1980.
- [177] C. C. J. Roothaan. New developments in molecular orbital theory. *Reviews of Modern Physics*, 23(2):69–89, apr 1951.
- [178] F. Coester. Bound states of a many-particle system. *Nuclear Physics*, 7:421–424, jun 1958.
- [179] F. Coester and H. Kümmel. Short-range correlations in nuclear wave functions. *Nuclear Physics*, 17:477–485, jun 1960.
- [180] J Cizek and J Paldus. Coupled cluster approach. *Physica Scripta*, 21(3-4):251–254, jan 1980.
- [181] Rodney J. Bartlett. Coupled-cluster approach to molecular structure and spectra: a step toward predictive quantum chemistry. *The Journal of Physical Chemistry*, 93(5):1697–1708, mar 1989.
- [182] Per-Olov Löwdin. Quantum theory of many-particle systems. i. physical interpretations by means of density matrices, natural spin-orbitals, and convergence problems in the method of configurational interaction. *Physical Review*, 97(6):1474–1489, mar 1955.

- [183] B. O. Roos. *Lecture notes in quantum chemistry*. Springer-Verlag, Berlin New York, 1992.
- [184] Chr. Møller and M. S. Plesset. Note on an approximation treatment for many-electron systems. *Physical Review*, 46(7):618–622, oct 1934.
- [185] L. H. Thomas. The calculation of atomic fields. *Mathematical Proceedings of the Cambridge Philosophical Society*, 23(05):542–548, jan 1927.
- [186] E. Fermi. Un metodo statistico per la determinazione di alcune proprietà dell’atomo. *Rend. Accad. Naz. Lincei*, 6:602–607, 1927.
- [187] P. A. M. Dirac. Note on exchange phenomena in the thomas atom. *Mathematical Proceedings of the Cambridge Philosophical Society*, 26(03):376, jul 1930.
- [188] E. Teller. On the stability of molecules in the thomas-fermi theory. *Rend. Accad. Naz. Lincei*, 34(4):627–630, oct 1962.
- [189] Wolfram Koch and Max C. Holthausen. *A Chemist’s Guide to Density Functional Theory*. Wiley-VCH, 2015.
- [190] *Density Functional Theory (Nato Science Series B: (closed))*. Springer, 1995.
- [191] P. Hohenberg and W. Kohn. Inhomogeneous electron gas. *Phys. Rev.*, 136(3B):B864–B871, nov 1964.
- [192] W. Kohn and L. J. Sham. Self-consistent equations including exchange and correlation effects. *Physical Review*, 140(4A):A1133–A1138, nov 1965.
- [193] Richard M. Martin. *Electronic Structure: Basic Theory and Practical Methods (Vol 1)*. Cambridge University Press, 2004.
- [194] D. M. Ceperley and B. J. Alder. Ground state of the electron gas by a stochastic method. *Physical Review Letters*, 45(7):566–569, aug 1980.
- [195] J. P. Perdew and Alex Zunger. Self-interaction correction to density-functional approximations for many-electron systems. *Phys. Rev. B*, 23:5048–5079, May 1981.
- [196] Frank Herman, John P. Van Dyke, and Irene B. Ortenburger. Improved statistical exchange approximation for inhomogeneous many-electron systems. *Phys. Rev. Lett.*, 22:807–811, Apr 1969.
- [197] John P. Perdew and Yue Wang. Accurate and simple analytic representation of the electron-gas correlation energy. *Phys. Rev. B*, 45:13244–13249, Jun 1992.

- [198] John P. Perdew and Kieron Burke. Comparison shopping for a gradient-corrected density functional. *International Journal of Quantum Chemistry*, 57(3):309–319, 1996.
- [199] Sérgio Filipe Sousa, Pedro Alexandrino Fernandes, and Maria João Ramos. General performance of density functionals. *The Journal of Physical Chemistry A*, 111(42):10439–10452, oct 2007.
- [200] A. D. Becke. Density-functional exchange-energy approximation with correct asymptotic behavior. *Physical Review A*, 38(6):3098–3100, sep 1988.
- [201] Chengteh Lee, Weitao Yang, and Robert G. Parr. Development of the colle-salvetti correlation-energy formula into a functional of the electron density. *Physical Review B*, 37(2):785–789, jan 1988.
- [202] John P. Perdew and Wang Yue. Accurate and simple density functional for the electronic exchange energy: Generalized gradient approximation. *Physical Review B*, 33(12):8800–8802, jun 1986.
- [203] John P. Perdew, J. A. Chevary, S. H. Vosko, Koblar A. Jackson, Mark R. Pederson, D. J. Singh, and Carlos Fiolhais. Atoms, molecules, solids, and surfaces: Applications of the generalized gradient approximation for exchange and correlation. *Physical Review B*, 46(11):6671–6687, sep 1992.
- [204] John P. Perdew, Kieron Burke, and Matthias Ernzerhof. Generalized gradient approximation made simple. *Phys. Rev. Lett.*, 77(18):3865–3868, oct 1996.
- [205] Daniel Tunega, Tomáš Bučko, and Ali Zaoui. Assessment of ten DFT methods in predicting structures of sheet silicates: Importance of dispersion corrections. *The Journal of Chemical Physics*, 137(11):114105, sep 2012.
- [206] Evgeniy M. Myshakin Guozhen Zhang, W. A. Al-Saidi and Kenneth D. Jordan. Dispersion-corrected density functional theory and classical force field calculations of water loading on a pyrophyllite(001) surface. *J. Phys. Chem. C*, 116(32):17134–17141, jul 2012.
- [207] Federico Musso, Pierre Mignon, Piero Ugliengo, and Mariona Sodupe. Cooperative effects at water-crystalline silica interfaces strengthen surface silanol hydrogen bonding. an ab initio molecular dynamics study”. *Phys. Chem. Chem. Phys.*, 14:10507–10514, 2012.
- [208] Axel D. Becke. A new mixing of hartree–fock and local density-functional theories. *The Journal of Chemical Physics*, 98(2):1372–1377, jan 1993.

-
- [209] Eva Scholtzová, Daniel Tunega, and Ladislav Turi Nagy. Theoretical study of cation substitution in trioctahedral sheet of phyllosilicates. an effect on inner oh group. *Journal of Molecular Structure: Theochem*, 620(1):1 – 8, 2003.
- [210] Daniel Muñoz-Santiburcio, Joaquin Ortega-Castro, Claro Sainz-Díaz, F Huertas, and Alfonso Hernandez-Laguna. Theoretical study of the adsorption of 2-nitro-1-propanol on smectite surface models. 912:95–104, 10 2009.
- [211] Federico Musso, Mariona Sodupe, Marta Corno, and Piero Ugliengo. H-bond features of fully hydroxylated surfaces of crystalline silica polymorphs: A periodic b3lyp study. *The Journal of Physical Chemistry C*, 113(41):17876–17884, 2009.
- [212] M. De La Pierre, R. Orlando, L. Maschio, K. Doll, P. Ugliengo, and R. Dovesi. Performance of six functionals (LDA, PBE, PBESOL, b3lyp, PBE0, and WC1lyp) in the simulation of vibrational and dielectric properties of crystalline compounds. the case of forsterite mg_2sio_4 . *Journal of Computational Chemistry*, 32(9):1775–1784, apr 2011.
- [213] Attila Kovács, Jan Cz. Dobrowolski, Sławomir Ostrowski, and Joanna E. Rode. Benchmarking density functionals in conjunction with grimme's dispersion correction for noble gas dimers (ne_2 , ar_2 , kr_2 , xe_2 , rn_2). *International Journal of Quantum Chemistry*, 117(9):e25358, feb 2017.
- [214] Erin R. Johnson, Robert A. Wolkow, and Gino A. DiLabio. Application of 25 density functionals to dispersion-bound homomolecular dimers. *Chemical Physics Letters*, 394(4-6):334–338, aug 2004.
- [215] Jiří Černý and Pavel Hobza. The x3lyp extended density functional accurately describes h-bonding but fails completely for stacking. *Phys. Chem. Chem. Phys.*, 7(8):1624–1626, 2005.
- [216] P. Kolandaivel, D. Uma Maheswari, and L. Senthilkumar. The study of performance of DFT functional for van der waals interactions. *Computational and Theoretical Chemistry*, 1004:56–60, jan 2013.
- [217] Yan Zhao and Donald G. Truhlar. Benchmark databases for nonbonded interactions and their use to test density functional theory. *Journal of Chemical Theory and Computation*, 1(3):415–432, may 2005.
- [218] Kanchana S. Thanthiriwatte, Edward G. Hohenstein, Lori A. Burns, and C. David Sherrill. Assessment of the performance of DFT and DFT-D methods for describing

- distance dependence of hydrogen-bonded interactions. *Journal of Chemical Theory and Computation*, 7(1):88–96, jan 2011.
- [219] T. P. M. Goumans, Adrian Wander, Wendy A. Brown, and C. Richard A. Catlow. Structure and stability of the (001) α -quartz surface. *Phys. Chem. Chem. Phys.*, 9(17):2146–2152, 2007.
- [220] Joel Ireta, Jörg Neugebauer, and Matthias Scheffler. On the accuracy of DFT for describing hydrogen bonds: dependence on the bond directionality. *The Journal of Physical Chemistry A*, 108(26):5692–5698, jul 2004.
- [221] Mikhail V. Vener, Xavier Rozanska, and Joachim Sauer. Protonation of water clusters in the cavities of acidic zeolites: (h₂o)_n-h-chabazite, $n = 1-4$. *Physical Chemistry Chemical Physics*, 11(11):1702, 2009.
- [222] Jeffrey C. Grossman, Eric Schwegler, Erik W. Draeger, François Gygi, and Giulia Galli. Towards an assessment of the accuracy of density functional theory for first principles simulations of water. *The Journal of Chemical Physics*, 120(1):300–311, jan 2004.
- [223] Eric Schwegler, Jeffrey C. Grossman, François Gygi, and Giulia Galli. Towards an assessment of the accuracy of density functional theory for first principles simulations of water. ii. *The Journal of Chemical Physics*, 121(11):5400–5409, 2004.
- [224] P. H.-L. Sit and Nicola Marzari. Static and dynamical properties of heavy water at ambient conditions from first-principles molecular dynamics. *The Journal of Chemical Physics*, 122(20):204510, may 2005.
- [225] Thomas D. Kühne, Matthias Krack, and Michele Parrinello. Static and dynamical properties of liquid water from first principles by a novel car-parrinello-like approach. *Journal of Chemical Theory and Computation*, 5(2):235–241, 2009. PMID: 26610101.
- [226] Robert A. DiStasio, Biswajit Santra, Zhaofeng Li, Xifan Wu, and Roberto Car. The individual and collective effects of exact exchange and dispersion interactions on the ab initio structure of liquid water. *The Journal of Chemical Physics*, 141(8):084502, aug 2014.
- [227] Arindam Bankura, Anwesa Karmakar, Vincenzo Carnevale, Amalendu Chandra, and Michael L. Klein. Structure, dynamics, and spectral diffusion of water from first-principles molecular dynamics. *The Journal of Physical Chemistry C*, 118(50):29401–29411, dec 2014.

- [228] Michael J. Gillan, Dario Alfè, and Angelos Michaelides. Perspective: How good is DFT for water? *The Journal of Chemical Physics*, 144(13):130901, apr 2016.
- [229] Katrin Forster-Tonigold and Axel Groß. Dispersion corrected RPBE studies of liquid water. *The Journal of Chemical Physics*, 141(6):064501, aug 2014.
- [230] Stefan Grimme. Accurate description of van der waals complexes by density functional theory including empirical corrections. *Journal of Computational Chemistry*, 25(12):1463–1473, 2004.
- [231] Stefan Grimme. Semiempirical GGA-type density functional constructed with a long-range dispersion correction. *Journal of Computational Chemistry*, 27(15):1787–1799, 2006.
- [232] Stefan Grimme, Jens Antony, Stephan Ehrlich, and Helge Krieg. A consistent and accurate ab initio parametrization of density functional dispersion correction (DFT-d) for the 94 elements h-pu. *The Journal of Chemical Physics*, 132(15):154104, apr 2010.
- [233] CPMD, <http://www.cpmc.org/>, Copyright IBM Corp 1990-2015, Copyright MPI für Festkörperforschung Stuttgart 1997-2001.
- [234] James C. Phillips. Energy-band interpolation scheme based on a pseudopotential. *Physical Review*, 112(3):685–695, nov 1958.
- [235] D. R. Hamann, M. Schlüter, and C. Chiang. Norm-conserving pseudopotentials. *Physical Review Letters*, 43(20):1494–1497, nov 1979.
- [236] N. Troullier and José Luriaas Martins. Efficient pseudopotentials for plane-wave calculations. *Physical Review B*, 43(3):1993–2006, jan 1991.
- [237] M. Allen and D. Tildesley. *Computer simulation of liquids*. Oxford University Press, 1989.
- [238] C. W. Gear. The numerical integration of ordinary differential equations. *Mathematics of Computation*, 21(98):146–146, may 1967.
- [239] C.W. Gear. *Numerical initial value problems in ordinary differential equations*. Prentice-Hall series in automatic computation. Prentice-Hall, 1971.
- [240] Loup Verlet. Computer ”experiments” on classical fluids. i. thermodynamical properties of lennard-jones molecules. *Physical Review*, 159(1):98–103, jul 1967.

- [241] F. Y. Fraige and P. A. Langston. Integration schemes and damping algorithms in distinct element models. *Advanced Powder Technology*, 15(2):227–245, mar 2004.
- [242] William C. Swope, Hans C. Andersen, Peter H. Berens, and Kent R. Wilson. A computer simulation method for the calculation of equilibrium constants for the formation of physical clusters of molecules: Application to small water clusters. *The Journal of Chemical Physics*, 76(1):637–649, jan 1982.
- [243] Trygve Helgaker, Einar Uggerud, and Hans Jørgen Aa. Jensen. Integration of the classical equations of motion on ab initio molecular potential energy surfaces using gradients and hessians: application to translational energy release upon fragmentation. *Chemical Physics Letters*, 173(2-3):145–150, oct 1990.
- [244] Einar Uggerud and Trygve Helgaker. Dynamics of the reaction $\text{CH}_2\text{OH}^+ \rightarrow \text{CHO}^+ + \text{H}_2$. Translational energy release from ab initio trajectory calculations. *Journal of the American Chemical Society*, 114(11):4265–4268, may 1992.
- [245] R. Car and M. Parrinello. Unified approach for molecular dynamics and density-functional theory. *Phys. Rev. Lett.*, 55(22):2471–2474, nov 1985.
- [246] H. Hellmann. *Einführung in die Quantenchemie*. 1937.
- [247] R. P. Feynman. Forces in molecules. *Physical Review*, 56(4):340–343, aug 1939.
- [248] Walter J. Stevens and William H. Fink. Frozen fragment reduced variational space analysis of hydrogen bonding interactions. application to the water dimer. *Chemical Physics Letters*, 139(1):15–22, aug 1987.
- [249] Michael W. Schmidt, Kim K. Baldridge, Jerry A. Boatz, Steven T. Elbert, Mark S. Gordon, Jan H. Jensen, Shiro Koseki, Nikita Matsunaga, Kiet A. Nguyen, Shujun Su, Theresa L. Windus, Michel Dupuis, and John A. Montgomery. General atomic and molecular electronic structure system. *J. Comput. Chem.*, 14(11):1347–1363, nov 1993.
- [250] Mark S. Gordon and Michael W. Schmidt. Advances in electronic structure theory. In *Theory and Applications of Computational Chemistry*, pages 1167–1189. Elsevier BV, 2005.
- [251] Keiji Morokuma. Molecular orbital studies of hydrogen bonds. III. c[double bond]o[middle dot][middle dot][middle dot]h[single bond]o hydrogen bond in h2co[middle dot][middle dot][middle dot]h2o and h2co[middle dot][middle dot][middle dot]2h2o. *The Journal of Chemical Physics*, 55(3):1236, 1971.

-
- [252] B. Liu and A. D. McLean. Accurate calculation of the attractive interaction of two ground state helium atoms. *The Journal of Chemical Physics*, 59(8):4557–4558, oct 1973.
- [253] B. Liu and A. D. McLean. The interacting correlated fragments model for weak interactions, basis set superposition error, and the helium dimer potential. *The Journal of Chemical Physics*, 91(4):2348–2359, aug 1989.
- [254] Frans B. van Duijneveldt, Jeanne G. C. M. van Duijneveldt-van de Rijdt, and Joop H. van Lenthe. State of the art in counterpoise theory. *Chemical Reviews*, 94(7):1873–1885, nov 1994.
- [255] S.F. Boys and F. Bernardi. The calculation of small molecular interactions by the differences of separate total energies. some procedures with reduced errors. *Molecular Physics*, 19(4):553–566, oct 1970.
- [256] Glenn J. Martyna and Mark E. Tuckerman. A reciprocal space based method for treating long range interactions in ab initio and force-field-based calculations in clusters. *The Journal of Chemical Physics*, 110(6):2810–2821, feb 1999.
- [257] M. J. Frisch, G. W. Trucks, H. B. Schlegel, G. E. Scuseria, M. A. Robb, J. R. Cheeseman, G. Scalmani, V. Barone, B. Mennucci, G. A. Petersson, H. Nakatsuji, M. Caricato, X. Li, H. P. Hratchian, A. F. Izmaylov, J. Bloino, G. Zheng, J. L. Sonnenberg, M. Hada, M. Ehara, K. Toyota, R. Fukuda, J. Hasegawa, M. Ishida, T. Nakajima, Y. Honda, O. Kitao, H. Nakai, T. Vreven, J. A. Montgomery, Jr., J. E. Peralta, F. Ogliaro, M. Bearpark, J. J. Heyd, E. Brothers, K. N. Kudin, V. N. Staroverov, R. Kobayashi, J. Normand, K. Raghavachari, A. Rendell, J. C. Burant, S. S. Iyengar, J. Tomasi, M. Cossi, N. Rega, J. M. Millam, M. Klene, J. E. Knox, J. B. Cross, V. Bakken, C. Adamo, J. Jaramillo, R. Gomperts, R. E. Stratmann, O. Yazyev, A. J. Austin, R. Cammi, C. Pomelli, J. W. Ochterski, R. L. Martin, K. Morokuma, V. G. Zakrzewski, G. A. Voth, P. Salvador, J. J. Dannenberg, S. Dapprich, A. D. Daniels, Ö. Farkas, J. B. Foresman, J. V. Ortiz, J. Cioslowski, and D. J. Fox. Gaussian09 Revision E.01. Gaussian Inc. Wallingford CT 2009.
- [258] Bastien Belzunces, Sophie Hoyau, Jérôme Cuny, and Fabienne Bessac. Pesticide interaction with environmentally important cations: A molecular dynamics and DFT study of metamitron and fenhexamid. *Computational and Theoretical Chemistry*, 1117:220–234, oct 2017.
- [259] W. Matthew C. Foulkes and Roger Haydock. Tight-binding models and density-functional theory. *Physical Review B*, 39(17):12520–12536, jun 1989.

- [260] D. Porezag, Th. Frauenheim, Th. Köhler, G. Seifert, and R. Kaschner. Construction of tight-binding-like potentials on the basis of density-functional theory: Application to carbon. *Physical Review B*, 51(19):12947–12957, may 1995.
- [261] M. Elstner, D. Porezag, G. Jungnickel, J. Elsner, M. Haugk, Th. Frauenheim, S. Suhai, and G. Seifert. Self-consistent-charge density-functional tight-binding method for simulations of complex materials properties. *Physical Review B*, 58(11):7260–7268, sep 1998.
- [262] T. Heine, M. Rapacioli, J. Cuny, S. Patchkovskii, J. Frenzel, A. Koster, P. Calaminici, H.A. Duarte, S. Escalante, R. Flores-Moreno, A. Goursot, J. Reveles, D. Salahub, and A. Vela. deMonNano.
- [263] Shuichi Nosé and M.L. Klein. Constant pressure molecular dynamics for molecular systems. *Molecular Physics*, 50(5):1055–1076, dec 1983.
- [264] Shūichi Nosé. A molecular dynamics method for simulations in the canonical ensemble. *Molecular Physics*, 52(2):255–268, jun 1984.
- [265] Shuichi Nosé. A unified formulation of the constant temperature molecular dynamics methods. *The Journal of Chemical Physics*, 81(1):511–519, jul 1984.
- [266] William G. Hoover. Canonical dynamics: Equilibrium phase-space distributions. *Physical Review A*, 31(3):1695–1697, mar 1985.
- [267] A.K. Soper. The radial distribution functions of water and ice from 220 to 673 K and at pressures up to 400 MPa. *Chemical Physics*, 258(2-3):121–137, aug 2000.
- [268] Lawrie B. Skinner, Congcong Huang, Daniel Schlesinger, Lars G. M. Pettersson, Anders Nilsson, and Chris J. Benmore. Benchmark oxygen-oxygen pair-distribution function of ambient water from x-ray diffraction measurements with a wide q-range. *The Journal of Chemical Physics*, 138(7):074506, feb 2013.
- [269] Giovanni Bussi and Michele Parrinello. Stochastic thermostats: comparison of local and global schemes. *Computer Physics Communications*, 179(1-3):26–29, jul 2008.
- [270] Michele Ceriotti, Giovanni Bussi, and Michele Parrinello. Langevin equation with colored noise for constant-temperature molecular dynamics simulations. *Phys. Rev. Lett.*, 102:020601, Jan 2009.
- [271] Michele Ceriotti, Giovanni Bussi, and Michele Parrinello. Colored-noise thermostats à la carte. *Journal of Chemical Theory and Computation*, 6(4):1170–1180, apr 2010.

- [272] Yu. I. Naberukhin. The pair distribution function of liquid water: Truncation problem in light of recent x-ray diffraction data. *Journal of Molecular Liquids*, 239:45–48, aug 2017.
- [273] I-Chun Lin, Ari P. Seitsonen, Ivano Tavernelli, and Ursula Rothlisberger. Structure and dynamics of liquid water from ab initio molecular dynamics—comparison of BLYP, PBE, and revPBE density functionals with and without van der waals corrections. *Journal of Chemical Theory and Computation*, 8(10):3902–3910, oct 2012.
- [274] L. B. Skinner, C. J. Benmore, J. C. Neuefeind, and J. B. Parise. The structure of water around the compressibility minimum. *The Journal of Chemical Physics*, 141(21):214507, dec 2014.
- [275] David H. Brookes and Teresa Head-Gordon. Family of oxygen–oxygen radial distribution functions for water. *The Journal of Physical Chemistry Letters*, 6(15):2938–2943, aug 2015.
- [276] Pascal Clausen. *Release kinetics of volatiles from smectite clay minerals*. PhD thesis, STI, Lausanne, 2009.
- [277] John G. Kirkwood. Statistical mechanics of fluid mixtures. *The Journal of Chemical Physics*, 3(5):300–313, may 1935.
- [278] Glenn M. Torrie and John P. Valleau. Monte carlo free energy estimates using non-boltzmann sampling: Application to the sub-critical lennard-jones fluid. *Chemical Physics Letters*, 28(4):578–581, oct 1974.
- [279] G.M. Torrie and J.P. Valleau. Nonphysical sampling distributions in monte carlo free-energy estimation: Umbrella sampling. *Journal of Computational Physics*, 23(2):187–199, feb 1977.
- [280] Benoît Roux. The calculation of the potential of mean force using computer simulations. *Computer Physics Communications*, 91(1-3):275–282, sep 1995.
- [281] Shankar Kumar, John M. Rosenberg, Djamel Bouzida, Robert H. Swendsen, and Peter A. Kollman. The weighted histogram analysis method for free-energy calculations on biomolecules. i. the method. *Journal of Computational Chemistry*, 13(8):1011–1021, oct 1992.
- [282] Grossfield Alan. "WHAM: the weighted histogram analysis method", version 2.0.9.1.

- [283] I. Bakó, J. Hutter, and G. Pálinkás. Car–parrinello molecular dynamics simulation of the hydrated calcium ion. *The Journal of Chemical Physics*, 117(21):9838–9843, dec 2002.
- [284] Tünde Megyes, Tamás Grósz, Tamás Radnai, Imre Bakó, and Gábor Pálinkás. Solvation of calcium ion in polar solvents: an x-ray diffraction and ab initio study. *The Journal of Physical Chemistry A*, 108(35):7261–7271, sep 2004.
- [285] Waheed A. Adeagbo, Nikos L. Doltsinis, Michael Burchard, Walter V. Maresch, and Thomas Fockenberg. Ca²⁺ solvation as a function of p, t, and pH from ab initio simulation. *The Journal of Chemical Physics*, 137(12):124502, sep 2012.
- [286] Yaspal S. Badyal, Adrian C. Barnes, Gabriel J. Cuello, and John M. Simonson. Understanding the effects of concentration on the solvation structure of ca²⁺ in aqueous solution. II: insights into longer range order from neutron diffraction isotope substitution. *The Journal of Physical Chemistry A*, 108(52):11819–11827, dec 2004.
- [287] Mor M. Naor, Keith Van Nostrand, and Christoph Dellago. Car–parrinello molecular dynamics simulation of the calcium ion in liquid water. *Chemical Physics Letters*, 369(1-2):159–164, feb 2003.
- [288] Takashi Ikeda, Mauro Boero, and Kiyoyuki Terakura. Hydration properties of magnesium and calcium ions from constrained first principles molecular dynamics. *The Journal of Chemical Physics*, 127(7):074503, aug 2007.
- [289] Guomin Yang, Ivars Neretnieks, and Michael Holmboe. Atomistic simulations of cation hydration in sodium and calcium montmorillonite nanopores. *The Journal of Chemical Physics*, 147(8):084705, aug 2017.
- [290] Raúl Monsalvo, Liberto de Pablo, and M. Lourdes Chávez. Hydration of calcium montmorillonite at basin conditions: A monte carlo molecular simulation. *Revista Mexicana de Ciencias Geológicas*, 2006.
- [291] Neal T. Skipper, Peter A. Lock, James O. Titiloye, Jan Swenson, Zakaria A. Mirza, W. Spencer Howells, and Felix Fernandez-Alonso. The structure and dynamics of 2-dimensional fluids in swelling clays. *Chemical Geology*, 230(3-4):182–196, jun 2006.
- [292] Meysam Makaremi, Kenneth D. Jordan, George D. Guthrie, and Evgeniy M. Myshakin. Multiphase monte carlo and molecular dynamics simulations of water

and CO₂ intercalation in montmorillonite and beidellite. *The Journal of Physical Chemistry C*, 119(27):15112–15124, jul 2015.

Abstract

Pesticides are widely employed molecules for crop protection in France and all over the world. When these substances are spread an important quantity reaches soils. In the present thesis, pesticide fate is under study. For this purpose, three pesticides have been selected: atrazine, metamitron and fenhexamid ; and the most abundant smectite clay type, montmorillonite, has been chosen. The computational simulations conducted in this thesis use the Density Functional Theory (DFT) formalism. The first part of this thesis treats a static study of atrazine interaction with pyrophyllite and montmorillonite. In the following chapters, Car-Parrinello Molecular Dynamics through DFT is used. This study begins with isolated pesticides, metamitron and fenhexamid, then their complexes with one or two Na^+ and Ca^{2+} . Finally, the adsorption of these entities, in the presence of water or not, onto a montmorillonite surface, is considered using periodic calculations. Within the second chapter of the present work, results from geometry optimisations in gas phase are presented. The third part develops the obtained results on the adsorption of metamitron and fenhexamid over the chosen clay model. In the last chapter of this thesis, some of the most stable structures of each adsorbed pesticide onto the surface have been solvated and a study of fenhexamid desorption from the montmorillonite surface using Umbrella Sampling has been done. This work allowed to quantify theoretically the free energy barrier to overcome to desorb fenhexamid from the hydrated montmorillonite.

Résumé

Les pesticides sont des molécules utilisées en grandes quantités en France et dans le monde entier pour la protection des cultures. Lorsque ces substances sont répandues une grande quantité rejoint les sols. Dans cette thèse, le devenir de pesticides dans le sol est étudié. Pour cela, trois pesticides ont été sélectionnés : l'atrazine, la métamitrone et le fenhexamide ; et une argile de type montmorillonite a été choisie. Les simulations menées lors de cette thèse emploient le formalisme de la Théorie de la Fonctionnelle de la Densité (DFT). La première partie de cette thèse porte sur l'étude statique de l'interaction de l'atrazine avec la pyrophyllite et la montmorillonite. Dans les chapitres suivants, la Dynamique Moléculaire Car-Parrinello en DFT est utilisée. L'étude débute par les pesticides seuls, métamitrone et fenhexamide, puis leurs complexes avec un ou deux cations Na^+ et Ca^{2+} . Ensuite, l'adsorption de ces entités, en présence ou non d'eau, sur une surface de montmorillonite, est envisagée à l'aide de calculs périodiques. Dans le second chapitre de ce travail, des résultats issus d'optimisations de géométries en phase gazeuse sont présentés. La troisième partie développe les résultats obtenus pour l'adsorption de la métamitrone et du fenhexamide sur le modèle d'argile choisi. Dans le dernier chapitre, certaines des structures les plus stables de chaque pesticide adsorbé sur la surface ont été solvatées et une étude de la désorption du fenhexamide de la surface de montmorillonite a été réalisée à l'aide de la méthode Umbrella Sampling. Ce travail a permis de quantifier théoriquement la barrière d'énergie libre à franchir pour désorber le fenhexamide de la montmorillonite hydratée.